NASA
Technical
Paper
2333
c.2
August 1984

Fuselage and Nozzle Pressure Distributions of a 1/12-Scale F-15 Propulsion Model at Transonic Speeds

Effect of Fuselage Modifications and Nozzle Variables

Odis C. Pendergraft, Jr.,
and George T. Carson, Jr.

NASA

NASA Technical Paper 2333

1984

Fuselage and Nozzle Pressure Distributions of a 1/12-Scale F-15 Propulsion Model at Transonic Speeds

Effect of Fuselage Modifications and Nozzle Variables

Odis C. Pendergraft, Jr.,
and George T. Carson, Jr.

Langley Research Center
Hampton, Virginia

National Aeronautics
and Space Administration

Scientific and Technical Information Branch

SUMMARY

Static-pressure-coefficient distributions on the forebody, afterbody, and nozzles of a 1/12-scale F-15 propulsion model have been determined in the Langley 16-Foot Transonic Tunnel for Mach numbers from 0.60 to 1.20, angles of attack from -2° to 7°, and ratio of jet total pressure to free-stream static pressure from 1 (jet off) up to about 7, depending on Mach number. The effects of nozzle geometry (both symmetric and asymmetric) and horizontal-tail deflection on the pressure distributions were investigated. Boundary-layer total-pressure profiles were also determined at two locations ahead of the nozzles on the top nacelle surface. Reynolds number varied from about 1.0×10^7 to 1.3×10^7 per meter, depending on Mach number.

Results of the wind-tunnel test program indicate that the flow field surrounding the nozzles is very complex, always resulting in nonuniform pressure distributions around the circumference of the nozzles and quite often resulting in separated flow regions, especially for the dry power nozzles. Different geometry on the right-hand nozzle from that on the left-hand nozzle produced large changes in the surface pressure-coefficient distributions and integrated axial force on the instrumented left nozzle.

INTRODUCTION

The reduction of propulsion system losses for twin engines installed in a fighter-type aircraft has been a difficult problem, because of the inability to adequately predict the effect of the jet engine exhaust flows and other variables on the airframe. Even current computer technologies cannot adequately handle the masses of data input needed to model the very complex flow fields surrounding the exhaust nozzles and adjacent airframe components.

One of the best ways to gain further understanding of this complex flow field is to conduct both subscale wind-tunnel tests and full-scale flight tests with configurations and instrumentation as nearly identical as possible. In practice, such wind-tunnel and flight tests can rarely be conducted, since the evolution of flight hardware usually involves substantial changes from the models used in the development stages of the design. Further differences usually arise because of simplification of details on subscale models, such as elimination of small inlets, vents, antennas, and steps on the model surfaces.

To improve the understanding of flow interactions between the propulsion system and the airframe, NASA has conducted model and flight tests of the F-15. In 1975, Langley Research Center obtained an existing 1/12-scale F-15 propulsion model, which would be available indefinitely and could be modified as needed for tests. At about the same time, Dryden Flight Research Facility of the Ames Research Center received the number 2 and number 8 prototype aircraft to conduct flight programs investigating engine-airframe interactions. With the proper modifications to the existing 1/12-scale model, along with newly instrumented nozzle hardware for both the model and the aircraft, subscale and full-scale data were obtained on identical configurations (except for the inlets, which on the model were faired over), with identical pressure-orifice locations and at identical test parameters (except for Reynolds number).

For the first tests of this model in the Langley 16-Foot Transonic Tunnel, reported in reference 1, the model was modified to incorporate the larger production vertical tails, notched horizontal-tail leading edges, and raked wing tips. Ventral fins on the afterbody were removed, and some small details, such as the vertical-tail antenna fairings, were added. Three axisymmetric nozzle sets were fabricated with geometries to match those expected on the full-scale aircraft at flight conditions matching those possible in the wind tunnel. The static-pressure orifices on the model nozzles were located to match those on the aircraft. For the present tests, which were conducted after the flight tests, two additional sets of nozzles for the 1/12-scale model were fabricated to match additional intermediate afterburning power settings used during the full-scale flight tests. Also, several small actuator fairings, vents, and nacelle surface steps were added to the afterbody of the model.

The purpose of both wind-tunnel investigations was to establish a data base of static-pressure distributions and integrated nozzle axial force to be used for comparison with those from the full-scale flight tests (refs. 2 and 3). The three nozzle configurations tested in the first phase represented maximum dry power (Power lever angle (PLA) = 83°), intermediate afterburning power (PLA = 112°), and maximum afterburning power (PLA = 130°), and the two additional nozzle configurations represented intermediate afterburning power settings (PLA = 103° and 108°). Along with these two new nozzles, the nozzles representing PLA = 83° and 112° were used for the present tests.

SYMBOLS

A_e/A_t ratio of nozzle exit area to nozzle throat area

a mean-line designation fraction of the chord from leading edge over which loading is uniform at the ideal angle of attack, $\frac{x_w}{c}$

$C_{A,n}$ integrated axial-force coefficient for left-hand nozzle only positive in the drag direction (see eq. (1))

$C_{p,boom}$ tail boom pressure coefficient, $\frac{p_\ell - p_\infty}{q_\infty}$

C_p^* pressure coefficient at a sonic point, $\frac{0.5283(1 + 0.2M^2)^{3.5} - 1}{0.7M^2}$

$C_{p,f}$ fuselage pressure coefficient, $\frac{p_\ell - p_\infty}{q_\infty}$

$C_{p,n}$ nozzle pressure coefficient, $\frac{p_\ell - p_\infty}{q_\infty}$

$C_{p,nac}$ nacelle pressure coefficient, $\frac{p_\ell - p_\infty}{q_\infty}$

c local chord length, m

HRL height of left boundary-layer rake, 3.556 cm

HRR height of right boundary-layer rake, 3.632 cm

ℓ or L reference length from nose of model to tip of booms (158.689 cm)

M free-stream Mach number

NPR nozzle pressure ratio, $p_{t,j}/p_\infty$

PLA power lever angle (throttle position)

p_ℓ local static pressure, Pa

$p_{t,j}$ jet total pressure, Pa

p_∞ free-stream static pressure, Pa

$p_{t,\infty}$ free-stream total pressure, Pa

q_∞ free-stream dynamic pressure, Pa

x or X longitudinal distance measured downstream from model nose (see fig. 3(a)), cm

x_n longitudinal distance upstream from nozzle exit (see fig. 4), cm

x_w longitudinal distance from wing leading edge, positive rearward, m

x' longitudinal distance downstream from nozzle connect station, or F.S. 165.423 (see fig. 4), cm

Z height of boundary-layer probe above model surface, cm

α angle of attack, deg

β_L left-hand nozzle boattail angle, deg

β_n nozzle boattail angle (both nozzles), deg

β_R right-hand nozzle boattail angle, deg

δ_h horizontal-tail deflection, positive with L.E. up, deg

δ_r rudder deflection, negative right, deg

ϕ meridian angle, measured from top of left-hand nozzle in clockwise direction when looking upstream, deg

Abbreviations:

A/B afterburning

AFT afterbody pressure orifices (15), aft of metric break

B.L. buttock line, spanwise distance from vertical plane of symmetry, cm

FF fuselage pressure orifices (21), forward of metric break

F.S. fuselage station (see fig. 1), cm

L.E. leading edge

SRL left-hand boundary-layer rake static-pressure probe

SRR right-hand boundary-layer rake static-pressure probe

TRL left-hand boundary-layer rake total-pressure probes (5)

TRR right-hand boundary-layer rake total-pressure probes (5)

W.L. water line, vertical distance from horizontal reference plane, cm

Subscripts:

bot bottom orifice row

top top orifice row

350, 182 approximate meridian angle (e.g., 350 denotes 349.85°)

APPARATUS AND PROCEDURE

Wind Tunnel and Tests

This investigation was conducted in the Langley 16-Foot Transonic Tunnel, a single-return continuous-flow atmospheric wind tunnel with a slotted octagonal test section measuring 4.8 m diametrically to midflat centerline. With the aid of a compressor system, which draws air through slots in the test section for $M > 1.05$, the test section airspeed is continuously variable between Mach numbers of 0.20 and 1.30. Further details on dimensions and the operating characteristics of the 16-Foot Transonic Tunnel can be found in reference 4.

Model data were taken at Mach numbers of 0.60, 0.80, and 0.90 for the dry power nozzle configuration. Data were taken at Mach numbers of 0.90 and 1.20 for the afterburning power nozzle configurations. Reynolds number varied from about 1.0×10^7 to about 1.3×10^7 per meter for the test Mach number range. Model angle of attack varied from -2° to 7° corresponding to steady-state and maneuver conditions for the full-scale aircraft at the Mach numbers indicated above. Sideslip angle was zero throughout the test program. The ratio of jet total pressure to free-stream static pressure was varied from approximately 1 (jet off) to about 7, depending on Mach number and nozzle power setting (geometry and throat area), in an attempt to cover the operational range of nozzle pressure ratio for the full-scale aircraft. Horizontal-tail deflection was varied from 2.5° (leading edge up) to -4° and rudder deflection was set at 0° and -5° (trailing edge left) to determine the effects of these control deflections on afterbody and nozzle pressure distributions.

To match some of the wind-tunnel Mach number and angle of attack conditions of reference 1 and still maintain a particular power lever angle (PLA) on the left-hand engine, the full-scale aircraft was flown with the right-hand engine at various intermediate afterburning power settings, and therefore, the boattail angle on the

right-hand nozzle often differed from that on the left-hand nozzle (held at constant PLA). Likewise, during the current wind-tunnel investigation, several configurations with asymmetric nozzle boattail angles (different left-hand and right-hand PLA) were tested as indicated below to determine the effect on the left-hand nozzle static-pressure distributions and integrated nozzle axial force. The maximum afterburning power nozzles (PLA = 130°) were not retested in the present investigation, since $M \leq 1.20$ could not be maintained on the full-scale aircraft at this high thrust level.

β_L	β_R	δ_h	M
18.45°	15.05°	0°, -3°	0.90
18.45°	9.63°	-2°	0.90, 0.80
18.45°	7.72°	-4°	0.90
15.05°	18.45°	0°	0.90, 0.60
9.63°	15.05°	2.5°	1.20, 0.90

Boundary-layer transition was fixed on the model by means of 0.13- to 0.20-cm-wide strips of No. 120 carborundum grains sparsely distributed in a thin film of lacquer. The transition strips (or boundary-layer trips) were located 1.78 cm downstream of the wing leading edges, 1.02 cm downstream of the horizontal-stabilizer leading edge, 0.89 cm downstream of the twin-vertical-tail leading edges, and in a ring around the nose 7.62 cm downstream of the nose apex (F.S. 24.613). The methods described in references 5 and 6 were used to determine the locations for these trips and the grain size.

Model and Support System

A sketch showing the principal dimensions of the 1/12-scale F-15 model is shown in figure 1, and photographs of the model mounted in the Langley 16-Foot Transonic Tunnel are shown in figure 2. The dashed diagonal line across the closed inlet fairing in the side view in figure 1 indicates the location of the inlet side plate leading edges on the aircraft. The model inlet fairings were blended into the external inlet surfaces at the inlet leading edges (fig. 2(a)). The inlet fairings on the model were constructed to represent an inlet rotation angle of 0° on the full-scale aircraft. Further details of the model and aircraft geometry can be found in table I and in references 1, 7, 8, and 9.

High-pressure air at about room temperature (294 K) was used to simulate the nozzle exhausts of the twin-jet configuration. Compressed air was routed through a 3.97-cm-diameter passage drilled through the strut and into a high-pressure plenum (6.895 MPa maximum) located in the model. Air was throttled through 25 orifices, each having a diameter of 0.7938 cm (12.371 cm^2 total area), to a low-pressure plenum (1.034 MPa maximum) and then divided into two flow passages (45.604 cm^2 each) for the two closely spaced exhaust nozzles. Although the model did not contain the balance used in reference 1, much of the same model hardware was used for the present tests with a dummy balance installed to hold the afterbody parts. For the present tests, the metric break location (F.S. 138.107) is used only as a demarcation line between the forebody and the afterbody.

The locations of the external static-pressure orifices on the forebody and afterbody of the fuselage are shown in the model sketches of figure 3. The axial

locations of the fuselage orifices are also given in table II, along with span locations (B.L.) and water line locations (W.L.) where necessary to define positions on the model surface.

Sketches of the various nozzles showing their geometry are given in figure 4. These nozzle configurations correspond to actual power settings on the full-scale engines. The geometry of the dry power nozzle (β_n = 18.45°) corresponds very closely to all low-Mach-number (M < 1.10) dry power settings (actual geometry is for PLA = 83°). The geometry of the low-Mach-number intermediate afterburning nozzle (β_n = 15.05°) corresponds to PLA = 103°, and the geometries for the high-Mach-number intermediate afterburning power settings (β_n = 9.63° and 7.72°) correspond to PLA = 108° and 112° for M > 1.10. Note that the dry power and low-Mach-number afterburning power nozzles (PLA = 83° and 103°) have a smooth external surface contour, whereas both high-Mach-number afterburning power nozzles (PLA = 108° and 112°) have a "kink" in their surfaces at F.S. 167.828. (See fig. 4.) The coordinates of the external nozzle boattails are given in table III for each configuration, and the locations of the 42 nozzle static-pressure orifices are given for each power setting in table IV. All external boattail static-pressure orifices were incorporated in the left-hand nozzle (looking upstream) as shown in figure 5. Some irregularities in the orifice locations resulted from consideration of mounting locations on the full-scale nozzles (see note at ϕ = 301.85° in fig. 5).

Details of the fuselage modifications are presented in figure 6. These changes were made in an effort to more nearly duplicate the details on the full-scale aircraft. The nose boom was added because its large size (2.74 m long on the aircraft) could have some impact on boundary-layer development and vortex flow formation. The nozzle actuator fairings and the afterburner fuel vents were added because of their proximity to nozzle and afterbody orifice locations. During the aircraft flight tests and before the current wind-tunnel tests, it was found from comparing wind-tunnel data of reference 1 with the flight data that the engine bay cooling flow caused large changes in the nozzle pressure coefficients nearest the engine bay cooling exit annulus (see fig. 6(d) for details). To better duplicate this feature, a step was added to the model as shown in figure 6(d) and the aircraft was flown with the upper half and then the lower half of the exit annulus alternately sealed. The boundary-layer rakes tested on the model, shown in figure 7, were about the same relative size and at the same fuselage locations as those flown on the aircraft. The smaller size of the model rakes limited the number of total-pressure probes to 5 compared with 10 on the full-scale aircraft. During tests on the model with "all fuselage modifications," the rakes were installed unless otherwise stated.

Instrumentation

Two 48-port pressure-scanning devices, referenced to the wind-tunnel static pressure, were used to measure 15 afterbody static pressures and 21 forebody static pressures. The 42 nozzle static pressures were measured directly with individual gages. The pressure-scanning devices were cycled through in approximately 1 minute with a dwell time of 1/2 second on each port. Gages used with the pressure-scanning devices were mounted on the scanner bodies, resulting in almost instantaneously stabilized pressures to the gages. The jet total pressure in each of the tail pipes was measured with an individual gage, and jet total temperature was measured with an iron-constantan stagnation thermocouple probe. Combined mass flow for the two jet exhausts was measured with an electronic turbine flowmeter.

Data Reduction

The recorded external static-pressure data were used to compute standard pressure coefficients. The external pressure axial-force coefficients on the left-hand nozzle boattail were obtained by a numerical summation of the local nozzle static-pressure coefficients multiplied by an axially projected area assigned to each of the 42 nozzle orifices and all divided by the reference area:

$$C_{A,n} = \frac{1}{A_{REF}} \sum_{i=1}^{42} C_{p,n,i} A_{n,i} \tag{1}$$

where $C_{p,n,i}$ is the nozzle pressure coefficient calculated for nozzle orifice i, $A_{n,i}$ is the axially projected area assigned to nozzle orifice i, and the model reference area A_{REF} is the reference wing area, 0.3923 m^2.

Model angle of attack α was computed from the strut pitch angle. This angle was corrected for sting deflection caused by bending under aerodynamic load. A flow angularity adjustment of 0.1°, which is the average angle measured in the Langley 16-Foot Transonic Tunnel, was applied to the computed angles of attack. Nozzle pressure ratio was obtained by dividing the jet total pressure by the tunnel free-stream static pressure.

RESULTS

The results of the investigation are presented in the following figures:

The figures are indexed according to fuselage modification in table V and according to nozzle geometry in table VI.

DISCUSSION

In the following discussion, the pressure-coefficient plots in figure 8 contain dashed lines between two values of x/l. These dashed lines indicate an area of

uncertainty where the data were faired on the basis of other data (fig. 9) or experience, instead of being faired between the points shown.

Fuselage Pressure-Coefficient Distributions

Upper surface centerline.- Static-pressure-coefficient distributions on the top of the fuselage along the centerline are presented in figures 8 to 20 at $M = 0.60$, 0.80, and 0.90 for the model with dry power nozzles and at $M = 0.90$ and 1.20 for the model with A/B power nozzles.

The figures are indexed according to fuselage modification in table V and according to nozzle geometry in table VI. Each plot contains data at various angles of attack. Separate plots are presented for a jet-off and a jet-on nozzle pressure ratio (NPR) at each Mach number. The data show that increasing angle of attack causes a general decrease in pressure coefficient along the upper fuselage. NPR had only a small effect and, as expected, on only the static-pressure coefficients farthest aft.

Lower surface centerline.- Similar static-pressure-coefficient distributions on the bottom of the fuselage along the centerline are presented in figures 21 to 33. For these figures jet-off and jet-on data at each Mach number are presented in separate plots on the same page. Increasing angle of attack caused a general increase in the level of pressure coefficients which was, as expected, an opposite effect to that found on the top surface. Jet operation generally caused some increase in the pressure coefficients at the orifices farthest aft, especially for $M = 0.90$.

Nacelle and nozzle centerline.- Figures 34 to 46 and 47 to 59 present static-pressure-coefficient distributions on the top and bottom surfaces, respectively, of the engine nacelles and nozzle boattails. Note from figure 5 that the nozzle static-pressure orifices were not located exactly on the top (10° off) and bottom (2° off). Locations of the forebody/afterbody break, the start of the nozzle boattail, the kink in the nozzle surface, and the nozzle exit are indicated by tick marks on the bottom border of figures 34(a) and 47(a). The nozzle surface kink at F.S. 167.828 occurs between the variable and fixed external nozzle surfaces on the aircraft when the nozzle exit and throat areas are opened for high-Mach-number A/B power settings (figs. 4(c) and 4(d)). Note that there is a change in the horizontal scale increment from the left-hand plots (0.05 per division) to the right-hand plots (0.01 per division). In figures 47 to 59, the pressure coefficients for the first (most forward) static-pressure orifice on the nozzle lower surface ($x/l = 0.898$) are plotted in both the left-hand and the right-hand plots to assist the reader in the transition between the two plots. This was not possible for figures 34 to 46 because the most forward orifice on the top surface of the nozzle was not usable.

The data in these two sets of figures exhibit trends with angle of attack similar to those for the top and bottom surfaces of the fuselage along the centerline. Since there are nacelle and nozzle orifices near the nozzle exits, much more effect of jet operation is evident (figs. 34 to 59) than was observed along the fuselage centerline. Discussion of jet operation on the nozzle pressure coefficients will be presented in the section entitled "Nozzle Pressure-Coefficient Distributions," where nozzle boattail pressure data are presented for all meridian angles around the nozzles. Because of an instrumentation malfunction, the pressure distribution data from $x/l = 0.88$ to 0.94 could not be presented in figure 43.

Inside boom surface.- Static-pressure-coefficient distributions along the top inside surface of the left-hand tail boom (see fig. 3(b) for orifice locations) are presented in figures 60 to 67. Only small pressure-coefficient changes along this surface are generally indicated for increasing nozzle pressure ratio. Curve shape changes between $M = 0.90$ and 1.20 (compare figs. 65(a) and 65(b), for example) because of a sharp reduction in pressure coefficient for the last orifice as Mach number increases to 1.20. More significant is the low level of pressure in this region for all Mach numbers, probably caused by the low-pressure field between the twin vertical tails in combination with the expansion process between the vertical tail and adjacent nacelle and nozzle surfaces.

Effect of Fuselage Modifications

Nose boom.- Comparing the data of figure 8 with those of figure 9, for $M = 0.60$ and 0.90, indicates no discernible difference in the top centerline pressure distributions for the unmodified model and the model with only the nose boom added. The same is also true for the model with all fuselage modifications and the model with all modifications except the nose boom; compare figure 11 with figures 15 and 16. Comparing figure 21 with 22 and figure 24 with figures 28 and 29 also indicates no effect of the nose boom on the bottom centerline pressure coefficients. The same result is also indicated for the top and bottom pressure coefficients along the left-hand nacelle centerline.

A/B fuel vents and nozzle actuator fairings.- Addition of the afterburner fuel vents (simulated with small airfoil shaped blades with trailing edges at $x/l = 0.807$; see fig. 6(c)) to the bottom of the model afterbody produces little or no effect on the static-pressure-coefficient distributions except at $x/l = 0.808$ (compare fig. 49 with fig. 48). At $x/l = 0.808$, a large decrease in pressure occurs, especially for $M = 0.90$. At $x/l = 0.845$, the pressure coefficient with the vent suddenly increases to approximately the value without the vent. This sudden increase indicates a possible standing shock wave located behind the afterburner vents at $M = 0.90$, since pressure-coefficient values less than that required for supersonic flow ($C_p^* = -0.1878$ for $M = 0.90$) occur at $x/l = 0.808$, just ahead of the indicated shock.

Figure 48 may also be compared with figure 49 to determine how adding the nozzle actuator fairings (see fig. 6(b)) affects the bottom nacelle and nozzle pressure-coefficient distributions. A slight increase in $C_{p,n}$ is noted at $x/l = 0.904$, but none of the other nozzle orifices on the 182° row (the closest to the fairing) are noticeably affected.

Engine bay cooling vent around nozzle (step).- In order to better match the model nacelle shape ahead of the nozzles to that on the real aircraft, small annular steps were added to simulate the engine bay cooling vents without exhausting airflow. Details of this afterbody modification are shown in figure 6(d). Comparing the nozzle pressure-coefficient distributions of figure 68 for the unmodified model with the distributions of figure 70 for the model with all modifications indicates that adding the step ahead of the nozzles increased the pressure coefficients near the beginning of the nozzles. This increase generally occurs between $\phi = 180°$ and 302° and most consistently for $M = 0.60$ and 0.80, when there is less separated flow; but large differences also occur at $\phi = 181.85°$ for $M = 0.90$. Minimum $C_{p,n}$ values varied from -0.29 to -0.49 for the unmodified afterbody compared with -0.20 to -0.42 for the modified (step added) afterbody.

Though not true for all conditions, addition of this step ahead of the nozzles tended to flatten the nozzle boattail static-pressure-coefficient distributions.

Nacelle boundary-layer rakes.- The effect on the nacelle and nozzle pressure-coefficient distributions of adding the boundary-layer rakes can be determined by several comparisons. The effect on upper nacelle and nozzle pressure coefficients of installing both boundary-layer rakes (see fig. 7) can be seen by comparing figure 39 (rakes off) with figure 40 (rakes on) for $\delta_h = -2°$. Static pressure at $x/l = 0.684$ is significantly increased (particularly at $M = 0.90$) when the rake is installed. The static-pressure orifice at $x/l = 0.684$ is located on the nacelle upper surface directly underneath the probe tips of the forward, left-hand boundary-layer rake (see locations indicated in fig. 40(a)). The flow blockage caused by the rake tubes and strut probably accounts for the increased pressure coefficient at this station. For these data, no other noticeable changes occur for the various Mach numbers, angles of attack, and NPR's tested. Comparing figure 38 with figures 41 and 42 for $\delta_h = 0°$ yields the same results for the nacelle pressures; the rakes produced only small inconsistent effects on the upper nozzle pressure coefficients.

Further insight into the effects of rake installation on the nozzle pressure-coefficient distributions can be gained by comparing figure 71 (no rakes) with figure 72 (aft, right-hand rake only installed) and with figure 73 (both rakes installed). In these figures, the data at $\phi = 349.85°$, $61.85°$, and $85.85°$ might be affected by the aft rake installed on the opposite nacelle. The close agreement between the data of figures 71 and 72 indicates no effect on the left-hand nozzle of installing the aft rake on the right-hand nacelle at the subsonic Mach numbers tested ($M = 0.60$, 0.80, and 0.90). Also, when the forward, left-hand rake is installed, along with the aft, right-hand rake, there are no noticeable differences in the left-hand nozzle pressure-coefficient distributions (compare fig. 71 with fig. 73); thus, no significant effects of the boundary-layer rakes on the left-hand-nozzle pressure-coefficient distributions are indicated at the subsonic Mach numbers investigated. Although installation of the aft, right-hand rake did not affect left-hand nozzle static pressures, effects on the right-hand nozzle static pressures would have probably been observed had static-pressure instrumentation been present on the right-hand nozzle.

Nozzle Pressure-Coefficient Distributions

Dry power nozzles.- Static-pressure-coefficient distributions on the left-hand dry power nozzle at eight meridian angles around the nozzle are presented in figures 68 to 76. Each page presents data at a specific combination of Mach number and angle of attack for several nozzle pressure ratios. The view in figure 5 looking upstream at the dry power nozzle shows the locations of the pressure orifice rows relative to the tail boom fairing and nozzle interfairing. Note that the free-stream flow over the orifice rows at $\phi = 85.85°$ and $277.85°$ is at least partially blocked by the fairings, especially at positive angles of attack; whereas the rows at $\phi = 181.85°$ and $349.85°$ would experience the least interference from the surrounding structure. As previously indicated in reference 1 for the unmodified model, the external flow exhibits good pressure recovery on the nozzles at $M = 0.60$ except in the region adjacent to the nozzle interfairing ($\phi = 61.85°$, $85.85°$, and $133.85°$). Even for a relatively low Mach number of 0.60, the rapidly diverging channel between the steeply boattailed nozzles (boattail angles of $18.45°$) appears to produce flow separation in this region (see figs. 68(a) to 68(d)). With increasing Mach number, the amount of nozzle external flow separation increases. At $M = 0.80$ (figs. 68(e) to 68(i)), a separated region appears adjacent to and above the outboard tail boom

fairing (ϕ = 277.85° and 301.85°), especially for $\alpha \geq 3°$. At M = 0.90, the flow separation covers nearly the entire nozzle (figs. 68(j) to 68(m)). For M = 0.90, the nozzle external flow is generally attached on only the bottom surface (ϕ = 181.85°) of the nozzle at jet-on conditions. The largest effects of NPR occur between the jet-off and the lowest jet-on NPR, and only small changes are evident with increasing NPR above that value.

Results presented in references 1 and 7 indicate that horizontal-tail and rudder deflection can affect nozzle static-pressure distributions. Thus, during the current investigation, tests were made to determine the effects of small control surface deflection on the nozzle static-pressure-coefficient distributions, as an aid in matching full-scale flight test data. Figures 68, 69, 70, 74, and 75 are for $\delta_h = 0°$ and $\delta_r = 0°$; while figures 71, 72, and 73 are for $\delta_h = -2°$ and $\delta_r = 0°$; and figure 76 is for $\delta_h = 0°$ and $\delta_r = -5°$. Data for ϕ = 349.85° and 61.85° in figure 76 were not recorded properly because of pressure scanner problems, so only at ϕ = 277.85° and 301.85° are data available for deflected rudder conditions on the top of the nozzle adjacent to the tail boom and vertical tail. Although the effects of both horizontal- and vertical-tail control surface deflections on the static-pressure-coefficient distributions appear to be small, it was shown in reference 1 that large deflections of the horizontal tails ($\delta_h = -10°$) may substantially increase the integrated nozzle axial-force coefficient. Data from reference 7 indicate that rudder deflections of -10° have little effect on nozzle axial force at low angles of attack, but substantially decrease nozzle axial force at high angles of attack. Further comments on the effects of control surface deflection will be delayed until the integrated nozzle axial-force coefficients are discussed.

Dry power nozzle in the presence of A/B power nozzle.- During flight tests of the full-scale aircraft, it was necessary to operate the right-hand nozzle at A/B power settings while maintaining the left-hand nozzle at the dry power setting in order to match some of the wind-tunnel test conditions. Consequently, as mentioned earlier, the wind-tunnel model was tested to determine the effects on the pressure-coefficient distributions over the left-hand, dry power nozzle of operating the right-hand nozzle at various intermediate A/B power settings. Data for $\beta_L = 18.45°$ and $\beta_R = 15.05°$ are given in figure 77 for $\delta_h = 0°$ and figure 78 for $\delta_h = -3°$, both for M = 0.90 only. Data for $\beta_L = 18.45°$ and $\beta_R = 9.63°$ are given in figure 79 for $\delta_h = -2°$ at M = 0.80 and 0.90; data for $\beta_L = 18.45°$ and $\beta_R = 7.72°$ are given in figure 80 for $\delta_h = -4°$ at M = 0.90 only. Comparing figures 74 and 75 with figure 77 shows how changing the right-hand nozzle boattail angle from 18.45° to 15.05° affects the left-hand nozzle (dry power) static-pressure-coefficient distributions for $\delta_h = 0°$ and M = 0.90. Comparing figure 73 with figure 79 shows how changing the right-hand nozzle boattail angle from 18.45° to 9.63° affects the left-hand nozzle (dry power) static-pressure-coefficient distributions for $\delta_h = -2°$ and M = 0.80 and 0.90. As expected, the right-hand nozzle boattail angle (power setting) does strongly affect the left-hand nozzle static pressures. Consistent trends are not obvious from these data, but these pressures clearly depend on β_R, orifice location (ϕ and x/ℓ), jet operation, and control surface deflection.

Intermediate A/B power nozzles.- Static-pressure-coefficient distributions on the three intermediate A/B power nozzle configurations at the eight meridian angles are presented in figures 81 and 82 for $\beta_n = 15.05°$, in figure 84 for $\beta_n = 9.63°$, and in figure 86 for $\beta_n = 7.72°$. Reducing the boattail angle to 15.05° from 18.45° tends to improve the pressure recovery on the nozzles (compare figs. 74 and 75 for $\beta_n = 18.45°$ with fig. 81 for $\beta_n = 15.05°$ at M = 0.90, both at $\delta_h = 0°$). Reduction of the boattail angle to 9.63° and then to 7.72° (see figs. 84 and 86) further improves the boattail pressure recovery on the nozzles at M = 0.90, but at these

lower boattail angles (high power settings), the disturbance caused by the kink in the juncture between the fixed and movable parts of the boattail also changes the shape of the static-pressure-coefficient distributions, especially for $\phi = 181.85°$. At $M = 1.20$, operation of the jet (NPR) has much stronger effects on the nozzle boattail pressure-coefficient distributions than at $M = 0.90$, especially at the downstream end near the nozzle exit. See, for example, figure 81(e) at $\phi = 181.85°$ and 349.85°. In regions of totally separated flow (see data at $\phi = 61.85°$, 85.85°, and 133.85° in fig. 81(e), for example), extremely large jet effects are also noted. As the nozzle boattail angle is decreased, also decreasing the tendency of the flow to separate, the effects of increasing NPR are also decreased at $\phi = 349.85°$ and 181.85°. Compare figure 81(e) for $\beta_n = 15.05°$ with figure 84(e) for $\beta_n = 9.63°$ and with figure 86(e) for $\beta_n = 7.72°$ at $M = 1.20$ and $\alpha = 0°$. This decrease in effect of NPR may also be in part due to the increased A_e/A_t with decreased boattail angle, hence causing less pluming of the exhaust with increasing NPR.

A/B power nozzle in the presence of dry power nozzle.- Static-pressure-coefficient distributions on the left-hand intermediate A/B power nozzle ($\beta_L = 15.05°$) in the presence of the right-hand dry power nozzle ($\beta_R = 18.45°$) are presented in figure 83 for $M = 0.60$ and 0.90. Comparing figures 81(a) through 81(d) with figures 83(e) through 83(h) at $M = 0.90$ indicates that changing the right-hand nozzle from $\beta_R = 15.05°$ to $\beta_R = 18.45°$ has some effect on the left-hand intermediate A/B power nozzle ($\beta_L = 15.05°$). The effects are smaller than the effects of right-hand A/B power nozzle on left-hand dry power nozzle, but significant effects do occur (for example, see $\phi = 133.85°$, especially at $\alpha = 6°$). The small differences observed should produce slightly greater jet-on nozzle drag, which will be discussed in the section on integrated nozzle axial-force coefficients.

A/B power nozzle in the presence of different A/B power nozzle.- Static-pressure-coefficient distributions on the left-hand intermediate A/B power nozzle ($\beta_L = 9.63°$) in the presence of a different right-hand intermediate A/B power nozzle ($\beta_R = 15.05°$) are presented in figure 85 for $M = 0.90$ and 1.20. Since the data of figure 85 were taken with $\delta_h = 2.5°$, no direct comparison with data for which only the right-hand nozzle boattail angle changes is possible, but comparing figure 84 with figure 85 indicates again that changing the right-hand nozzle from $\beta_R = 9.63°$ to $\beta_R = 15.05°$ may signifcantly affect the left-hand nozzle ($\beta_L = 9.63°$). As before, this will be discussed in more detail in the section on integrated nozzle axial-force coefficient.

Boundary-Layer Total-Pressure Profiles

Boundary-layer total-pressure profiles for the various configurations and conditions are presented in figures 87 to 92. Ratios of boundary-layer to free-stream total pressures are plotted versus the ratio of probe height to total rake height for the forward, left-hand rake (F.S. 133.172) and the aft, right-hand rake (F.S. 162.128) at a specific combination of Mach number and nozzle pressure ratio for various angles of attack. Note that a surface static-pressure ratio is plotted at $Z/HRL = 0$ and that rake probe static-pressure ratios are plotted at $Z/HRL = 1$ and $Z/HRR = 1$.

Effect of free-stream variables.- The effect of angle of attack is evident on each plot. Figure 90, for the model with all fuselage modifications, both boundary-layer rakes, and dry power nozzles shows this effect for $M = 0.60$, 0.80, and 0.90. Increasing angle of attack causes only slight reductions in total-pressure ratios for

the forward, left-hand rake. For the aft, right-hand rake, increasing angle of attack causes much larger reductions in the total-pressure ratios, especially for $M = 0.80$ and 0.90. The shapes of these curves indicate that boundary-layer thickness is increasing with angle of attack. The reduction in rake total-pressure ratio at the top of the aft, right-hand rake is believed to be caused by the fuselage/vertical-tails flow field and not by boundary-layer viscous effects.

Increasing Mach number appears to increase sensitivity to angle of attack for both rakes, but especially for the aft rake. There is also a noticeable decrease in the maximum value of total-pressure ratio attained with increasing Mach number (for examples, see figs. 90 and 91), especially for the aft rake at $M = 1.20$.

Effect of model variables.- The effect of operation of the jet (variation of NPR) can be determined by comparing two plots at a particular Mach number at jet-off and jet-on conditions. Compare figure 87(a) with 87(b) and figure 87(c) with 87(d) for examples of this comparison at $M = 0.60$ and 0.90. As expected, the effects of jet operation are small, since the rakes are ahead of the nozzle boattails, where the largest jet operation effects are usually found.

The effect of the forward, left-hand rake stream disturbance on the aft, right-hand rake pressure ratio profiles can be determined by comparing figure 88 with figure 89. Note in figure 88 that both jet-off and jet-on data for a given Mach number are presented on the same figure part, since no data exist for the forward, left-hand rake for this configuration. Therefore, compare the left-hand graph of figure 88(a) with the right-hand graph of figure 89(a) to determine the effect at $M = 0.60$ with the jet off. Also compare the right-hand graph of figure 88(a) to the right-hand graph of figure 89(b) to determine the effect at $M = 0.60$ and $NPR = 3.00$. As expected, there is little or no effect of the forward, left-hand rake on the aft, right-hand rake. Since the data presented in figures 88 to 90 were taken with a configuration having dry power nozzles ($\beta_n = 18.45°$), no testing was conducted at $M = 1.20$.

Comparing figure 89 for $\delta_h = -2°$ with figure 90 for $\delta_h = 0°$ indicates that small deflections of the horizontal tails had no significant effect on the boundary-layer total-pressure profiles.

Figure 87 for the modified model with the nose boom removed, can be compared with figure 90 with the nose boom installed to determine the effect of the nose boom on the boundary-layer total-pressure profiles for $M = 0.60$ and 0.90. The comparison indicates that there are no significant effects of the nose boom on the boundary layer at the aft rake location, but for some conditions, a loss in total-pressure ratio is indicated at the forward rake location. However, this reduction, which occurs at $M = 0.90$ for the configuration with the nose boom removed (an unexpected result), also occurs on other configurations with the nose boom installed (see figs. 91 and 92 for examples). A more likely explanation for the increased losses would be the deteriorating condition of the model surface with use, since the configuration with the nose boom removed was tested last.

Some of the data for the forward, left-hand rake were not included in figure 91 because of problems with the pressure scanning device at the beginning of the tunnel run for this configuration.

Integrated Nozzle Axial-Force Coefficients

Nozzle axial-force coefficients for the four boattail angles and combinations of different right-hand and left-hand boattail angles, all nozzle pressure ratios, and all test Mach numbers are plotted in figures 93 to 106 as a function of angle of attack. Axial force on the left-hand nozzle was obtained by assigning incremental longitudinal projected areas to each nozzle static-pressure orifice and then summing incremental forces to obtain nozzle axial force. When orifices were plugged or leaking, the area assigned to such orifices was divided among adjacent orifices. Data were taken at increasing angles of attack while holding nozzle pressure ratio constant at preset values. Figures 93 to 98 present data for the dry power nozzles (β_n = 18.45°) to show the effects of various fuselage modifications and horizontal-tail deflections on nozzle axial-force coefficient, while figures 99 to 106 include data for the intermediate afterburning power nozzles and all asymmetric nozzle combinations to show the effects of boattail angle and the influence of an adjacent nozzle with dissimilar boattail angle on the left-hand nozzle axial-force coefficient.

Effect of fuselage modification.- As mentioned earlier in the discussion on fuselage pressure-coefficient distributions, the addition of the nose boom, actuator fairings, A/B fuel vents, and annular steps ahead of the nozzles was an attempt to more closely match the real aircraft afterbody (see ref. 3 for aircraft details). Note that figures 34 to 38 and figures 68 to 70 show that the nose boom had no effect on the left-hand nozzle pressure-coefficient distributions, the actuator fairings caused a small local increase, the A/B fuel vents caused a small local decrease, and the annular nozzle steps caused a general increase in the static-pressure coefficients. The net result, largely caused by the annular step, was a reduction in the nozzle axial-force coefficient, as may be seen by comparing figures 93 and 95.

The nose boom was installed on the model and remained in place for the entire wind-tunnel test except for the first and last runs. The effect of removing the nose boom can be determined by comparing figure 94 (boom off) with figure 98 (boom on). This comparison indicates no effect on the nozzle axial force for the dry power nozzles at subsonic Mach numbers. A similar comparison can be made between figures 95 (rakes off) and 97 (rakes on) to determine the effect on left-hand nozzle axial-force coefficient of installing boundary-layer rakes just ahead of the right-hand nozzle and farther forward ahead of the left-hand nozzle on the left-hand nacelle. As expected from previous discussions of the static-pressure-coefficient distributions, nozzle axial-force coefficient again seems unaffected by the afterbody change for M = 0.60, 0.80, and 0.90 with dry power nozzles. Note that although left-hand nozzle axial-force coefficient was not affected by boundary-layer rake installation, it is possible that right-hand nozzle axial-force coefficient might have been affected because of the proximity of the aft, right-hand rake to the right-hand nozzle boattail. Unfortunately, instrumentation was not available to determine this effect.

Effect of horizontal-tail deflection.- As previously shown in reference 1, deflection of the horizontal tails had surprisingly strong effects on nozzle axial-force coefficient, considering their outboard location and the shielding effect of the vertical tails. In reference 1, the horizontal-tail surfaces were deflected a full -10° to determine the gross effects in a parametric manner. In the present study, much smaller deflections were set in an attempt to match specific flight test conditions; therefore, the effects of horizontal-tail deflection, if any, are much smaller than in the previous investigation. The effect of horizontal-tail deflection on nozzle axial-force coefficient can be seen by comparing figure 95 for δ_h = 0°

with figure 96 for $\delta_h = -2°$. Although the difference is small, nozzle axial-force coefficient is consistently higher by 0.0001 to 0.0003 for $\delta_h = -2°$ than for $\delta_h = 0°$.

Dry power nozzles.- Nozzle axial-force coefficients for the model with all fuselage modifications and dry power nozzles installed on both sides are presented in figures 97 and 98 for $M = 0.60$, 0.80, and 0.90. The effect of all configuration modifications, including addition of the boundary-layer rakes, to more closely match the full-scale aircraft can be determined by comparing figure 97 with figure 93, which presents data for the unmodified configuration. In general, these modifications reduced nozzle axial-force coefficient significantly at jet-off conditions, but only slightly at jet-on conditions. It is believed that most of the axial-force coefficient reduction results from the step (simulated annulus) installed ahead of the nozzles; however, some of the reduction probably results from the actuator fairings since a small increase in $C_{p,n}$ was observed for this modification.

Dry power nozzle in the presence of A/B power nozzle.- Nozzle axial-force coefficients for the left-hand dry power nozzle in the presence of a right-hand A/B power nozzle are presented in figure 99 for $\beta_R = 15.05°$, in figure 100 for $\beta_R = 9.63°$, and in figure 101 for $\beta_R = 7.72°$. Since these data were taken to match specific flight test points and the horizontal-tail deflections vary between the figures, no direct comparison is possible to show the effect of right-hand boattail angle on left-hand nozzle axial-force coefficient. However, one comparison can be made between figure 100 for $\beta_R = 9.63°$ at $\delta_h = -2°$ and figure 96 for $\beta_R = 18.4°$ at $\delta_h = -2°$. At $M = 0.80$, changing the right-hand nozzle from $\beta_R = 18.4°$ to $\beta_R = 9.63°$ increases left-hand, dry power nozzle axial-force coefficient at jet-off conditions and slightly decreases it at jet-on conditions. At $M = 0.90$, the same comparison indicates a decrease in integrated left-hand nozzle axial-force coefficient for both jet-off and jet-on conditions.

Intermediate A/B power nozzles.- Integrated left-hand nozzle axial-force coefficients for the three intermediate afterburning power nozzle configurations are presented in figure 102 for $\beta_n = 15.05°$, in figure 104 for $\beta_n = 9.63°$, and in figure 106 for $\beta_n = 7.72°$. Comparing these figures with figures 97 and 98 shows that as boattail angle is decreased, the integrated nozzle axial force (with jet off or on) also decreases at all test conditions.

A/B power nozzle in the presence of dry-power nozzle.- Integrated nozzle axial-force coefficients for the left-hand afterburning power nozzle in the presence of a right-hand, dry power nozzle are presented in figure 103 for $\beta_L = 15.05°$ and $\beta_R = 18.4°$. The effect of increasing the right-hand nozzle boattail angle from 15.05° to 18.4°. on the left-hand nozzle ($\beta_L = 15.05°$) axial force can be determined for only $M = 0.90$ by comparing figure 102 with figure 103. At $M = 0.90$, the change had little or no effect at jet-off conditions, but generally increased left-hand nozzle axial-force coefficient at jet-on conditions, especially for the higher angles of attack ($\alpha = 4°$ to 6°).

A/B power nozzle in the presence of different A/B power nozzle.- Integrated nozzle axial-force coefficients for the left-hand A/B power nozzle ($\beta_L = 9.63°$) in the presence of a different right-hand A/B power nozzle ($\beta_R = 15.05°$) are presented in figure 105 for $\delta_h = 2.5°$ at $M = 0.90$ and 1.20. Since the horizontal-tail deflection is set to match a specific flight test condition, no direct comparison can be made with other test data to determine the effect on the left-hand nozzle of increasing the right-hand nozzle boattail angle from 9.63° to 15.05°.

CONCLUSIONS

Static-pressure-coefficient distributions on the forebody, afterbody, and nozzles of a 1/12-scale F-15 propulsion model have been determined in the Langley 16-Foot Transonic Tunnel for Mach numbers from 0.60 to 1.20, angles of attack from -2° to 7°, and nozzle pressure ratios from 1 (jet-off) up to about 7, depending on Mach number. The effects of nozzle power setting (both symmetric and asymmetric), horizontal-tail deflection angle, and several other fuselage modifications on the pressure-coefficient distributions were also investigated. Boundary-layer total-pressure profiles were also determined at two locations ahead of the nozzles on the top nacelle surface. Reynolds number varied from about 1.0×10^7 to 1.3×10^7 per meter, depending on Mach number.

The wind-tunnel investigation to determine static-pressure-coefficient distributions, and boundary-layer total-pressure profiles, in the presence of operating jets has produced the following results:

1. Forebody and afterbody static pressures were affected by both angle of attack and Mach number, but only small increases in the aftmost pressures were caused by operation of the twin nozzle jets.

2. Addition of a small annular step around the nacelles ahead of the nozzles (to simulate the engine bay cooling vent) increased the nozzle pressure near the beginning of the nozzle boattail and decreased nozzle axial-force coefficient (positive in drag direction).

3. For the dry power, steeply boattailed nozzles, disturbances from the twin-engine nozzle interfairing and twin-tail booms caused some flow separation on the nozzle boattail at a mach number of 0.60. The separated flow regions on the nozzle grew progressively as Mach number increased, until the flow was nearly completely separated around the entire nozzle at a Mach number of 0.90.

4. Installation of the afterburner fuel vents and nozzle actuator fairings had small local effects but had no significant overall effect on static-pressure coefficients, or integrated nozzle axial force.

5. Addition of the nose boom had no noticeable effect on the model static-pressure coefficients.

6. Installation of the two boundary-layer rakes had little or no effect on the afterbody and left-hand nozzle pressures at the subsonic speeds tested except in the immediate vicinity of the rakes.

7. Asymmetric operation of the right-hand and left-hand nozzles produced significant but inconsistent changes in the integrated nozzle axial force for the left-hand nozzle at the several combinations of nozzle boattail angles.

Langley Research Center
National Aeronautics and Space Administration
Hampton, VA 23665
June 6, 1984

REFERENCES

1. Pendergraft, Odis C., Jr.: Fuselage and Nozzle Pressure Distributions on a 1/12-Scale F-15 Propulsion Model at Transonic Speeds. NASA TP-1521, 1979.

2. Nugent, Jack; Taillon, Norman V.; and Pendergraft, Odis C., Jr.: Status of a Nozzle-Airframe Study of a Highly Maneuverable Fighter. AIAA Paper 78-990, July 1978.

3. Nugent, Jack; Plant, Thomas J.; Davis, Robert A.; and Taillon, Norman V.: Pressures Measured in Flight on the Aft Fuselage and External Nozzle of a Twin-Jet Fighter. NASA TP-2017, 1983.

4. Corson, Blake W., Jr.; Runckel, Jack F.; and Igoe, William B.: Calibration of the Langley 16-Foot Transonic Tunnel With Test Section Air Removal. NASA TR R-423, 1974.

5. Braslow, Albert L.; Hicks, Raymond M.; and Harris, Roy V., Jr.: Use of Grit-Type Boundary-Layer-Transition Trips on Wind-Tunnel Models. NASA TN D-3579, 1966.

6. Braslow, Albert L.; and Knox, Eugene C.: Simplified Method for Determination of Critical Height of Distributed Roughness Particles for Boundary-Layer Transition at Mach Numbers From 0 to 5. NACA TN 4363, 1958.

7. Berrier, Bobby L.; and Maiden, Donald L.: Effect of Nozzle-Exhaust Flow on the Longitudinal Aerodynamic Characteristics of a Fixed-Wing, Twin-Jet Fighter Airplane Model. NASA TM X-2389, 1971.

8. Maiden, Donald L.; and Berrier, Bobby L.: Effect of Airframe Modifications on Longitudinal Aerodynamic Characteristics of a Fixed-Wing, Twin-Jet Fighter Airplane Model. NASA TM X-2523, 1972.

9. Pendergraft, O. C.: Comparison of Axisymmetric and Nonaxisymmetric Nozzles Installed on the F-15 Configuration. AIAA Paper 77-842, July 1977.

TABLE I.- MODEL DETAILS

Wing geometry:	
Airfoil sections	NACA 64AXXX with modified conical camber leading edge
At B.L. 16.299 (root section)	NACA 64A(5.5)(05.9) a = 0.8 modified
At B.L. 32.809	NACA 64A(5.5)(04.6) a = 0.8 modified
At B.L. 47.567	NACA 64A2(03.5) a = 0.8 modified
At B.L. 54.364 (tip section)	NACA 64A203 a = 0.8 modified
Reference area, m^2	0.3923
Span, cm	108.727
Mean aerodynamic chord, cm	40.498
Tip chord, cm	14.464
Taper ratio	0.250
Aspect ratio	3.007
L.E. sweep angle, deg	45.0
Dihedral angle, deg	-1.0
Horizontal-stabilizer geometry:	
Airfoil sections	Modified NACA 000X-64
At B.L. 14.817 (root section)	NACA 0005.5-64
At B.L. 19.050	NACA 0003.5-64
At B.L. 34.723 (tip section)	NACA 0002.5-64
Area (each), m^2	0.0359
Span, cm	71.755
Root chord, cm	29.041
Tip chord, cm	9.851
Taper ratio	0.339
Aspect ratio	2.046
L.E. sweep angle, deg	50.0
Dihedral angle, deg	0
Twist, deg	0
Vertical-tail geometry:	
Airfoil sections	NACA 000X-64
At W.L. 27.517 (root section)	NACA 0005-64
At W.L. 53.729 Itip secton)	NACA 0003.5-64
Area (each), m^2	0.0404
Span, cm	26.213
Root chord, cm	24.333
Tip chord, cm	6.481
Taper ratio	0.266
Aspect ratio	1.70
L.E. sweep angle, deg	36.57
Toe angle (L.E. out), deg	2.0
Twist, deg	0
Rudder area (each), m^2	0.0057

TABLE II.- FUSELAGE ORIFICE LOCATIONS FOR THE 1/12-SCALE F-15 PROPULSION MODEL

Orifice number	Fuselage station, cm	Buttock or water line, cm
FF 1	F.S. 36.779	B.L. 0.0
FF 2	F.S. 49.213	↓
FF 3	F.S. 59.030	
FF 4	F.S. 71.679	
FF 5	F.S. 85.217	
FF 6	F.S. 96.977	
FF 7	F.S. 109.423	
FF 8	F.S. 121.564	
FF 9	F.S. 133.175	
FF 10	↓	B.L. 5.961
FF 11		W.L. 21.229
FF 12		B.L. 5.961
FF 13		B.L. 0.0
FF 14	F.S. 109.423	B.L. 6.030
FF 15	F.S. 121.564	B.L. 6.030
FF 16	F.S. 133.175	B.L. 5.961
FF 17	F.S. 121.564	W.L. 21.229
FF 18	F.S. 133.175	W.L. 21.229
FF 19	F.S. 109.423	B.L. 6.030
FF 20	F.S. 121.564	B.L. 6.030
FF 21	F.S. 133.175	B.L. 5.961
AFT 1	F.S. 152.819	B.L. 0.0
AFT 2	F.S. 158.323	↓
AFT 3	F.S. 169.418	
AFT 4	F.S. 152.819	
AFT 5	F.S. 158.323	
AFT 6	F.S. 169.418	
AFT 7	F.S. 152.819	B.L. 5.687
AFT 8	F.S. 158.750	B.L. 5.839
AFT 9	F.S. 163.096	B.L. 5.547
AFT 10	F.S. 158.323	B.L. 12.106
AFT 11	F.S. 163.096	B.L. 12.106
AFT 12	F.S. 169.418	B.L. 12.106
AFT 13	F.S. 152.819	B.L. 5.687
AFT 14	F.S. 158.750	B.L. 5.687
AFT 15	F.S. 163.096	B.L. 5.547

TABLE III.- COORDINATES OF THE NOZZLE EXTERNAL CONTOURS

Low Mach number, maximum dry power, PLA = 83°		Low Mach number, intermediate A/B power, PLA = 103°		High Mach number, intermediate A/B power, PLA = 108°		High Mach number, intermediate A/B power, PLA = 112°		Remarks
x', cm (a)	Radius, cm	x', cm (a)	Radius, cm	x', cm (a)	Radius, cm	x', cm (a)	Radius, cm	
0.000	4.907	0.000	4.907	0.000	4.907	0.000	4.907	Blend for smooth contour
.234	4.897	.234	4.897	.234	4.897	.234	4.895	
.445	4.879	.445	4.879	.445	4.879	.445	4.879	
.655	4.862	.655	4.862	.655	4.862	.655	4.859	
.869	4.836	.869	4.836	.869	4.836	.869	4.834	
1.080	4.806	1.080	4.806	1.080	4.806	1.080	4.806	
1.290	4.775	1.290	4.775	1.290	4.775	1.290	4.770	
1.504	4.737	1.504	4.737	1.504	4.737	1.504	4.732	
1.715	4.694	1.715	4.694	1.715	4.694	1.715	4.689	
1.925	4.651	1.925	4.651	1.925	4.651	1.925	4.643	
2.139	4.600	2.139	4.600	2.139	4.600	2.139	4.590	
2.350	4.547	2.350	4.547	2.350	4.547	2.350	4.534	
(b)	(b)	2.405	4.531	2.405	4.531	2.405	4.519	←Change of slope
2.560	4.491	2.560	4.506	2.560	4.509	2.560	4.509	Blend for smooth contour
2.774	4.432	2.774	4.463	2.774	4.478	2.774	4.488	
2.985	4.366	2.985	4.409	2.985	4.443	2.985	4.468	
3.129	4.315	3.165	4.366	3.053	4.430	3.099	4.450	←Tangent point
7.739	2.776	7.859	3.104	7.920	3.604	7.915	3.792	Straight taper

[a]Measured downstream from F.S. 165.423.

[b]No change of slope.

TABLE IV.- AXIAL LOCATIONS OF NOZZLE BOATTAIL STATIC-PRESSURE ORIFICES

Maximum dry power: PLA = 83°

ϕ, deg	Nozzle orifice designation at axial location x_n,[a] cm, of -							
	0.676	1.176	1.740	2.301	3.145	4.270	[b]5.410	6.474
349.85		6		5	4	3	2	1
61.85		12		11	10	9	8	7
85.85		16		15		14		13
133.85		20		19	18	17		
181.85		26		25	24	23	22	21
229.85		30		29		28		27
277.85		34		33		32		31
301.85	42	41	40	39	38	37	36	35
x/l	0.933	0.931	0.928	0.924	0.919	0.912	0.904	0.898

Intermediate A/B power: PLA = 103°

ϕ, deg	Nozzle orifice designation at axial location x_n,[a] cm, of -							
	0.686	1.196	1.770	2.342	3.200	4.343	[b]5.550	6.599
349.85		6		5	4	3	2	1
61.85		12		11	10	9	8	7
85.85		16		15		14		13
133.85		20		19	18	17		
181.85		26		25	24	23	22	21
229.85		30		29		28		27
277.85		34		33		32		31
301.85	42	41	40	39	38	37	36	35
x/l	0.934	0.931	0.928	0.924	0.919	0.912	0.904	0.898

Intermediate A/B power: PLA = 108°

ϕ, deg	Nozzle orifice designation at axial location x_n,[a] cm, of -							
	0.686	1.219	1.806	2.390	3.266	4.435	[b]5.575	6.668
349.85		6		5	4	3	2	1
61.85		12		11	10	9	8	7
85.85		16		15		14		13
133.85		20		19	18	17		
181.85		26		25	24	23	22	21
229.85		30		29		28		27
277.85		34		33		32		31
301.85	42	41	40	39	38	37	36	35
x/l	0.934	0.932	0.928	0.925	0.919	0.912	0.904	0.898

Intermediate A/B power: PLA = 112°

ϕ, deg	Nozzle orifice designation at axial location x_n,[a] cm, of -							
	0.706	1.229	1.819	2.405	3.287	4.460	[b]5.649	6.668
349.85		6		5	4	3	2	1
61.85		12		11	10	9	8	7
85.85		16		15		14		13
133.85		20		19	18	17		
181.85		26		25	24	23	22	21
229.85		30		29		28		27
277.85		34		33		32		31
301.85	42	41	40	39	38	37	36	35
x/l	0.935	0.932	0.928	0.925	0.919	0.912	0.904	0.898

[a]Measured upstream from nozzle exit. See figure 5 for orifice locations.

[b]All orifices at this station offset 0.107 cm clockwise looking upstream.

TABLE V.- INDEX OF FIGURES ACCORDING TO FUSELAGE MODIFICATION

Nozzle configuration	Figures presenting plots of -							
	$(C_{p,f})_{top}$	$(C_{p,f})_{bot}$	$\frac{(C_{p,n})_{350}}{(C_{p,nac})_{top}}$	$\frac{(C_{p,n})_{182}}{(C_{p,nac})_{bot}}$	$C_{p,boom}$	$C_{p,n}$	$p/p_{t,\infty}$	$C_{A,n}$
Unmodified	8	21	34	47	60	68		93
With nose boom	9	22	35	48				
With nose boom, actuator fairings, and A/B vents	10	23	36	49				
With all modifications	14-20	27-33	40-46	53-59	61-67	73-86	89-92	97-106
With all modifications except nose boom	11	24	37	50		69	87	94
With all modifications except boundary-layer rakes	12, 13	25, 26	38, 39	51, 52		70, 71		95, 96
With all modifications except left boundary-layer rake						72	88	

TABLE VI.- INDEX OF FIGURES ACCORDING TO NOZZLE GEOMETRY

Nozzle configuration	Figures presenting plots of -							
	$(C_{p,f})_{top}$	$(C_{p,f})_{bot}$	$\frac{(C_{p,n})_{350}}{(C_{p,nac})_{top}}$	$\frac{(C_{p,n})_{182}}{(C_{p,nac})_{top}}$	$C_{p,boom}$	$C_{p,n}$	$p/p_{t,\infty}$	$C_{A,n}$
$\beta_n = 18.45°$	8-17	21-30	34-43	47-56	60-64	68-76	87-90	93-98
$\beta_n = 15.05°$	18	31	44	57	65	81, 82	91	102
$\beta_n = 9.63°$	19	32	45	58	66	84		104
$\beta_n = 7.72°$	20	33	46	59	67	86	92	106
$\beta_L = 18.45°$, $\beta_R = 15.05°$						77, 78		99
$\beta_L = 18.45°$, $\beta_R = 9.63°$						79		100
$\beta_L = 18.45°$, $\beta_R = 7.72°$						80		101
$\beta_L = 15.05°$, $\beta_R = 18.45°$						83		103
$\beta_L = 9.63°$, $\beta_R = 15.05°$						85		105

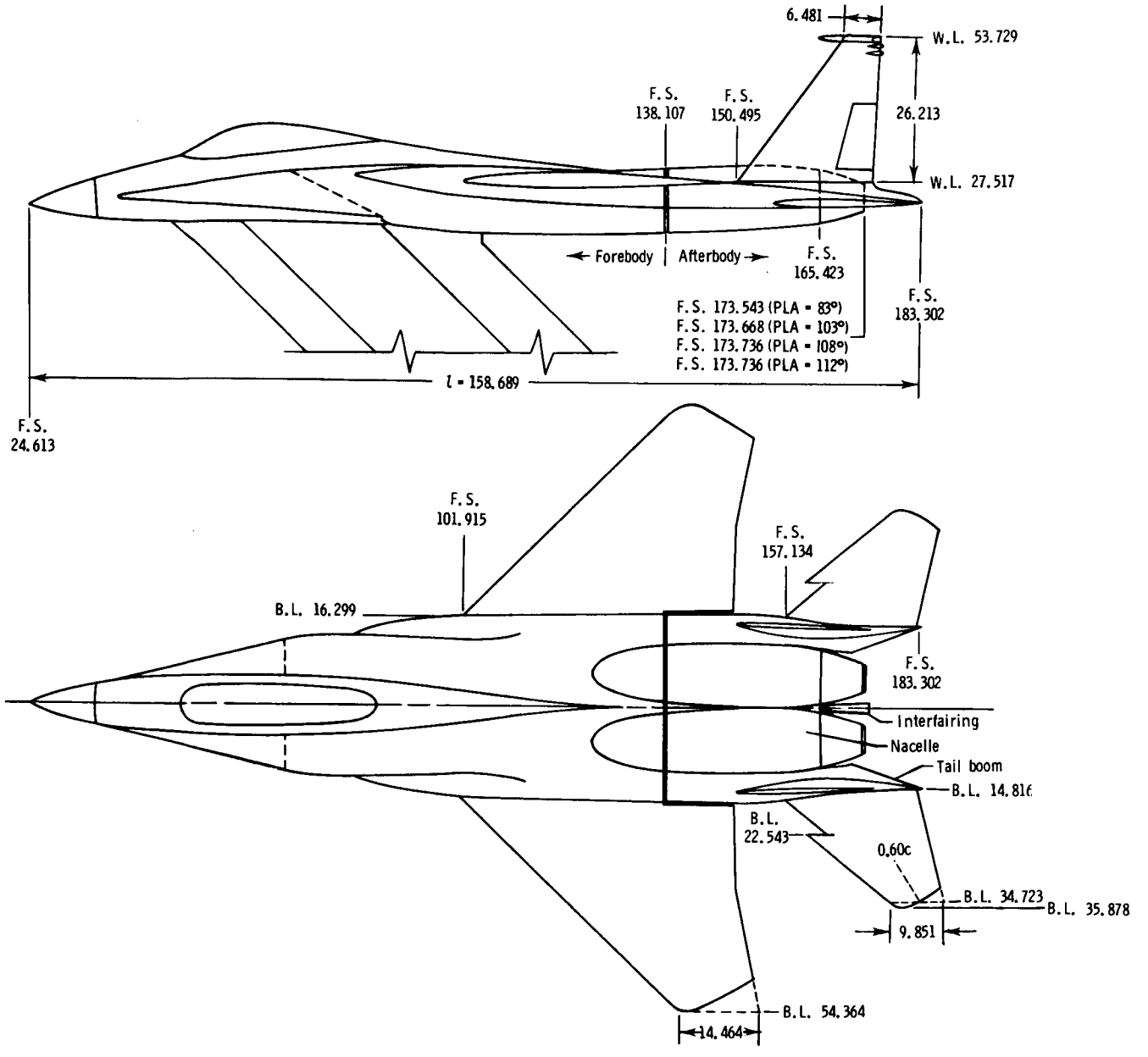

Figure 1.- Details of model geometry. (See also table I.) All linear dimensions are in centimeters.

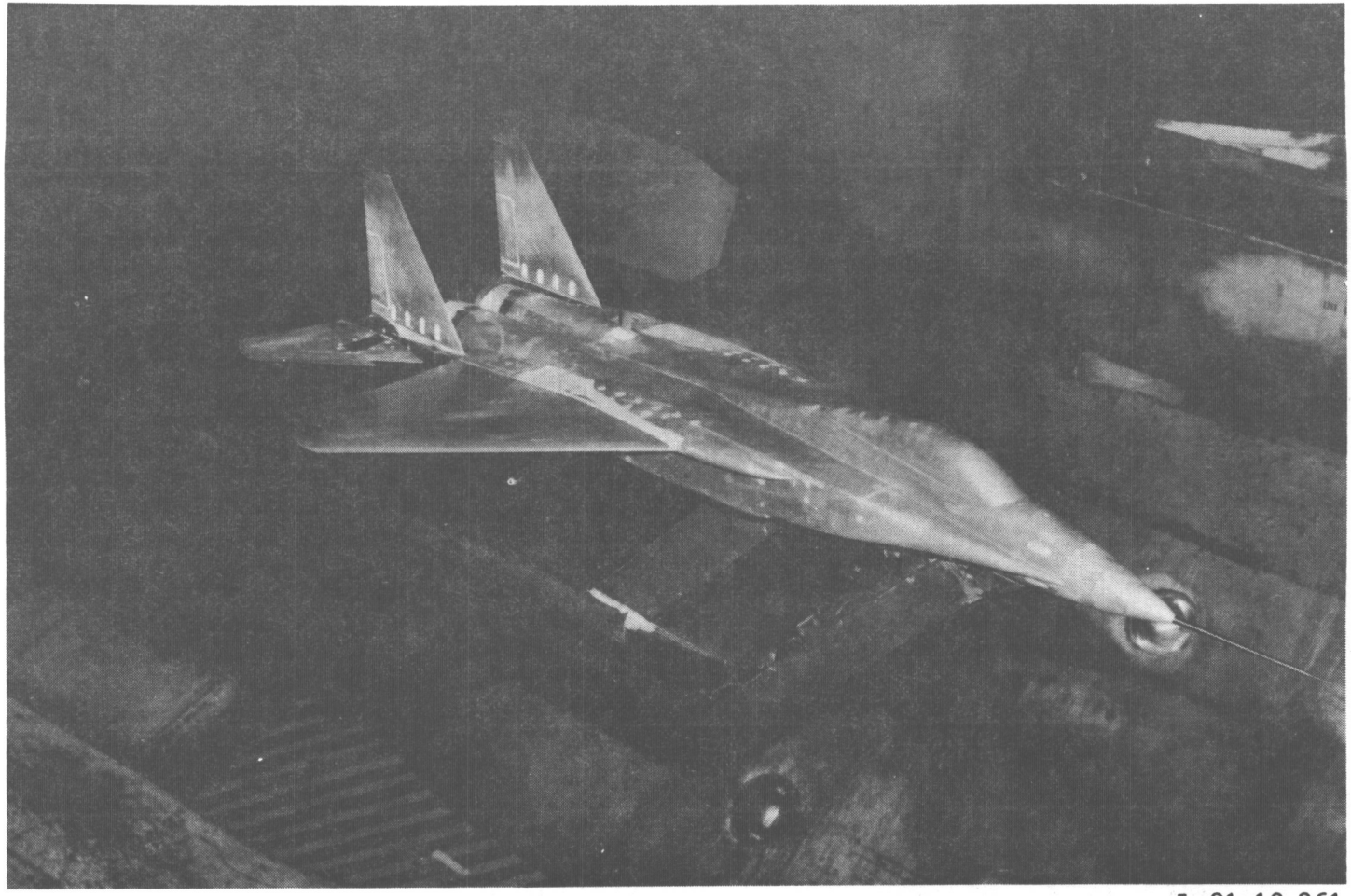

L-81-10,961

(a) Overall view of model with all fuselage modifications and dry power nozzles, showing nose boom.

Figure 2.- Photographs of 1/12-scale F-15 propulsion model installed in the Langley 16-Foot Transonic Tunnel.

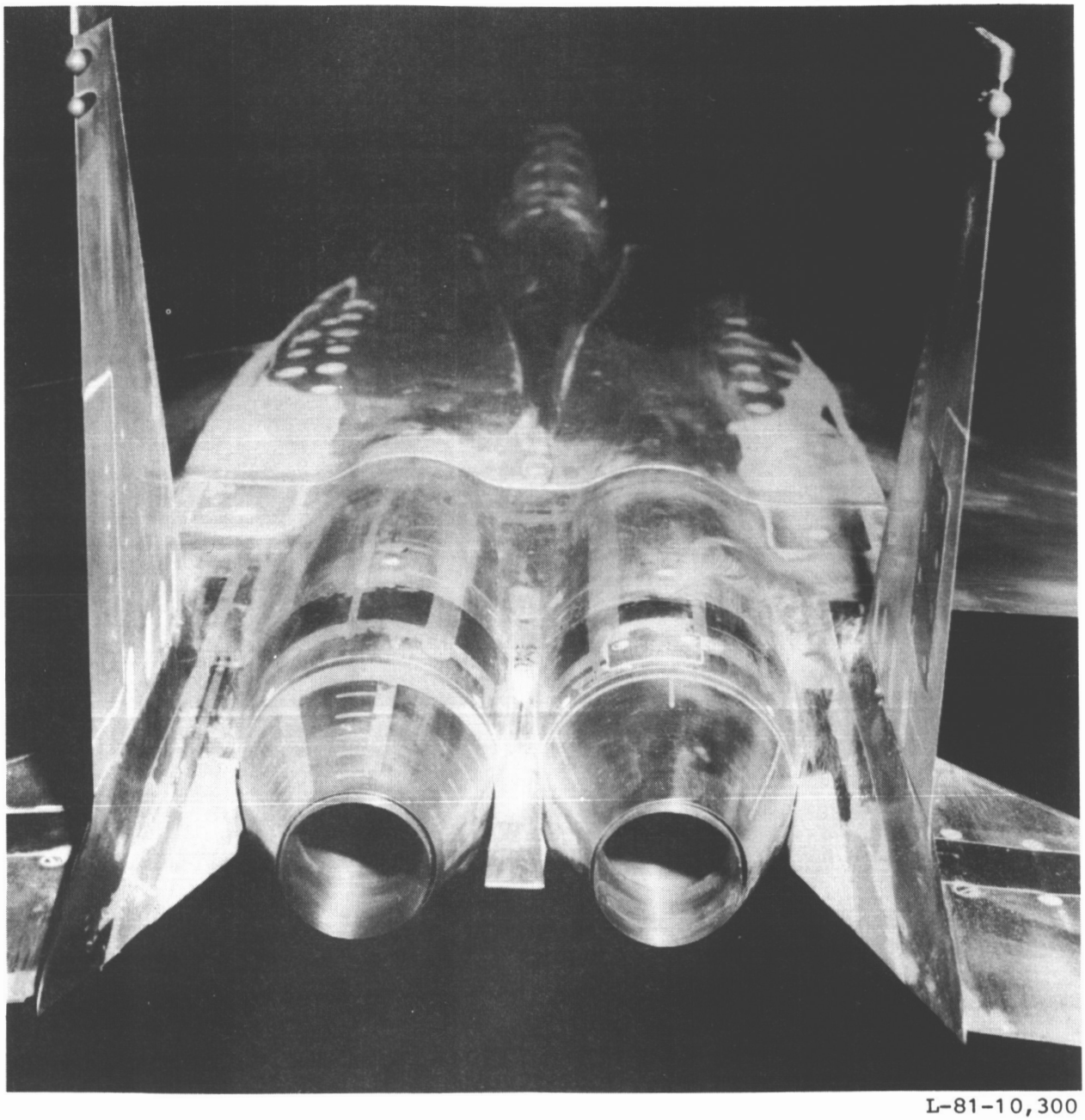

L-81-10,300

(b) View of unmodified afterbody with dry power nozzles installed.

Figure 2.- Continued.

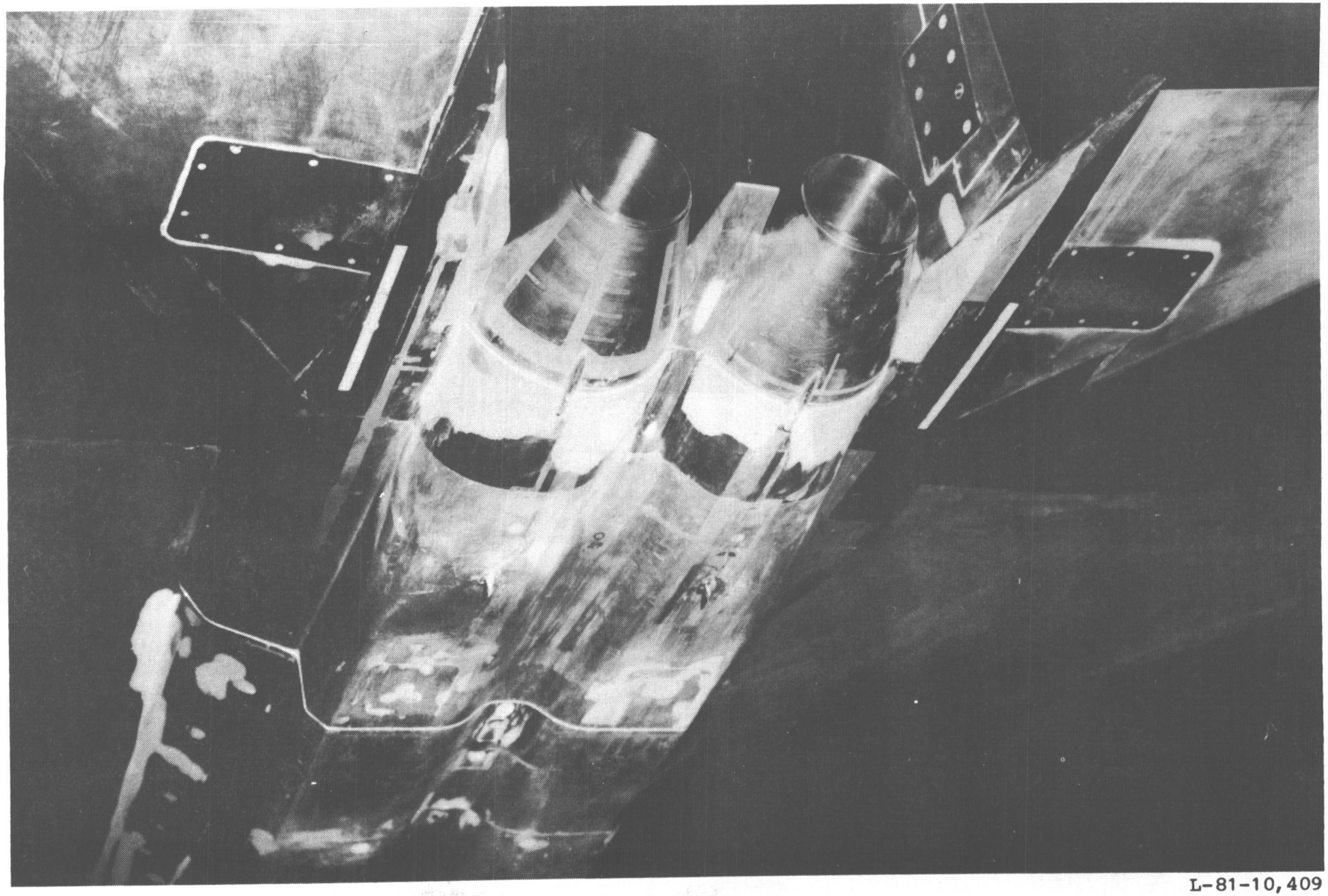

L-81-10,409

(c) Bottom view of afterbody showing actuator fairings, afterburner fuel vents, and simulated engine bay cooling annulus (sealed).

Figure 2.- Continued.

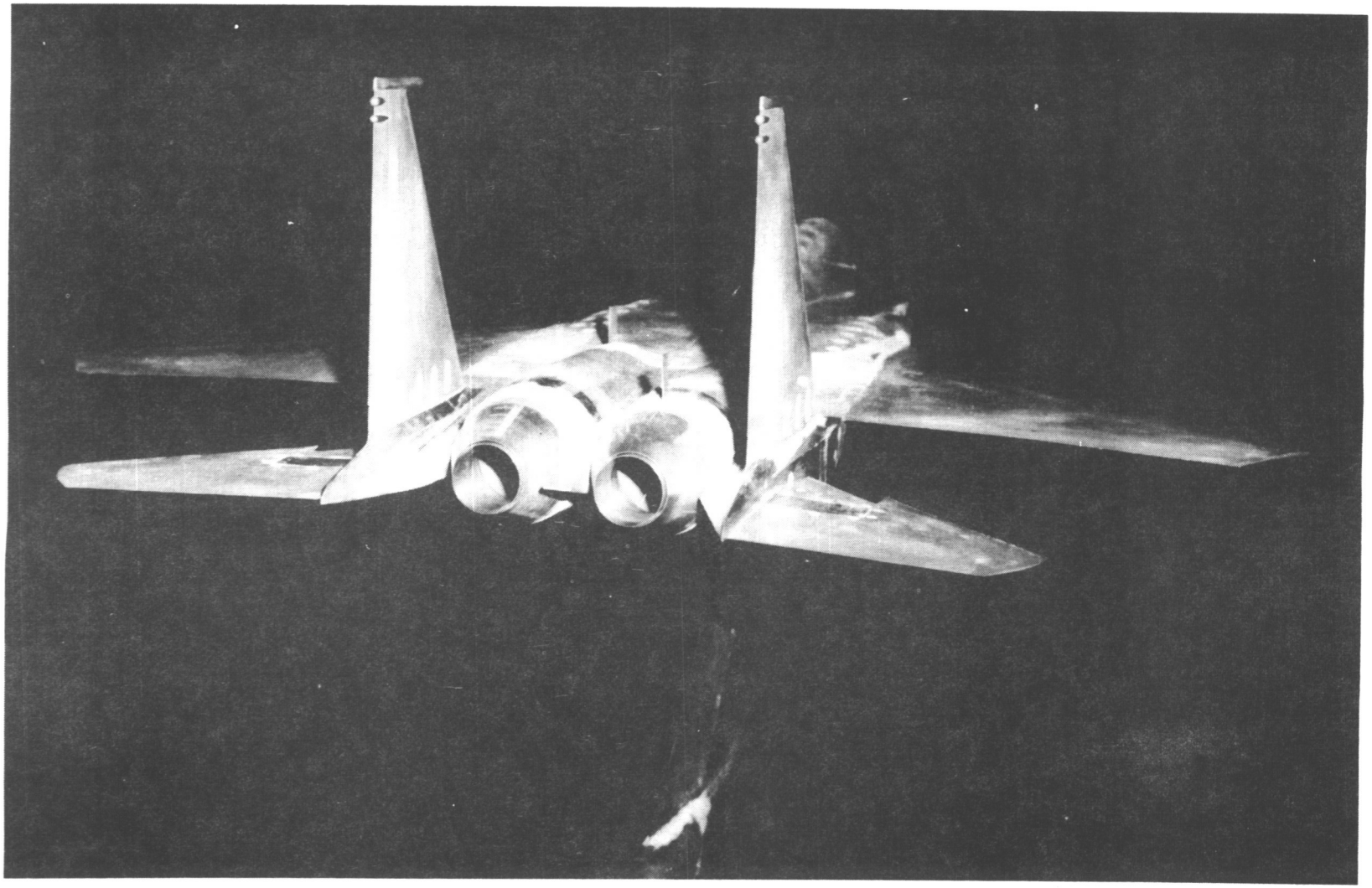

L-81-10,957

(d) View showing afterbody with modifications and boundary-layer rakes installed.

Figure 2.- Continued.

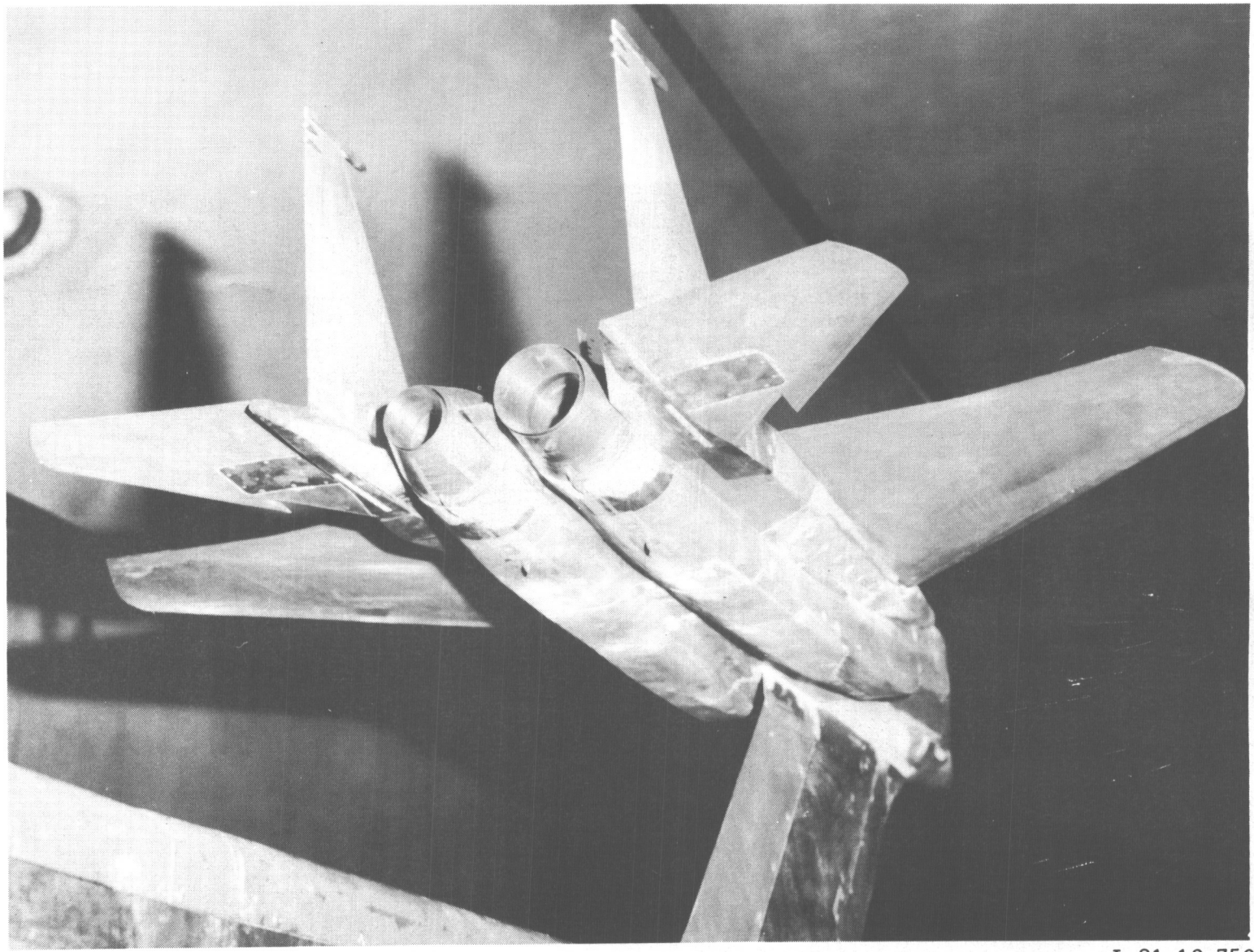

L-81-10,750

(e) View of model with left-hand dry power (PLA = 83°) and right-hand intermediate afterburning power (PLA = 112°) nozzles installed.

Figure 2.- Concluded.

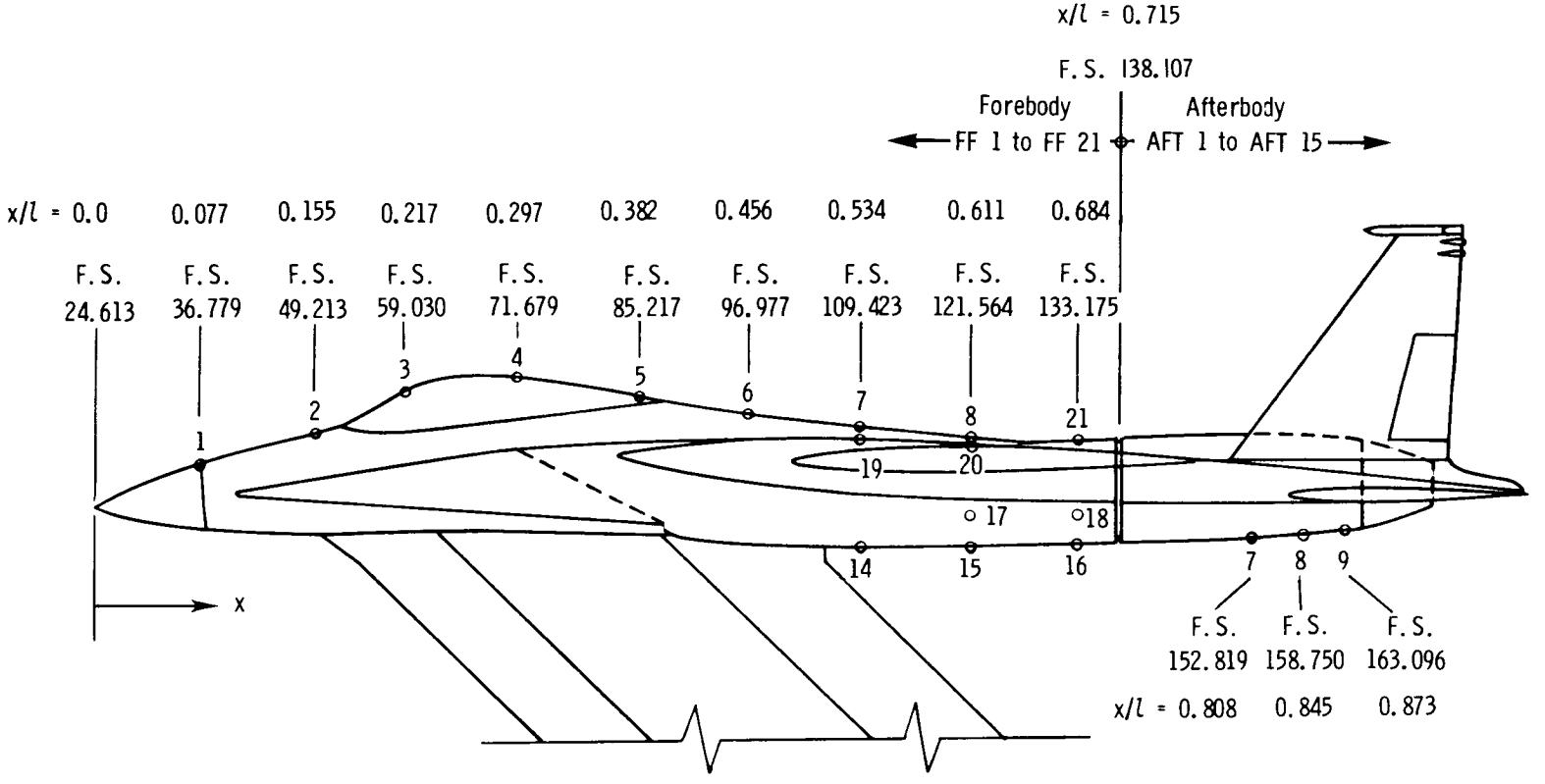

(a) Side view.

Figure 3.- Sketches showing static-pressure orifice locations on the forebody and afterbody. All dimensions are in centimeters.

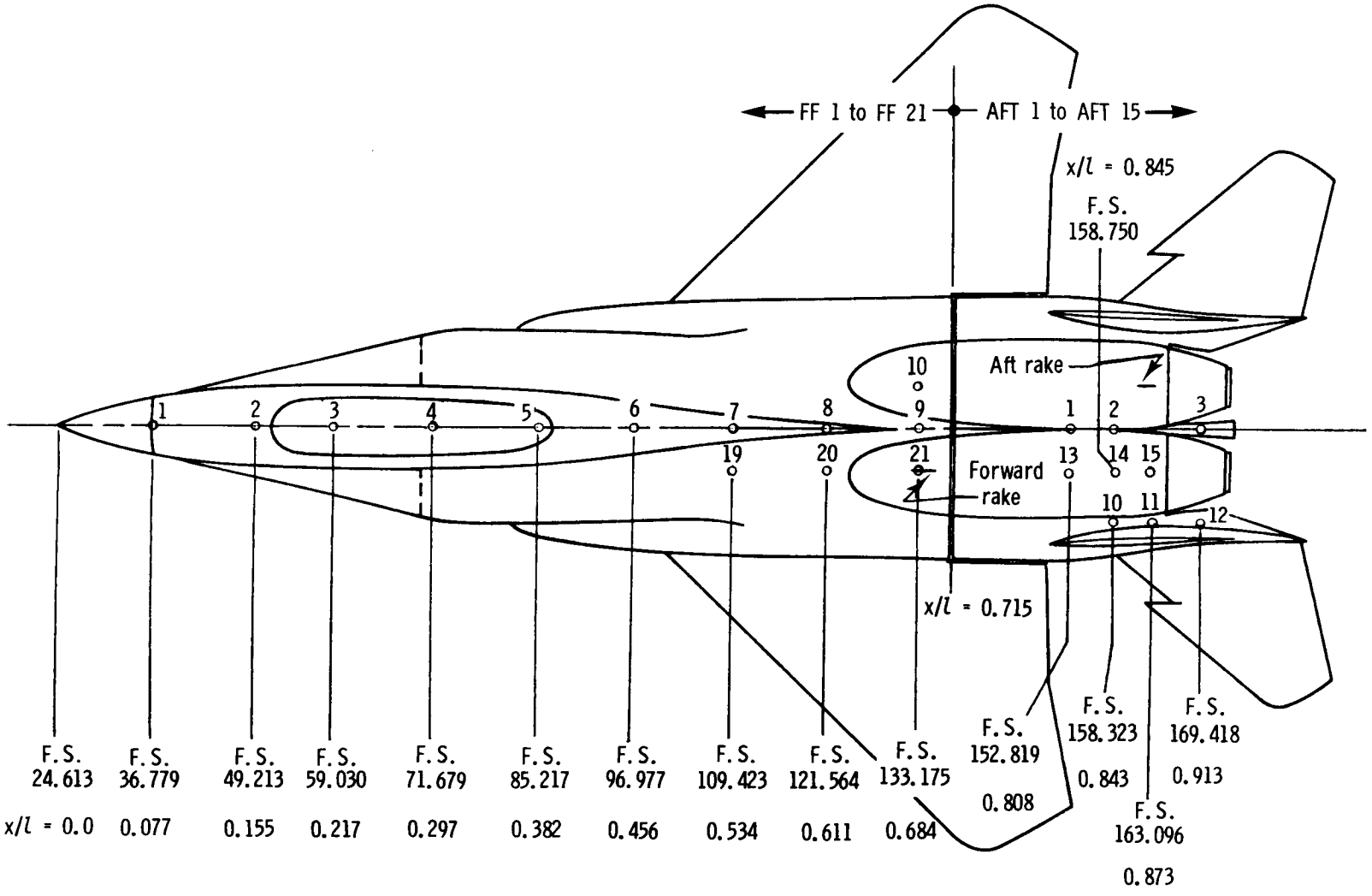

(b) Top view.

Figure 3.- Continued.

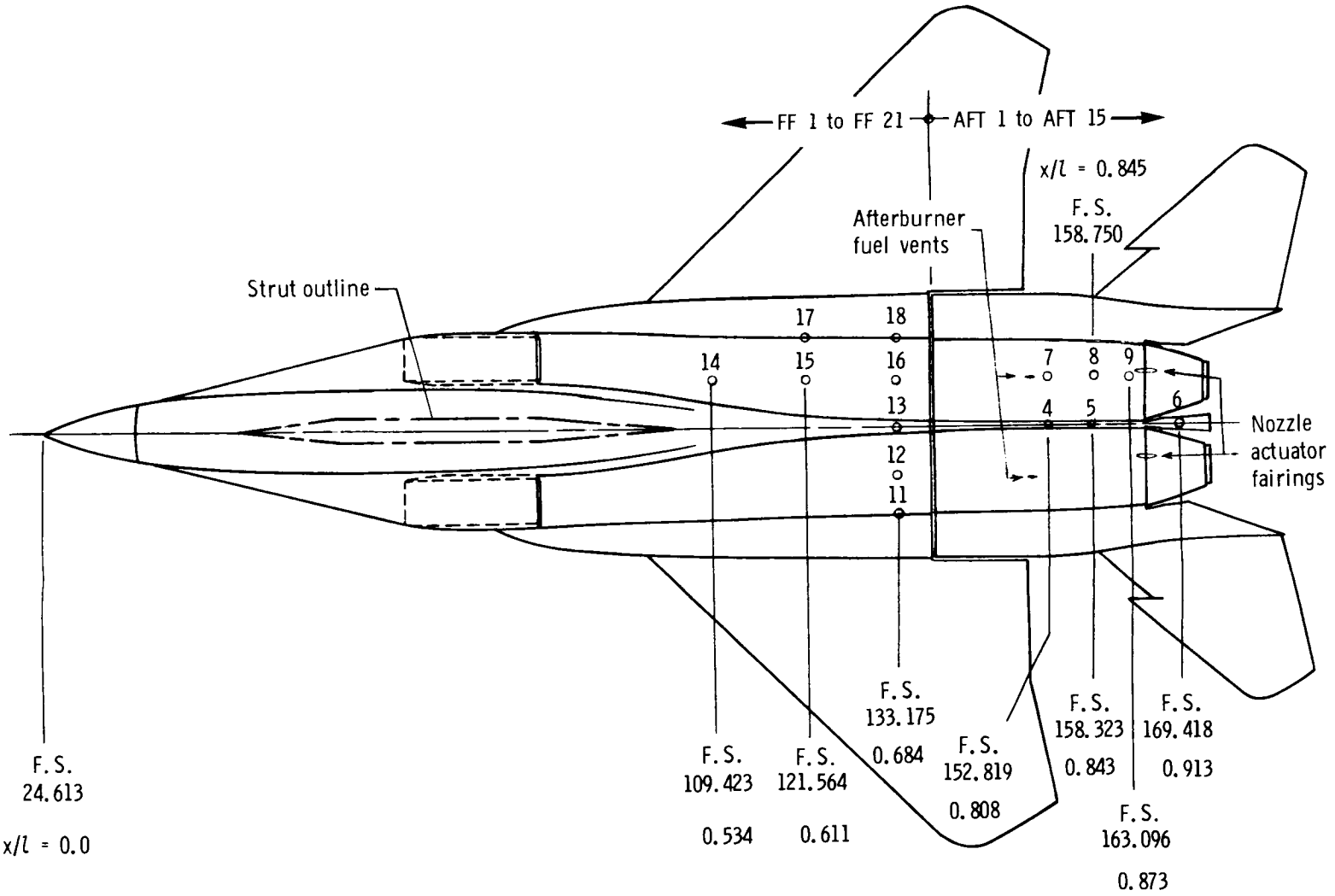

(c) Bottom view.

Figure 3.- Concluded.

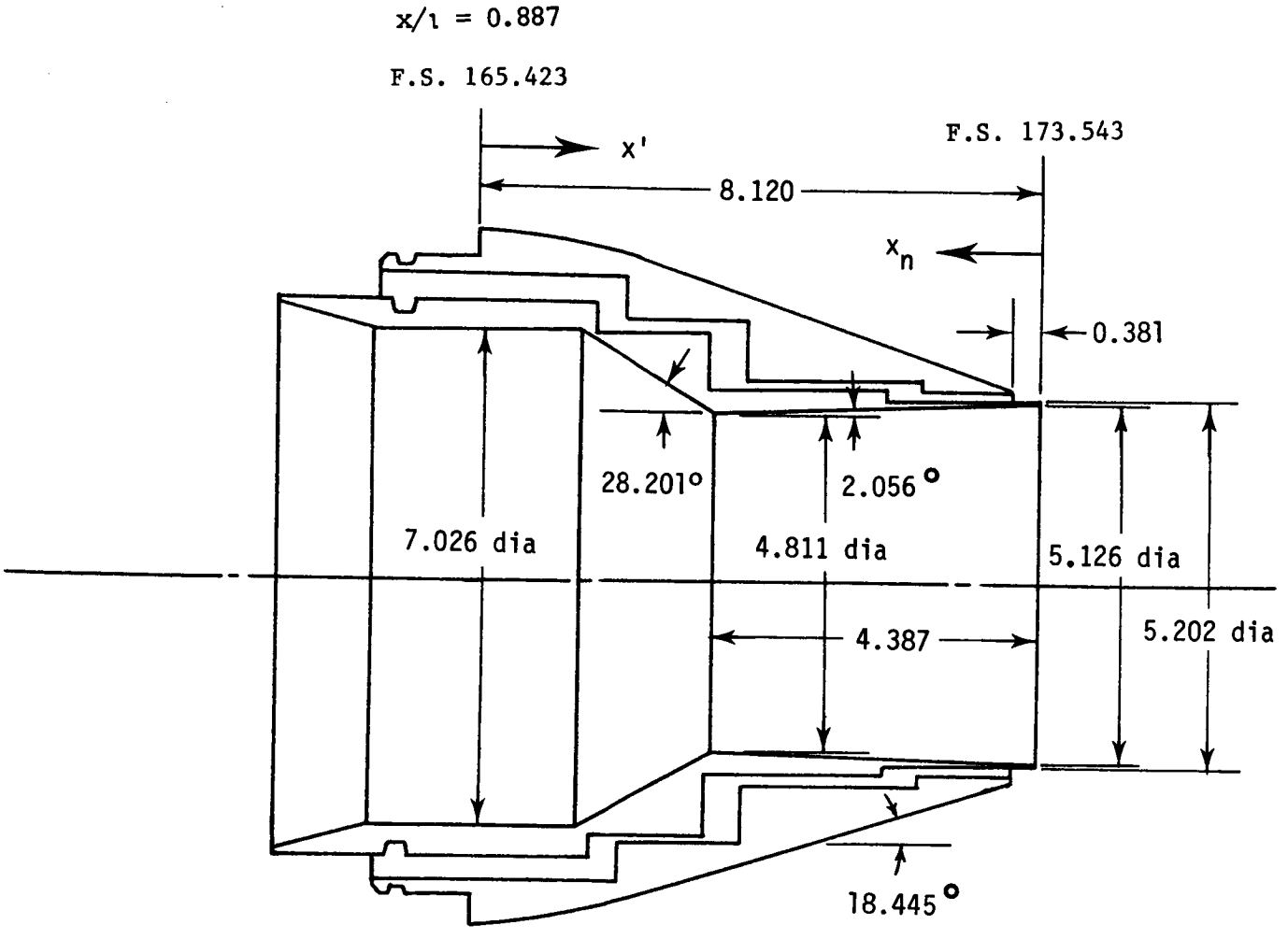

(a) Maximum dry power, low Mach number: PLA = 83°.

Figure 4.- Sketches of the various nozzle configurations. All linear dimensions are in centimeters.

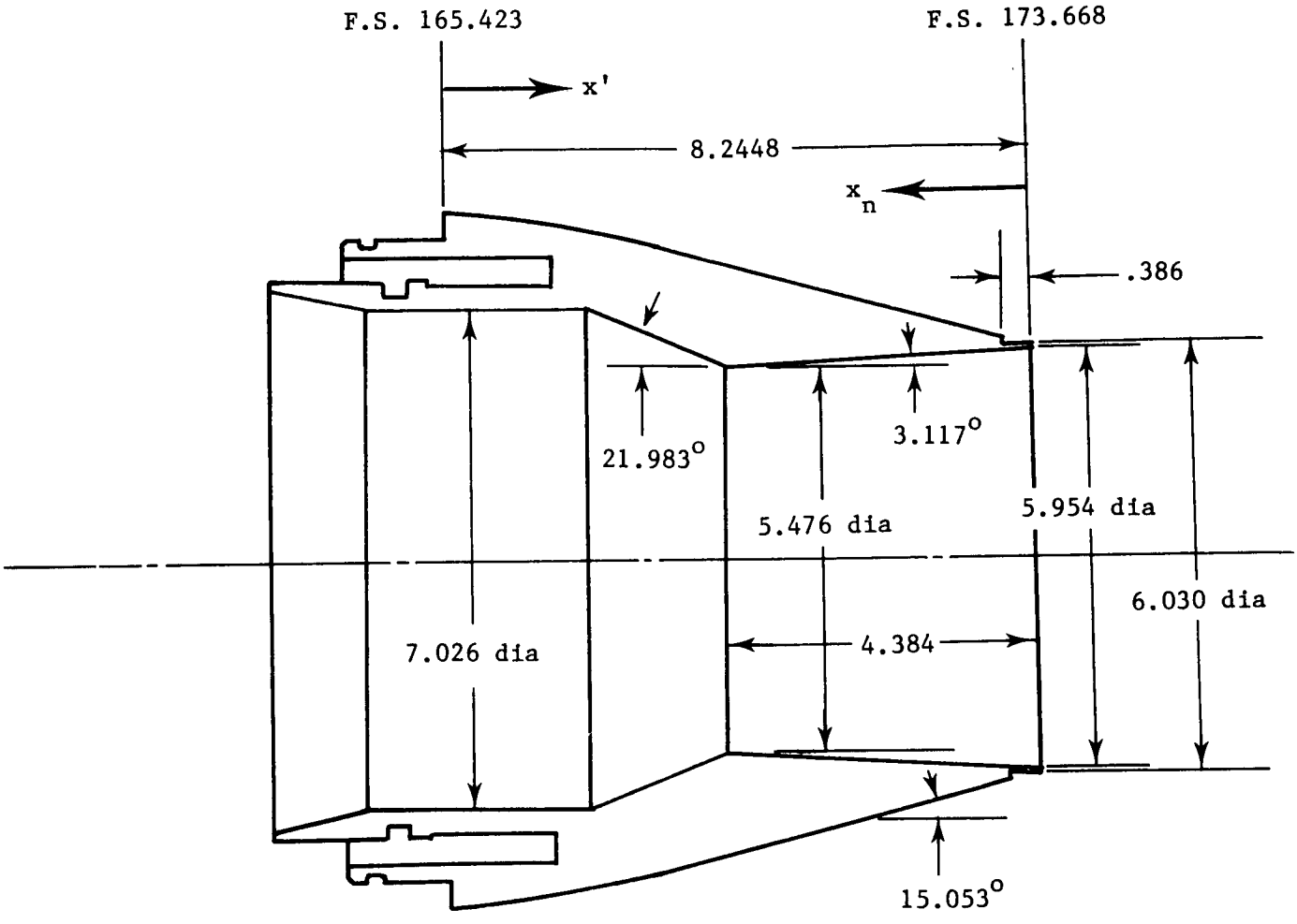

(b) Intermediate A/B power, low Mach number: PLA = 103°.

Figure 4.- Continued.

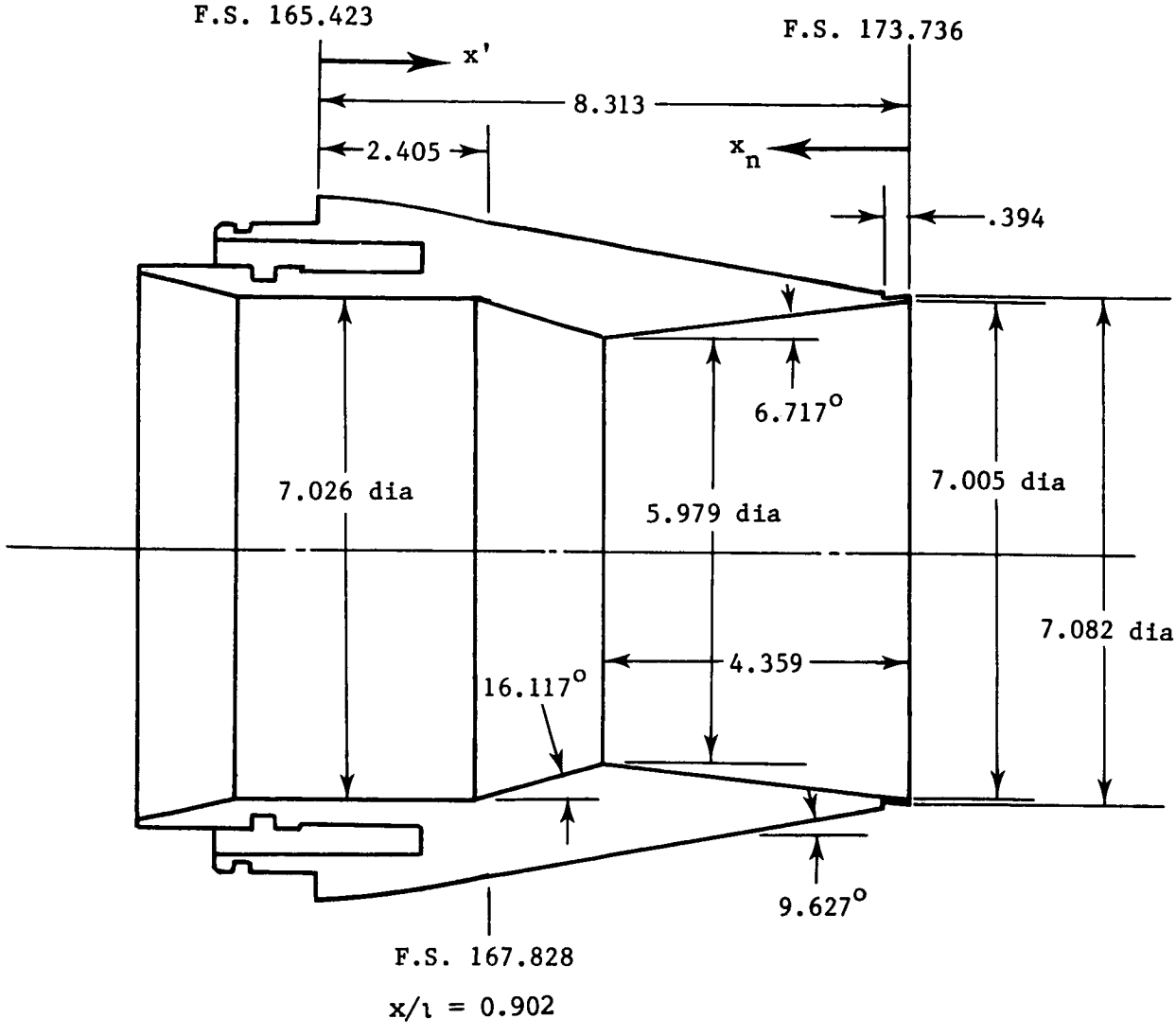

(c) Intermediate A/B power, high Mach number: PLA = 108°.

Figure 4.- Continued.

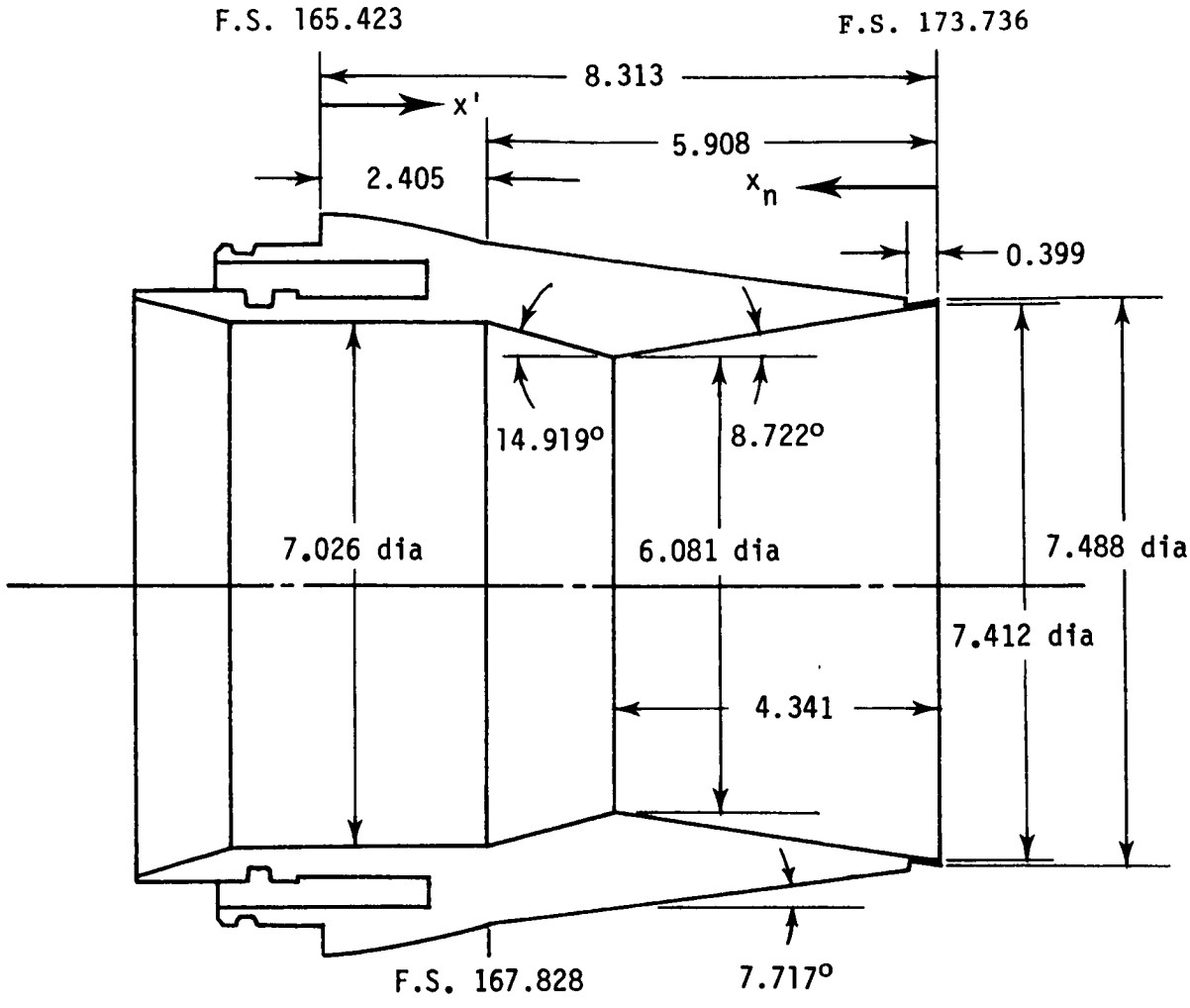

(d) Intermediate A/B power, high Mach number: PLA = 112°.

Figure 4.- Concluded.

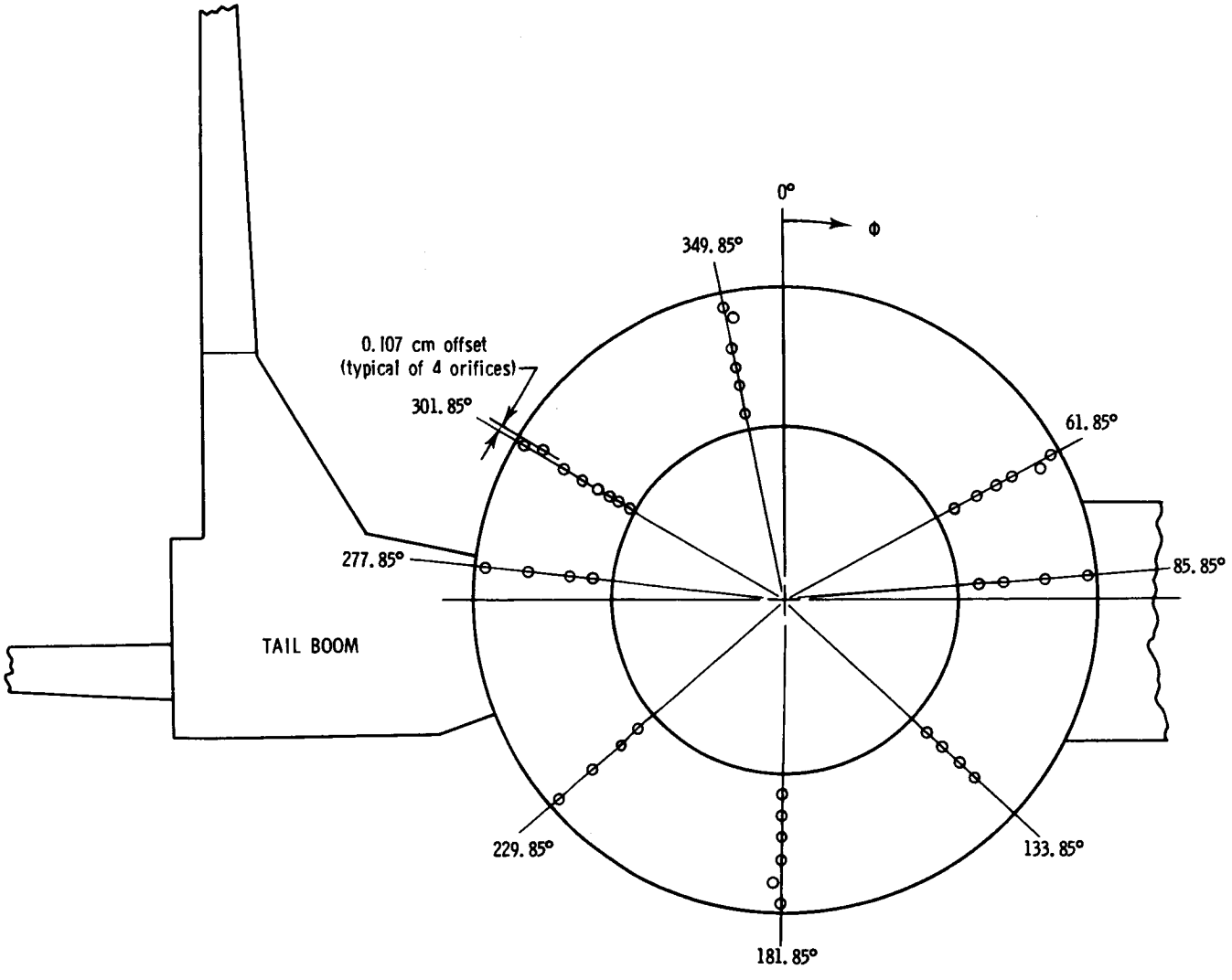

Figure 5.- Location of static-pressure orifices on left-hand nozzle boattail. View of left-hand dry power nozzle looking upstream.

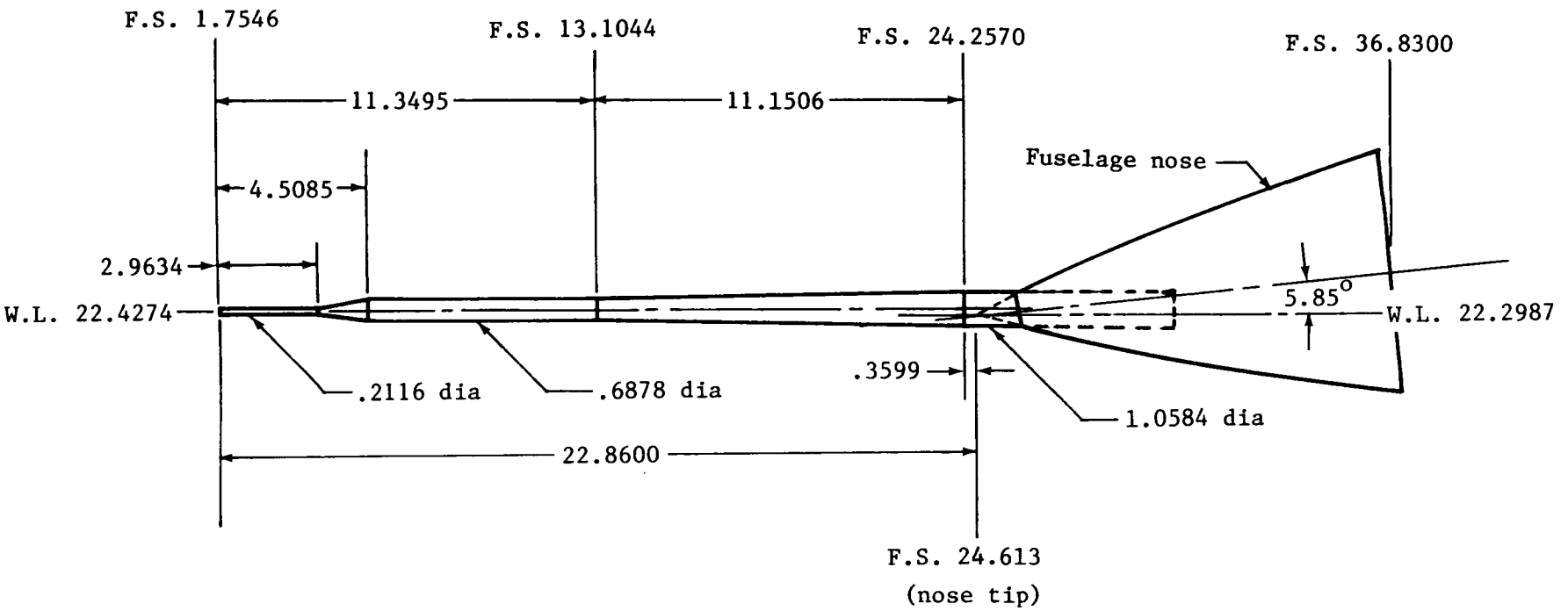

(a) Nose boom.

Figure 6.- Sketches of model modifications to match full-scale aircraft. All linear dimensions are in centimeters.

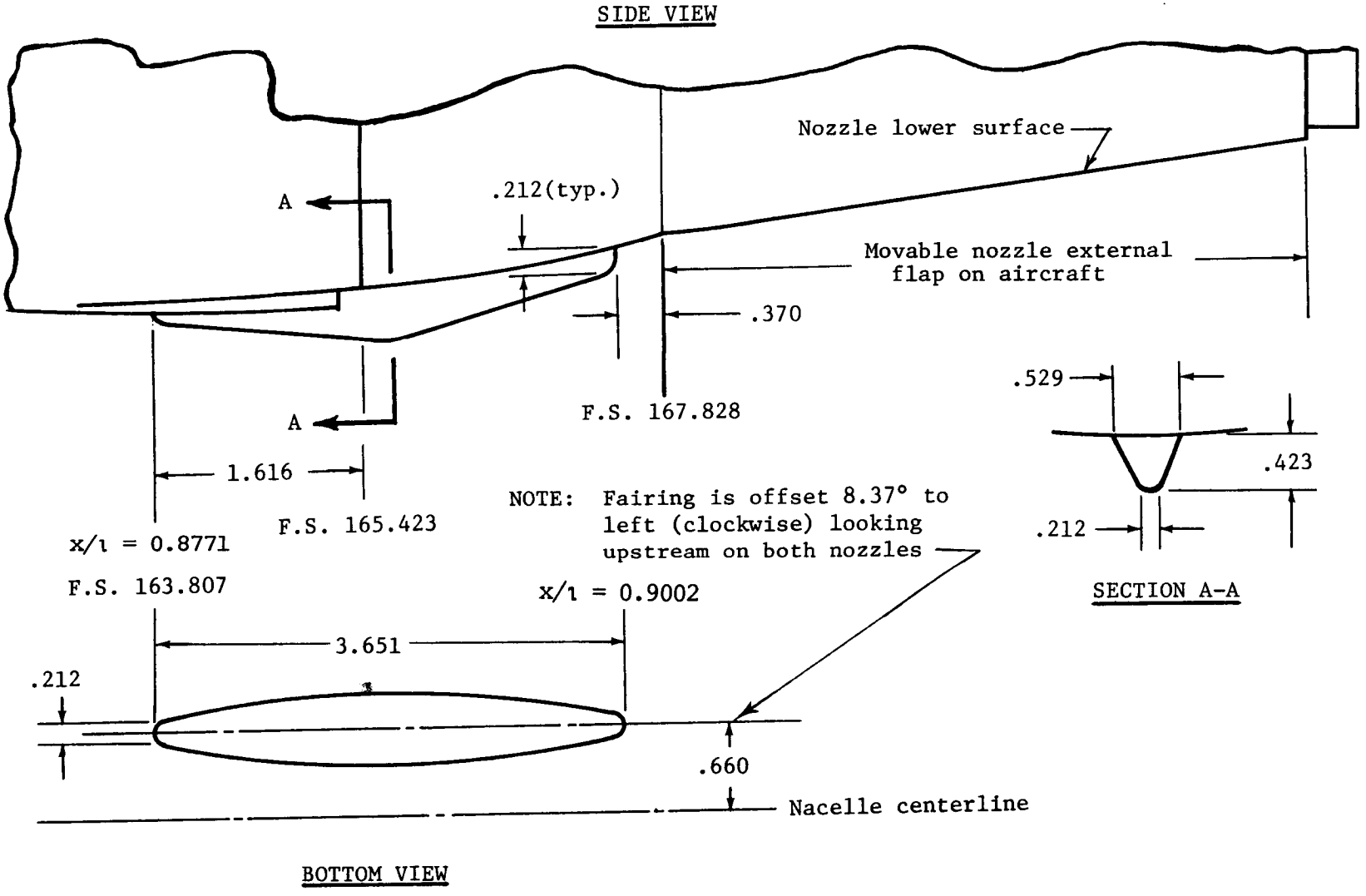

(b) Nozzle actuator fairings.

Figure 6.- Continued.

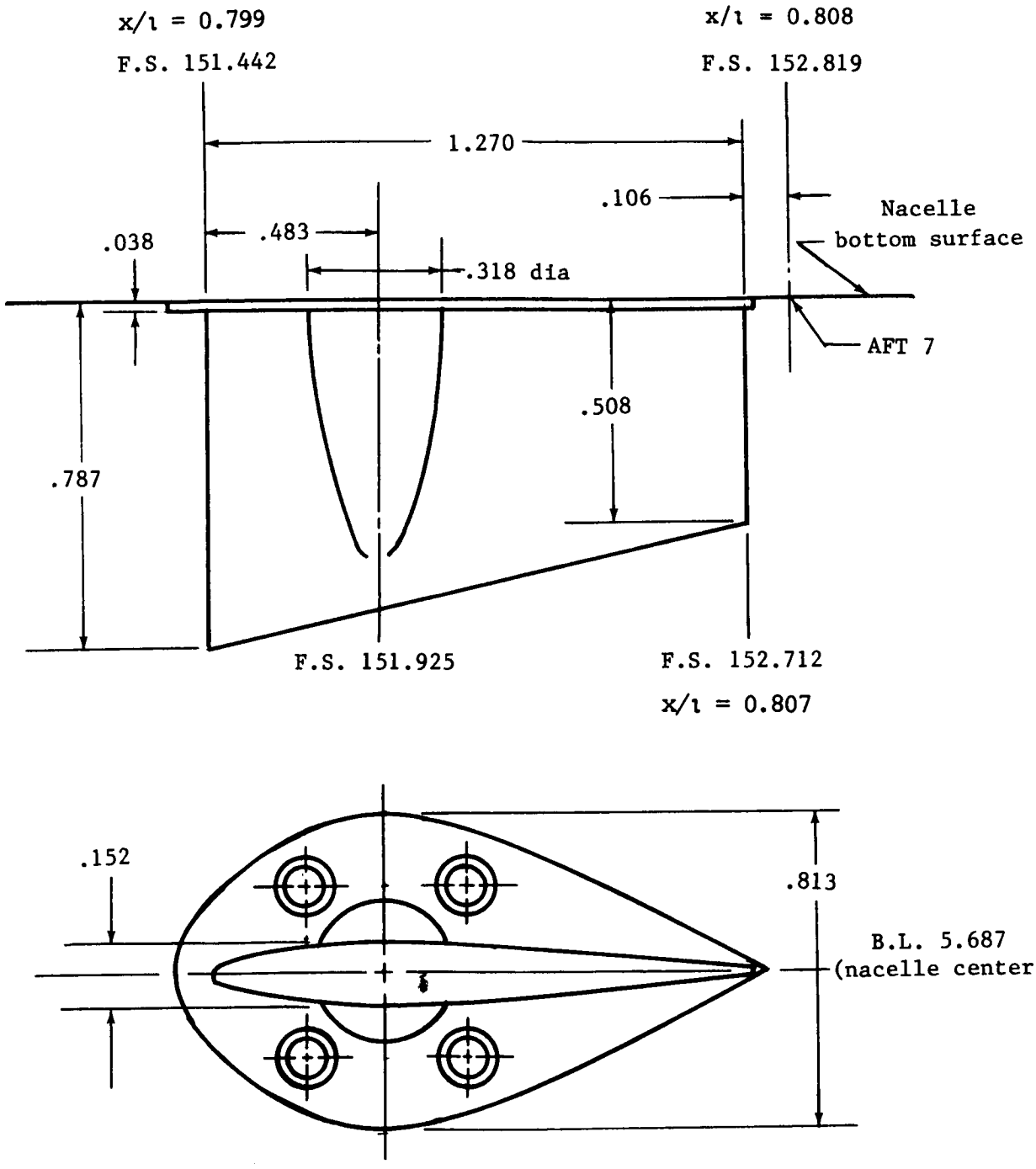

(c) Afterburner fuel vents.

Figure 6.- Continued.

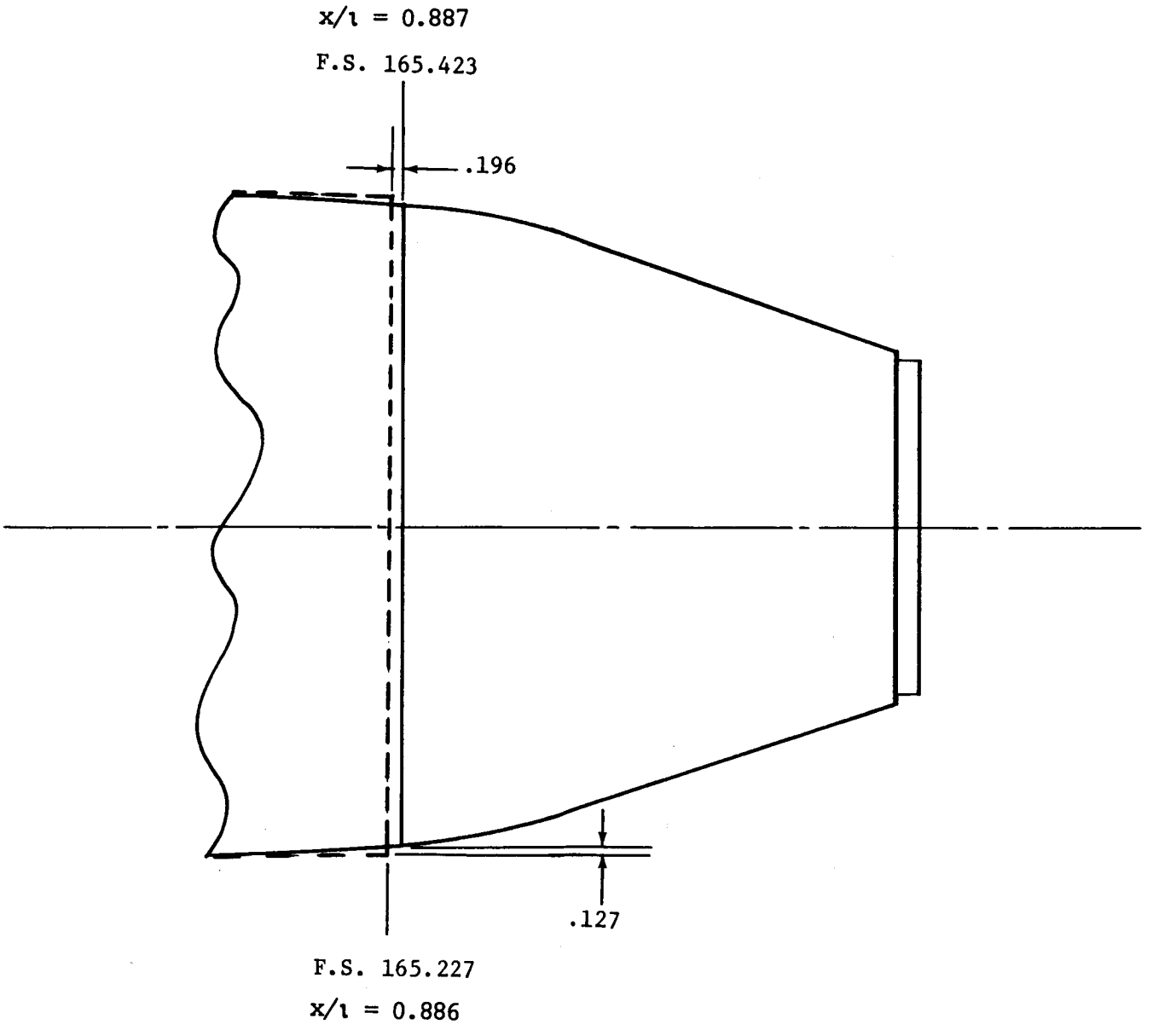

(d) Engine bay cooling exit annulus (sealed). Annulus modification shown as dashed lines.

Figure 6.- Concluded.

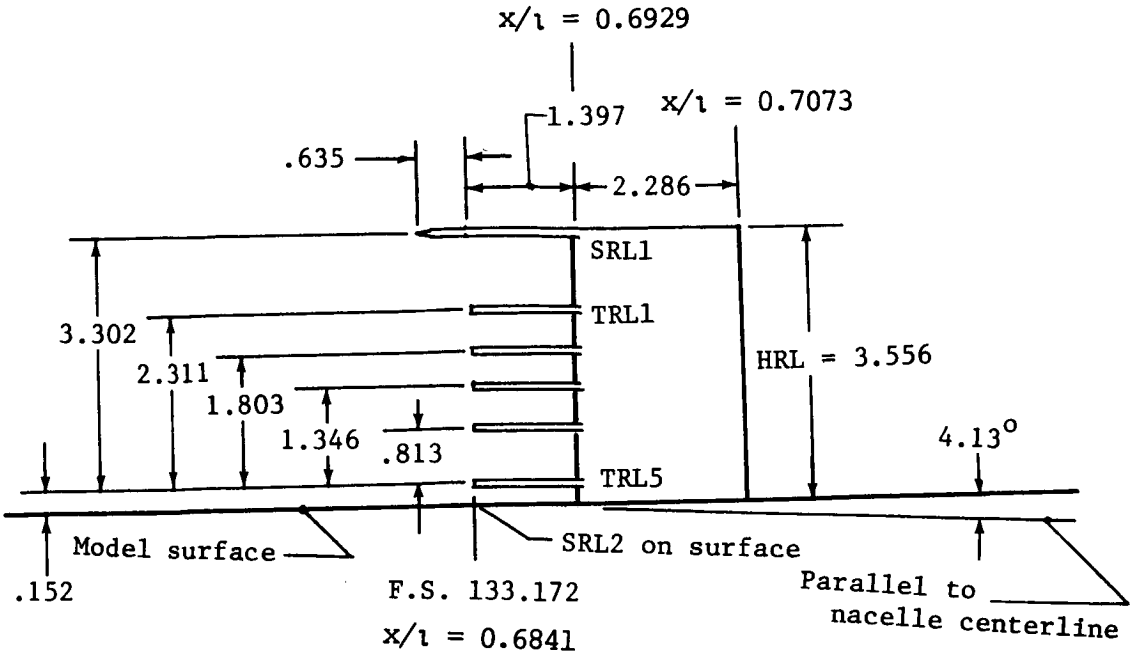

FORWARD LEFT-HAND RAKE

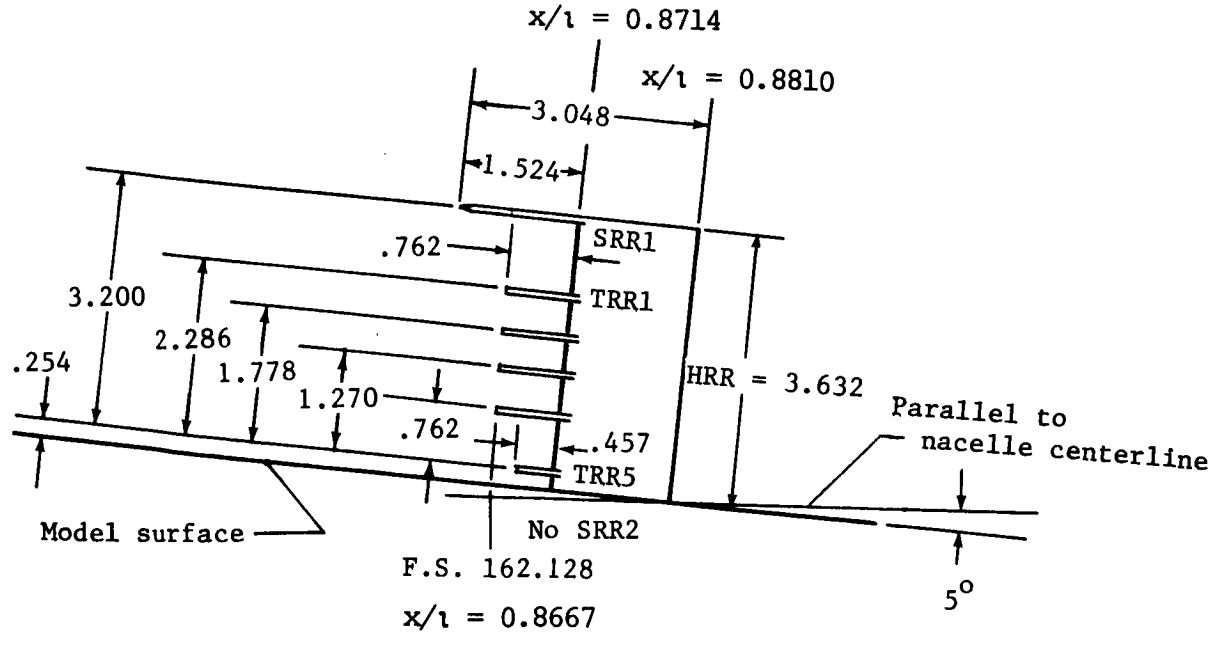

AFT RIGHT-HAND RAKE

Figure 7.- Details of forward and aft boundary-layer rakes. All dimensions are in centimeters except as noted.

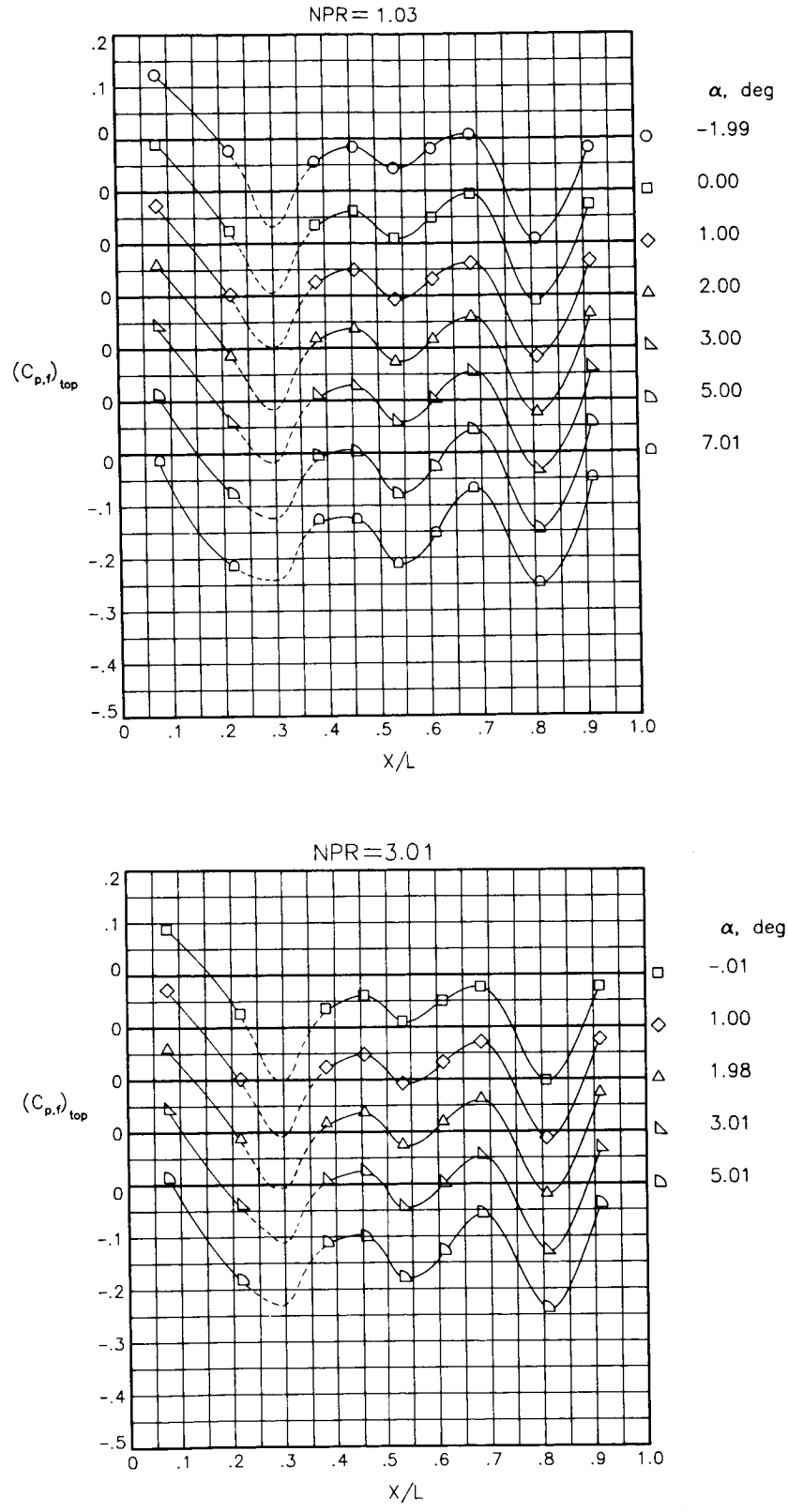

(a) M = 0.60.

Figure 8.- Static-pressure-coefficient distributions on top of fuselage along centerline for the unmodified model. β_n = 18.45°.

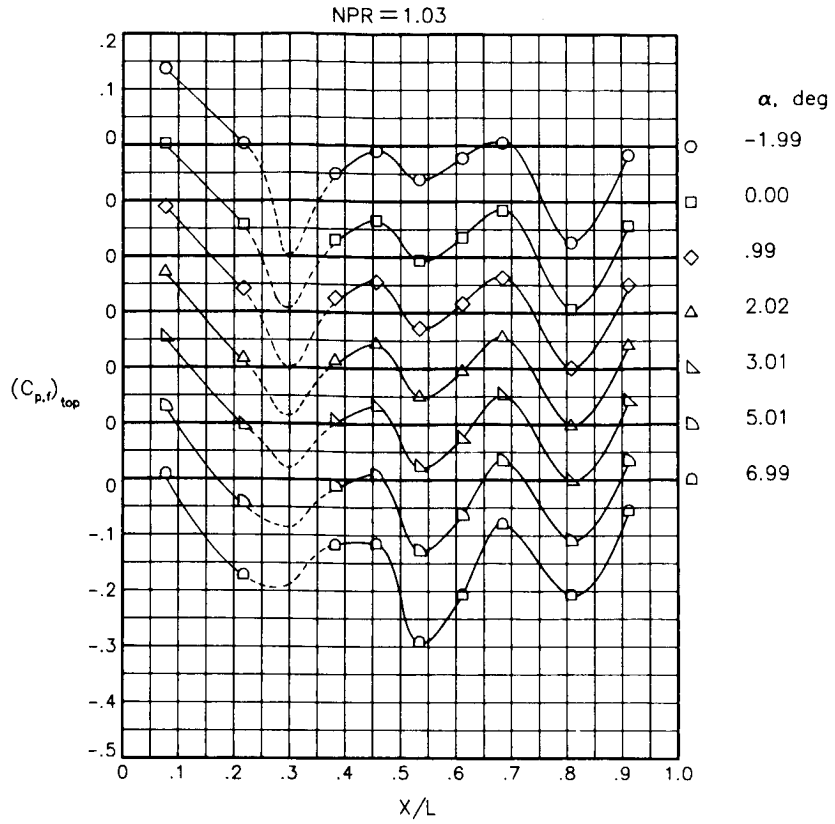

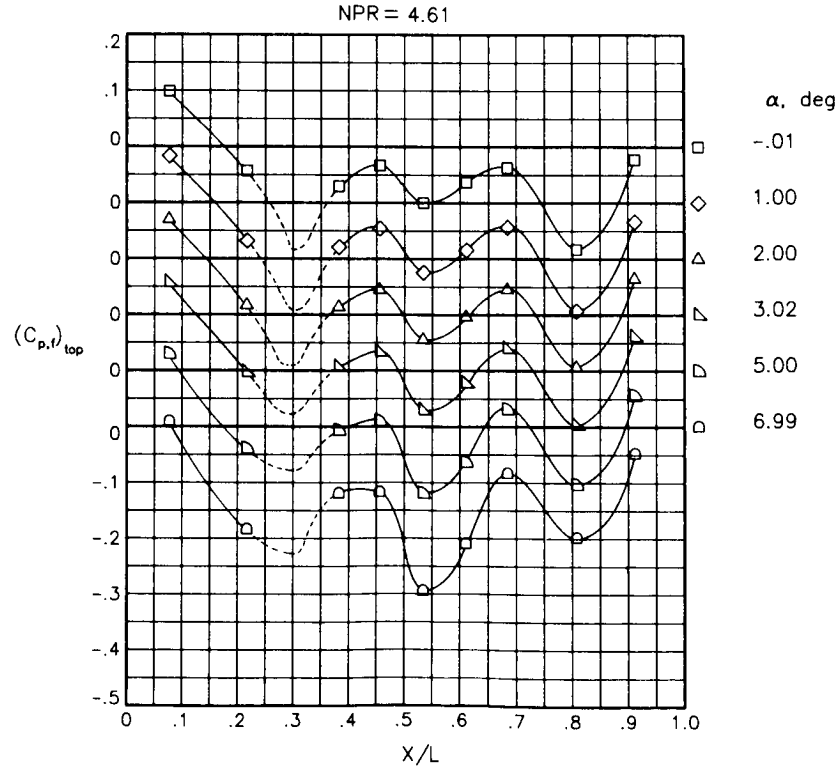

(b) M = 0.80.

Figure 8.- Continued.

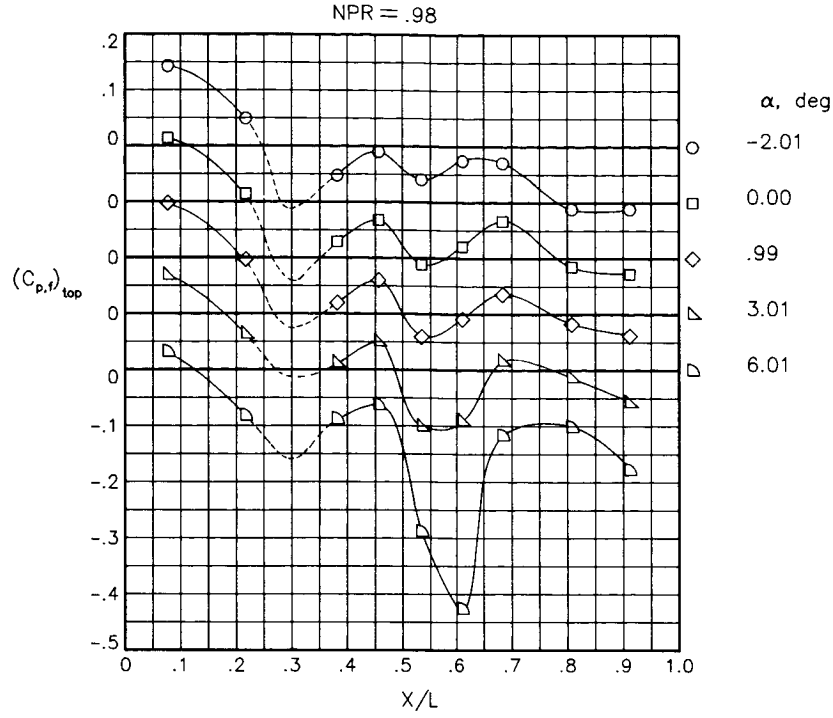

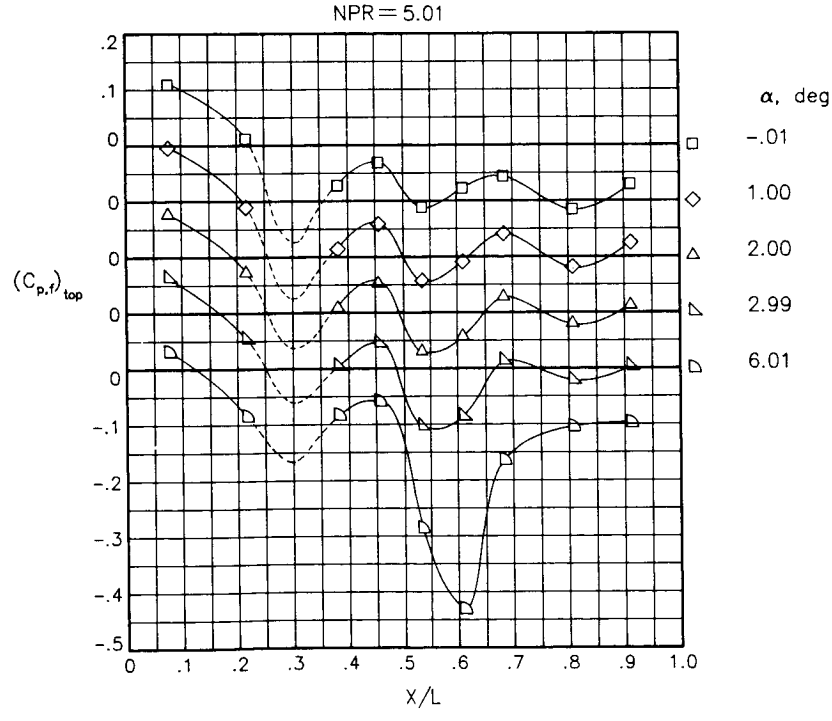

(c) M = 0.90.

Figure 8.- Concluded.

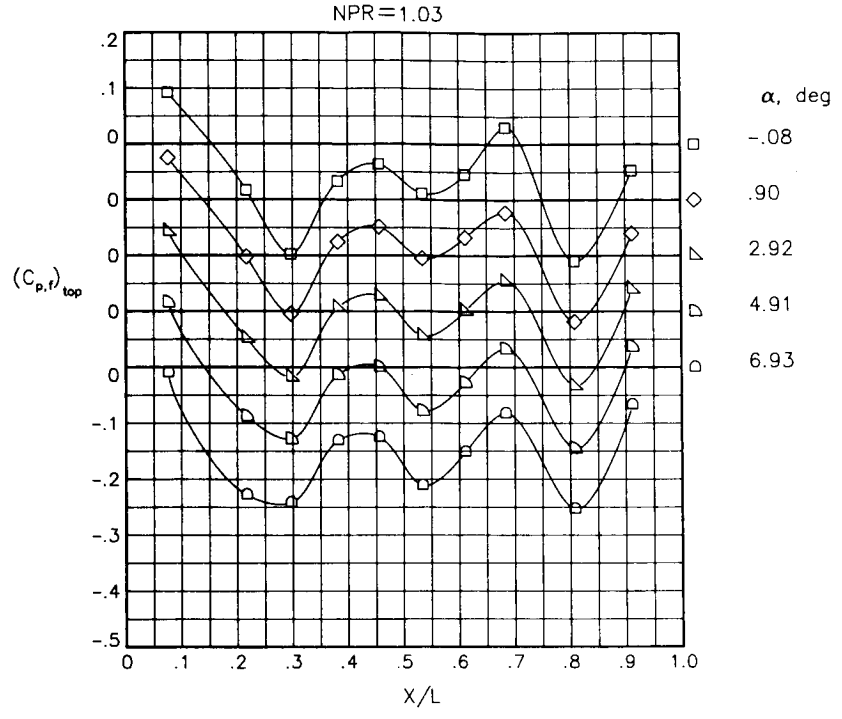

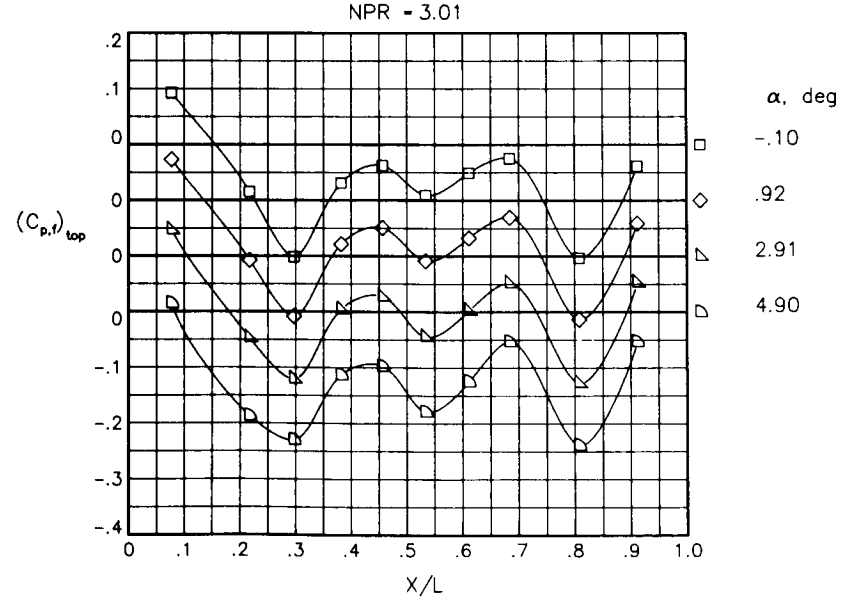

(a) M = 0.60.

Figure 9.- Static-pressure-coefficient distributions on top of fuselage along centerline for the model with nose boom. β_n = 18.45°.

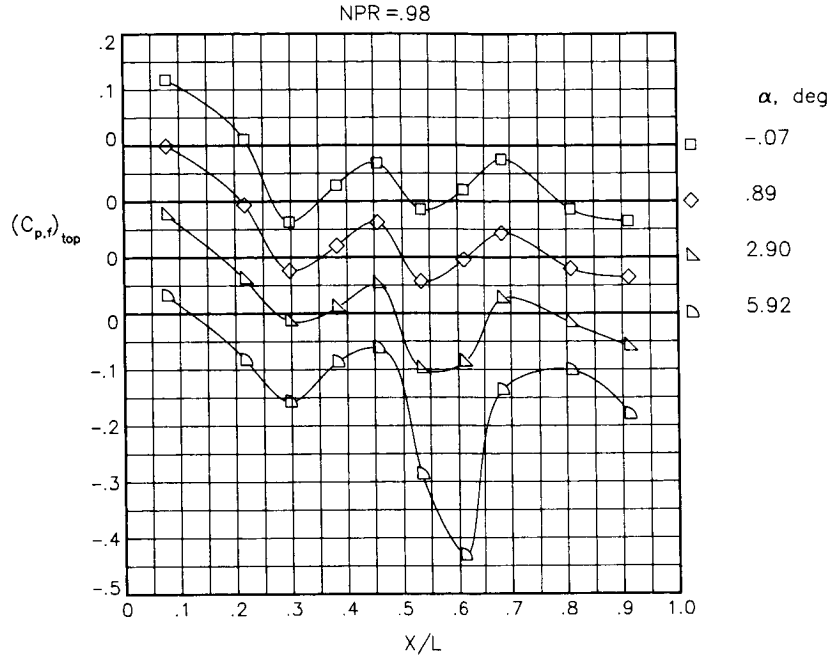

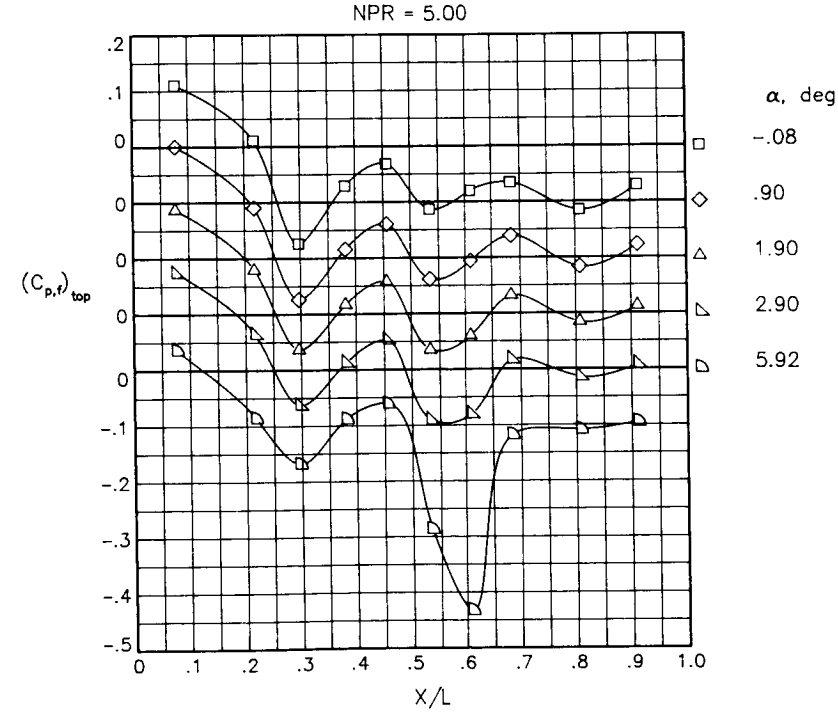

(b) M = 0.90.

Figure 9.- Concluded.

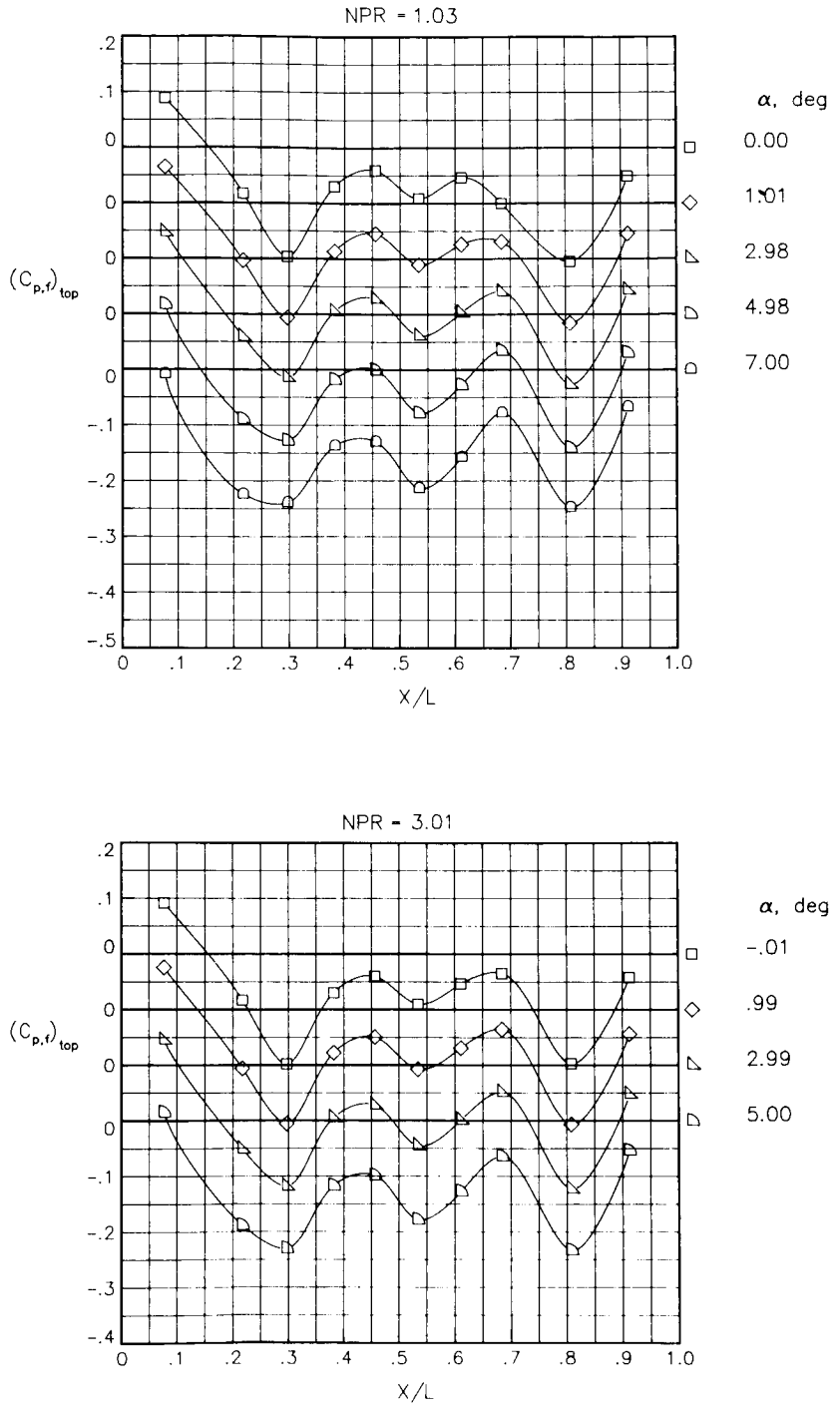

(a) M = 0.60.

Figure 10.- Static-pressure-coefficient distributions on top of fuselage along centerline for the model with nose boom, actuator fairings, and A/B vents. β_n = 18.45°.

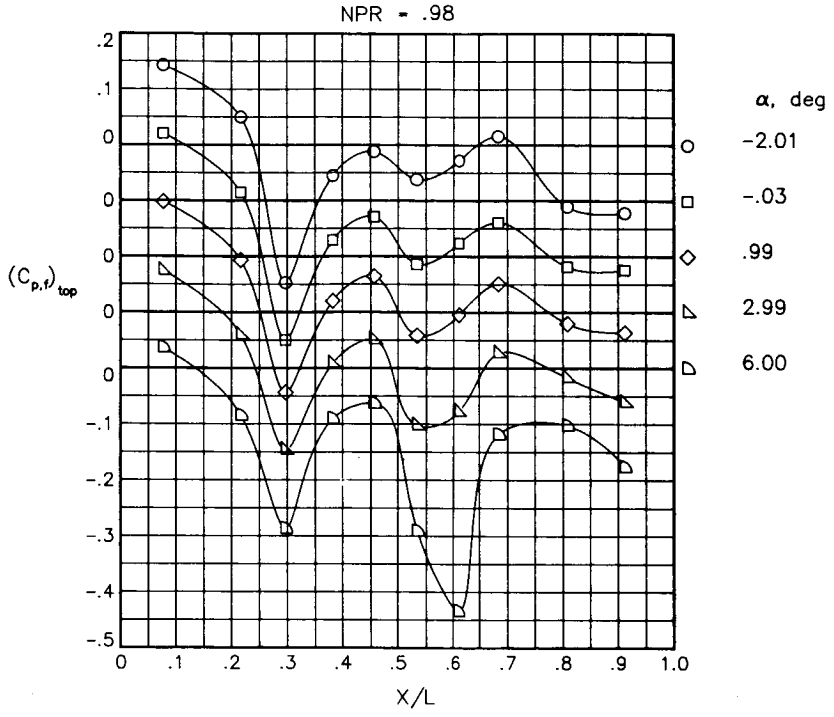

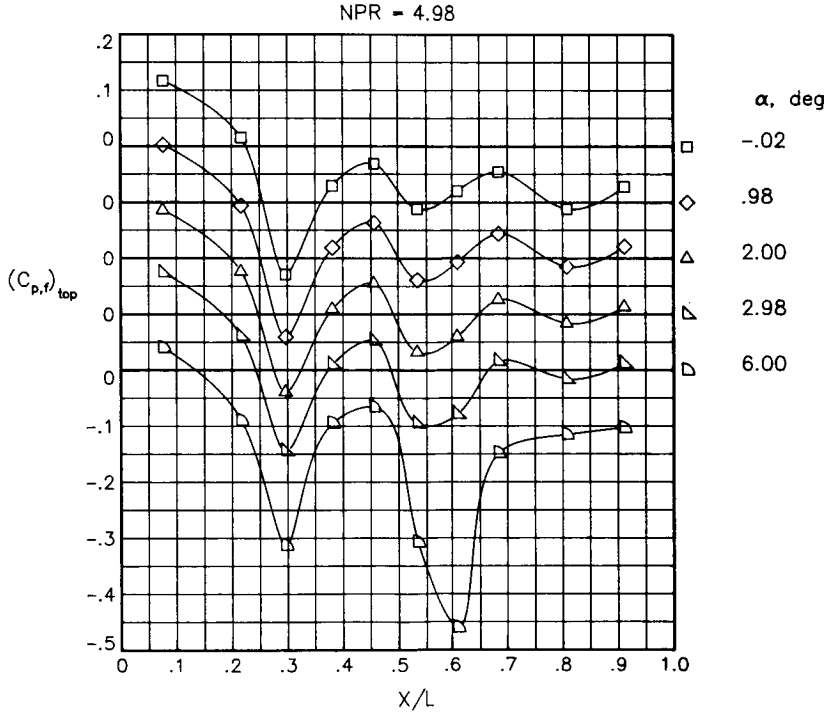

(b) M = 0.90.

Figure 10.- Concluded.

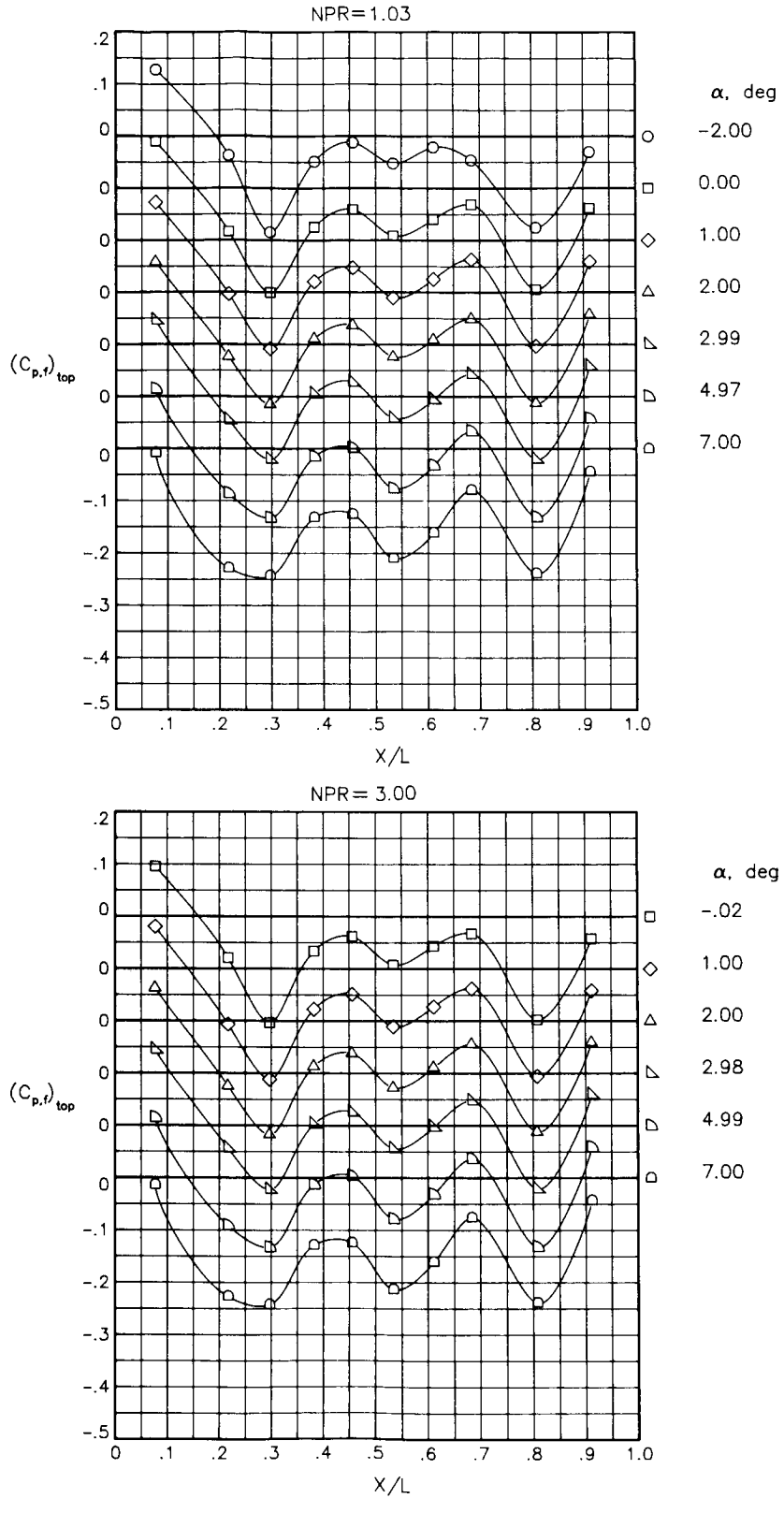

(a) M = 0.60.

Figure 11.- Static-pressure-coefficient distributions on top of fuselage along centerline for the model with all fuselage modifications except nose boom. β_n = 18.45°.

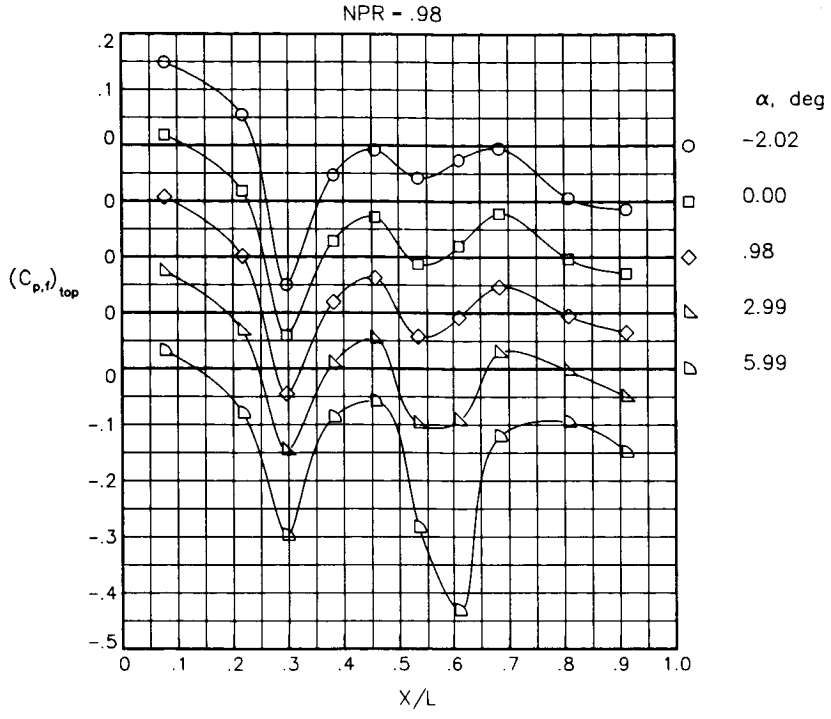

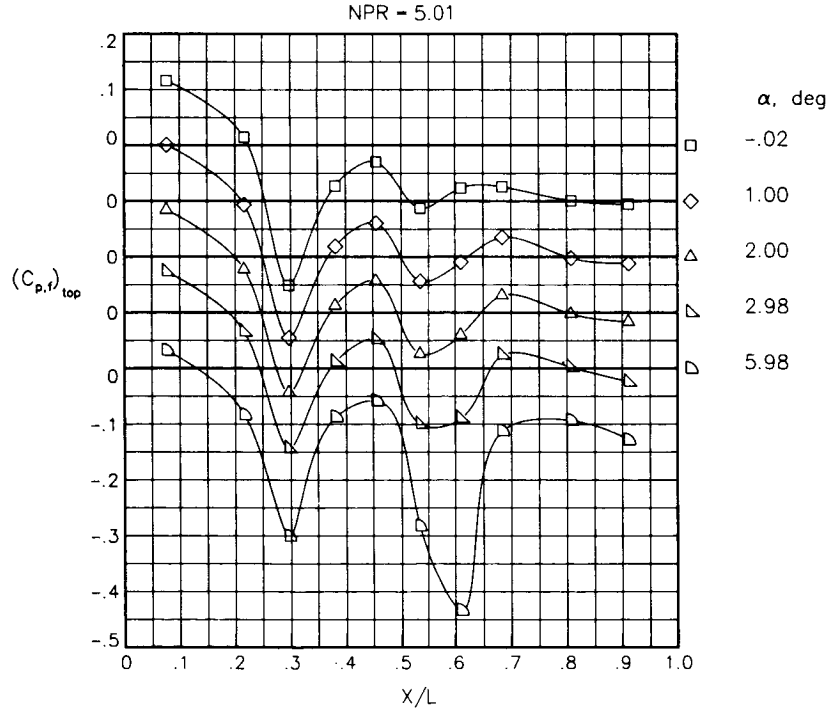

(b) M = 0.90.

Figure 11.- Concluded.

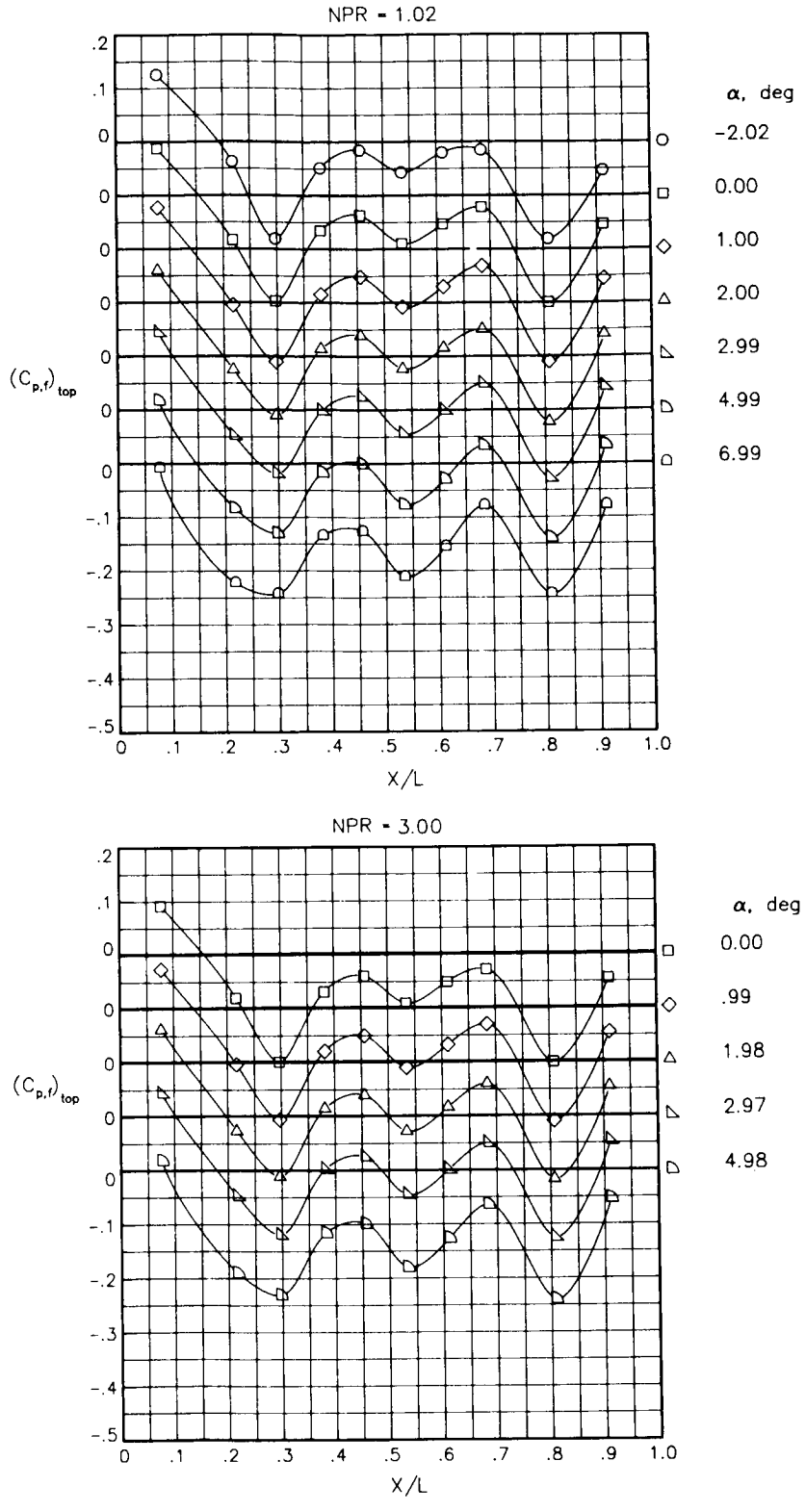

(a) M = 0.60.

Figure 12.- Static-pressure-coefficient distributions on top of fuselage along centerline for the model with nose boom, actuator fairings, A/B vents, and nozzle steps (no rakes). β_n = 18.45°.

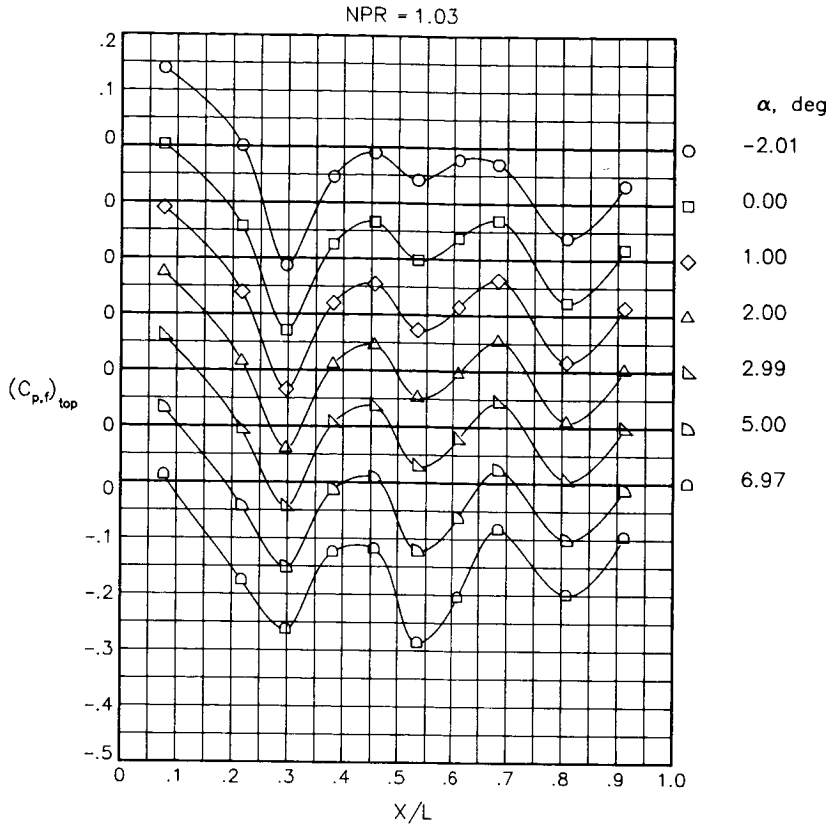

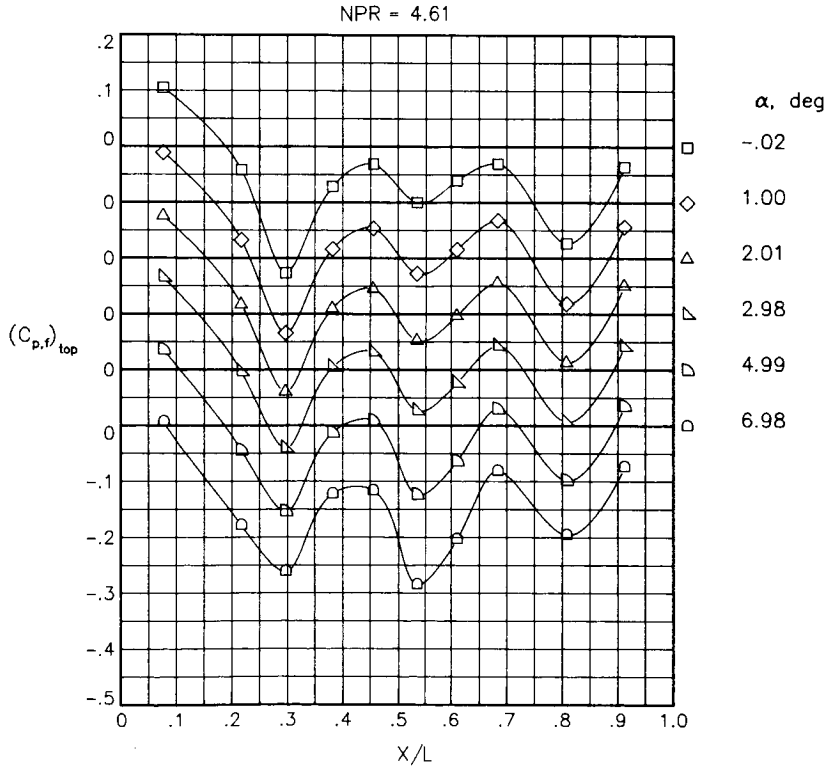

(b) M = 0.80.

Figure 12.- Continued.

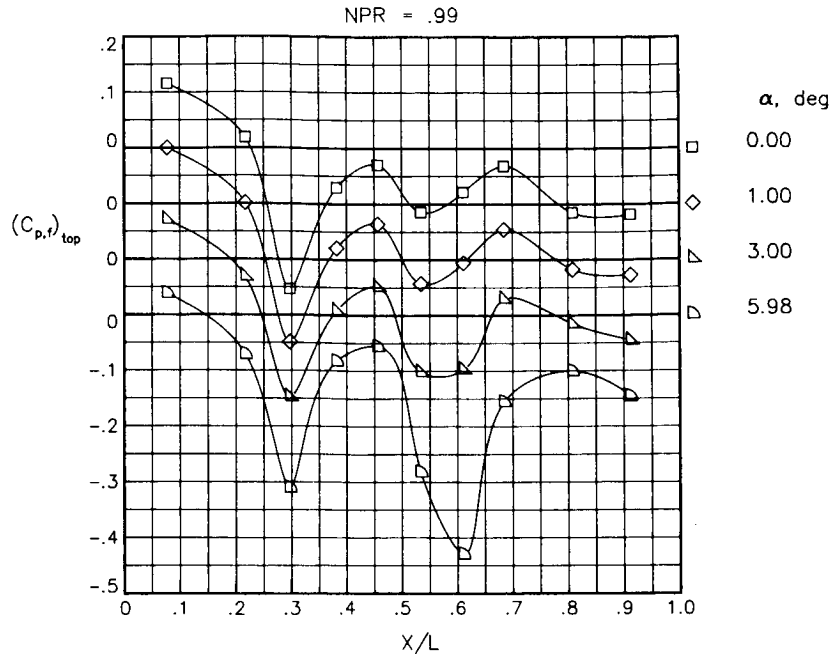

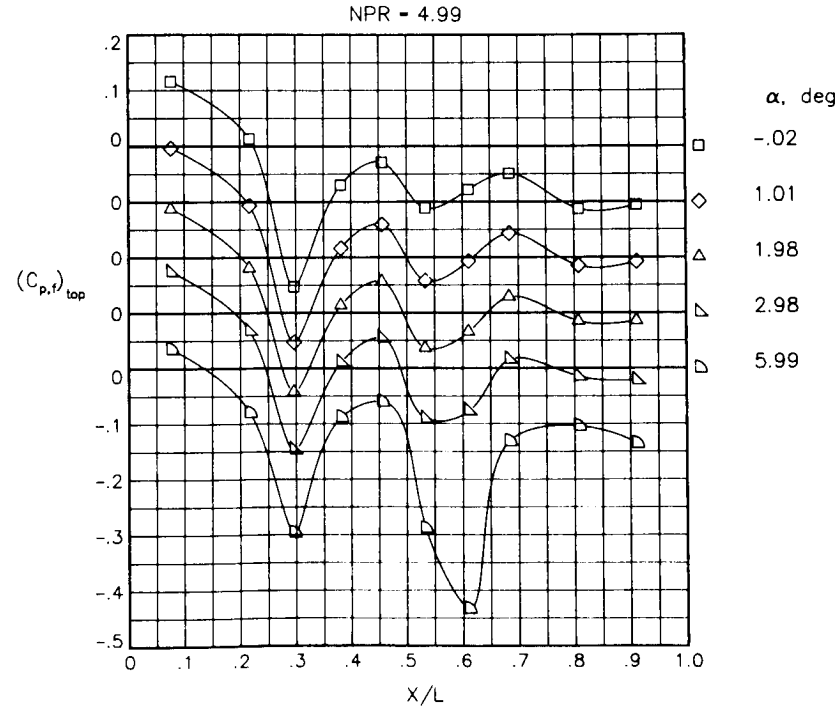

(c) M = 0.90.

Figure 12.- Concluded.

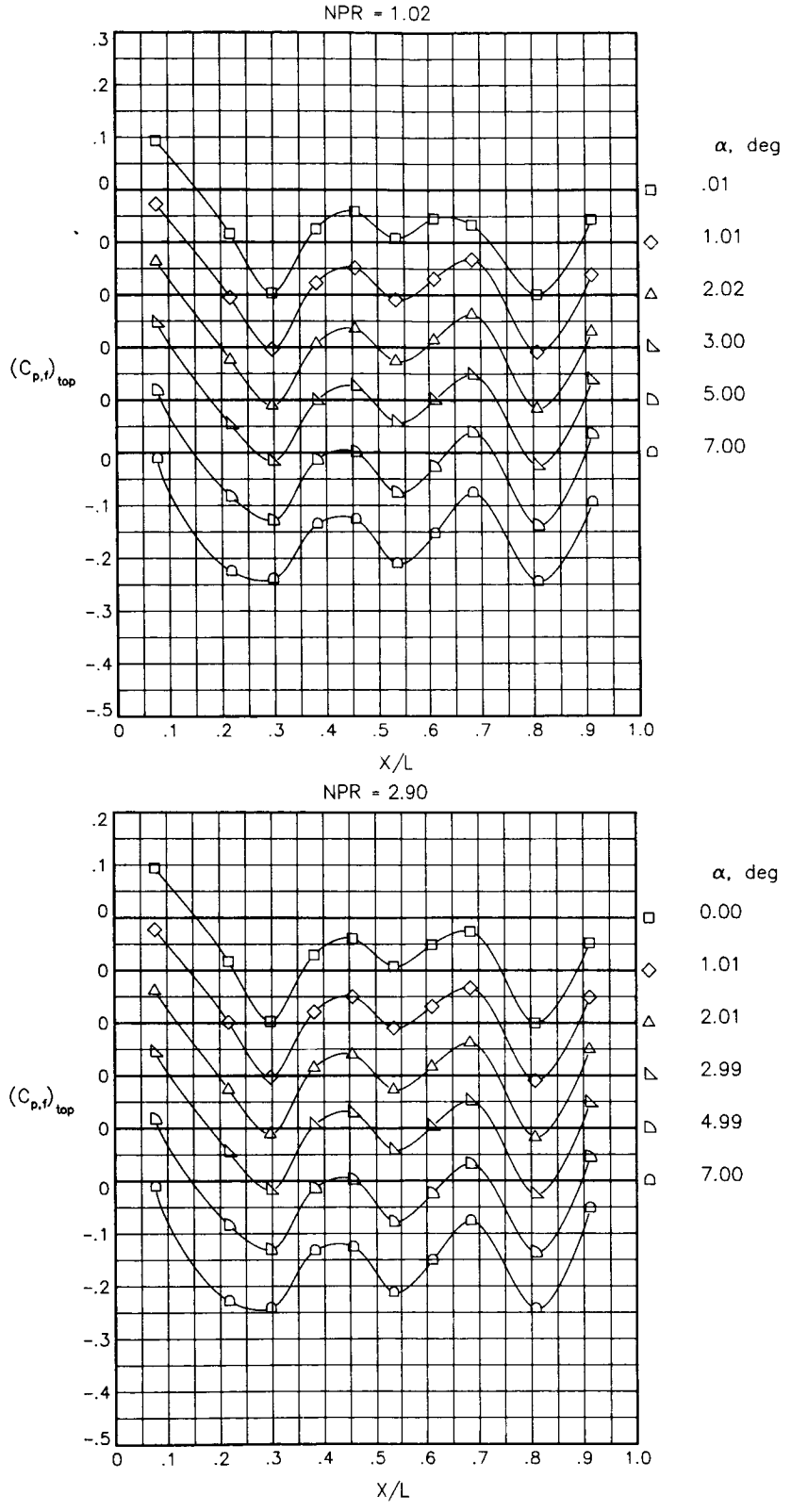

(a) M = 0.60.

Figure 13.- Static-pressure-coefficient distributions on top of fuselage along centerline for the model with nose boom, actuator fairings, A/B vents, and nozzle steps (no rakes). β_n = 18.45°; δ_h = -2°.

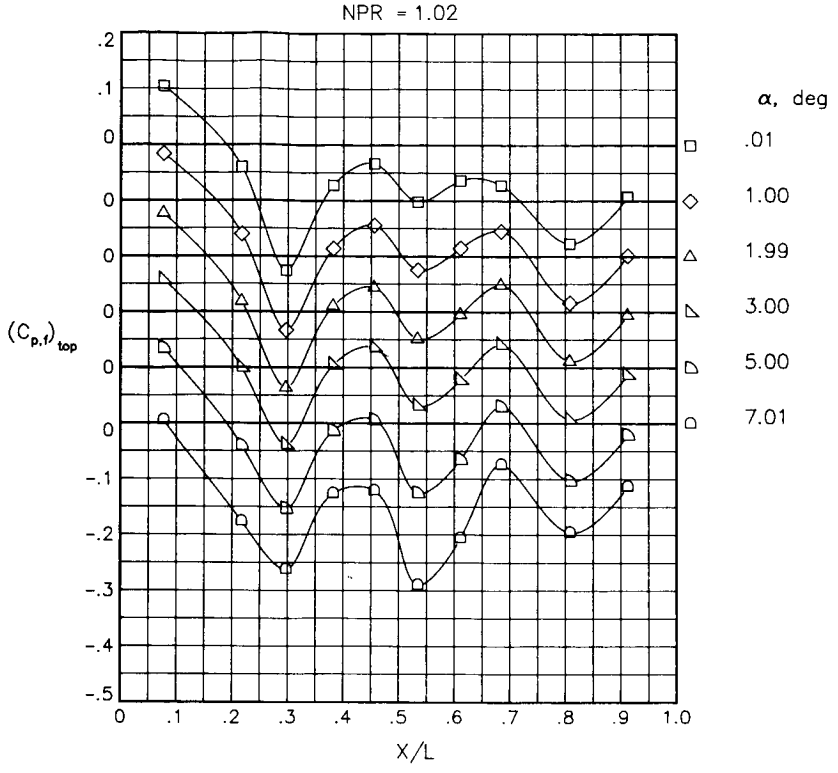

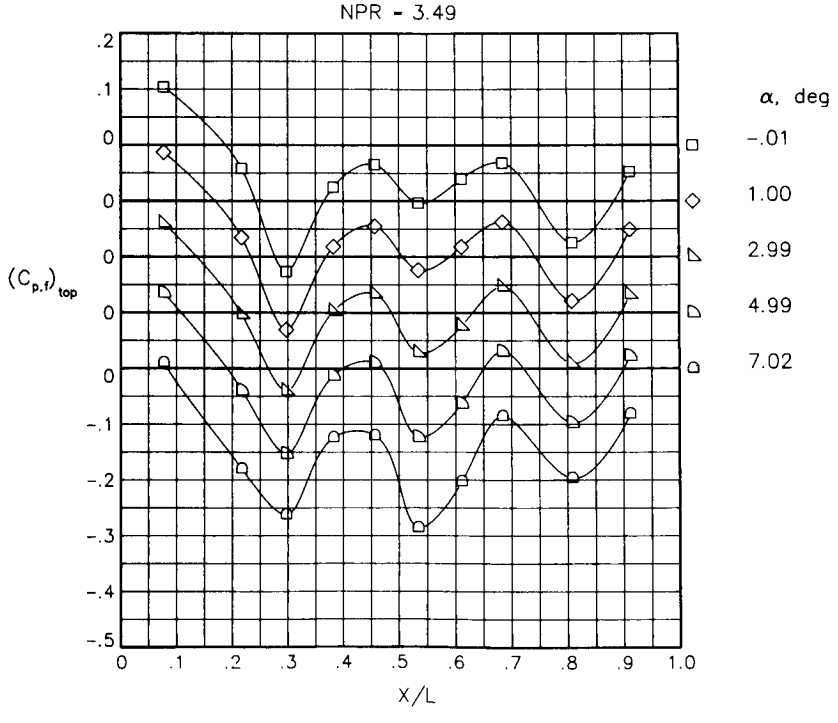

(b) M = 0.80.

Figure 13.- Continued.

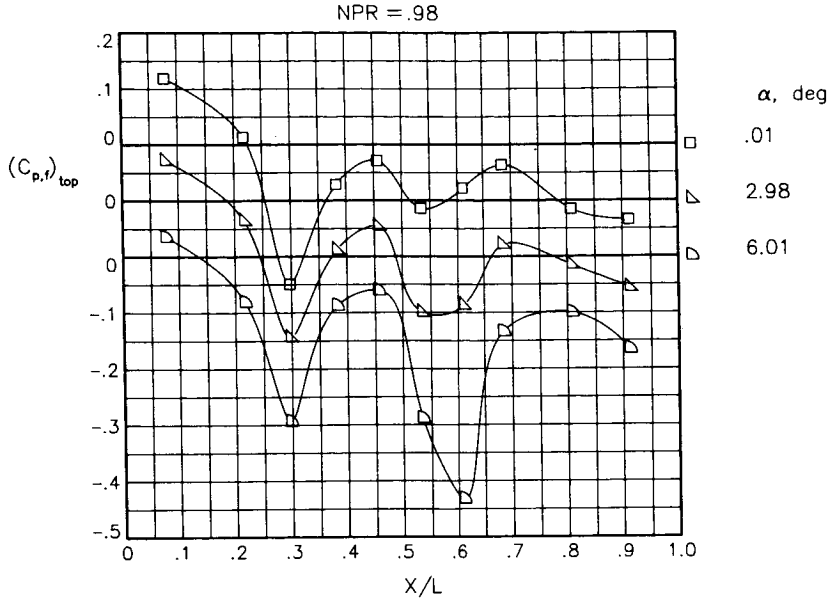

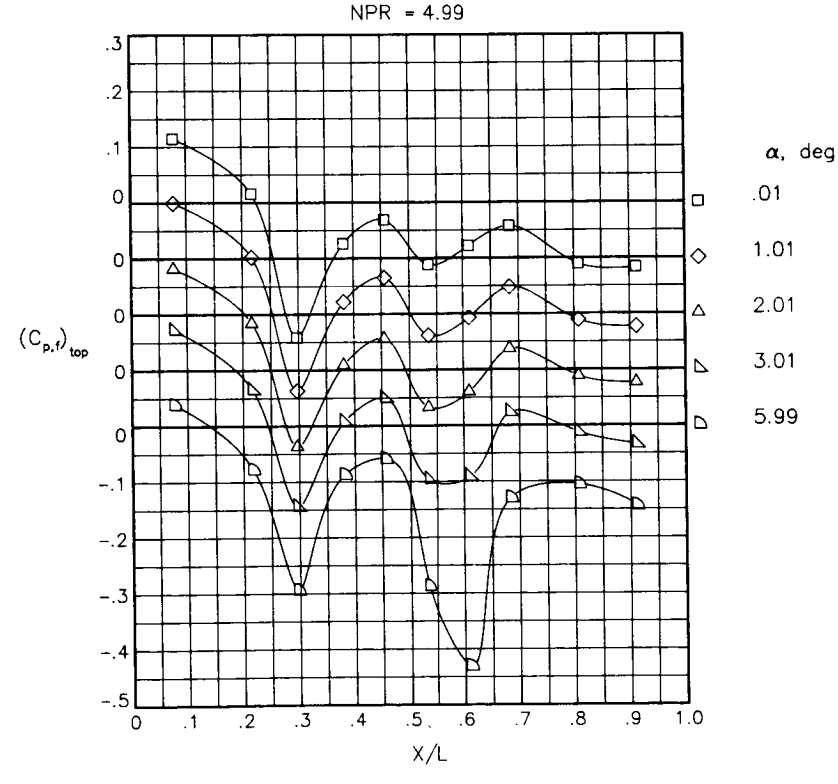

(c) M = 0.90.

Figure 13.- Concluded.

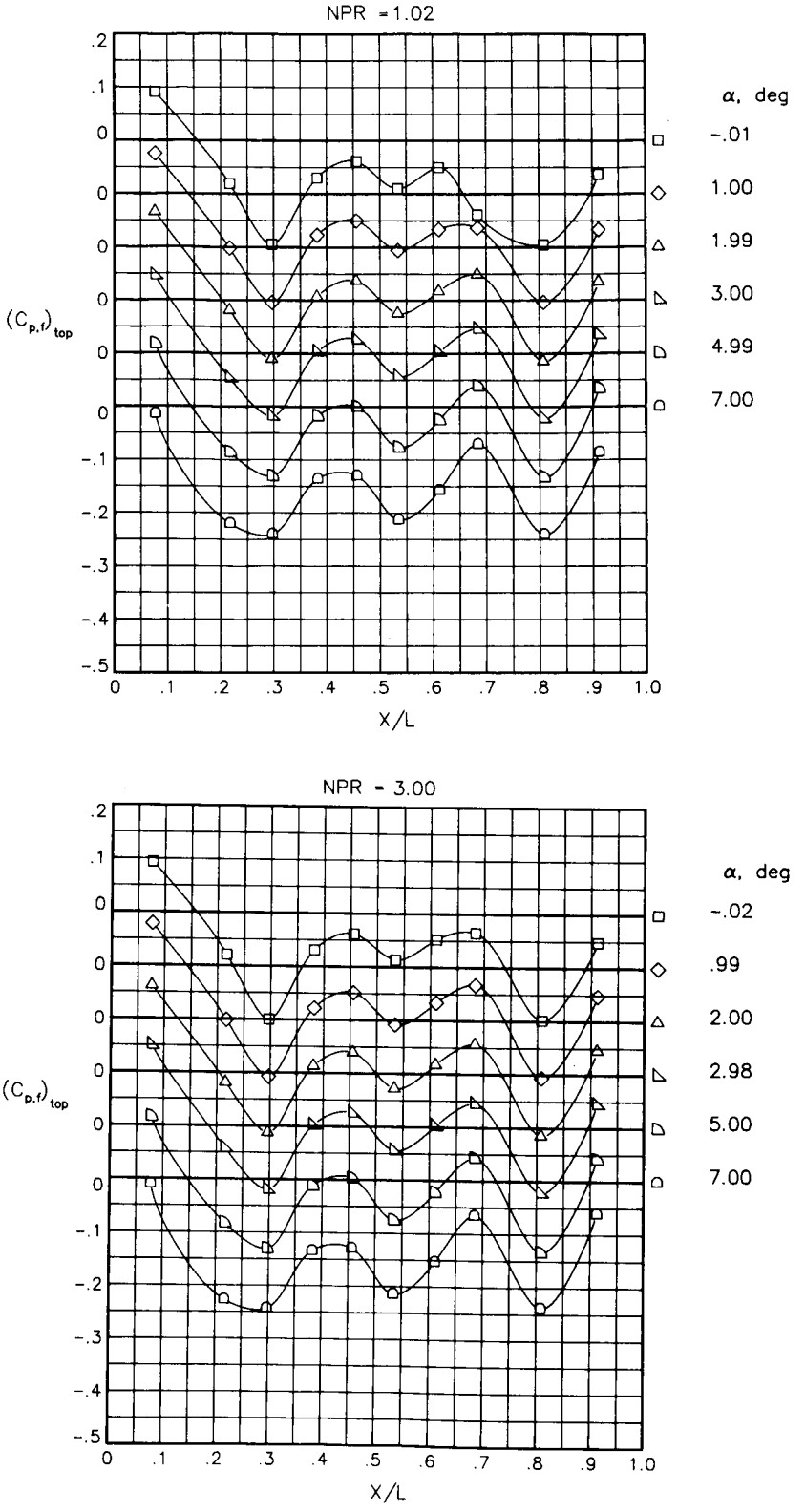

(a) M = 0.60.

Figure 14.- Static-pressure-coefficient distributions on top of fuselage along centerline for the model with all fuselage modifications. β_n = 18.45°; δ_h = -2°.

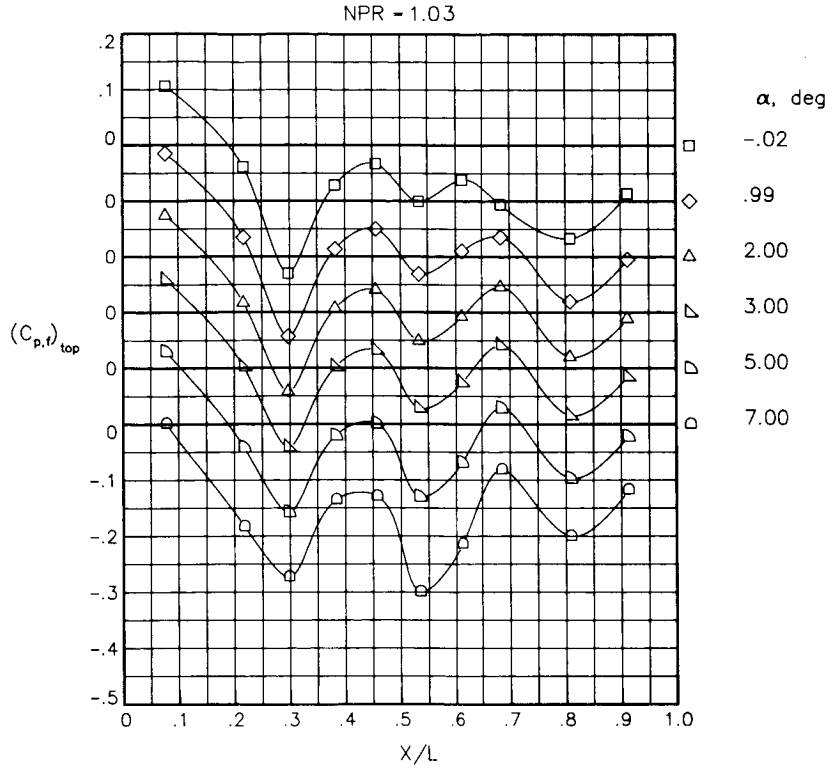

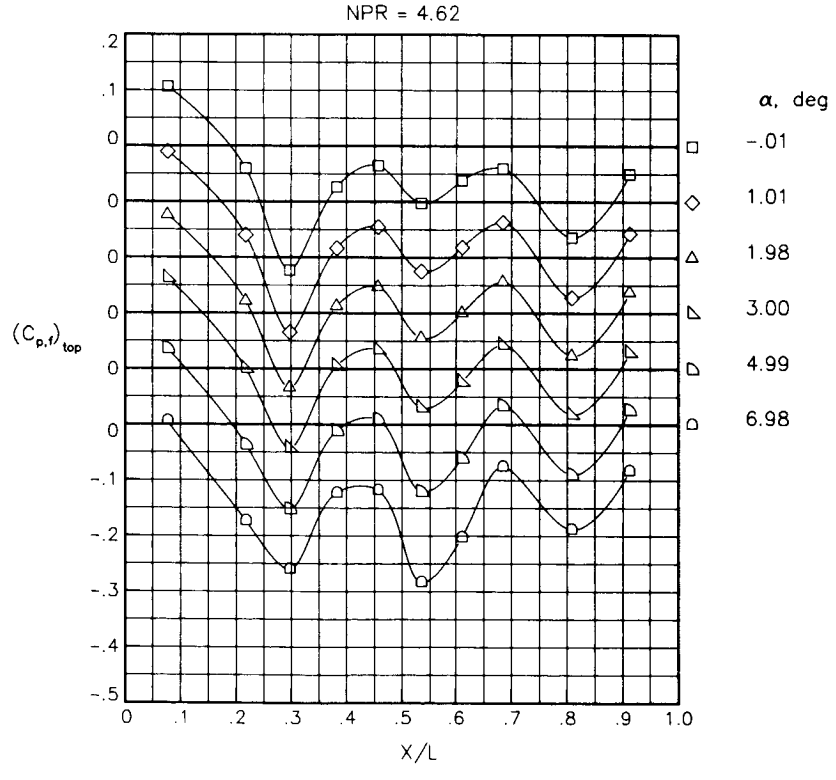

(b) M = 0.80.

Figure 14.- Continued.

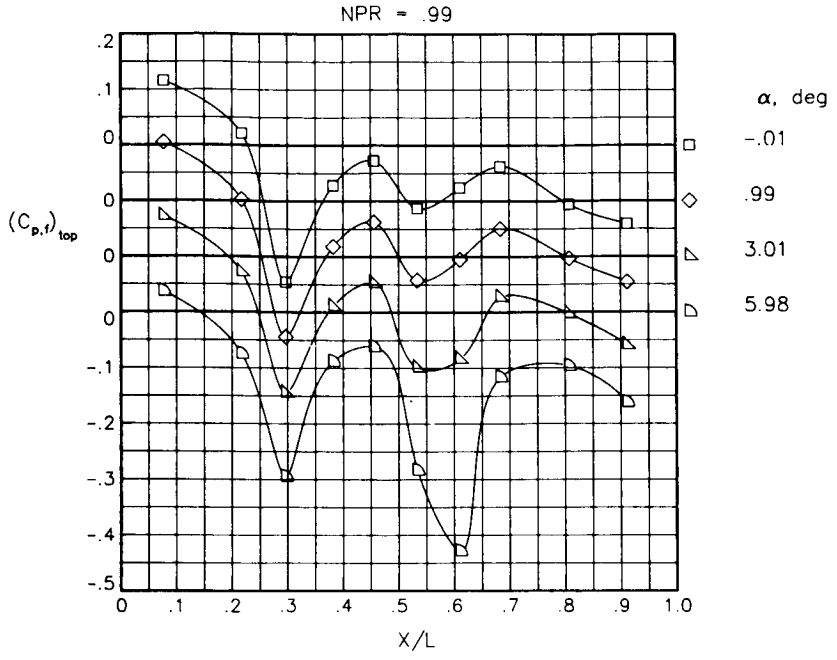

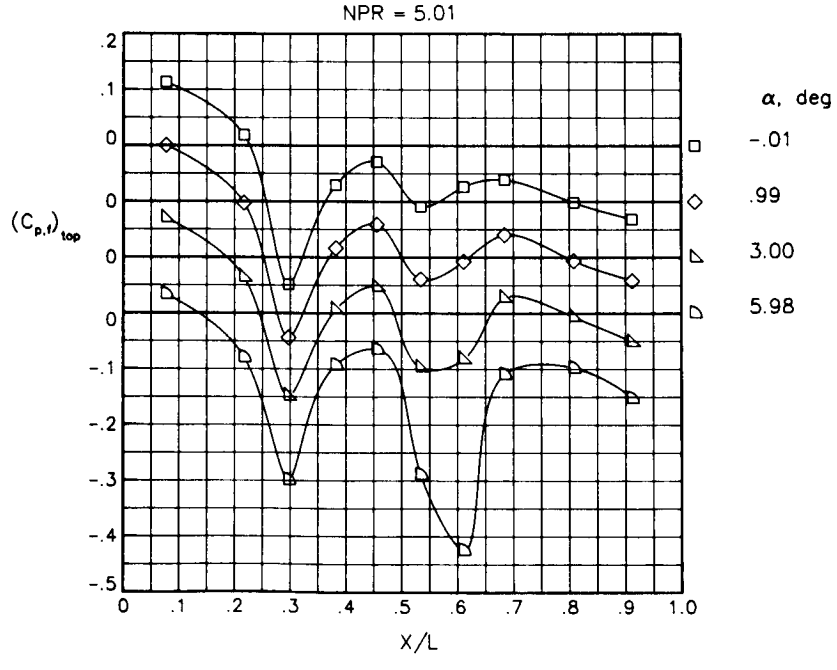

(c) M = 0.90.

Figure 14.- Concluded.

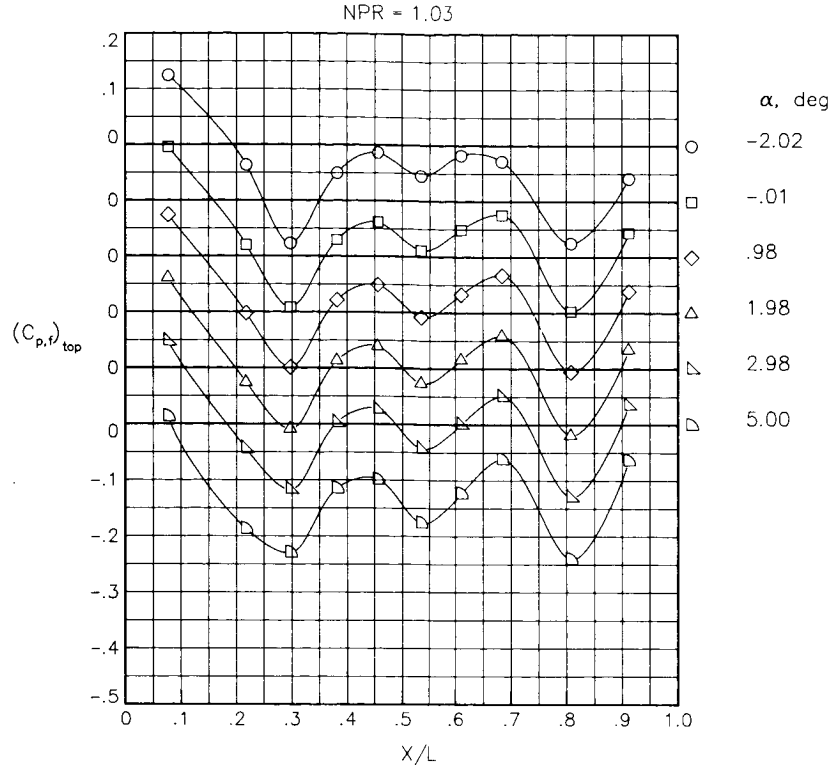

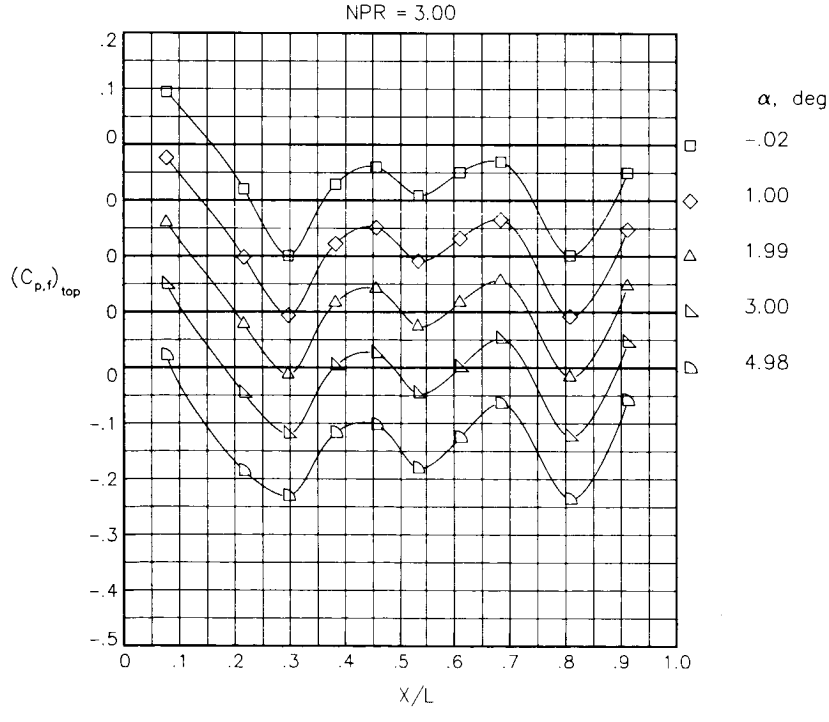

(a) M = 0.60.

Figure 15.- Static-pressure-coefficient distributions on top of fuselage along centerline for the model with all fuselage modifications. β_n = 18.45°.

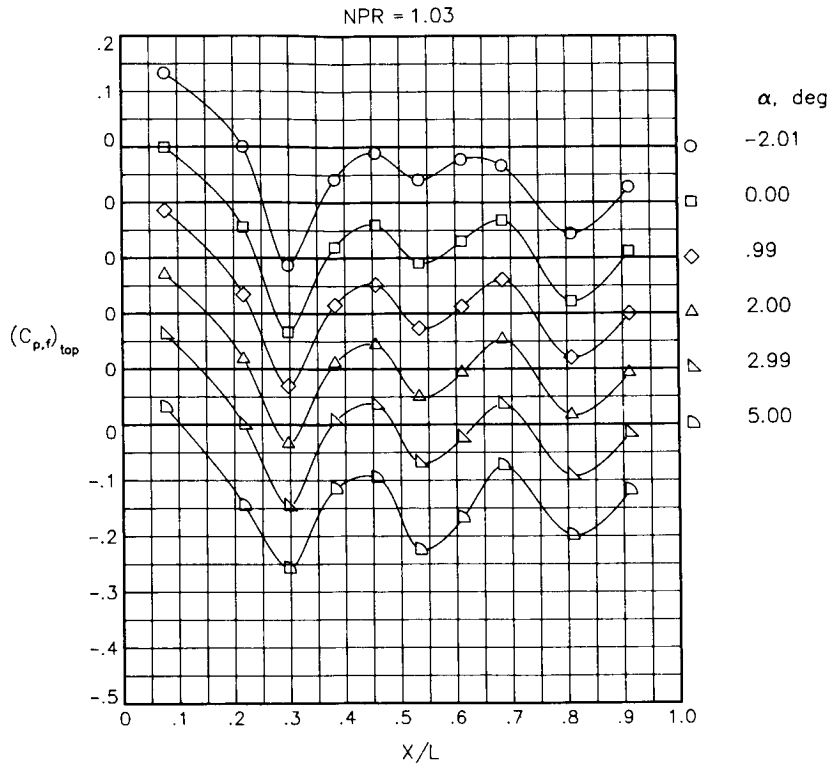

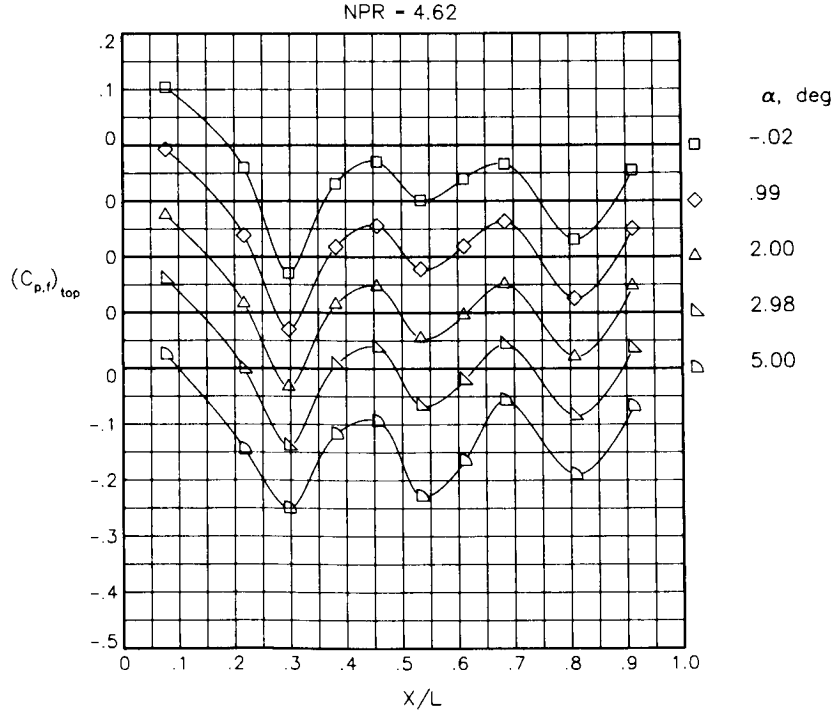

(b) M = 0.80.

Figure 15.- Continued.

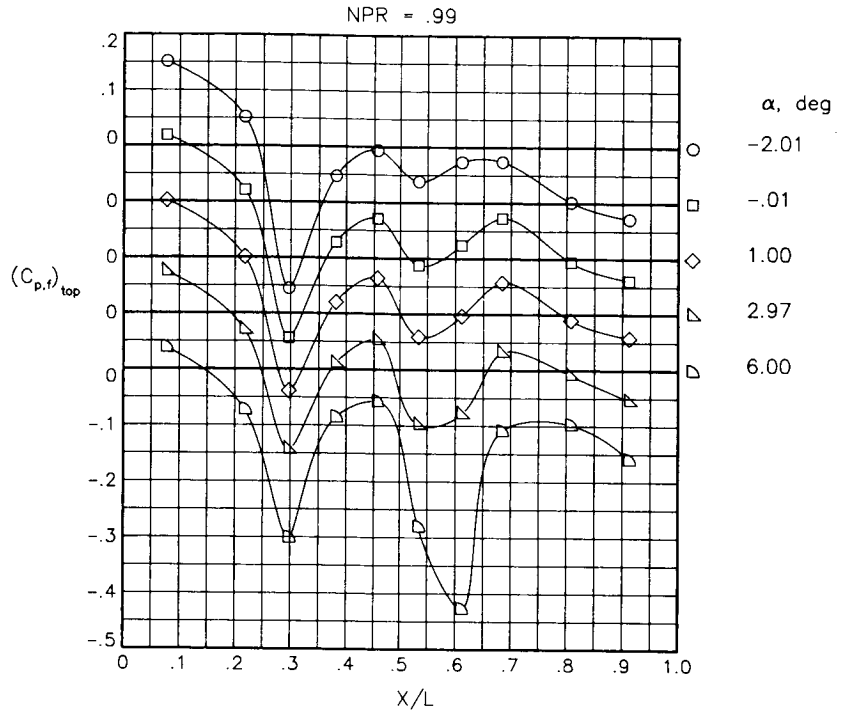

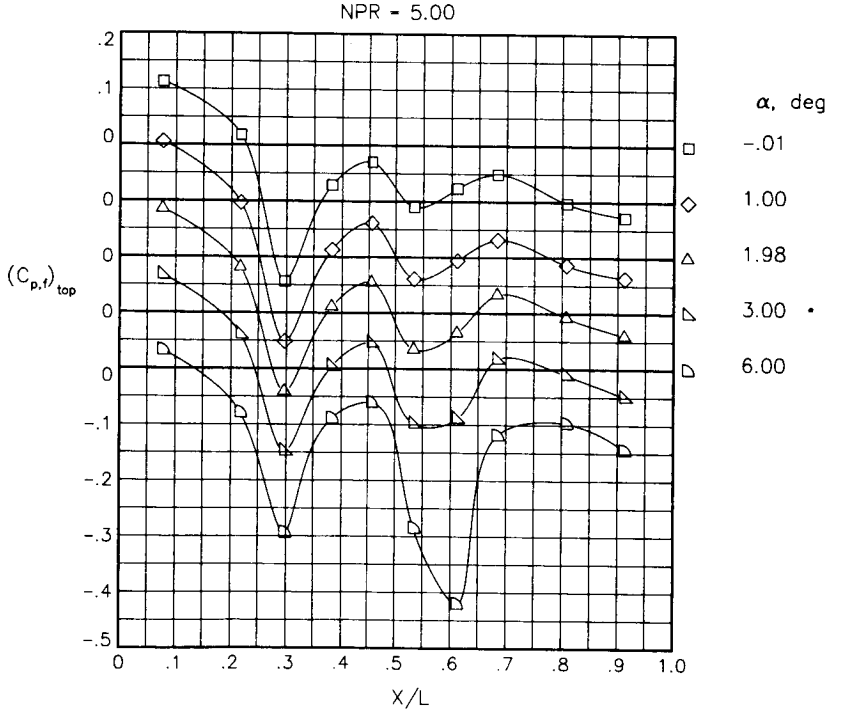

(c) M = 0.90.

Figure 15.- Concluded.

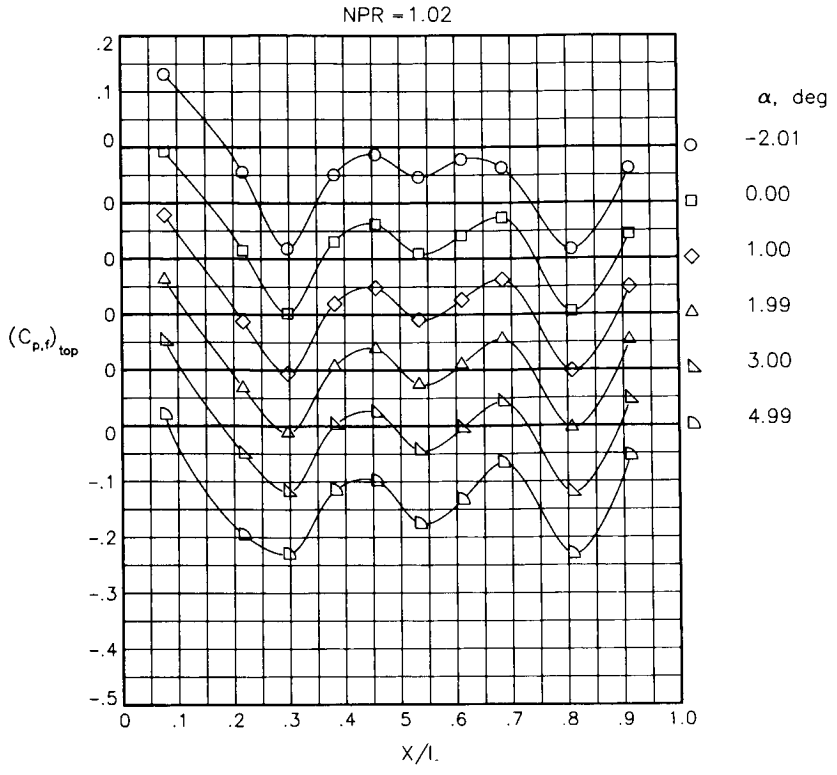

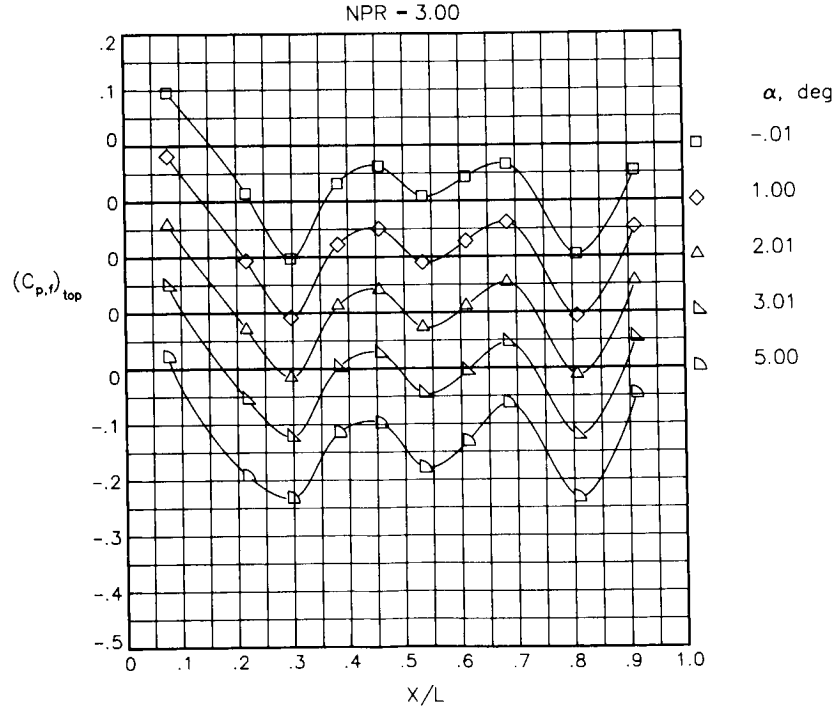

(a) M = 0.60.

Figure 16.- Static-pressure-coefficient distributions on top of fuselage along centerline for the model with all fuselage modifications. β_n = 18.45°. Repeat data.

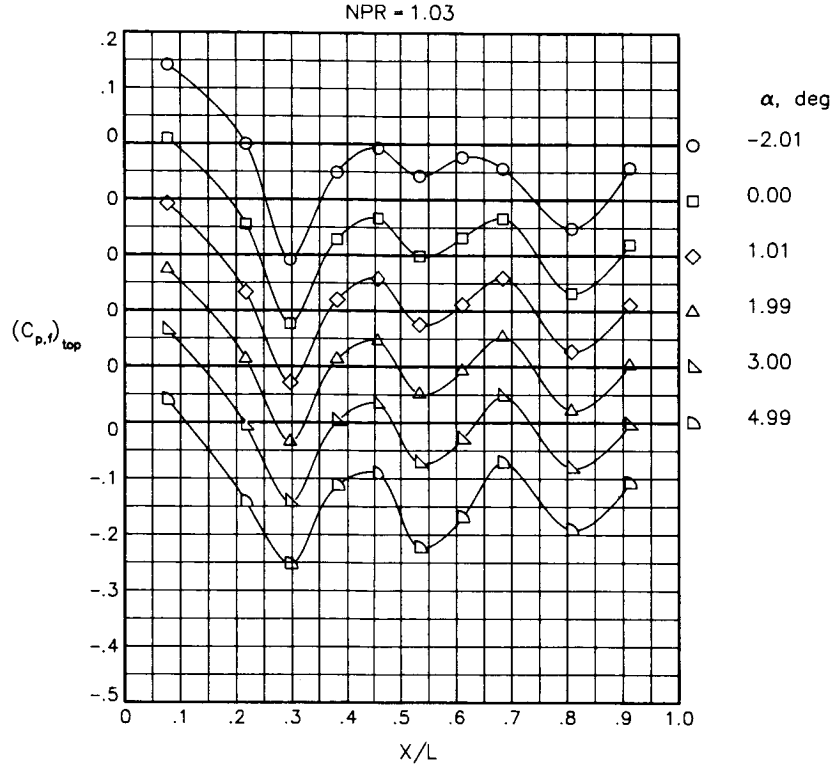

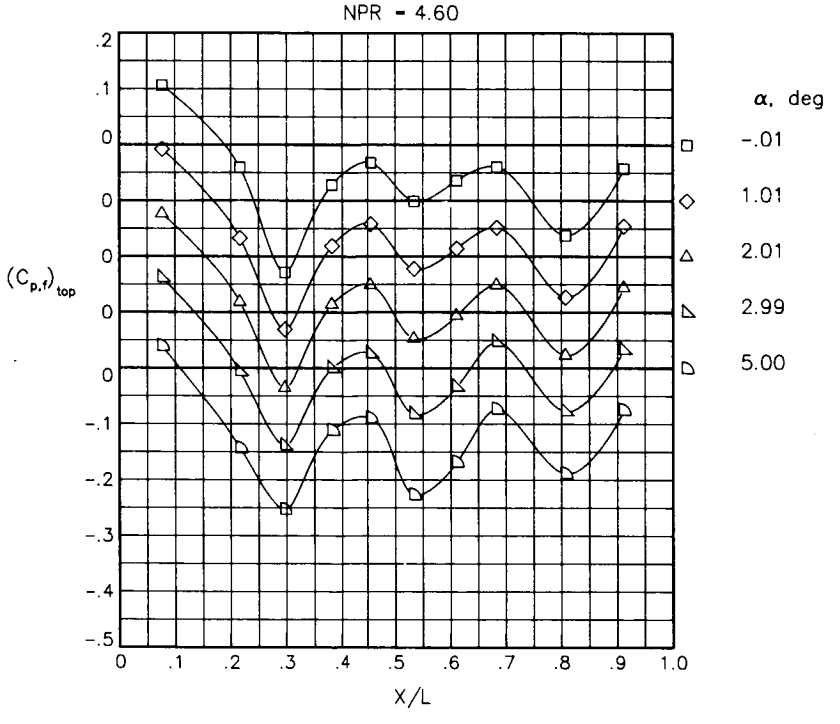

(b) M = 0.80.

Figure 16.- Continued.

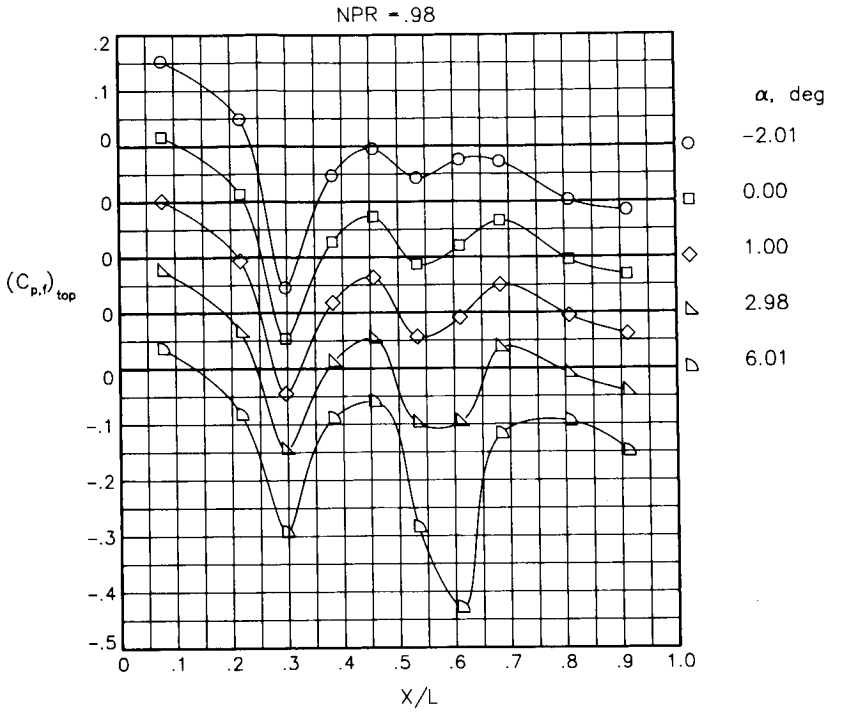

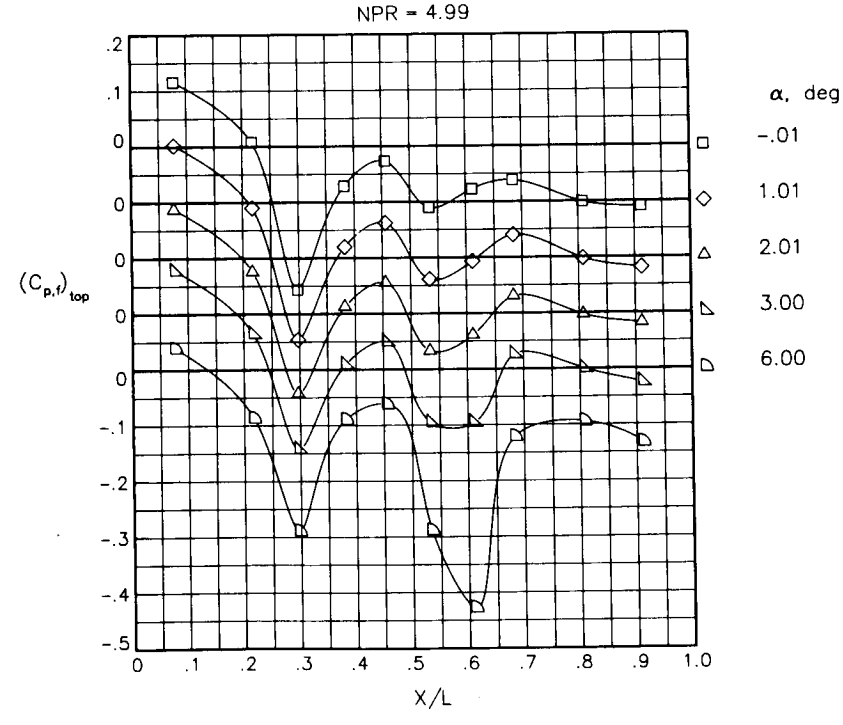

(c) M = 0.90.

Figure 16.- Concluded.

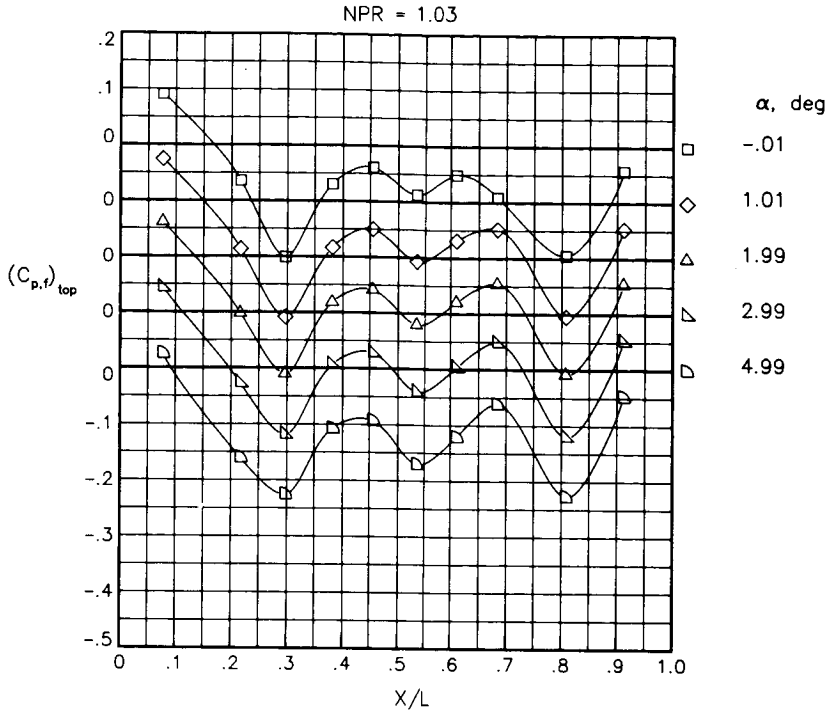

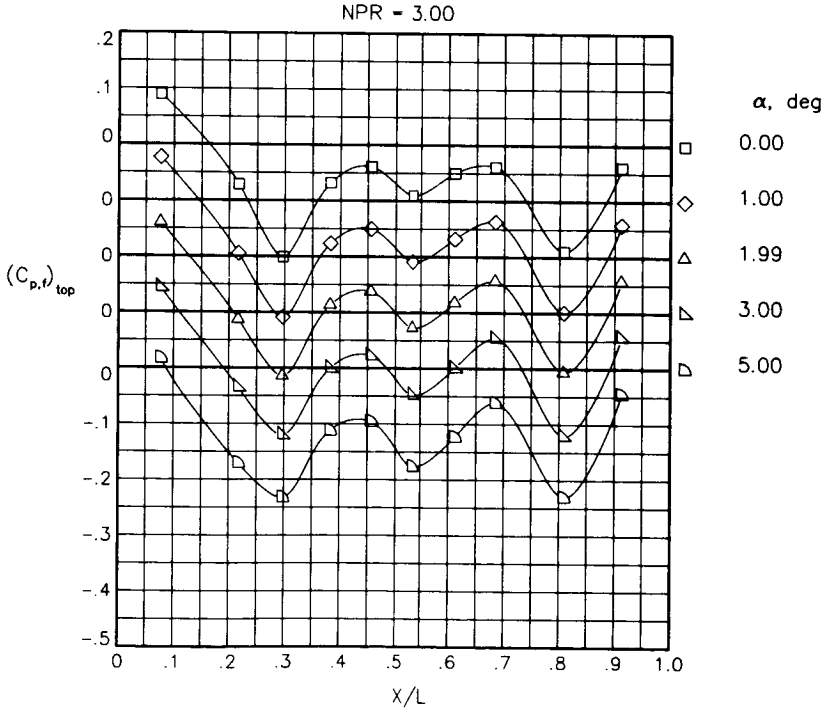

(a) M = 0.60.

Figure 17.- Static-pressure-coefficient distributions on top of fuselage along centerline for the model with all fuselage modifications. β_n = 18.45°; δ_h = -5°.

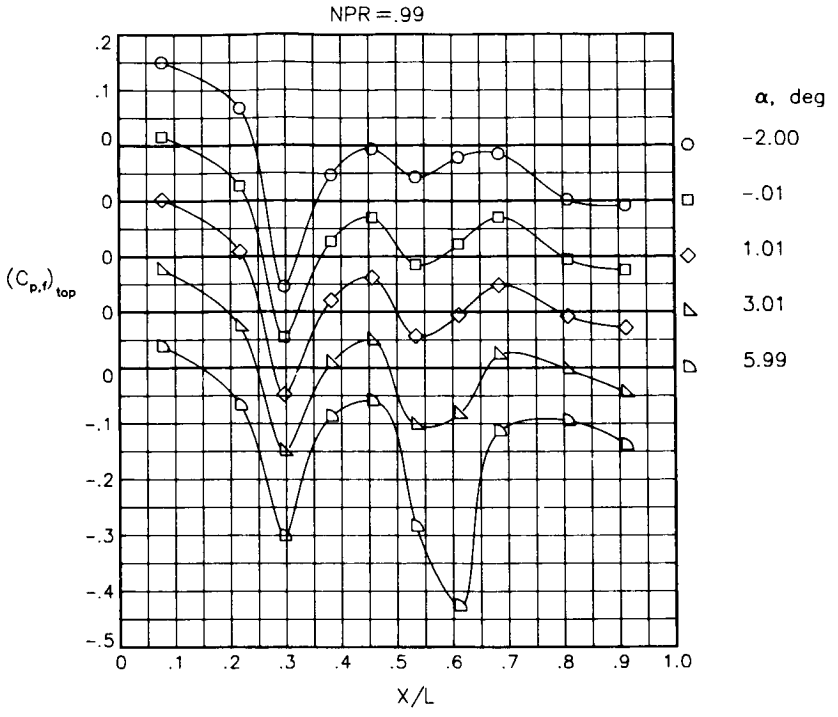

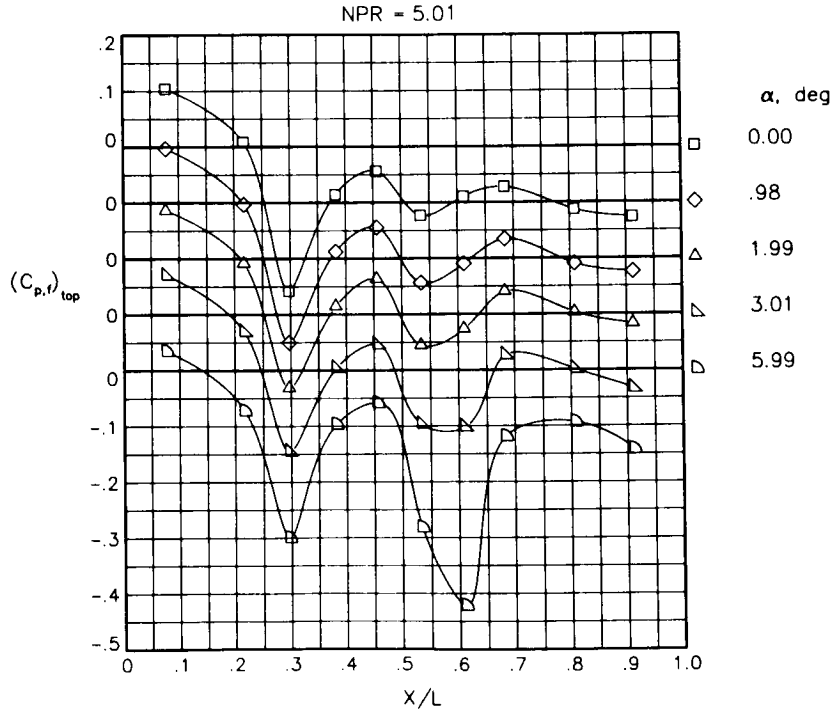

(b) M = 0.90.

Figure 17.- Concluded.

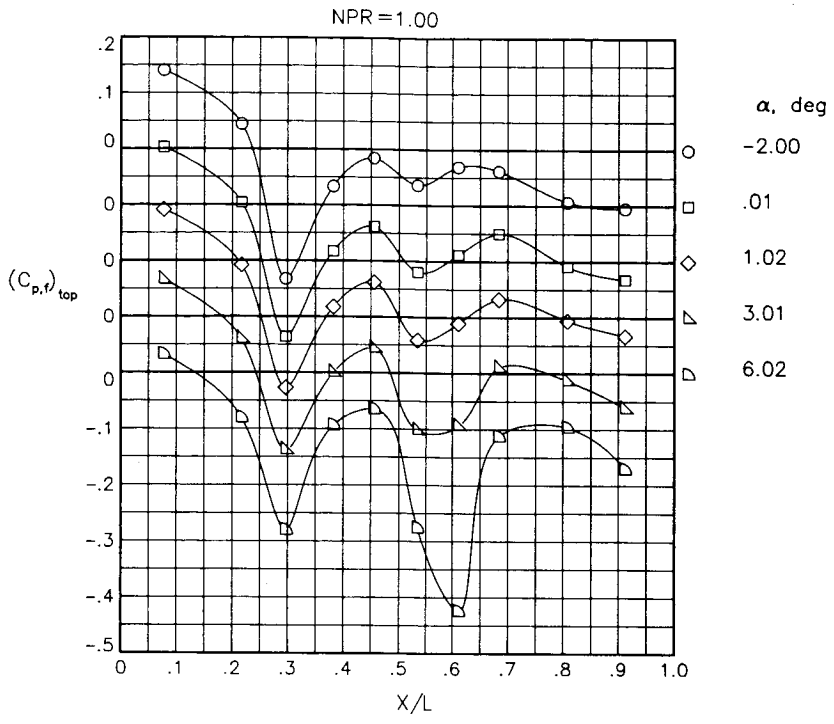

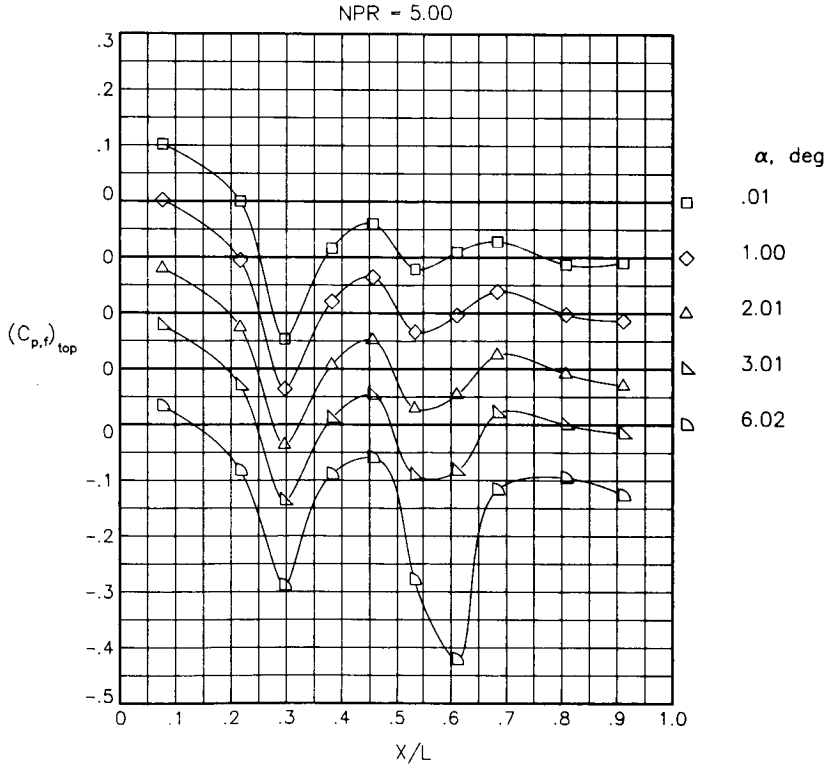

(a) M = 0.90.

Figure 18.- Static-pressure-coefficient distributions on top of fuselage along centerline for the model with all fuselage modifications. β_n = 15.05°.

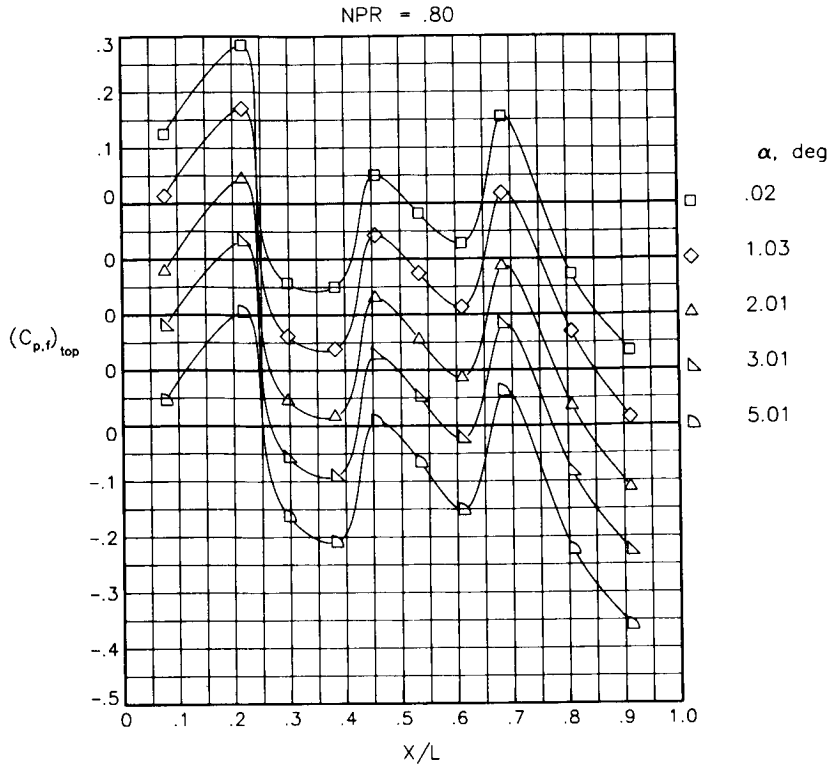

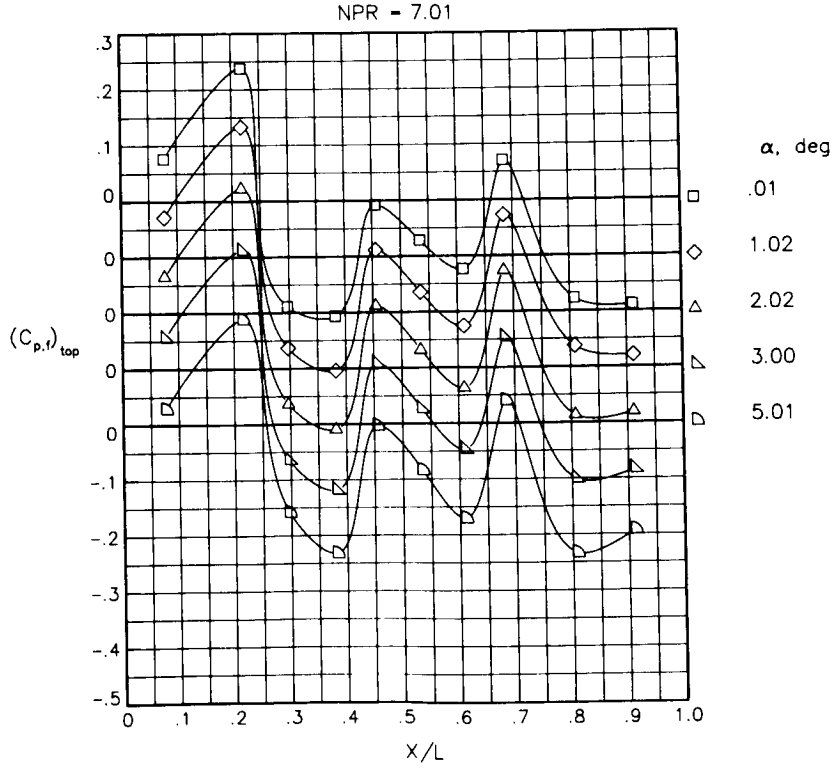

(b) M = 1.20.

Figure 18.- Concluded.

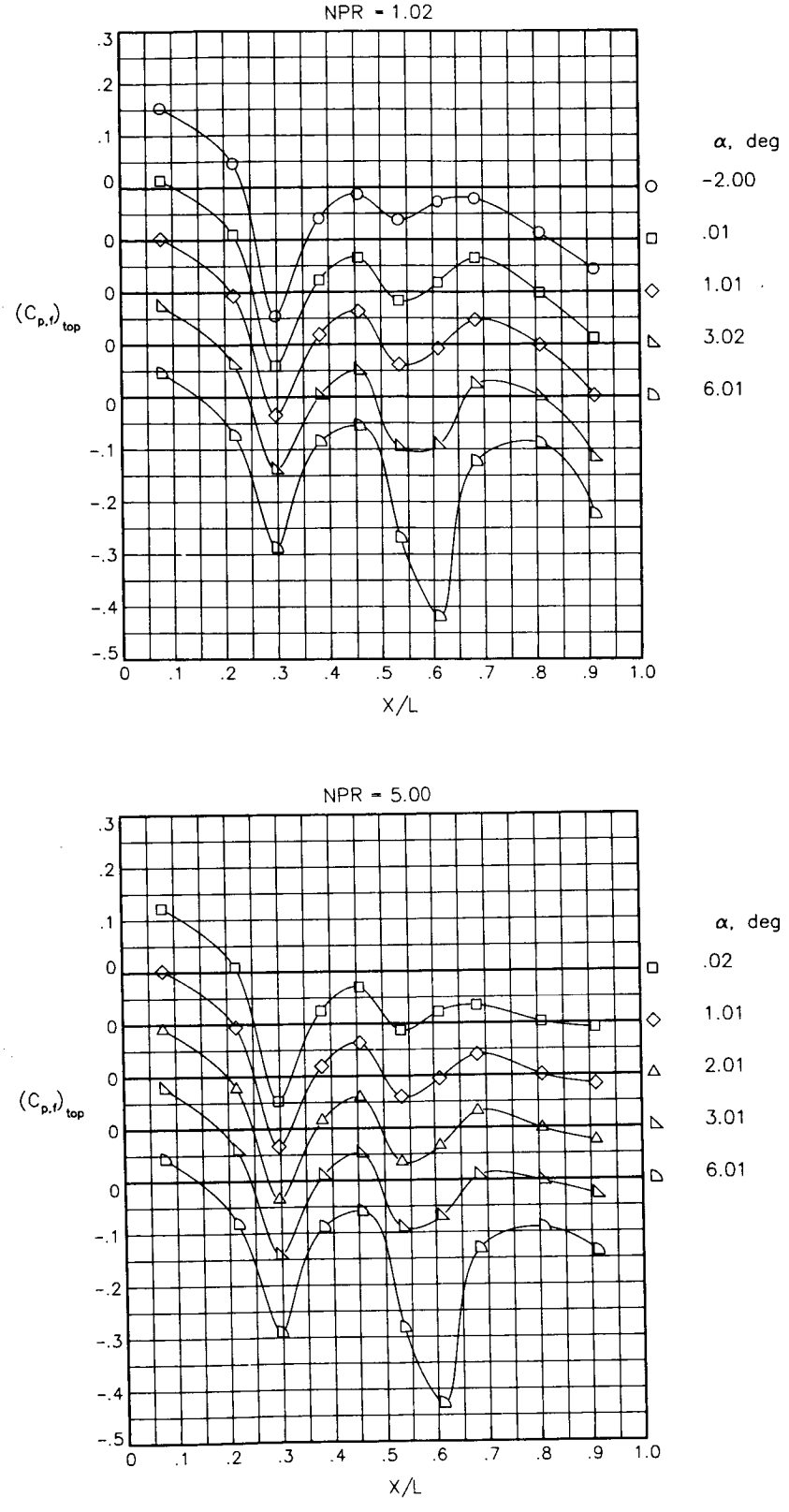

(a) M = 0.90.

Figure 19.- Static-pressure-coefficient distributions on top of fuselage along centerline for the model with all fuselage modifications. β_n = 9.63°.

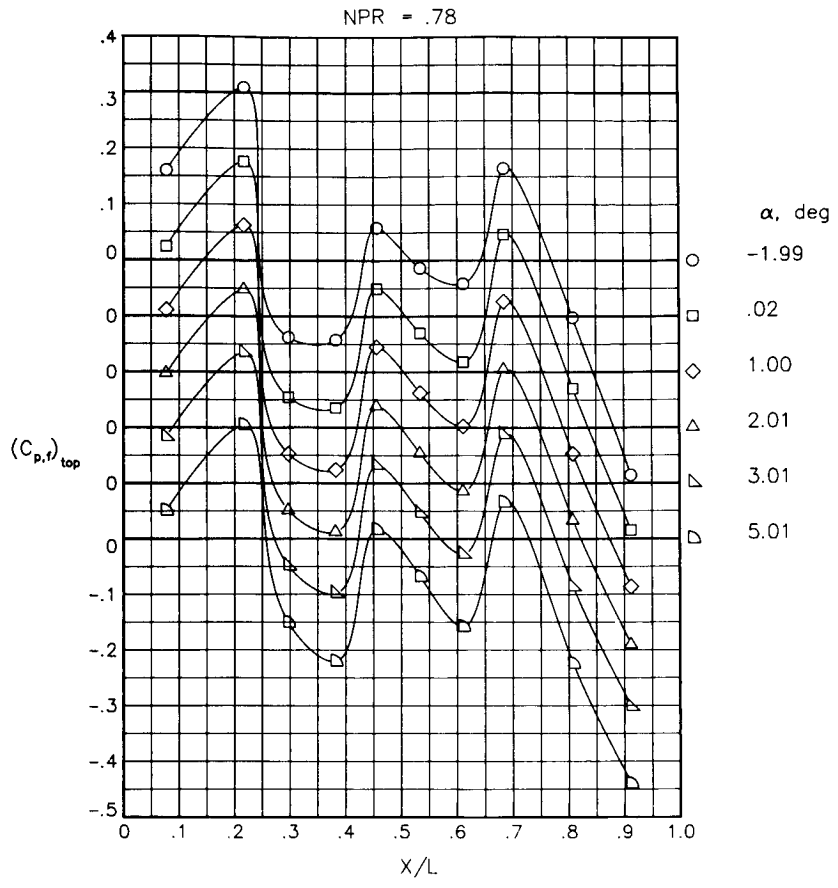

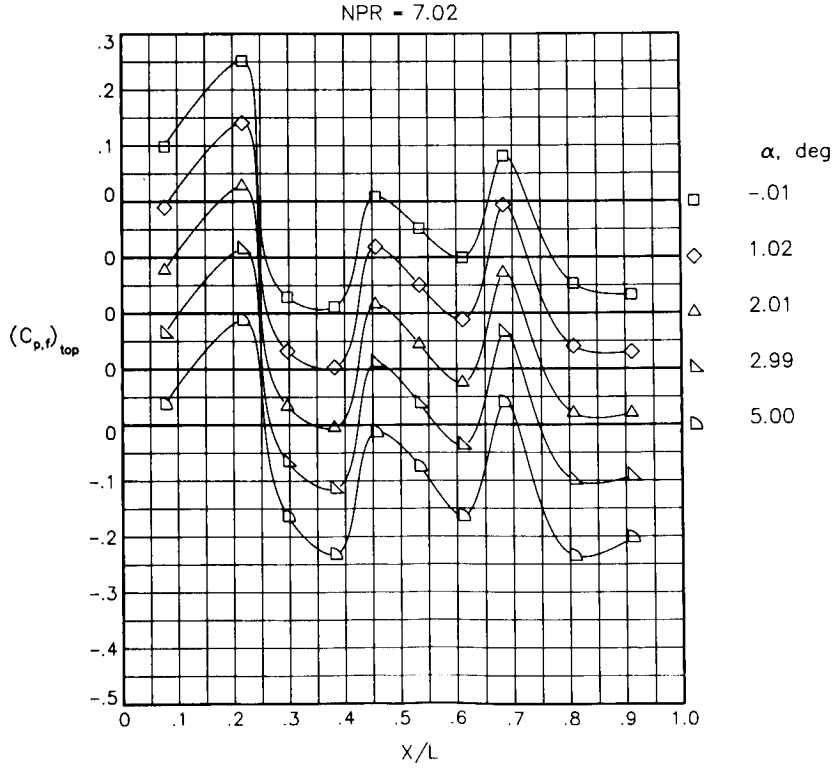

(b) M = 1.20.

Figure 19.- Concluded.

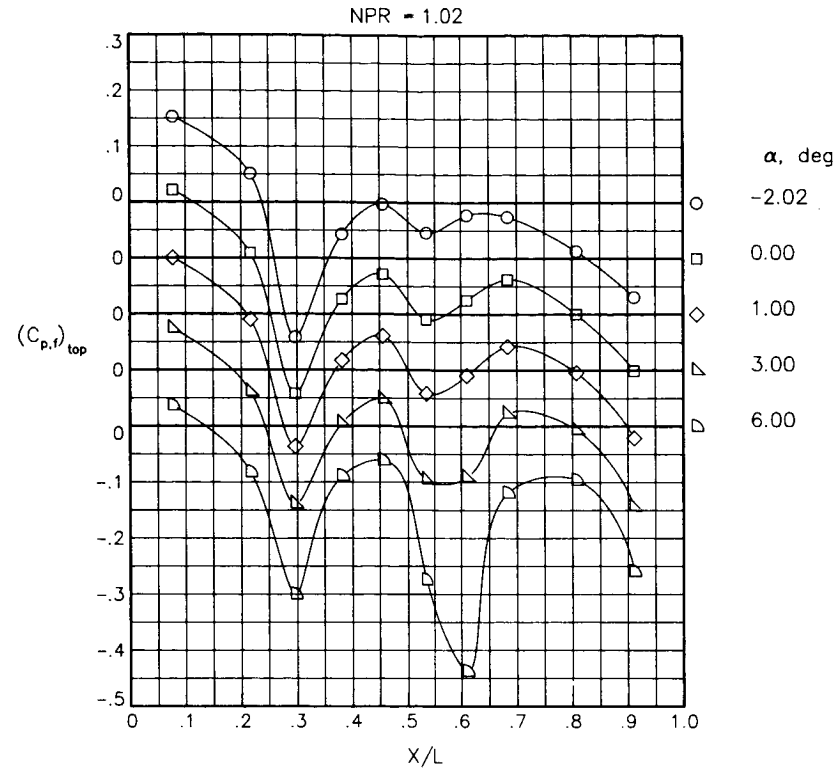

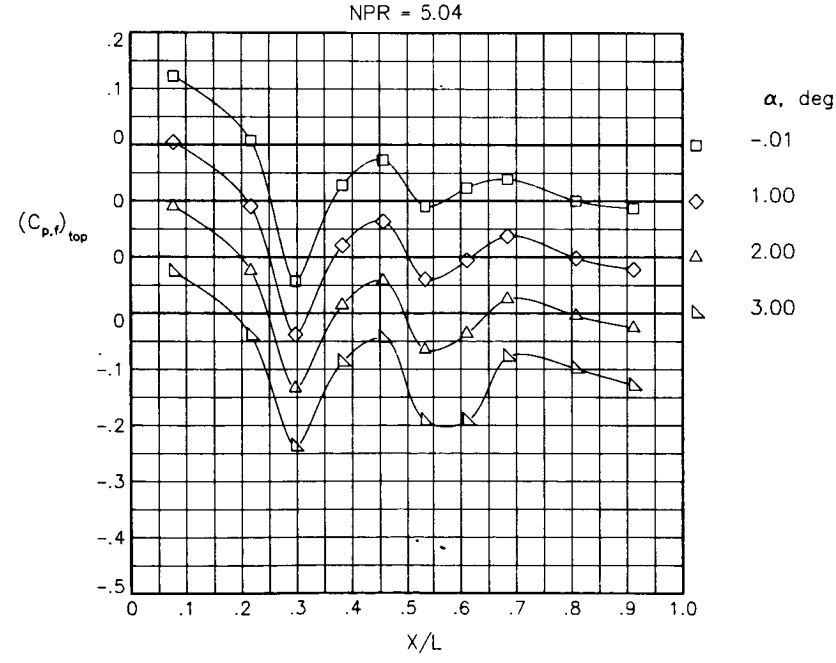

(a) M = 0.90.

Figure 20.- Static-pressure-coefficient distributions on top fuselage along centerline for the model with all fuselage modifications. β_n = 7.72°.

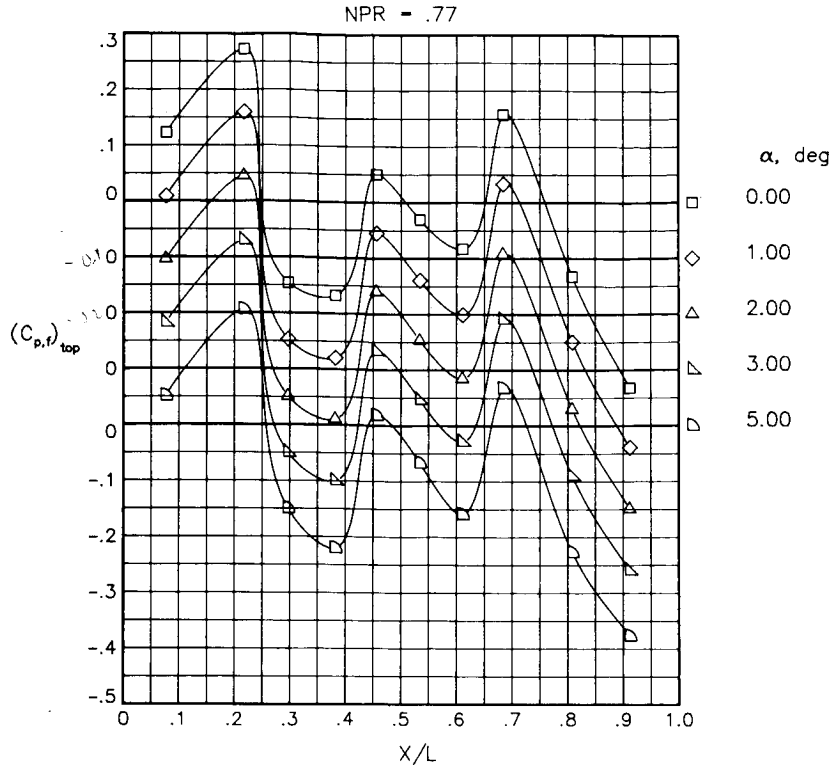

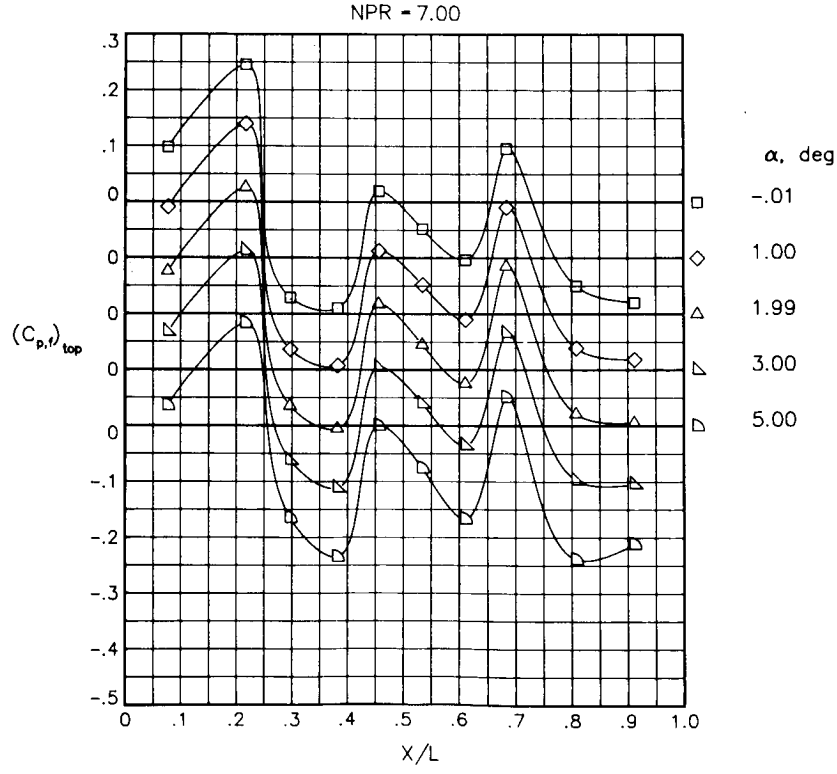

(b) M = 1.20.

Figure 20.- Concluded.

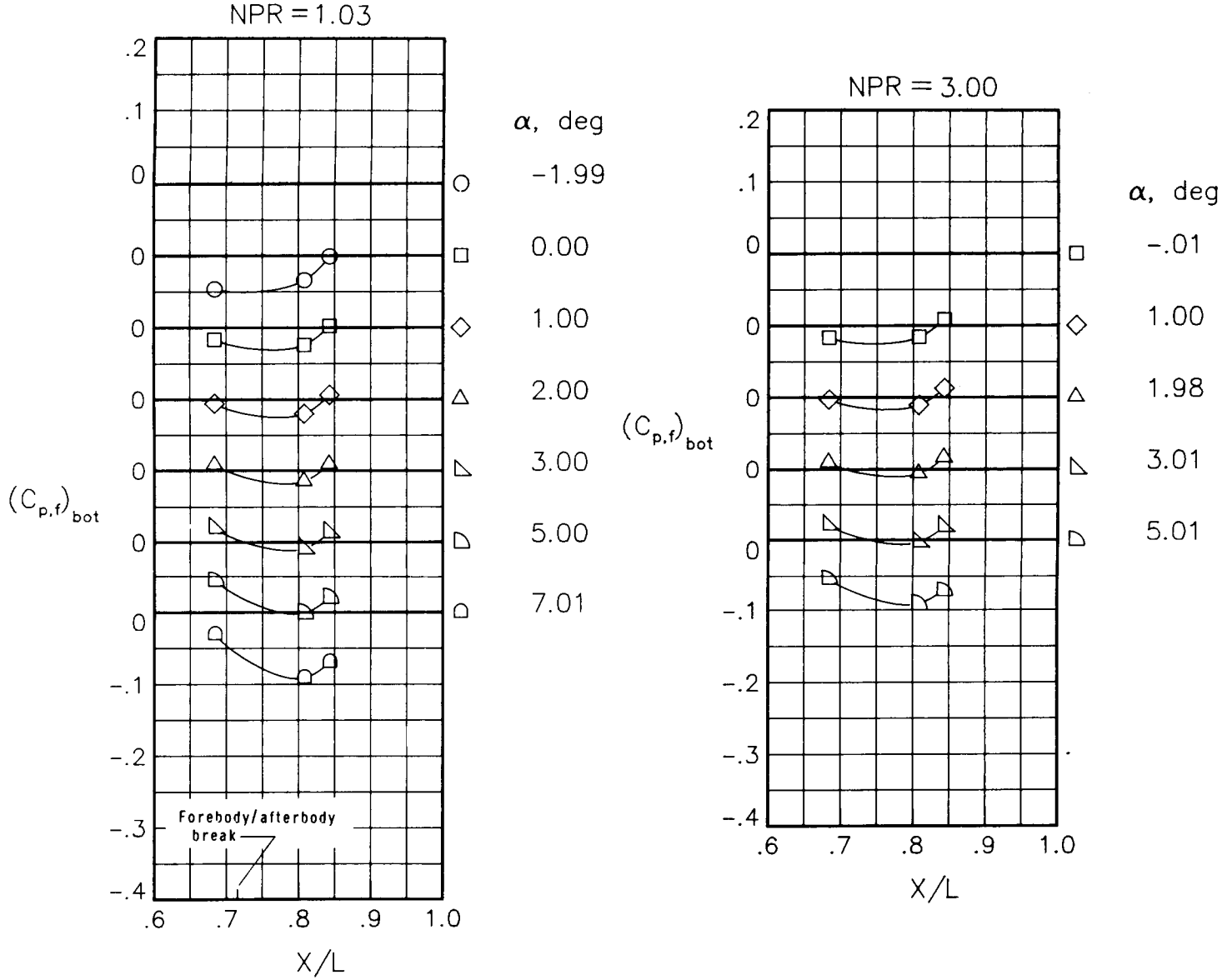

(a) M = 0.60.

Figure 21.- Static-pressure-coefficient distributions on bottom of fuselage engine interfairing along centerline for the unmodified model. β_n = 18.45°.

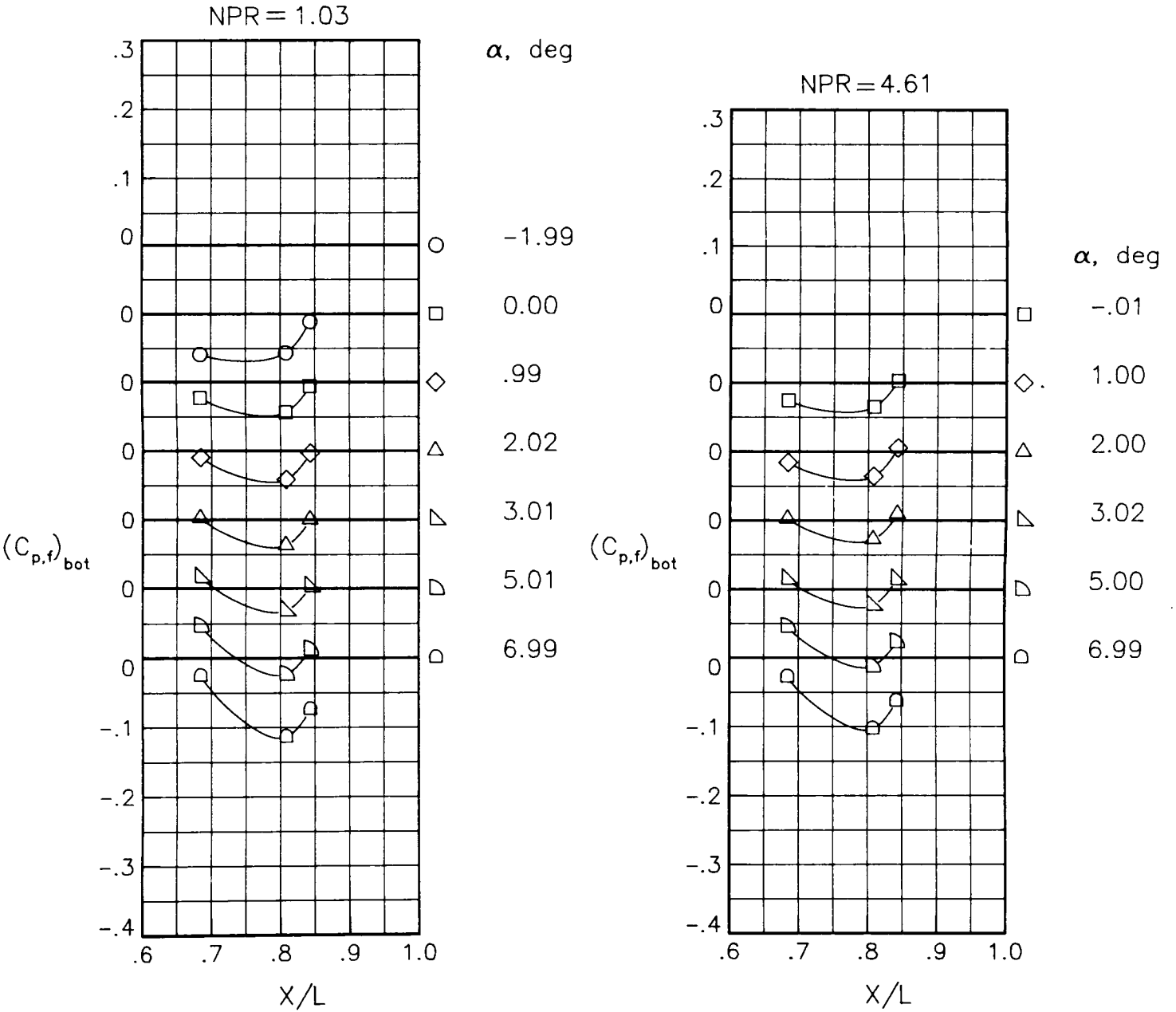

(b) M= 0.80.

Figure 21.- Continued.

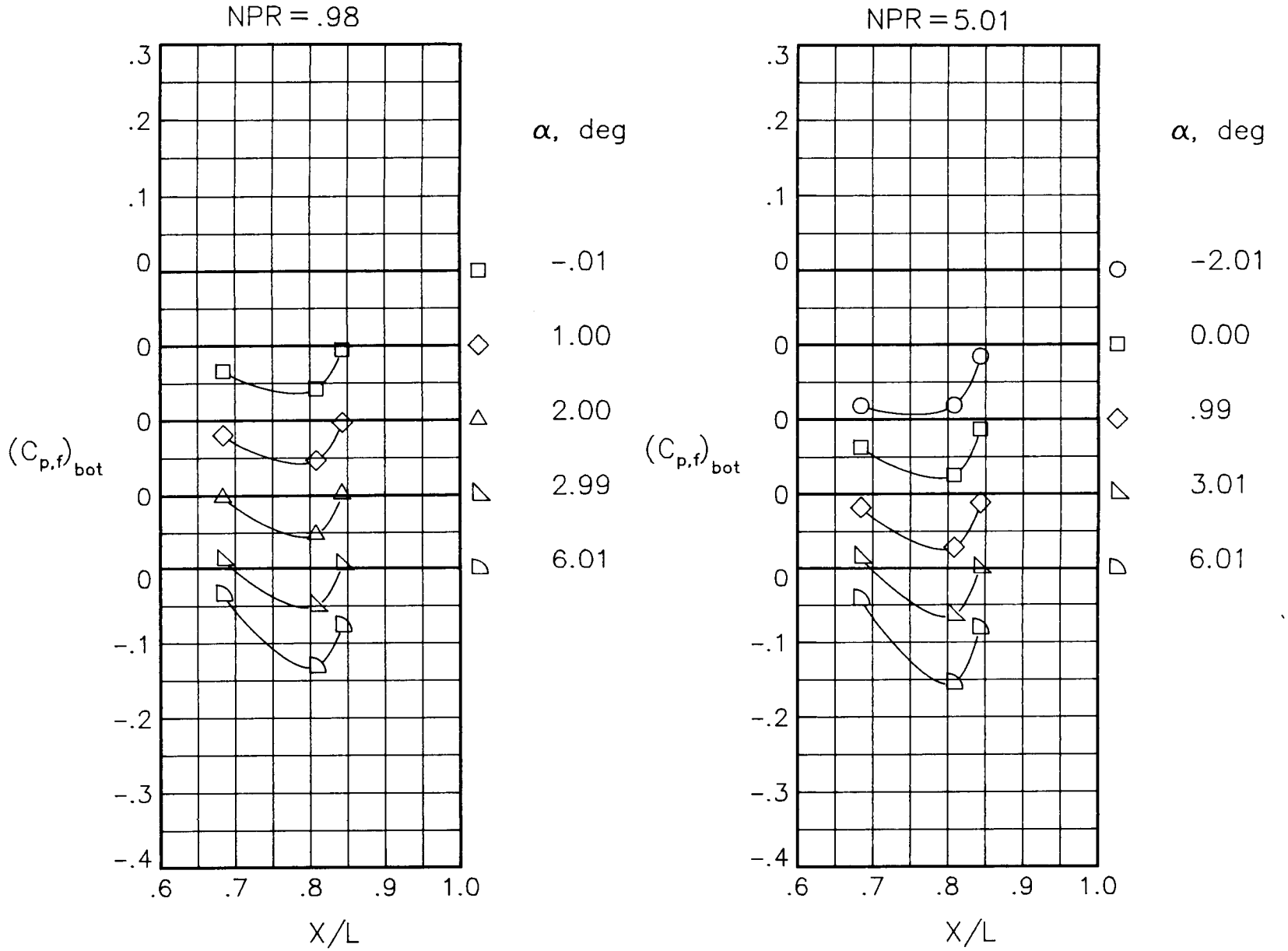

(c) M = 0.90.

Figure 21.- Concluded.

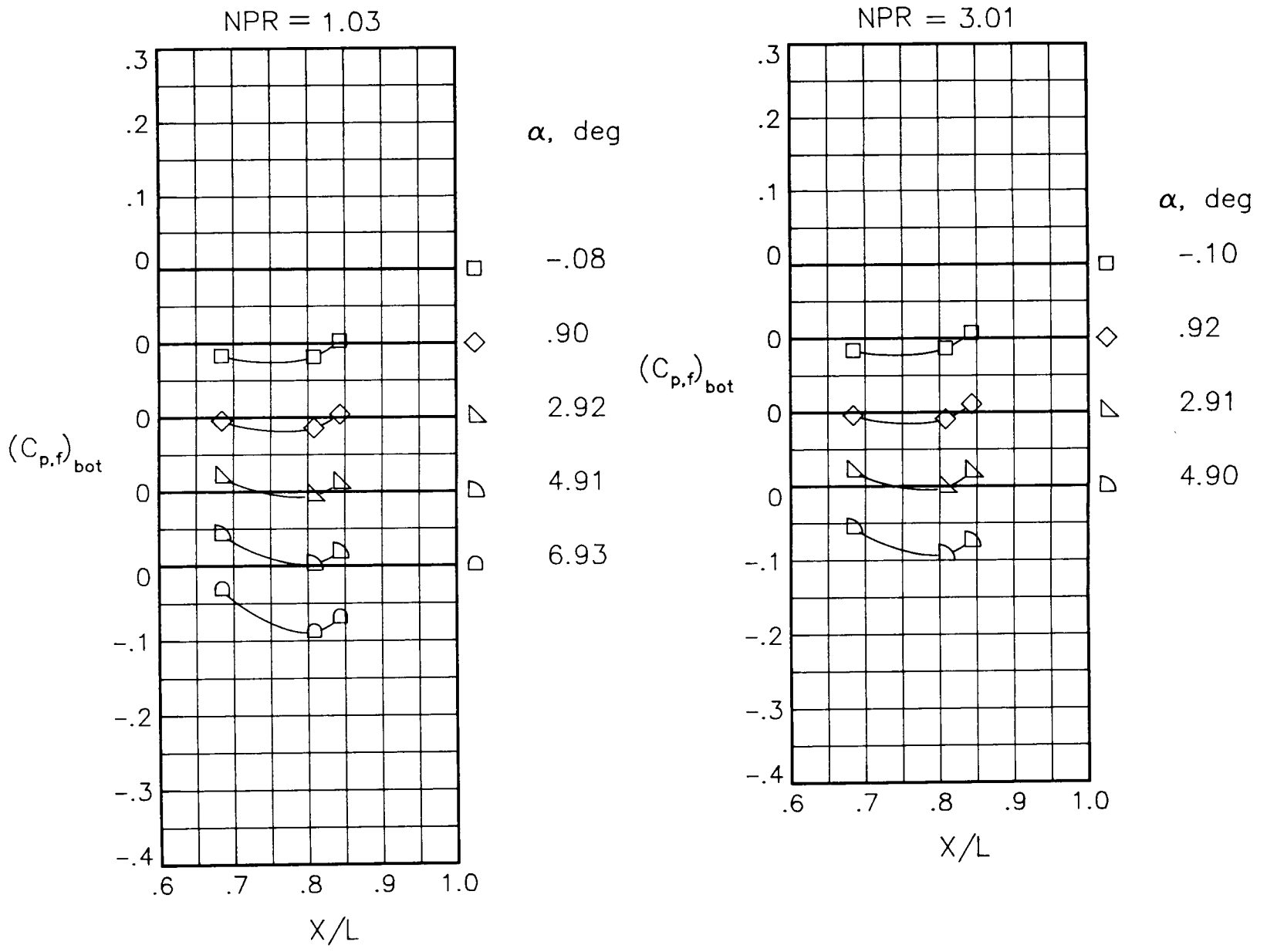

(a) M = 0.60.

Figure 22.- Static-pressure-coefficient distributions on bottom of fuselage engine interfairing along centerline for the model with nose boom. β_n = 18.45°.

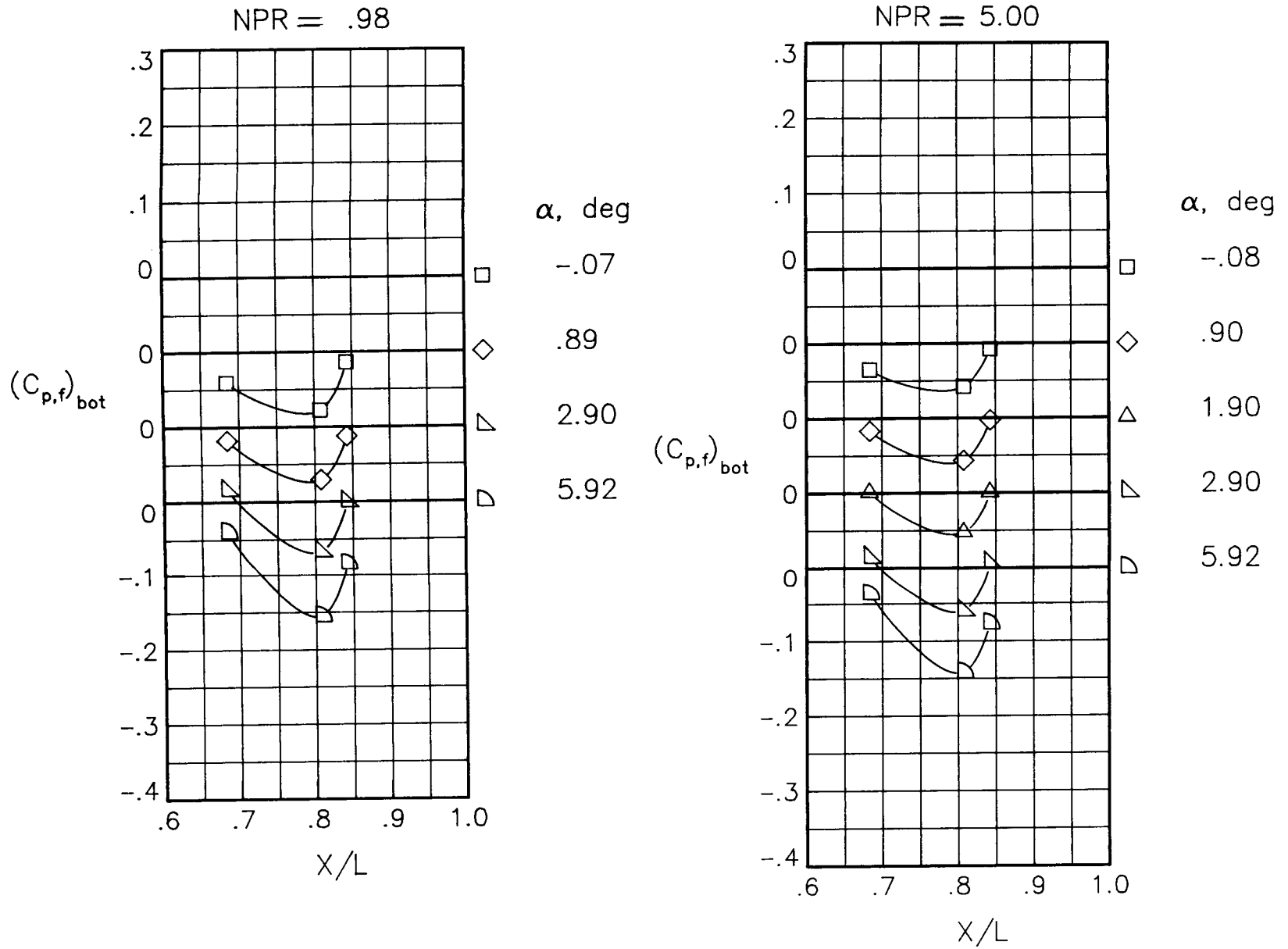

(b) M = 0.90.

Figure 22.- Concluded.

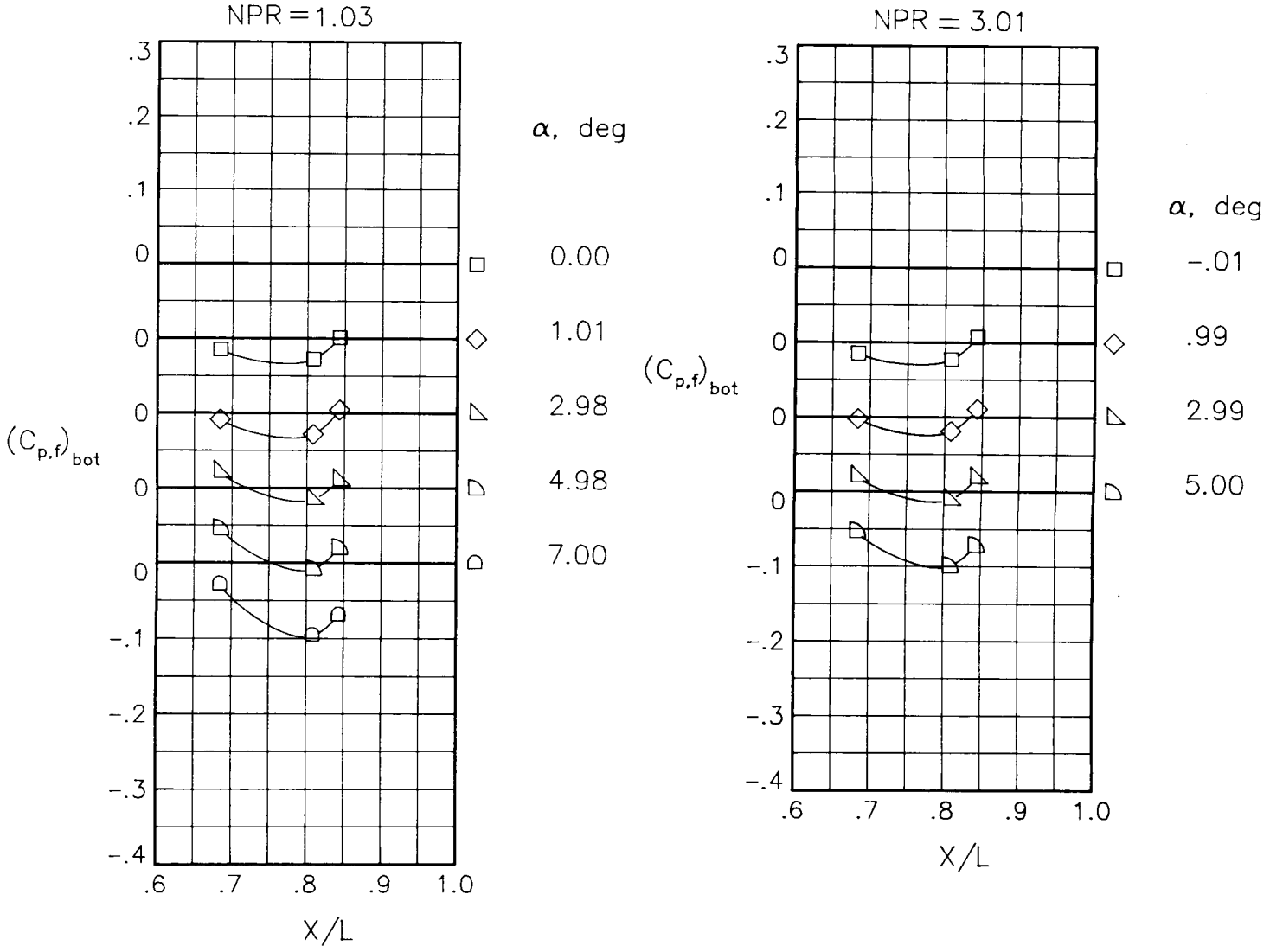

(a) M = 0.60.

Figure 23.- Static-pressure-coefficient distributions on bottom of fuselage engine interfairing along centerline for the model with nose boom, actuator fairings, and A/B vents. β_n = 18.45°.

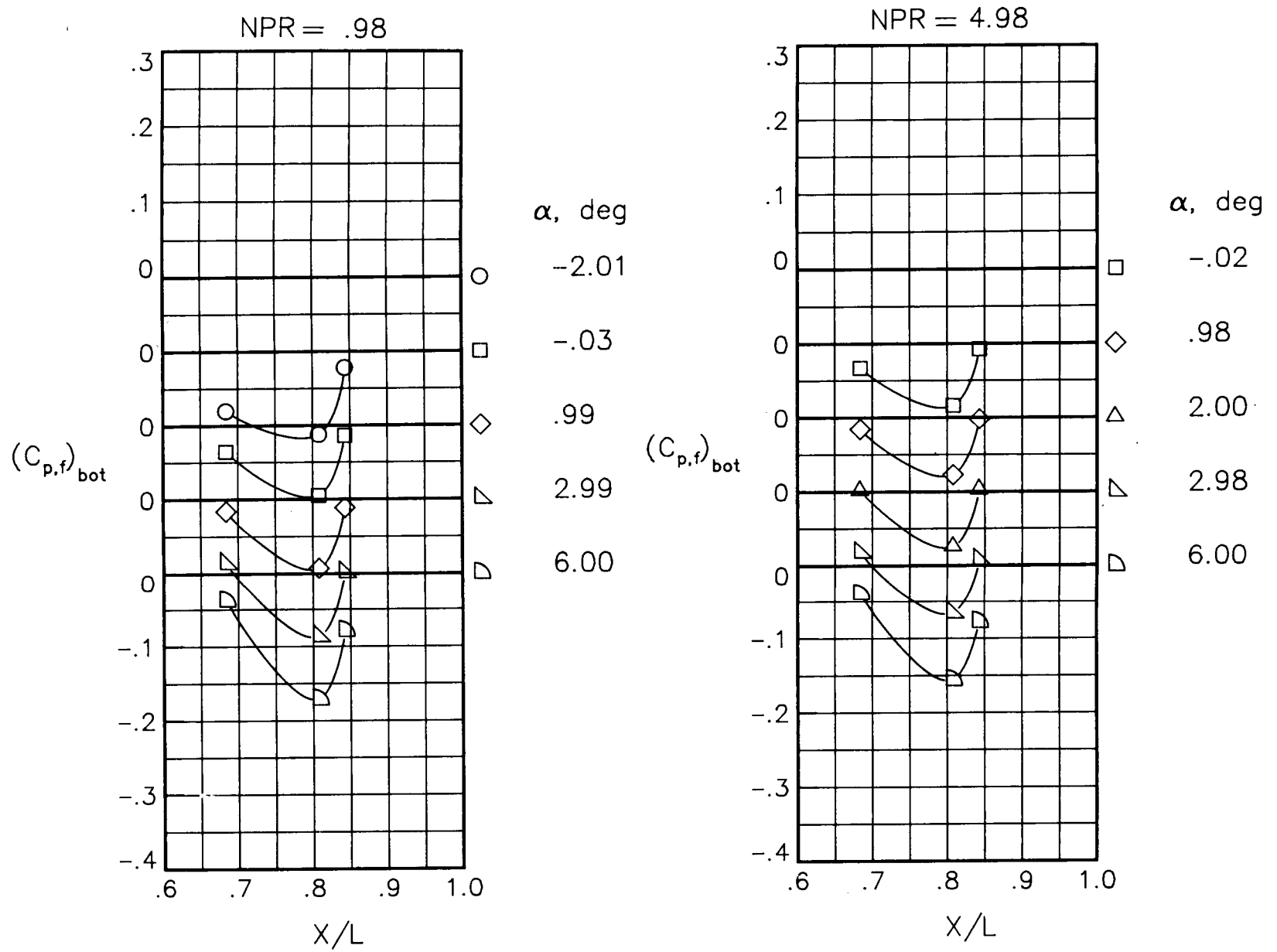

(b) M = 0.90.

Figure 23.- Concluded.

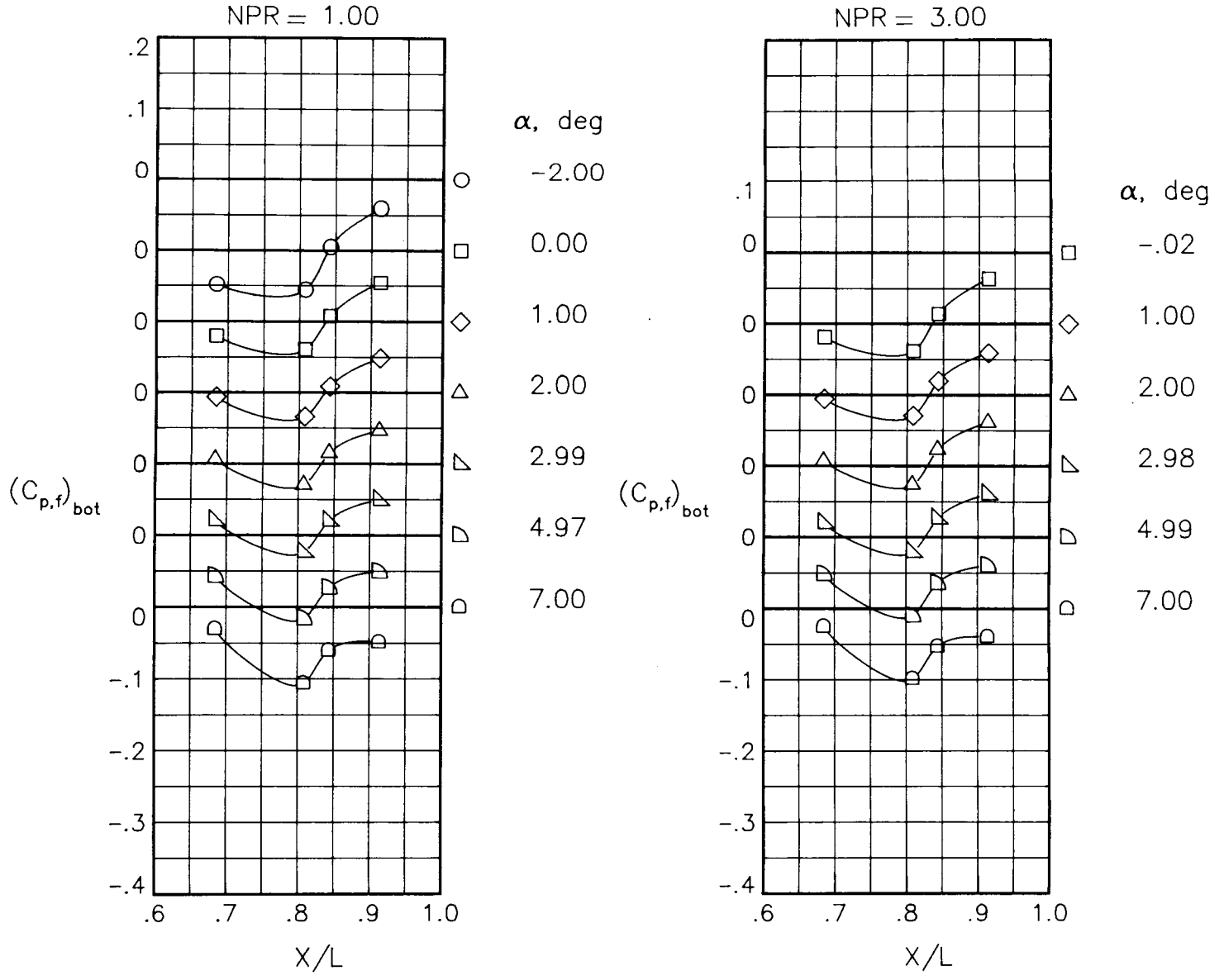

(a) M = 0.60.

Figure 24.- Static-pressure-coefficient distributions on bottom of fuselage engine interfairing along centerline for the model with all fuselage modifications except nose boom. β_n = 18.45°.

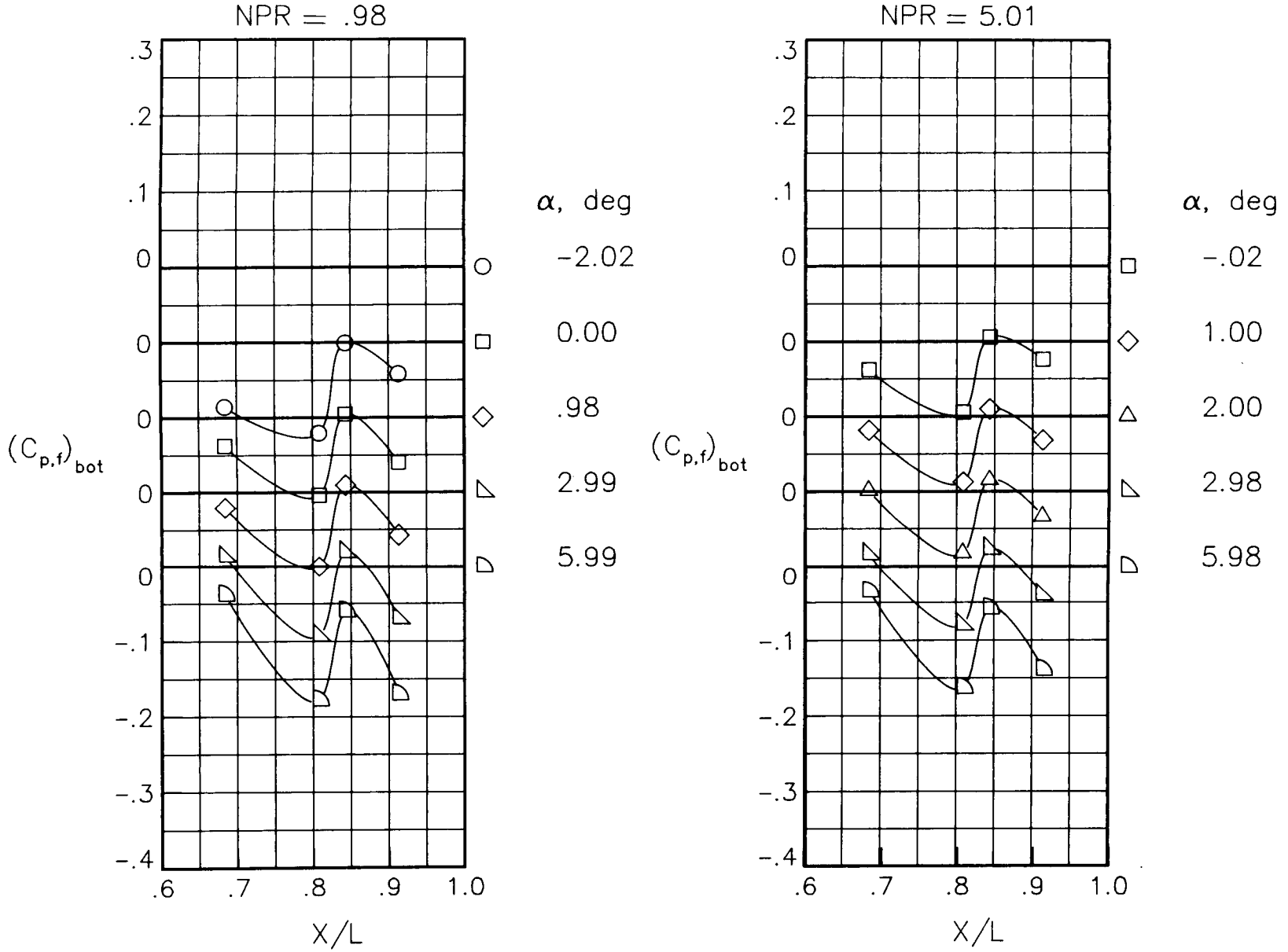

(b) M = 0.90.

Figure 24.- Concluded.

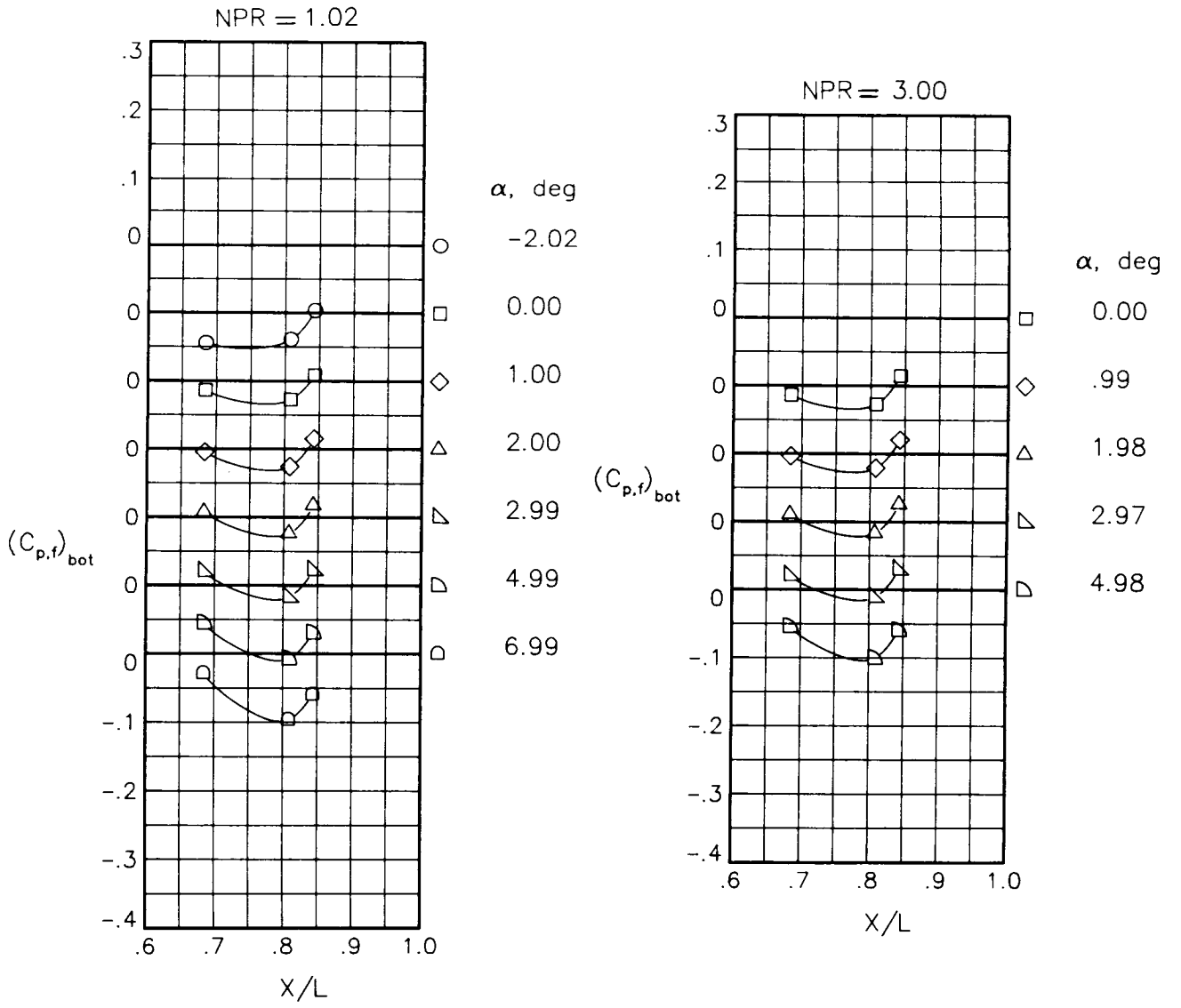

(a) M = 0.60.

Figure 25.- Static-pressure-coefficient distributions on bottom of fuselage engine interfairing along centerline for the model with nose boom, actuator fairings, A/B vents, and nozzle steps (no rakes). β_n = 18.45°.

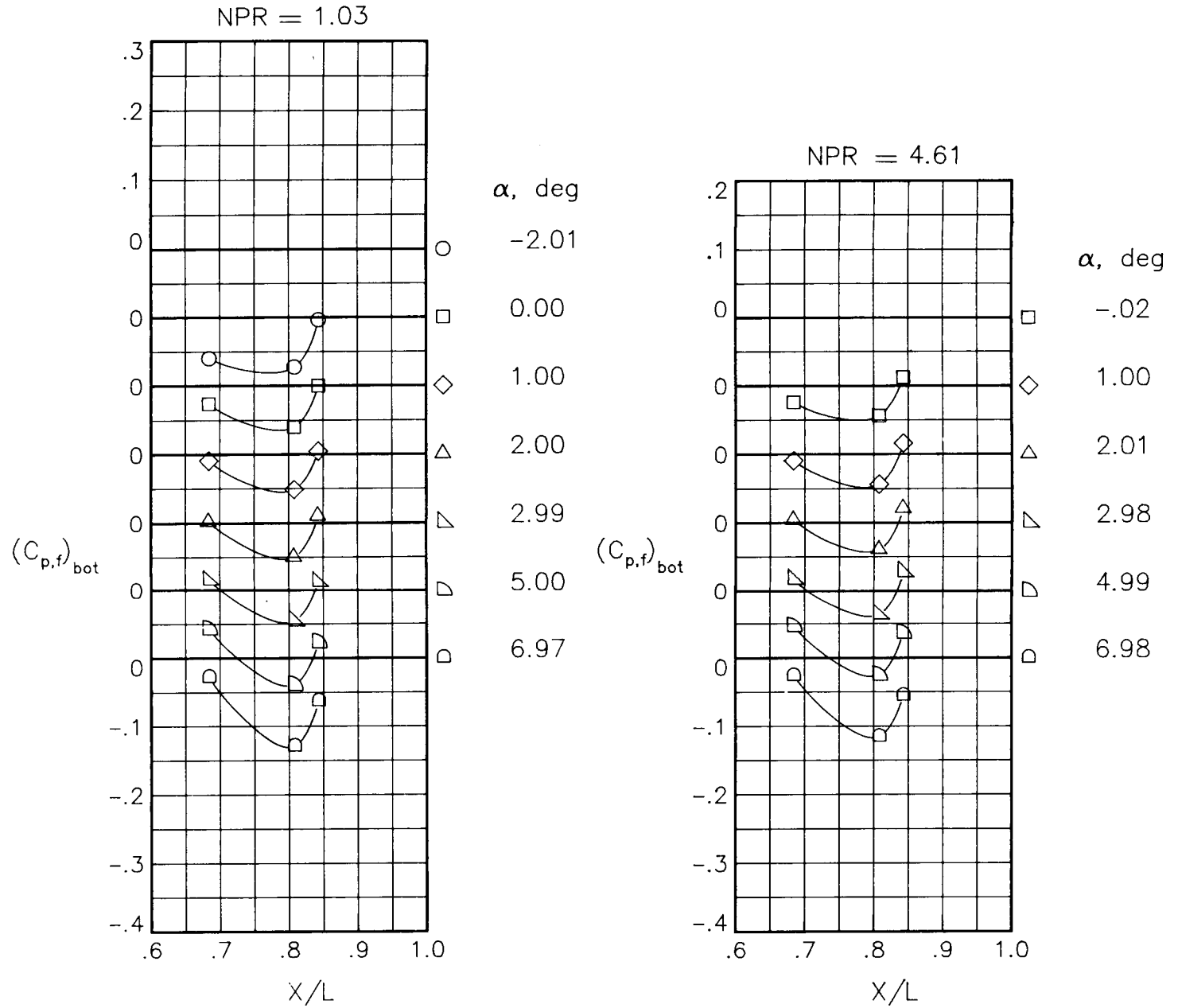

(b) M = 0.80.

Figure 25.- Continued.

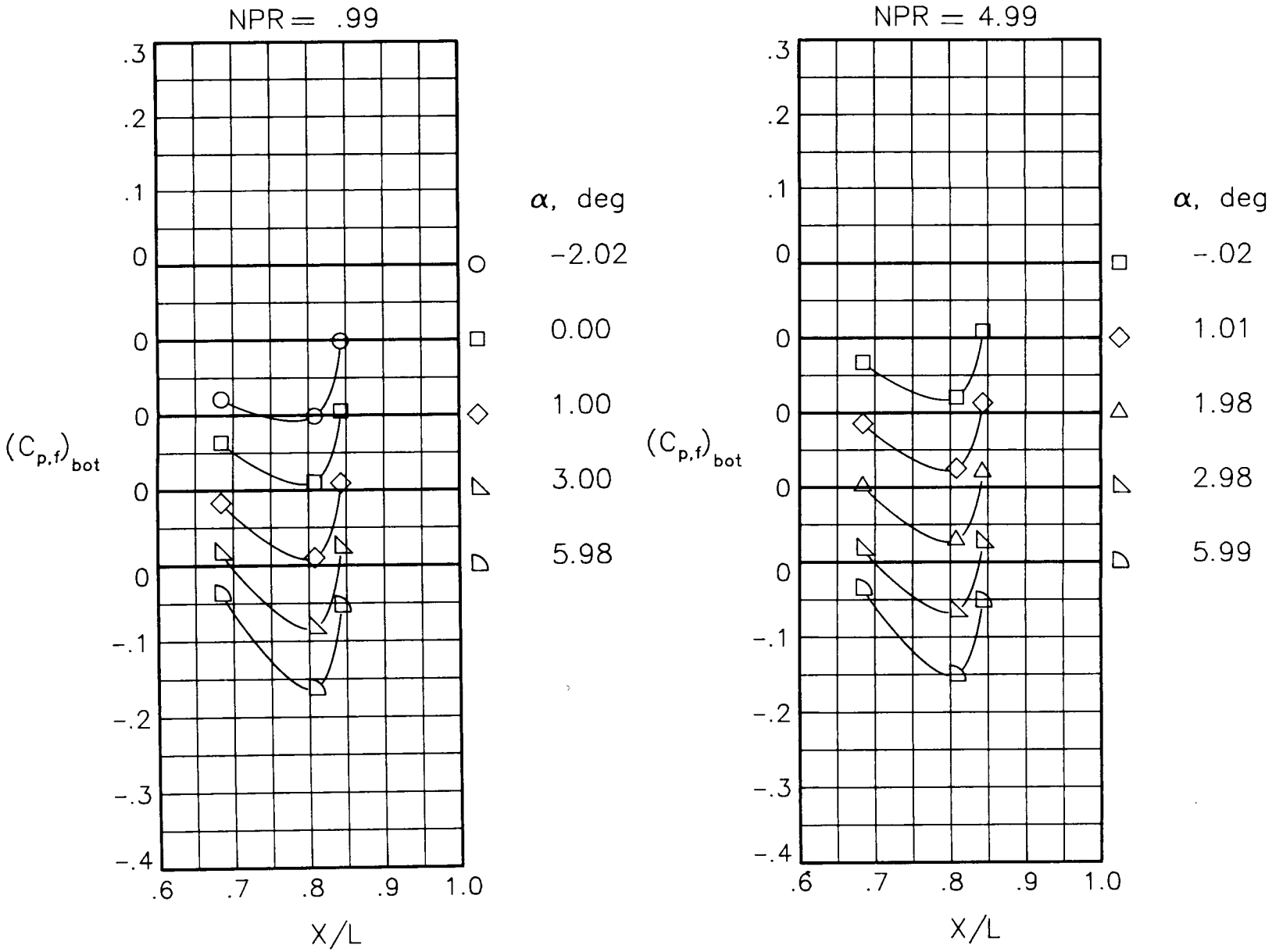

(c) M = 0.90.

Figure 25.- Concluded.

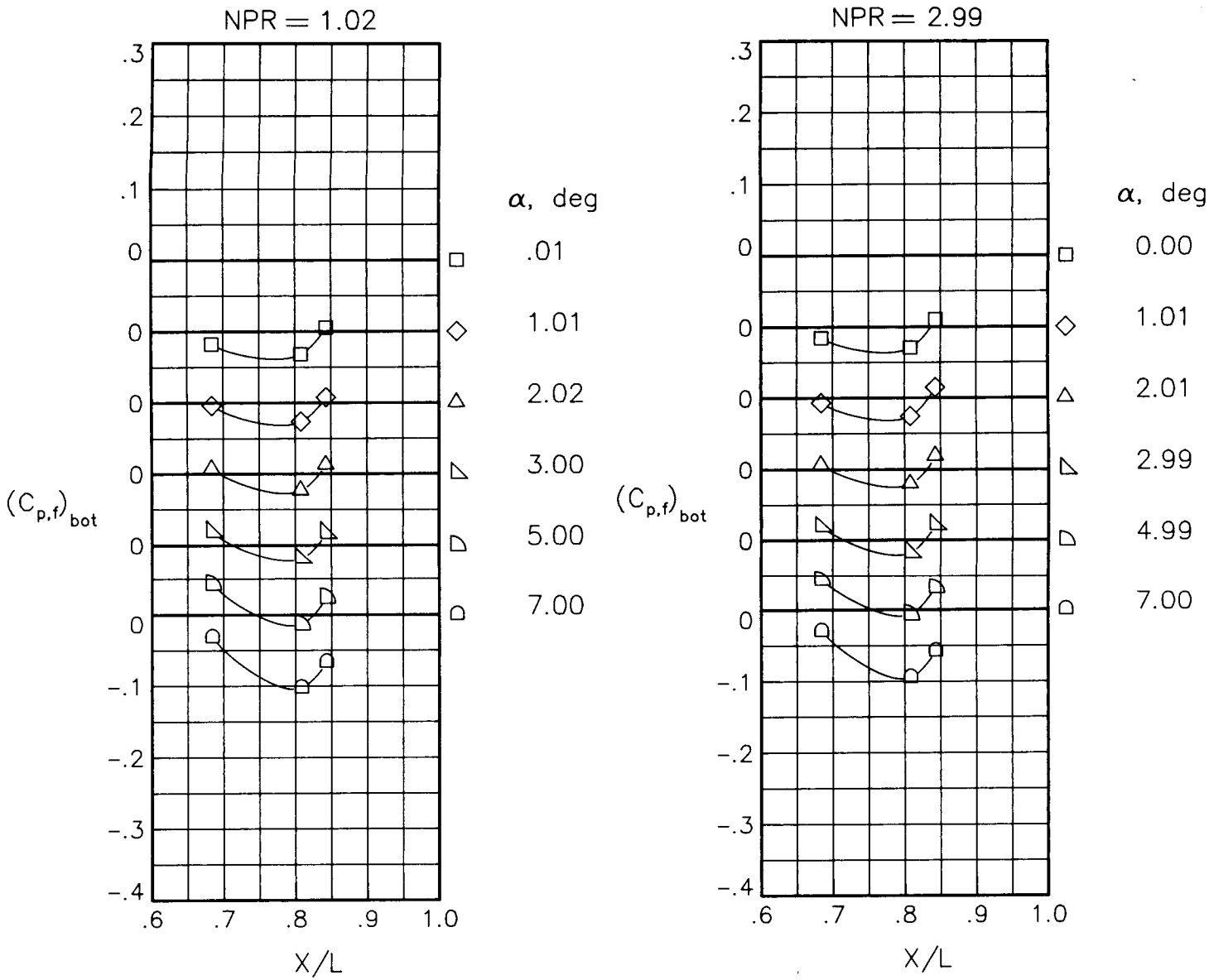

(a) M = 0.60.

Figure 26.- Static-pressure-coefficient distributions on bottom of fuselage engine interfairing along centerline for the model with nose boom, actuator fairings, A/B vents, and nozzle steps (no rakes). β_n = 18.45°; δ_h = -2°.

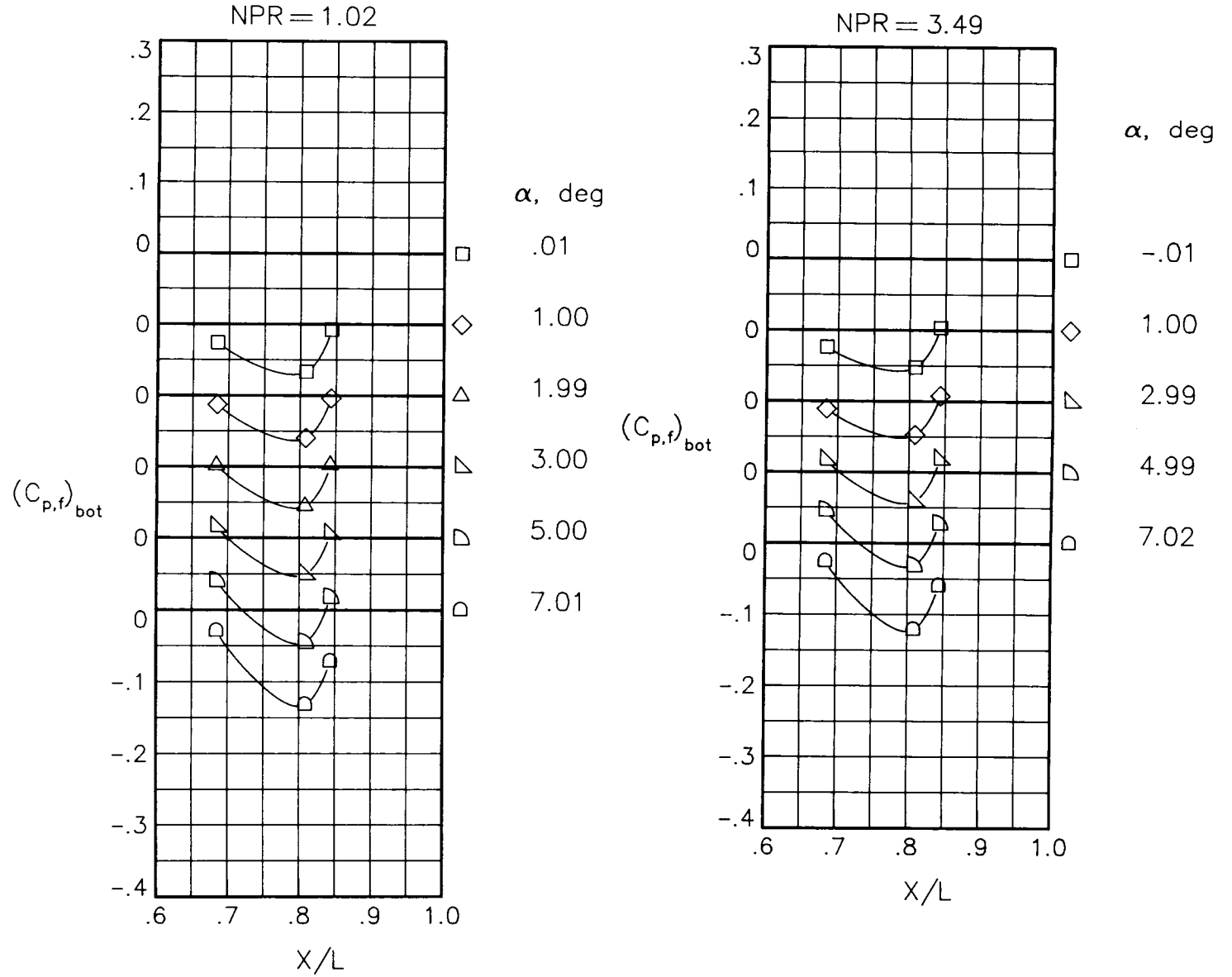

(b) M = 0.80.

Figure 26.- Continued.

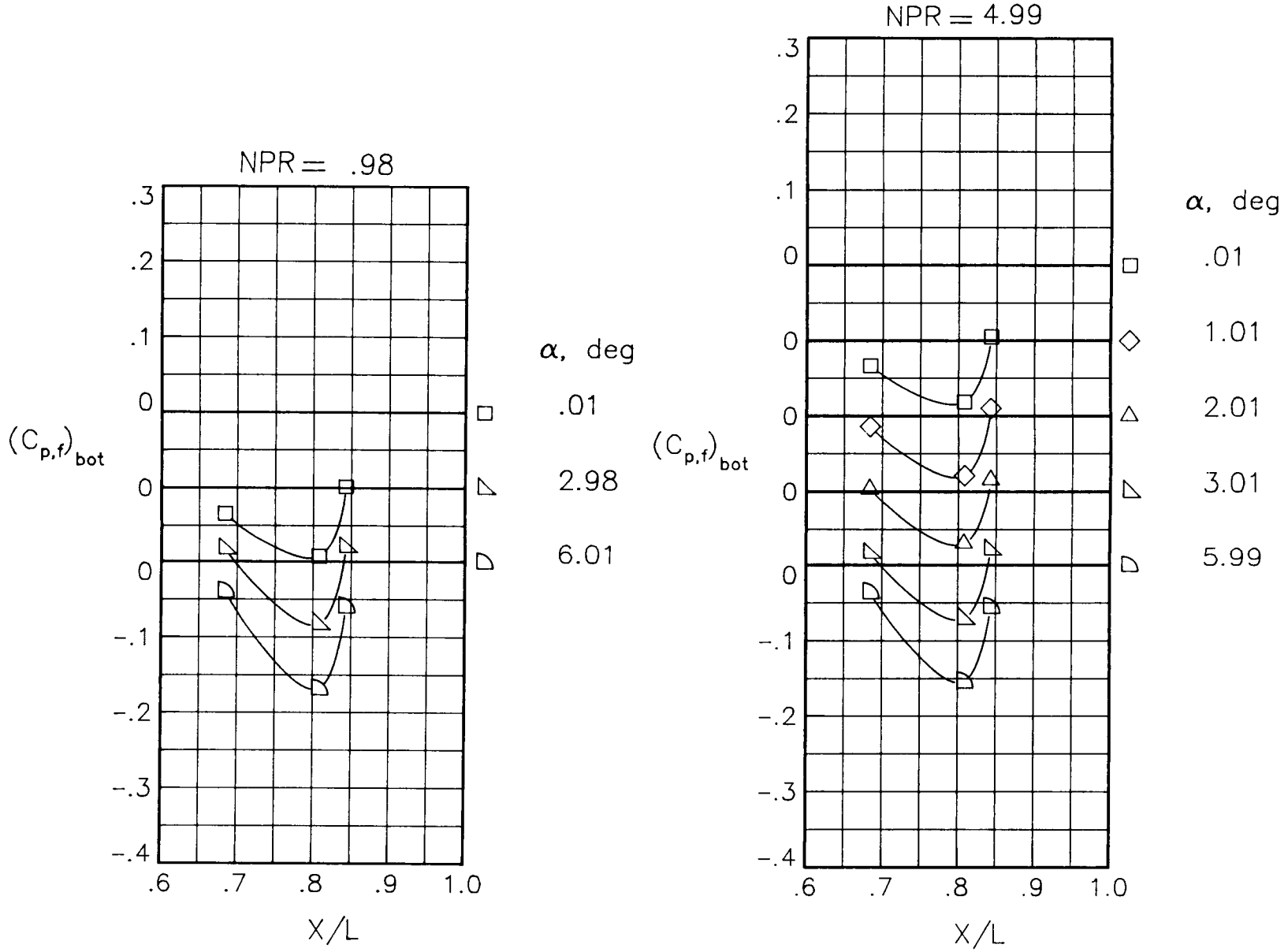

(c) M = 0.90.

Figure 26.- Concluded.

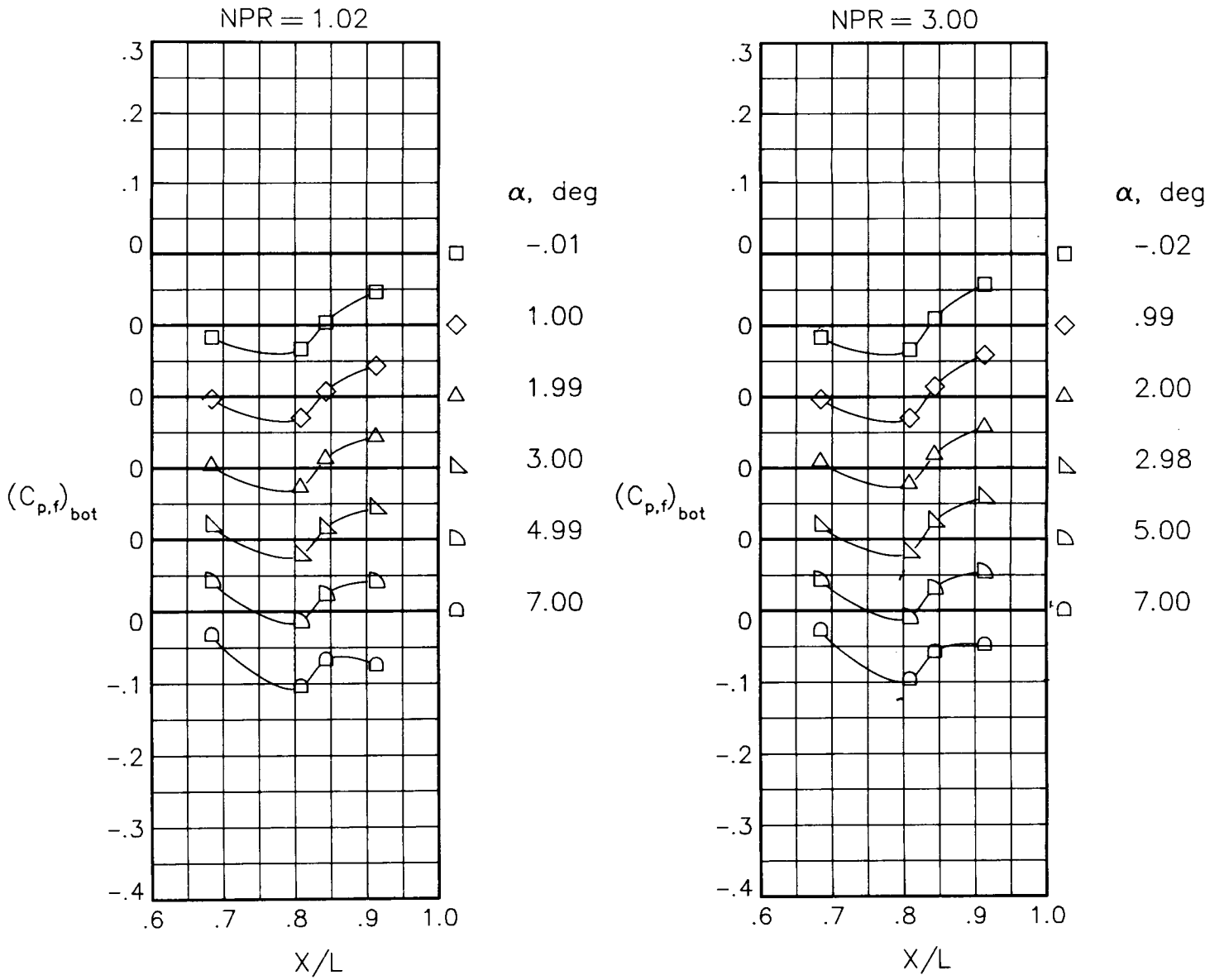

(a) M = 0.60.

Figure 27.- Static-pressure-coefficient distributions on bottom of fuselage engine interfairing along centerline for the model with all fuselage modifications. β_n = 18.45°; δ_h = -2°.

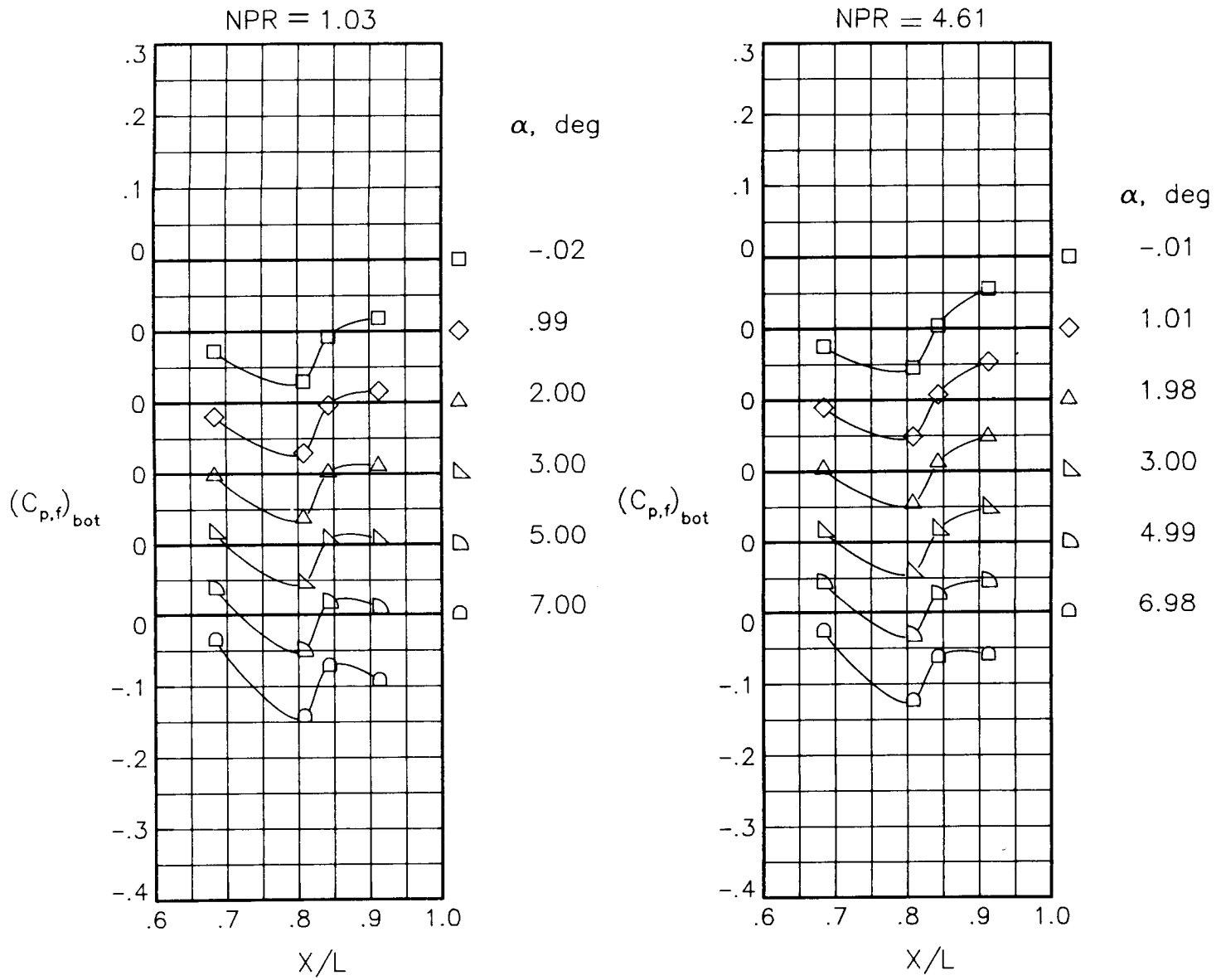

(b) M = 0.80.

Figure 27.- Continued.

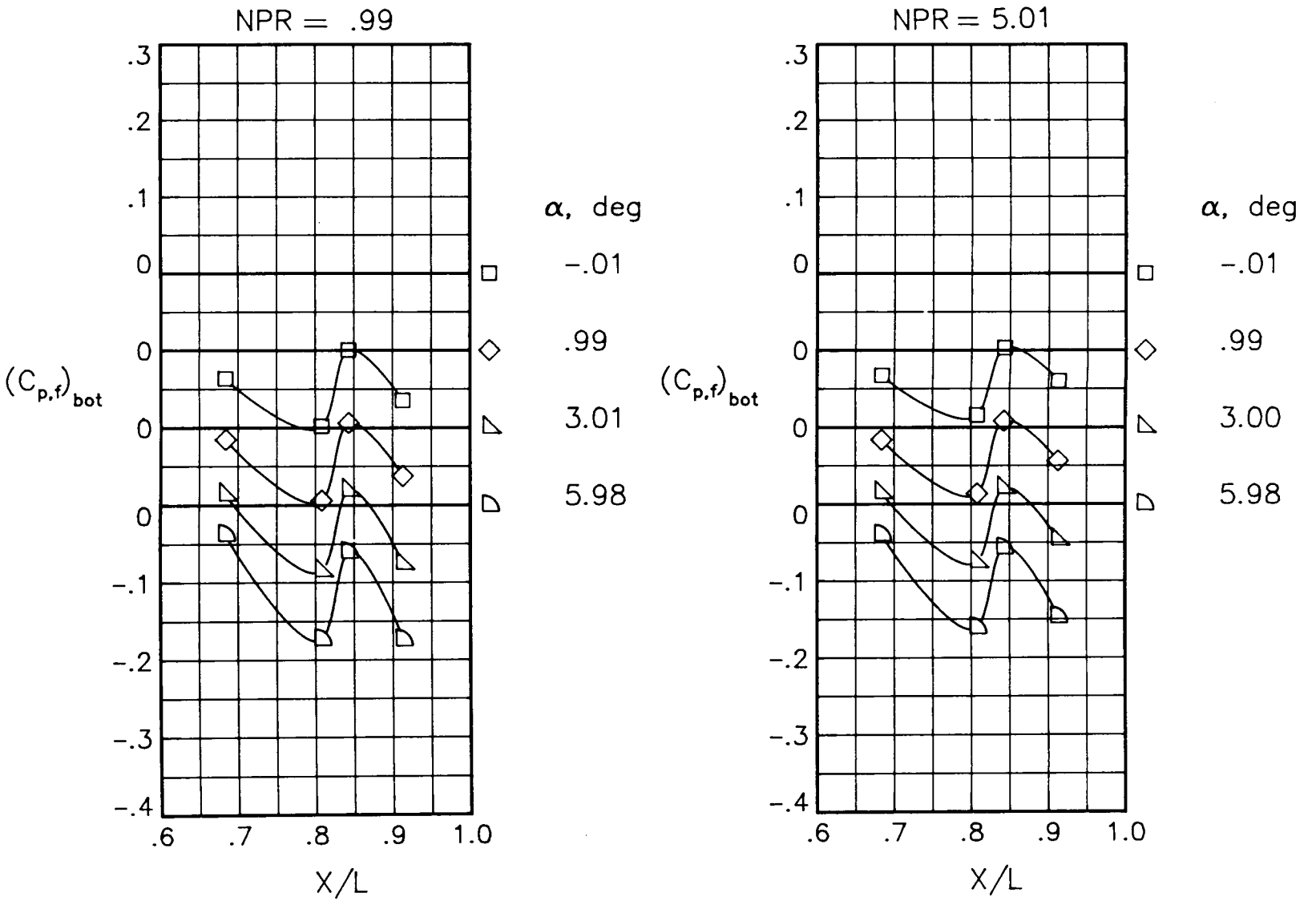

(c) M = 0.90.

Figure 27.- Concluded.

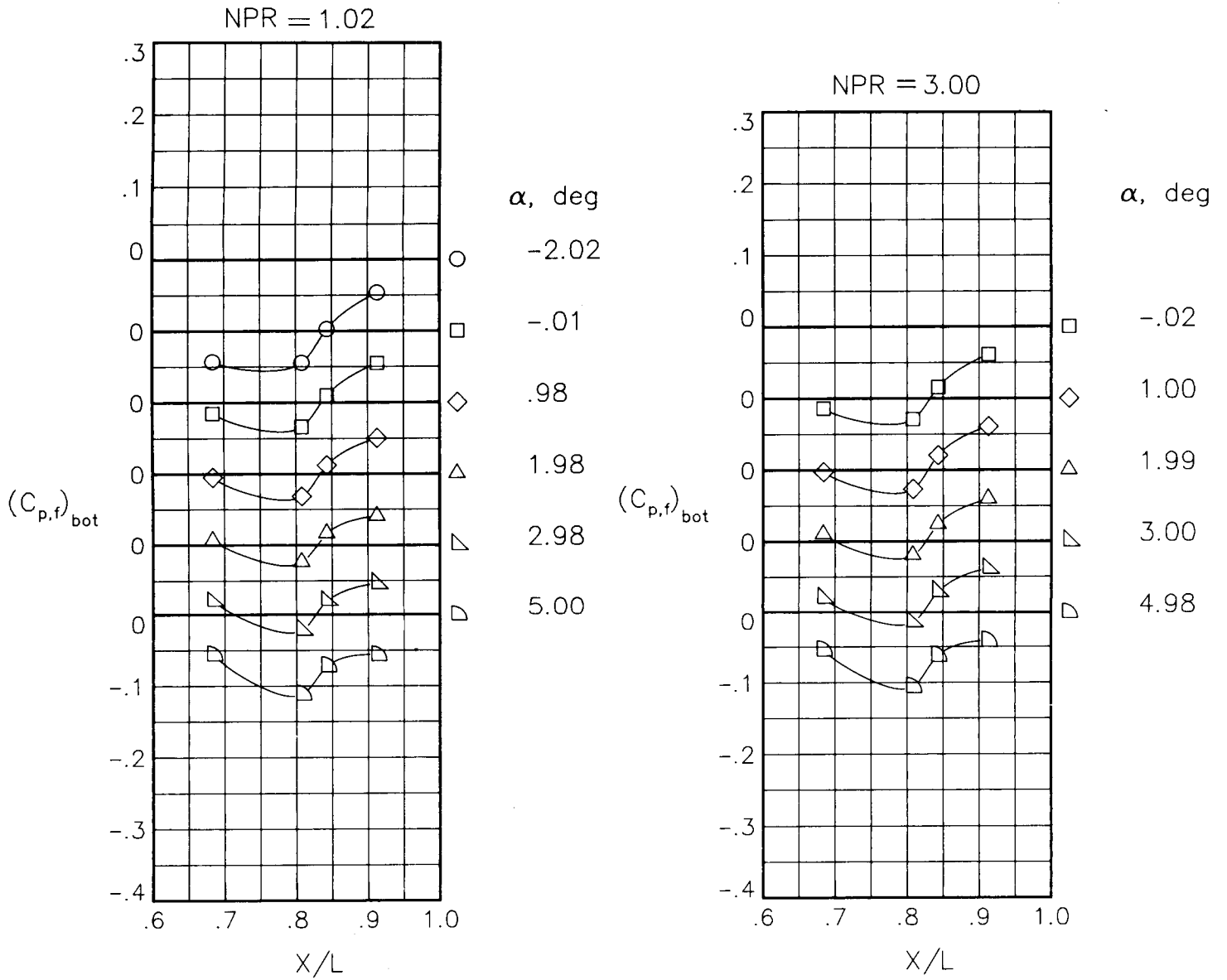

(a) M = 0.60.

Figure 28.- Static-pressure-coefficient distributions on bottom of fuselage engine interfairing along centerline for the model with all fuselage modifications. β_n = 18.45°.

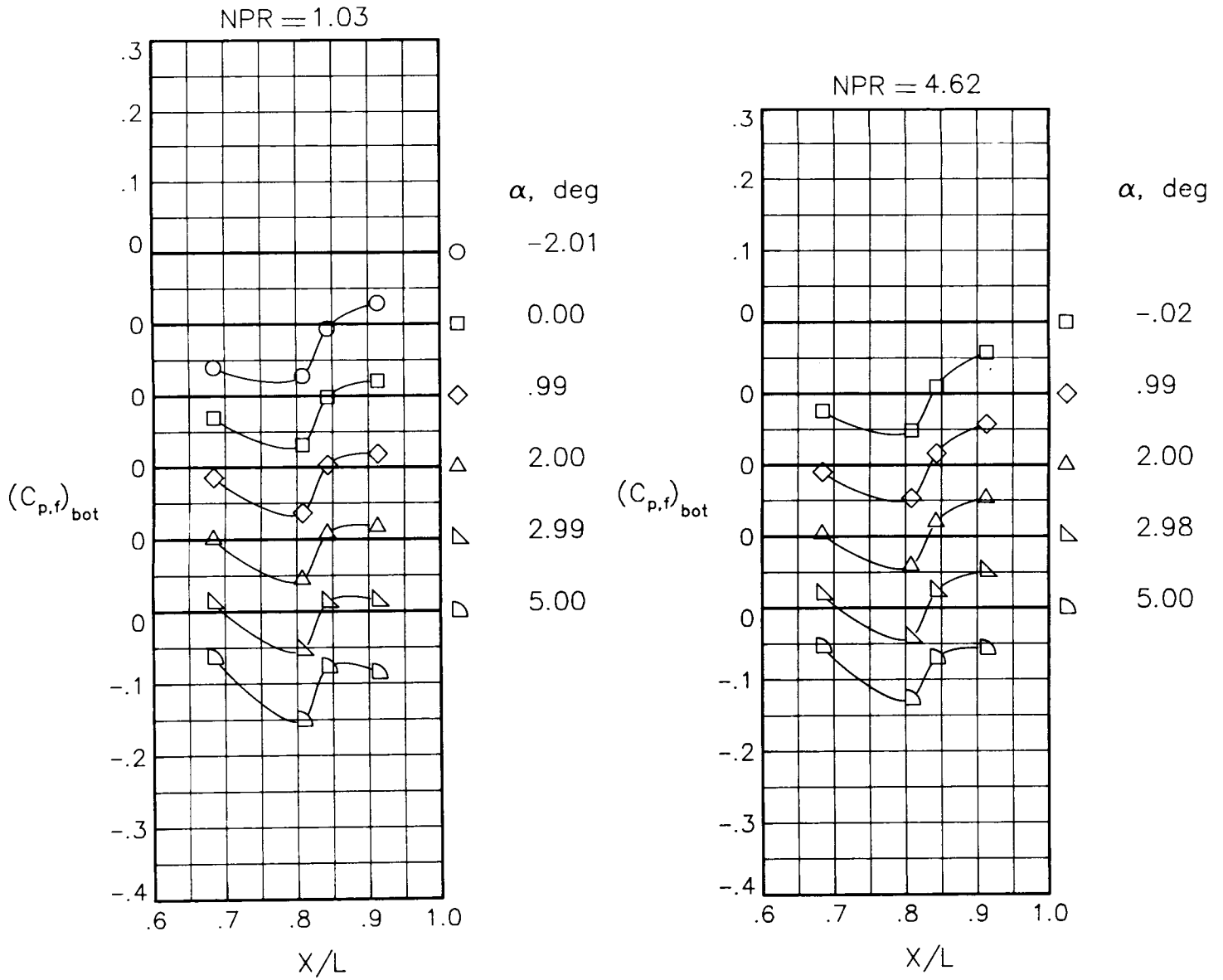

(b) M = 0.80.

Figure 28.- Continued.

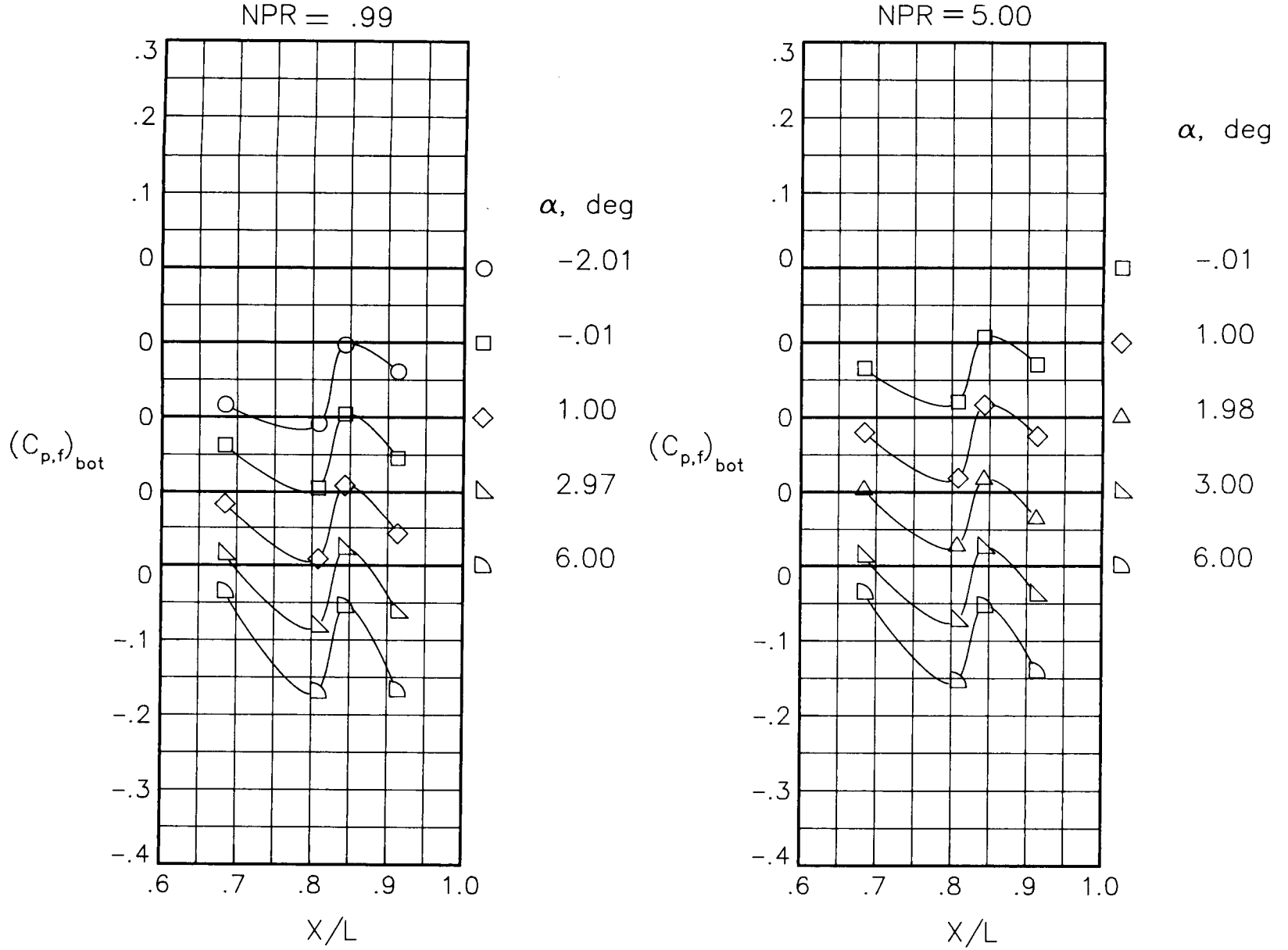

(c) M = 0.90.

Figure 28.- Concluded.

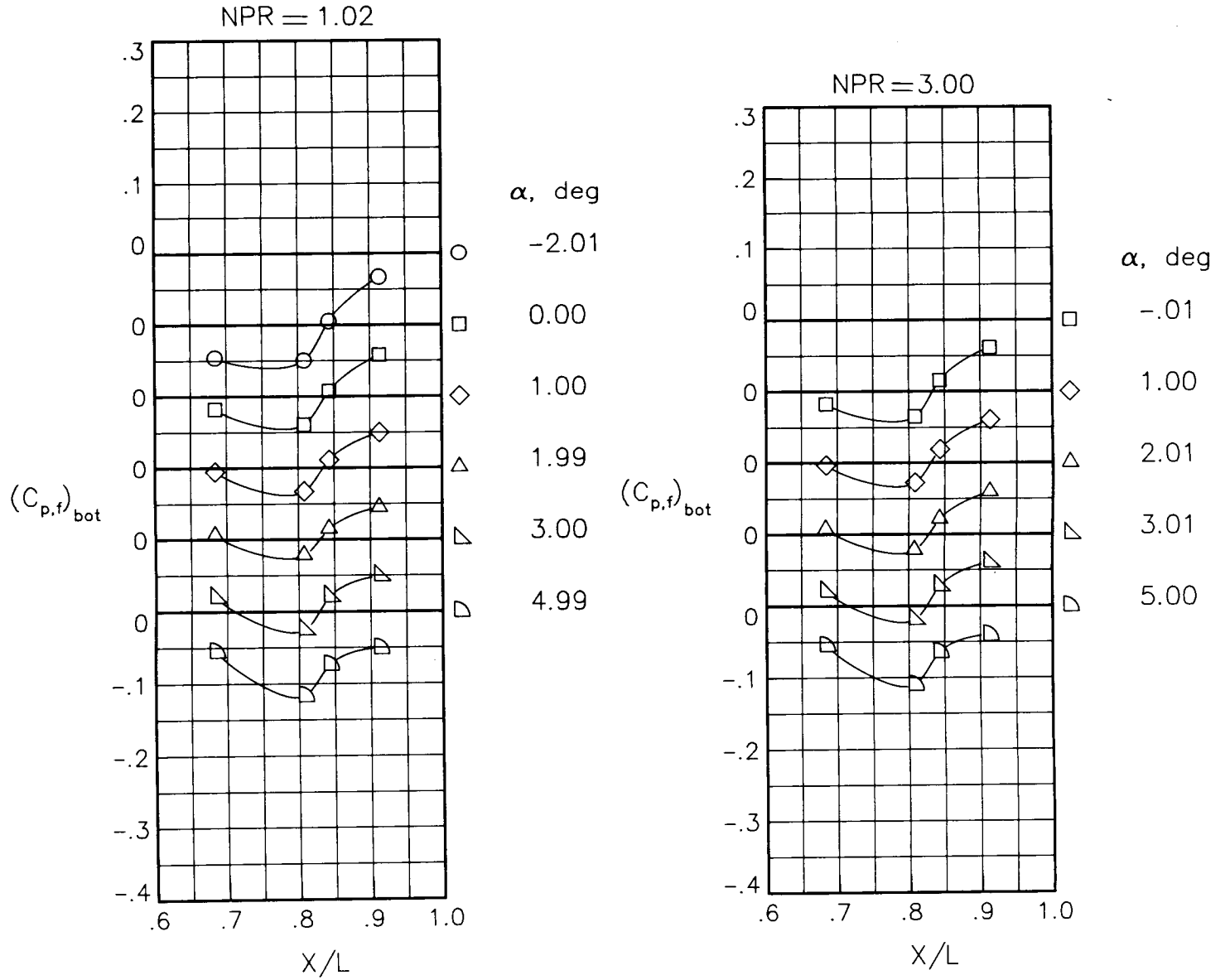

(a) M = 0.60.

Figure 29.- Static-pressure-coefficient distributions on bottom of fuselage engine interfairing along centerline for the model with all fuselage modifications. β_n = 18.45°. Repeat data.

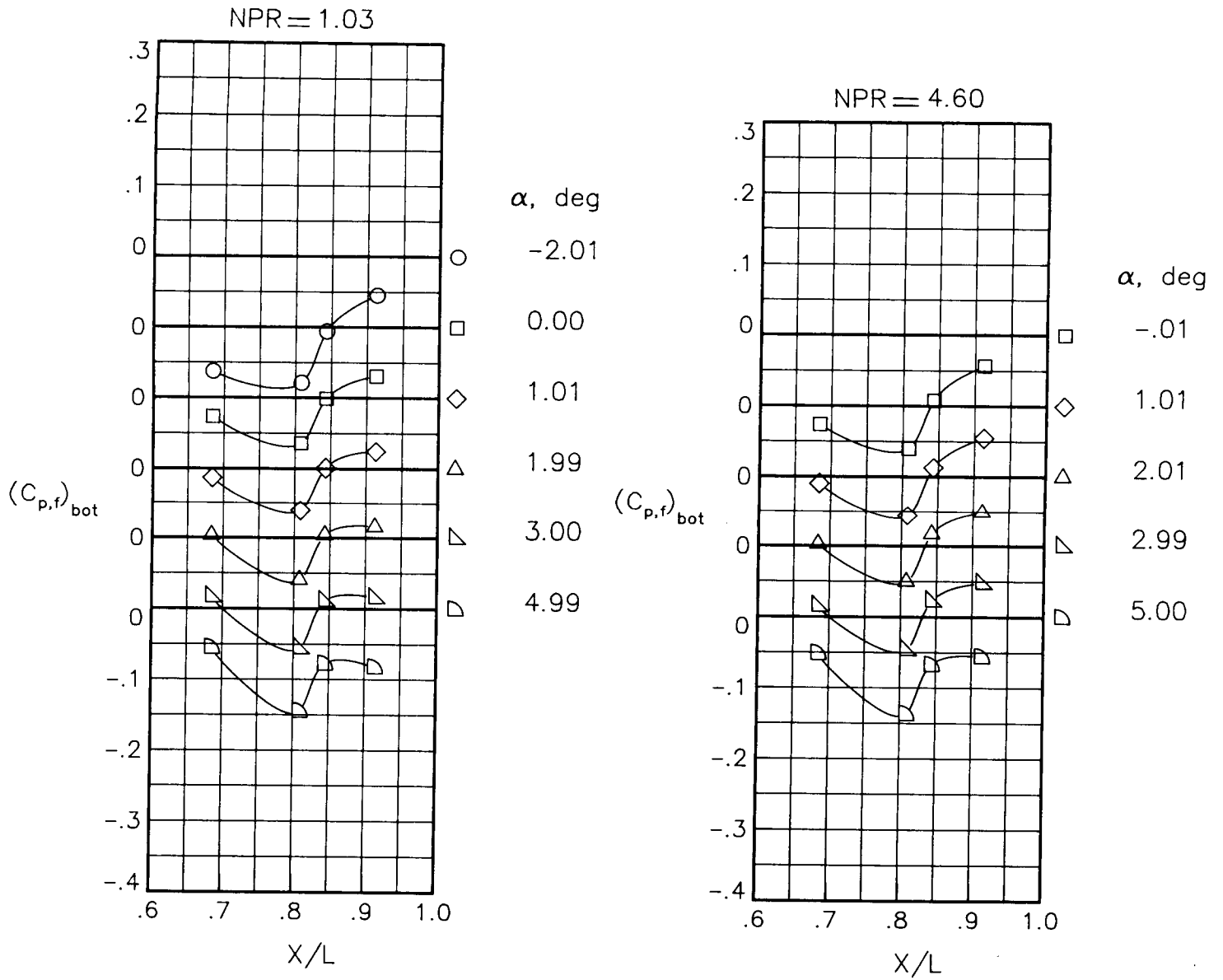

(b) M = 0.80.

Figure 29.- Continued.

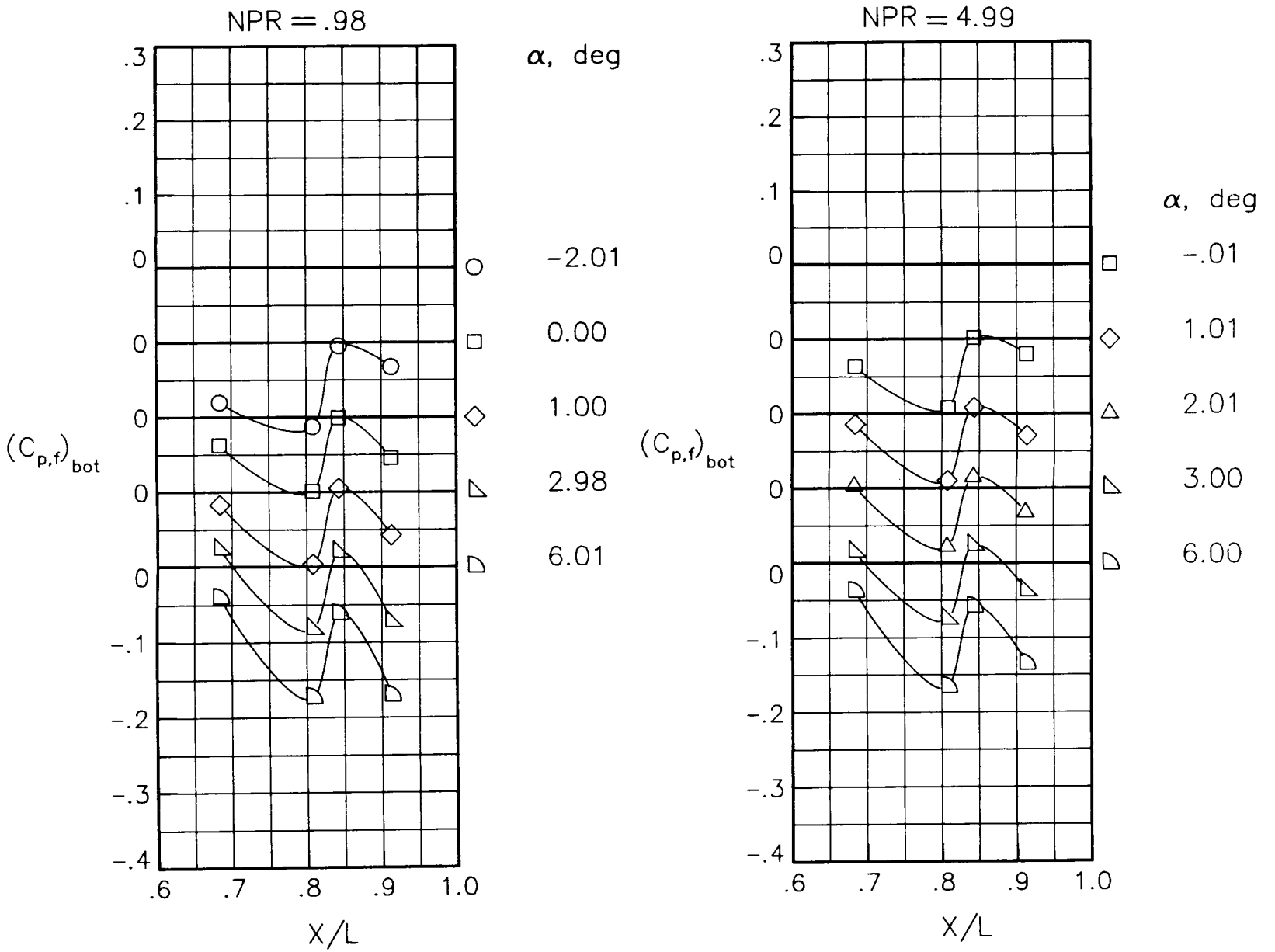

(c) M = 0.90.

Figure 29.- Concluded.

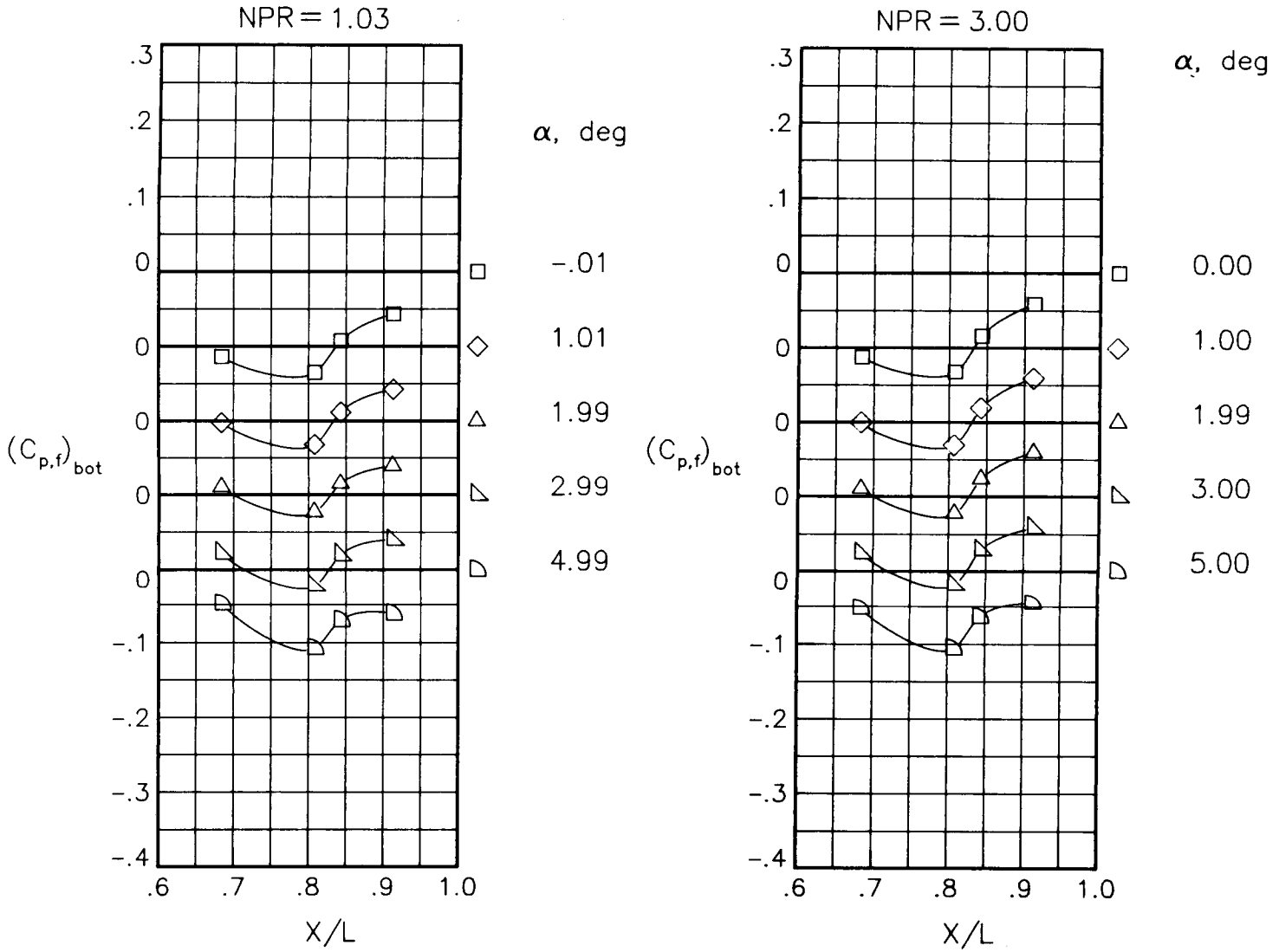

(a) M = 0.60.

Figure 30.- Static-pressure-coefficient distributions on bottom of fuselage engine interfairing along centerline for the model with all fuselage modifications. β_n = 18.45°; δ_r = -5°.

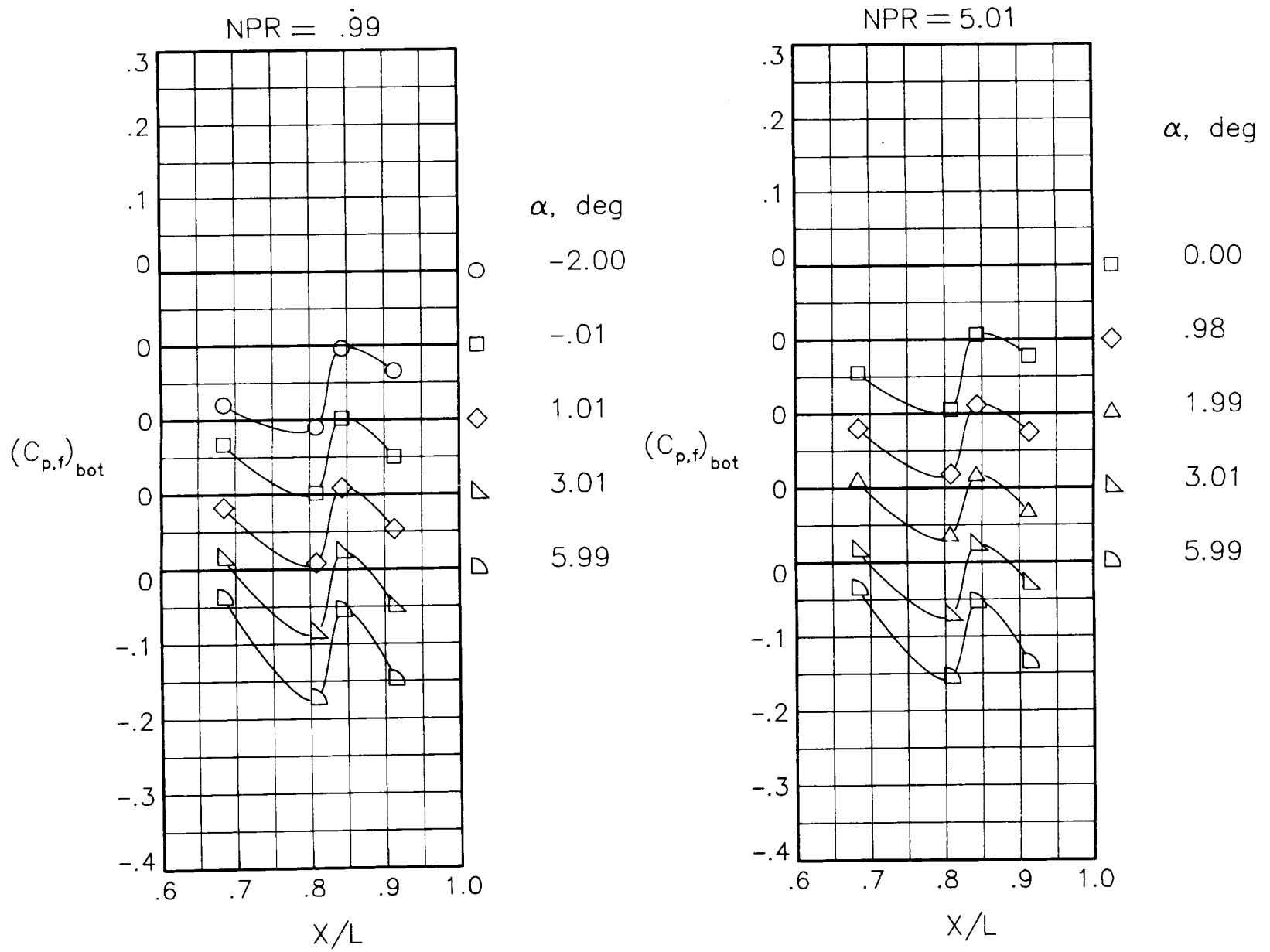

(b) M = 0.90.

Figure 30.- Concluded.

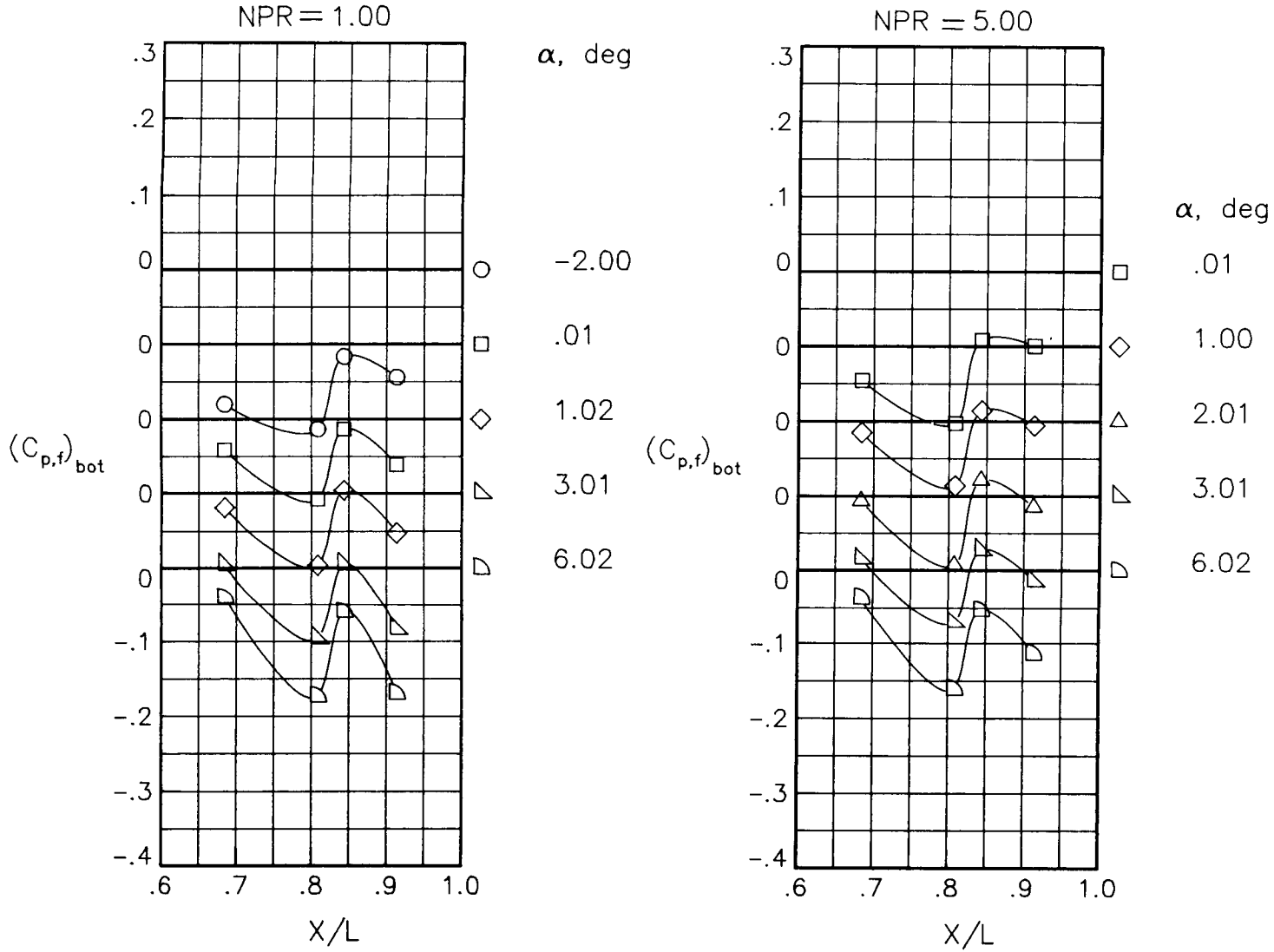

(a) M = 0.90.

Figure 31.- Static-pressure-coefficient distributions on bottom of fuselage engine interfairing along centerline for the model with all fuselage modifications. β_n = 15.05°.

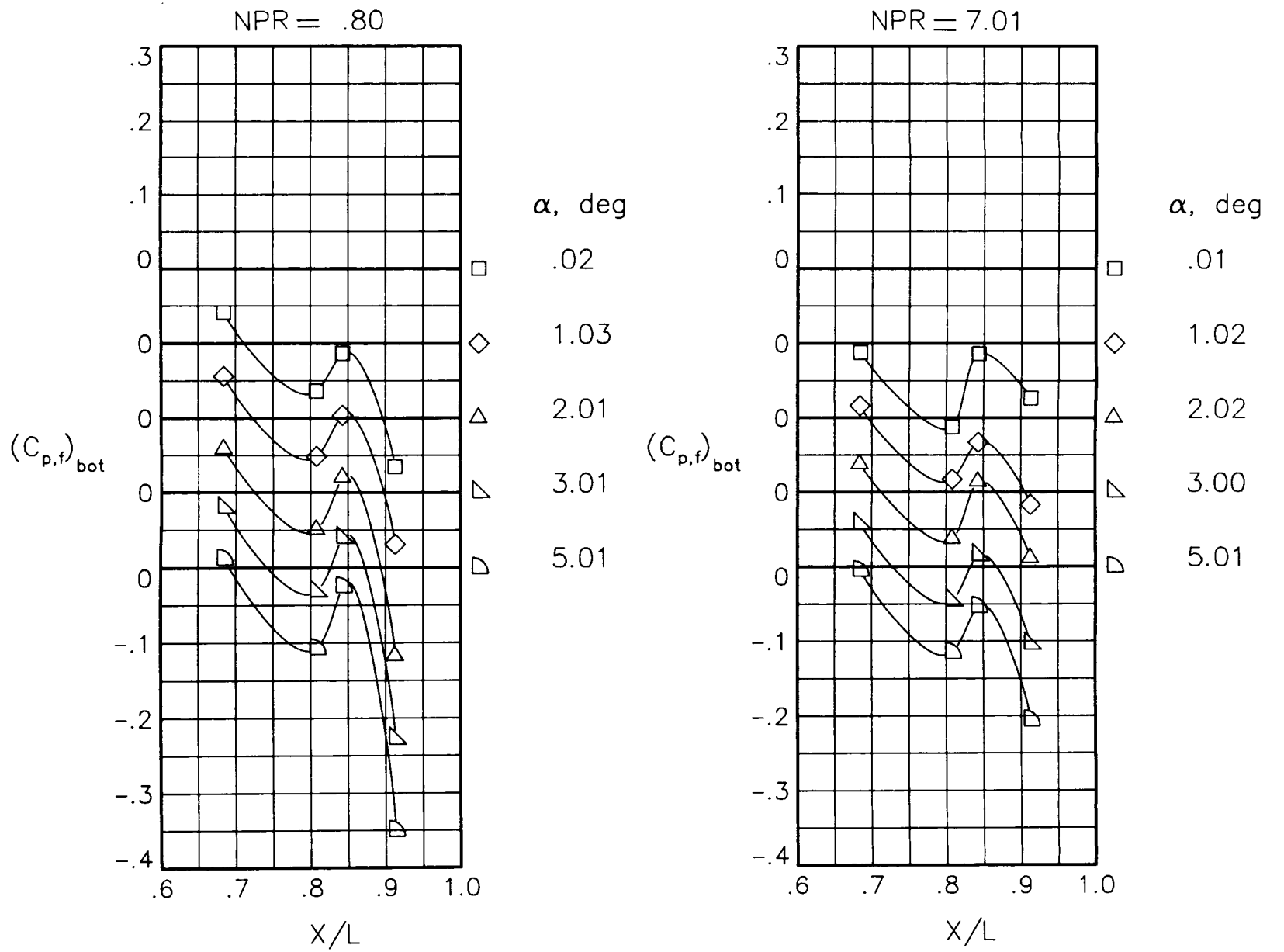

(b) M = 1.20.

Figure 31.- Concluded.

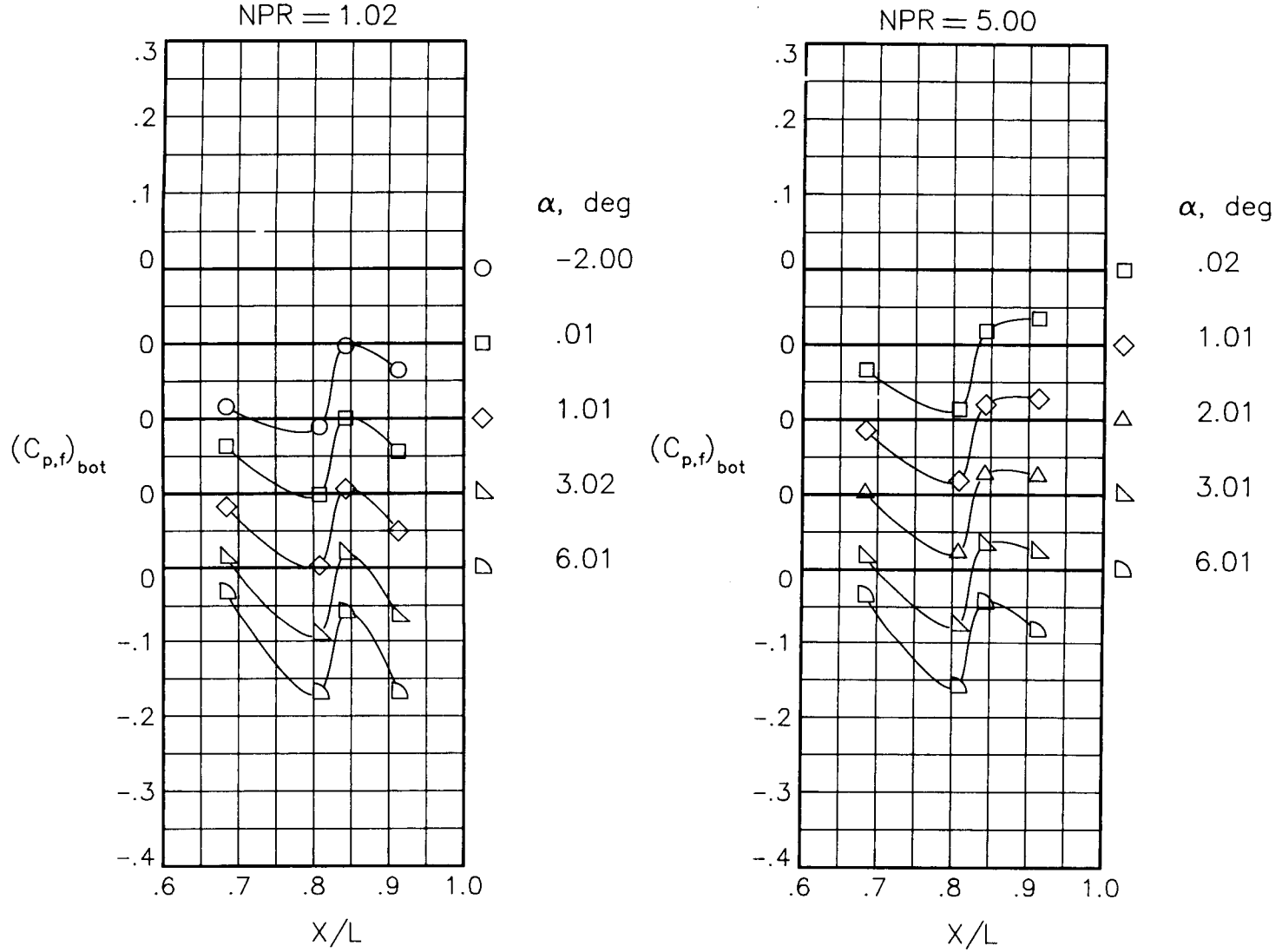

(a) M = 0.90.

Figure 32.- Static-pressure-coefficient distributions on bottom of fuselage engine interfairing along centerline for the model with all fuselage modifications. β_n = 9.63°.

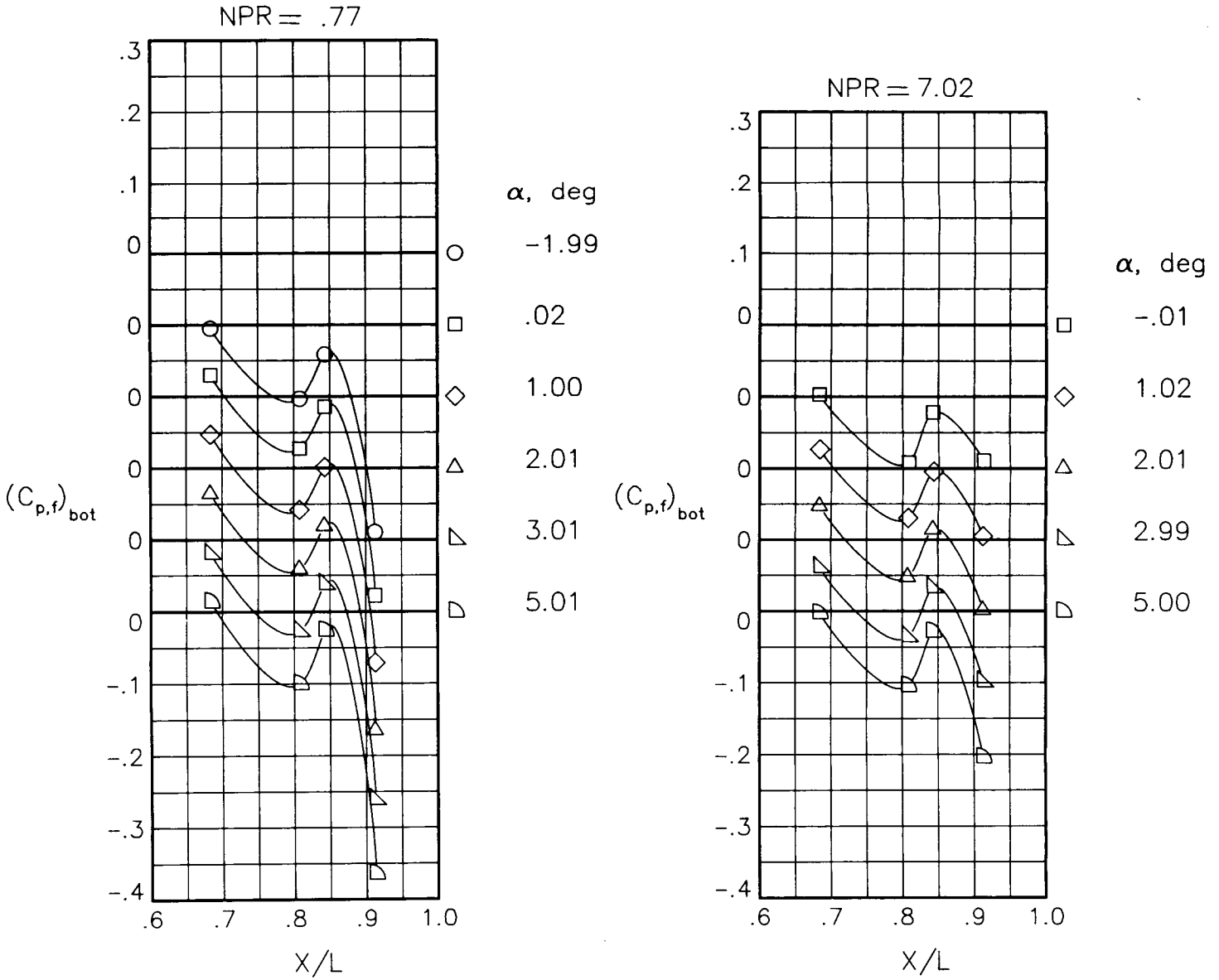

(b) M = 1.20.

Figure 32.- Concluded.

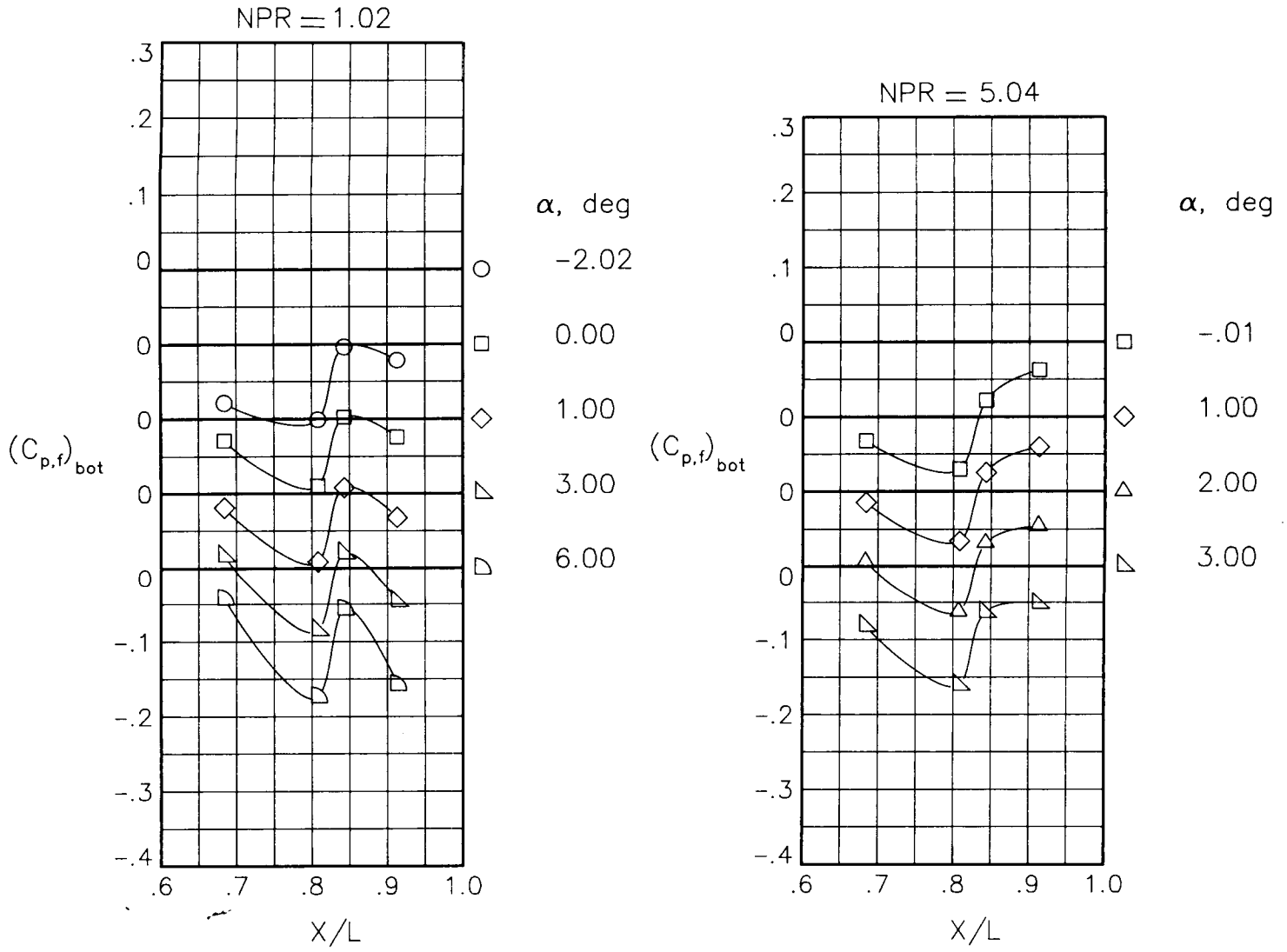

(a) M = 0.90.

Figure 33.- Static-pressure-coefficient distributions on bottom of fuselage engine interfairing along centerline for the model with all fuselage modifications. β_n = 7.72°.

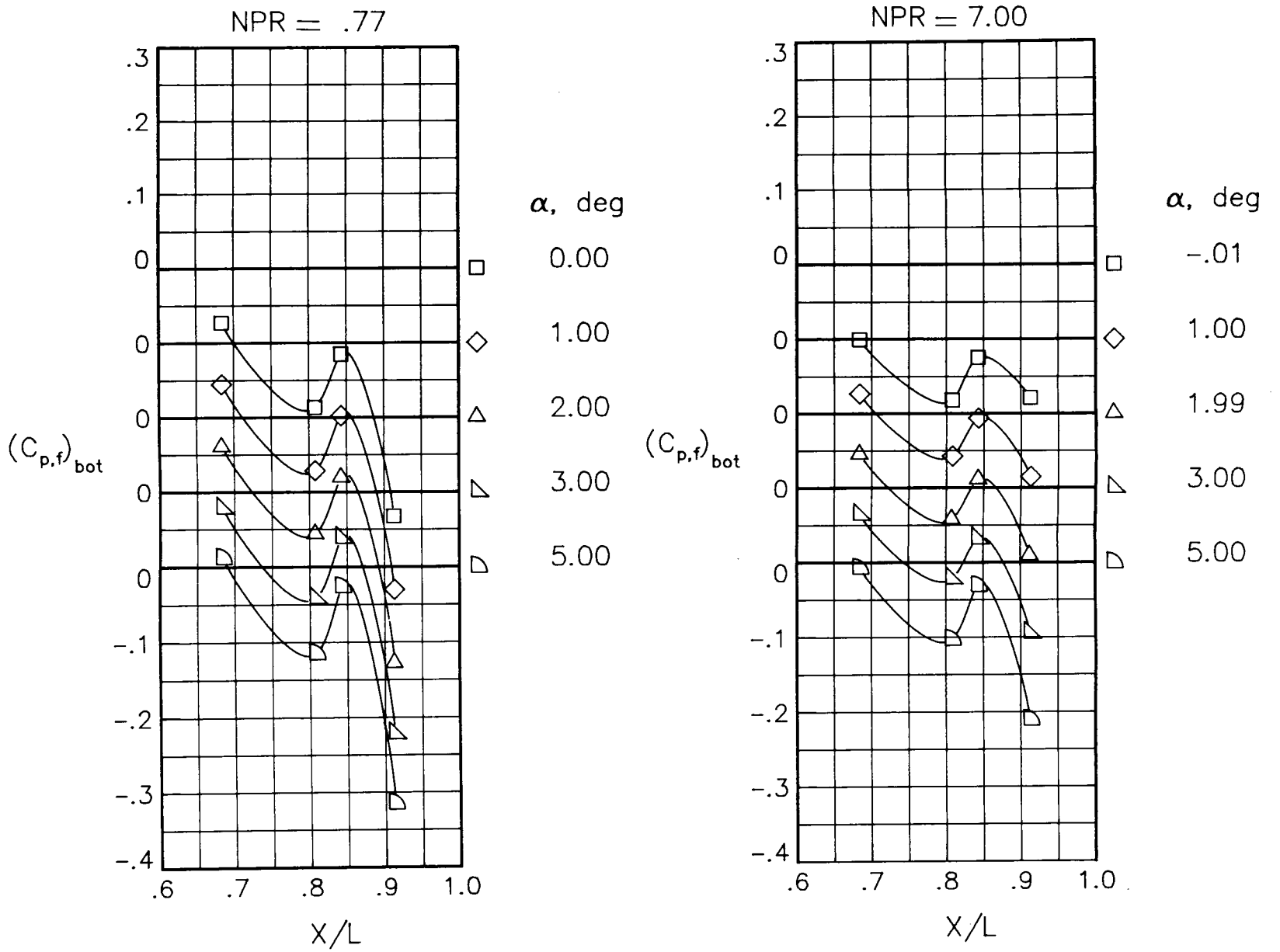

(b) M = 1.20.

Figure 33.- Concluded.

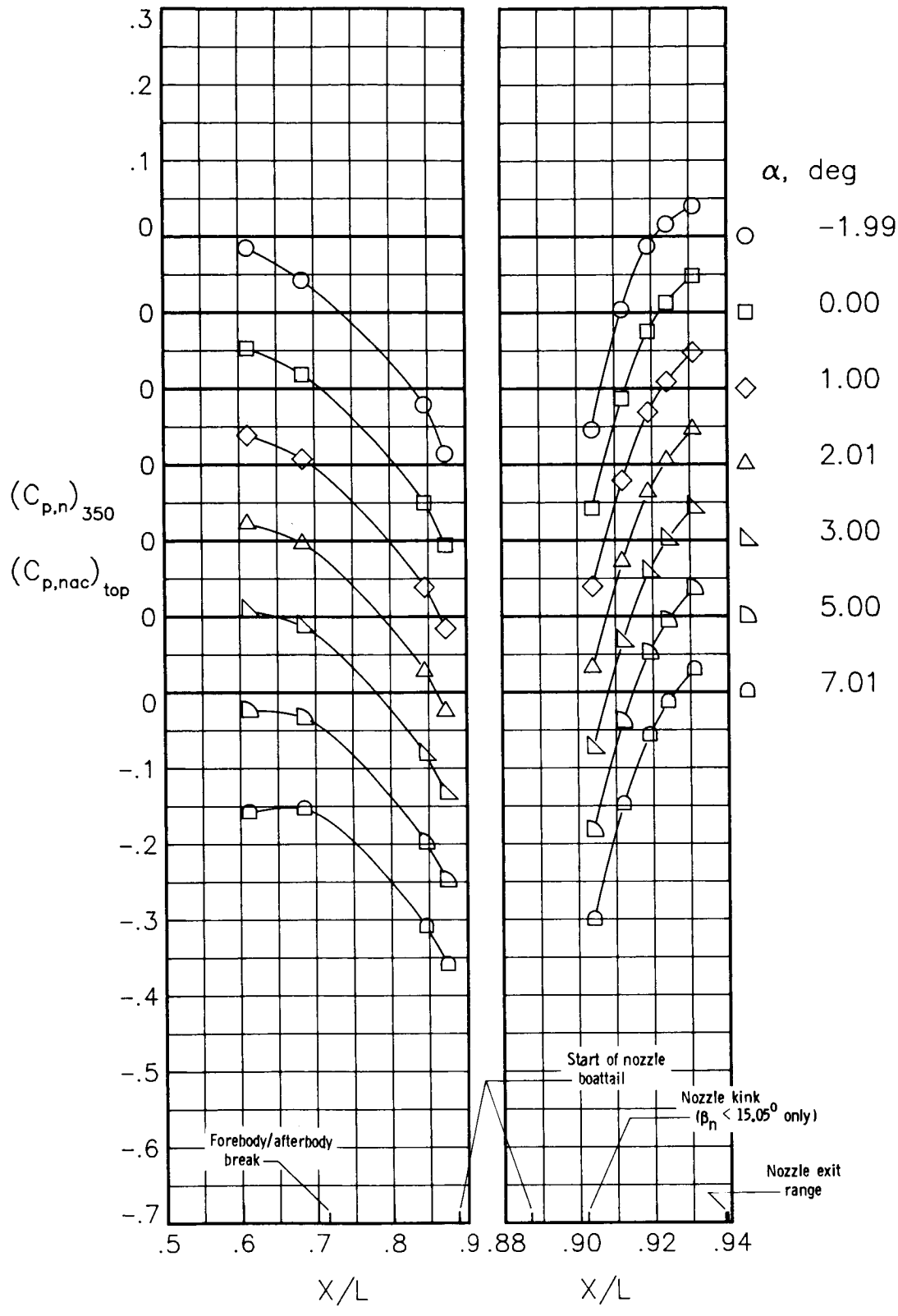

(a) M = 0.60; NPR = 1.00.

Figure 34.- Static-pressure-coefficient distributions on top of nacelle and nozzle for the unmodified model. β_n = 18.45°.

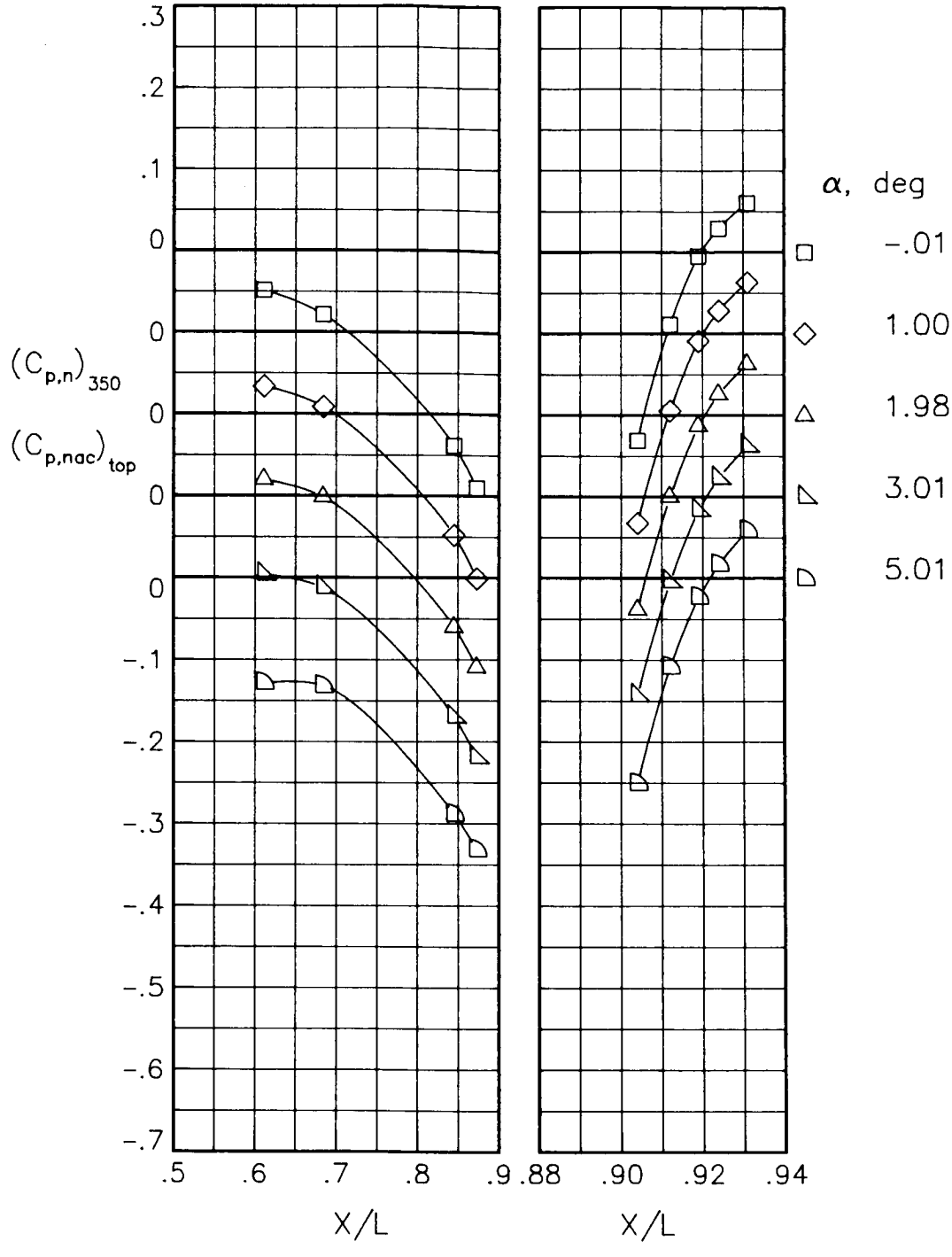

(b) M = 0.60; NPR = 3.00.

Figure 34.- Continued.

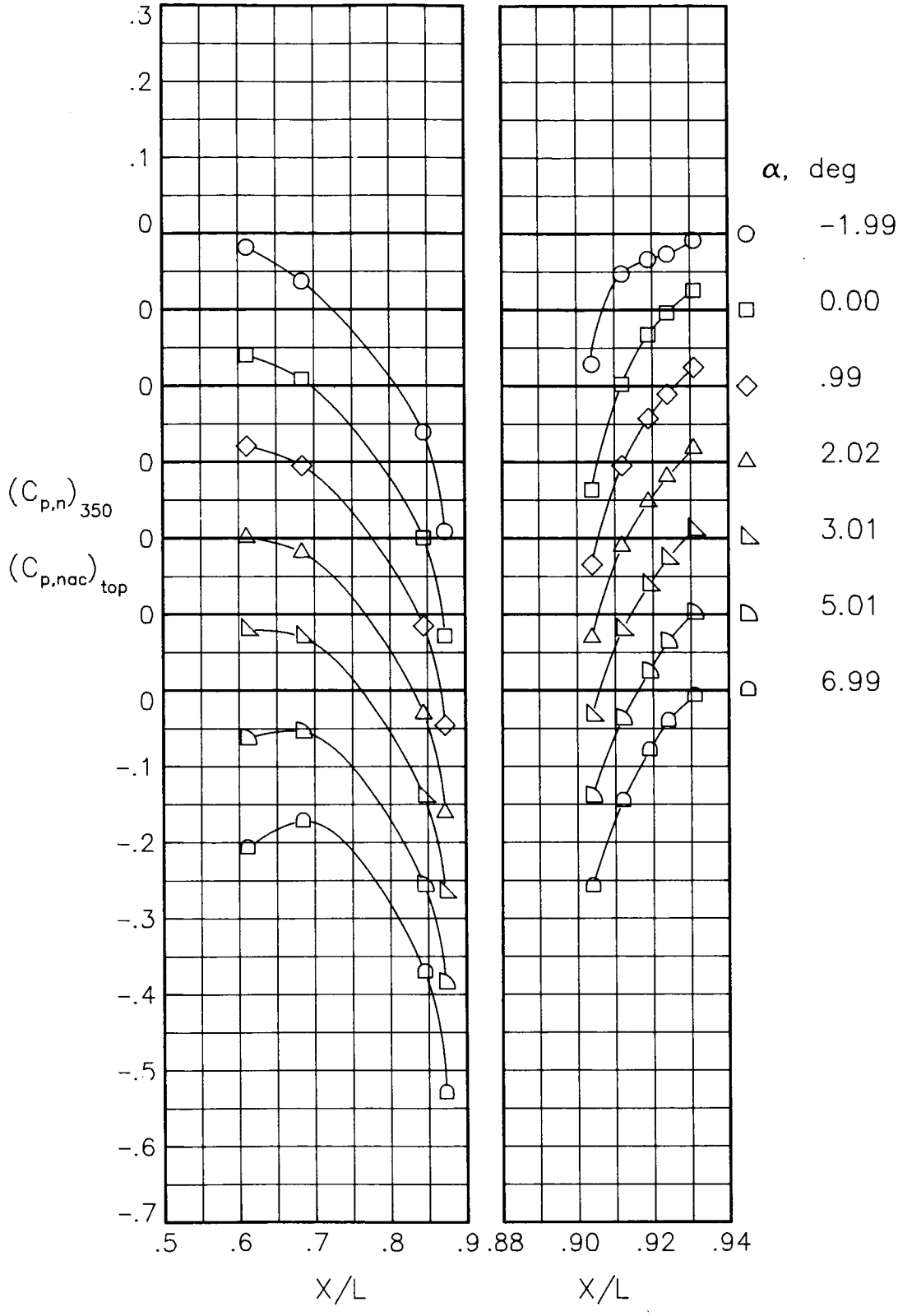

(c) M = 0.80; NPR = 1.00.

Figure 34.- Continued.

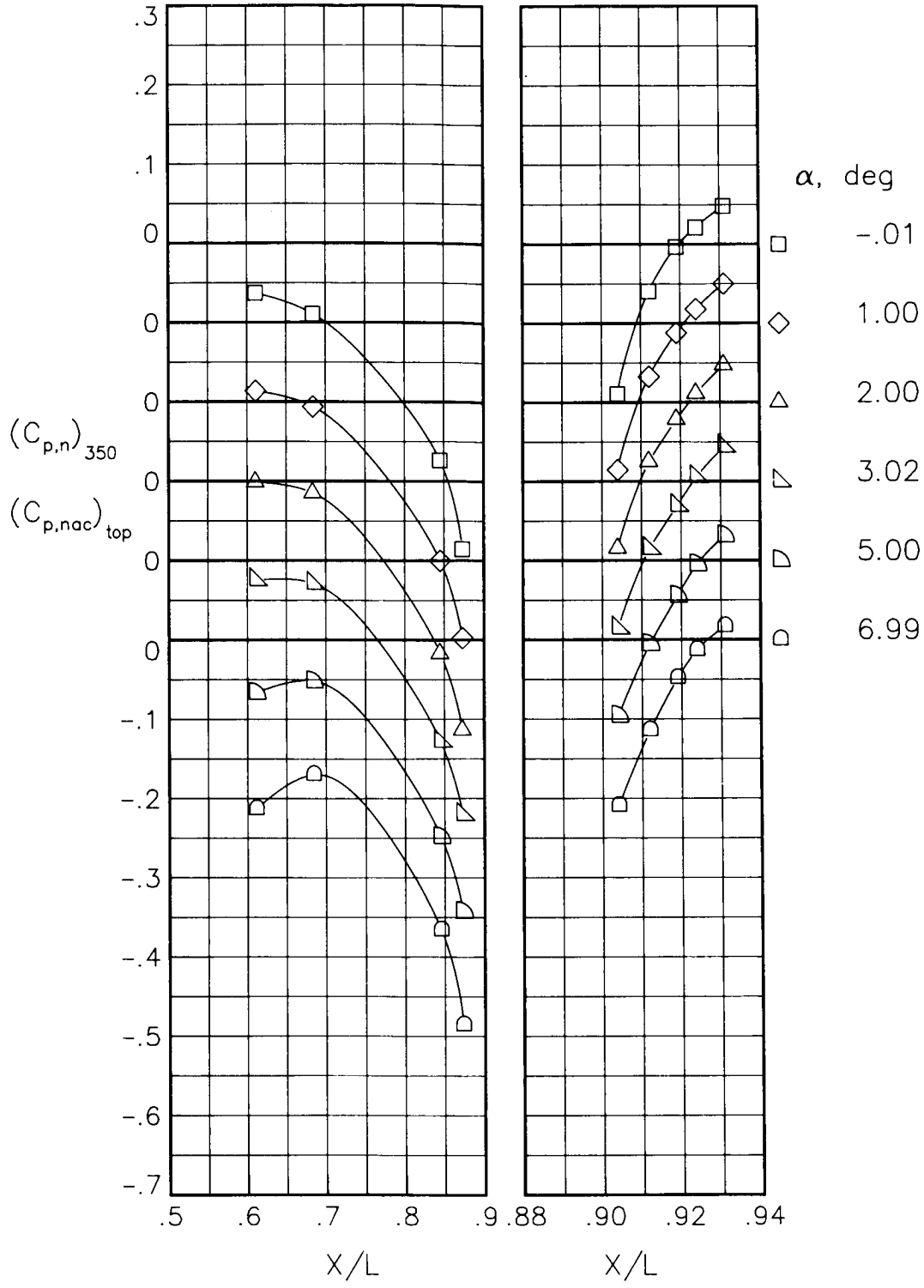

(d) M = 0.80; NPR = 4.60.

Figure 34.- Continued.

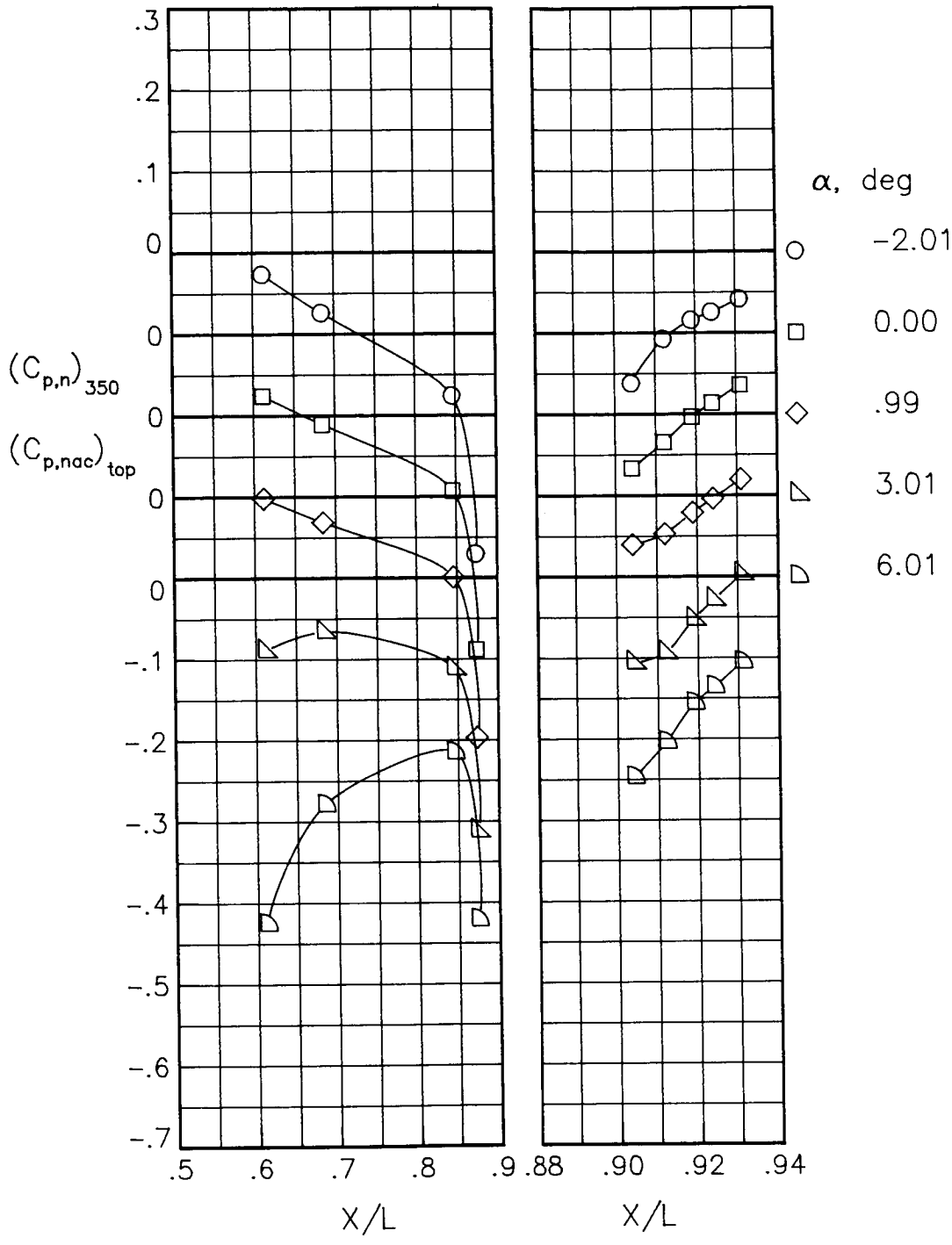

(e) M = 0.90; NPR = 1.00.

Figure 34.- Continued.

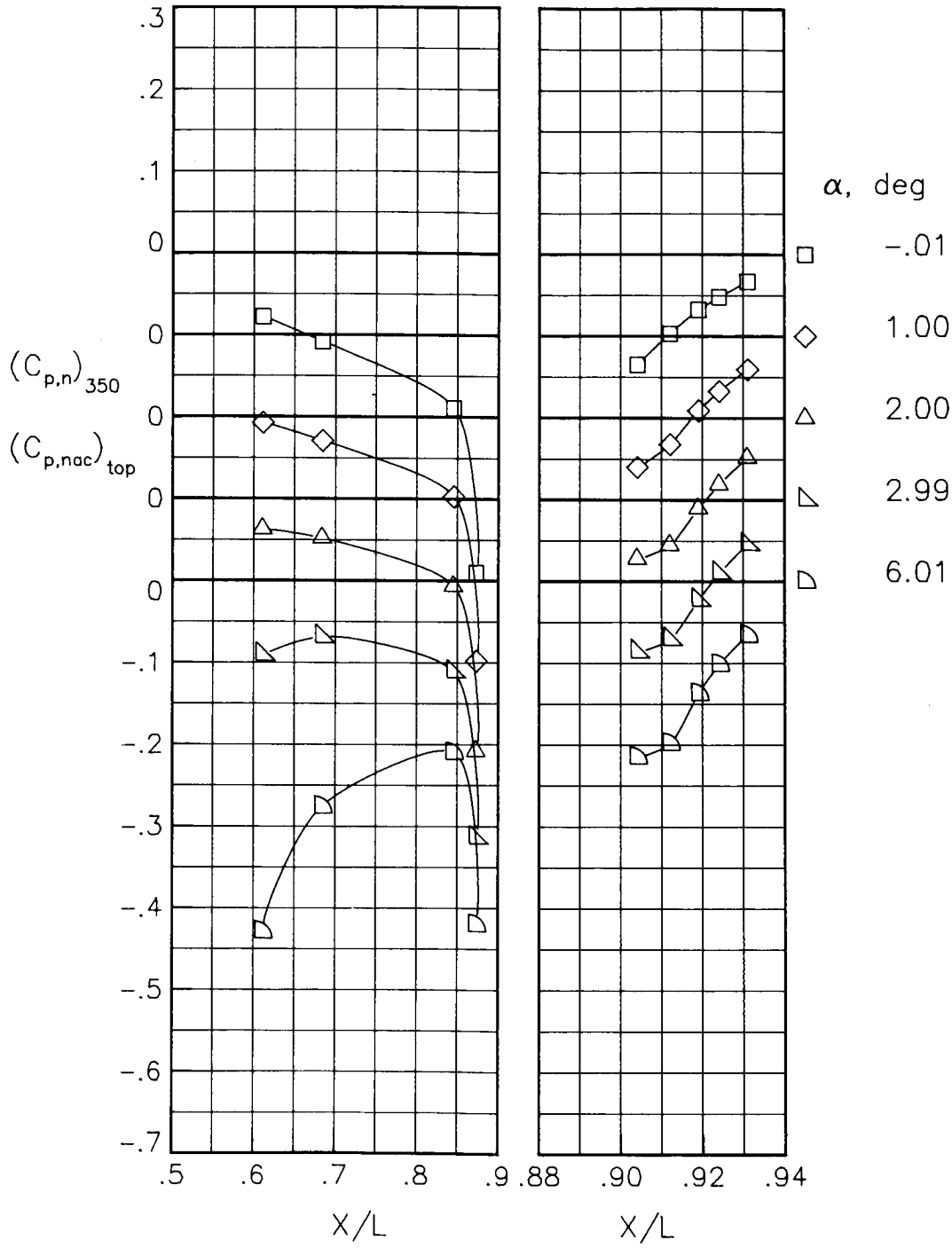

(f) M = 0.90; NPR = 5.00.

Figure 34.- Concluded.

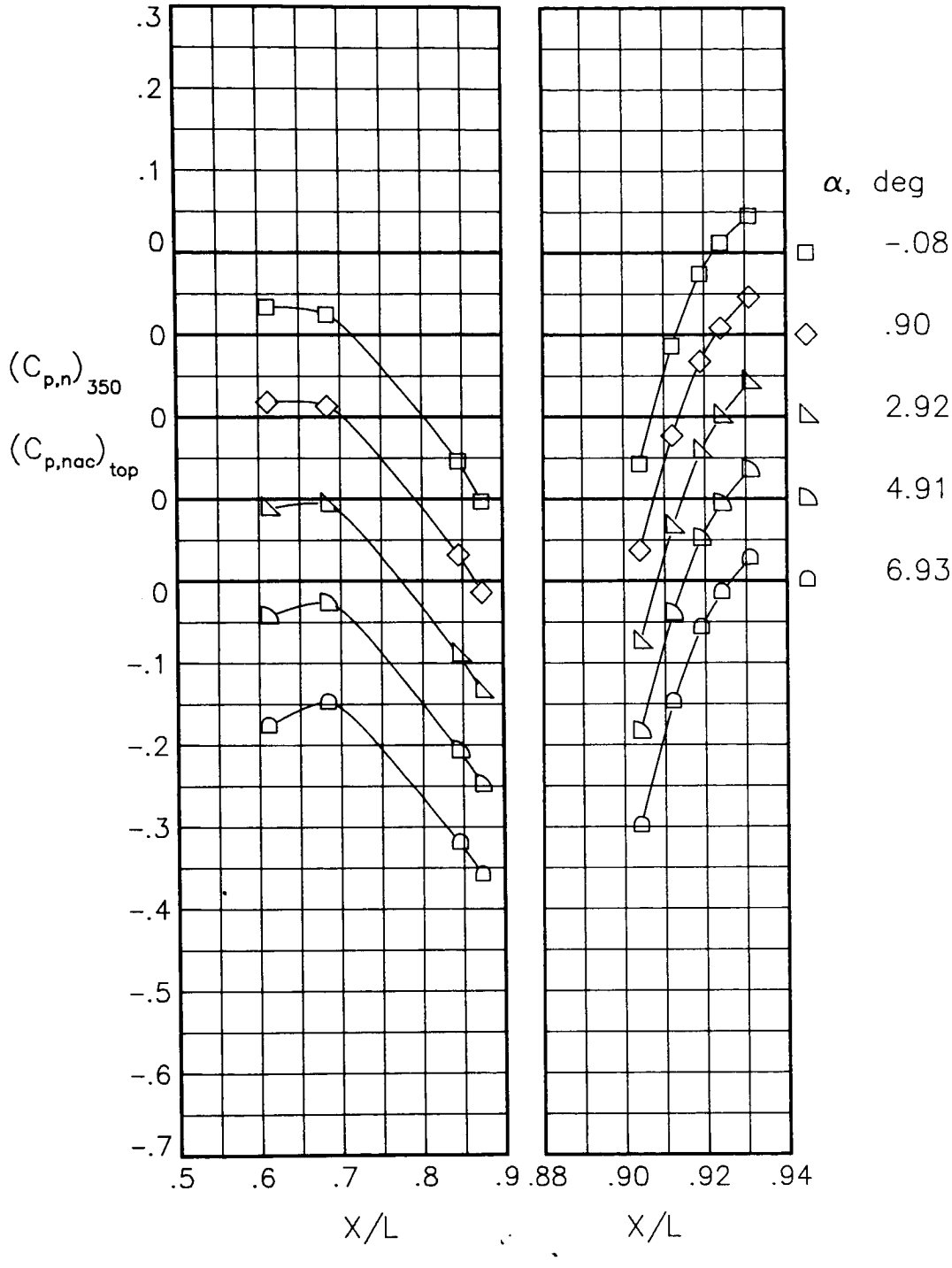

(a) M = 0.60; NPR = 1.00.

Figure 35.- Static-pressure-coefficient distributions on top of nacelle and nozzle for the model with nose boom. β_n = 18.45°.

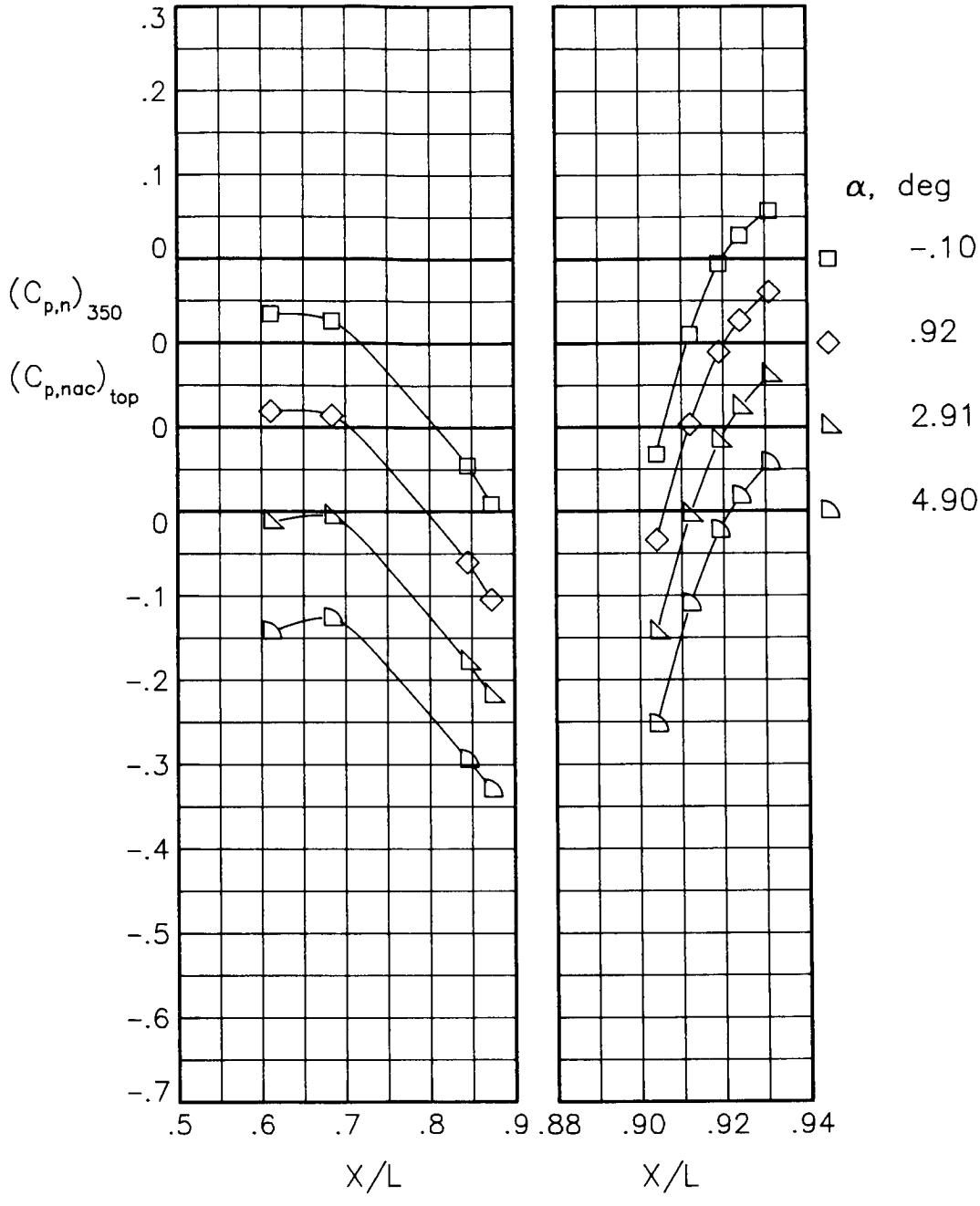

(b) M = 0.60; NPR = 3.00.

Figure 35.- Continued.

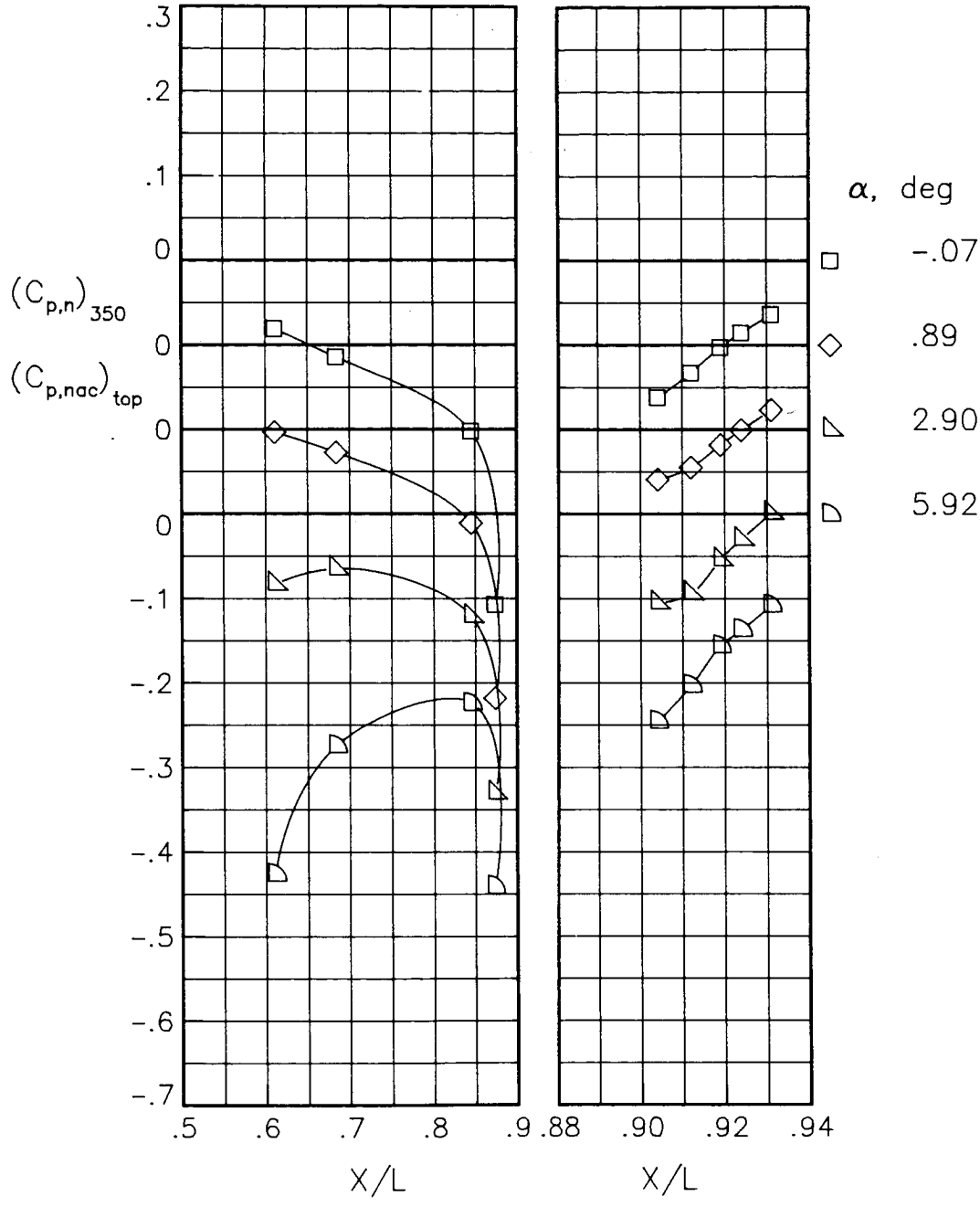

(c) M = 0.90; NPR = 1.00.

Figure 35.- Continued.

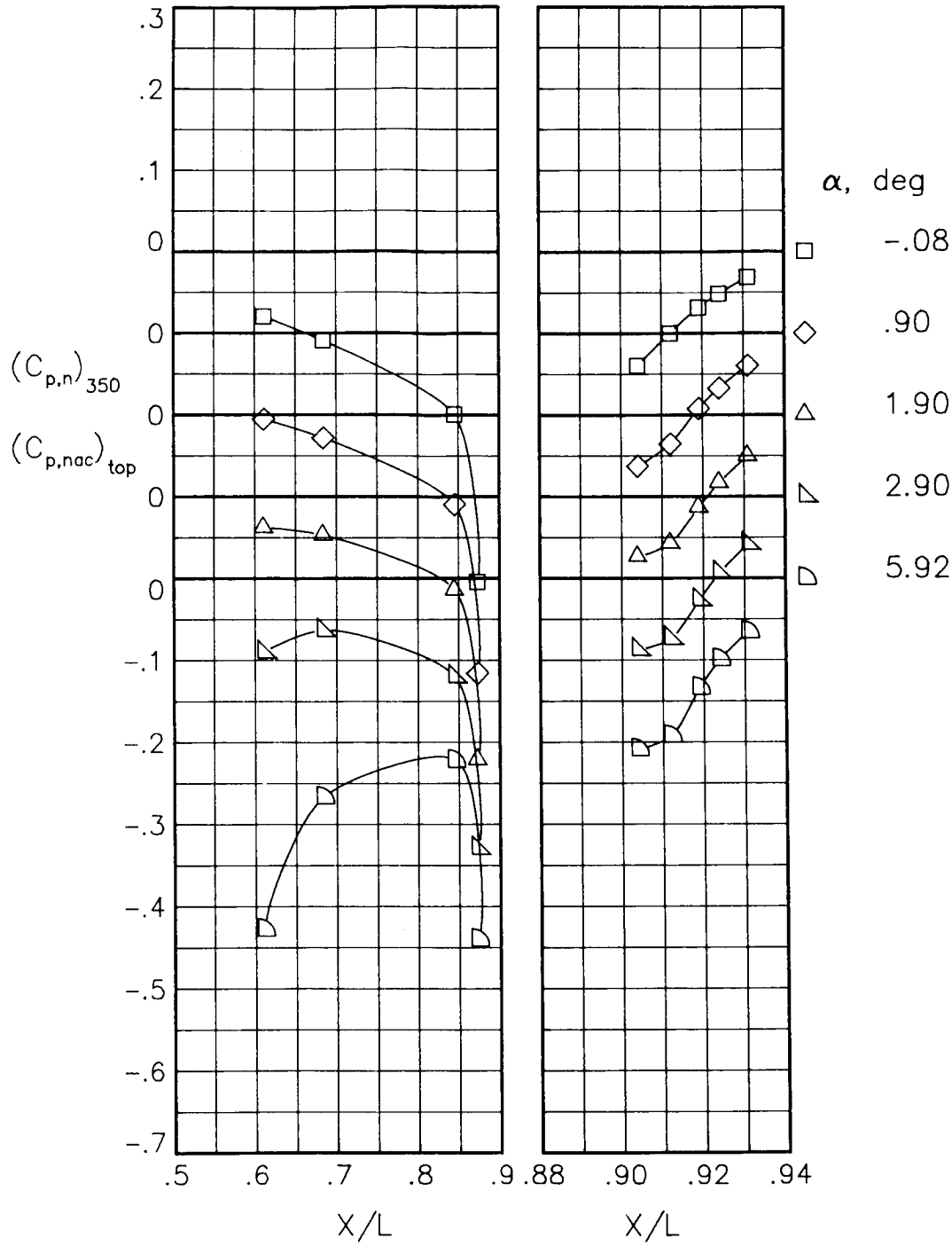

(d) M = 0.90; NPR = 5.00.

Figure 35.- Concluded.

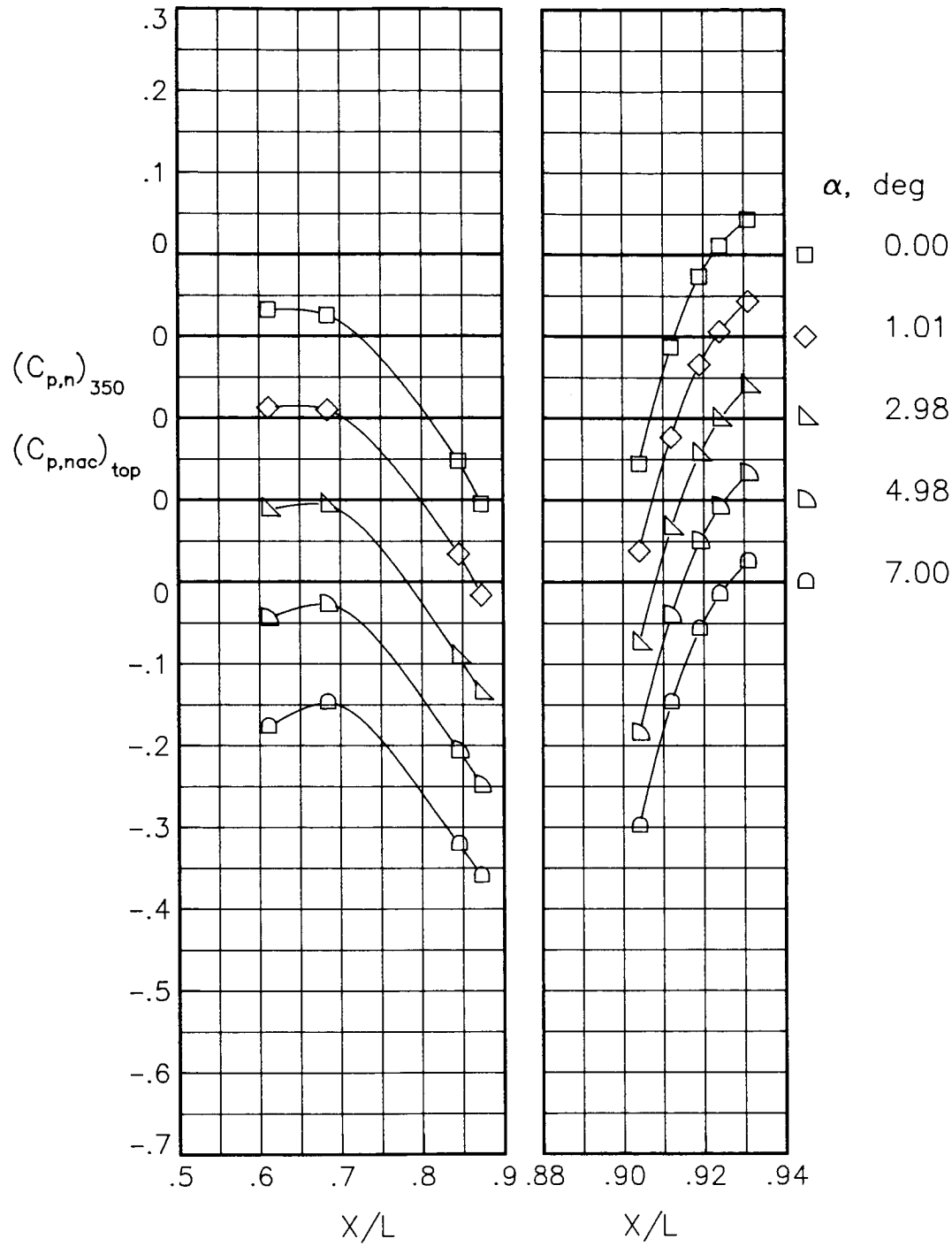

(a) M = 0.60; NPR = 1.00.

Figure 36.- Static-pressure-coefficient distributions on top of nacelle and nozzle for the model with nose boom, actuator fairings, and A/B vents. β_n = 18.45°.

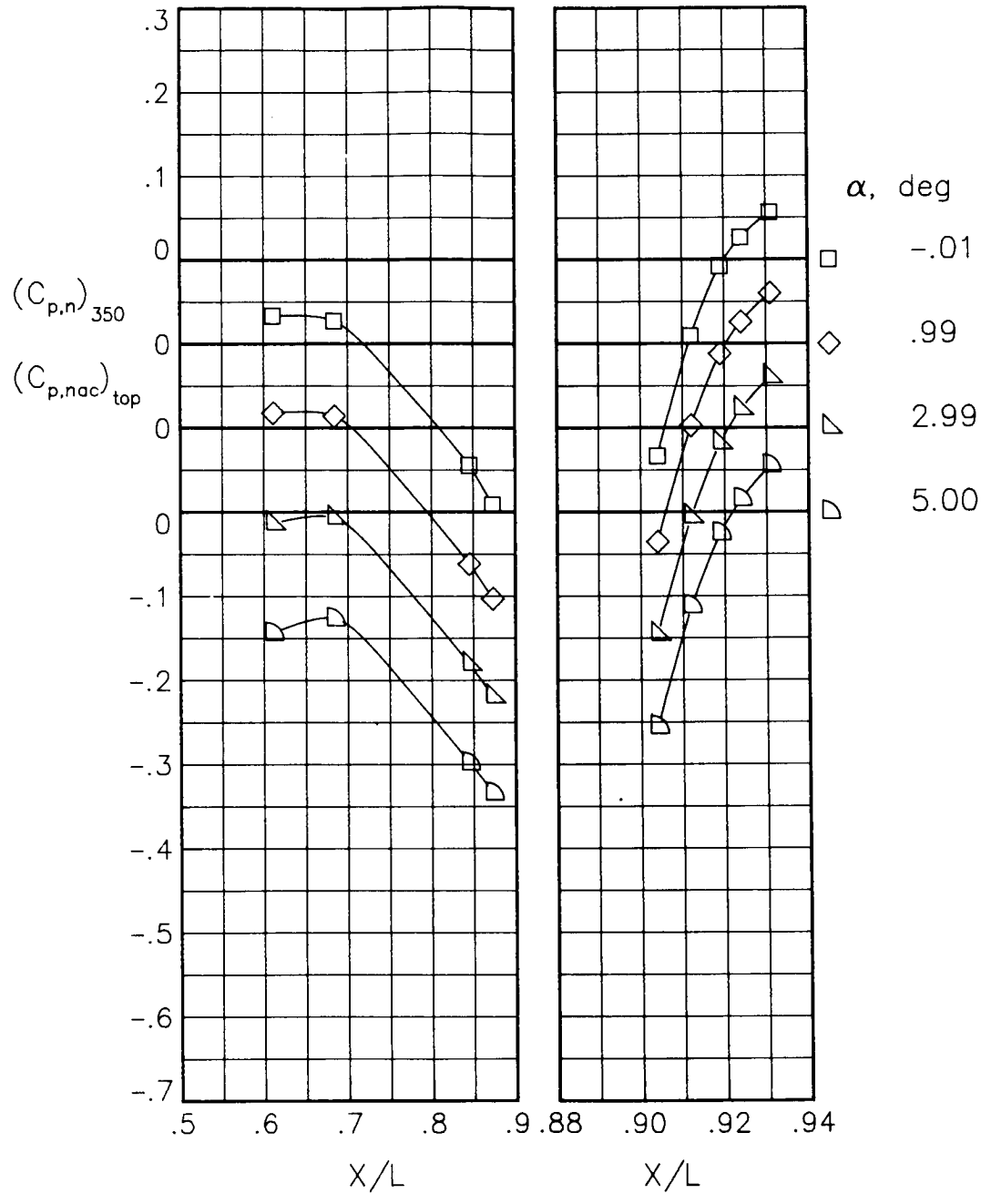

(b) M = 0.60; NPR = 3.00.

Figure 36.- Continued.

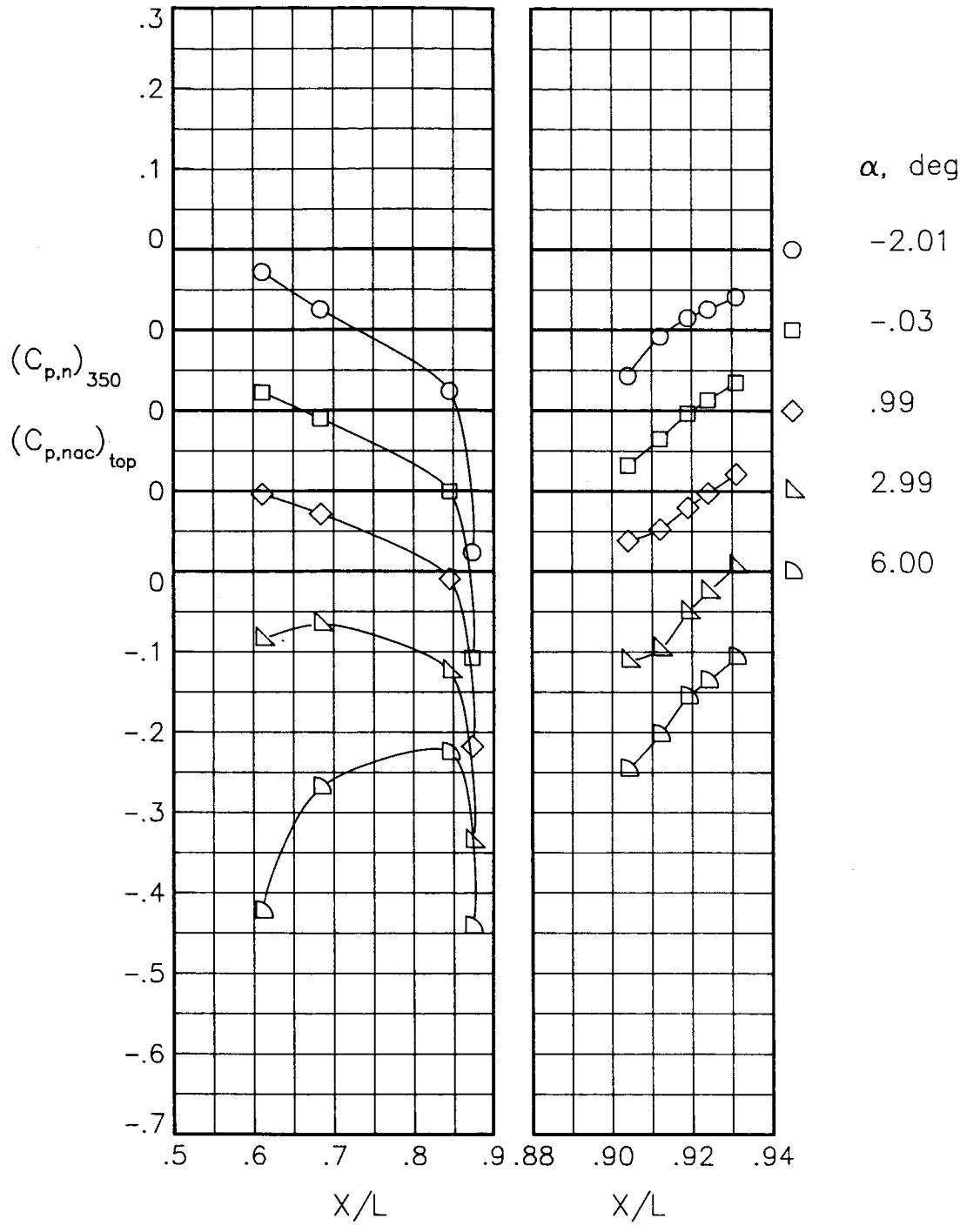

(c) M = 0.90; NPR = 1.00.

Figure 36.- Continued.

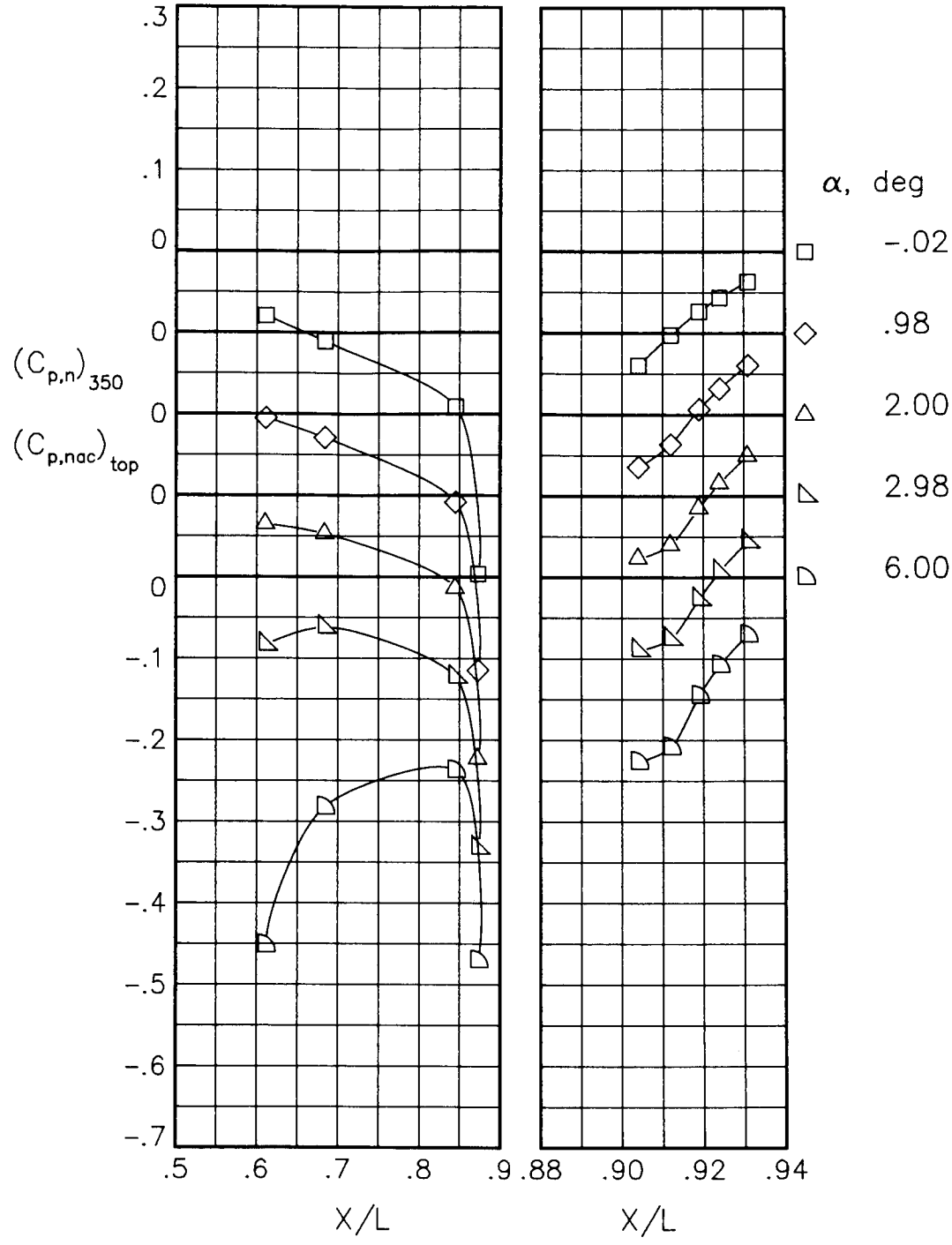

(d) M = 0.90; NPR = 5.00.

Figure 36.- Concluded.

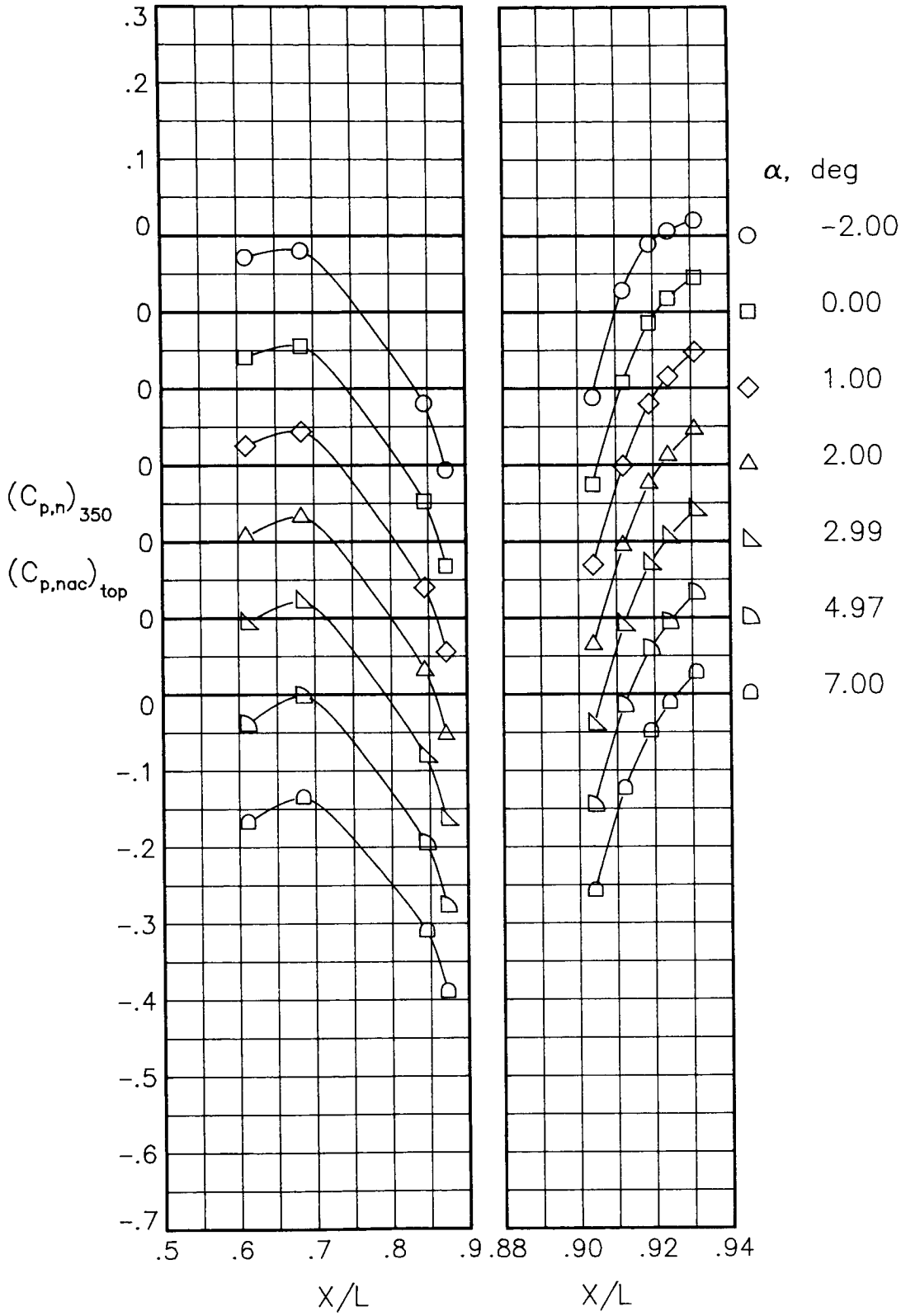

(a) M = 0.60; NPR = 1.00.

Figure 37.- Static-pressure-coefficient distributions on top of nacelle and nozzle for the model with all fuselage modifications except nose boom. β_n = 18.45°.

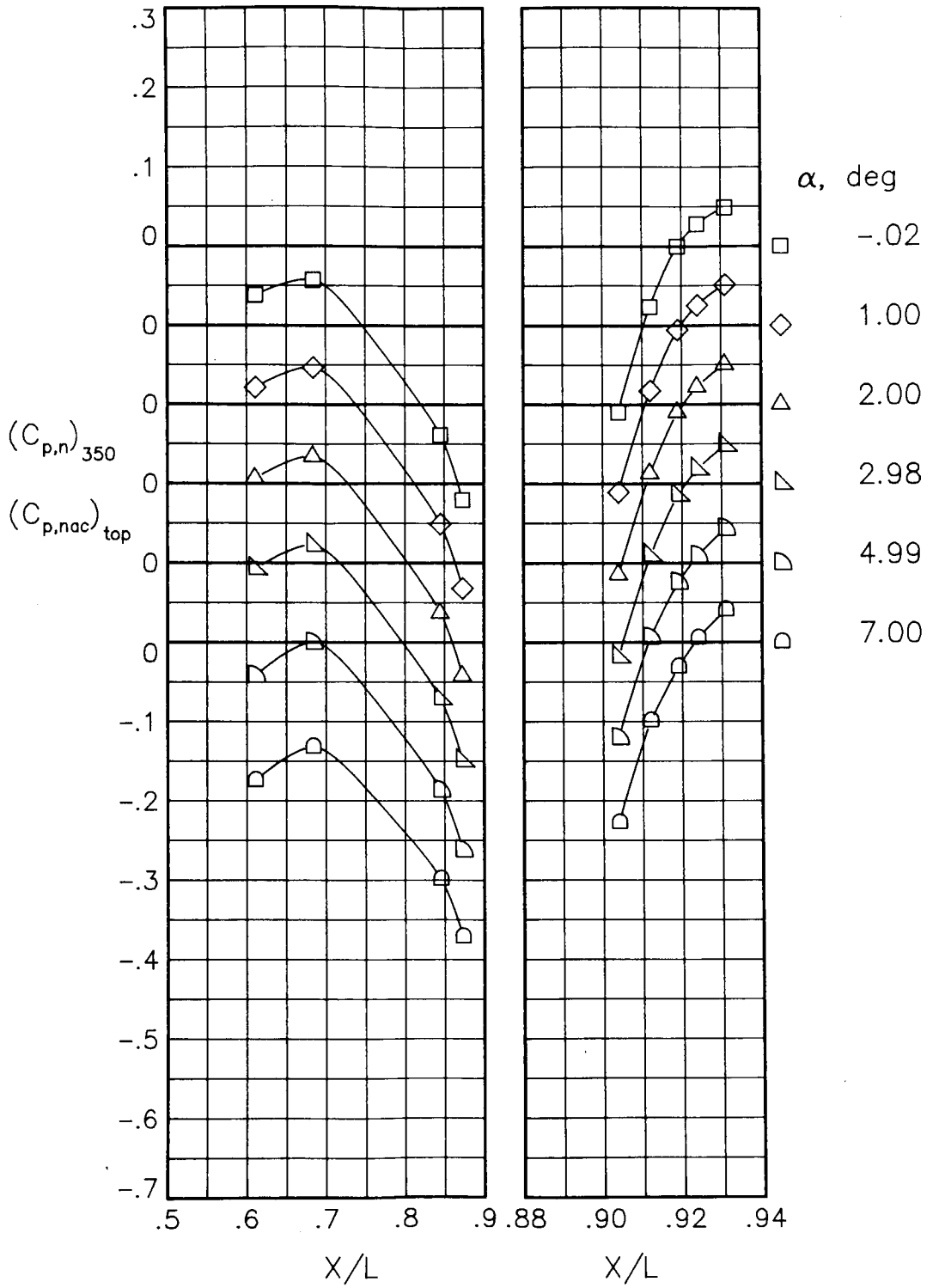

(b) M = 0.60; NPR = 3.00.

Figure 37.- Continued.

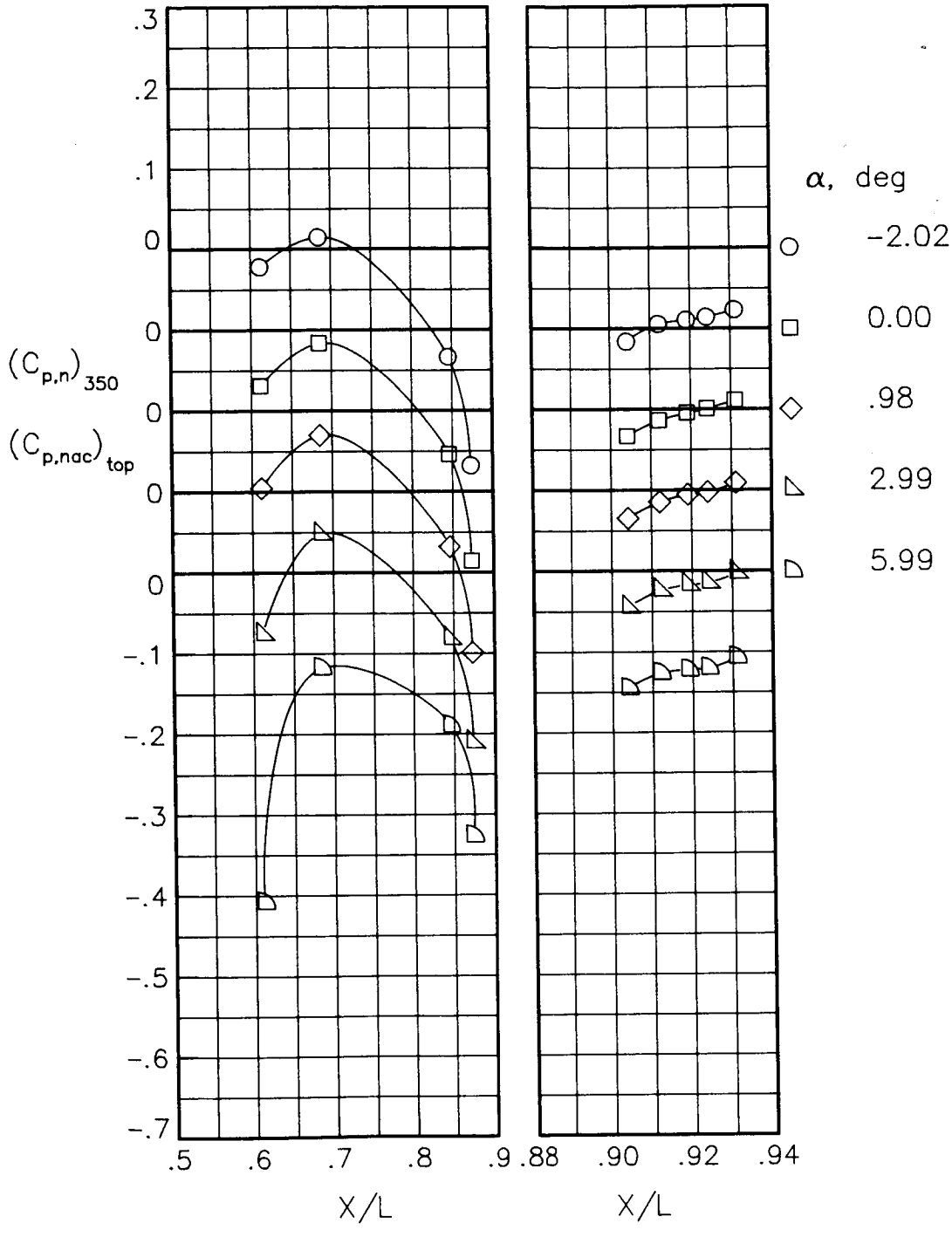

(c) M = 0.90; NPR = 1.00.

Figure 37.- Continued.

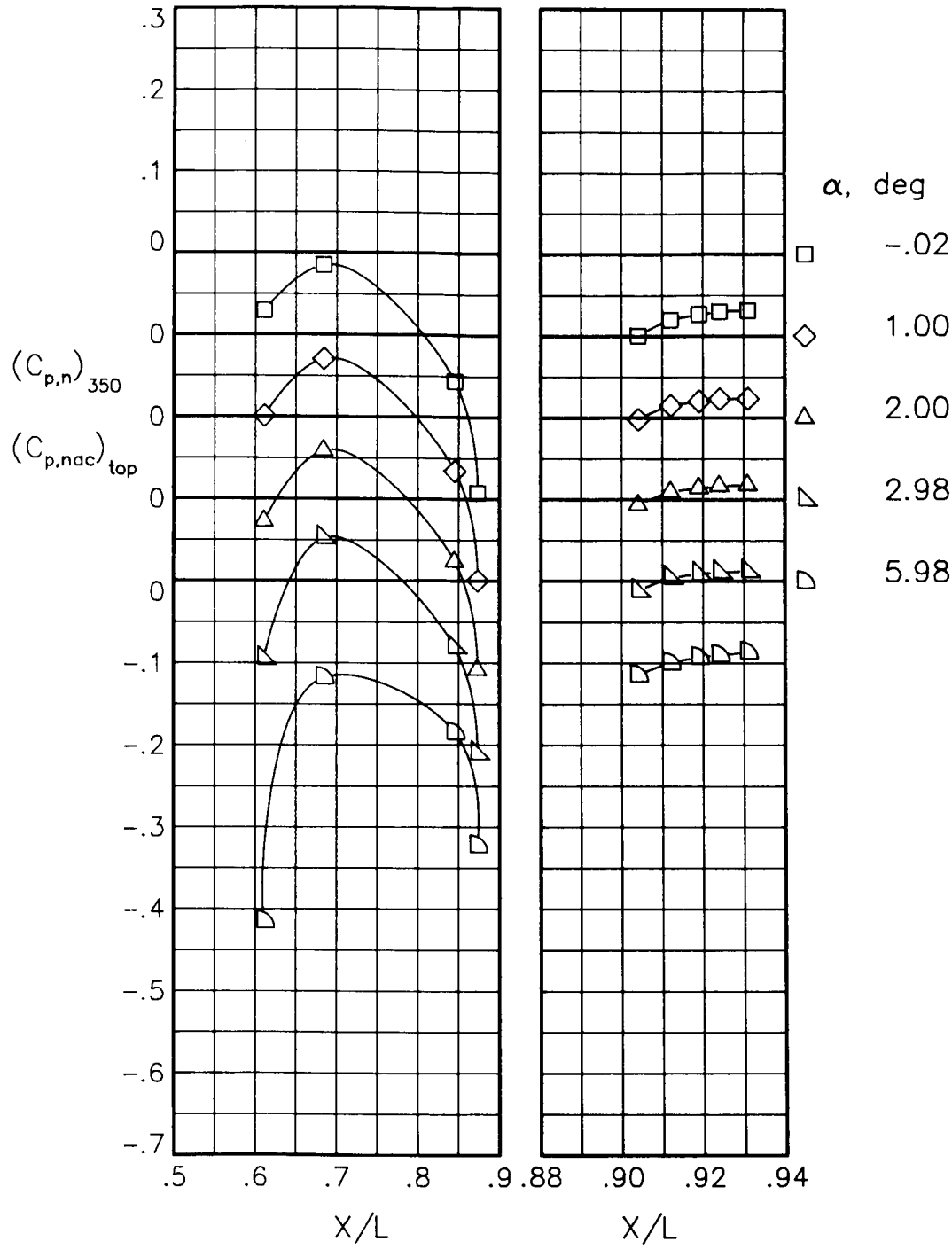

(d) M = 0.90; NPR = 5.00.

Figure 37.- Concluded.

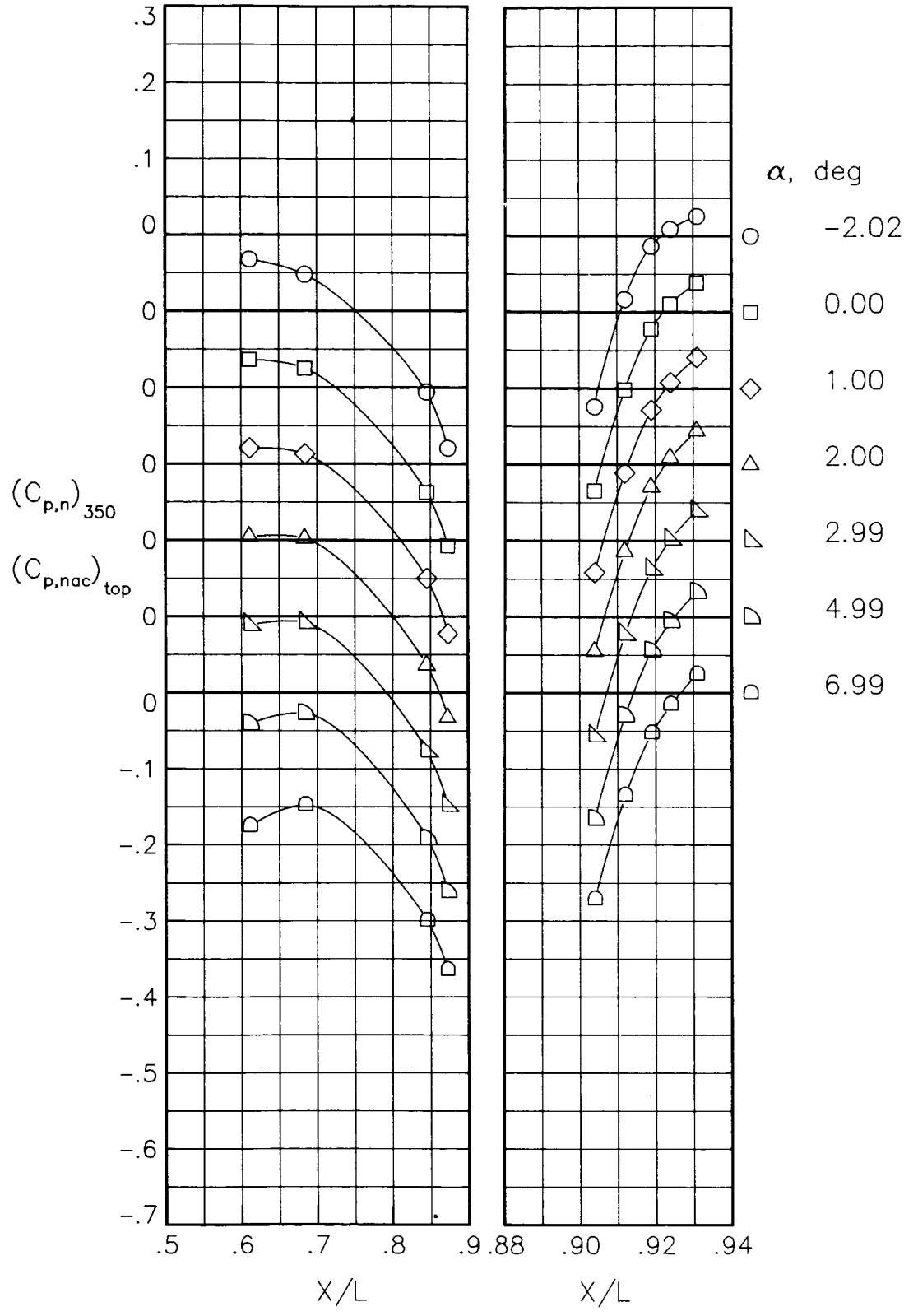

(a) M = 0.60; NPR = 1.00.

Figure 38.- Static-pressure-coefficient distributions on top of nacelle and nozzle for the model with nose boom, actuator fairings, A/B vents, and nozzle steps (no rakes). β_n = 18.45°.

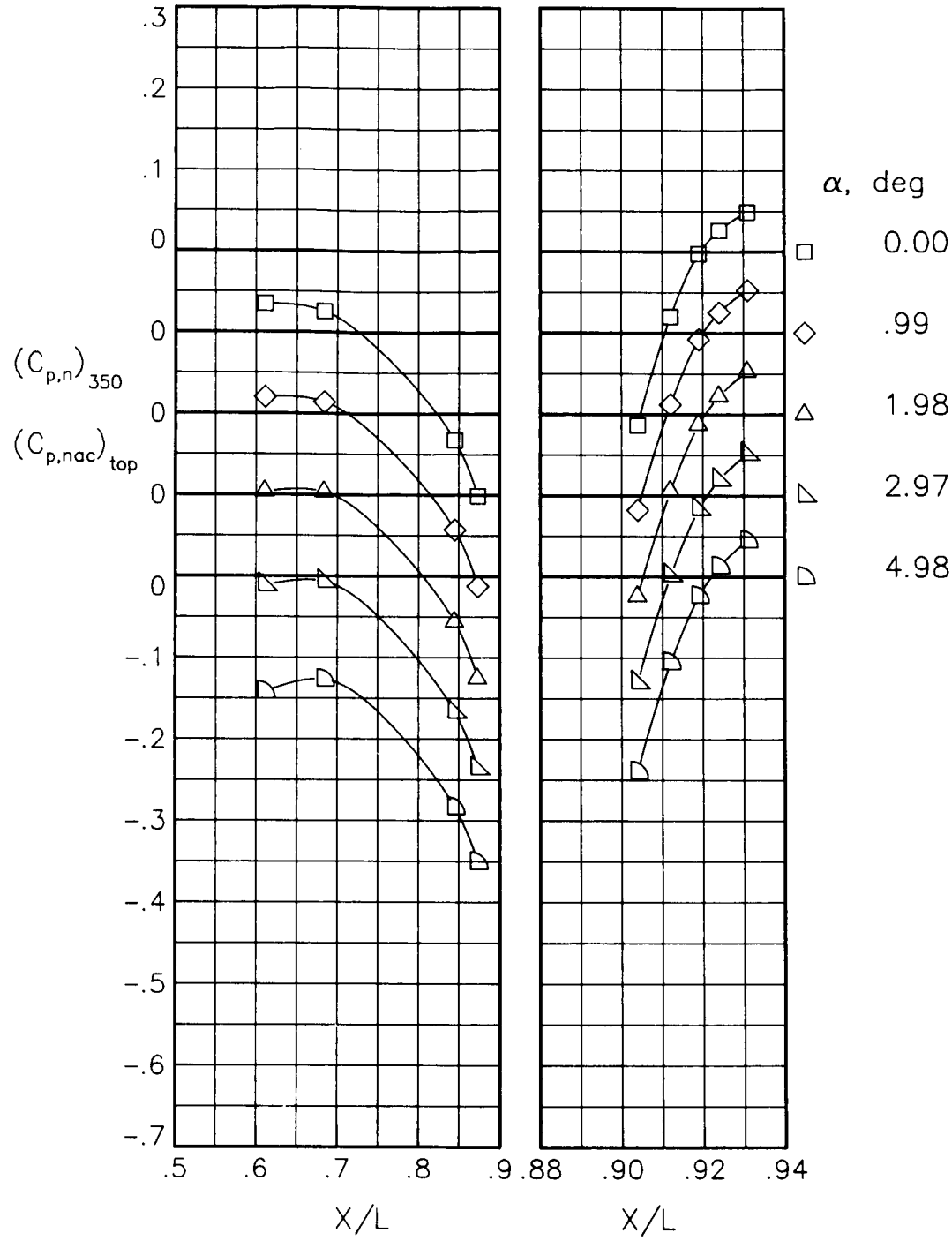

(b) M = 0.60; NPR = 3.00.

Figure 38.- Continued.

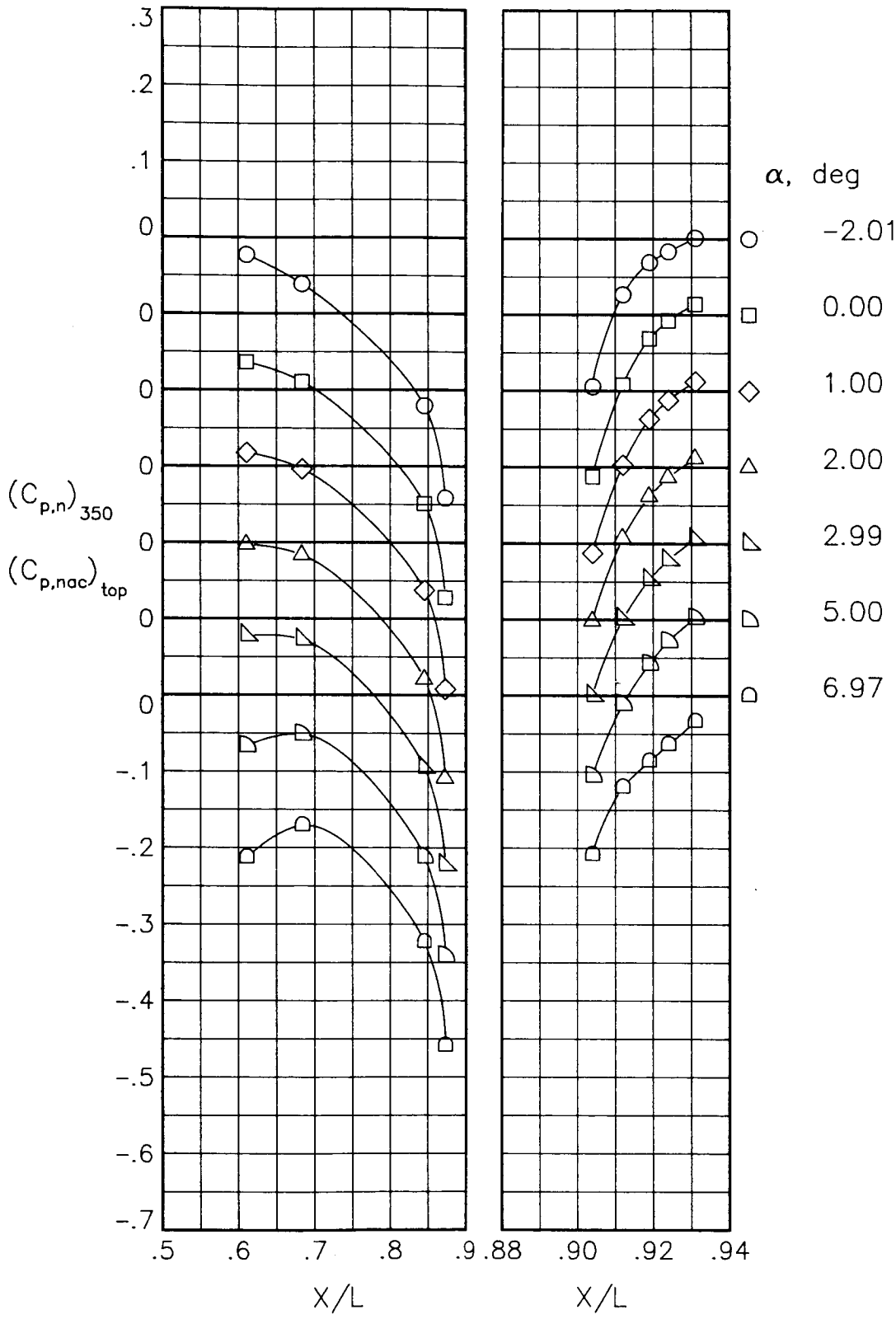

(c) M = 0.80; NPR = 1.00.

Figure 38.- Continued.

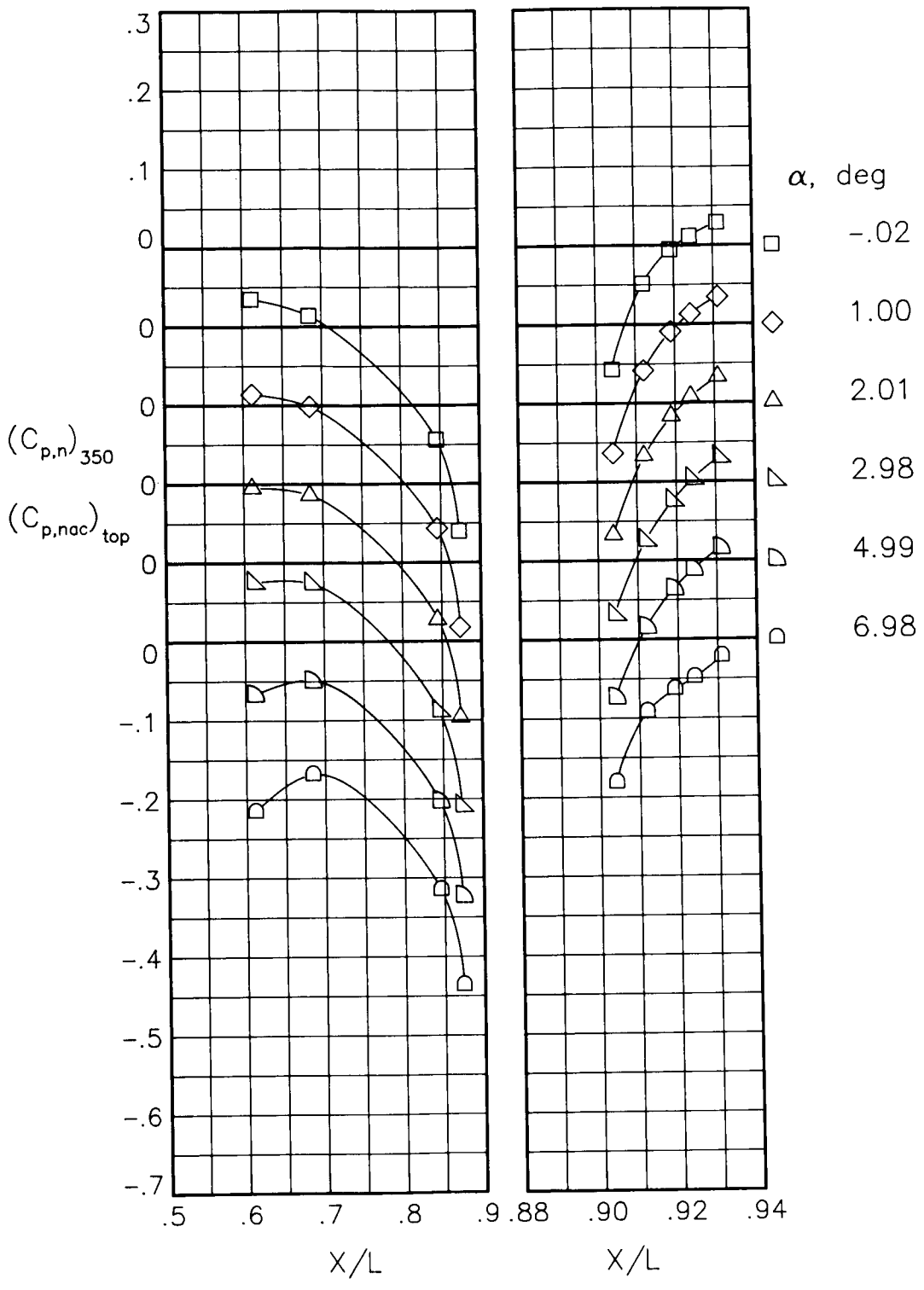

(d) M = 0.80; NPR = 4.60.

Figure 38.- Continued.

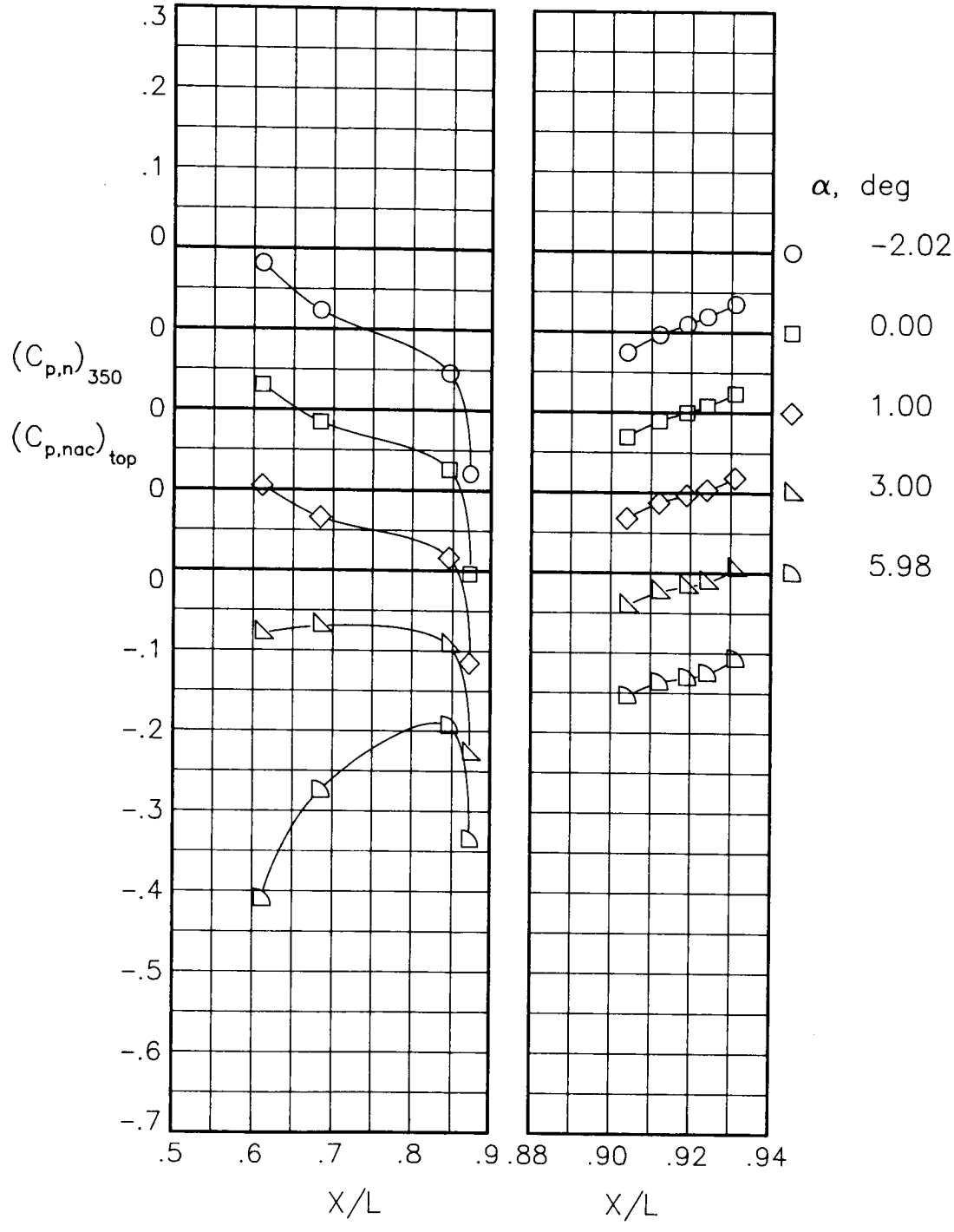

(e) M = 0.90; NPR = 1.00.

Figure 38.- Continued.

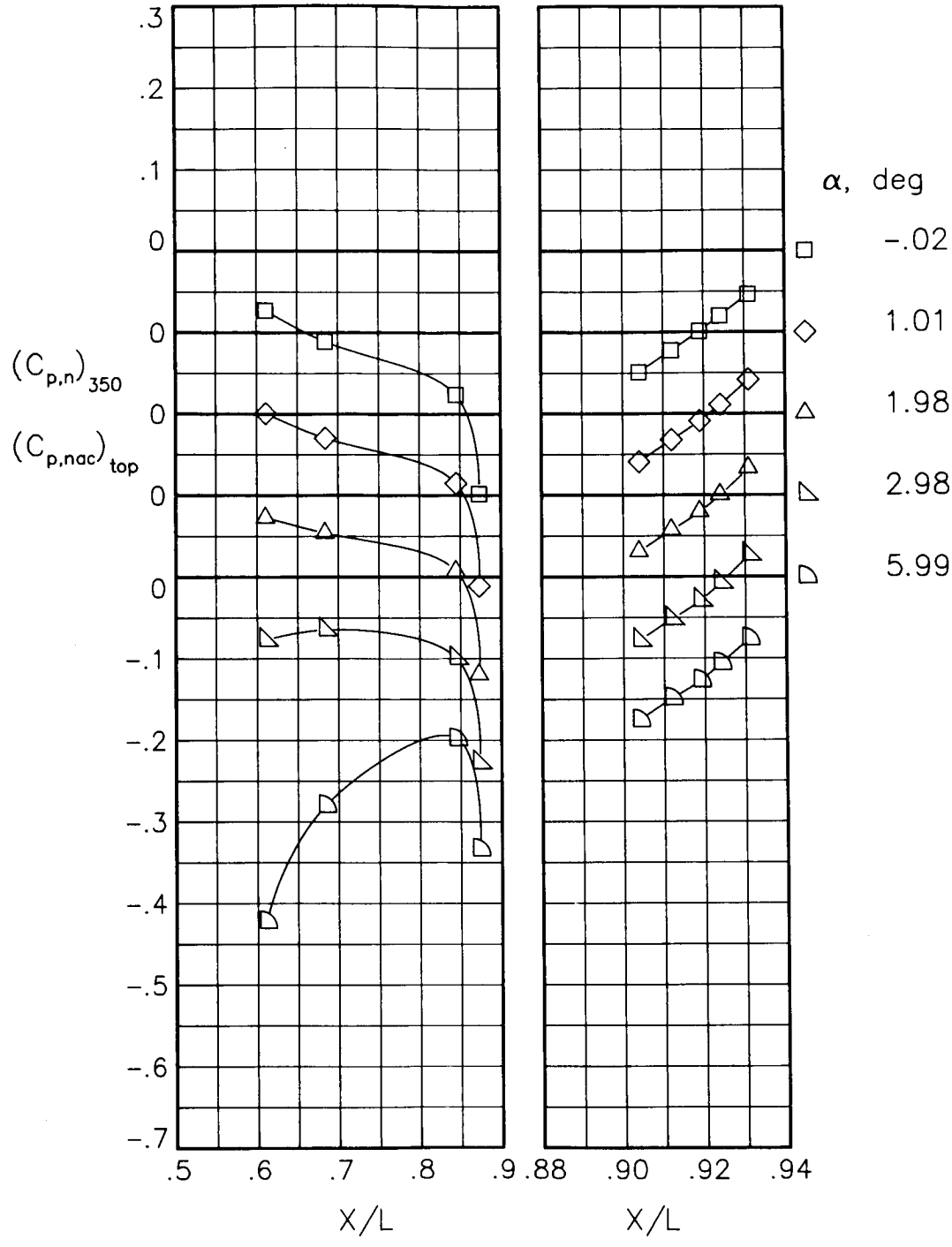

(f) M = 0.90; NPR = 5.00.

Figure 38.- Concluded.

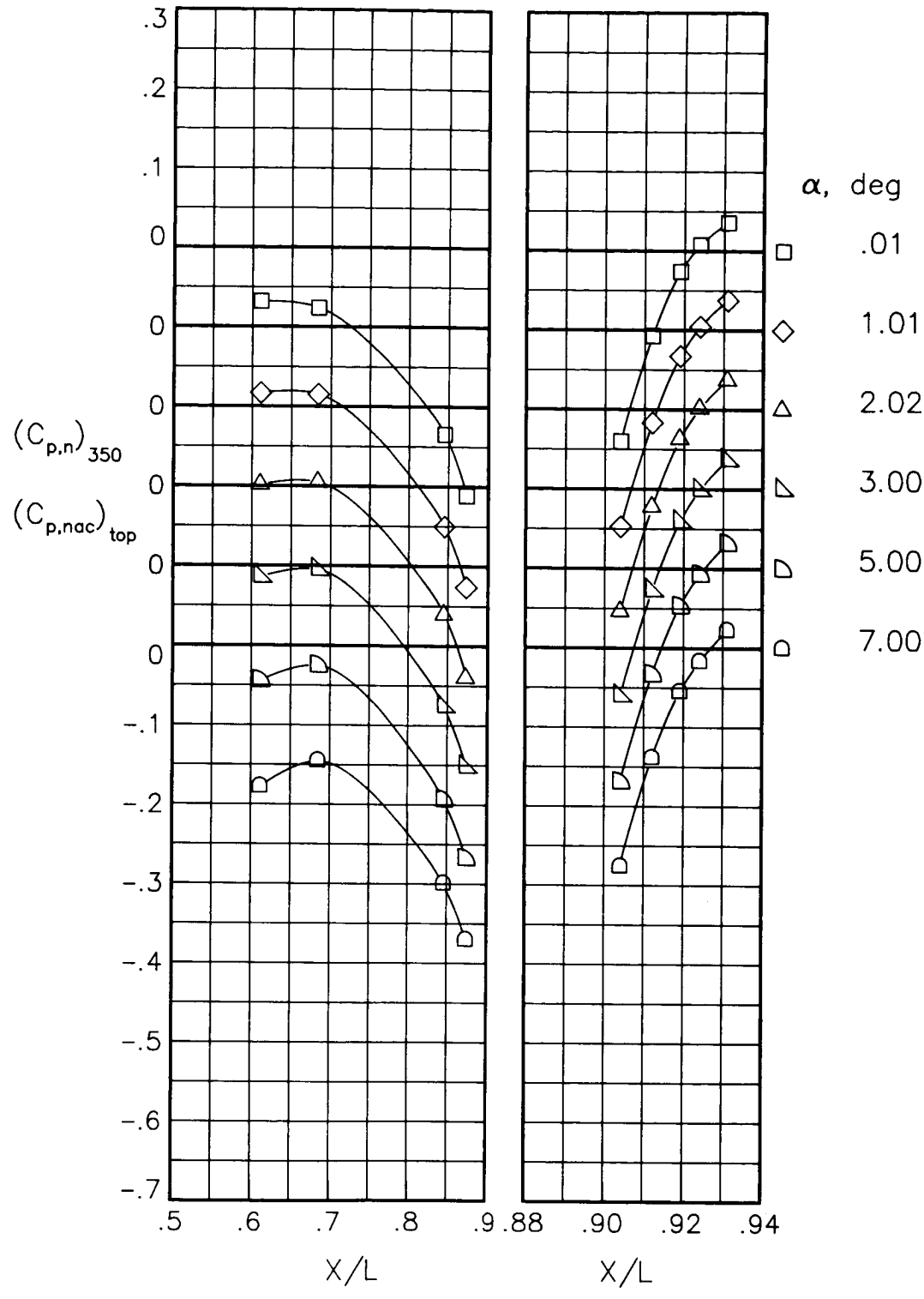

(a) M = 0.60; NPR = 1.00.

Figure 39.- Static-pressure-coefficient distributions on top of nacelle and nozzle for the model with nose boom, actuator fairings, A/B vents, and nozzle steps (no rakes). β_n = 18.45°; δ_h = -2°.

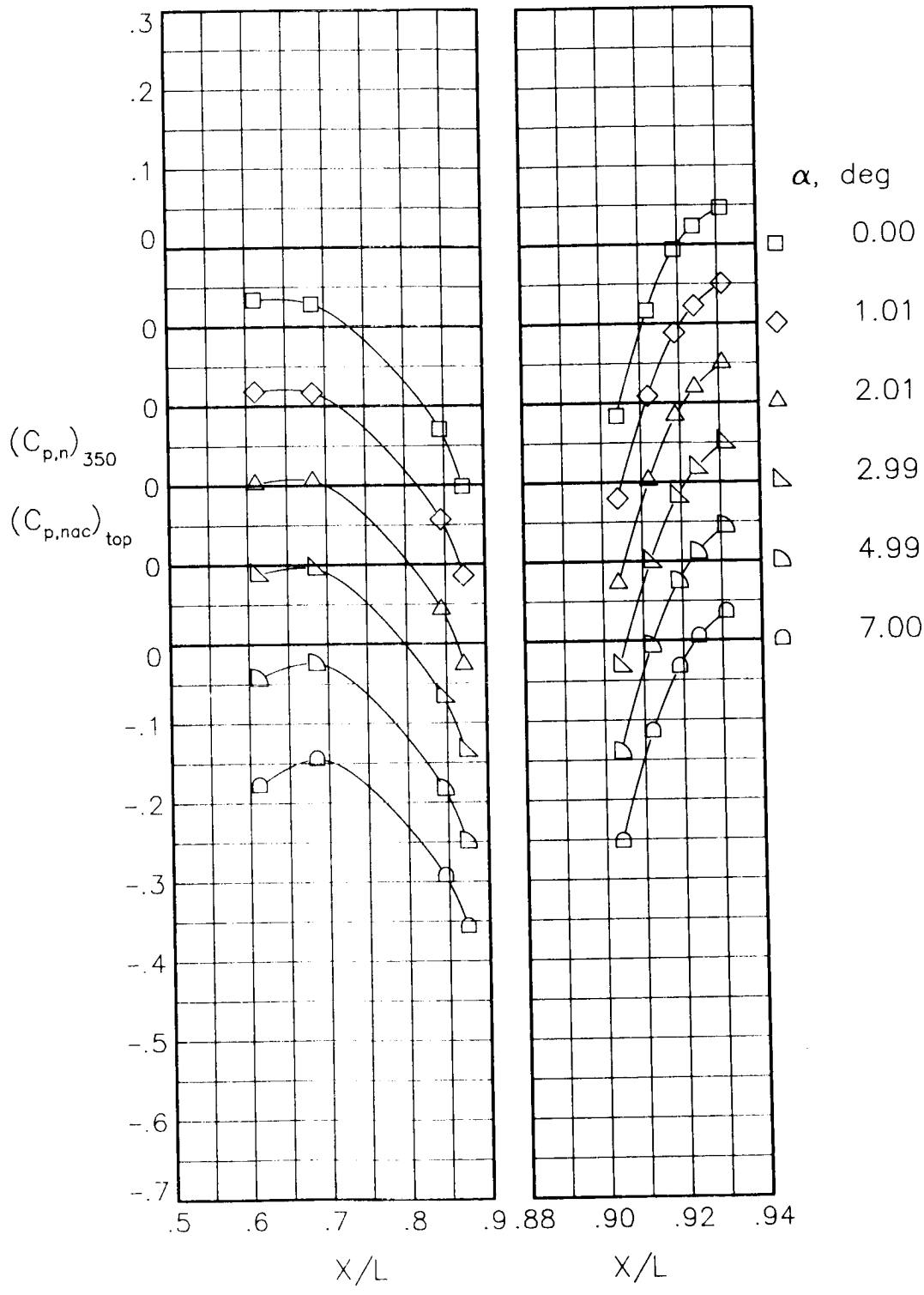

(b) M = 0.60; NPR = 3.00.

Figure 39.- Continued.

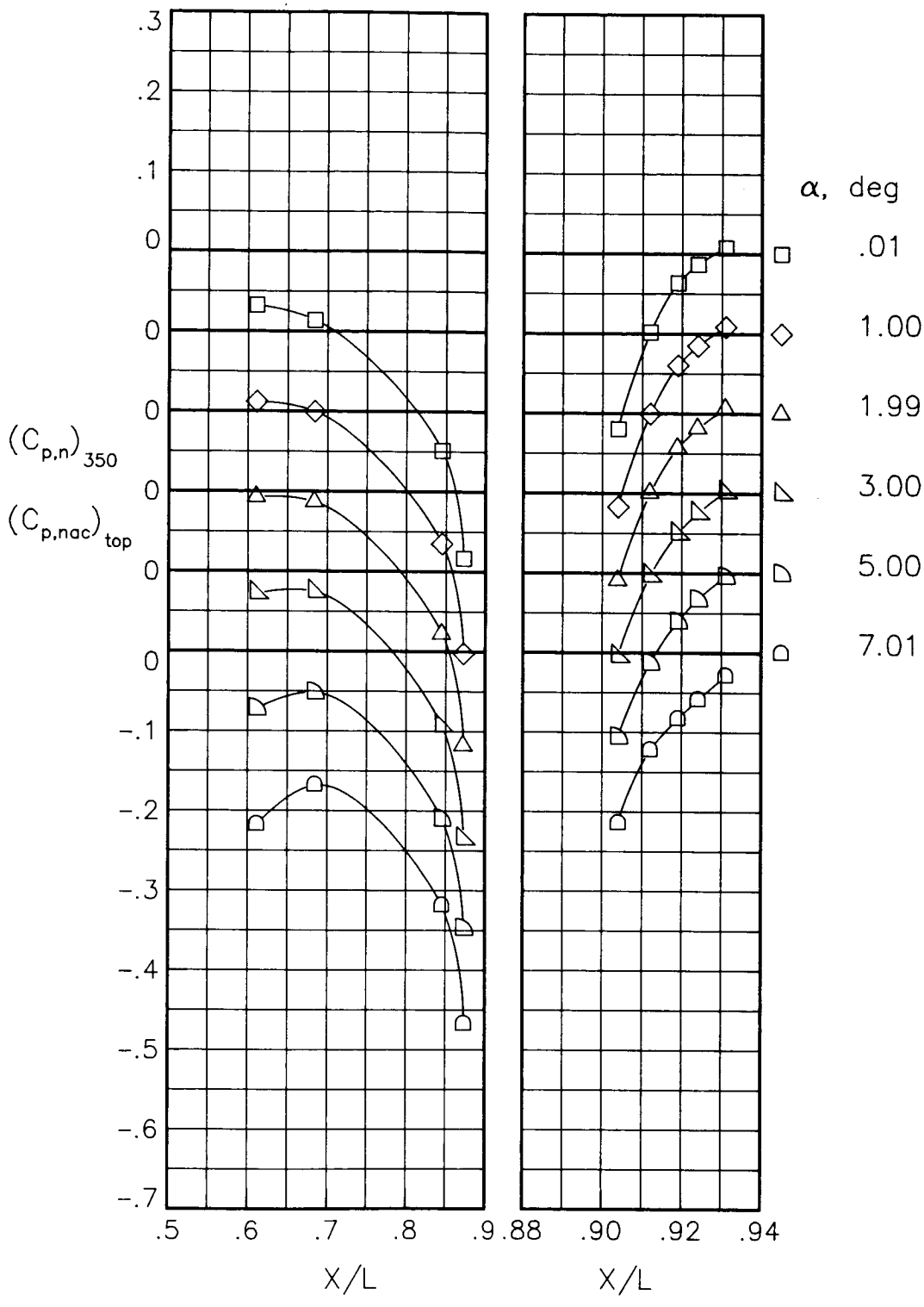

(c) M = 0.80; NPR = 1.00.

Figure 39.- Continued.

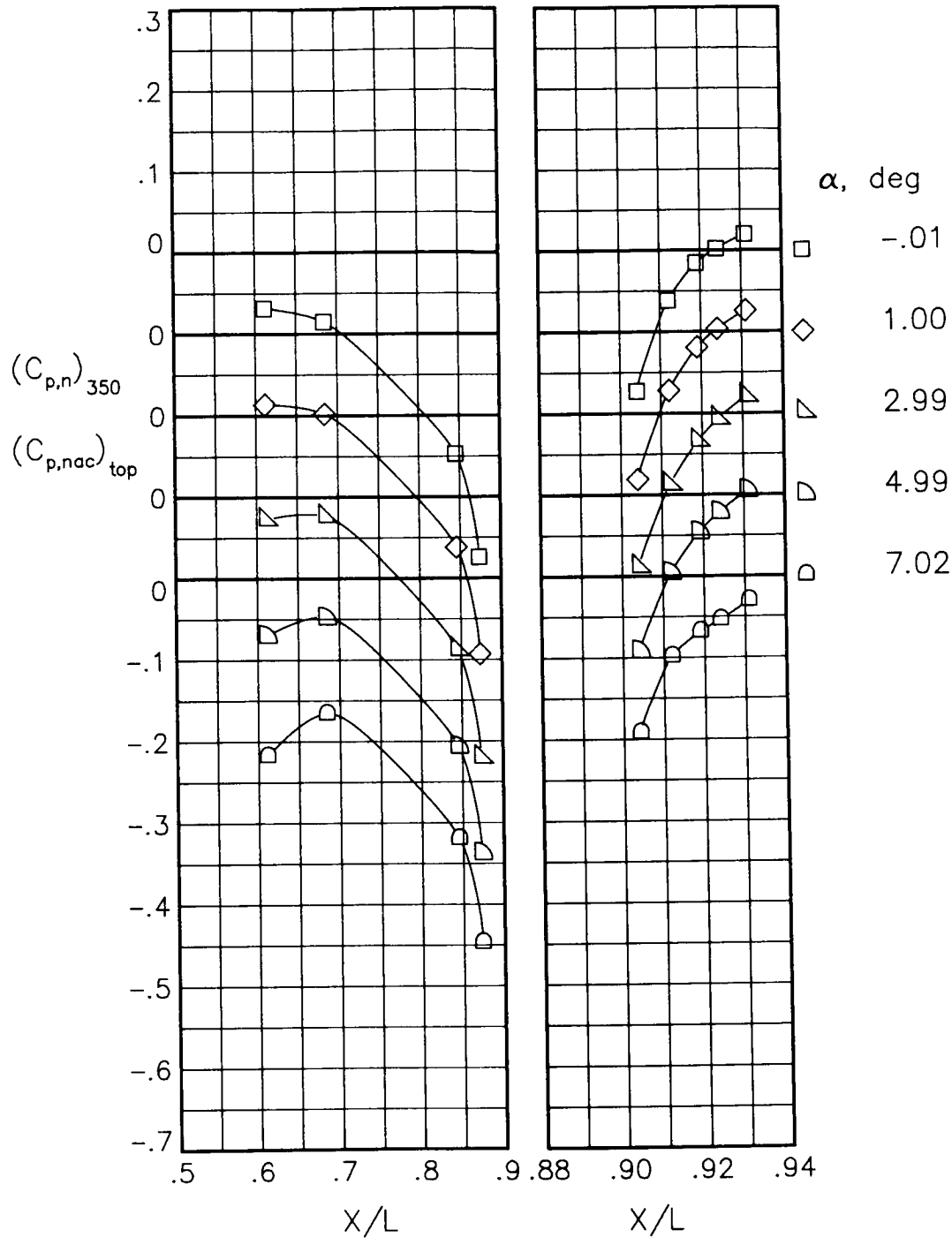

(d) M = 0.80; NPR = 4.60.

Figure 39.- Continued.

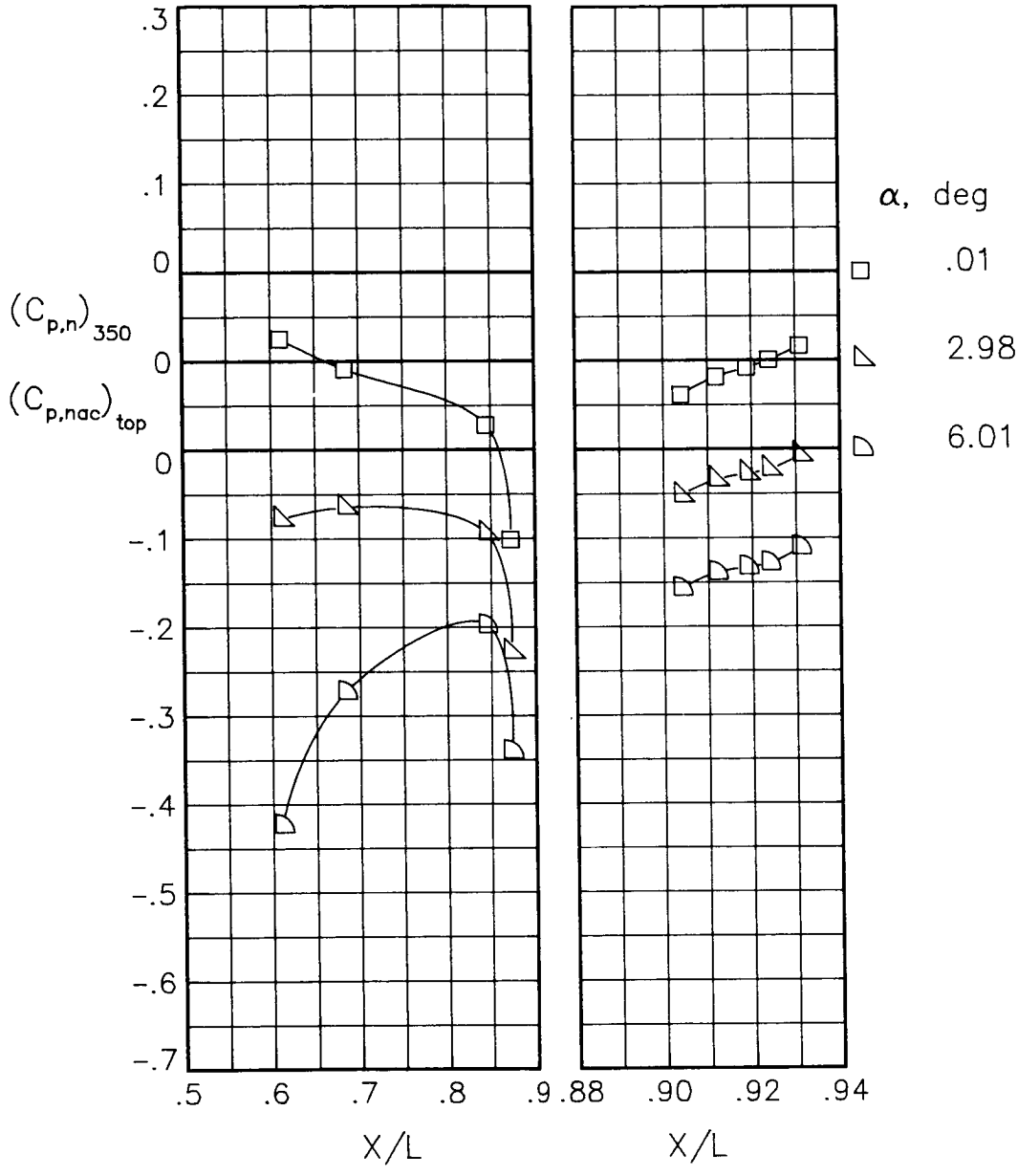

(e) M = 0.90; NPR = 1.00.

Figure 39.- Continued.

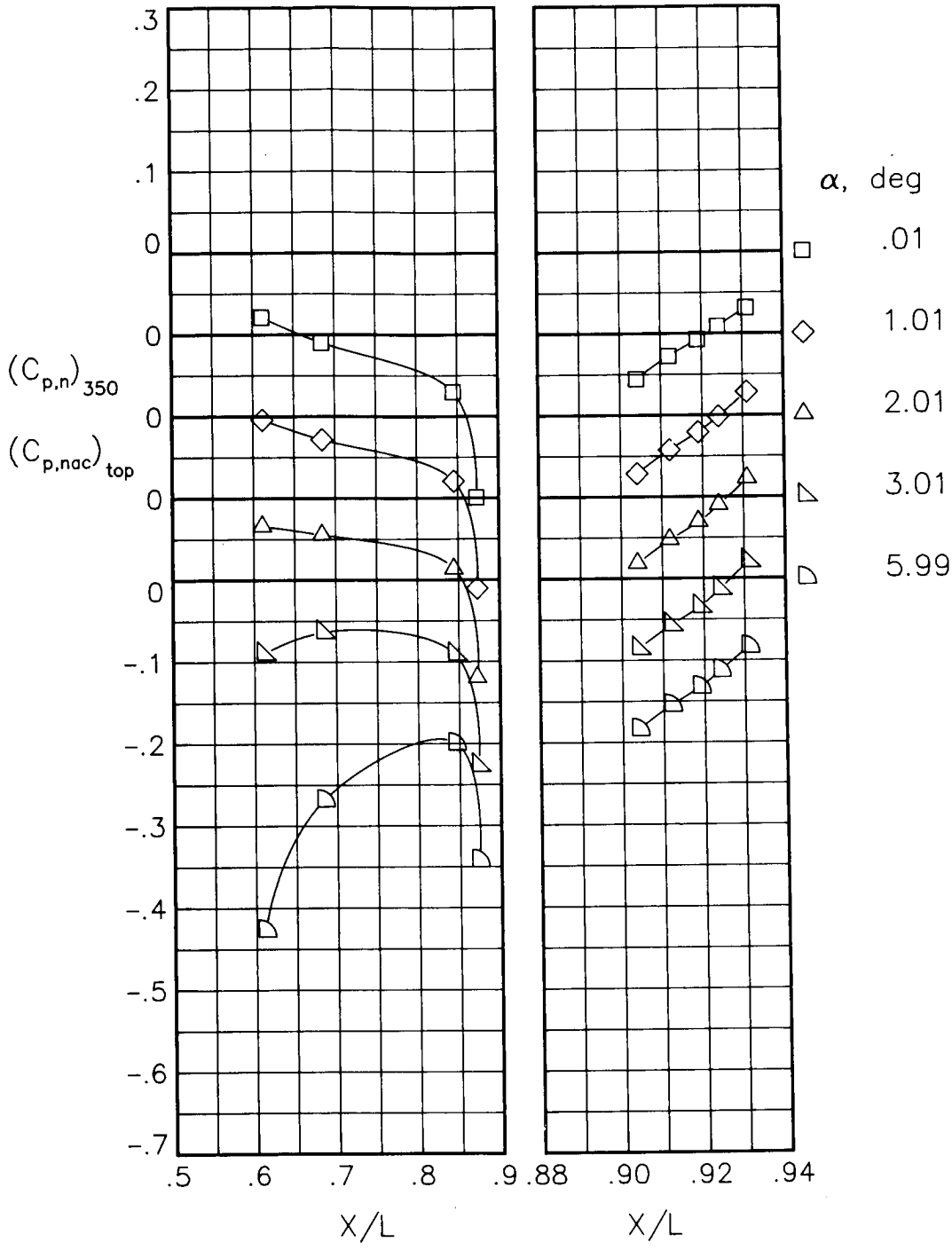

(f) M = 0.90; NPR = 5.00.

Figure 39.- Concluded.

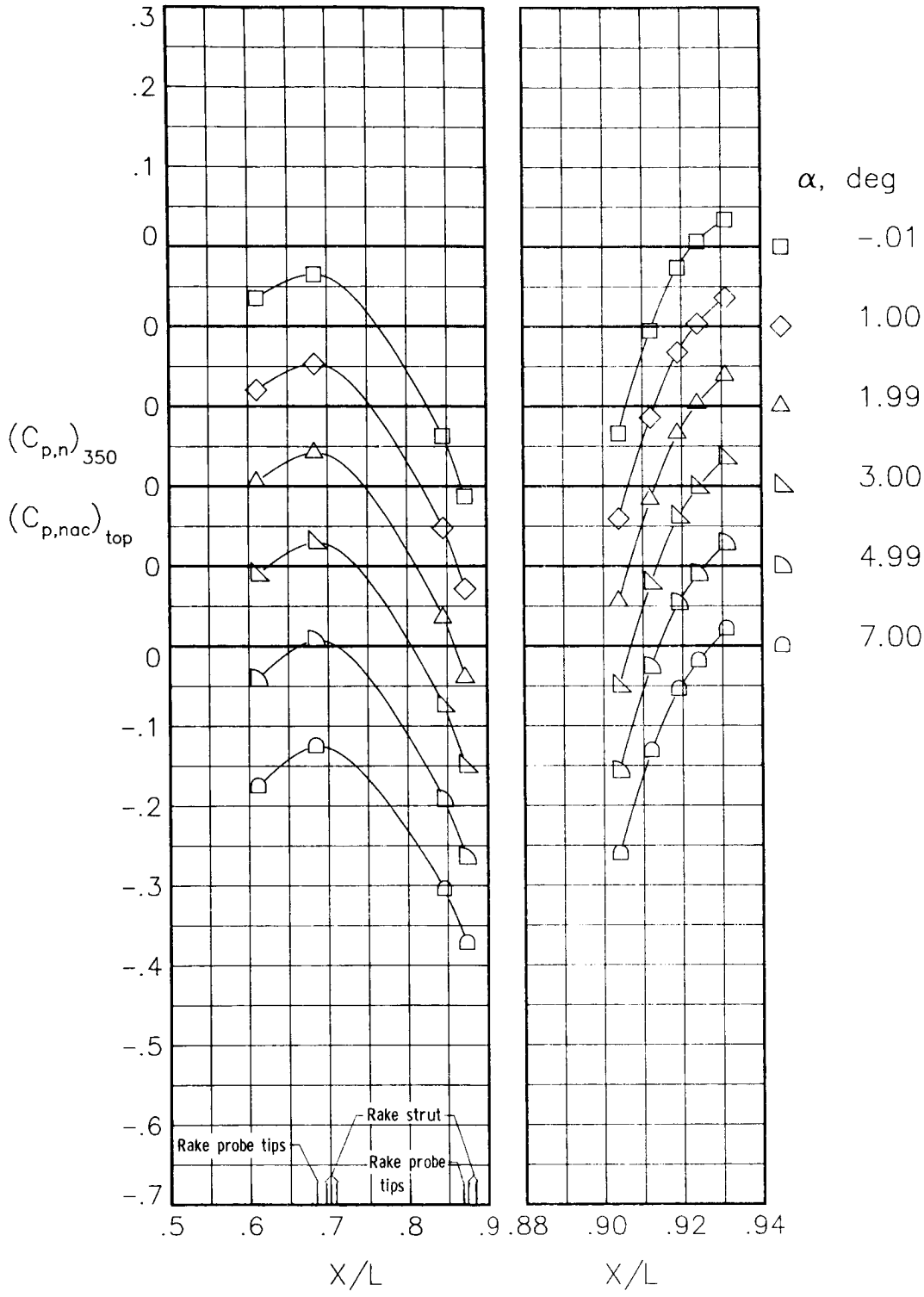

(a) M = 0.60; NPR = 1.00.

Figure 40.- Static-pressure-coefficient distributions on top of nacelle and nozzle for the model with all fuselage modifications. β_n = 18.45°; δ_h = -2°.

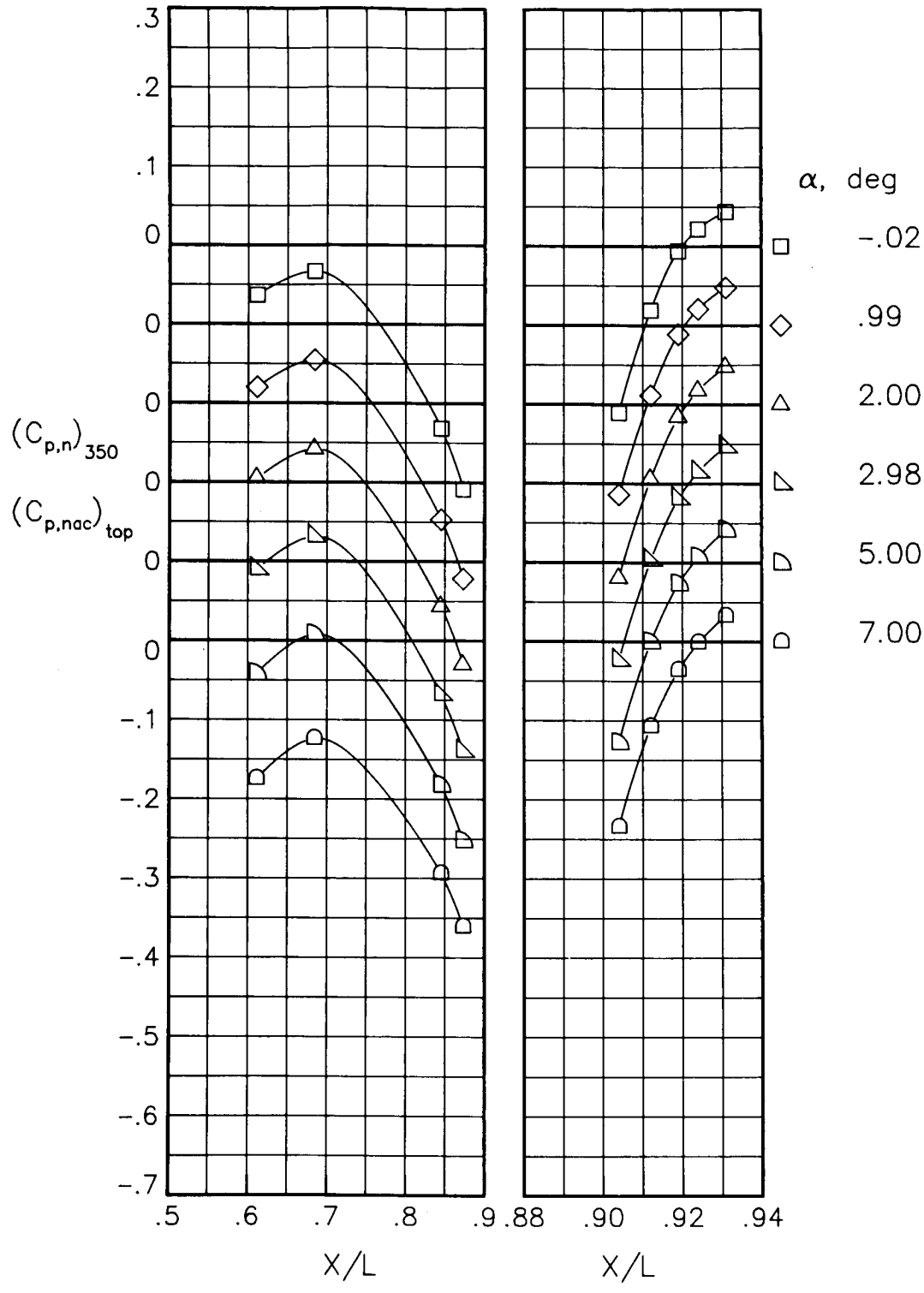

(b) M = 0.60; NPR = 3.00.

Figure 40.- Continued.

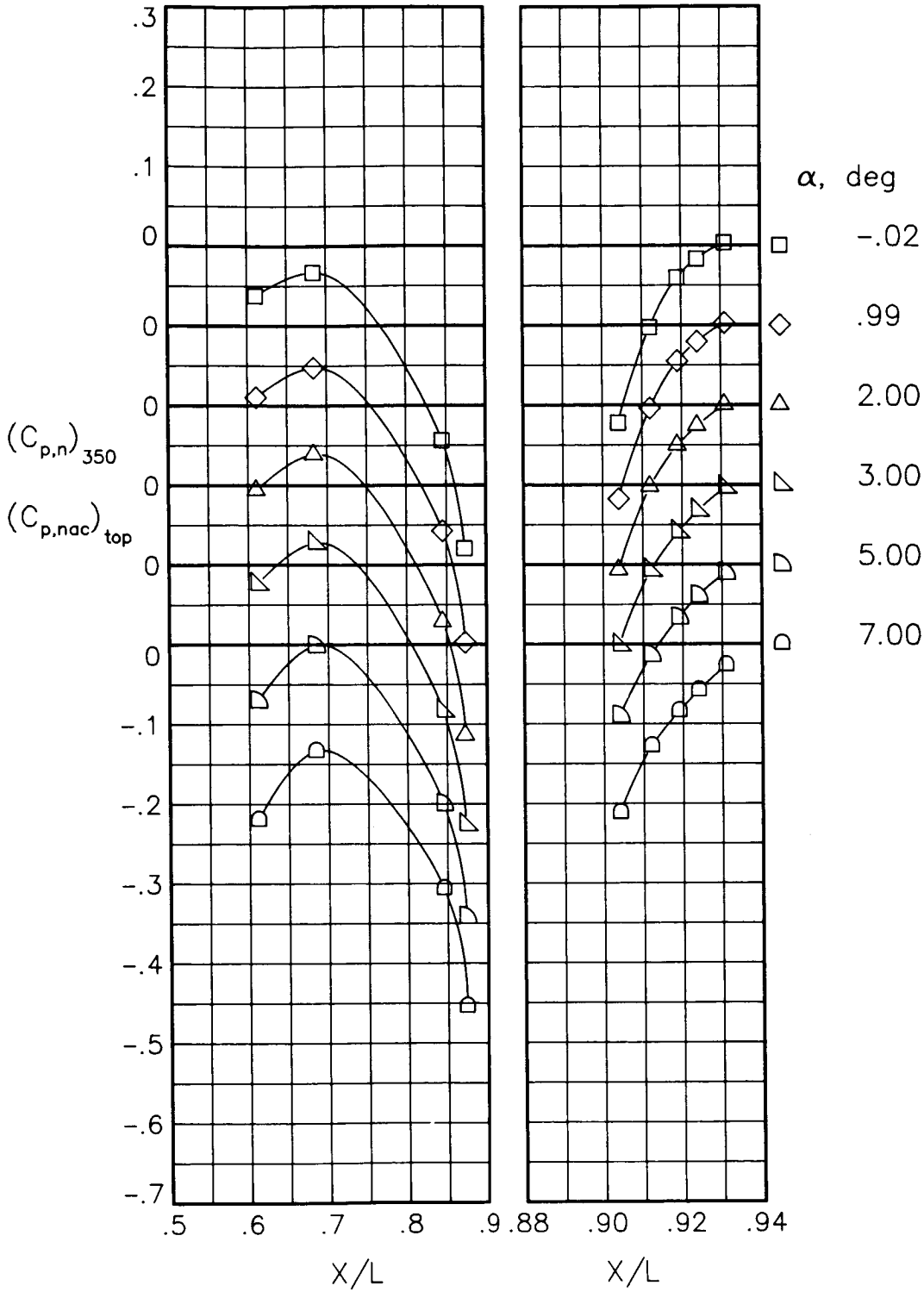

(c) M = 0.80; NPR = 1.00.

Figure 40.- Continued.

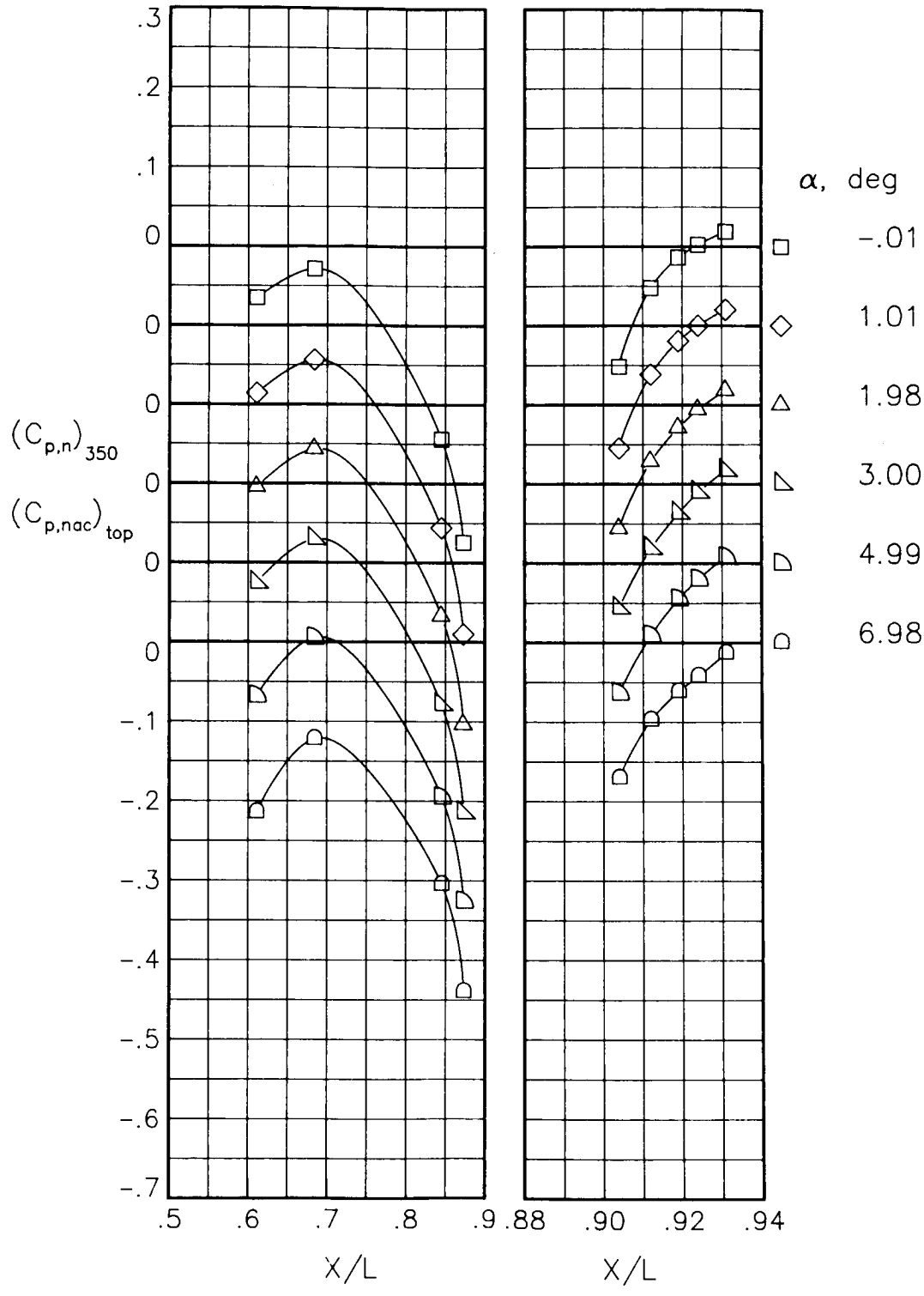

(d) M = 0.80; NPR = 4.60.

Figure 40.- Continued.

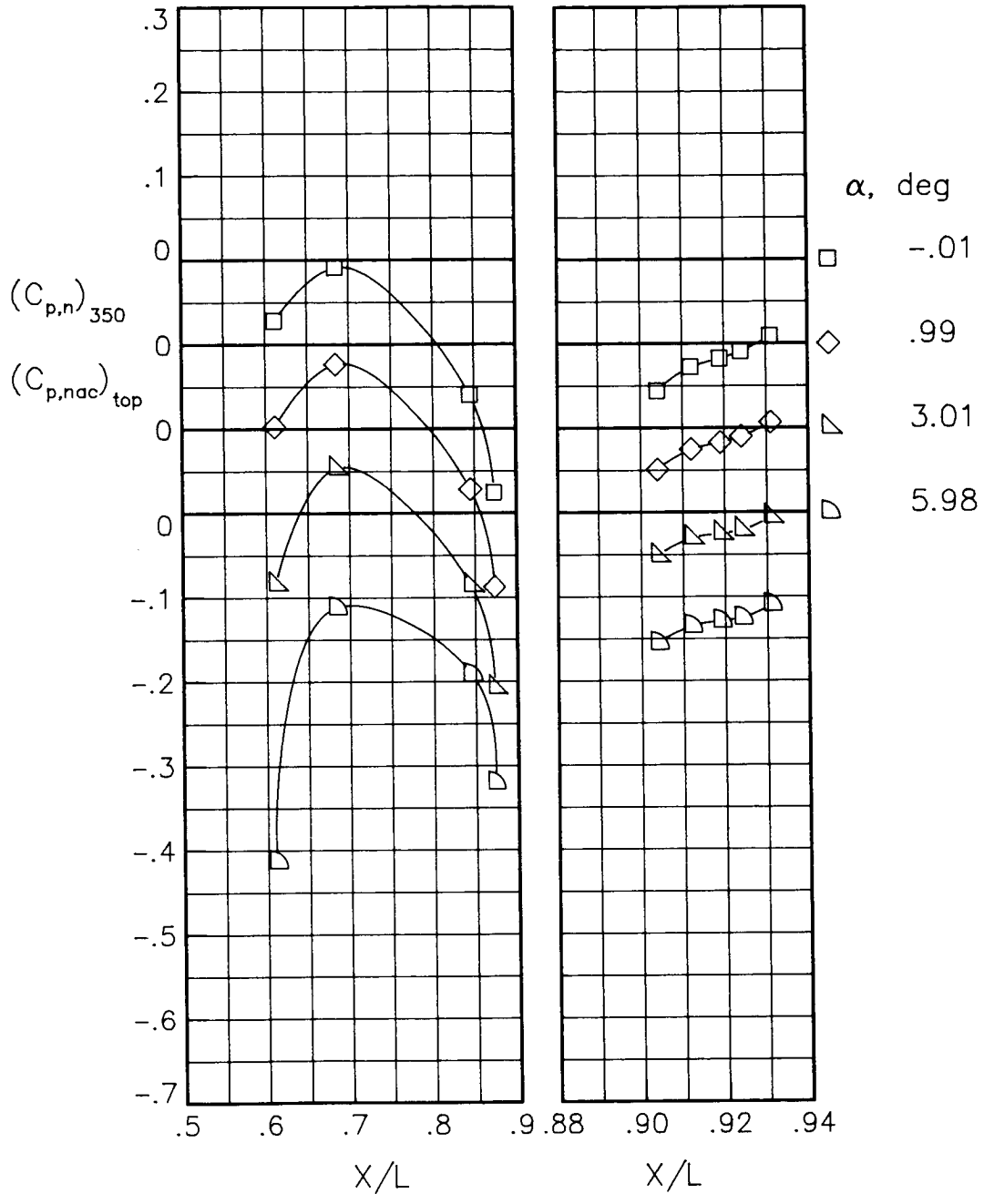

(e) M = 0.90; NPR = 1.00.

Figure 40.- Continued.

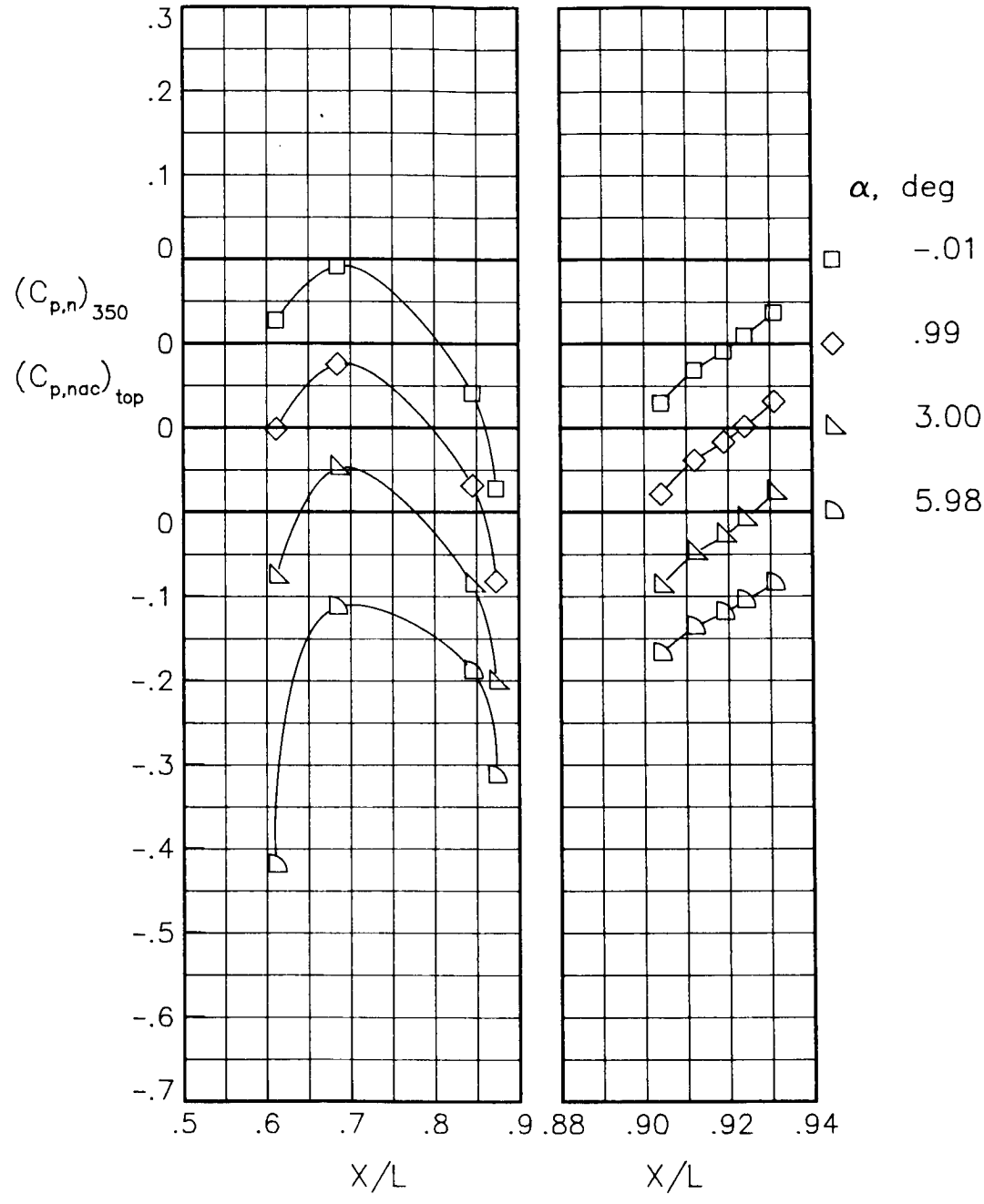

(f) M = 0.90; NPR = 5.00.

Figure 40.- Concluded.

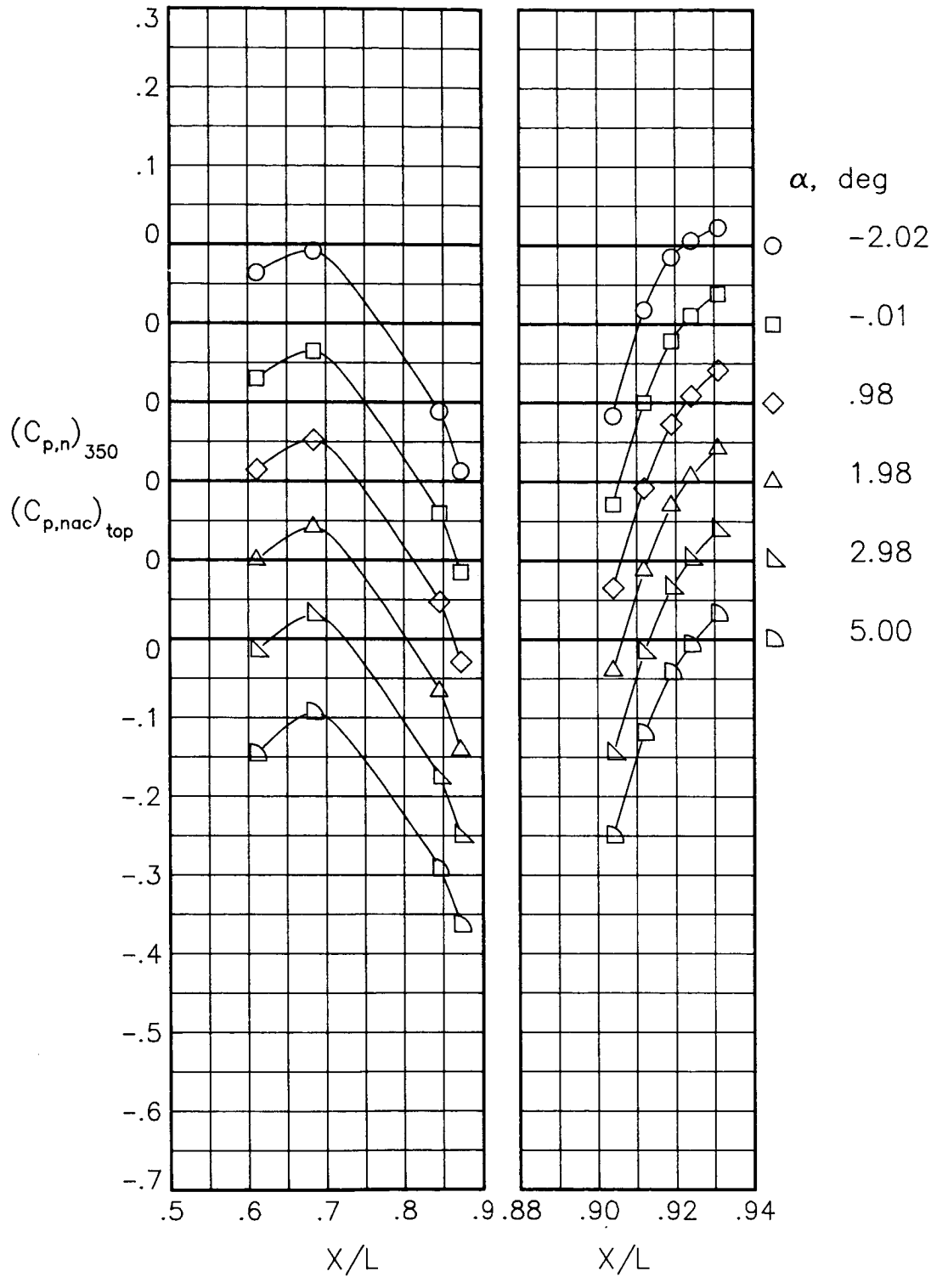

(a) M = 0.60; NPR = 1.00.

Figure 41.- Static-pressure-coefficient distributions on top of nacelle and nozzle for the model with all fuselage modifications. β_n = 18.45°.

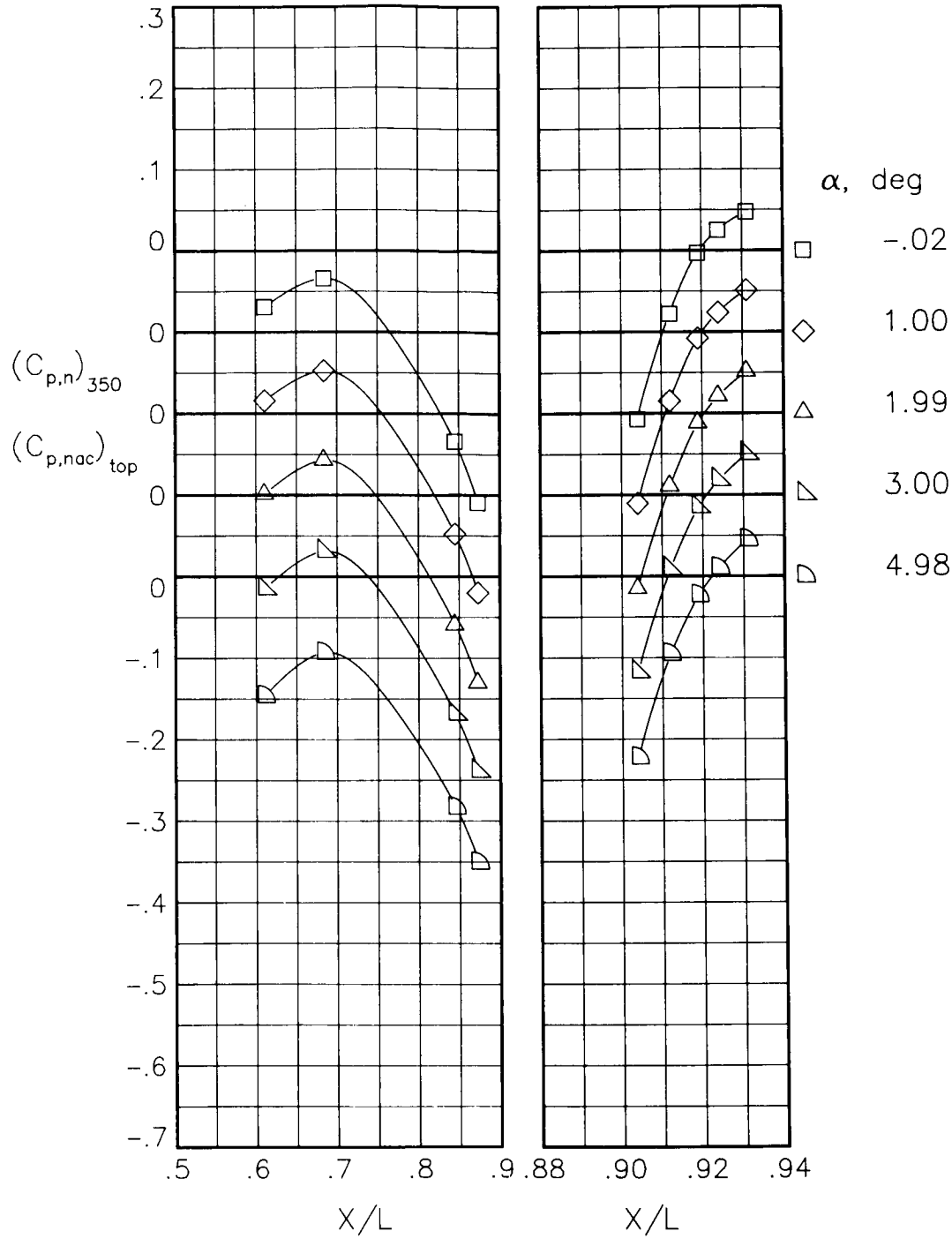

(b) M = 0.60; NPR = 3.00.

Figure 41.- Continued.

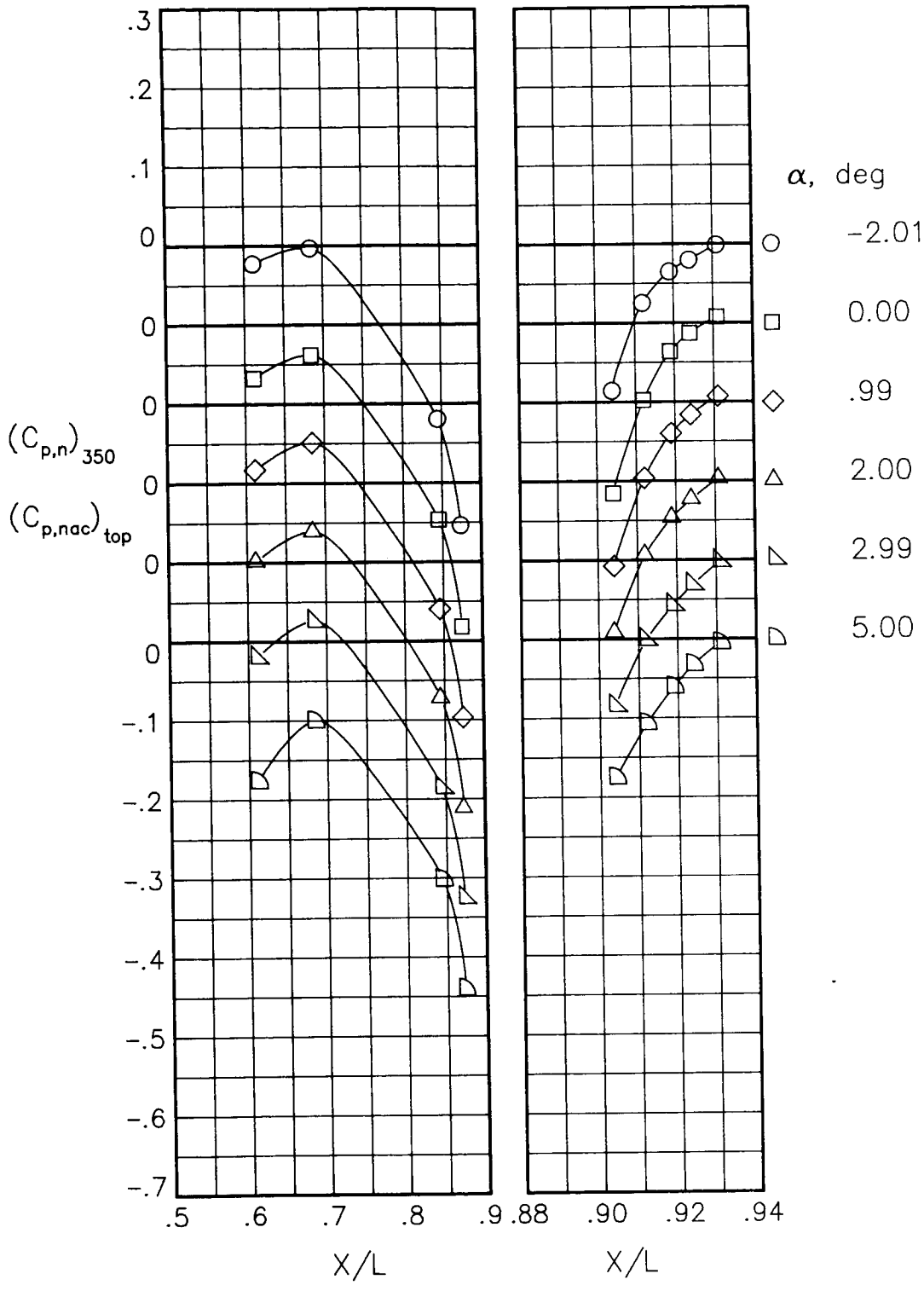

(c) M = 0.80; NPR = 1.00.

Figure 41.- Continued.

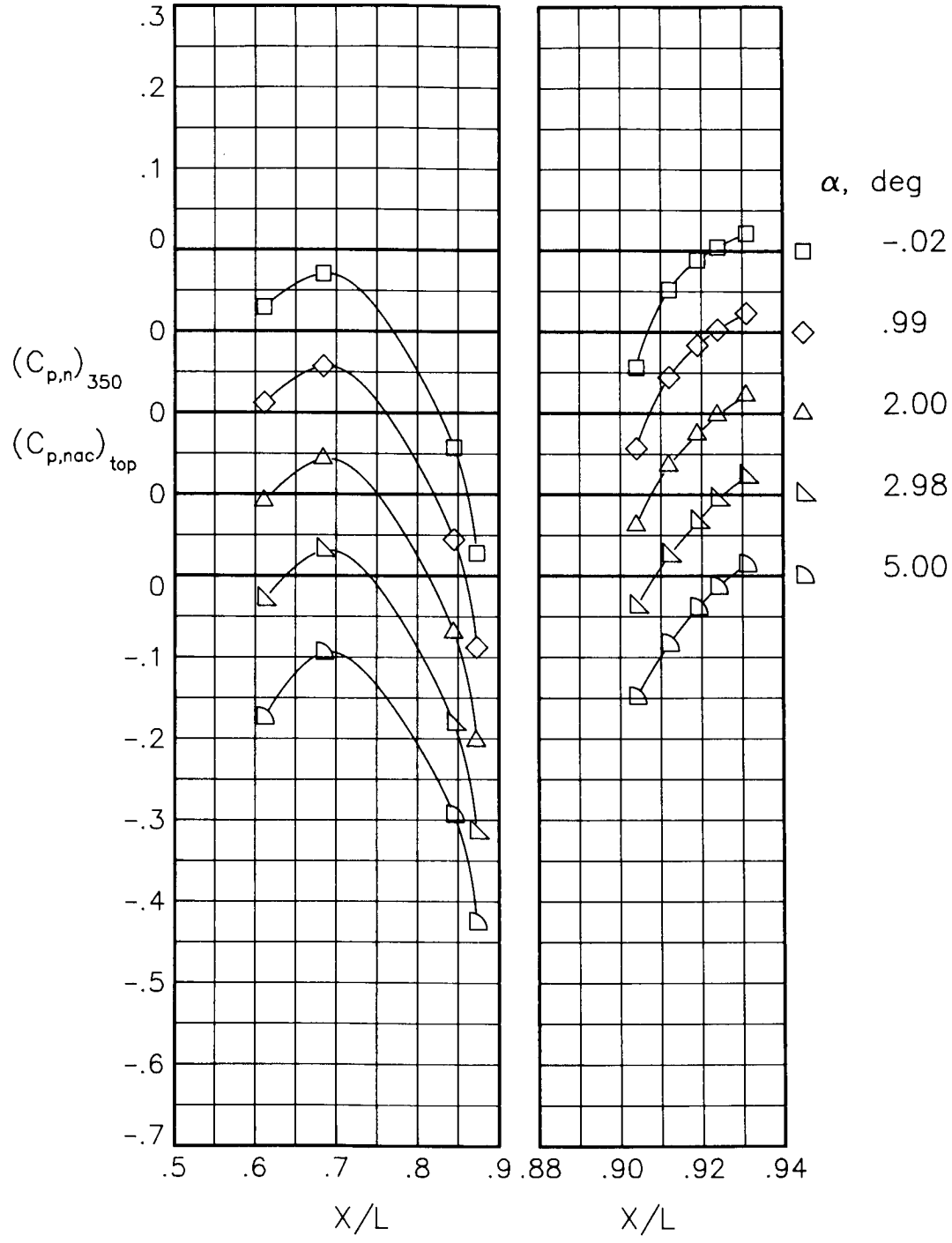

(d) M = 0.80; NPR = 4.60.

Figure 41.- Continued.

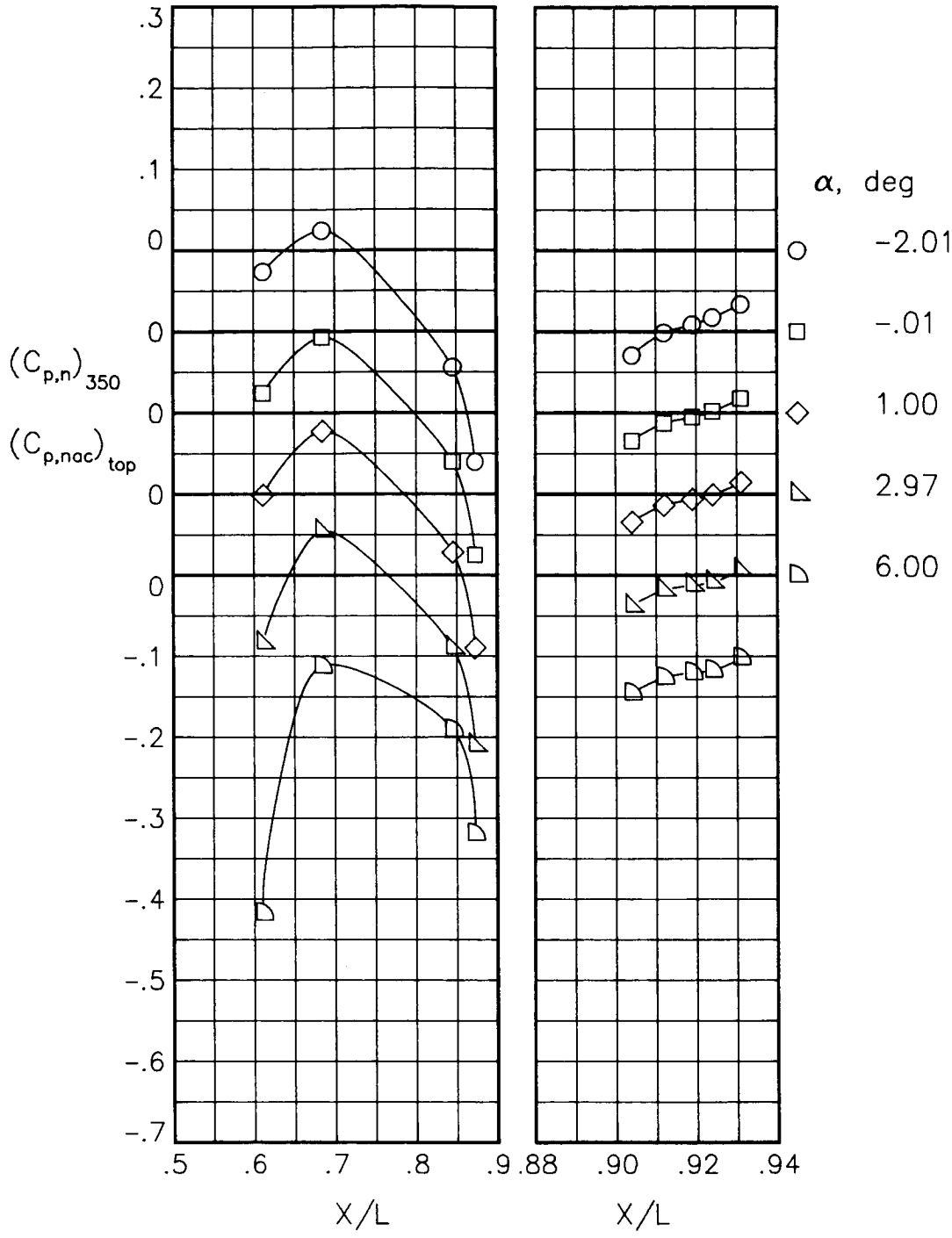

(e) M = 0.90; NPR = 1.00.

Figure 41.- Continued.

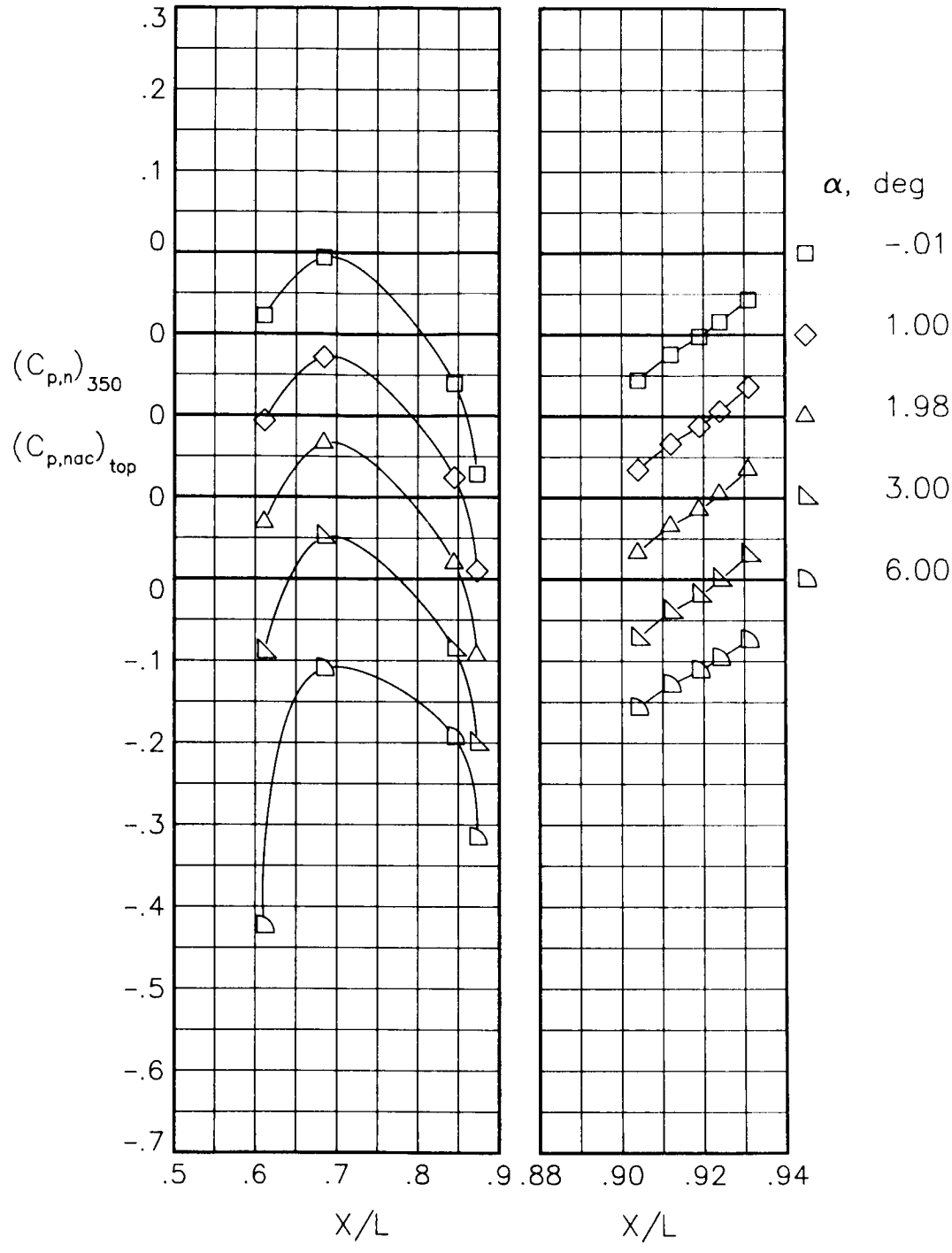

(f) M = 0.90; NPR = 5.00.

Figure 41.- Concluded.

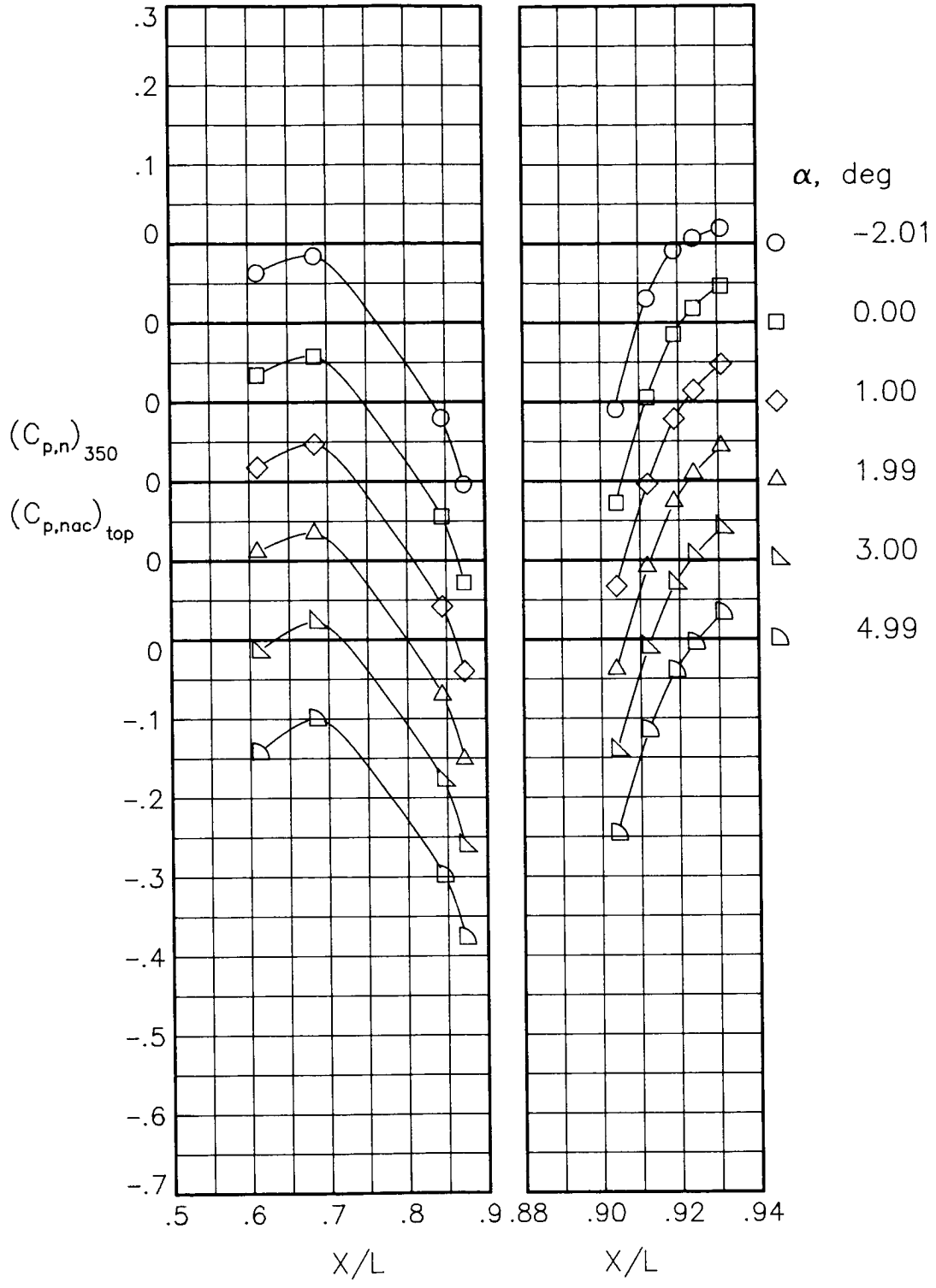

(a) M = 0.60; NPR = 1.00.

Figure 42.- Static-pressure-coefficient distributions on top of nacelle and nozzle for the model with all fuselage modifications. β_n = 18.45°. Repeat data.

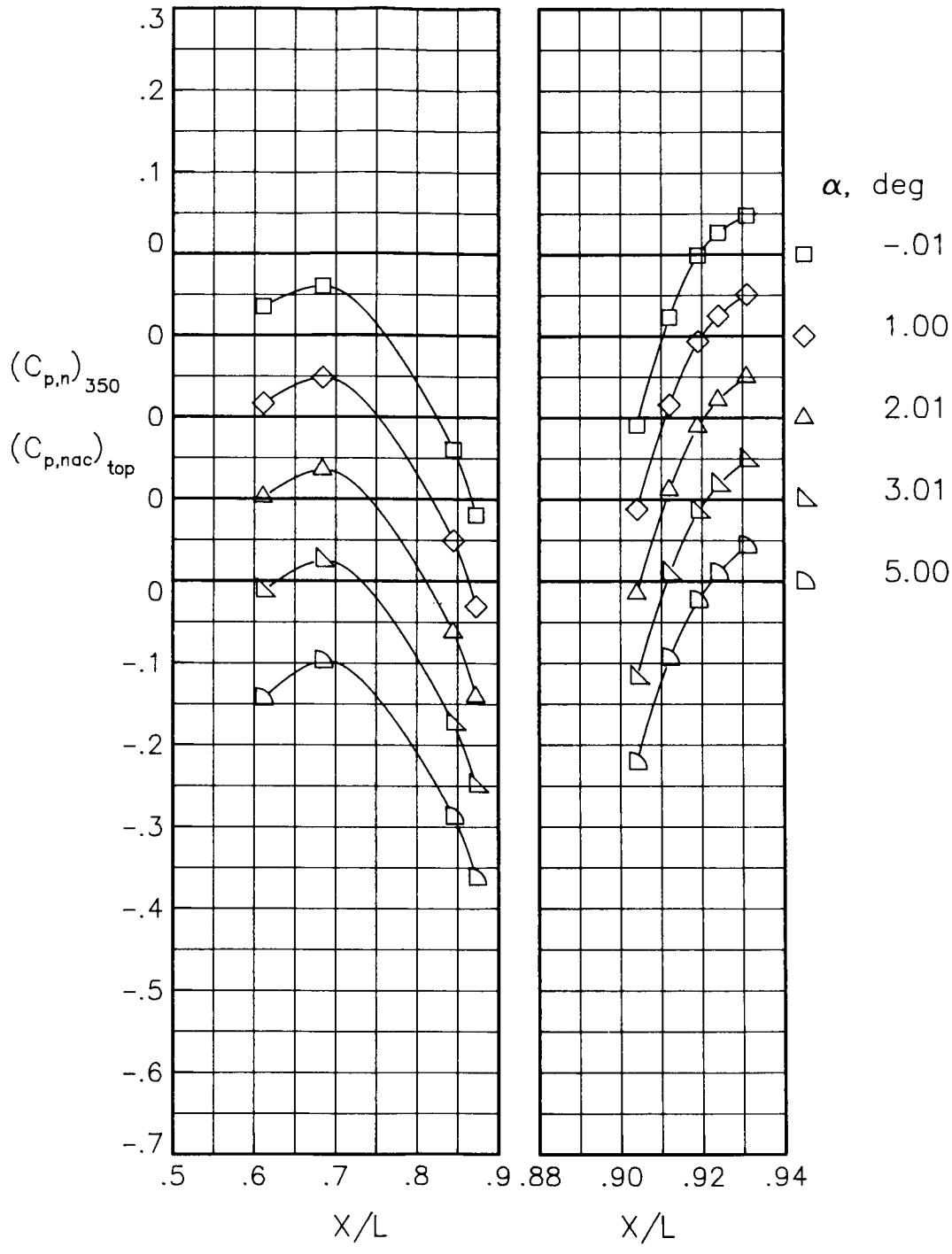

(b) M = 0.60; NPR = 3.00.

Figure 42.- Continued.

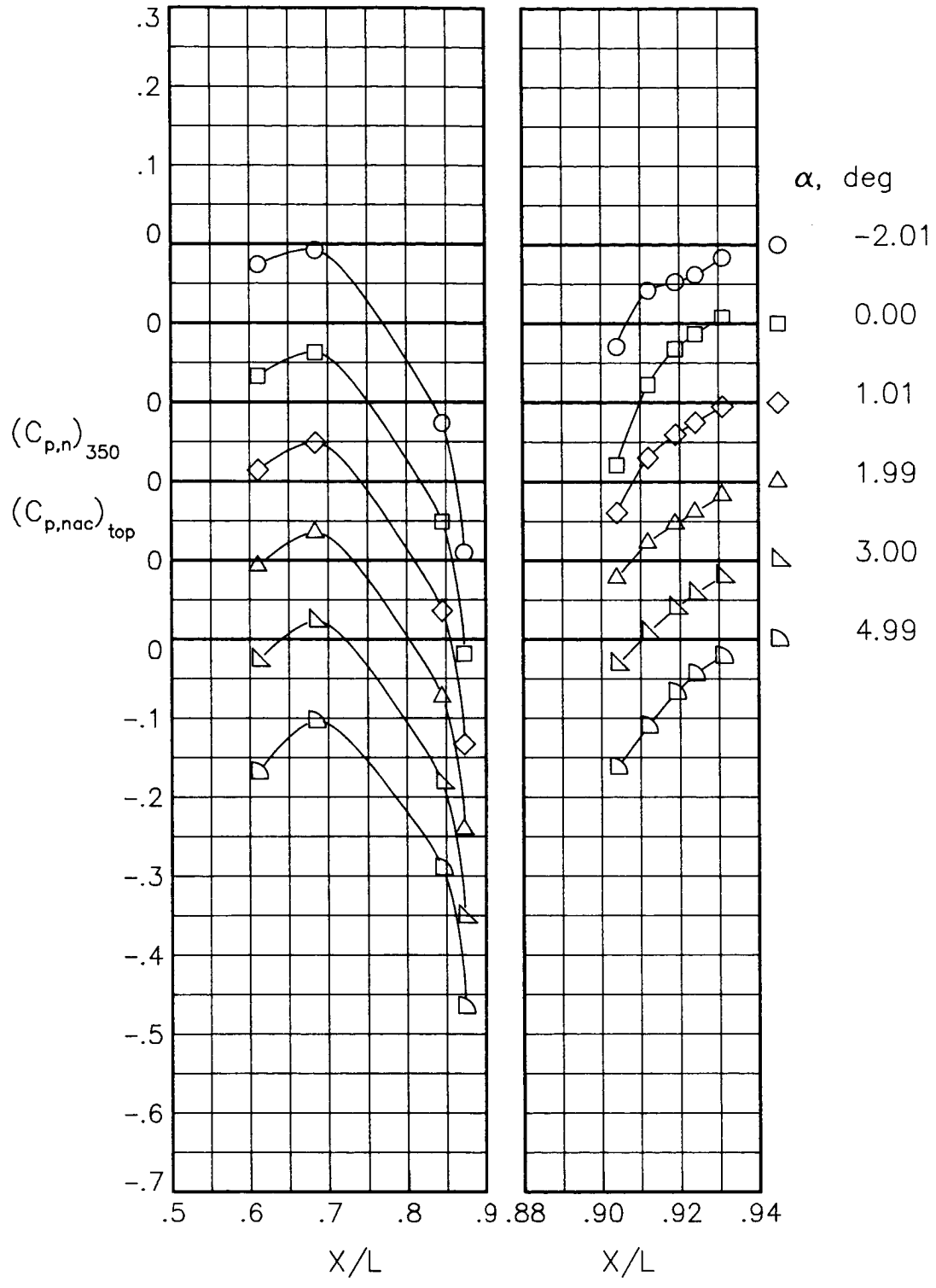

(c) M = 0.80; NPR = 1.00.

Figure 42.- Continued.

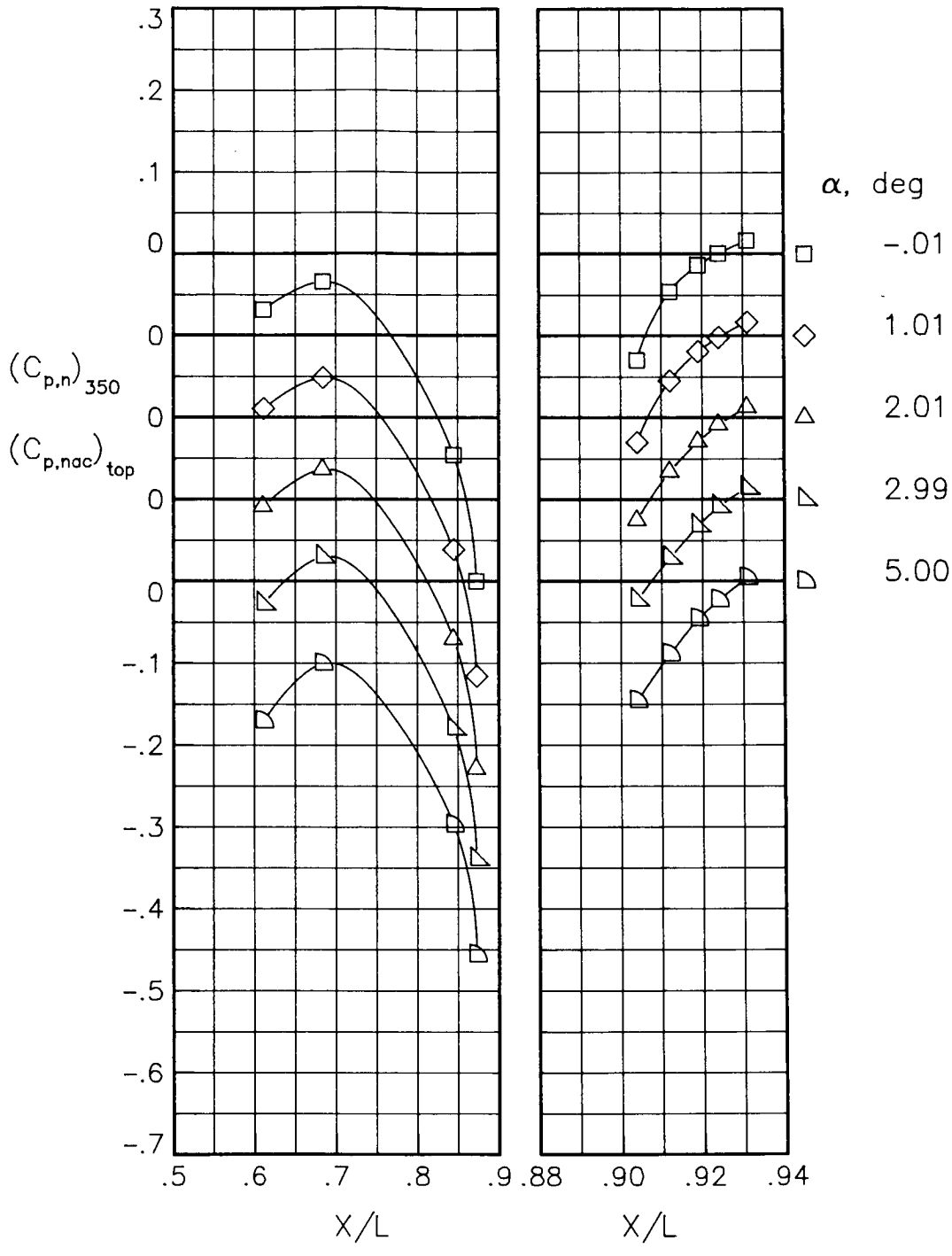

(d) M = 0.80; NPR = 4.60.

Figure 42.- Continued.

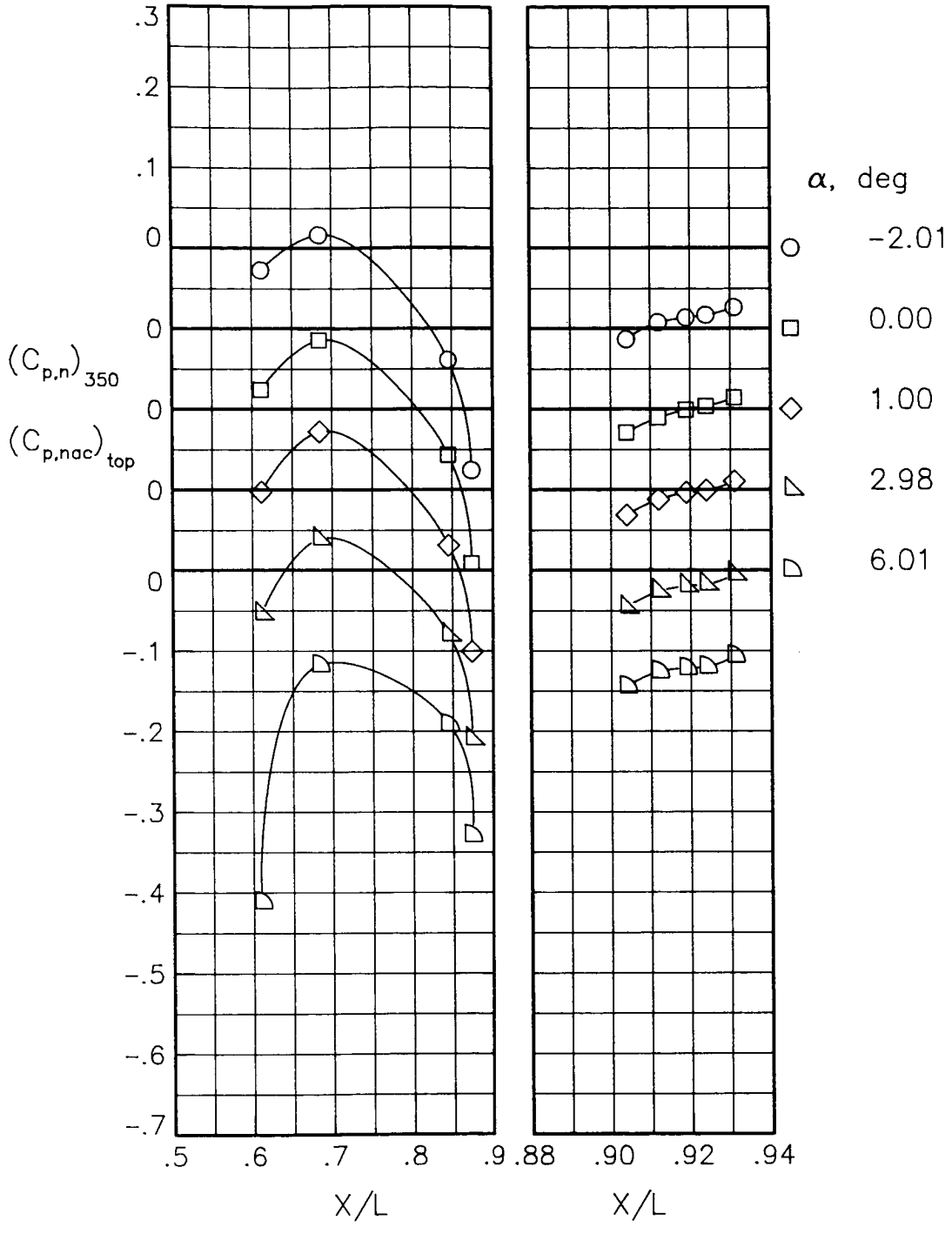

(e) M = 0.90; NPR = 1.00.

Figure 42.- Continued.

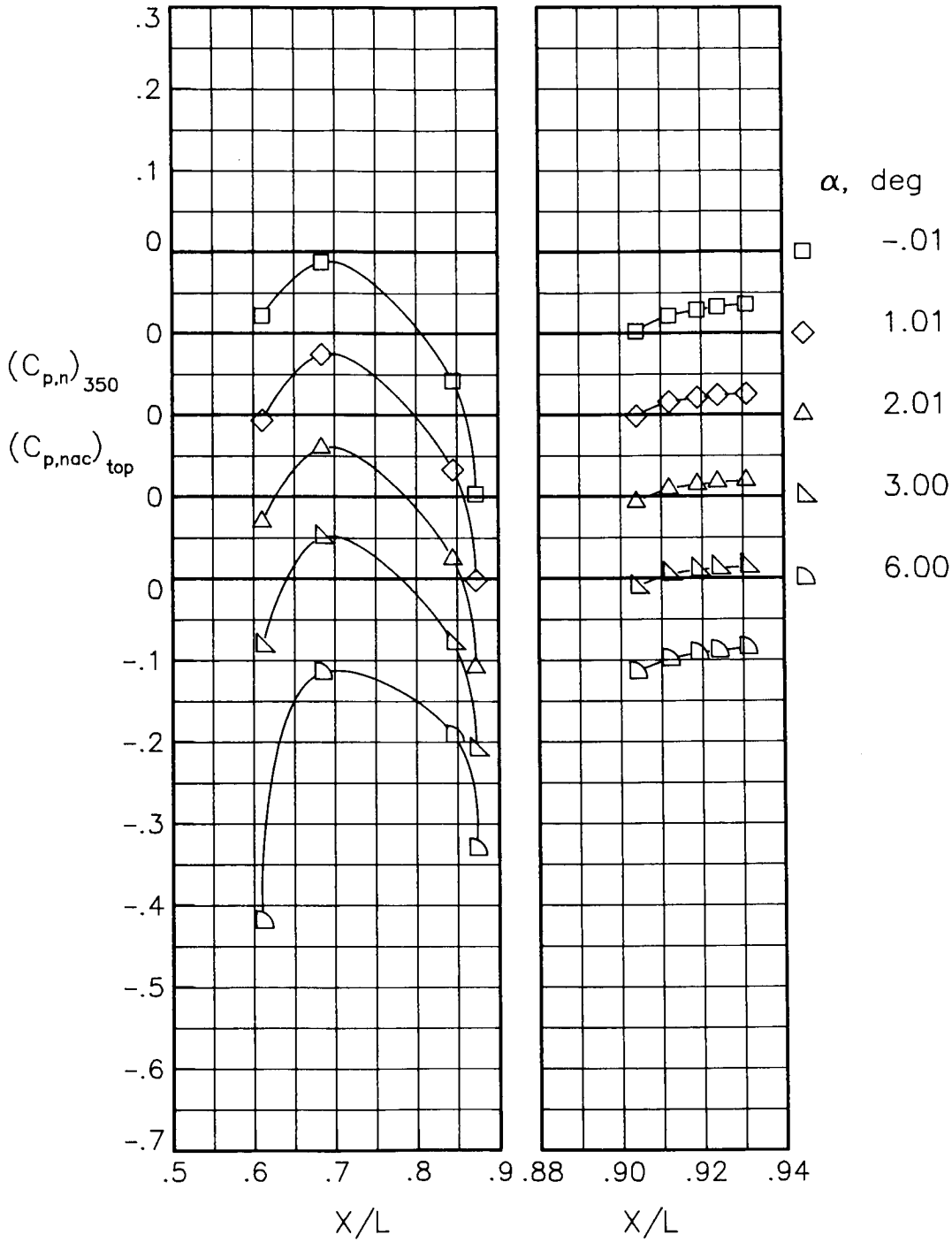

(f) M = 0.90; NPR = 5.00.

Figure 42.- Concluded.

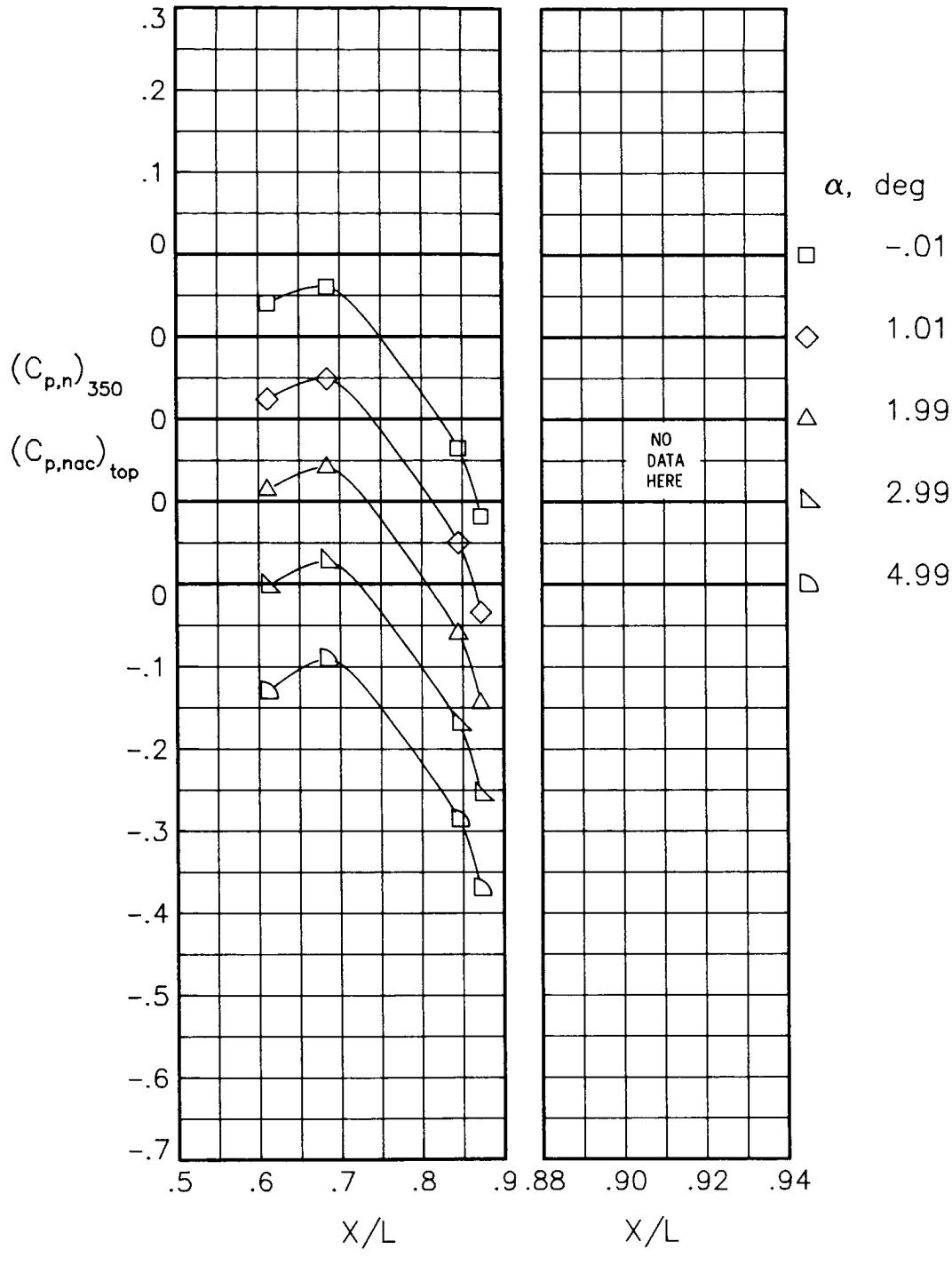

(a) M = 0.60; NPR = 1.00.

Figure 43.- Static-pressure-coefficient distributions on top of nacelle and nozzle for the model with all fuselage modifications. β_n = 18.45°; δ_h = -5°.

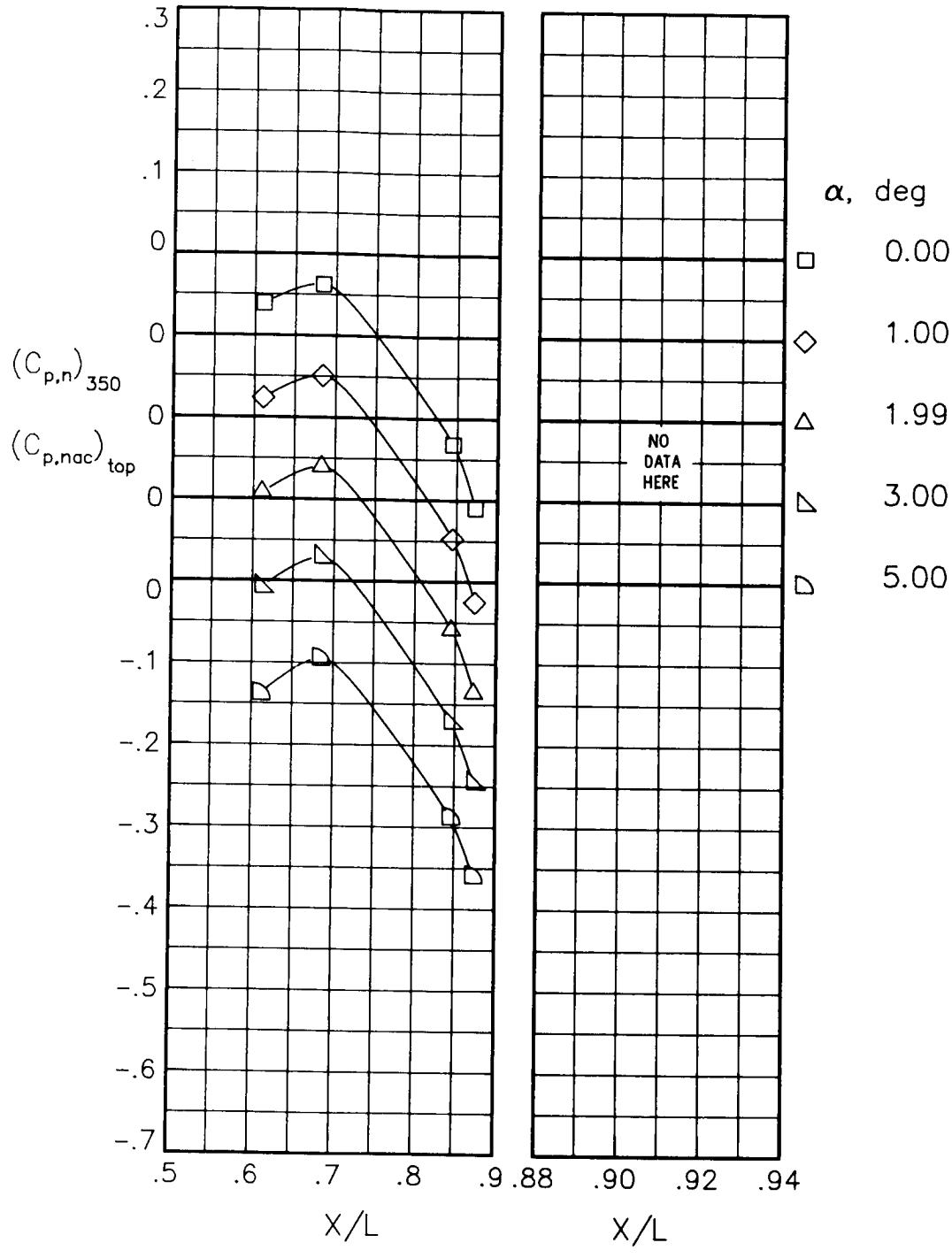

(b) M = 0.60; NPR = 3.00.

Figure 43.- Continued.

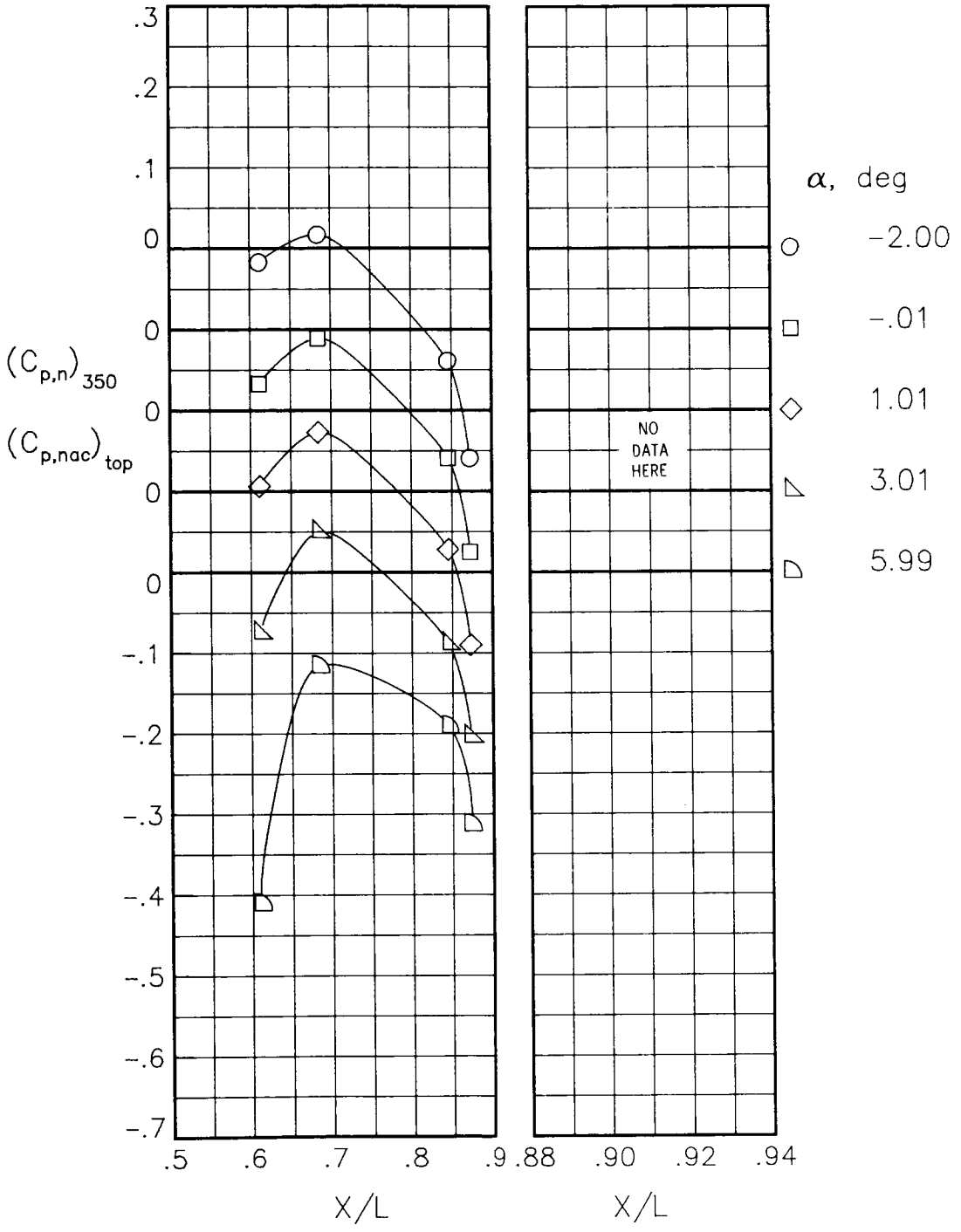

(c) M = 0.90; NPR = 1.00.

Figure 43.- Continued.

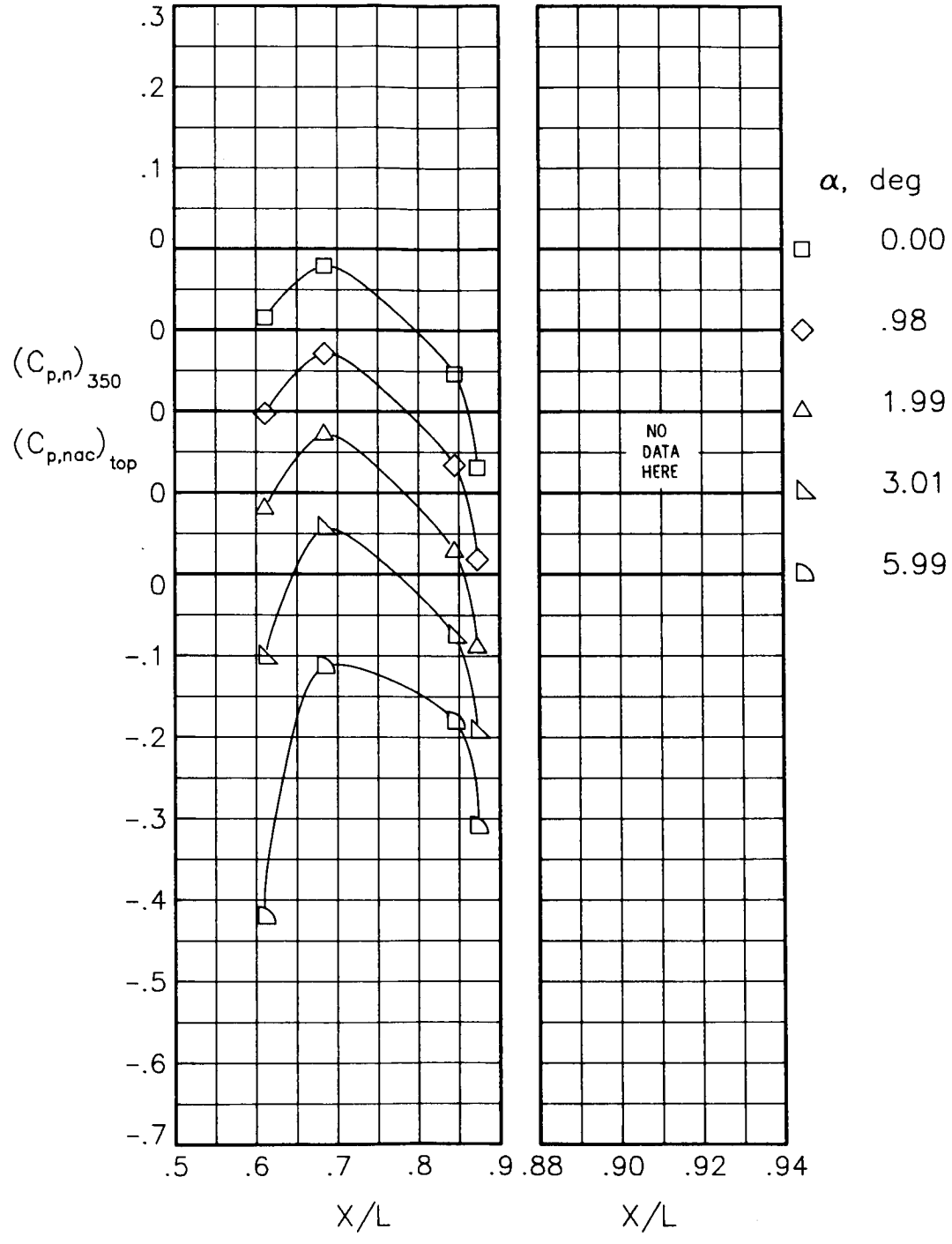

(d) M = 0.90; NPR = 5.00.

Figure 43.- Concluded.

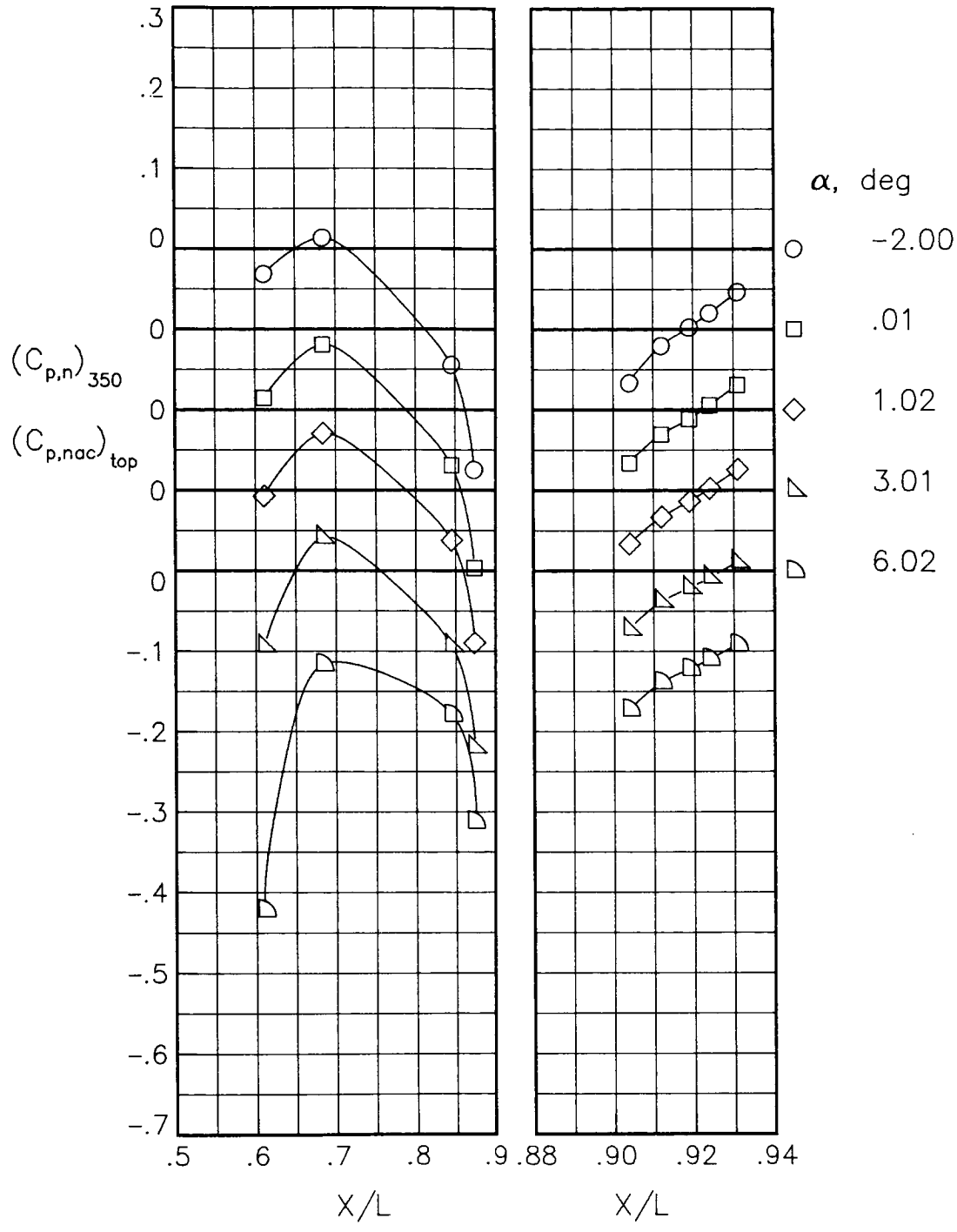

(a) M = 0.90; NPR = 1.00.

Figure 44.- Static-pressure-coefficient distributions on top of nacelle and nozzle for the model with all fuselage modifications. β_n = 15.05°.

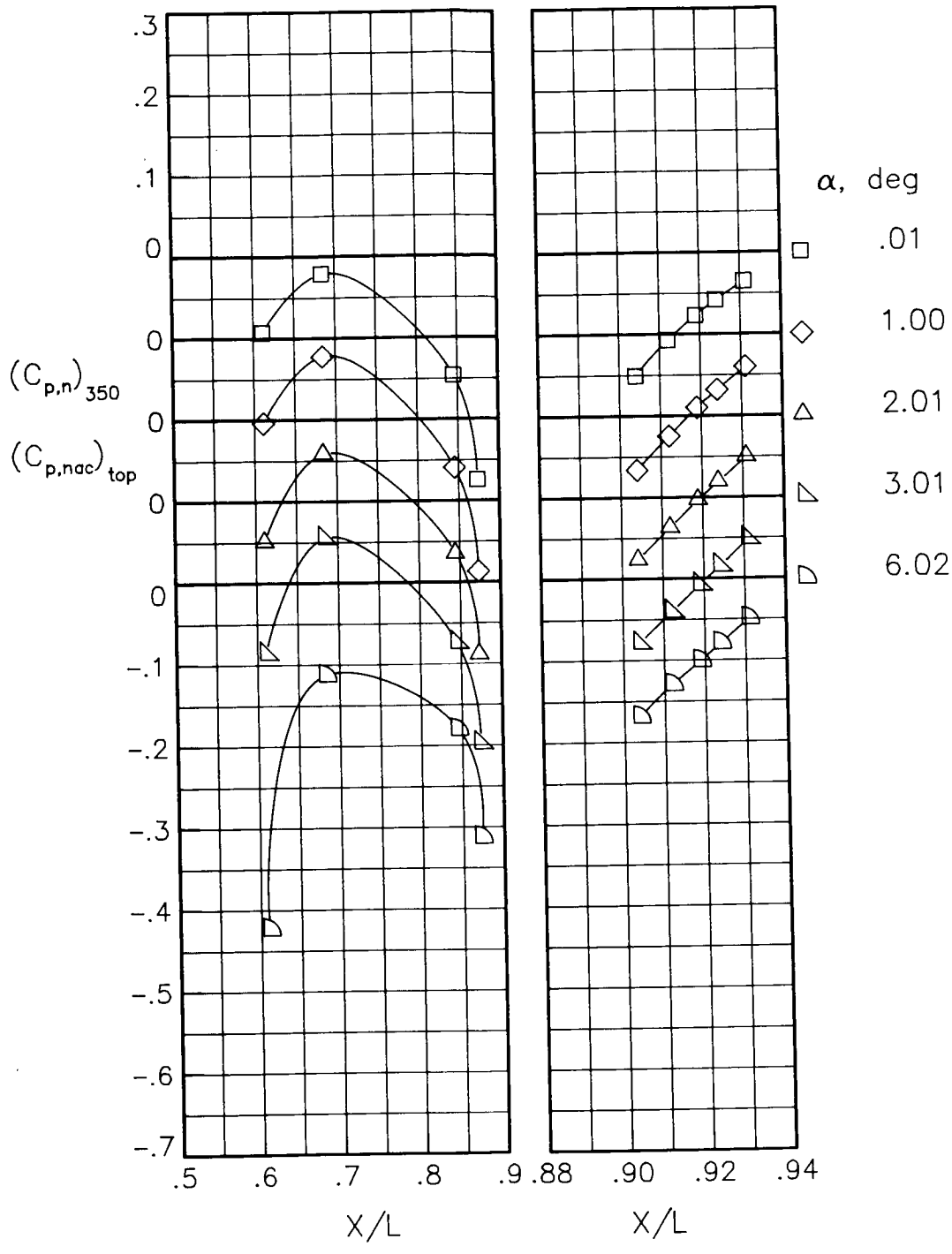

(b) M = 0.90; NPR = 5.00.

Figure 44.- Continued.

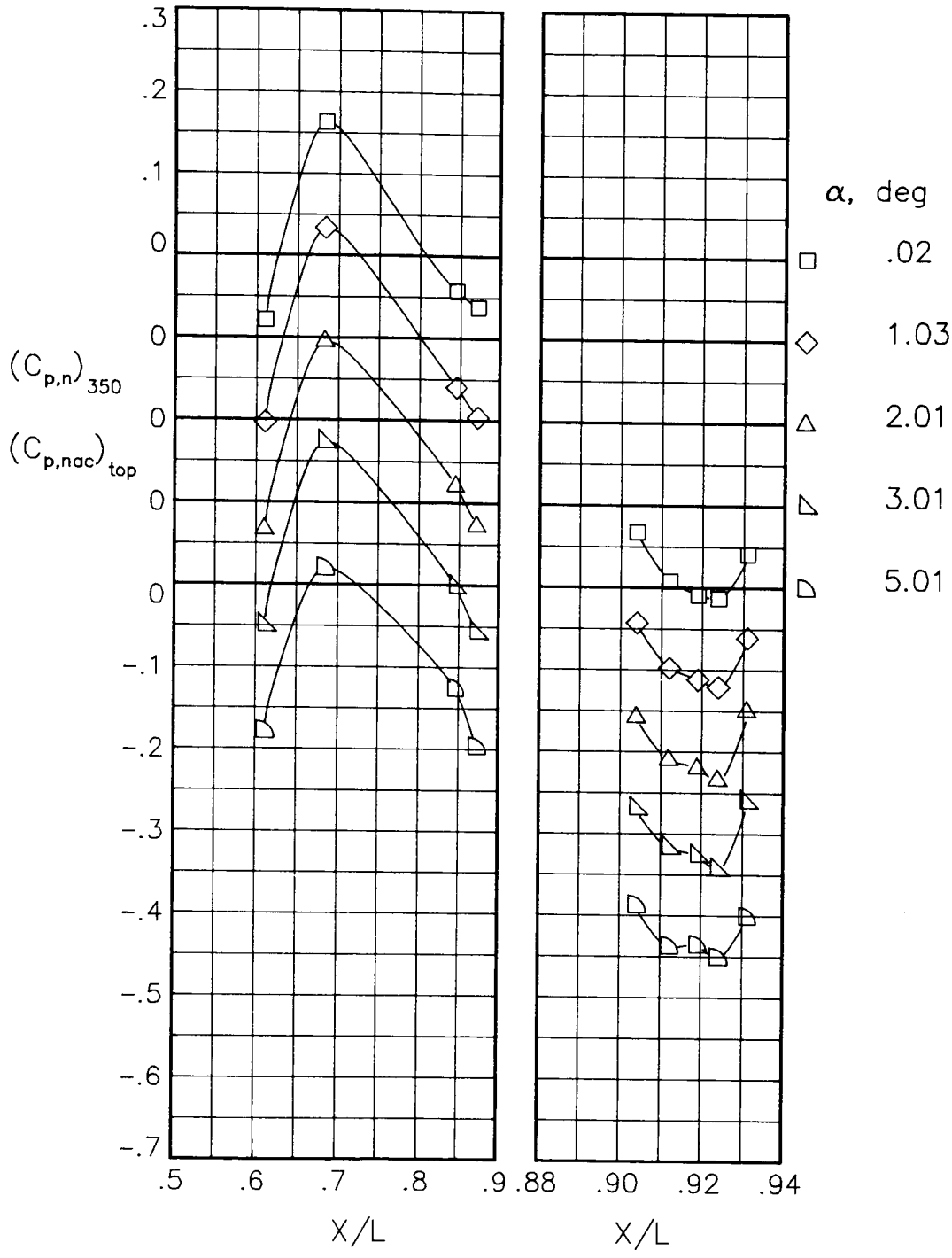

(c) M = 1.20; NPR = 1.00.

Figure 44.- Continued.

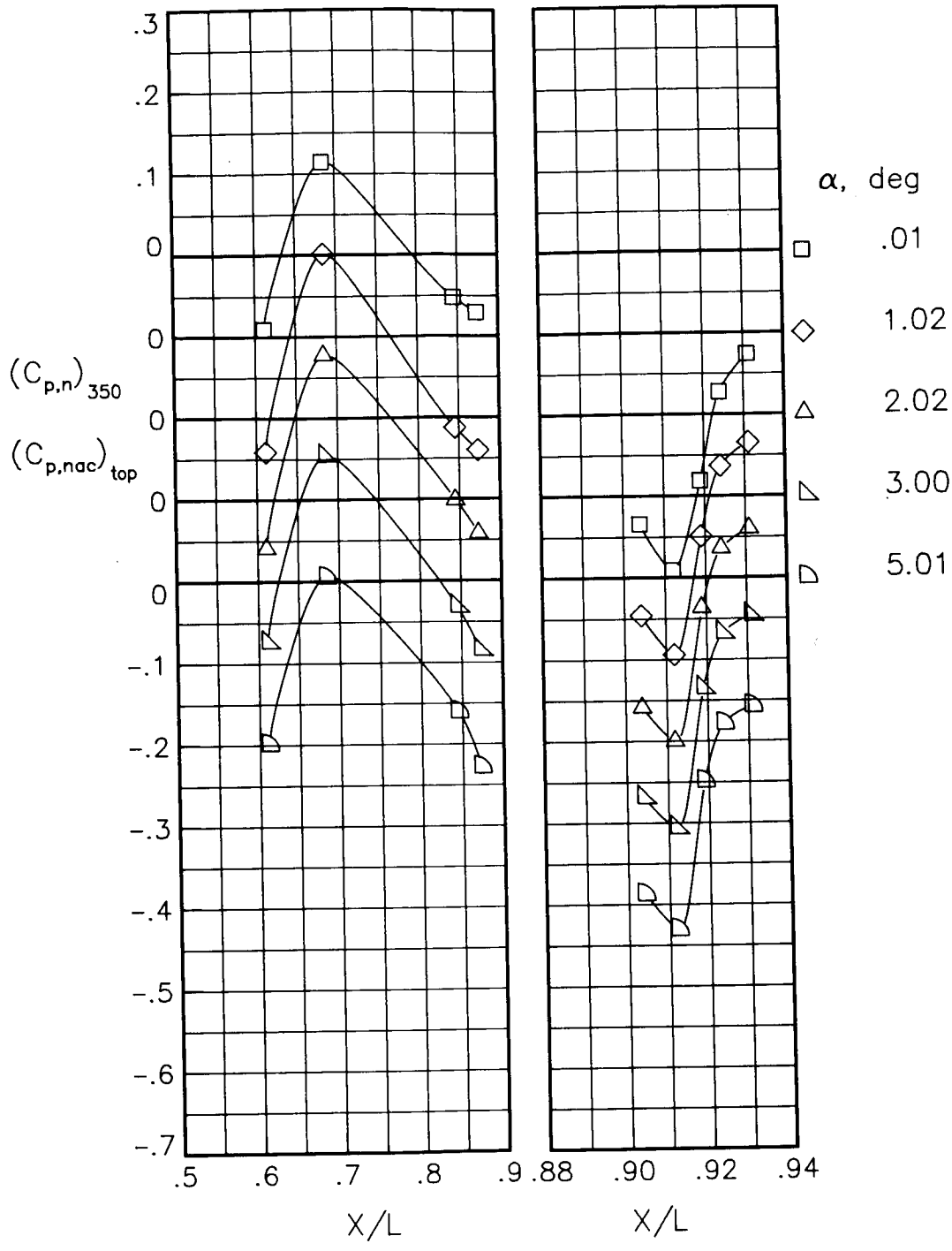

(d) M = 1.20; NPR = 7.00.

Figure 44.- Concluded.

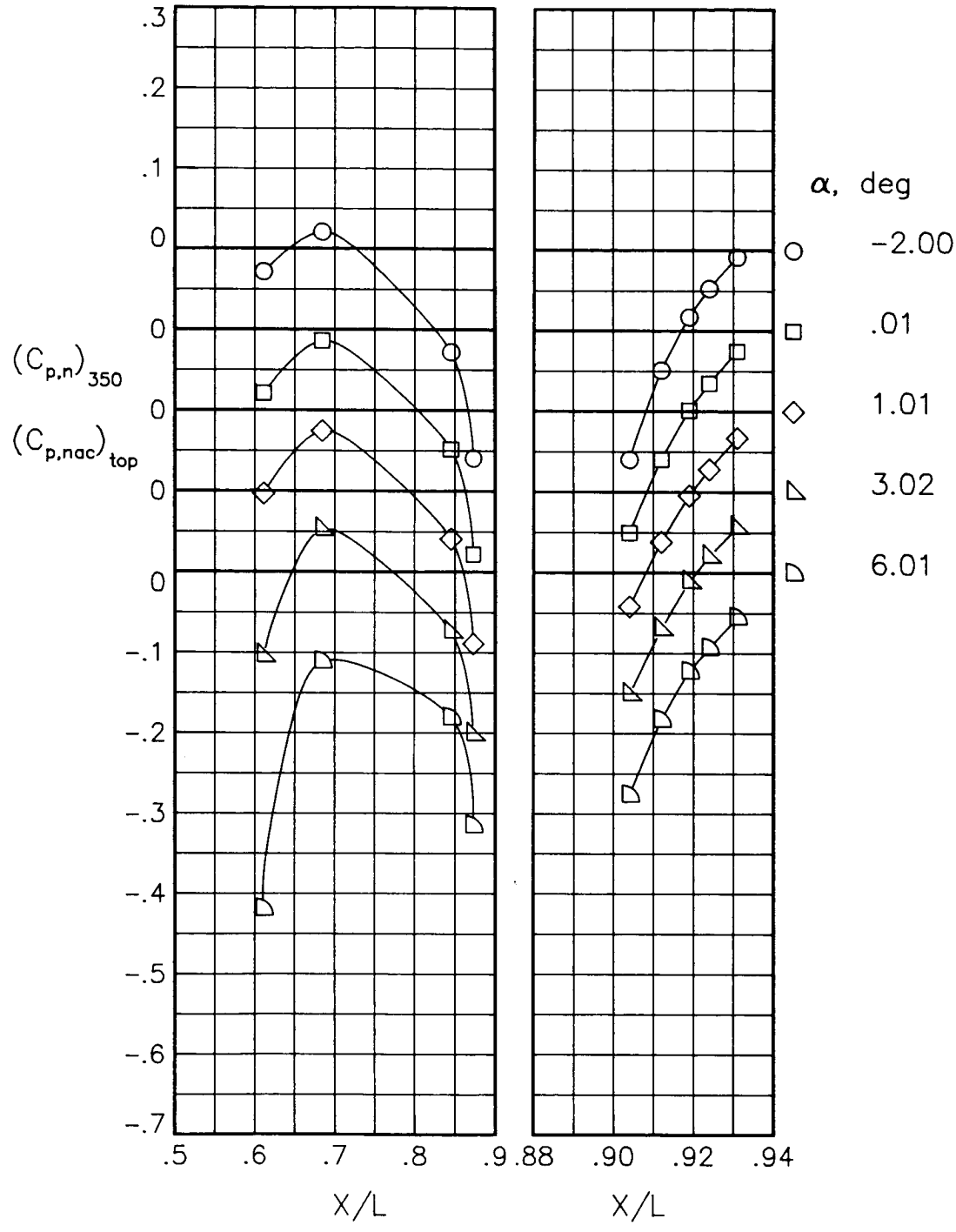

(a) M = 0.90; NPR = 1.00

Figure 45.- Static-pressure-coefficient distributions on top of nacelle and nozzle for the model with all fuselage modifications. β_n = 9.63°.

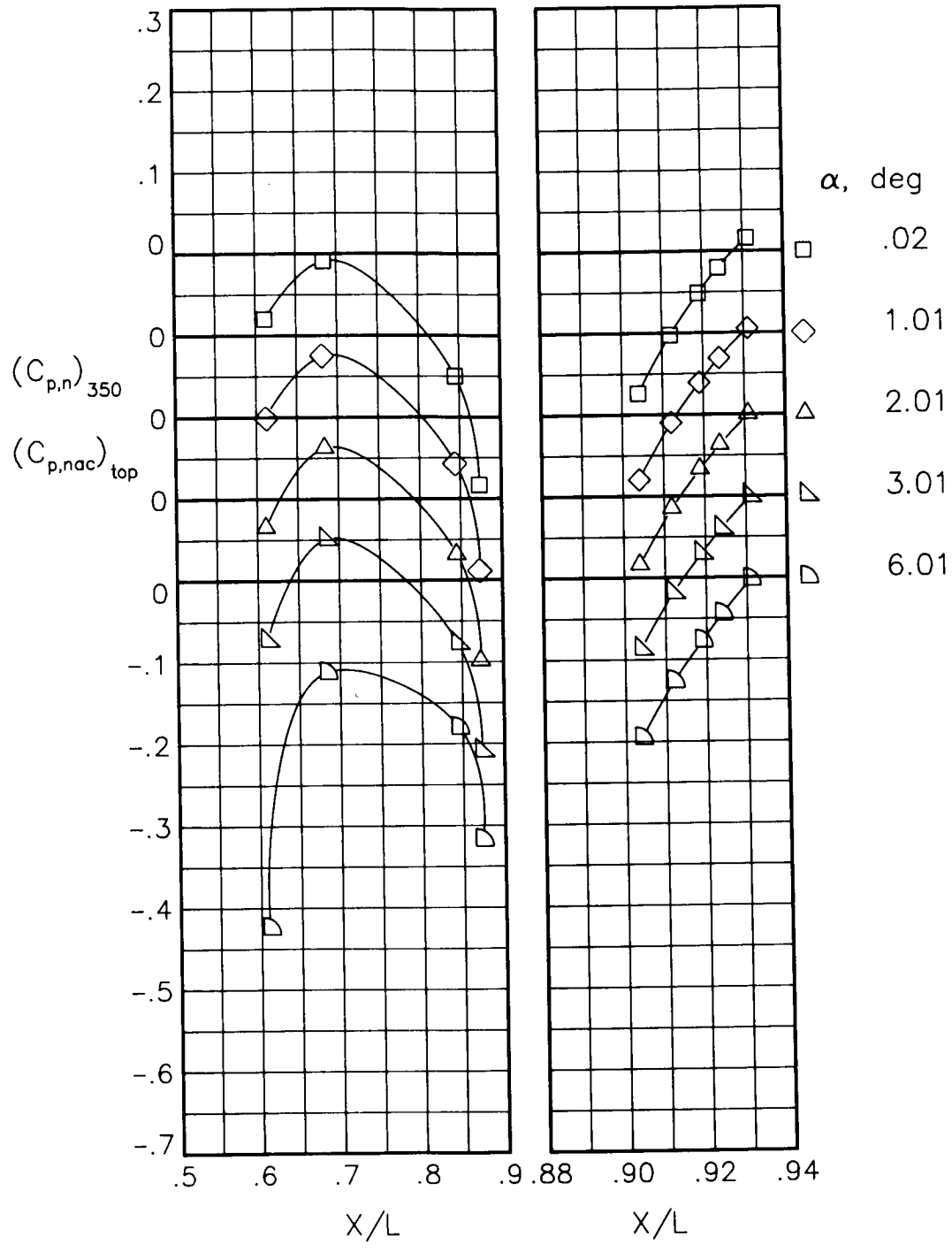

(b) M = 0.90; NPR = 5.00.

Figure 45.- Continued.

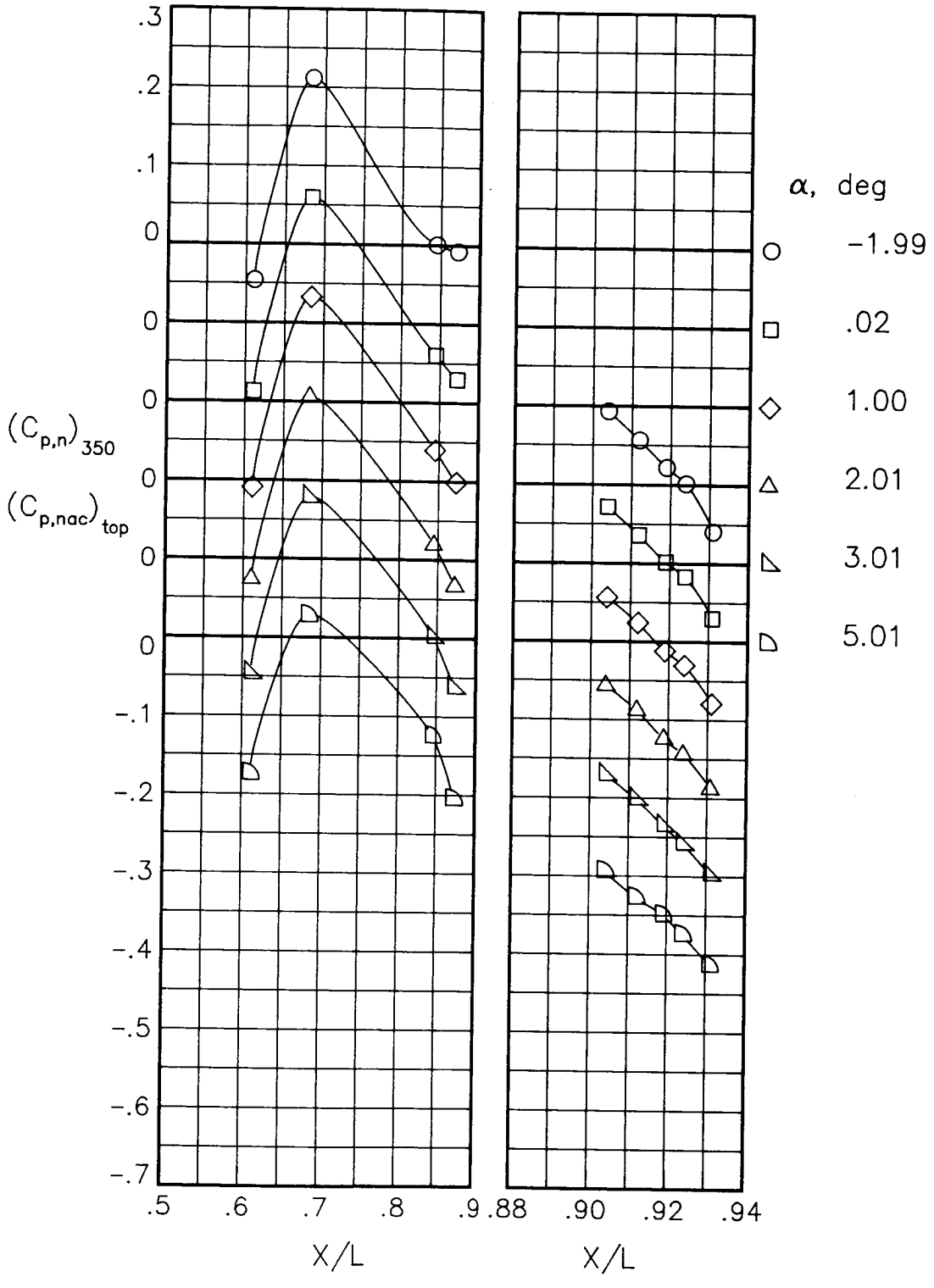

(c) M = 1.20; NPR = 1.00.

Figure 45.- Continued.

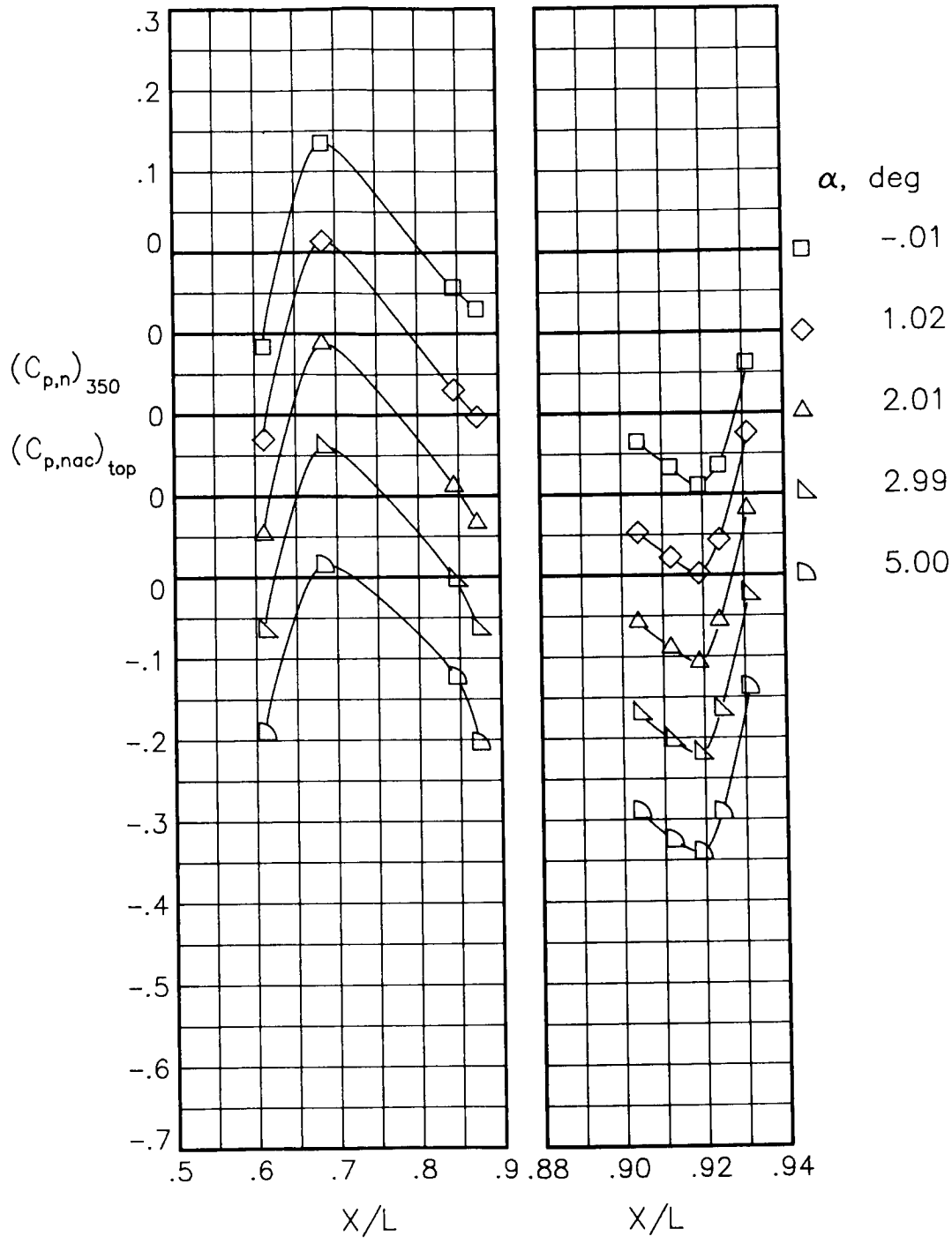

(d) M = 1.20; NPR = 7.00.

Figure 45.- Concluded.

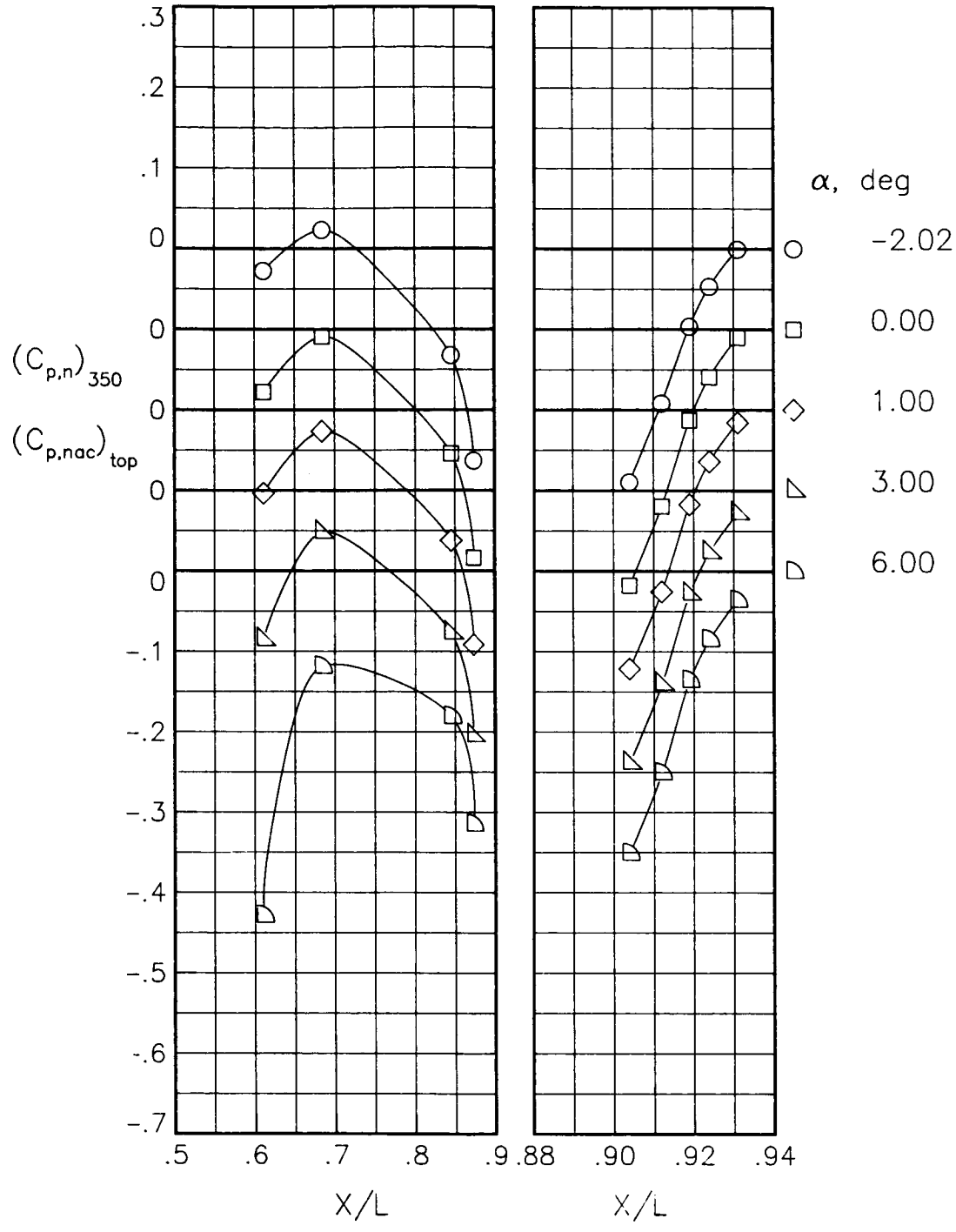

(a) M = 0.90; NPR = 1.00.

Figure 46.- Static-pressure-coefficient distributions on top of nacelle and nozzle for the model with all fuselage modifications. β_n = 7.72°.

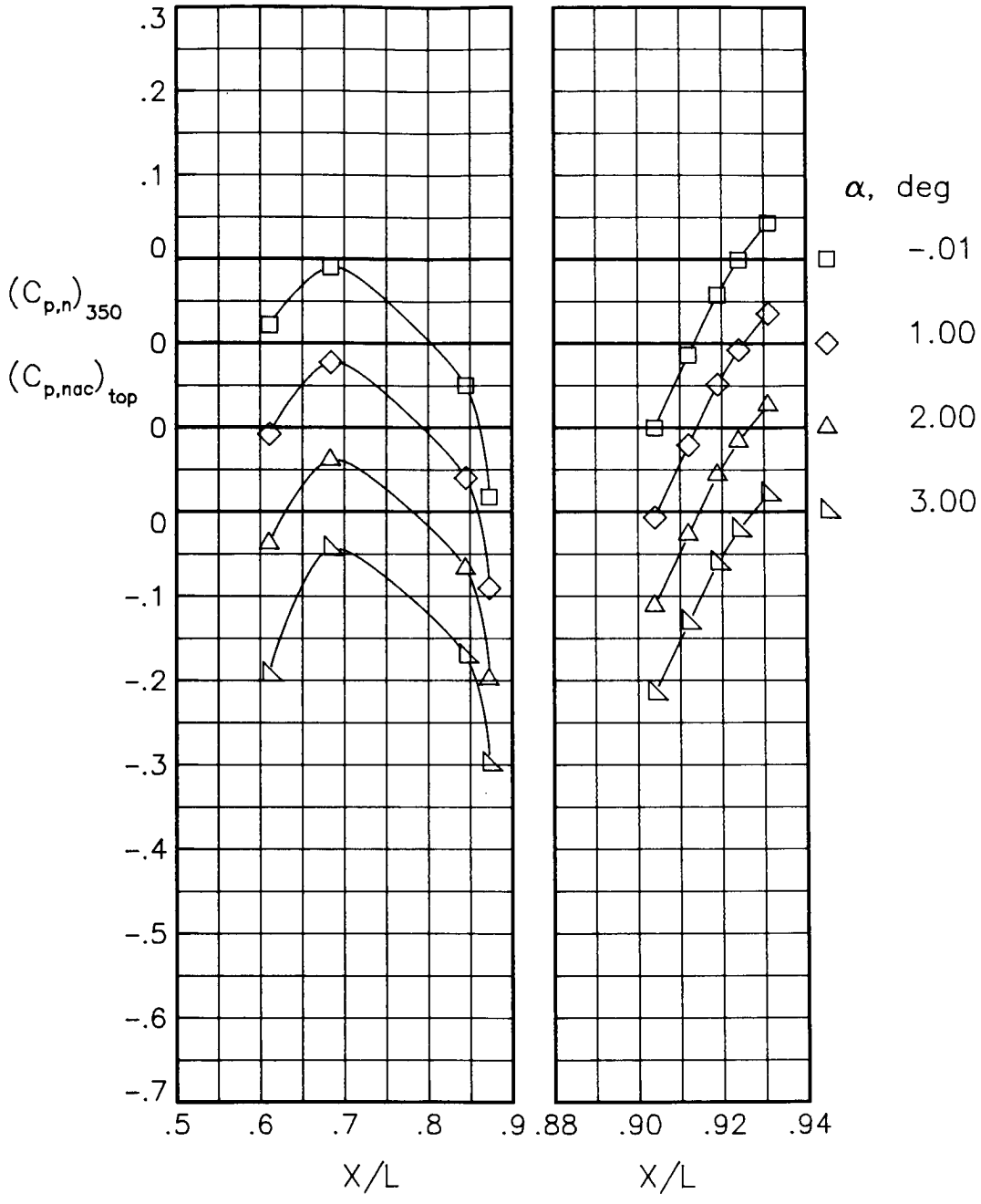

(b) M = 0.90; NPR = 5.00.

Figure 46.- Continued.

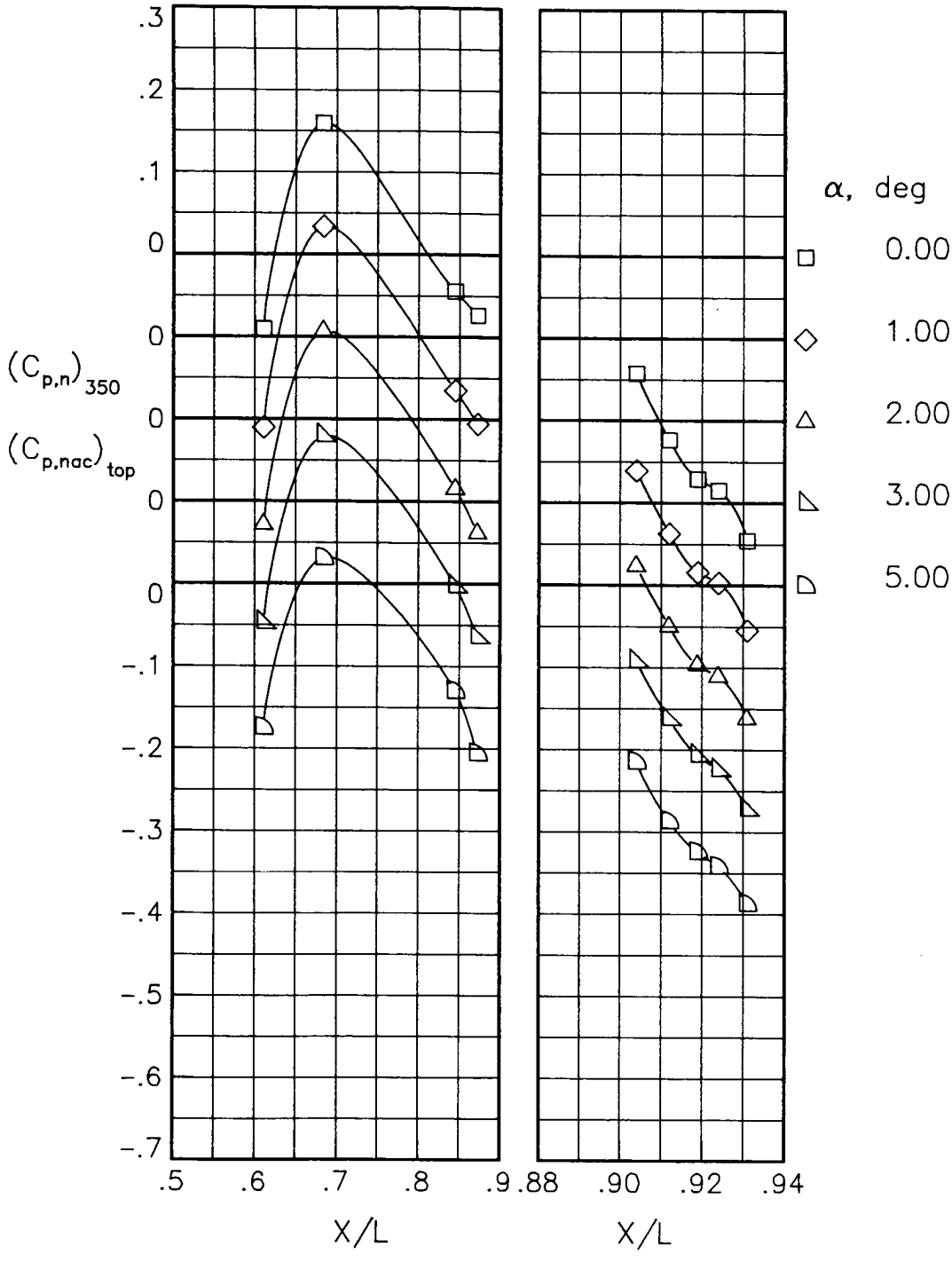

(c) M = 1.20; NPR = 1.00.

Figure 46.- Continued.

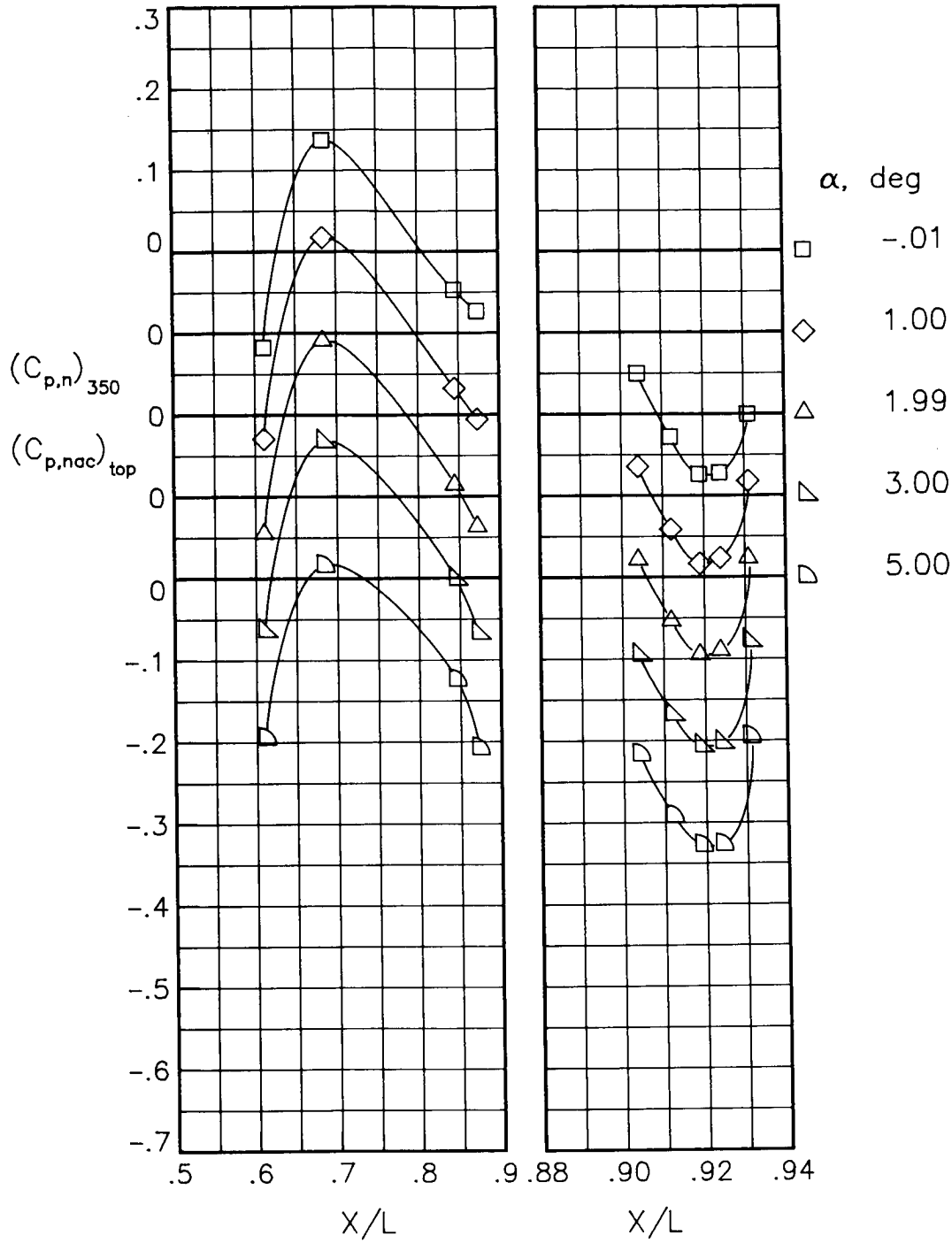

(d) M = 1.20; NPR = 7.00.

Figure 46.- Concluded.

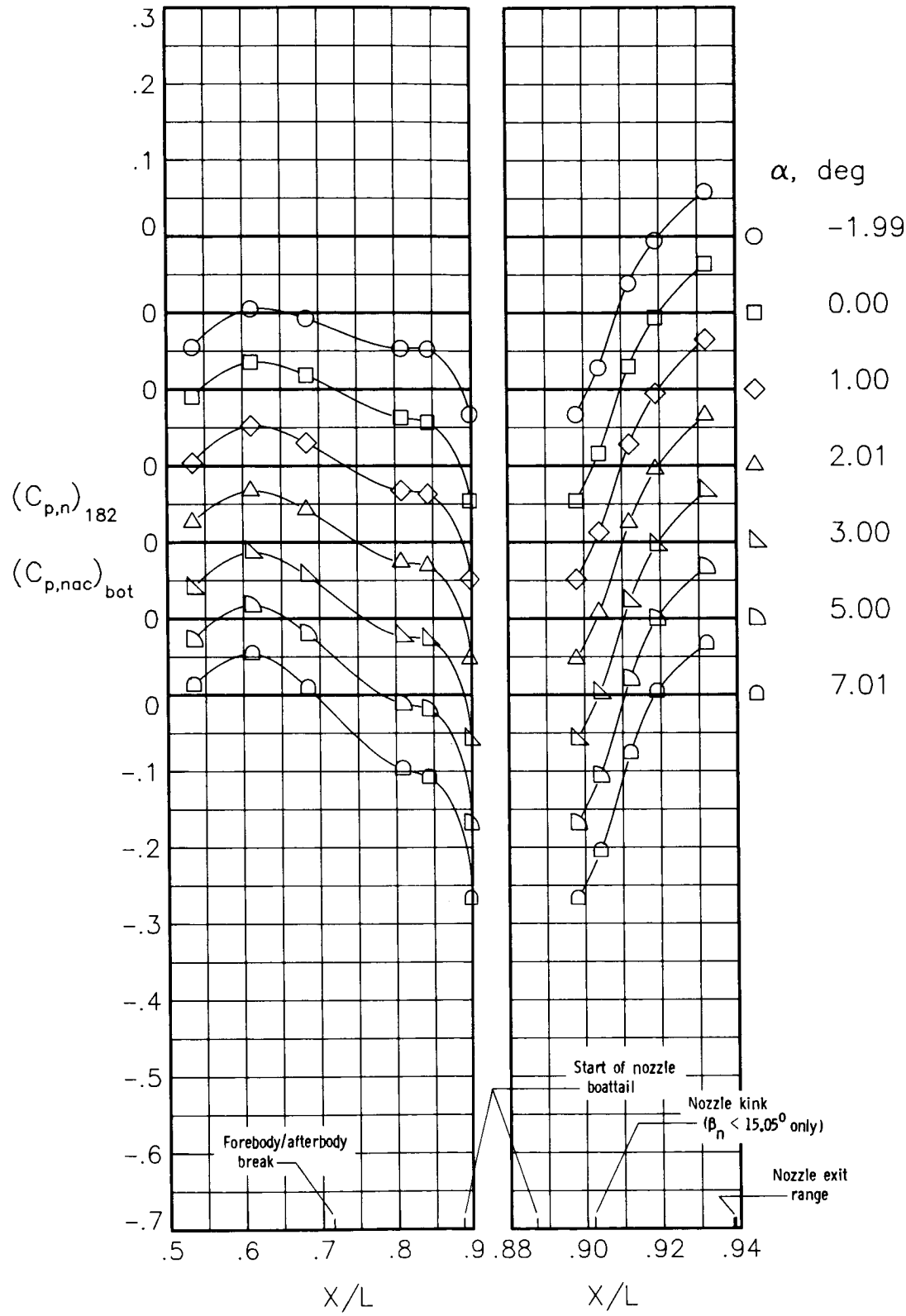

(a) M = 0.60; NPR = 1.00.

Figure 47.- Static-pressure-coefficient distributions on bottom of nacelle and nozzle for the unmodified model. β_n = 18.45°.

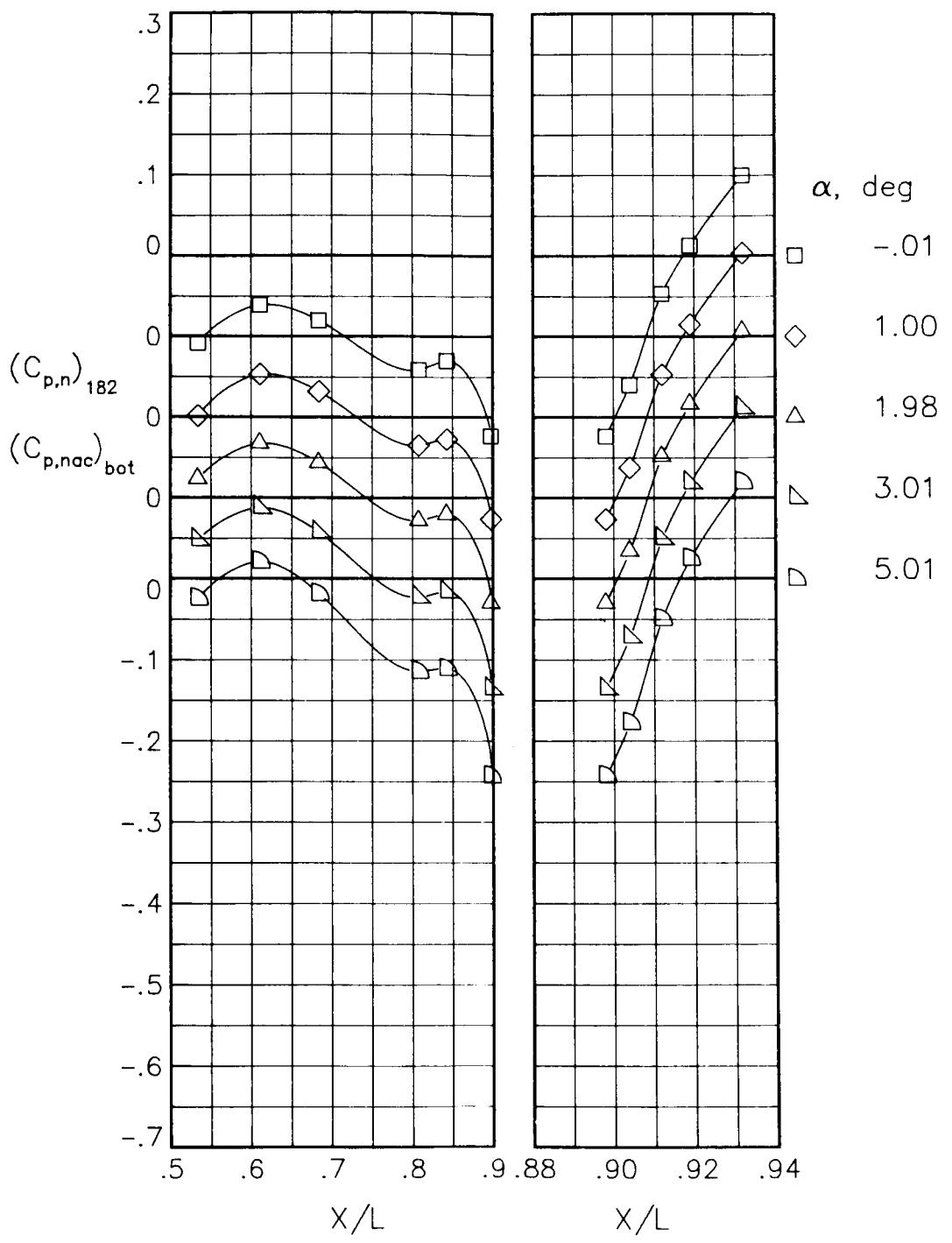

(b) M = 0.60; NPR = 3.00.

Figure 47.- Continued.

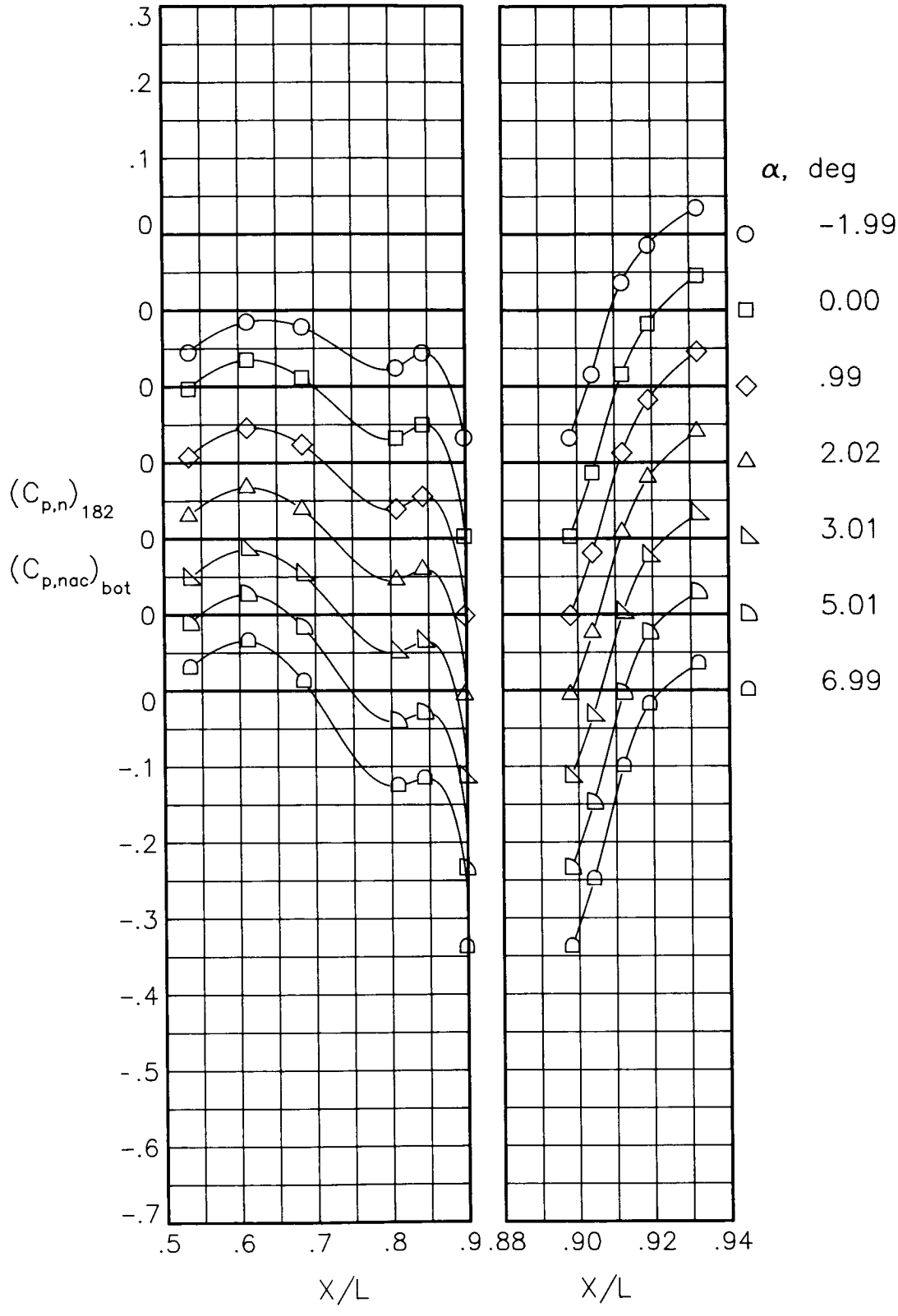

(c) M = 0.80; NPR = 1.00.

Figure 47.- Continued.

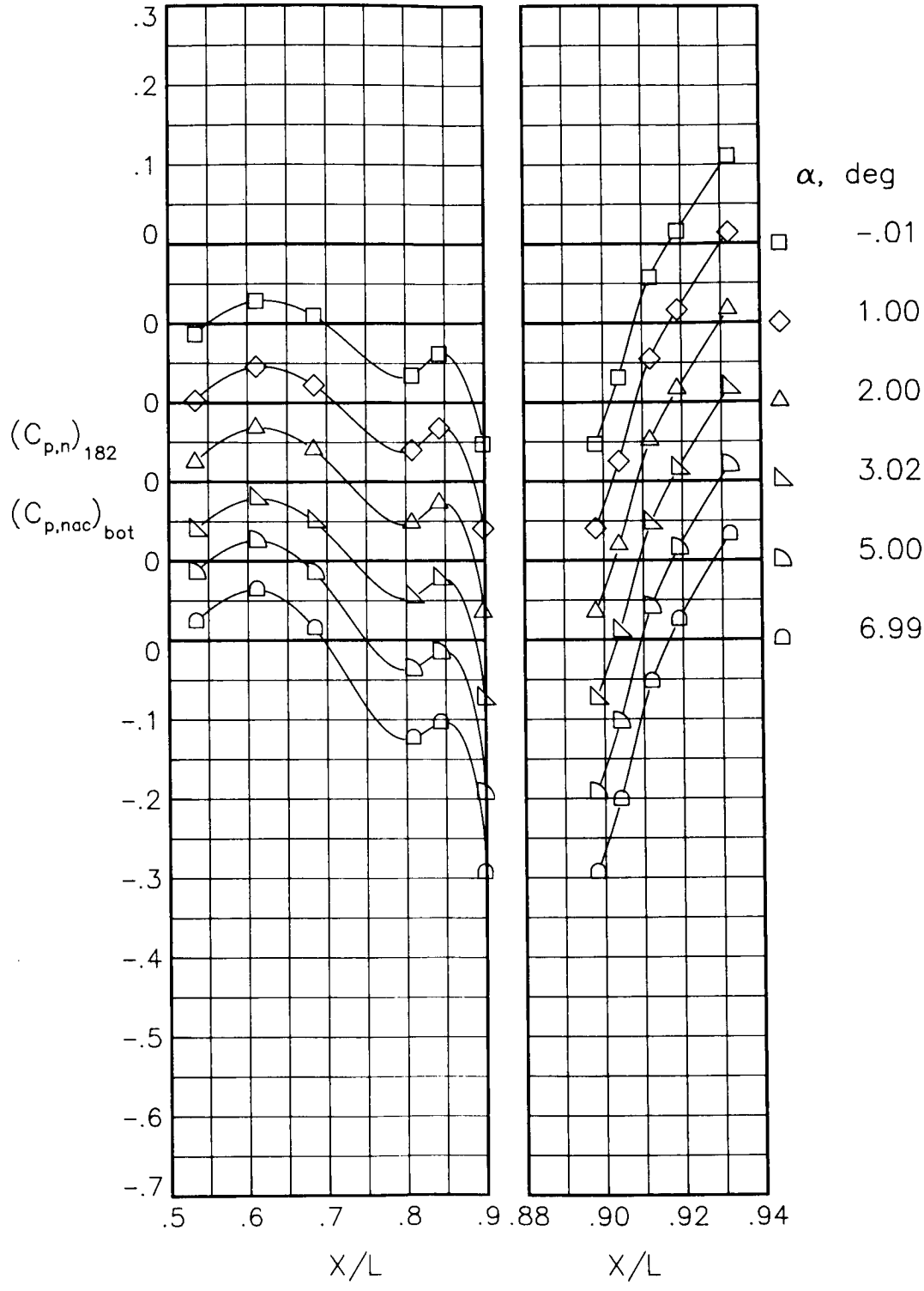

(d) M = 0.80; NPR = 4.60.

Figure 47.- Continued.

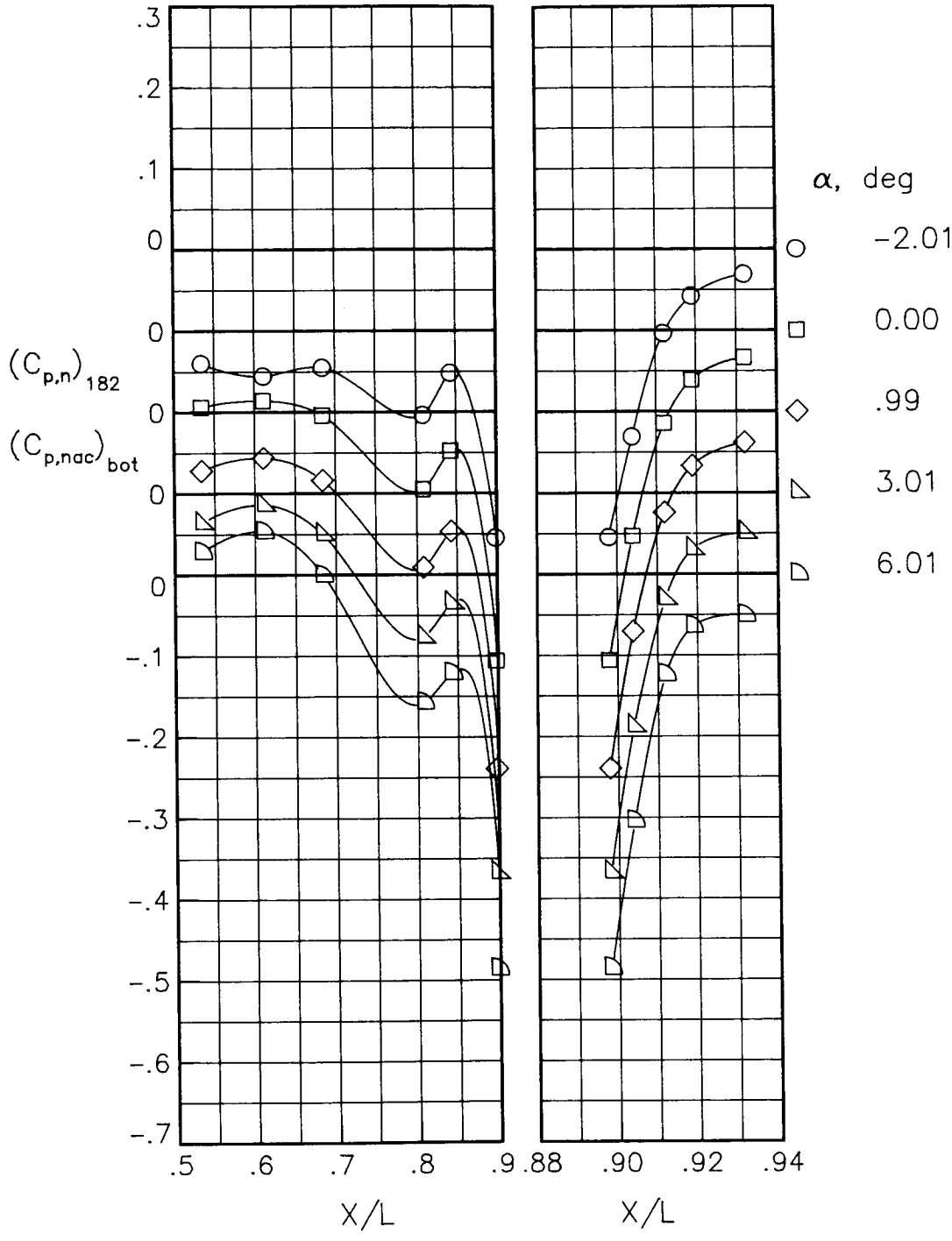

(e) M = 0.90; NPR = 1.00.

Figure 47.- Continued.

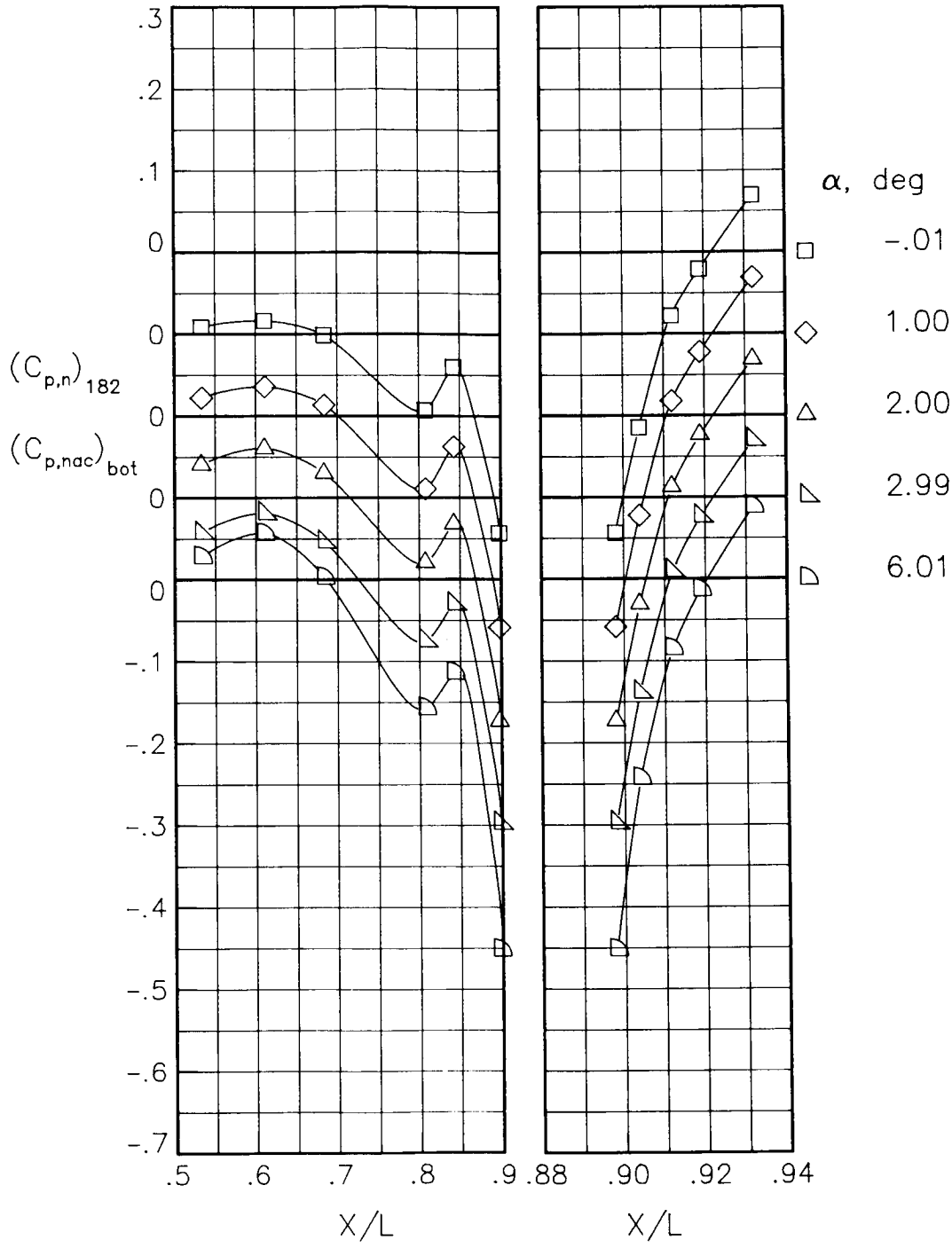

(f) M = 0.90; NPR = 5.00.

Figure 47.- Concluded.

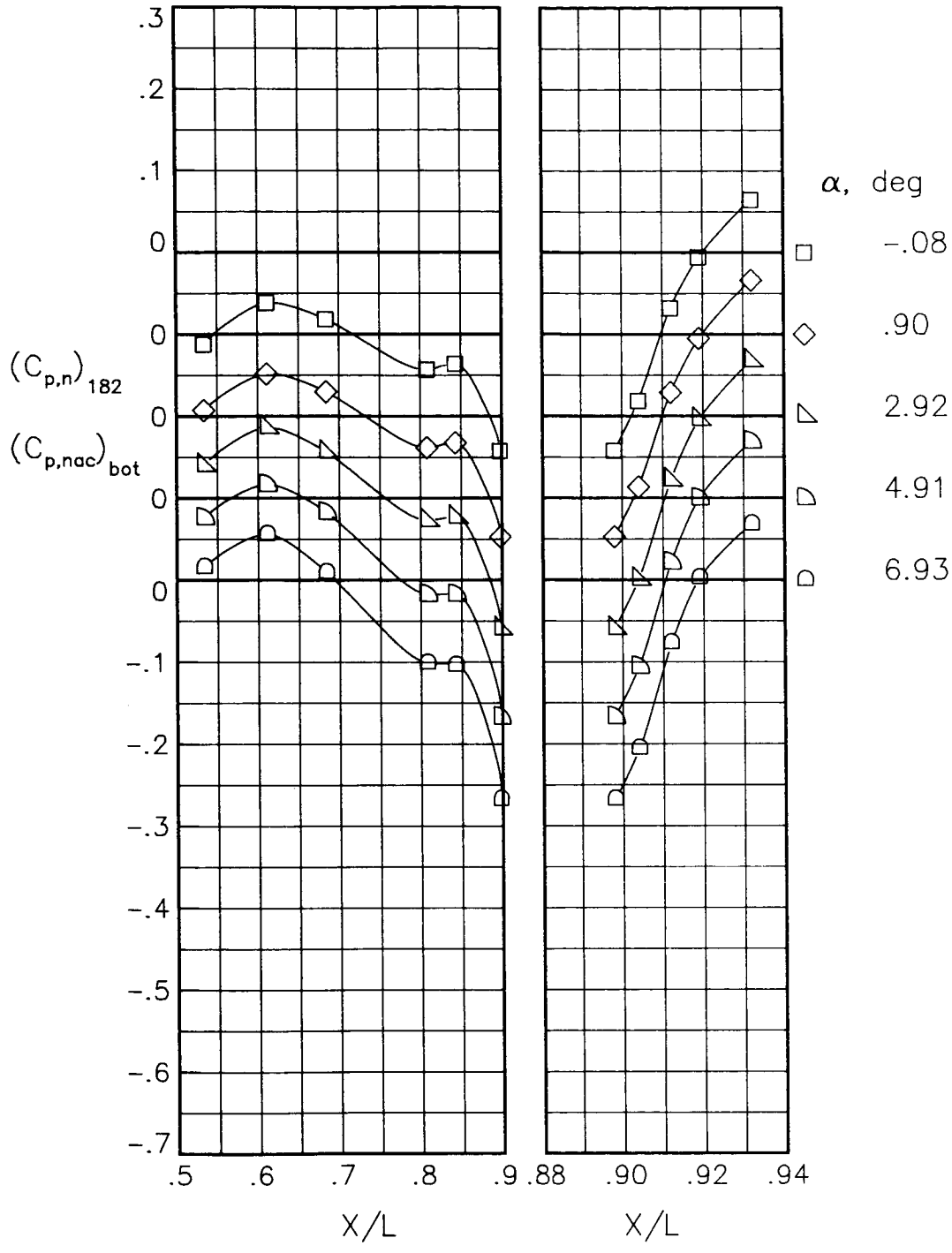

(a) M = 0.60; NPR = 1.00.

Figure 48.- Static-pressure-coefficient distributions on bottom of nacelle and nozzle for the model with nose boom. β_n = 18.45°.

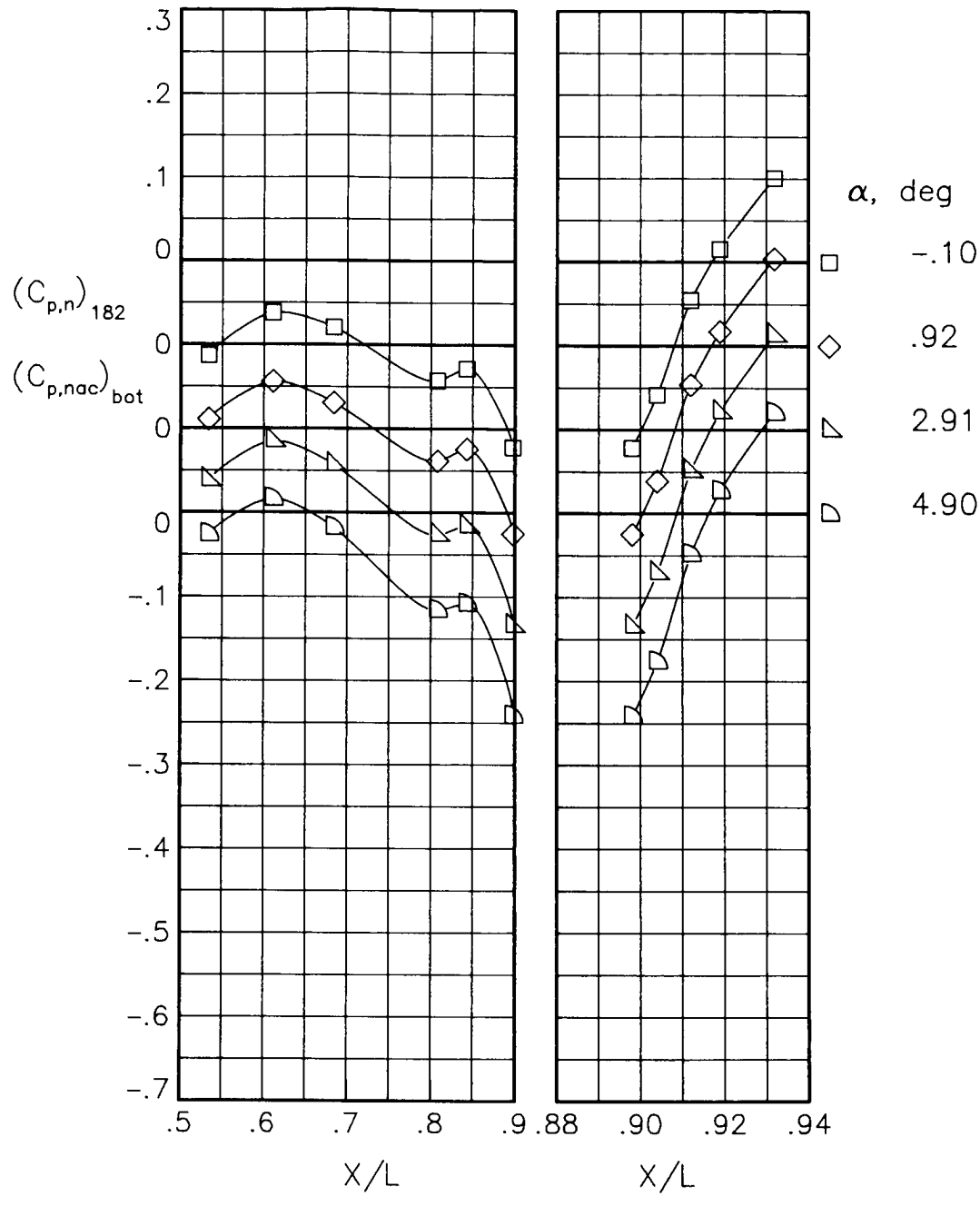

(b) M = 0.60; NPR = 3.00.

Figure 48.- Continued.

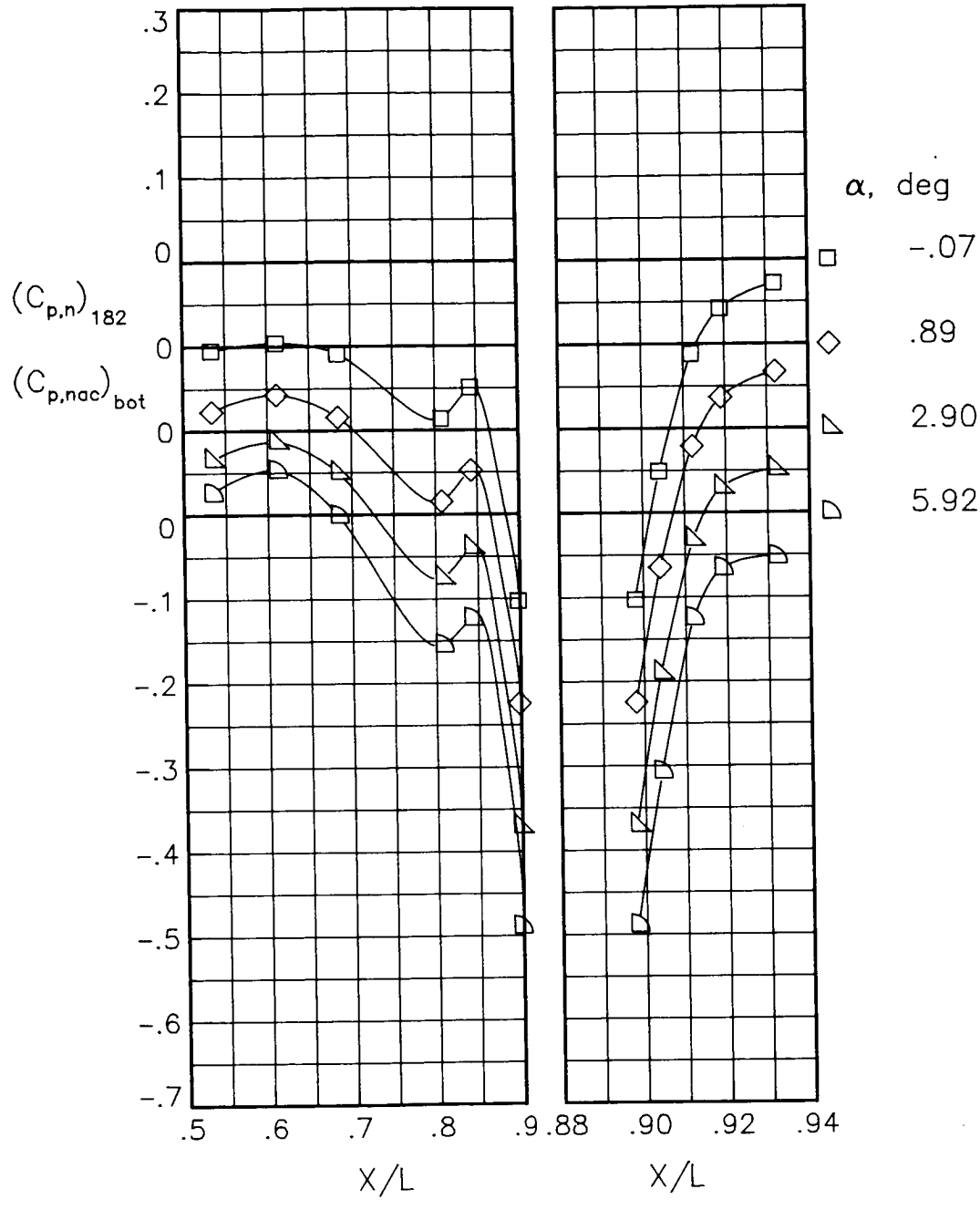

(c) M = 0.90; NPR = 1.00.

Figure 48.- Continued.

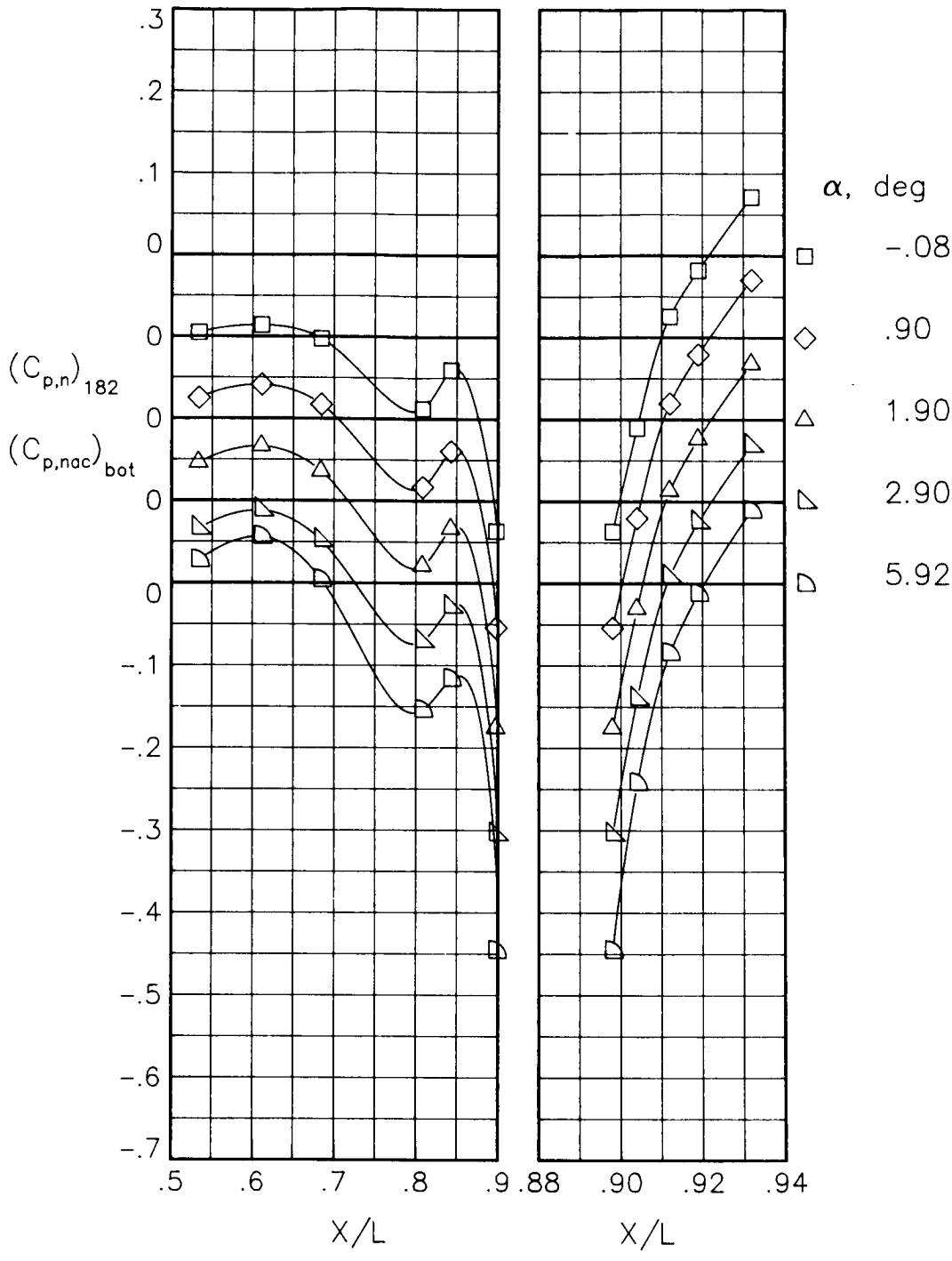

(d) M = 0.90; NPR = 5.00.

Figure 48.- Concluded.

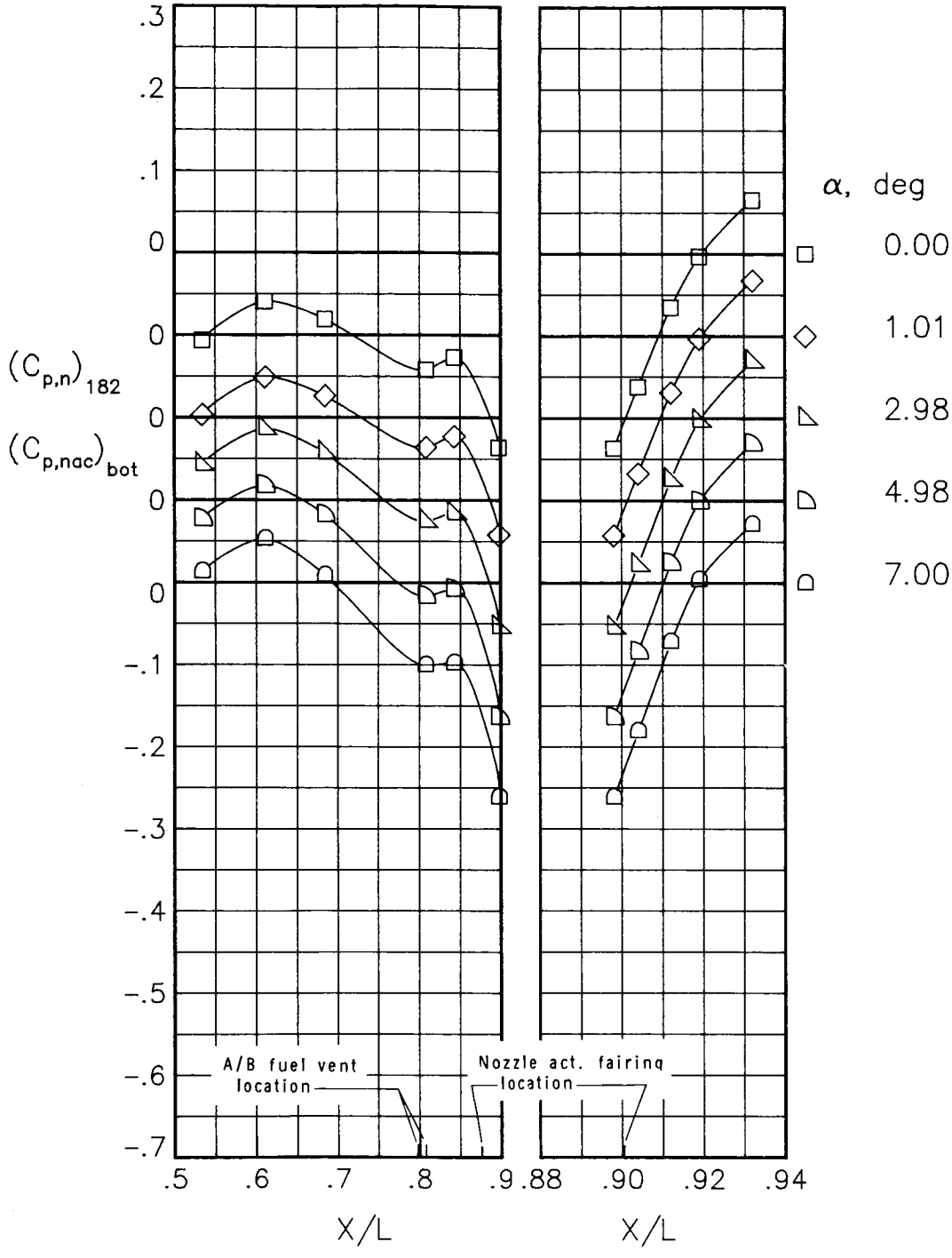

(a) M = 0.60; NPR = 1.00.

Figure 49.- Static-pressure-coefficient distributions on bottom of nacelle and nozzle for the model with nose boom, actuator fairings, and A/B vents. β_n = 18.45°.

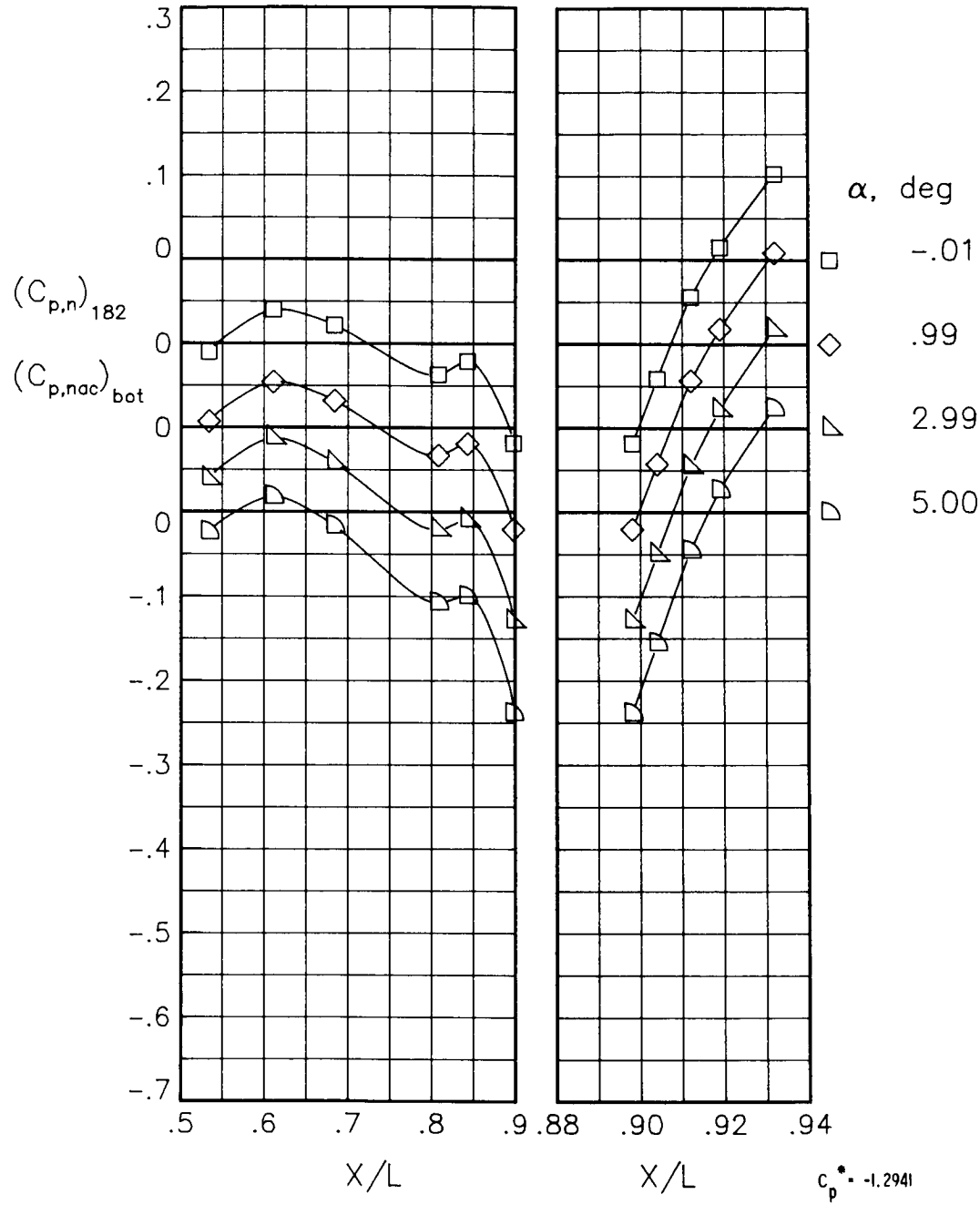

(b) M = 0.60; NPR = 3.00.

Figure 49.- Continued.

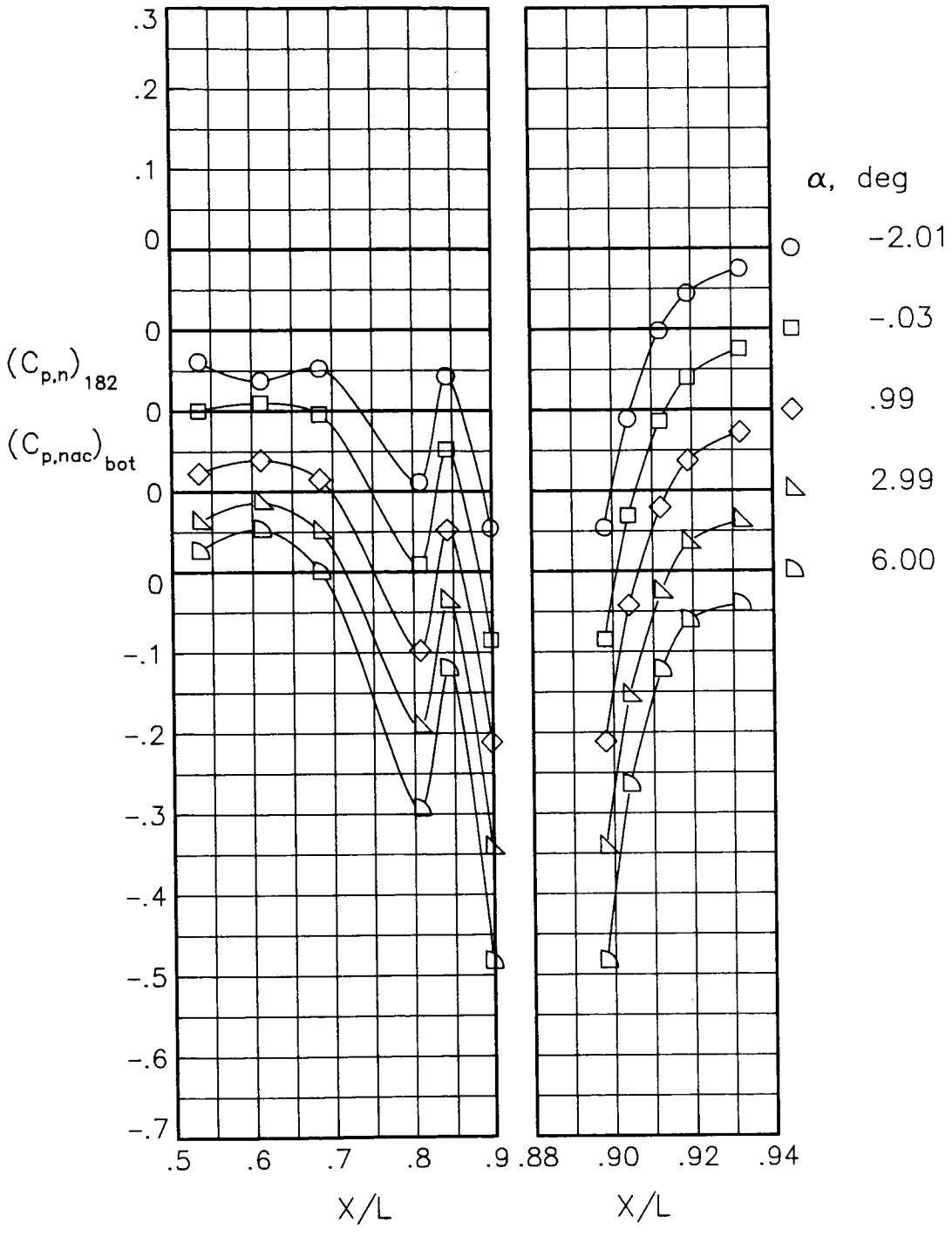

(c) M = 0.90; NPR = 1.00.

Figure 49.- Continued.

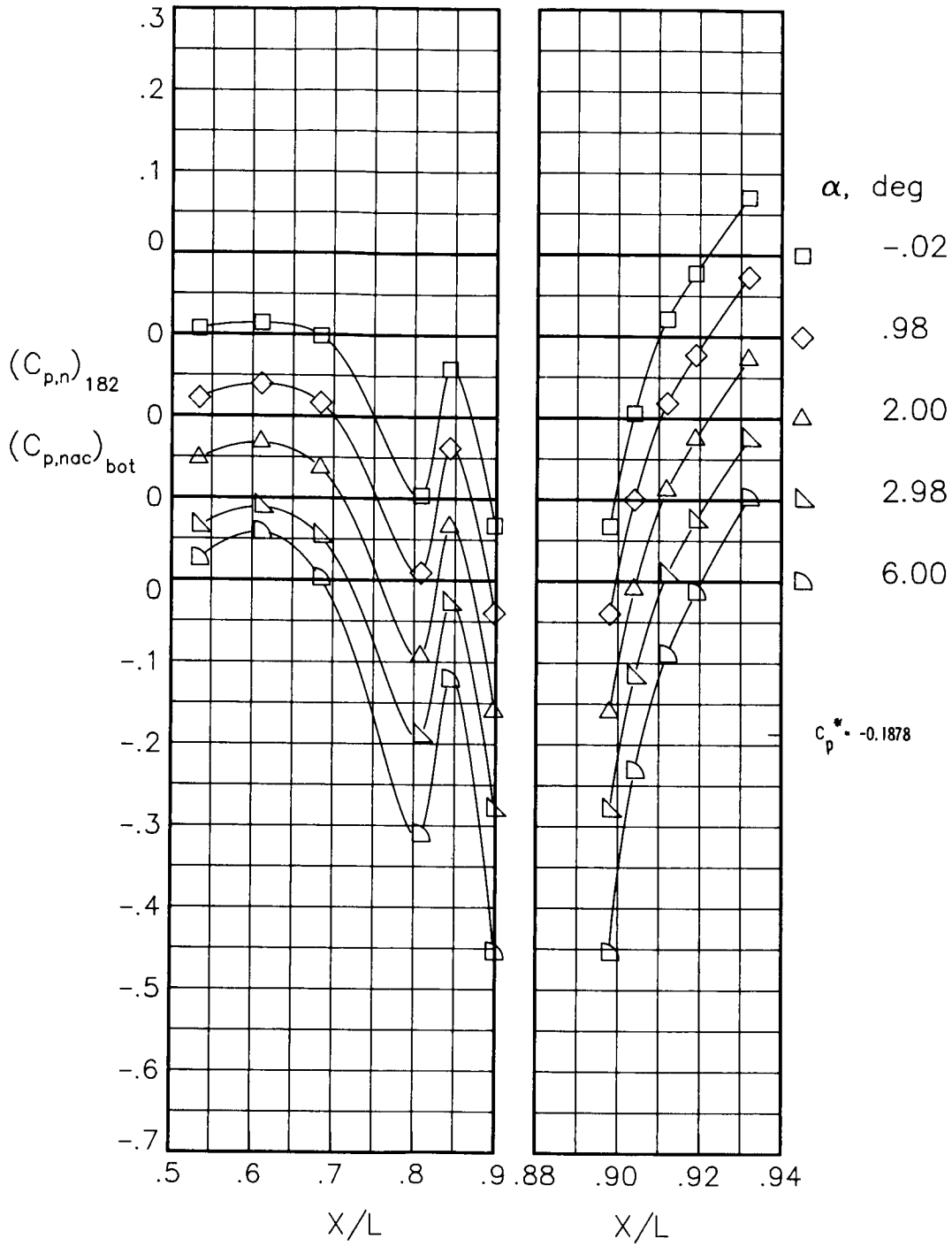

(d) M = 0.90; NPR = 5.00.

Figure 49.- Concluded.

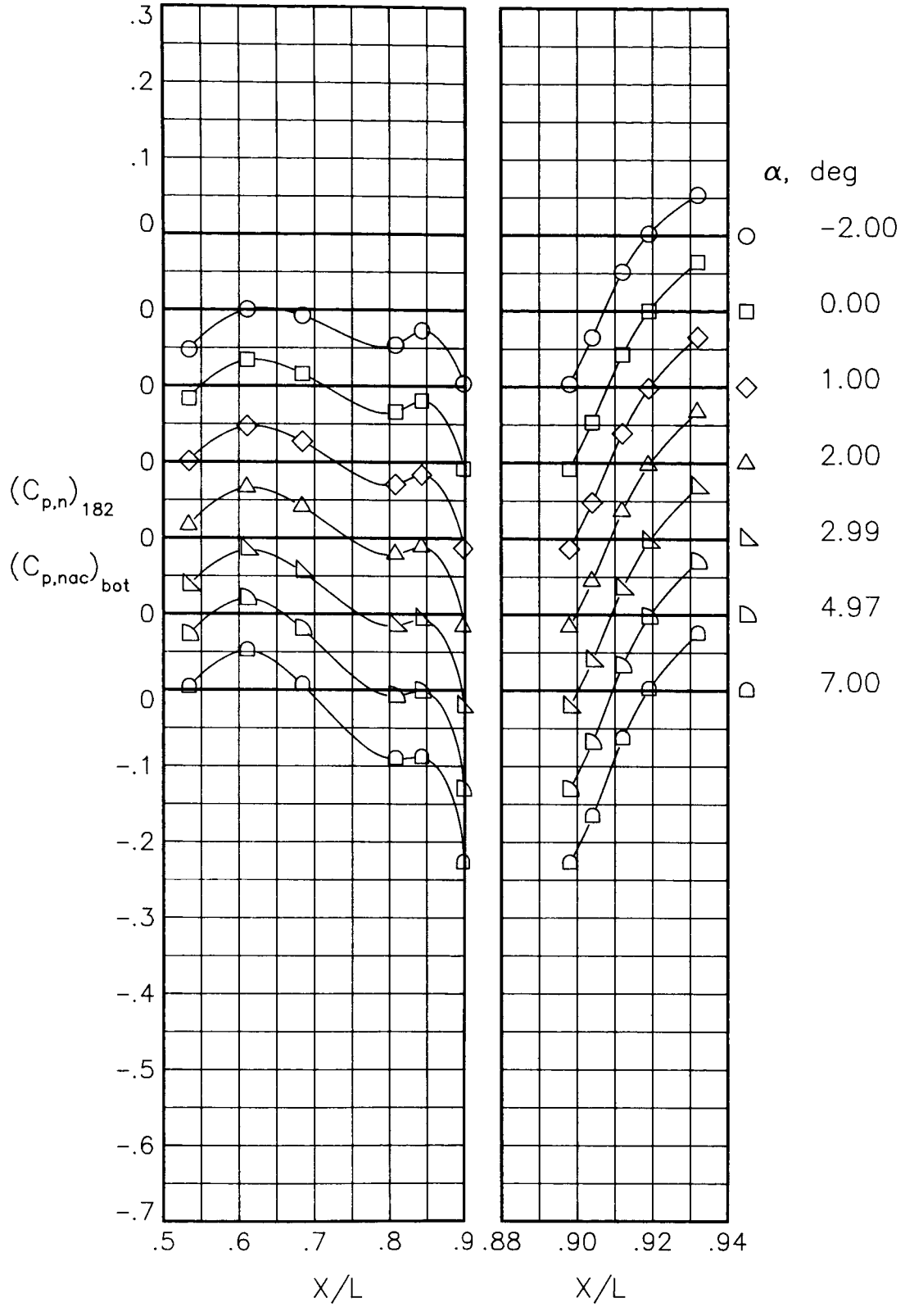

(a) M = 0.60; NPR = 1.00.

Figure 50.- Static-pressure-coefficient distributions on bottom of nacelle and nozzle for the model with all fuselage modifications except nose boom. β_n = 18.45°.

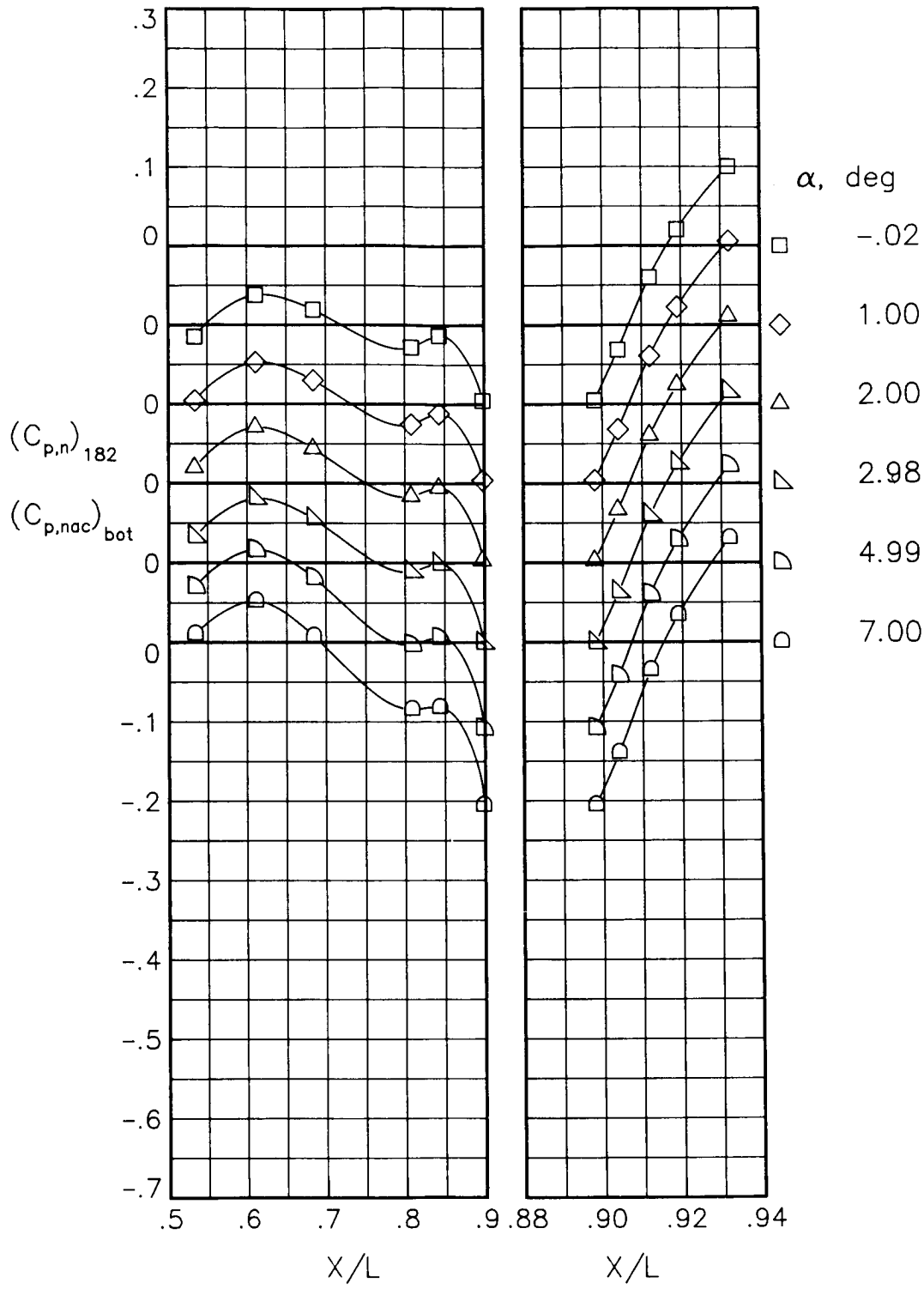

(b) M = 0.60; NPR = 3.00.

Figure 50.- Continued.

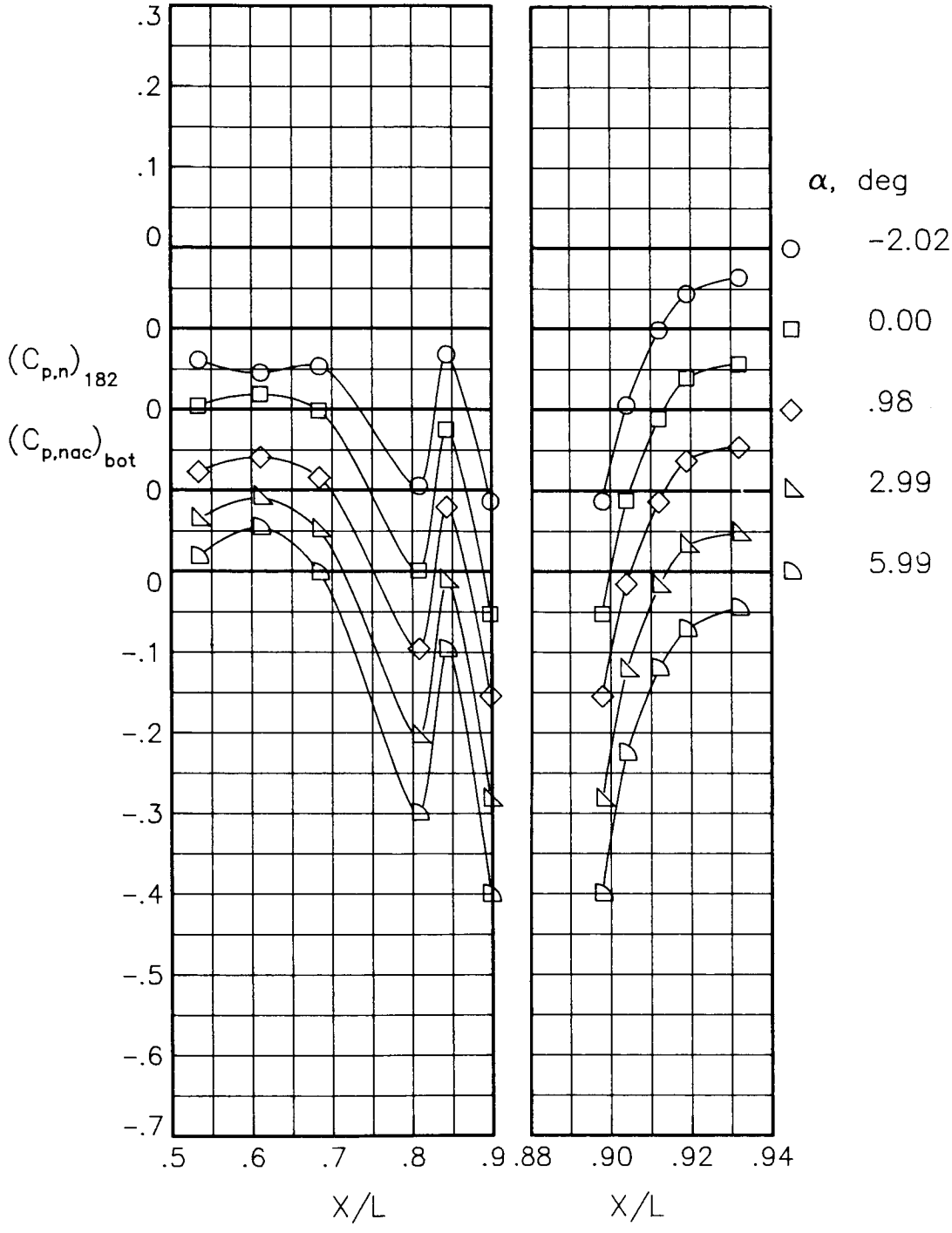

(c) M = 0.90; NPR = 1.00.

Figure 50.- Continued.

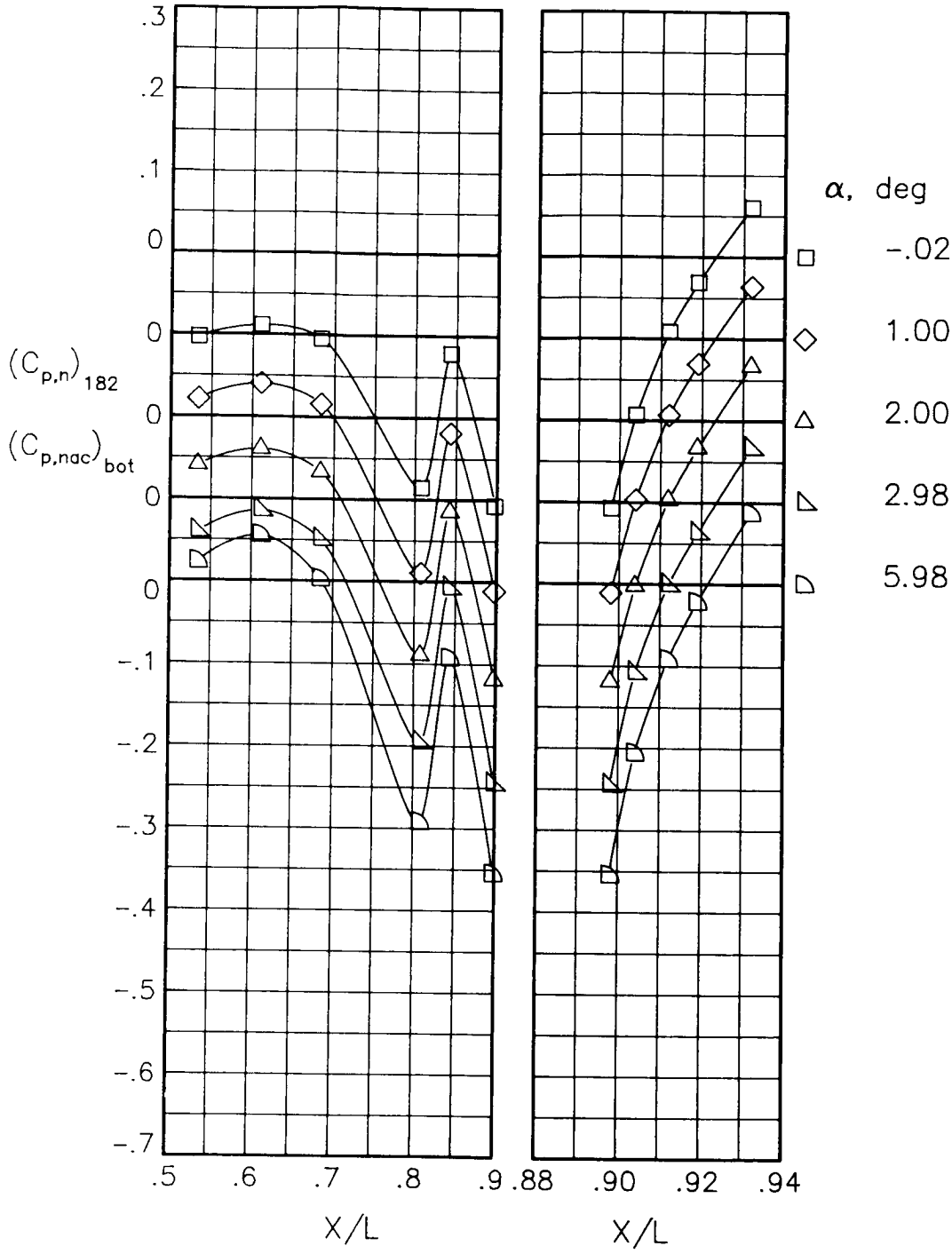

(d) M = 0.90; NPR = 5.00.

Figure 50.- Concluded.

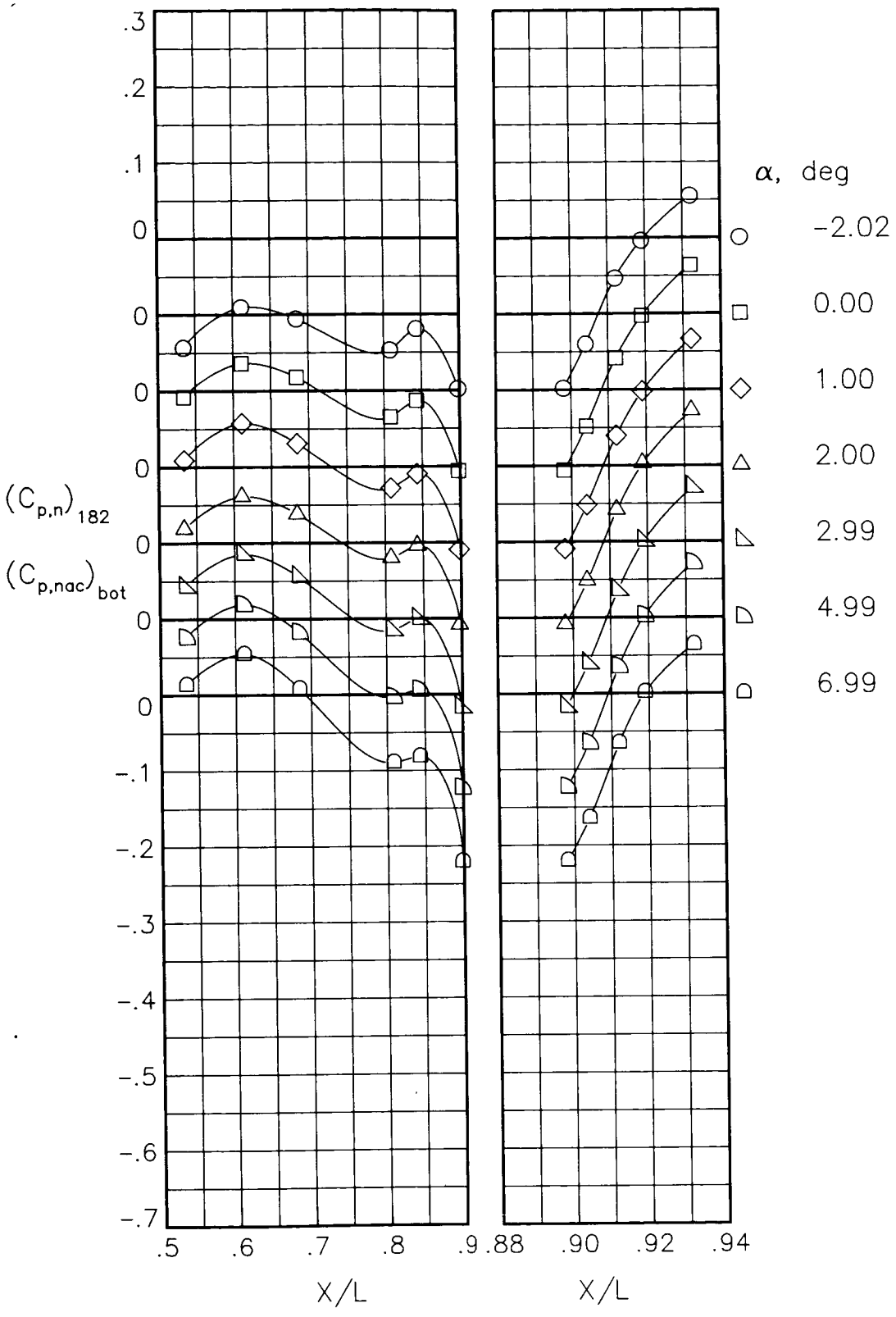

(a) M = 0.60; NPR = 1.00.

Figure 51.- Static-pressure-coefficient distributions on bottom of nacelle and nozzle for the model with nose boom, actuator fairings, A/B vents, and nozzle steps (no rakes). β_n = 18.45°.

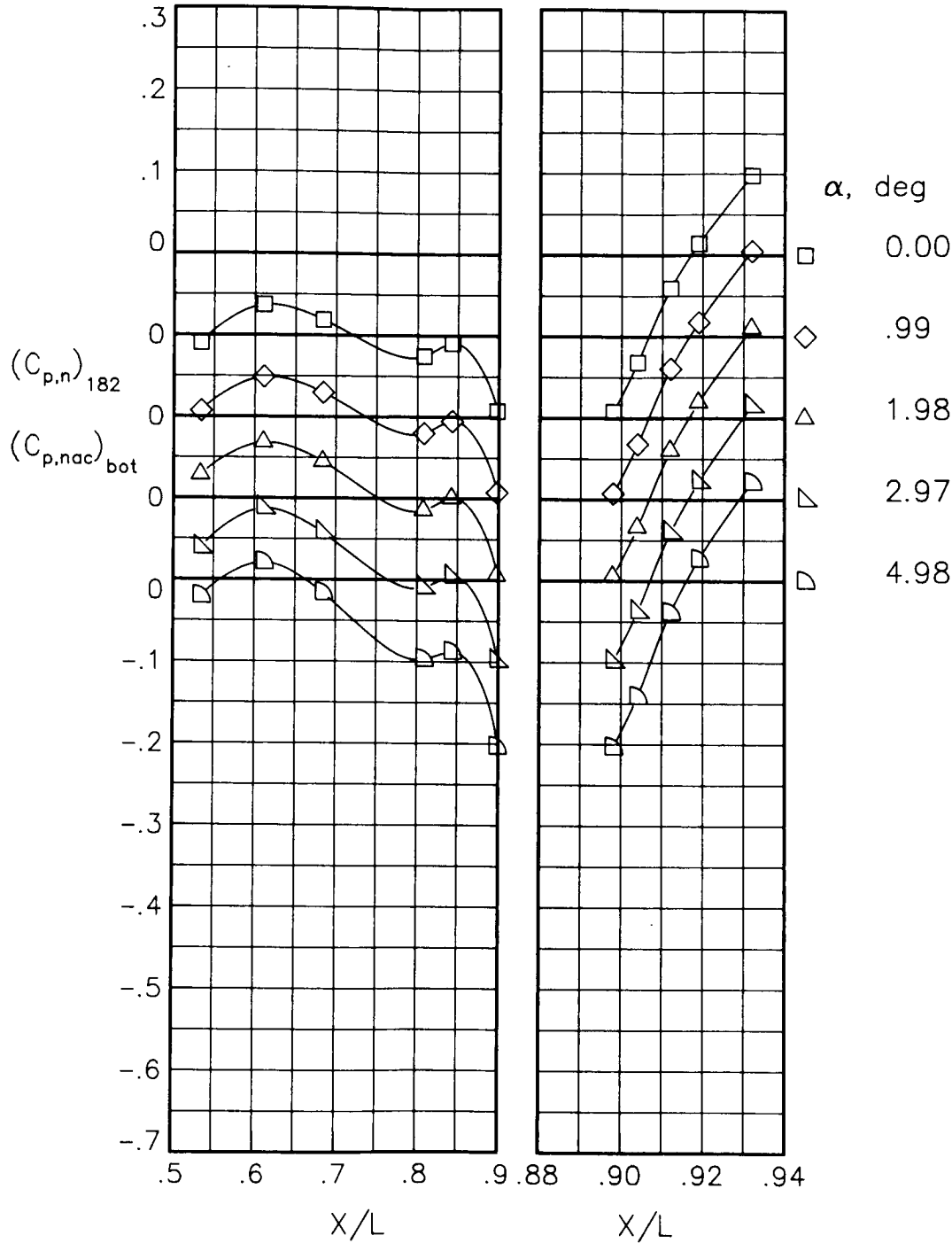

(b) M = 0.60; NPR = 3.00.

Figure 51.- Continued.

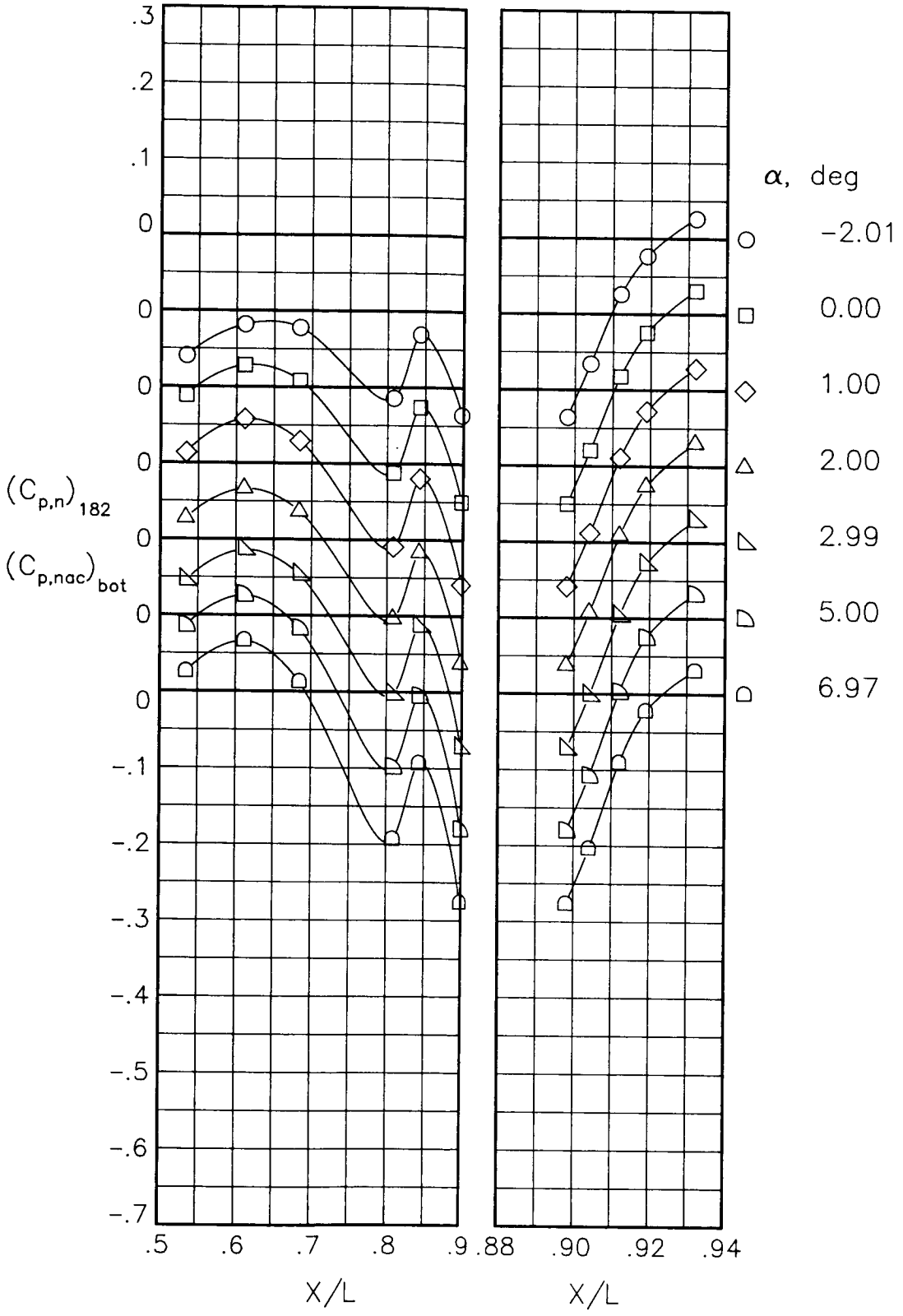

(c) M = 0.80; NPR = 1.00.

Figure 51.- Continued.

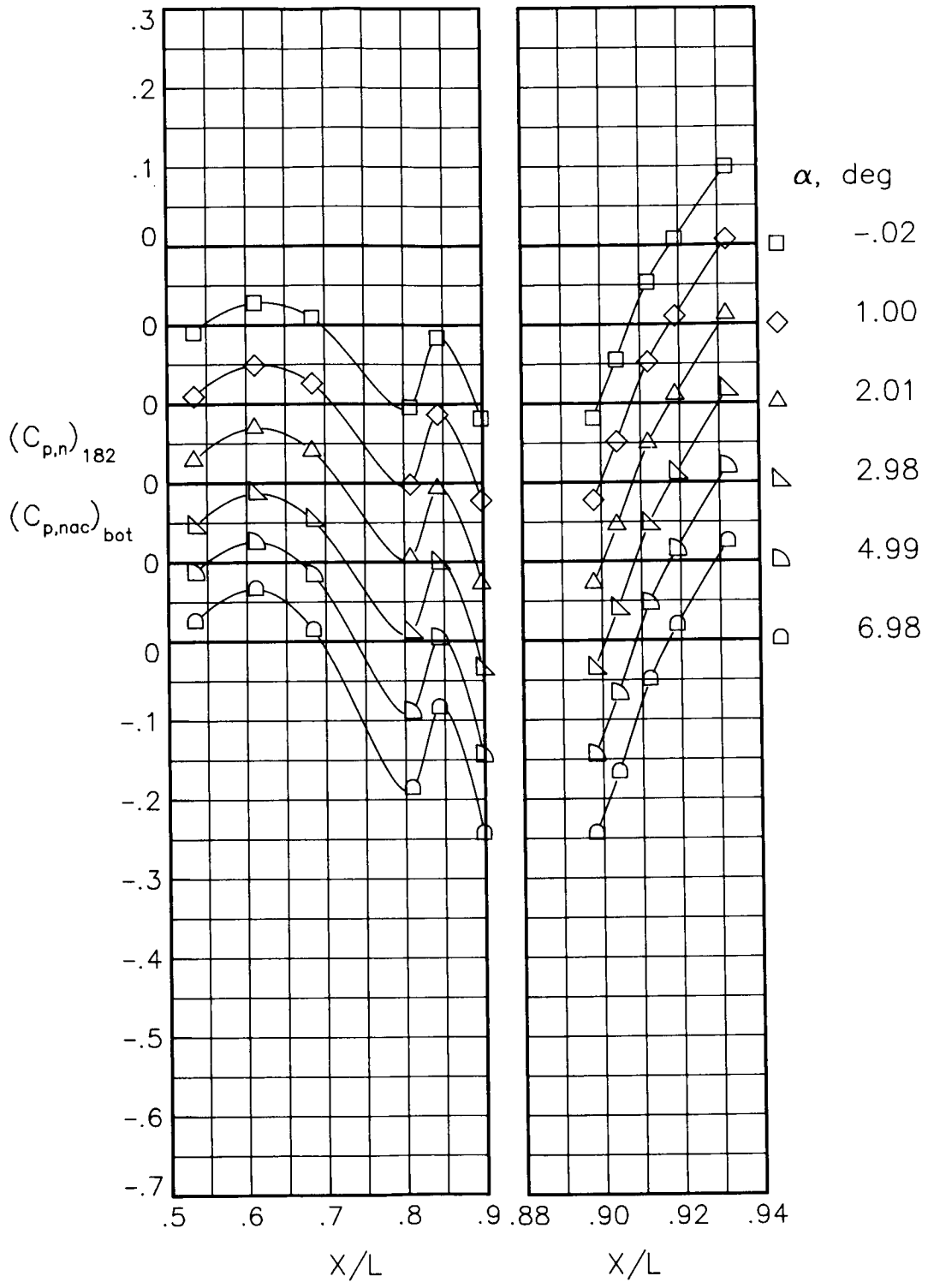

(d) M = 0.80; NPR = 4.60.

Figure 51.- Continued.

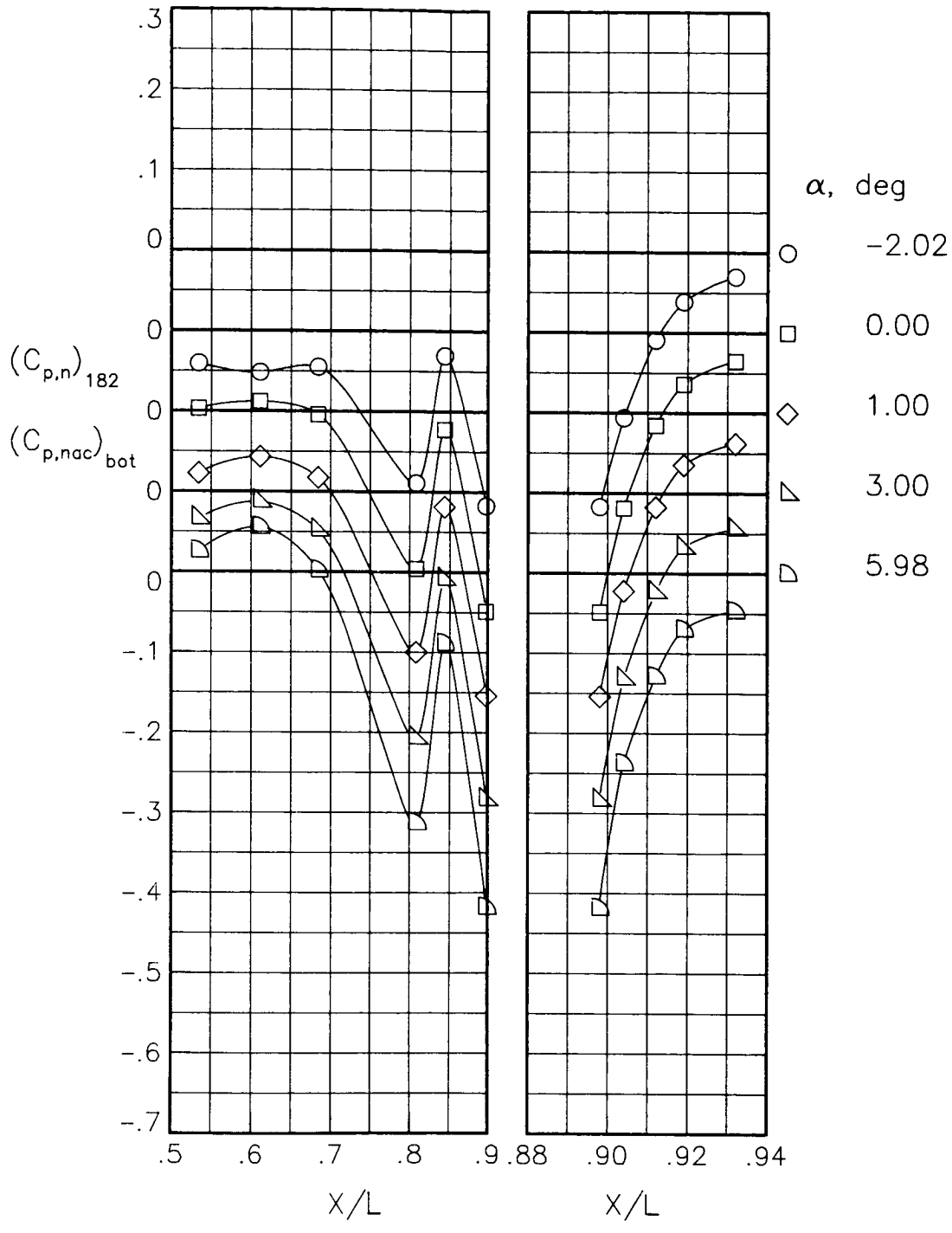

(e) M = 0.90; NPR = 1.00.

Figure 51.- Continued.

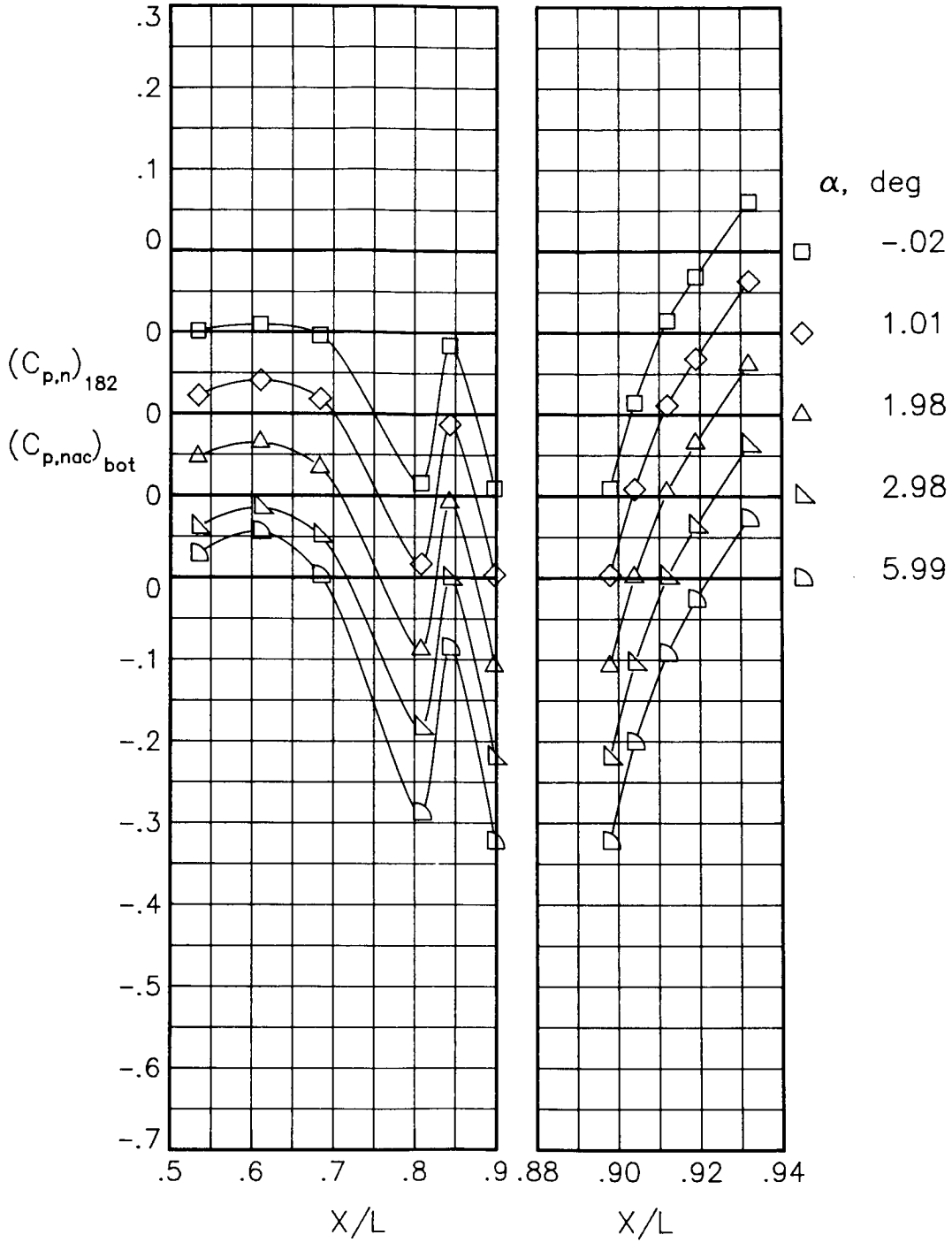

(f) M = 0.90; NPR = 5.00.

Figure 51.- Concluded.

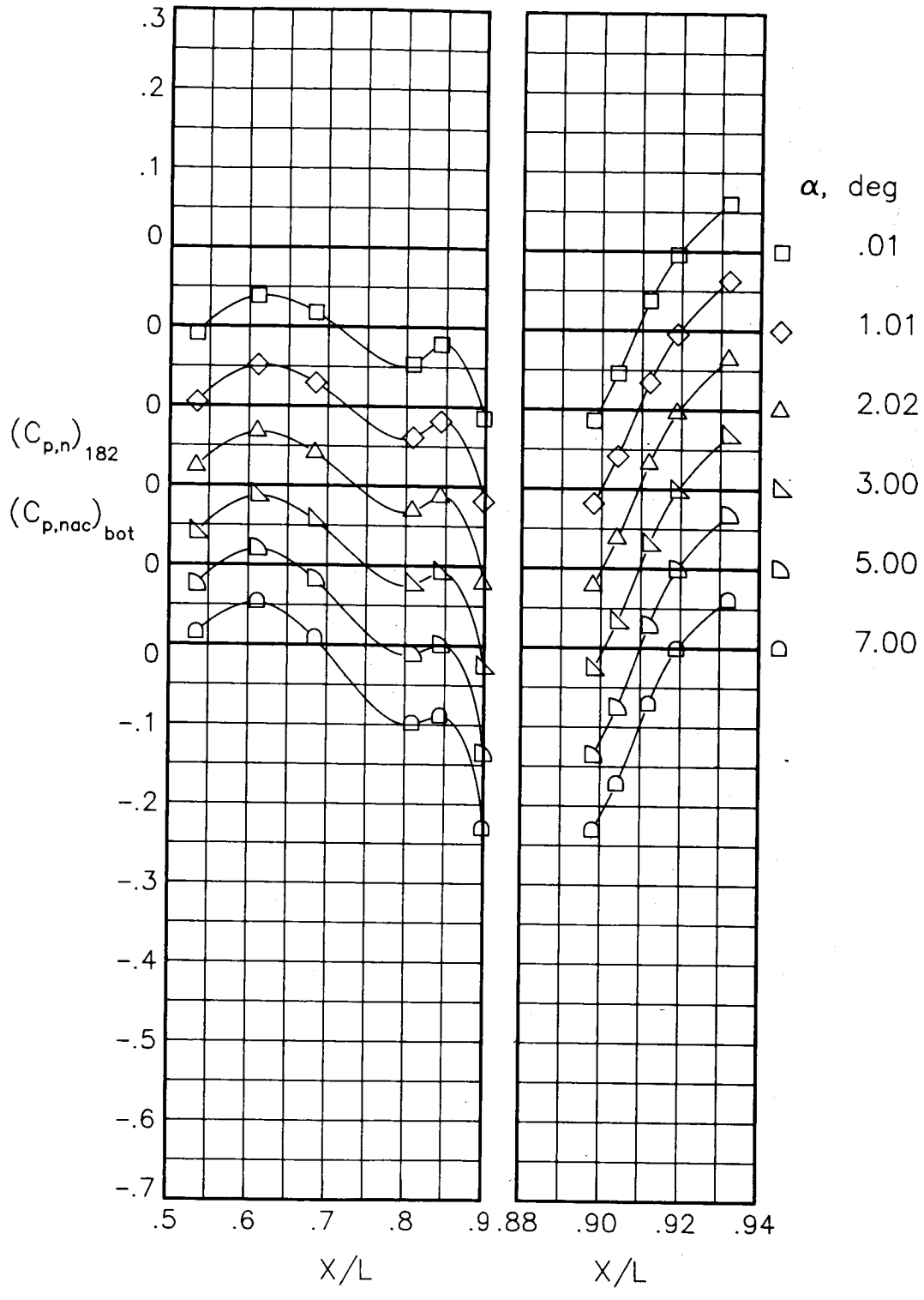

(a) M = 0.60; NPR = 1.00.

Figure 52.- Static-pressure-coefficient distributions on bottom of nacelle and nozzle for the model with nose boom, actuator fairings, A/B vents, and nozzle steps (no rakes). β_n = 18.45°; δ_h = -2°.

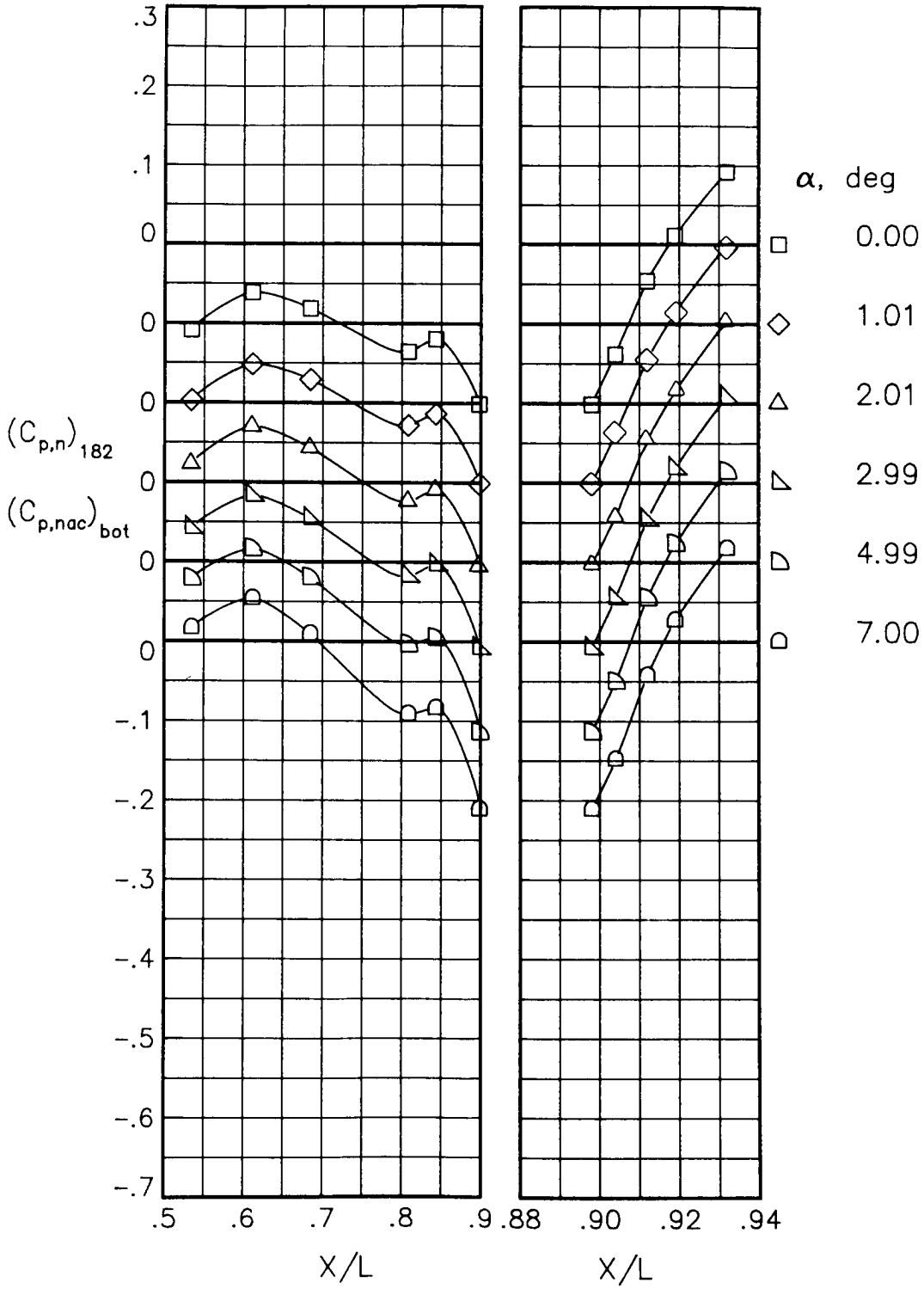

(b) M = 0.60; NPR = 3.00.

Figure 52.- Continued.

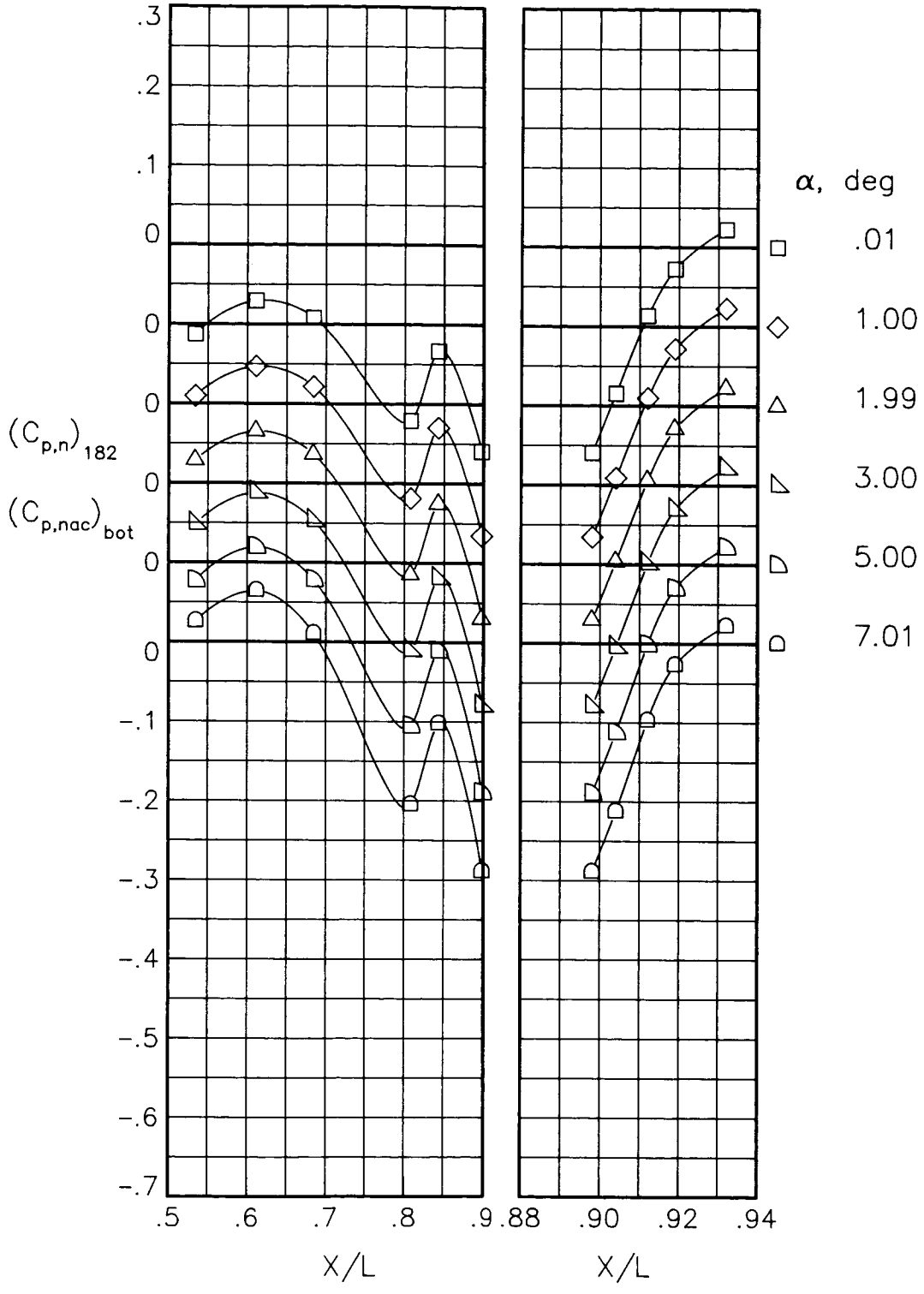

(c) M = 0.80; NPR = 1.00.

Figure 52.- Continued.

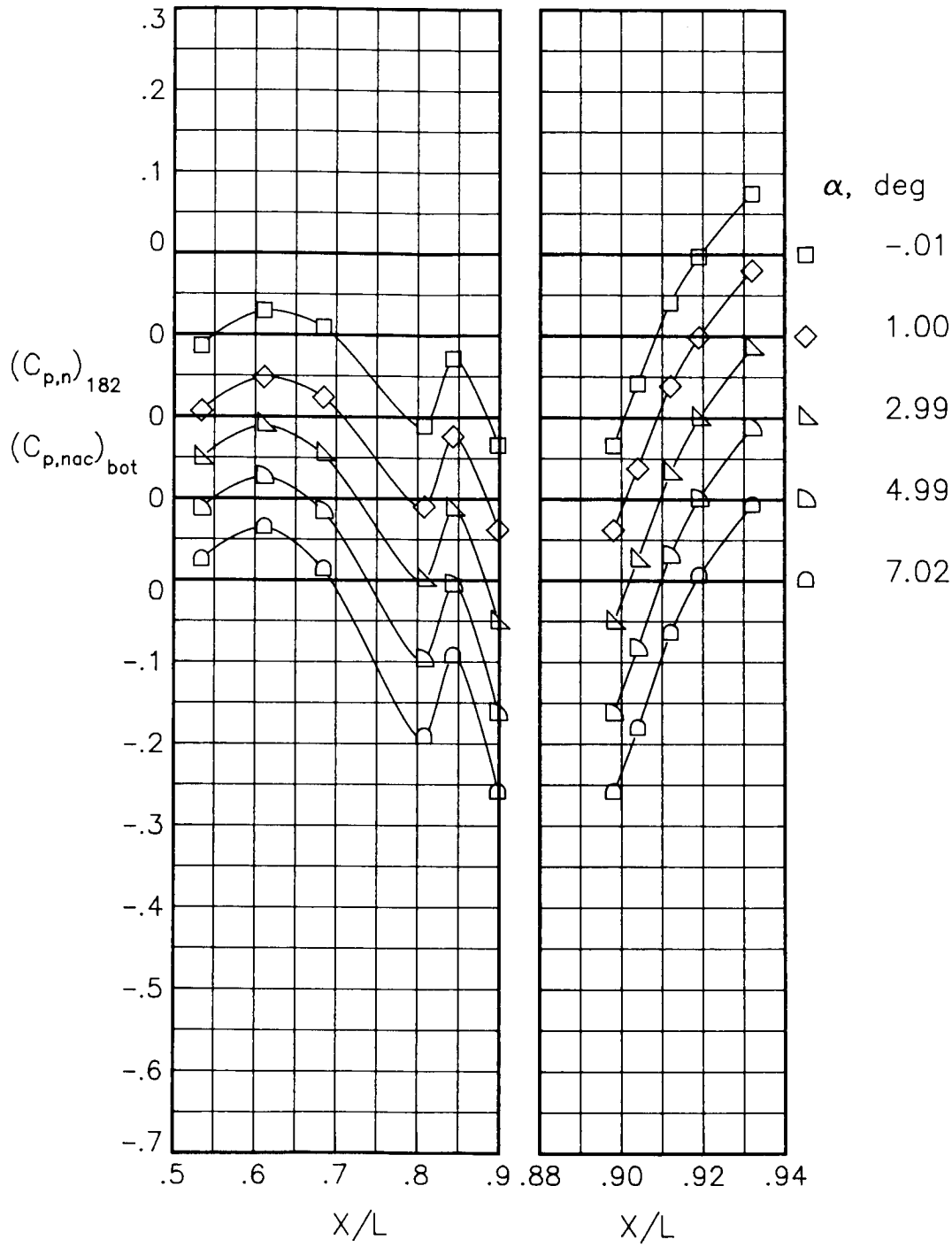

(d) M = 0.80; NPR = 3.50.

Figure 52.- Continued.

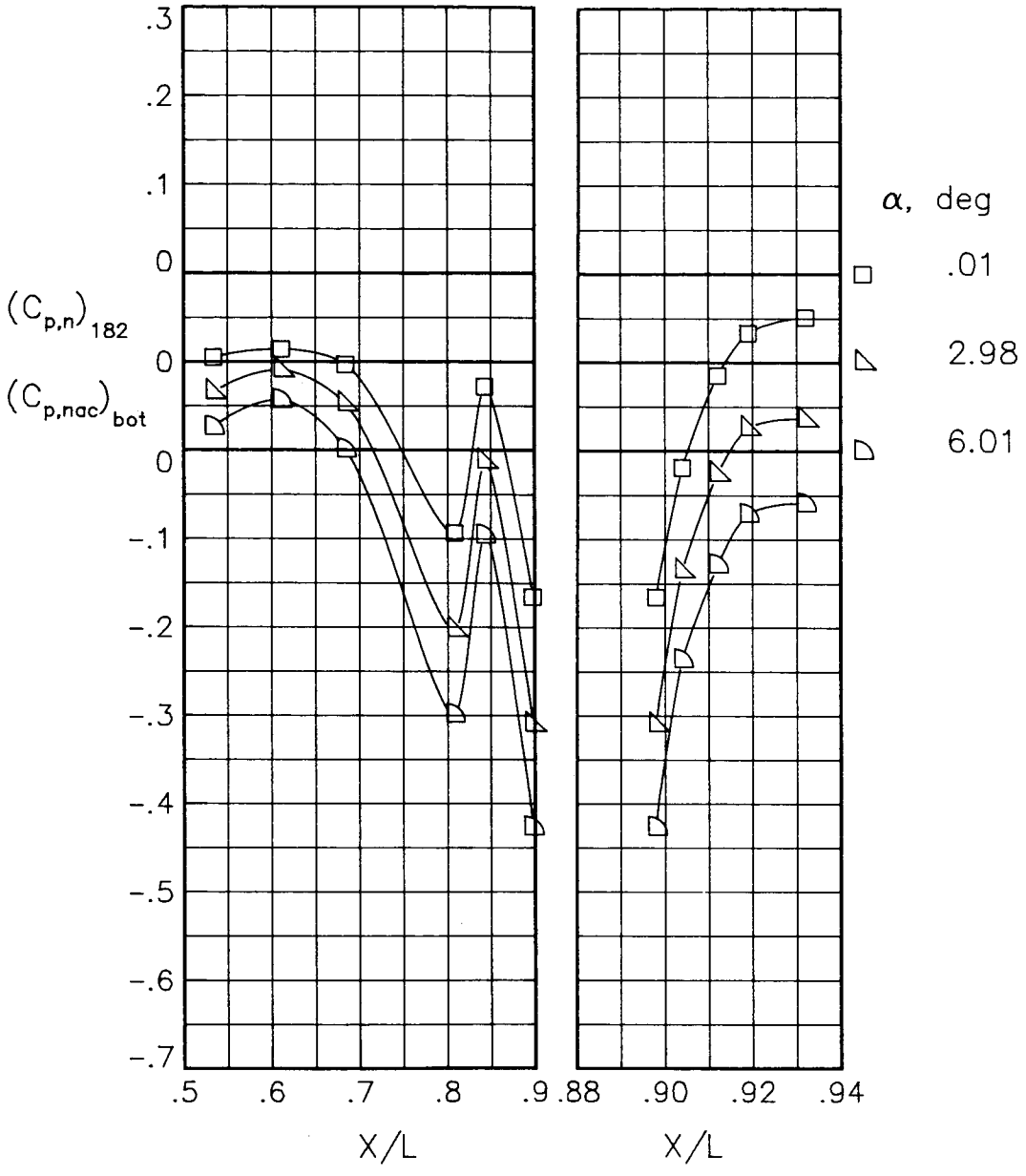

(e) M = 0.90; NPR = 1.00.

Figure 52.- Continued.

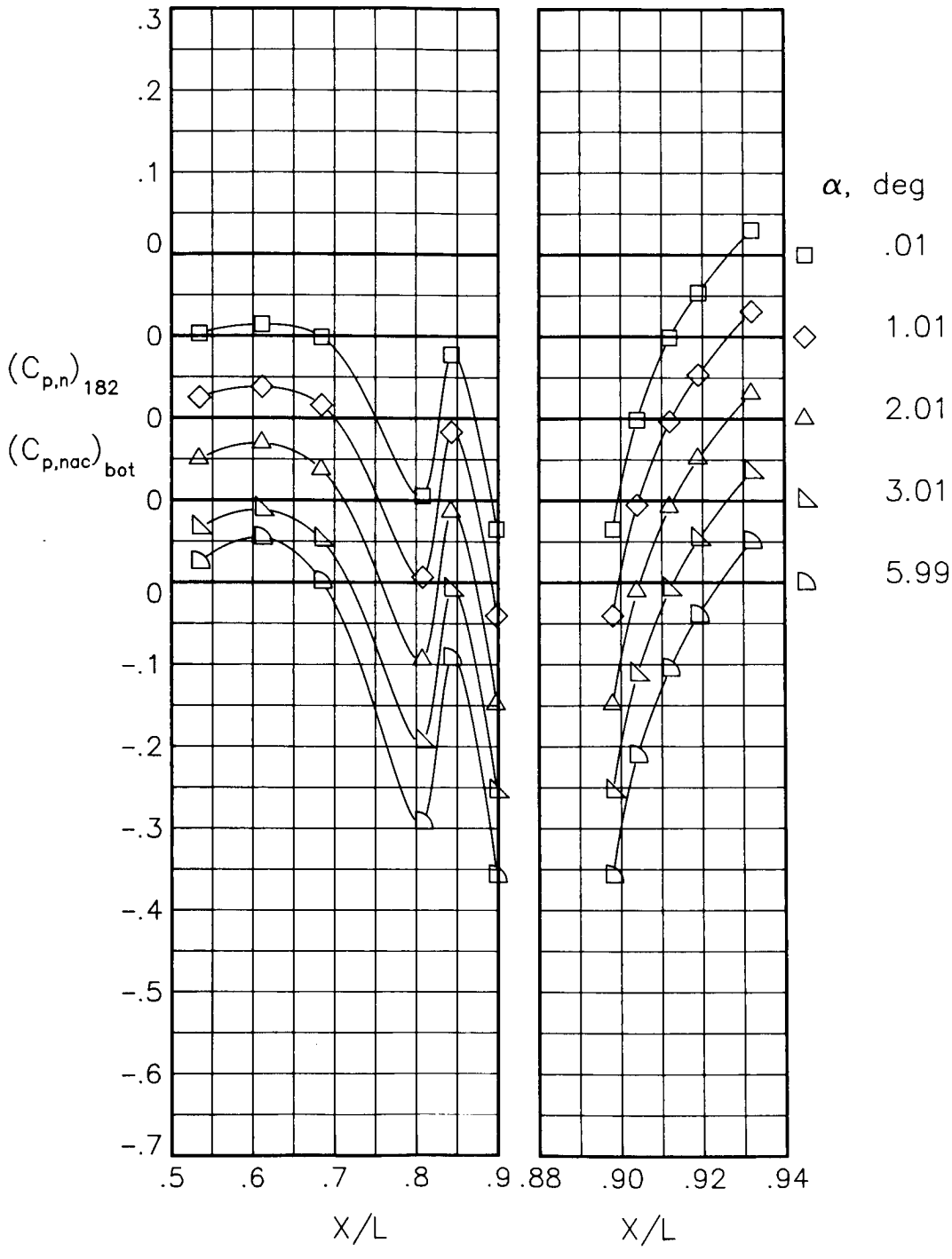

(f) M = 0.90; NPR = 5.00.

Figure 52.- Concluded.

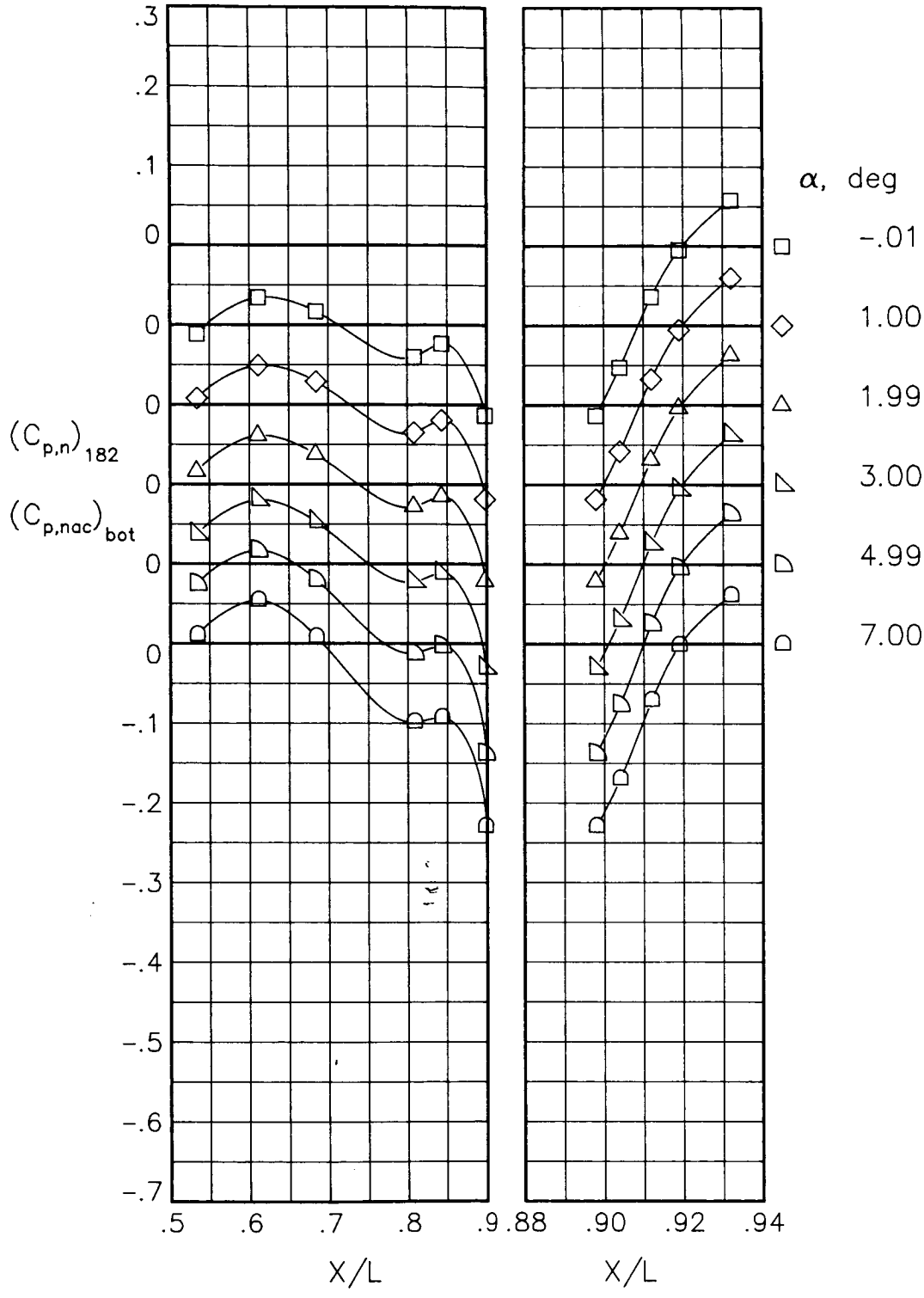

(a) M = 0.60; NPR = 1.00.

Figure 53.- Static-pressure-coefficient distributions on bottom of nacelle and nozzle for the model with all fuselage modifications. β_n = 18.45°; δ_h = -2°.

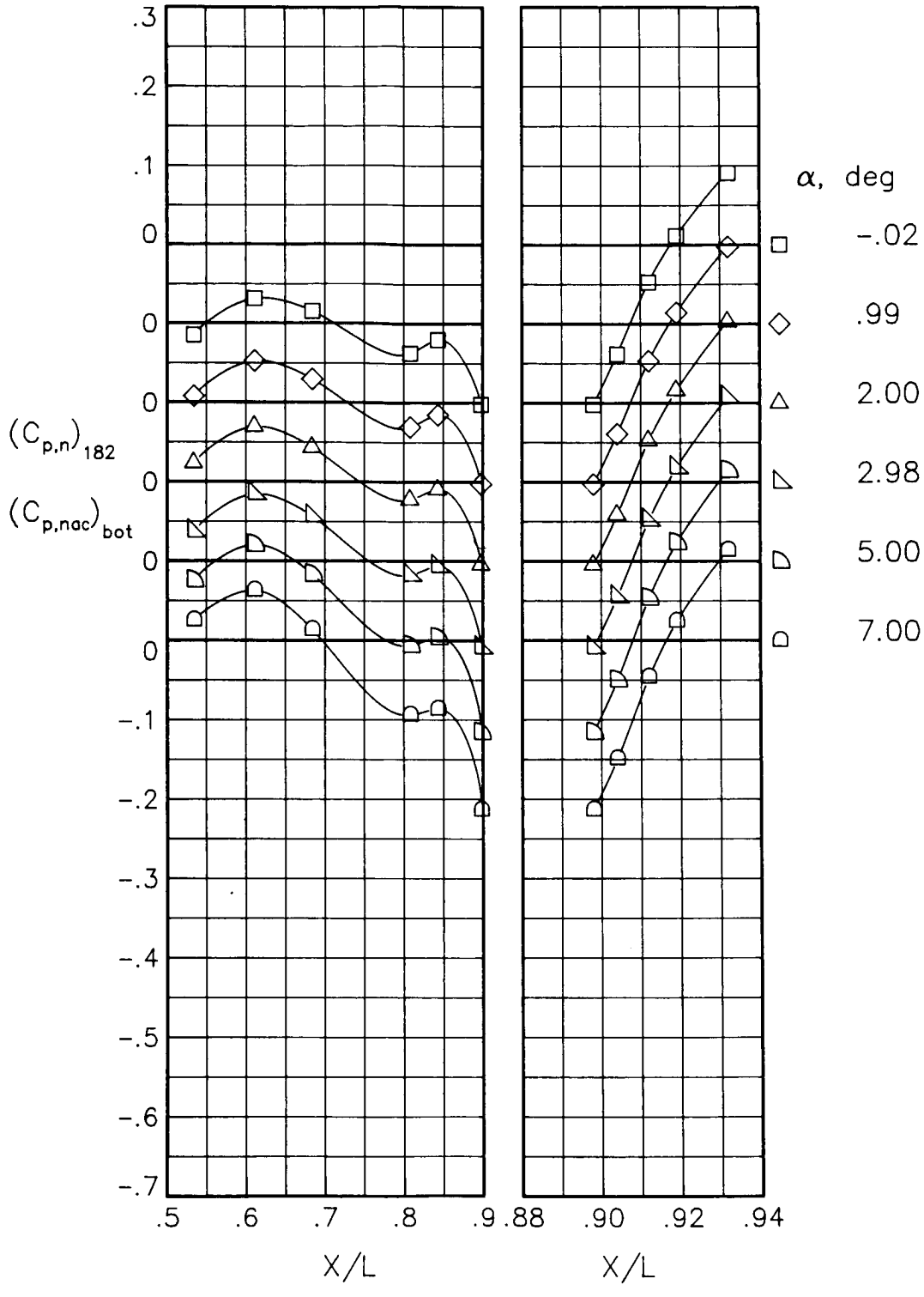

(b) M = 0.60; NPR = 3.00.

Figure 53.- Continued.

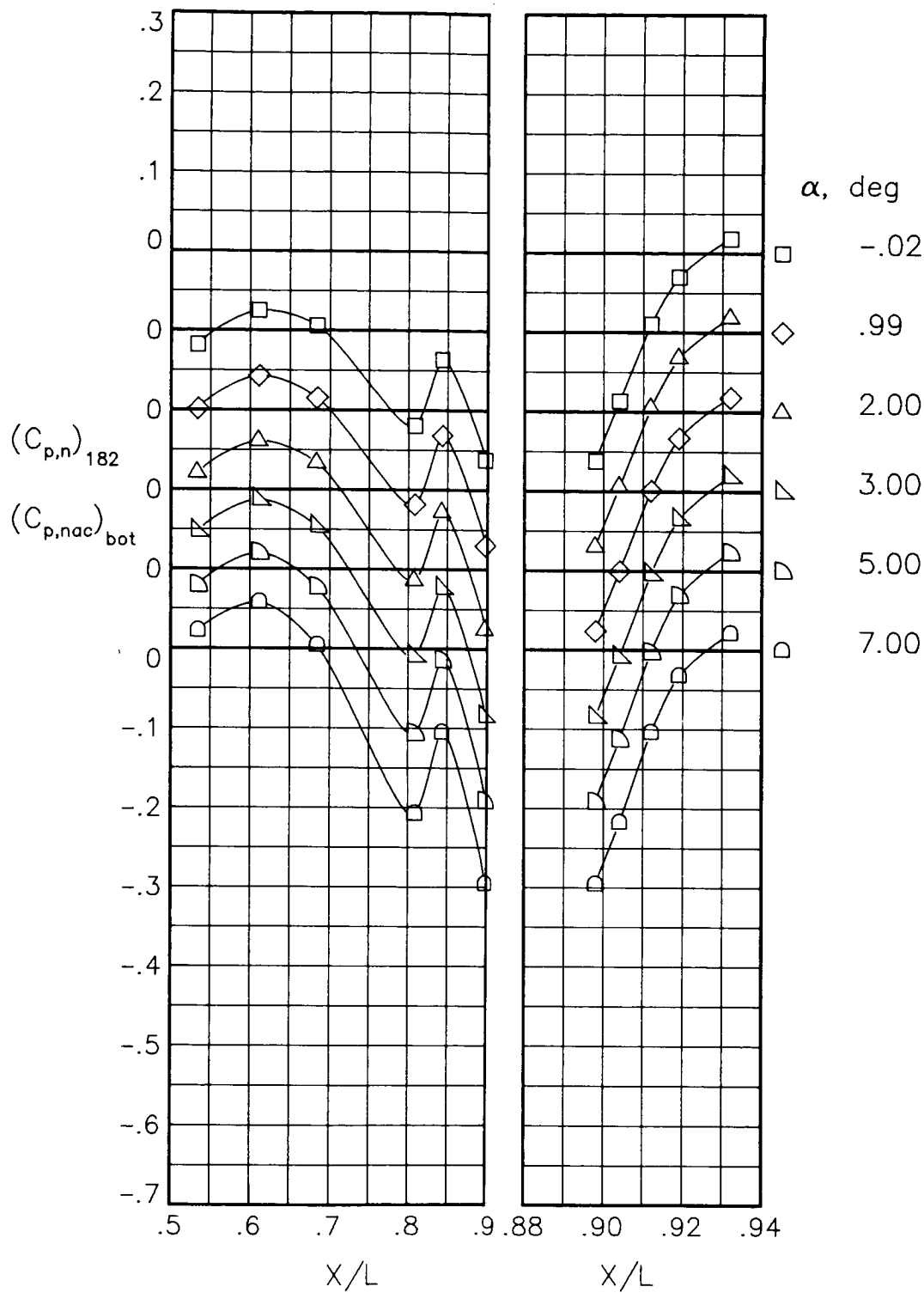

(c) M = 0.80; NPR = 1.00.

Figure 53.- Continued.

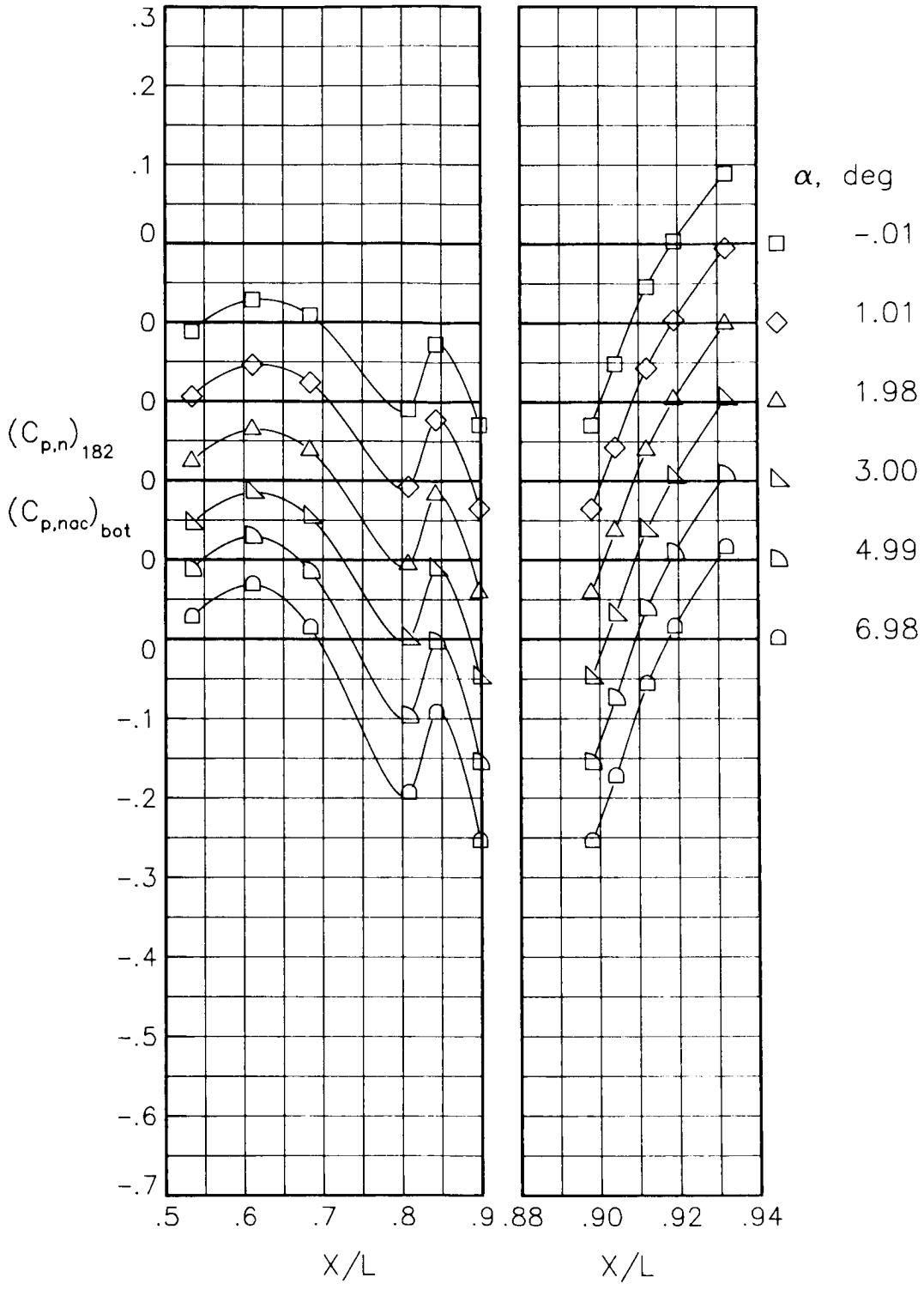

(d) M = 0.80; NPR = 4.60.

Figure 53.- Continued.

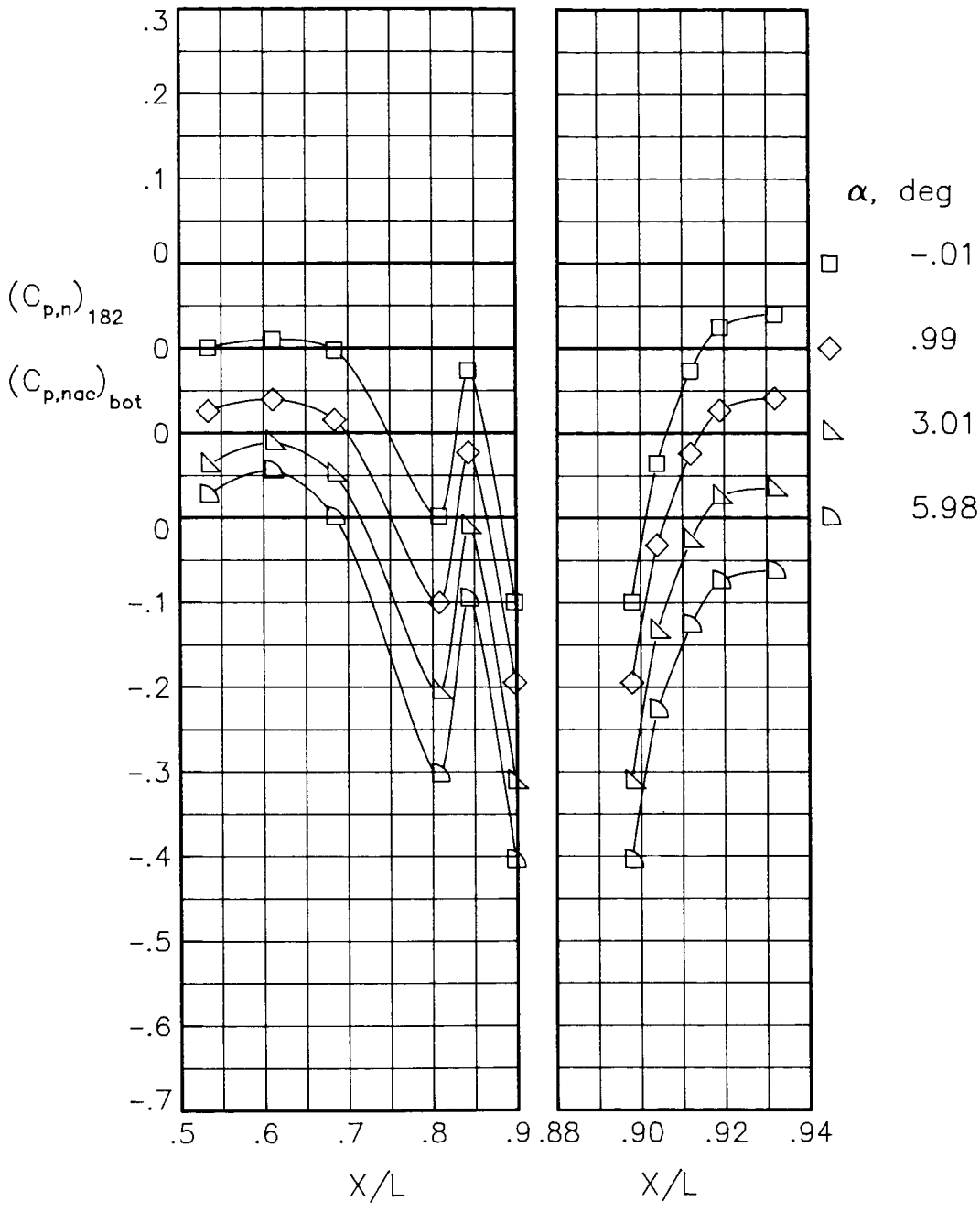

(e) M = 0.90; NPR = 1.00.

Figure 53.- Continued.

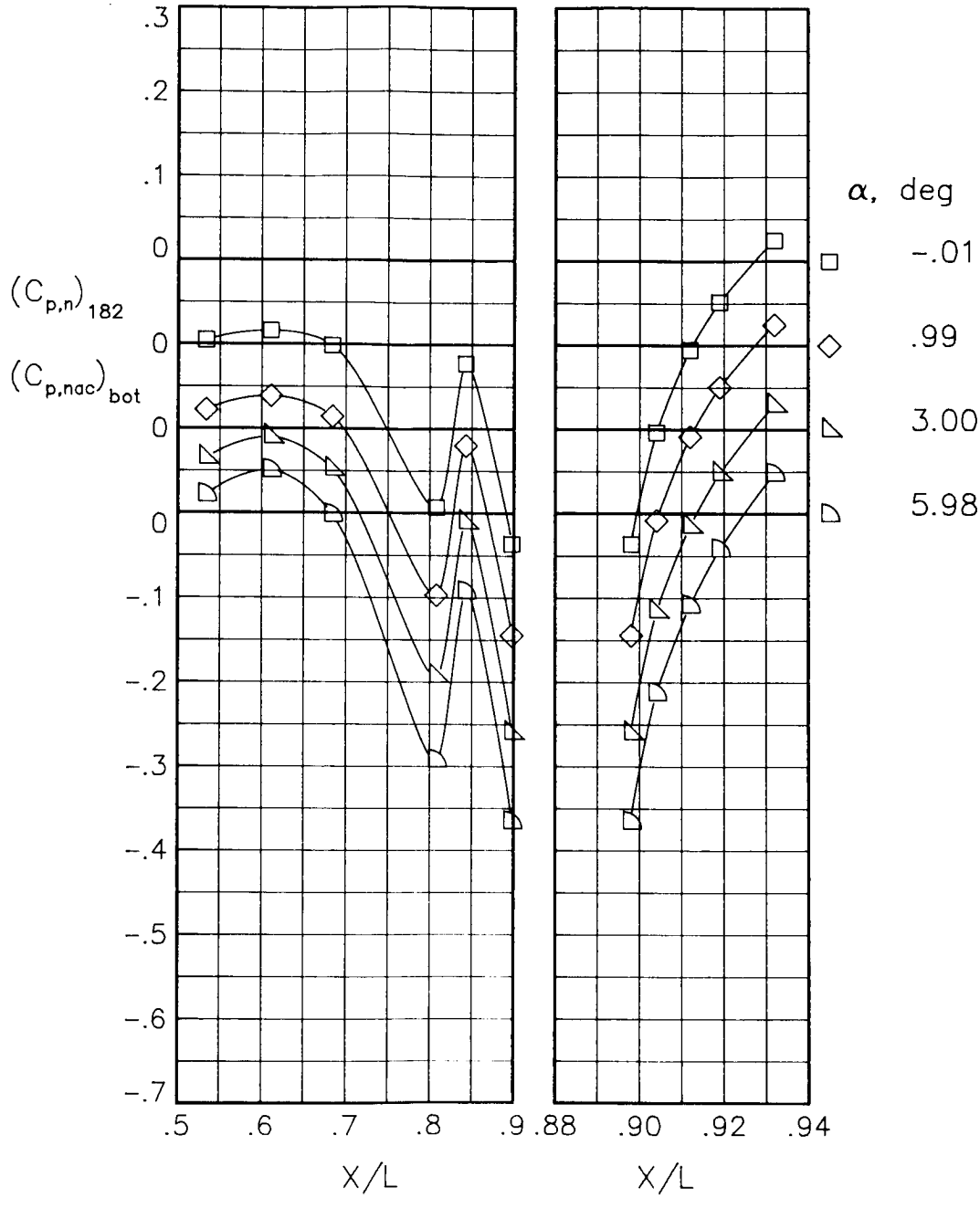

(f) M = 0.90; NPR = 5.00.

Figure 53.- Concluded.

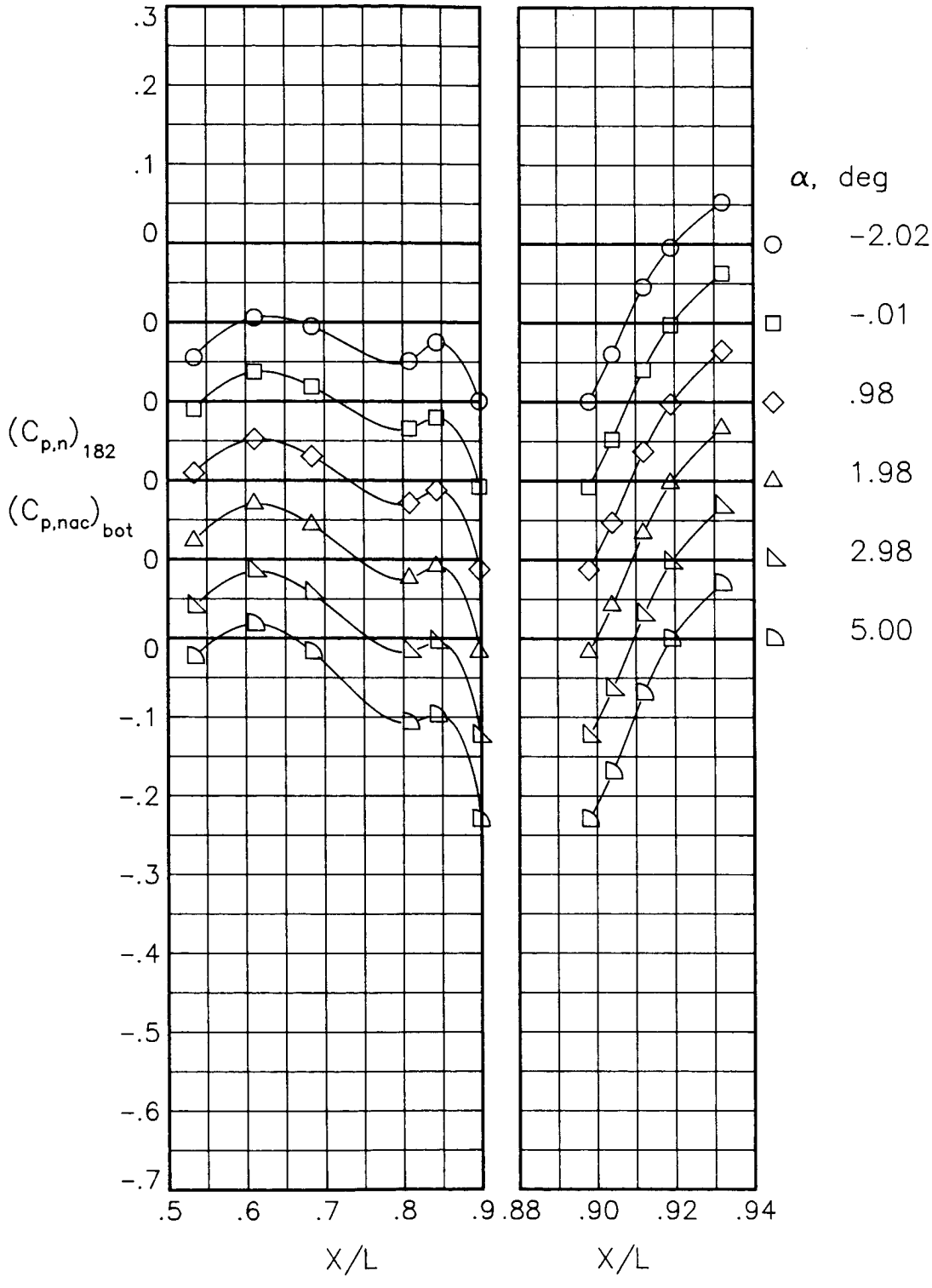

(a) M = 0.60; NPR = 1.00.

Figure 54.- Static-pressure-coefficient distributions on bottom of nacelle and nozzle for the model with all fuselage modifications. β_n = 18.45°.

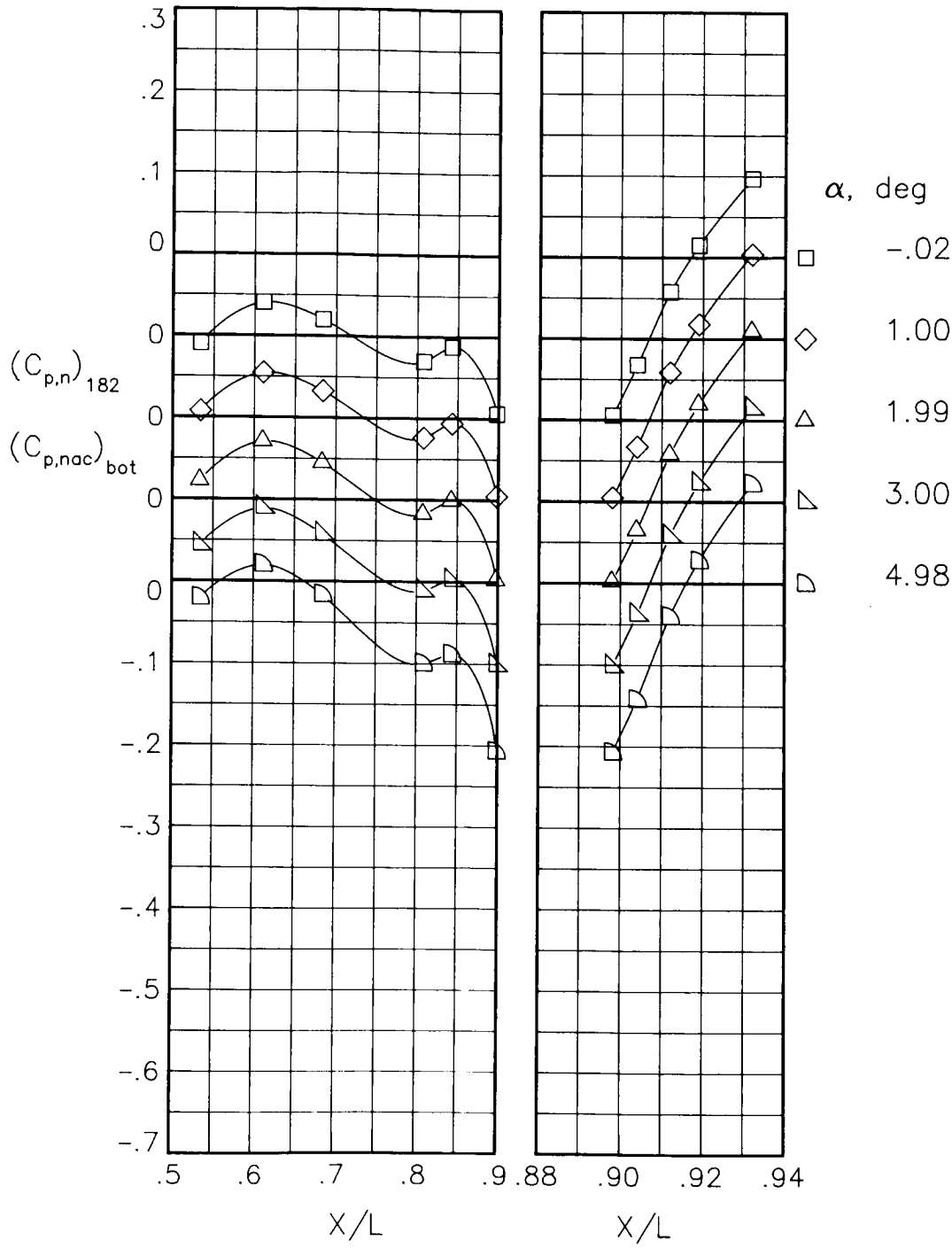

(b) M = 0.60; NPR = 3.00.

Figure 54.- Continued.

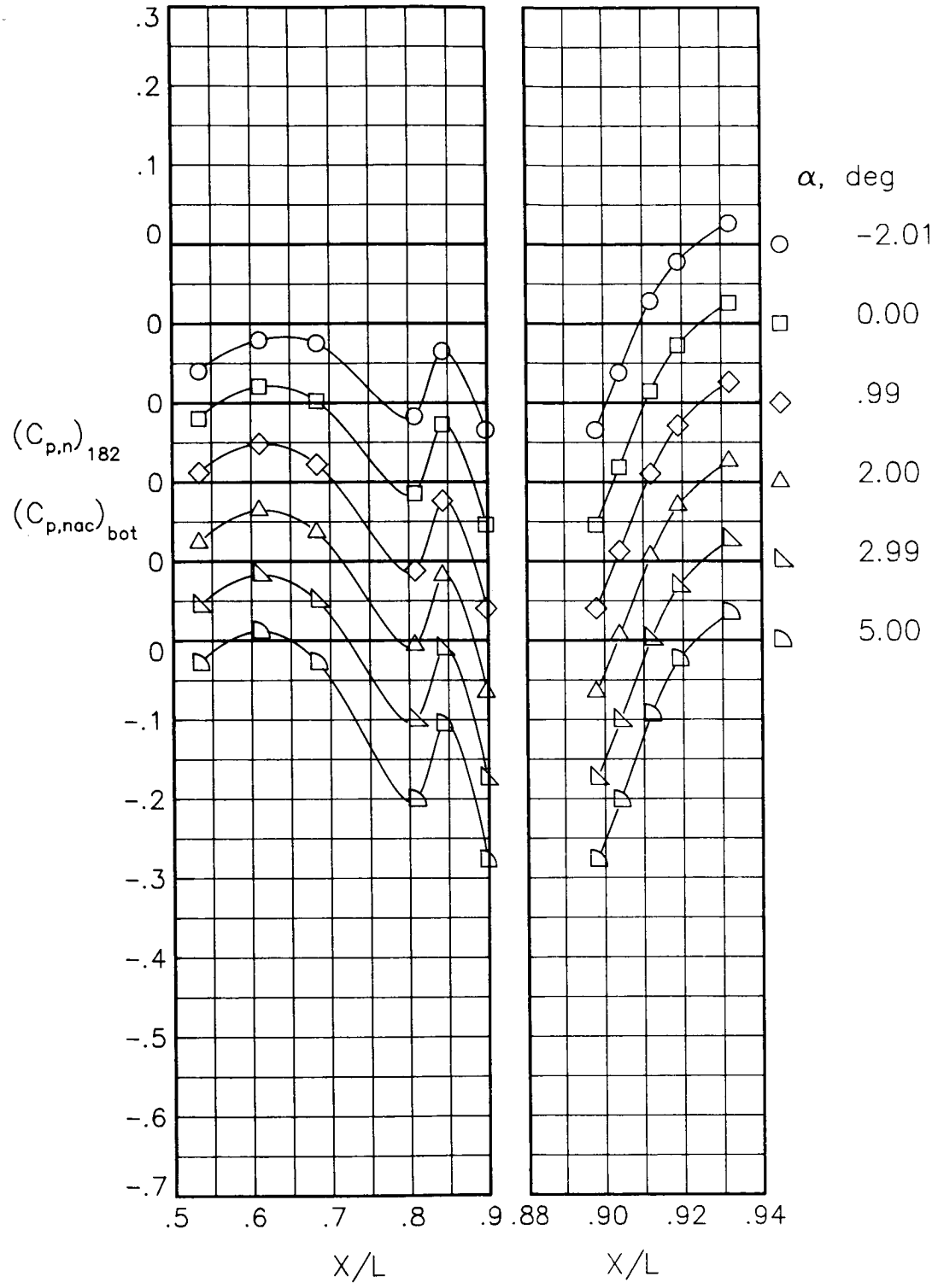

(c) M = 0.80; NPR = 1.00.

Figure 54.- Continued.

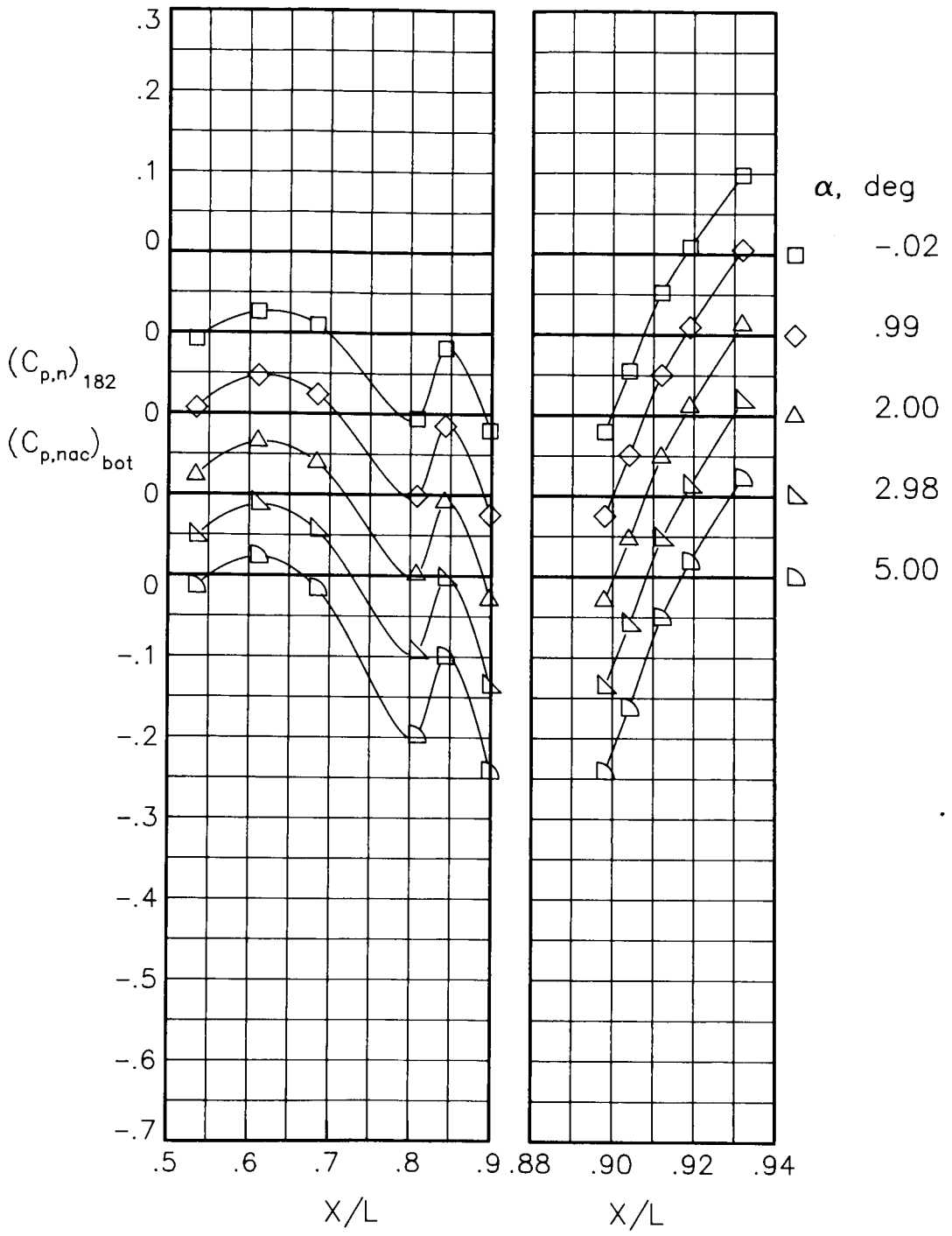

(d) M = 0.80; NPR = 4.60.

Figure 54.- Continued.

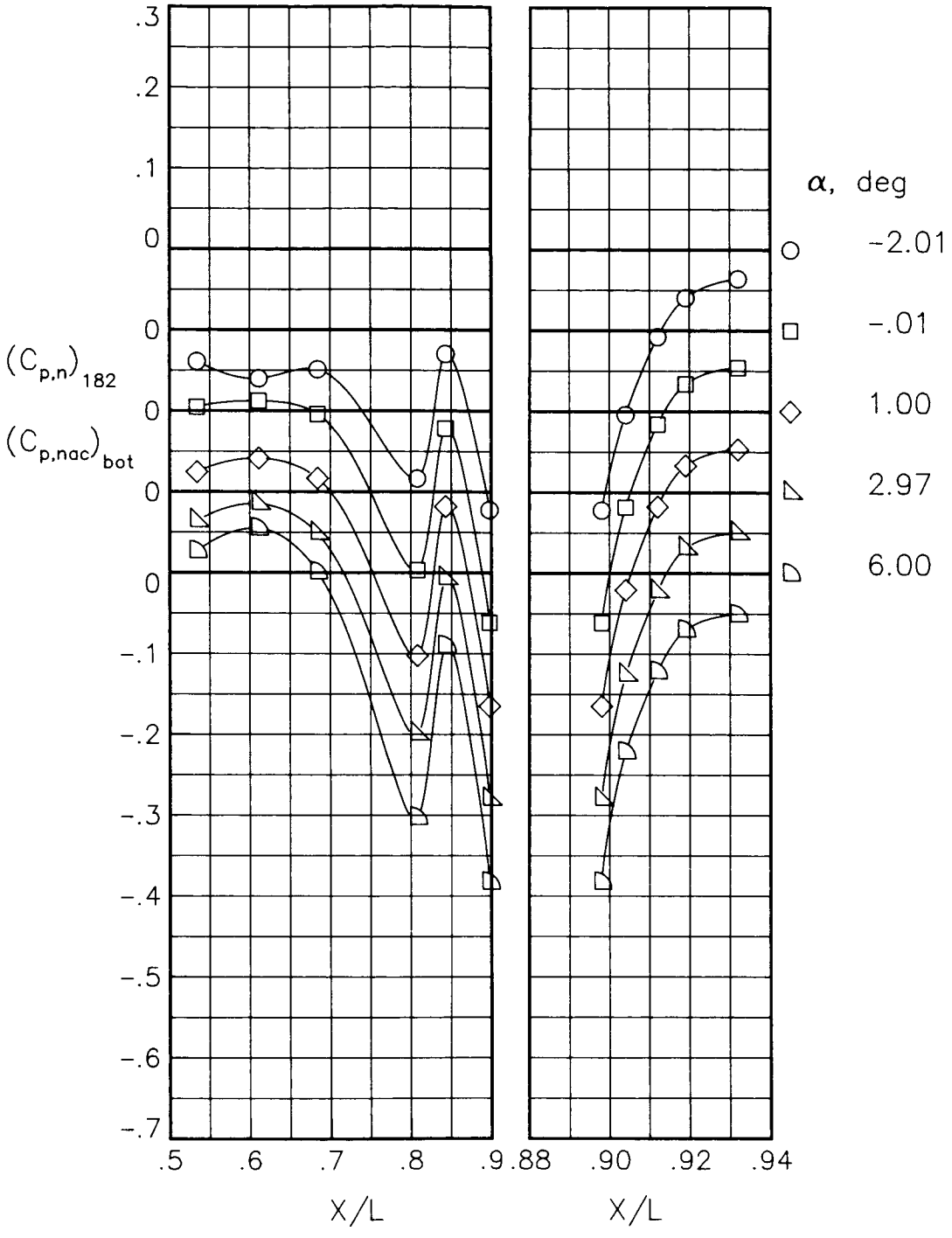

(e) M = 0.90; NPR = 1.00.

Figure 54.- Continued.

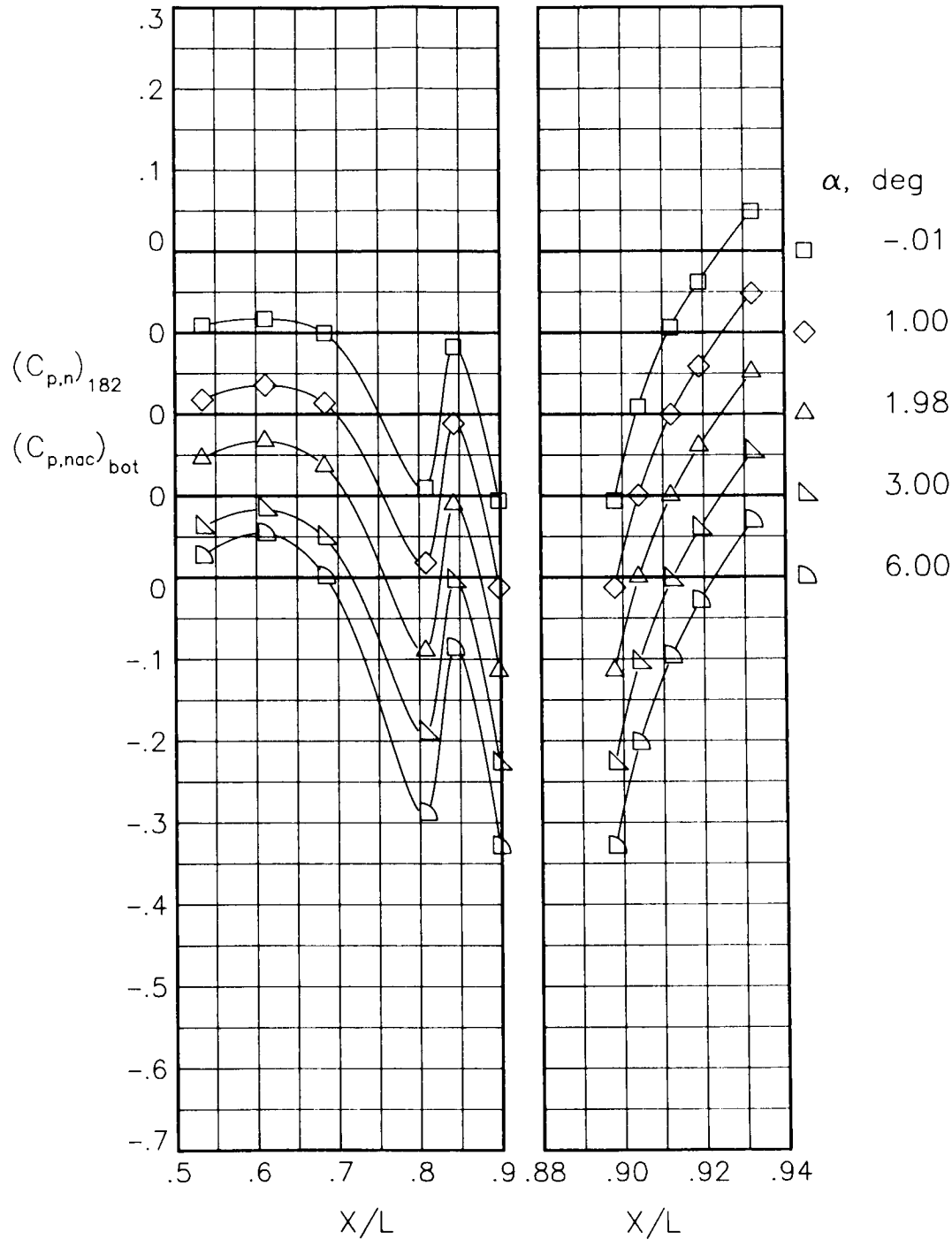

(f) M = 0.90; NPR = 5.00.

Figure 54.- Concluded.

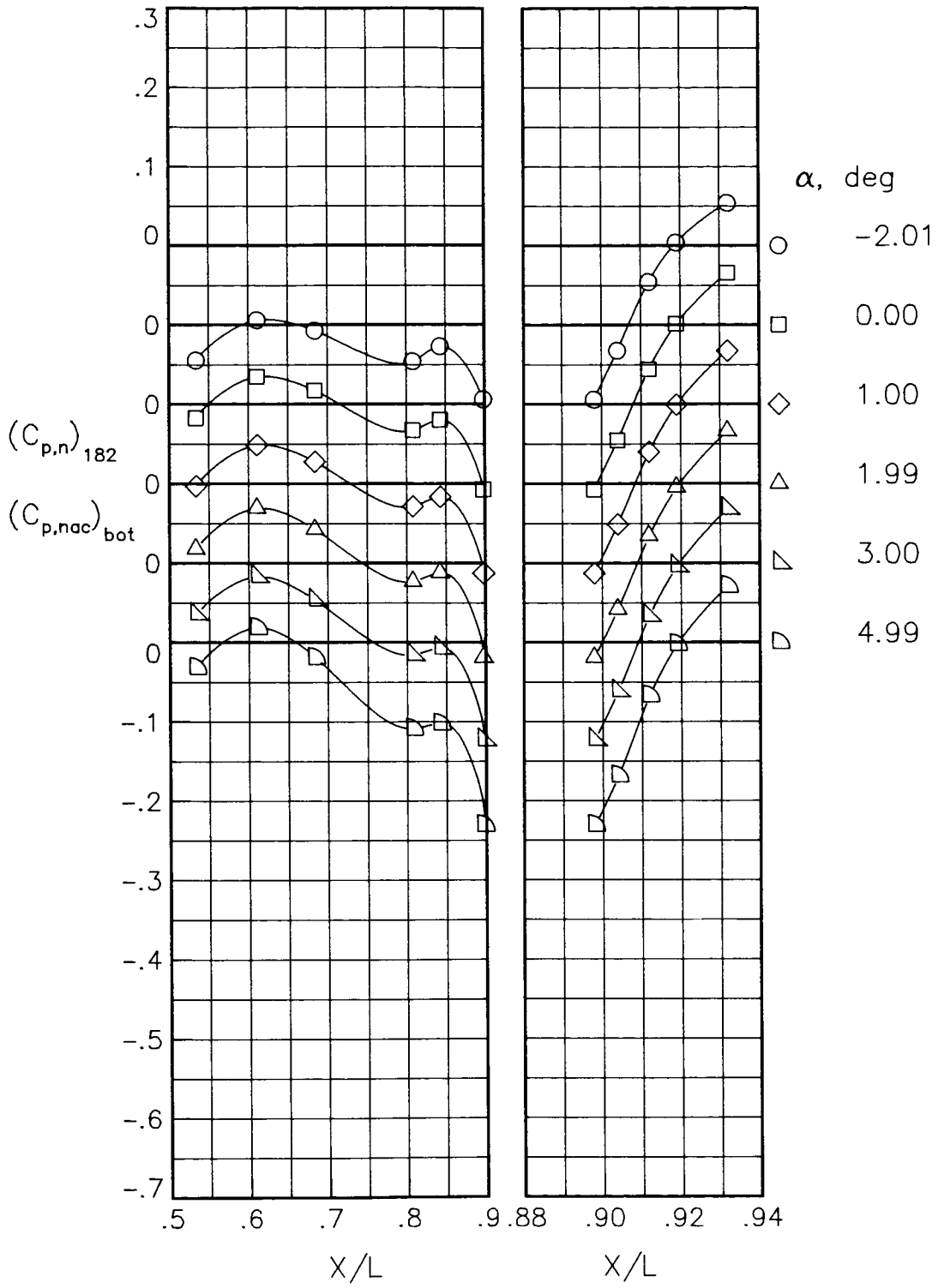

(a) M = 0.60; NPR = 1.00.

Figure 55.- Static-pressure-coefficient distributions on bottom of nacelle and nozzle for the model with all fuselage modifications. β_n = 18.45°. Repeat data.

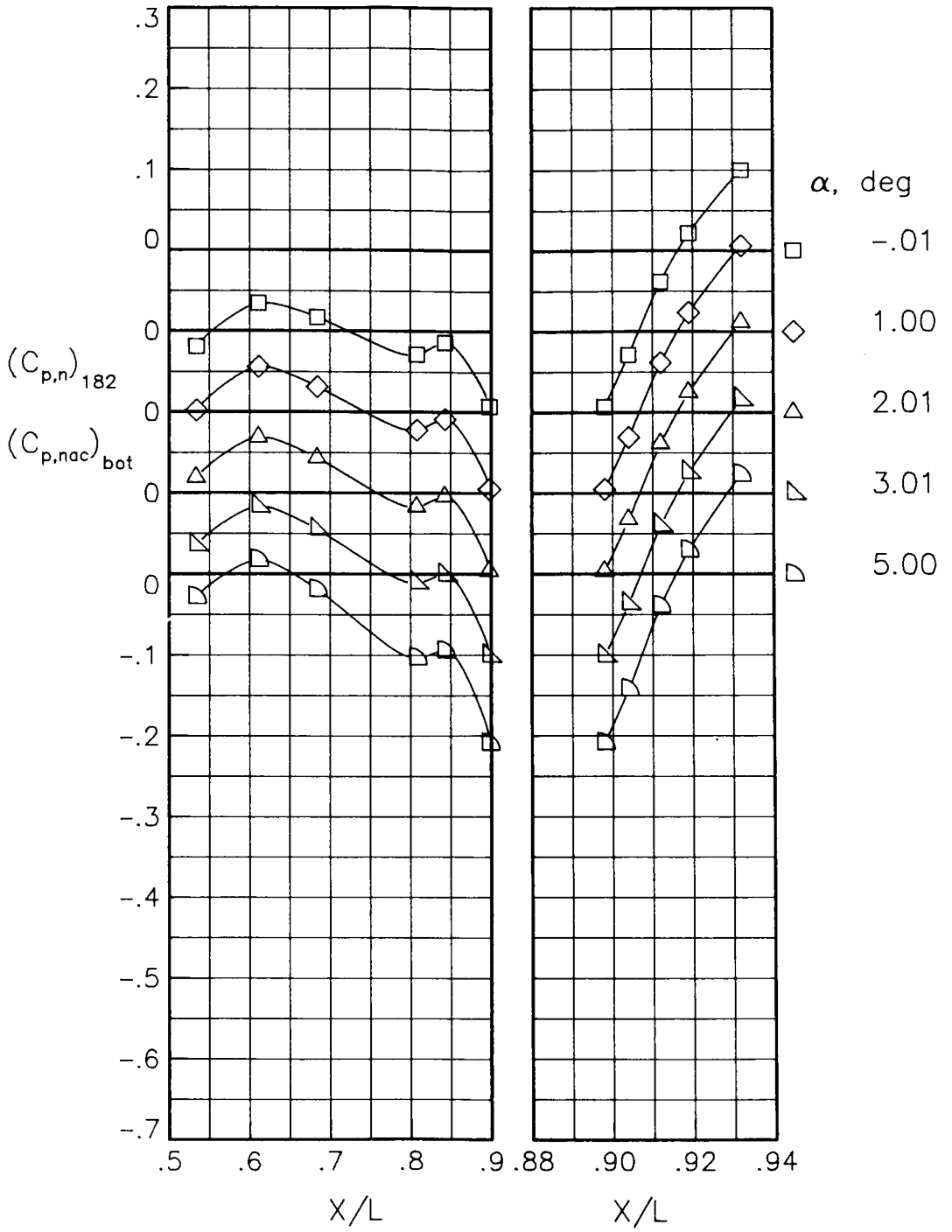

(b) M = 0.60; NPR = 3.00.

Figure 55.- Continued.

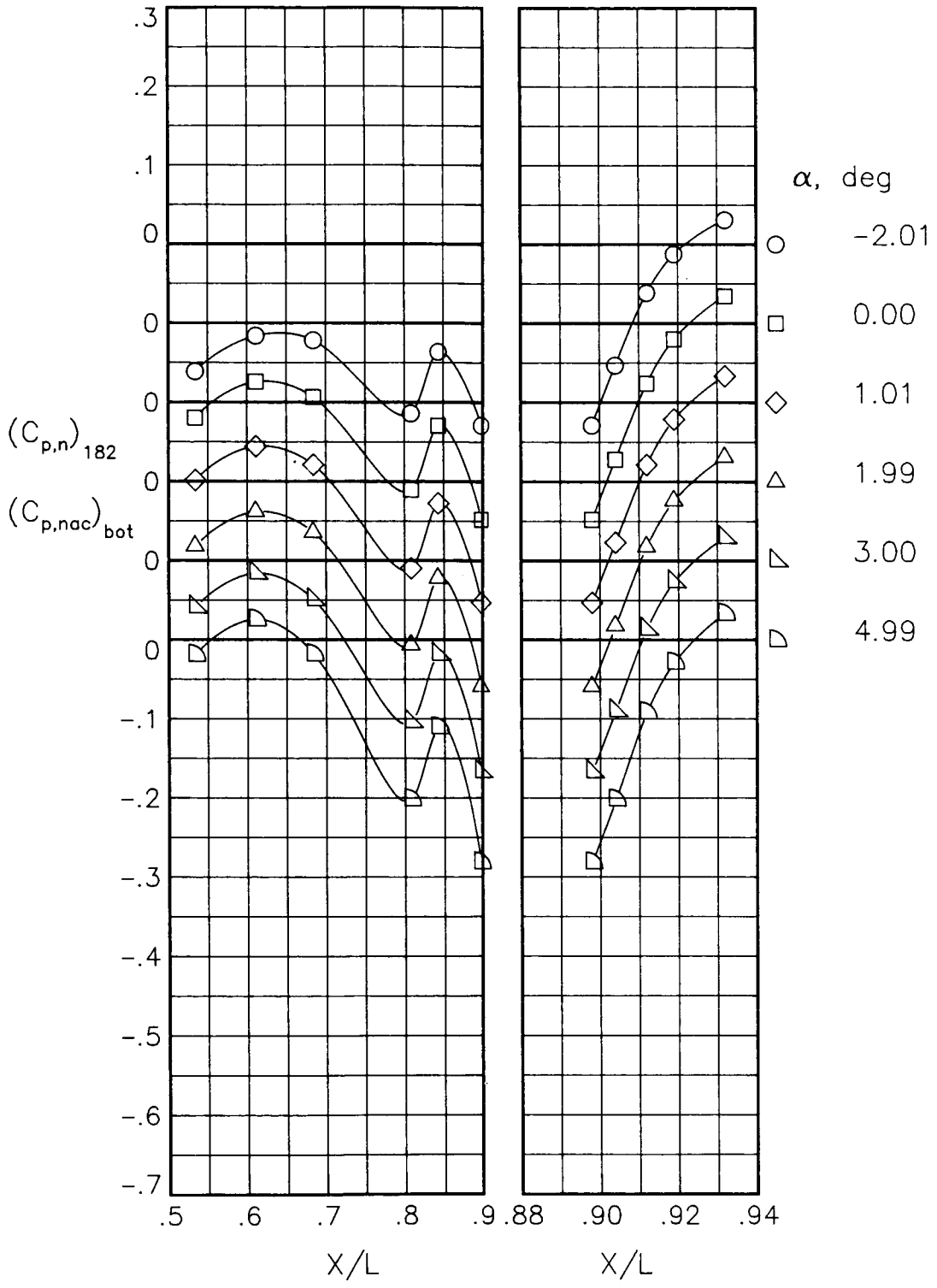

(c) M = 0.80; NPR = 1.00.

Figure 55.- Continued.

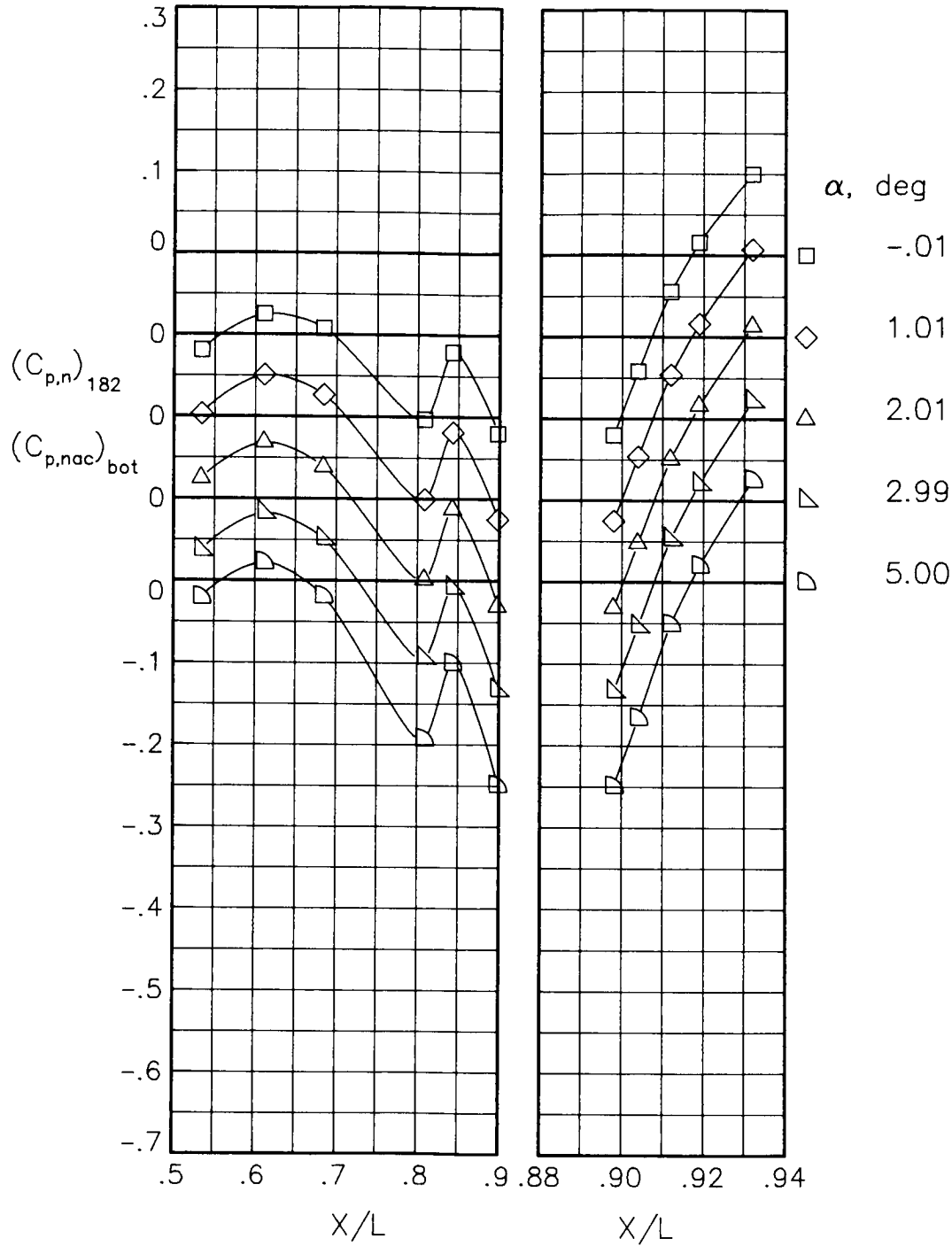

(d) M = 0.80; NPR = 4.60.

Figure 55.- Continued.

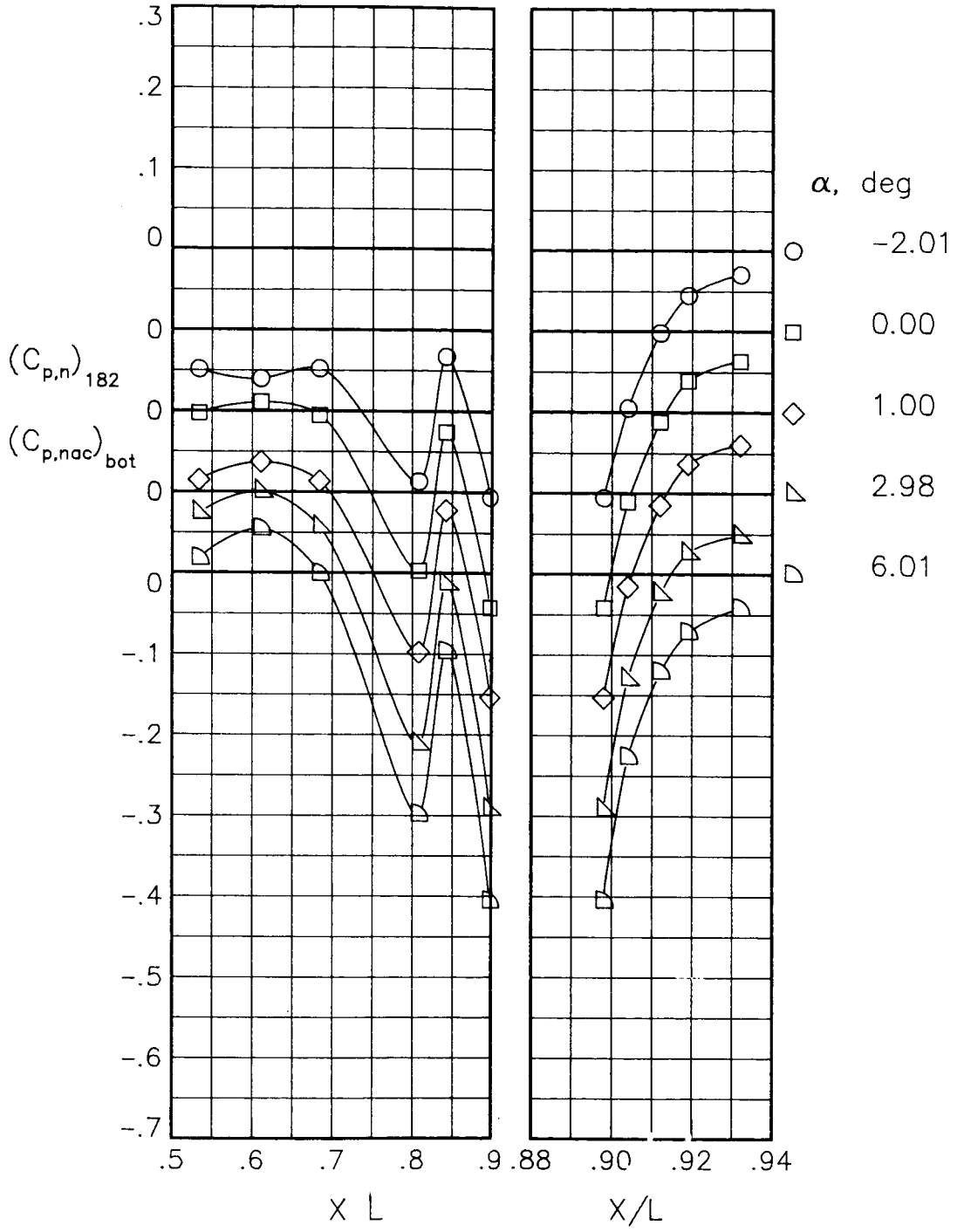

(e) M = 0.90; NPR = 1.00.

Figure 55.- Continued.

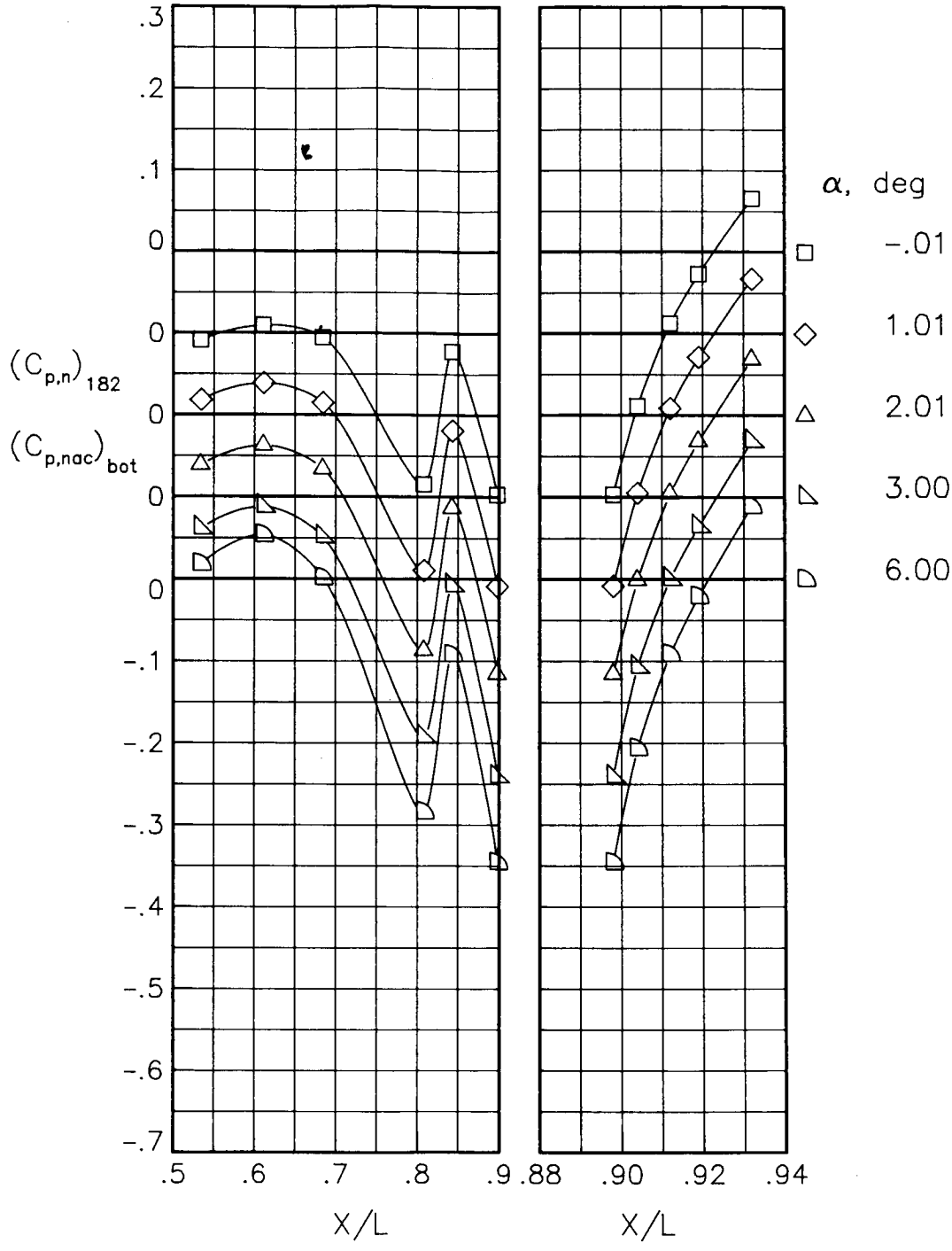

(f) M = 0.90; NPR = 5.00.

Figure 55.- Concluded.

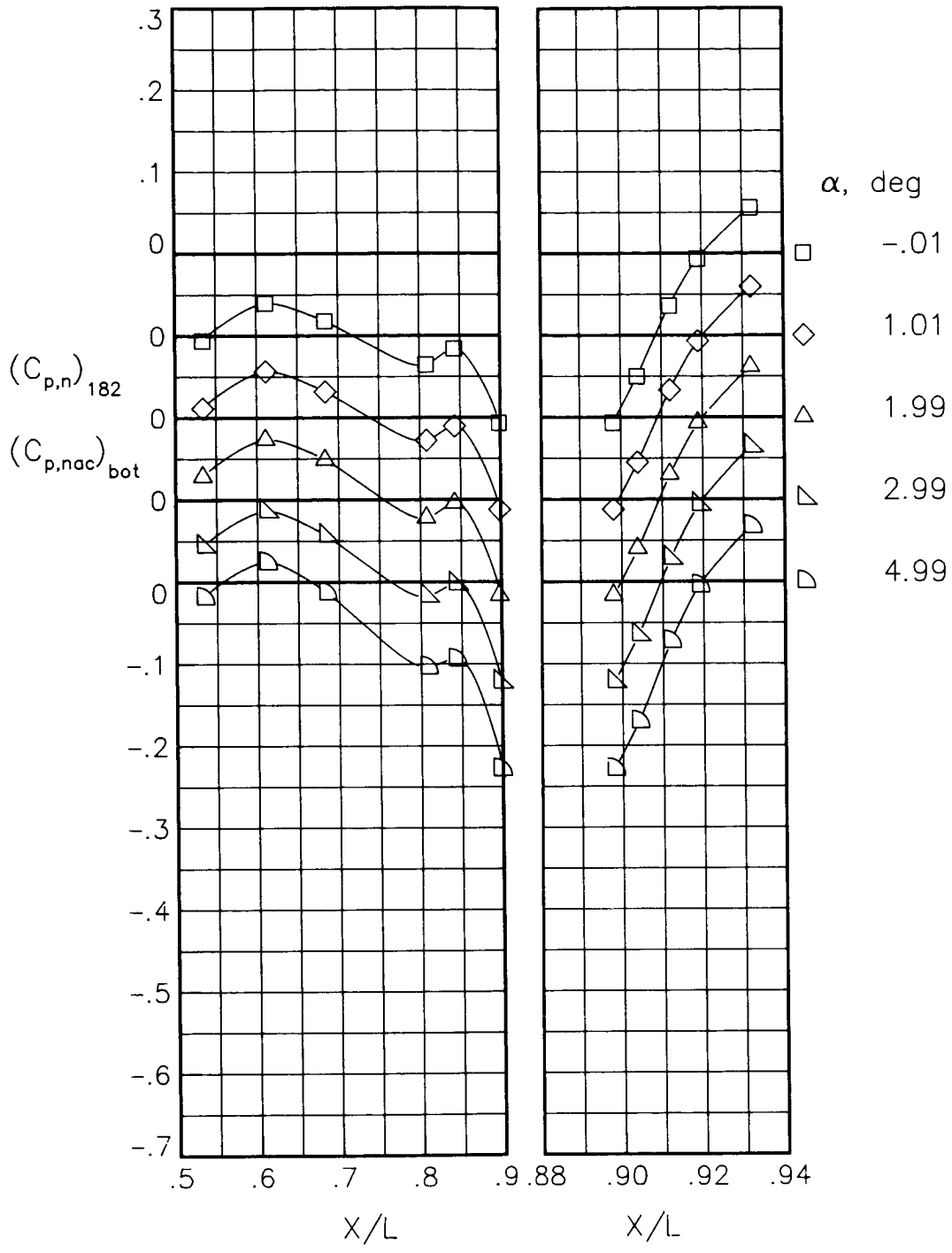

(a) M = 0.60; NPR = 1.00.

Figure 56.- Static-pressure-coefficient distributions on bottom of nacelle and nozzle for the model with all fuselage modifications. β_n = 18.45°; δ_r = -5°.

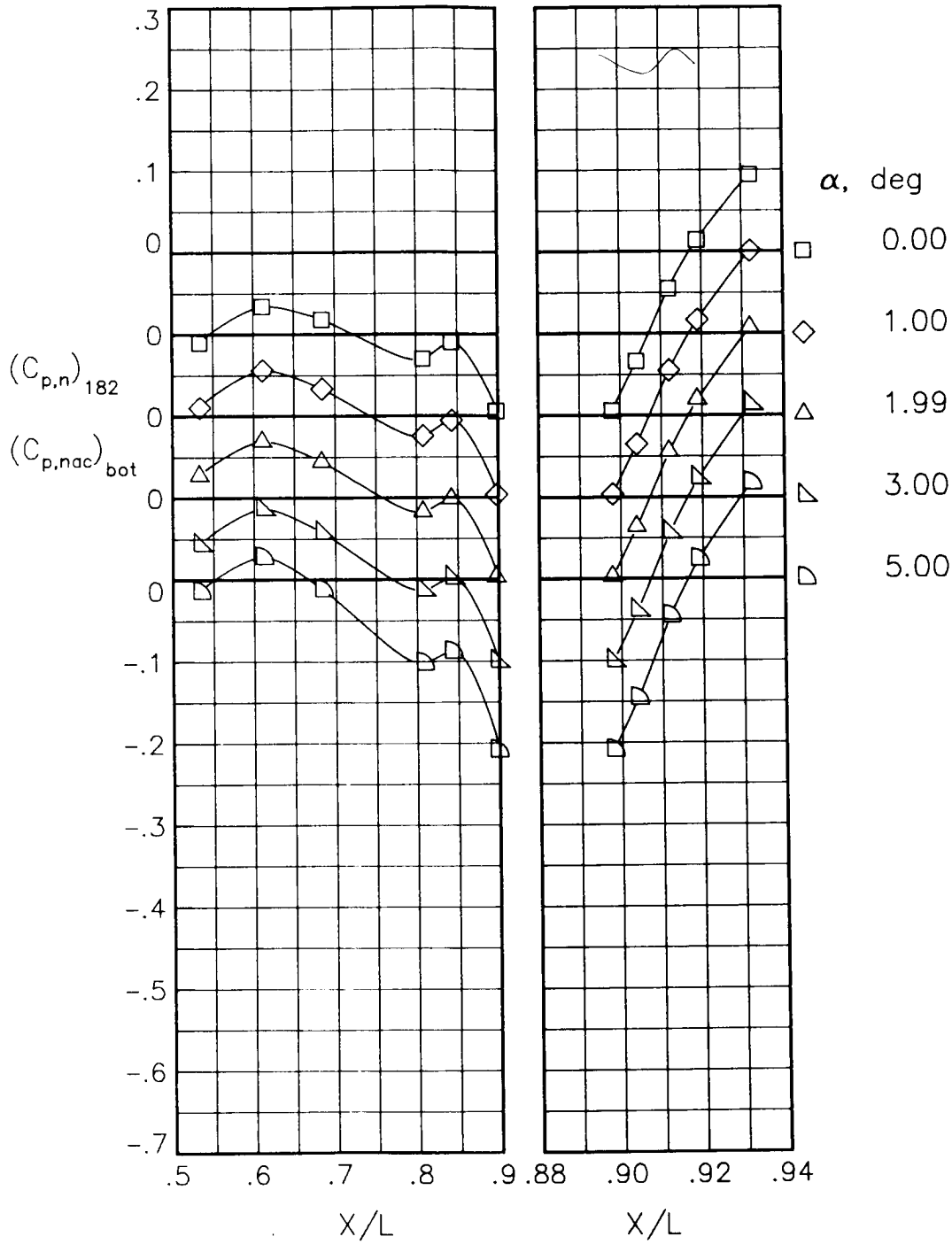

(b) M = 0.60; NPR = 3.00.

Figure 56.- Continued.

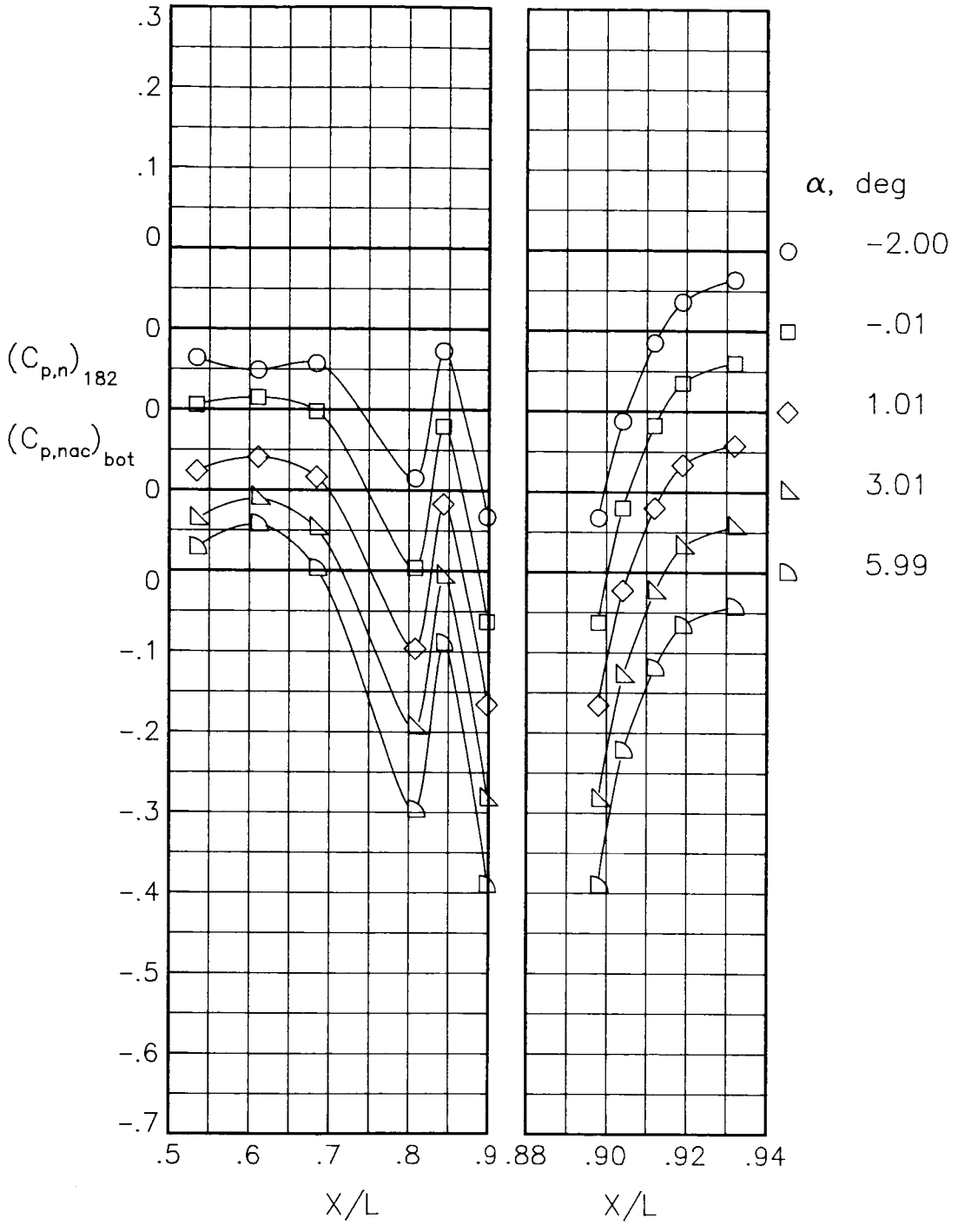

(c) M = 0.90; NPR = 1.00.

Figure 56.- Continued.

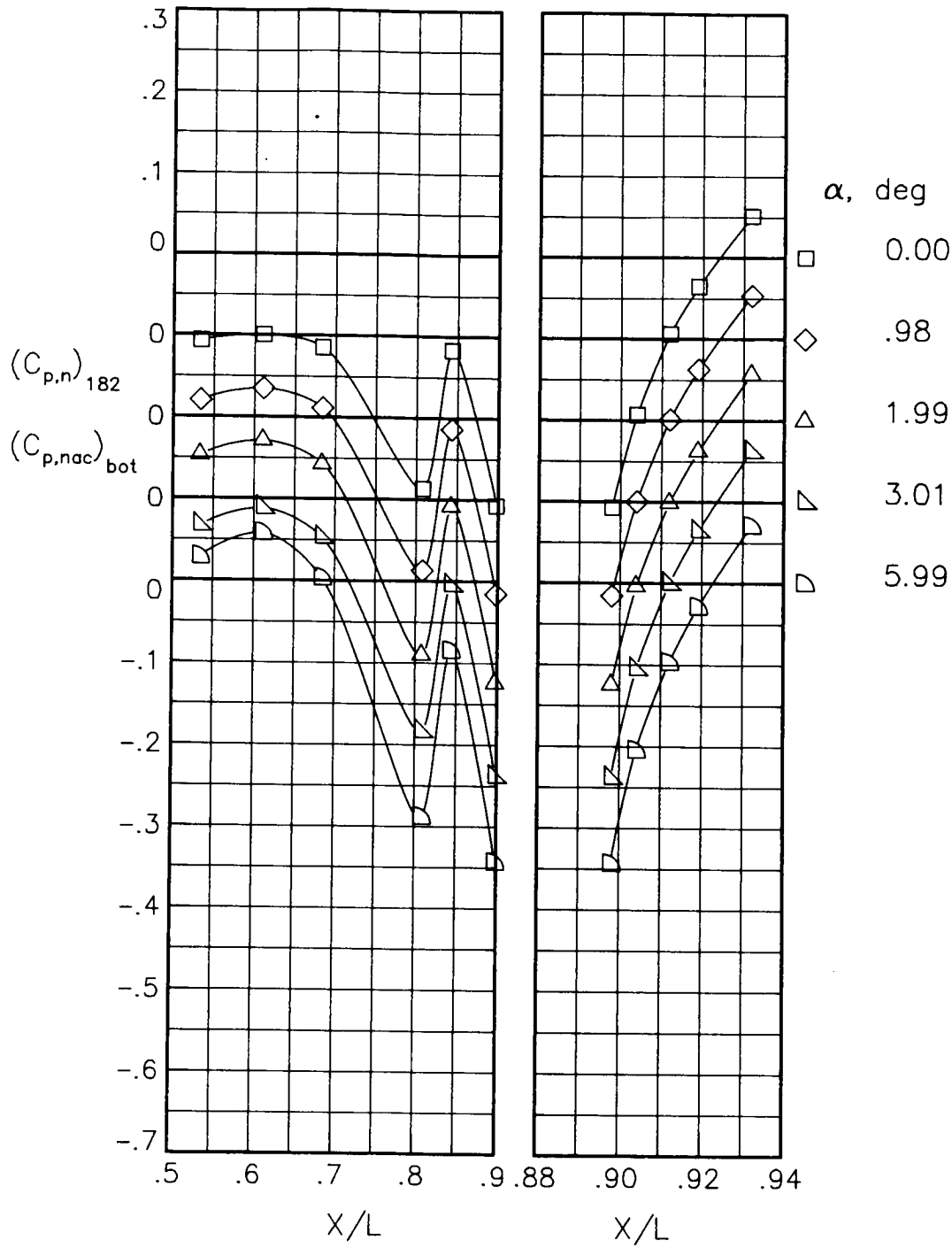

(d) M = 0.90; NPR = 5.00.

Figure 56.- Concluded.

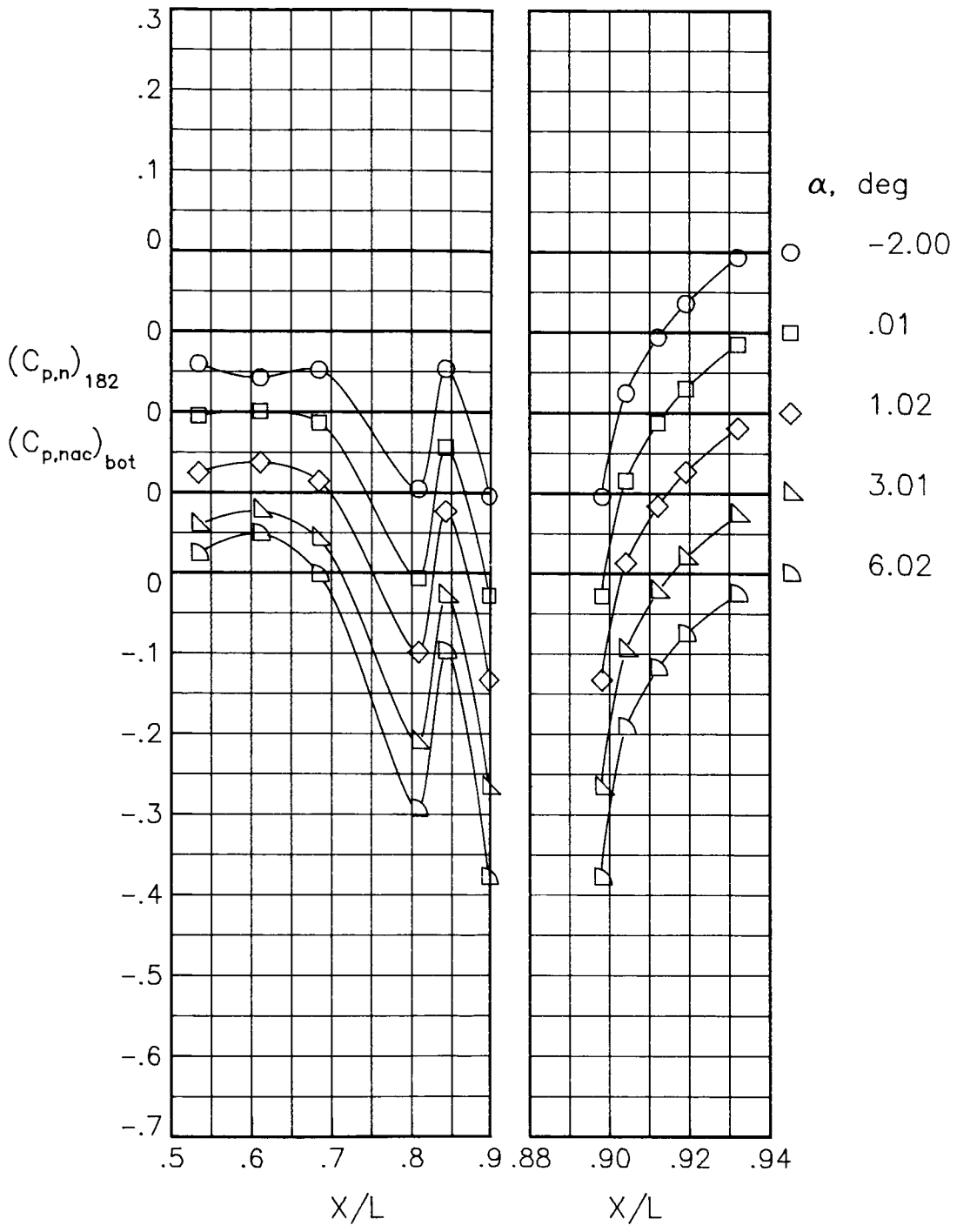

(a) M = 0.90; NPR = 1.00.

Figure 57.- Static-pressure-coefficient distributions on bottom of nacelle and nozzle for the model with all fuselage modifications. β_n = 15.05°.

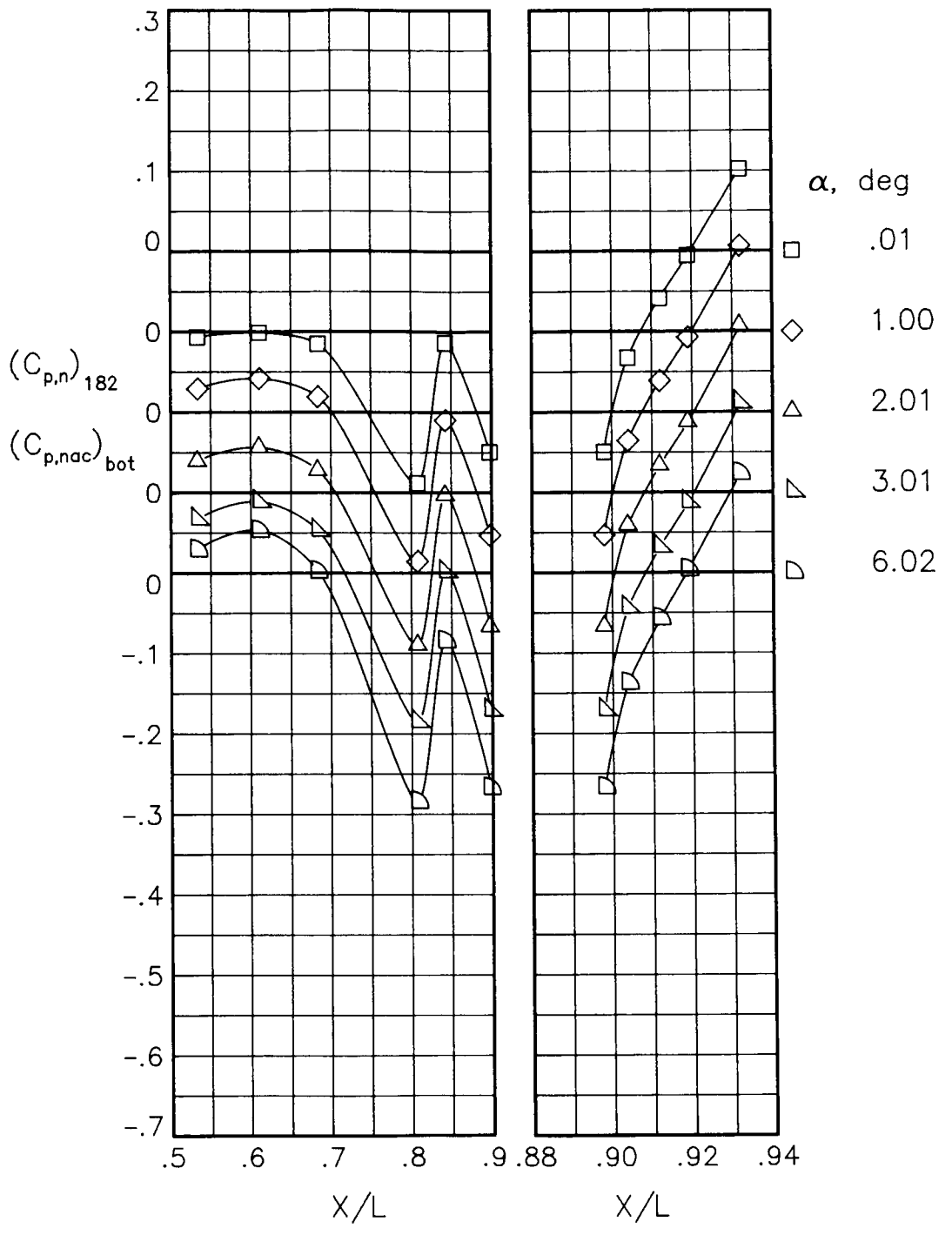

(b) M = 0.90; NPR = 5.00.

Figure 57.- Continued.

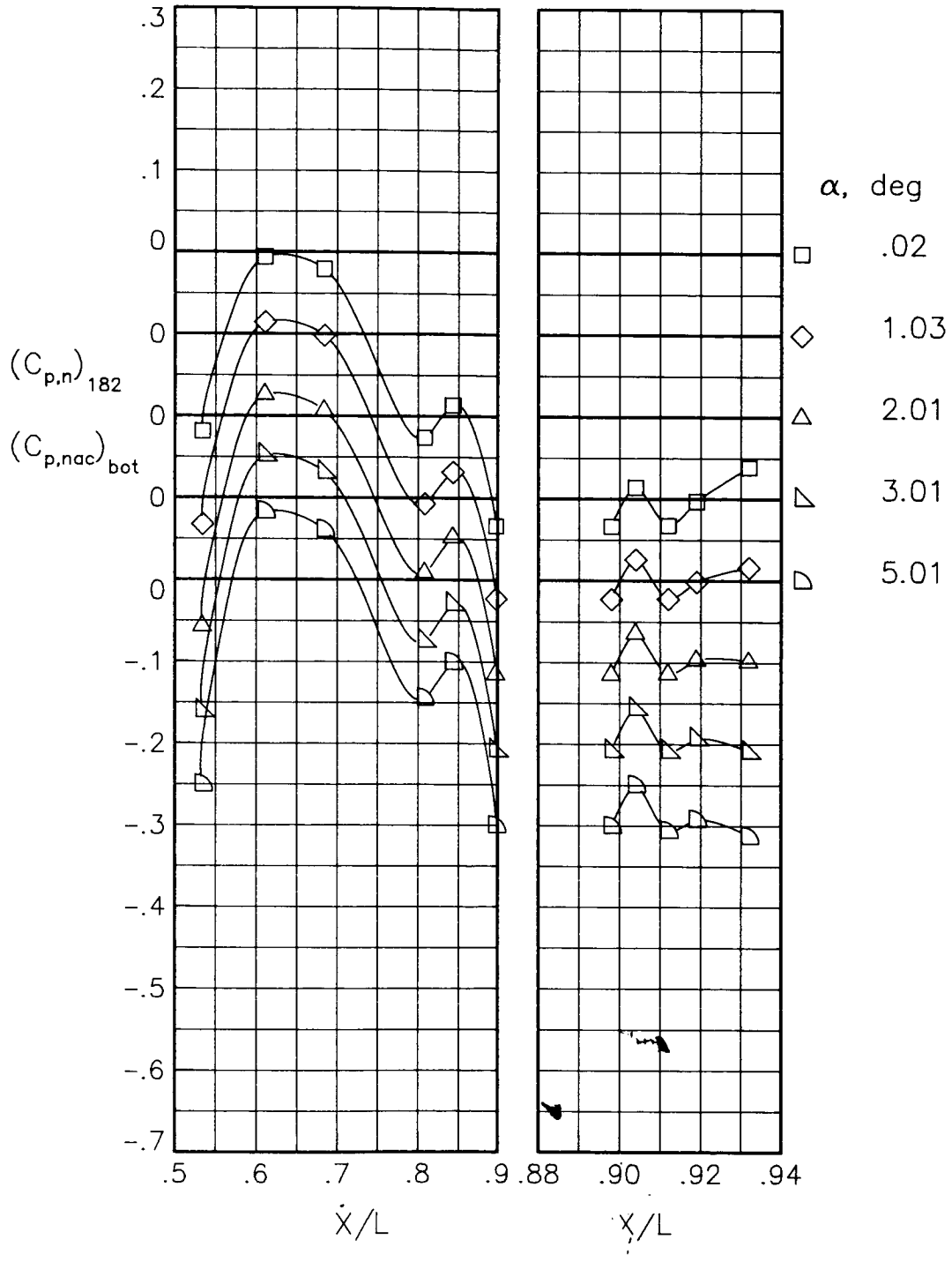

(c) M = 1.20; NPR = 1.00.

Figure 57.- Continued.

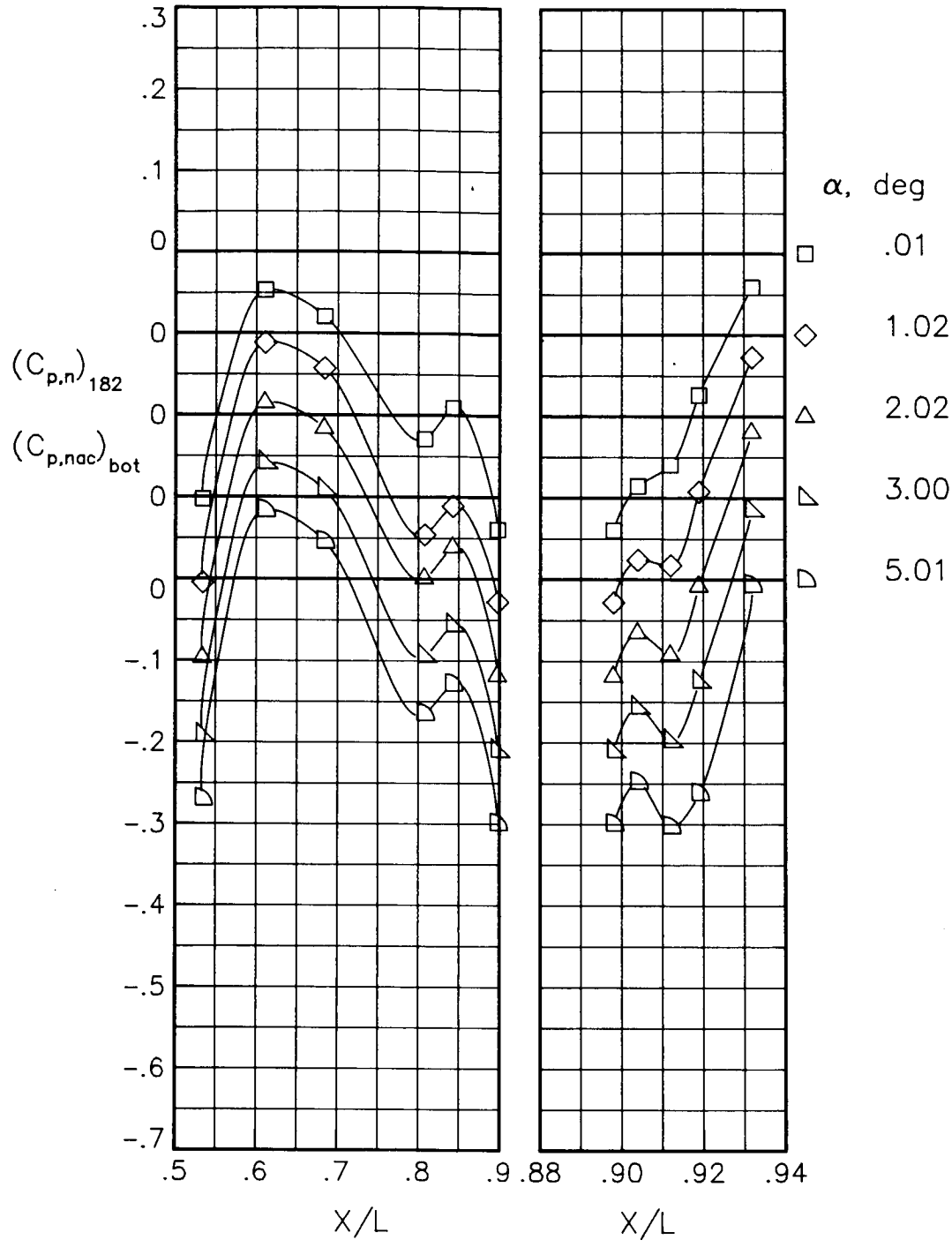

(d) M = 1.20; NPR = 7.00.

Figure 57.- Concluded.

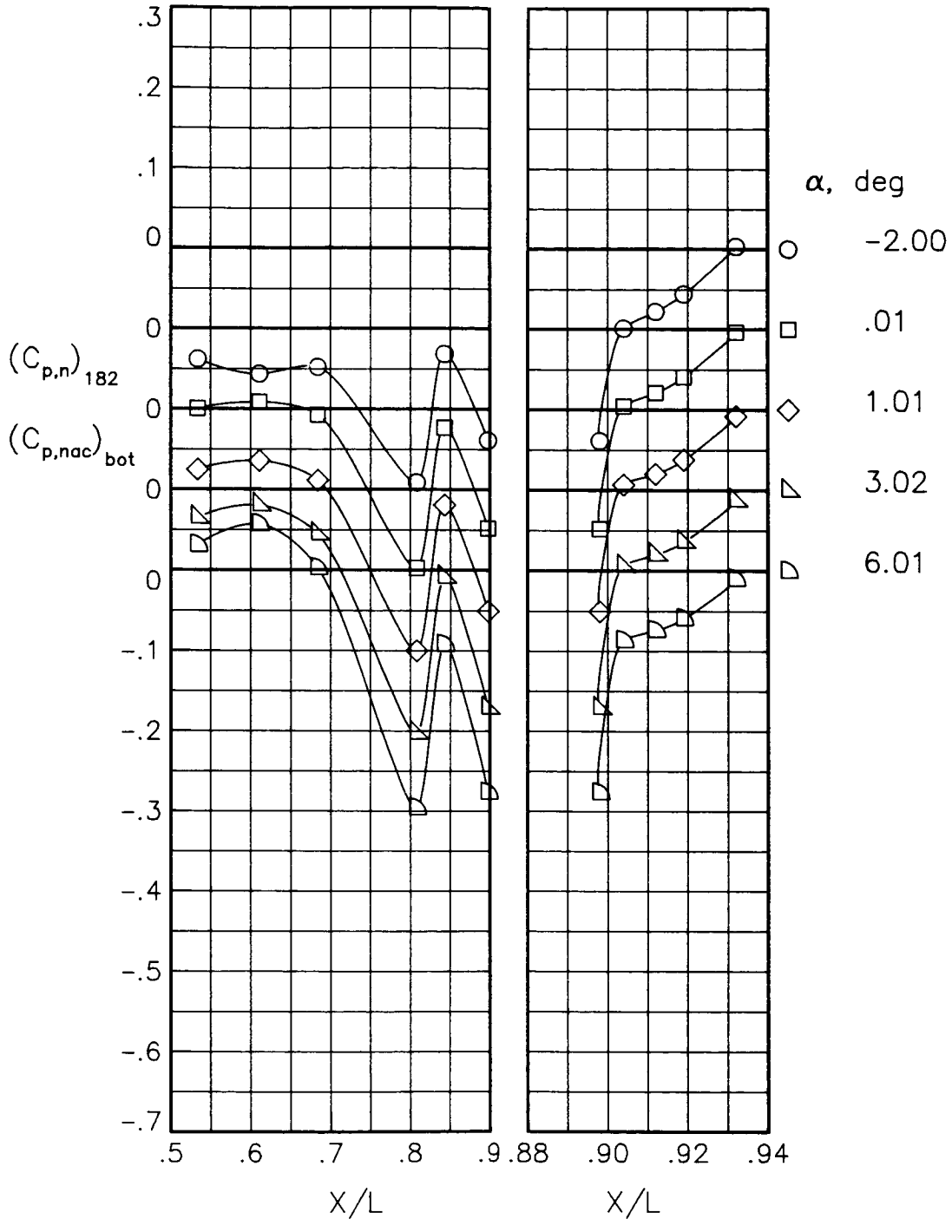

(a) M = 0.90; NPR = 1.00.

Figure 58.- Static-pressure-coefficient distributions on bottom of nacelle and nozzle for the model with all fuselage modifications. β_n = 9.63°.

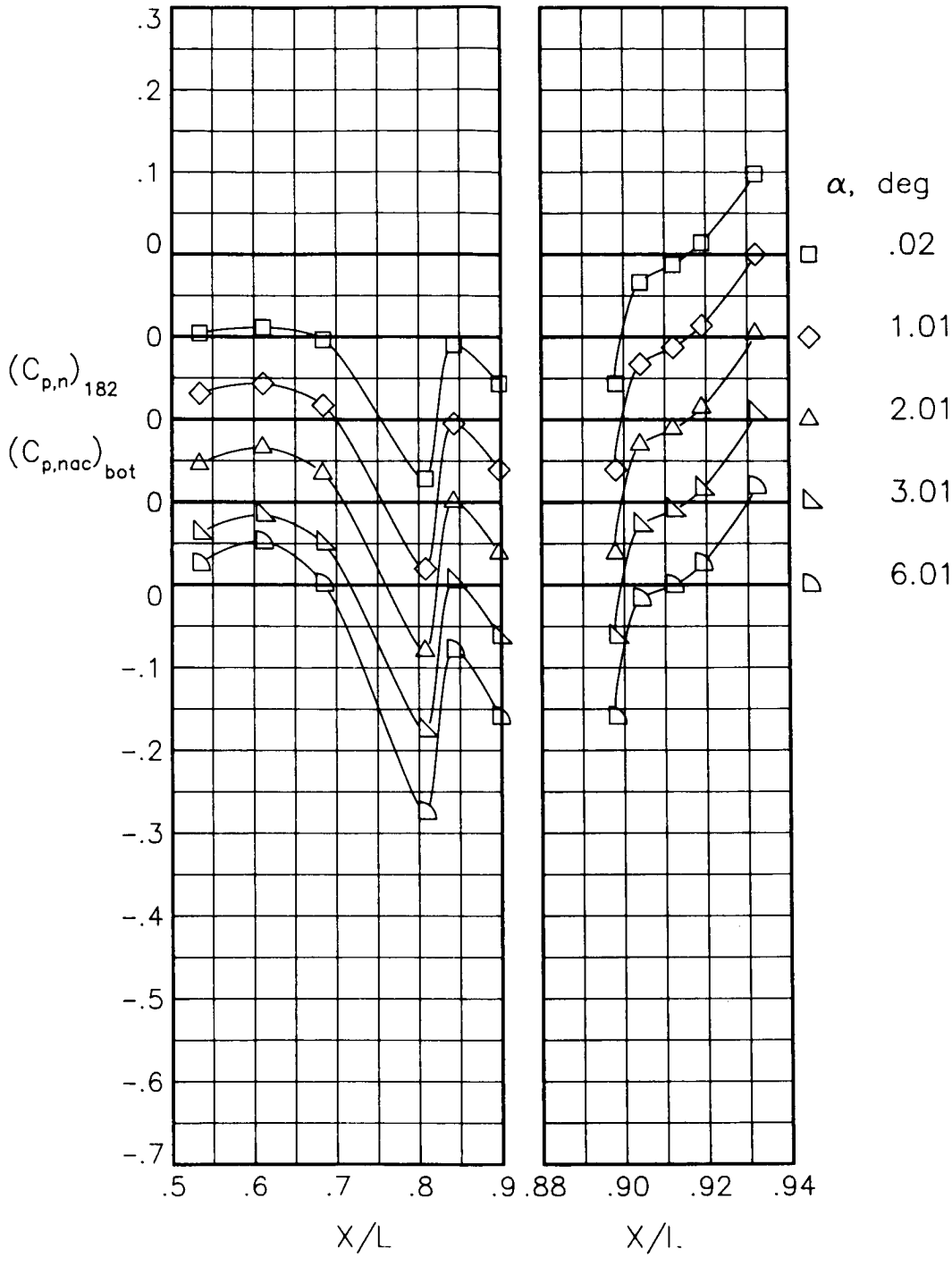

(b) M = 0.90; NPR = 5.00.

Figure 58.- Continued.

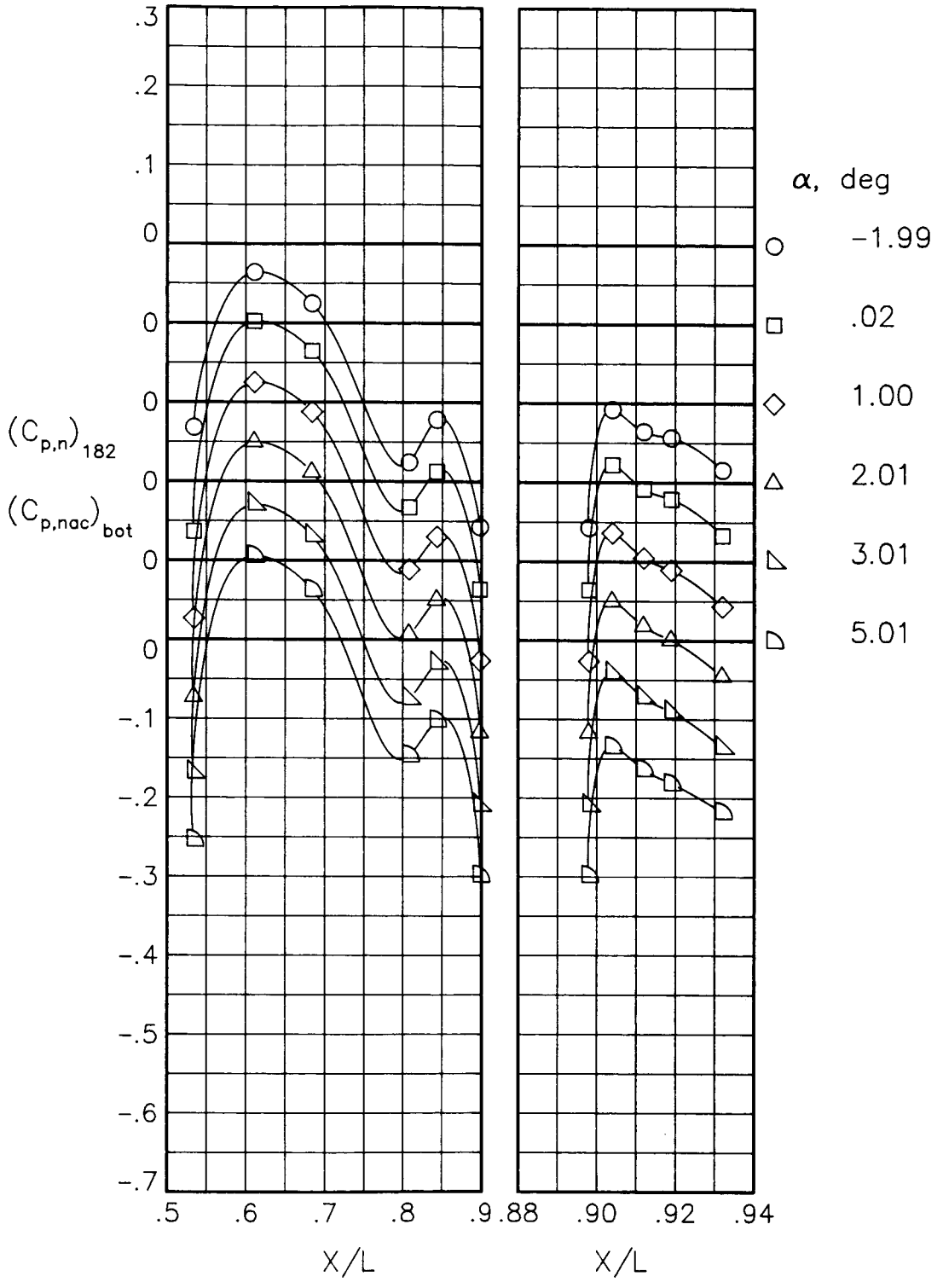

(c) M = 1.20; NPR = 1.00.

Figure 58.- Continued.

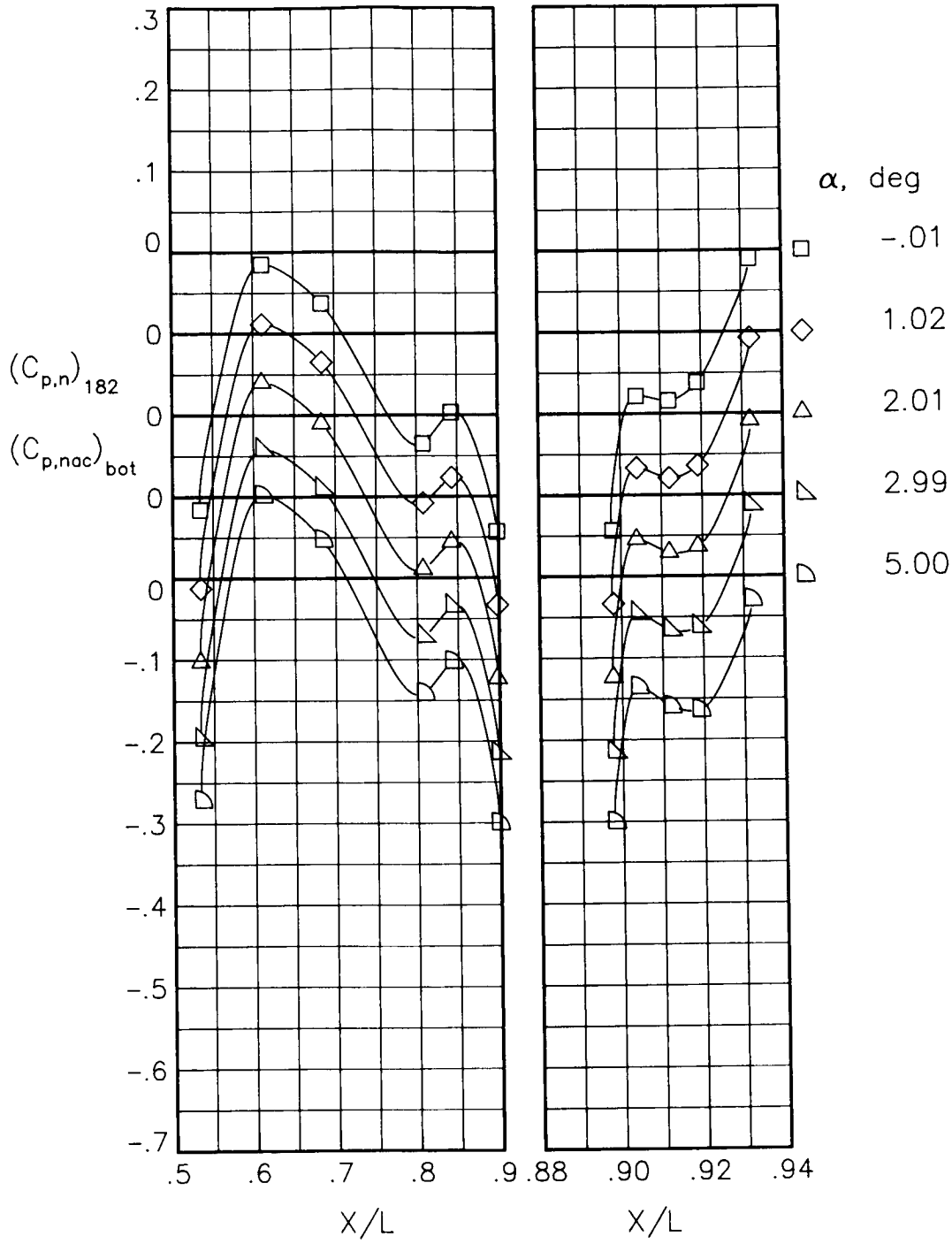

(d) M = 1.20; NPR = 7.00.

Figure 58.- Concluded.

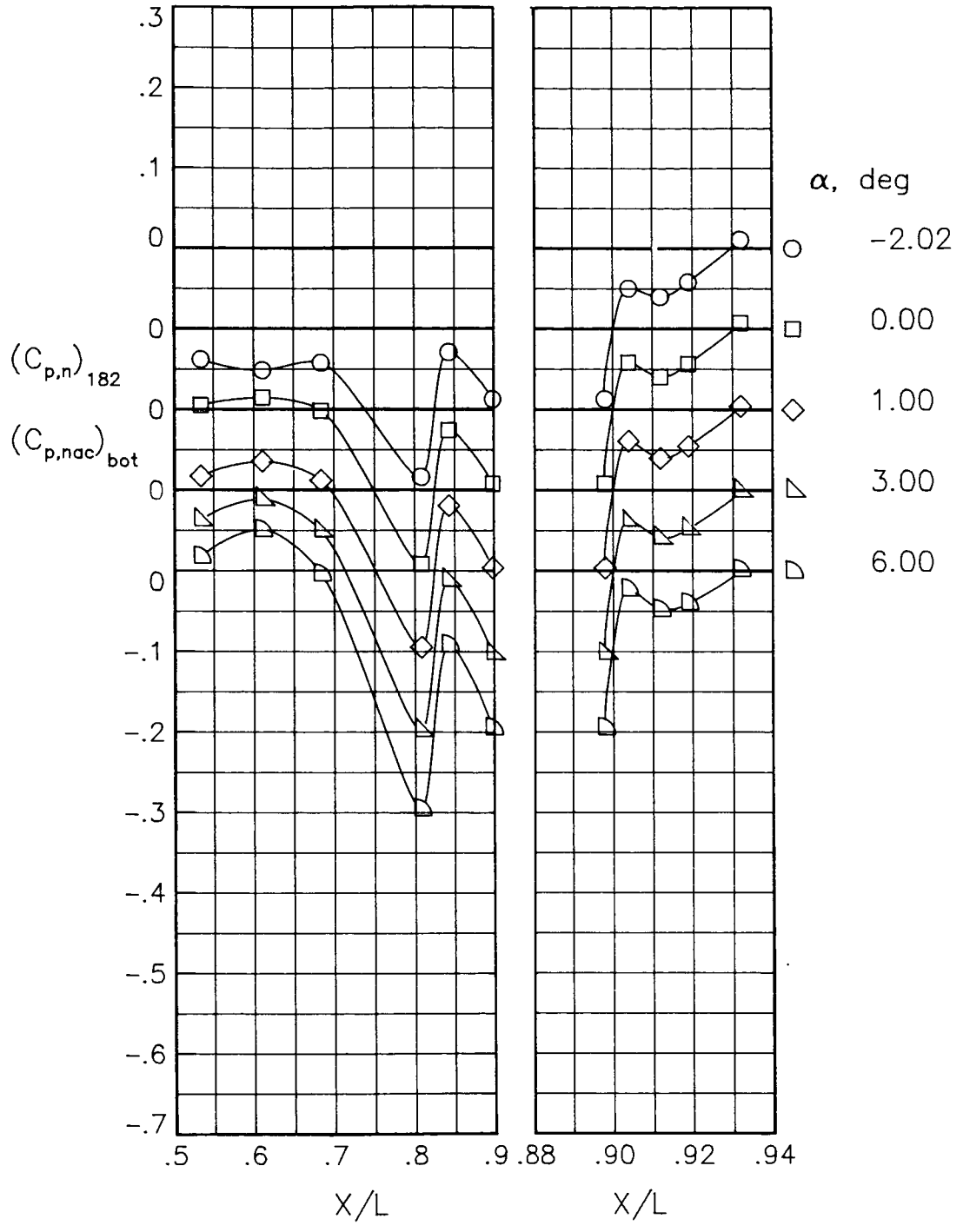

(a) M = 0.90; NPR = 1.00.

Figure 59.- Static-pressure-coefficient distributions on bottom of nacelle and nozzle for the model with all fuselage modifications. β_n = 7.72°.

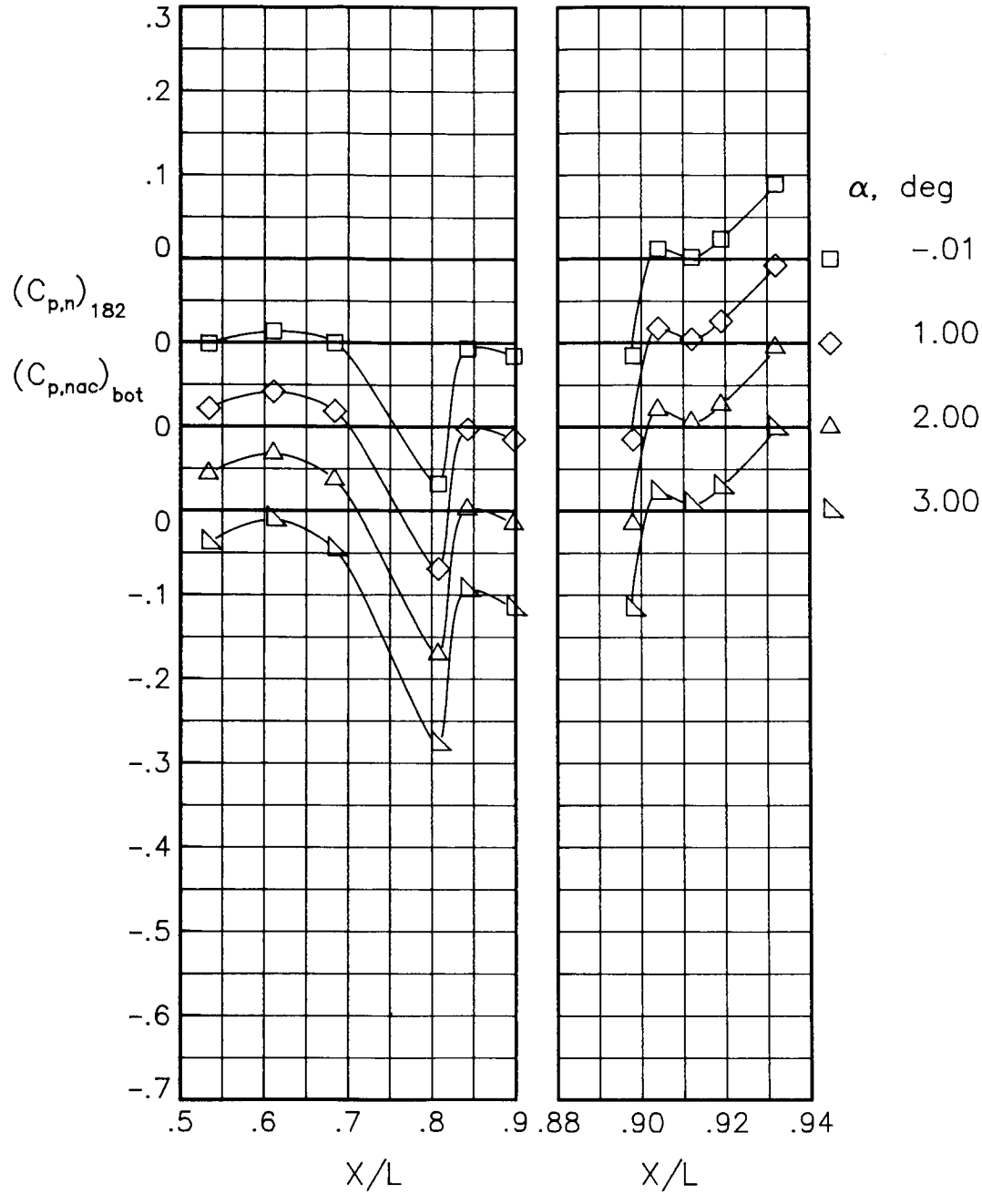

(b) M = 0.90; NPR = 5.00.

Figure 59.- Continued.

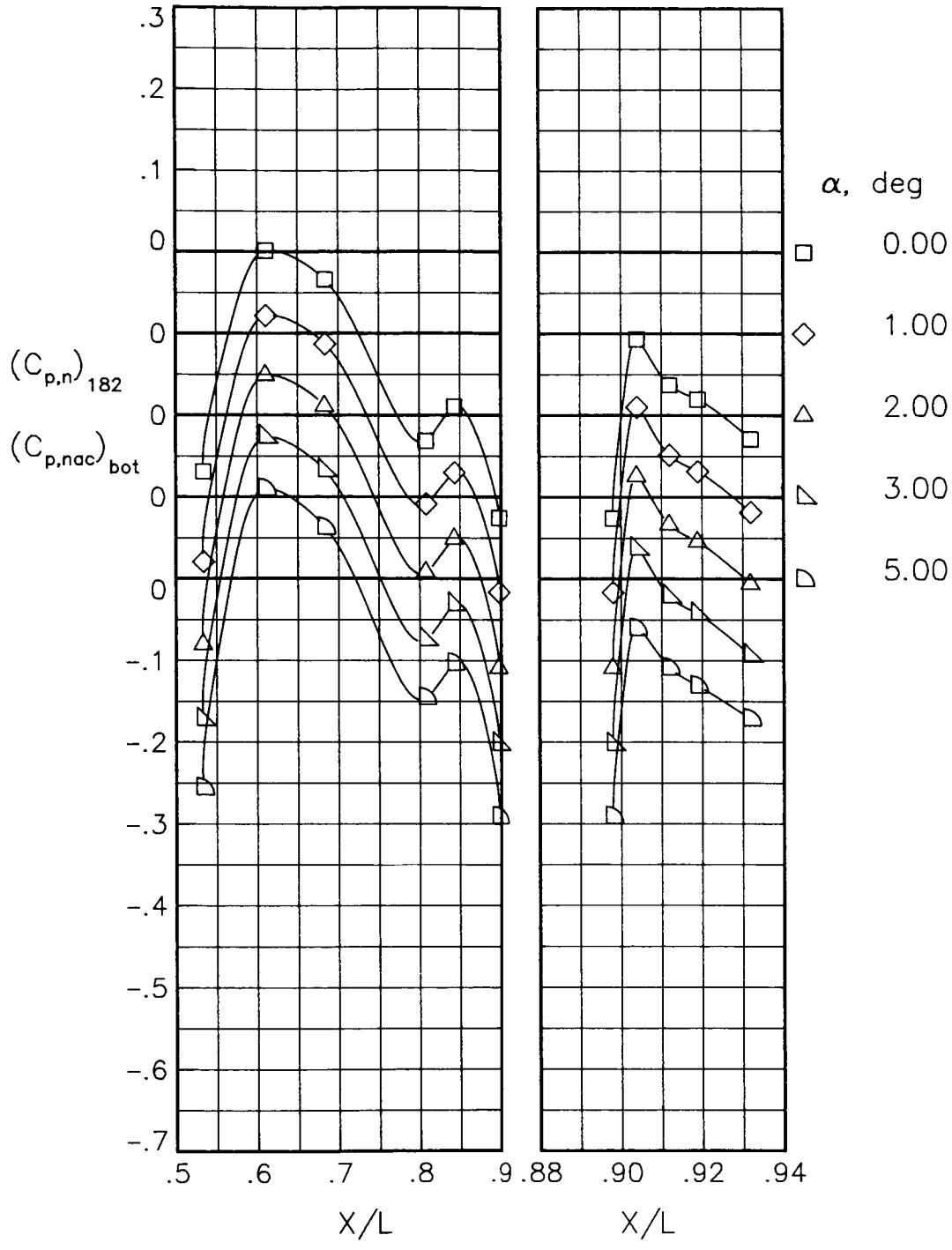

(c) M = 1.20; NPR = 1.00.

Figure 59.- Continued.

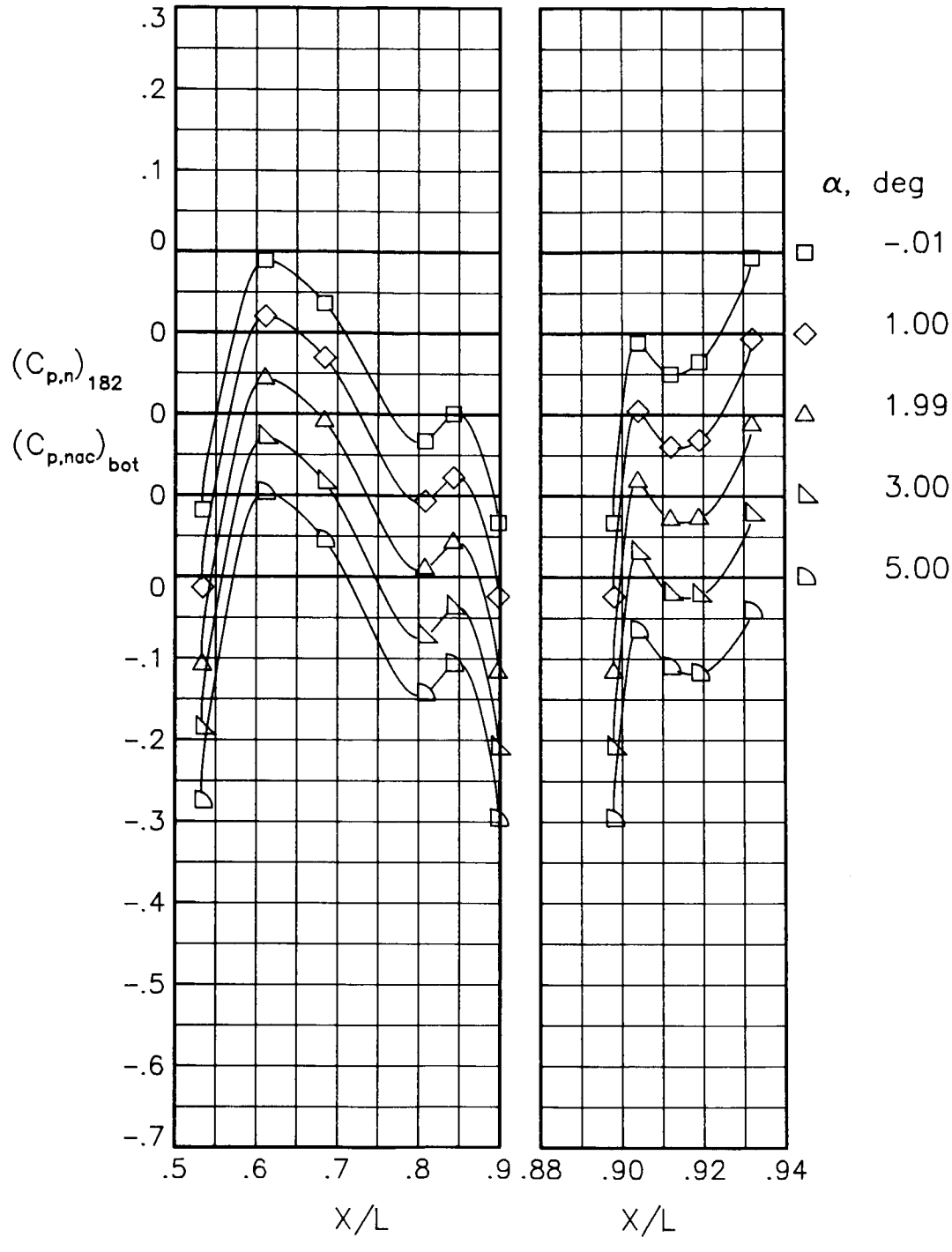

(d) M = 1.20; NPR = 7.00.

Figure 59.- Concluded.

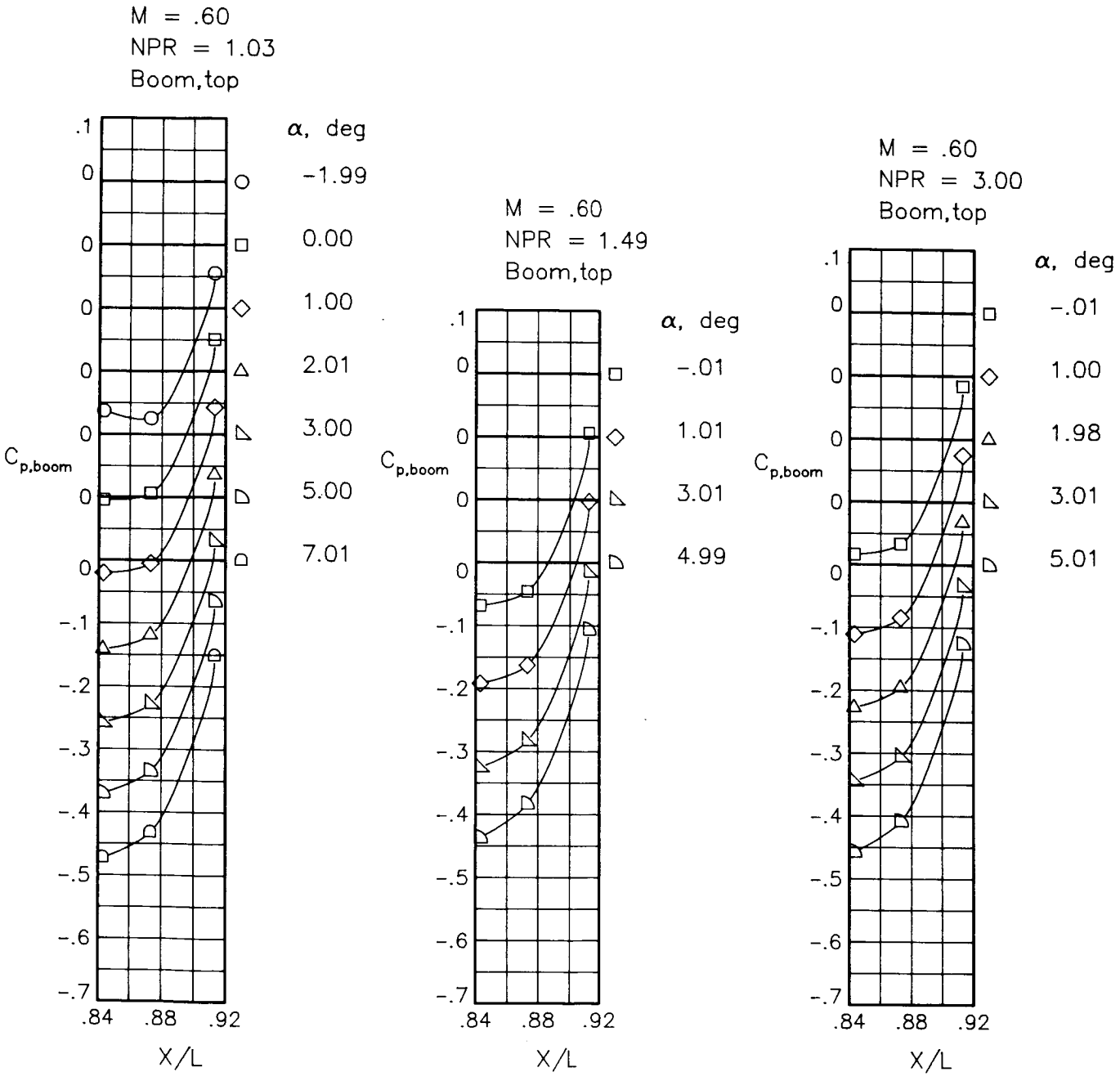

(a) M = 0.60.

Figure 60.- Static-pressure-coefficient distributions on top of tail boom for the unmodified model. β_n = 18.45°.

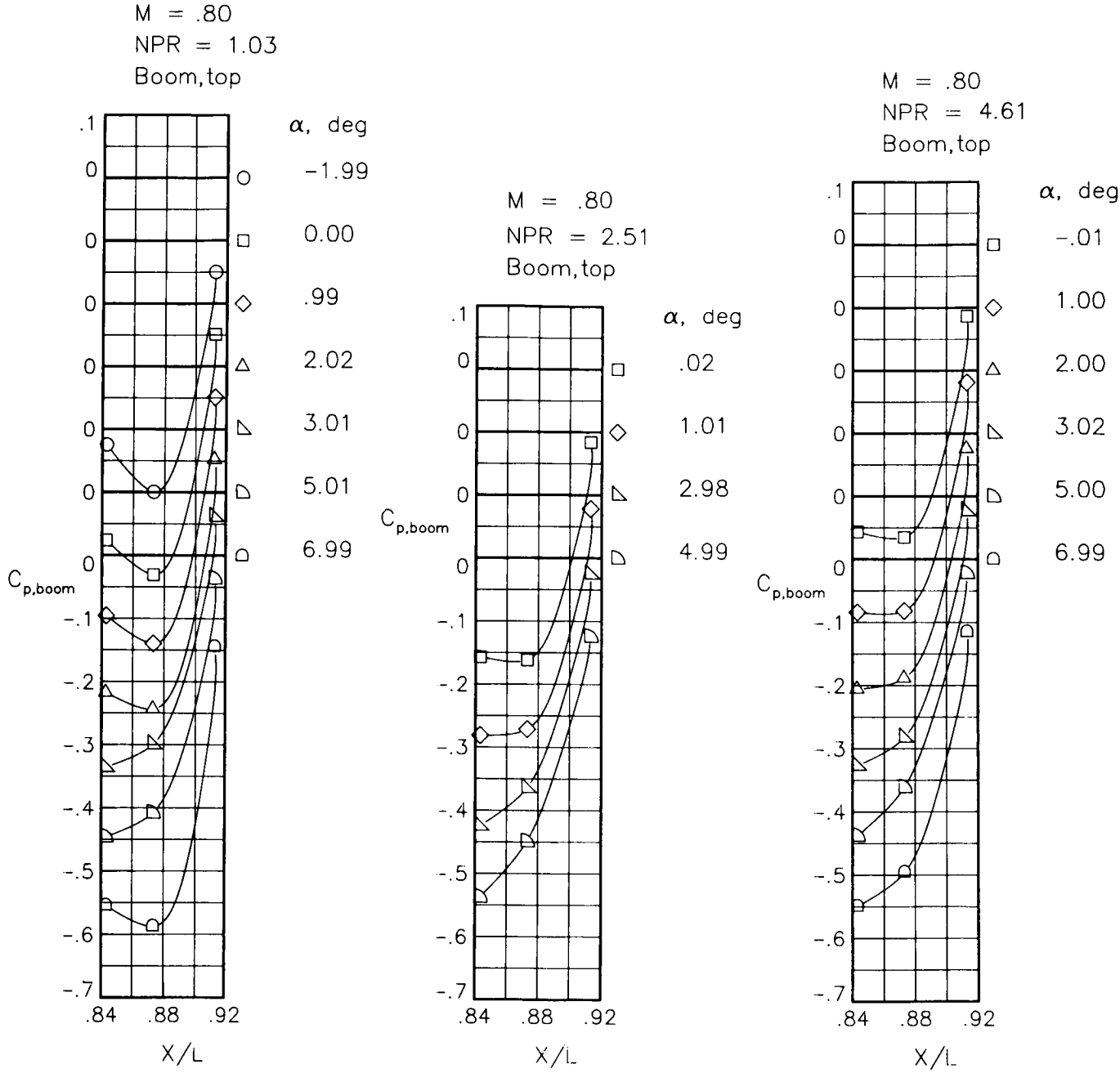

(b) M = 0.80.

Figure 60.- Continued.

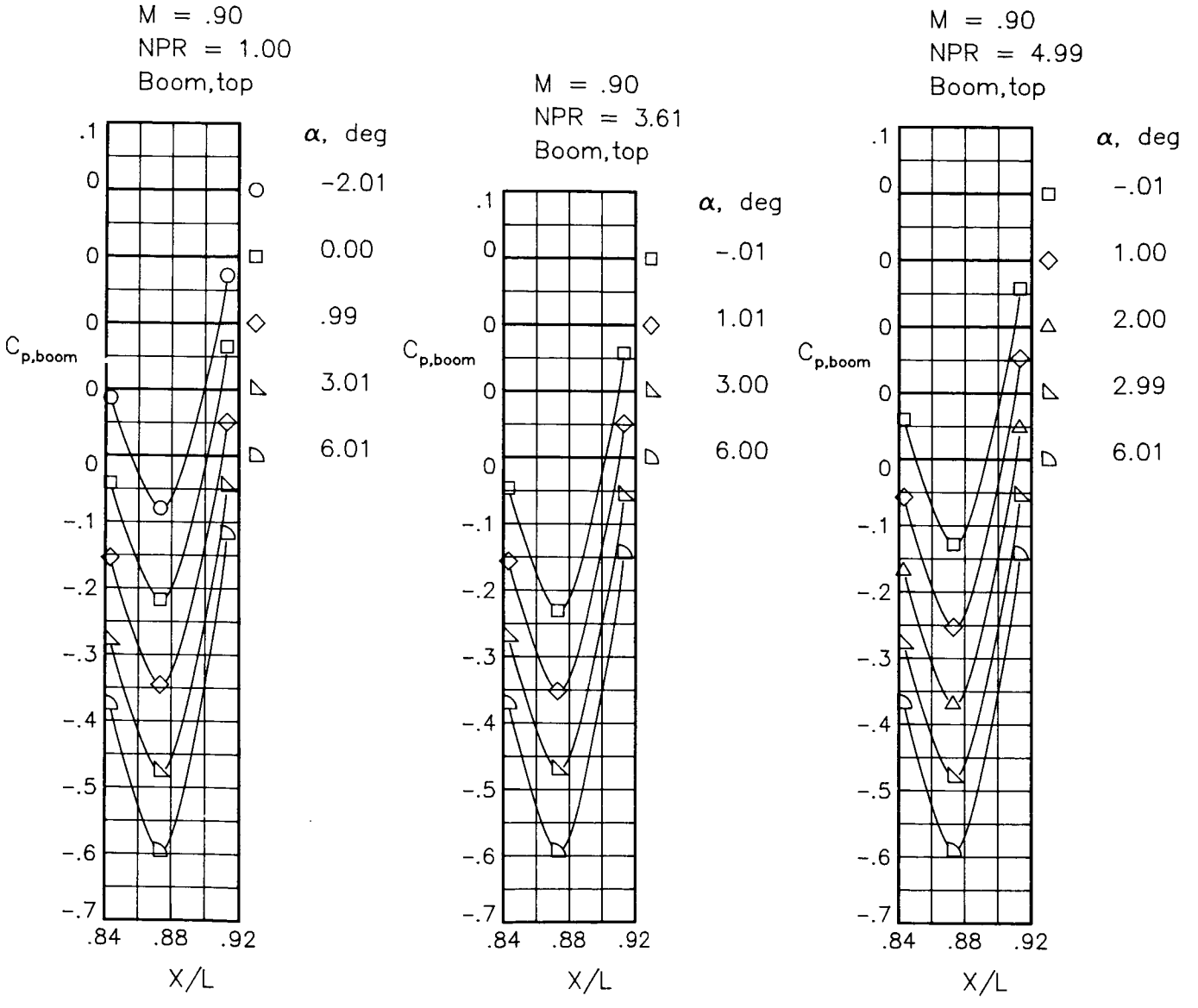

(c) M = 0.90.

Figure 60.- Concluded.

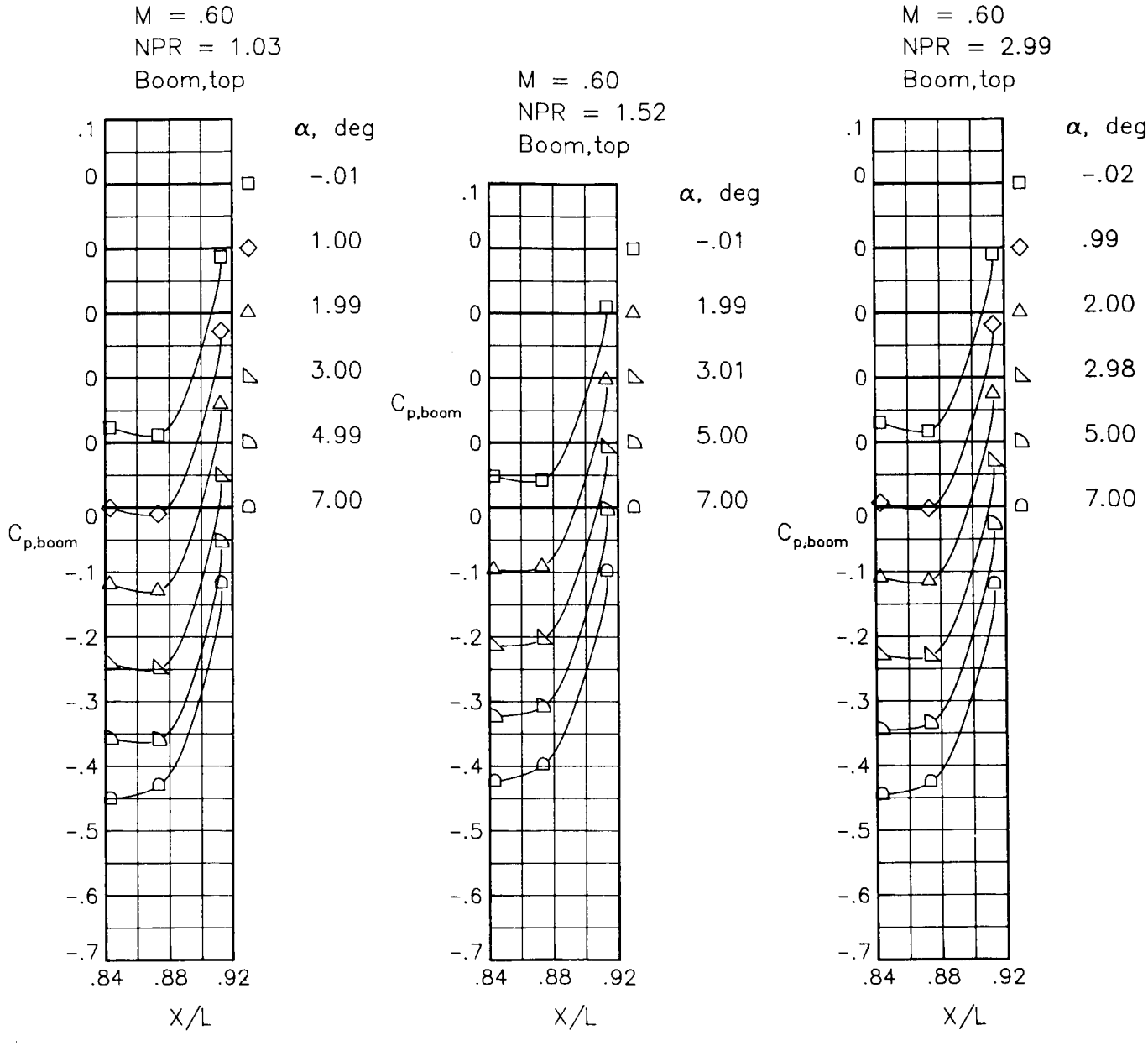

(a) M = 0.60.

Figure 61.- Static-pressure-coefficient distributions on top of tail boom for the model with all fuselage modifications. β_n = 18.45°; δ_h = -2°.

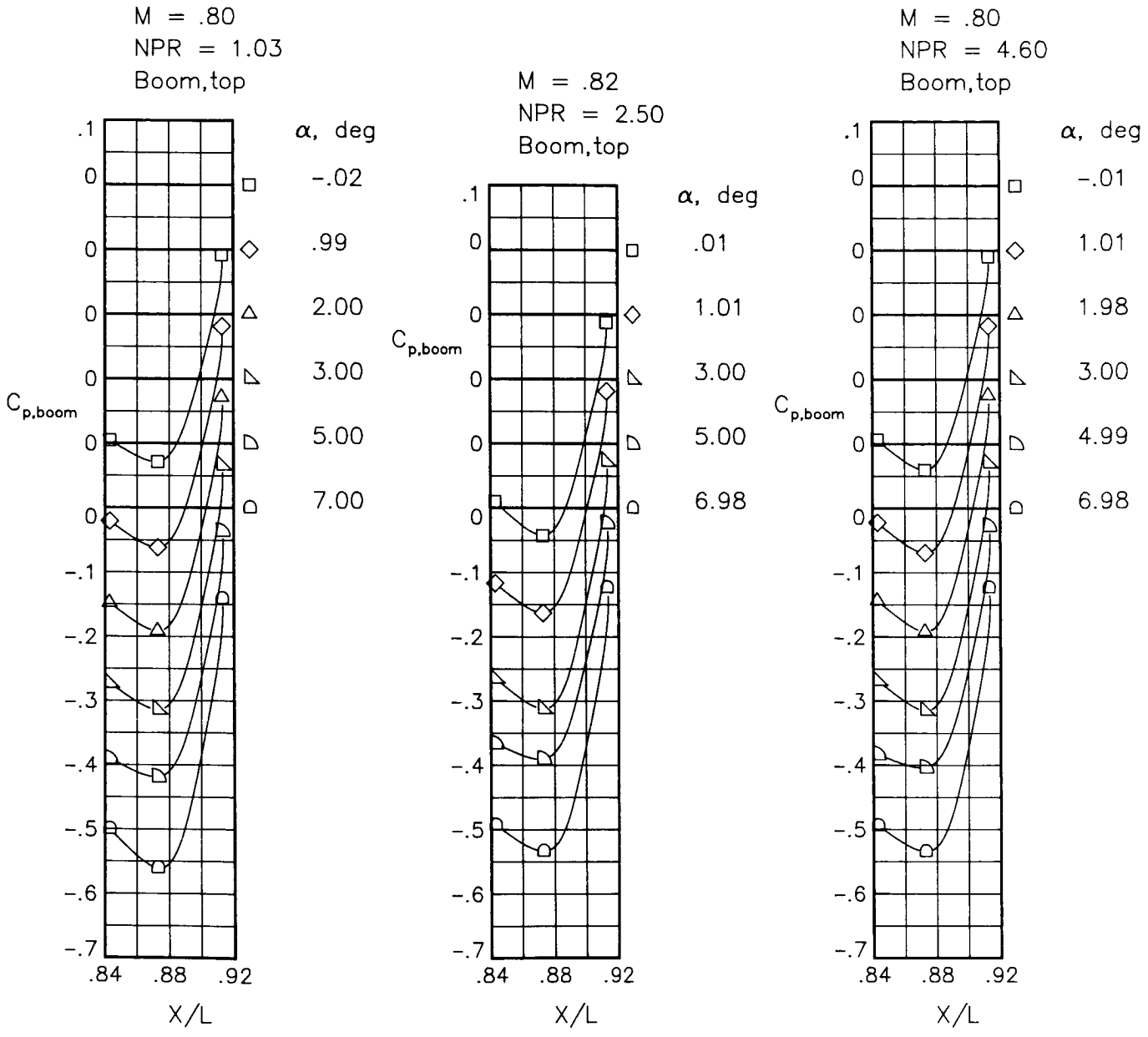

(b) M = 0.80.

Figure 61.- Continued.

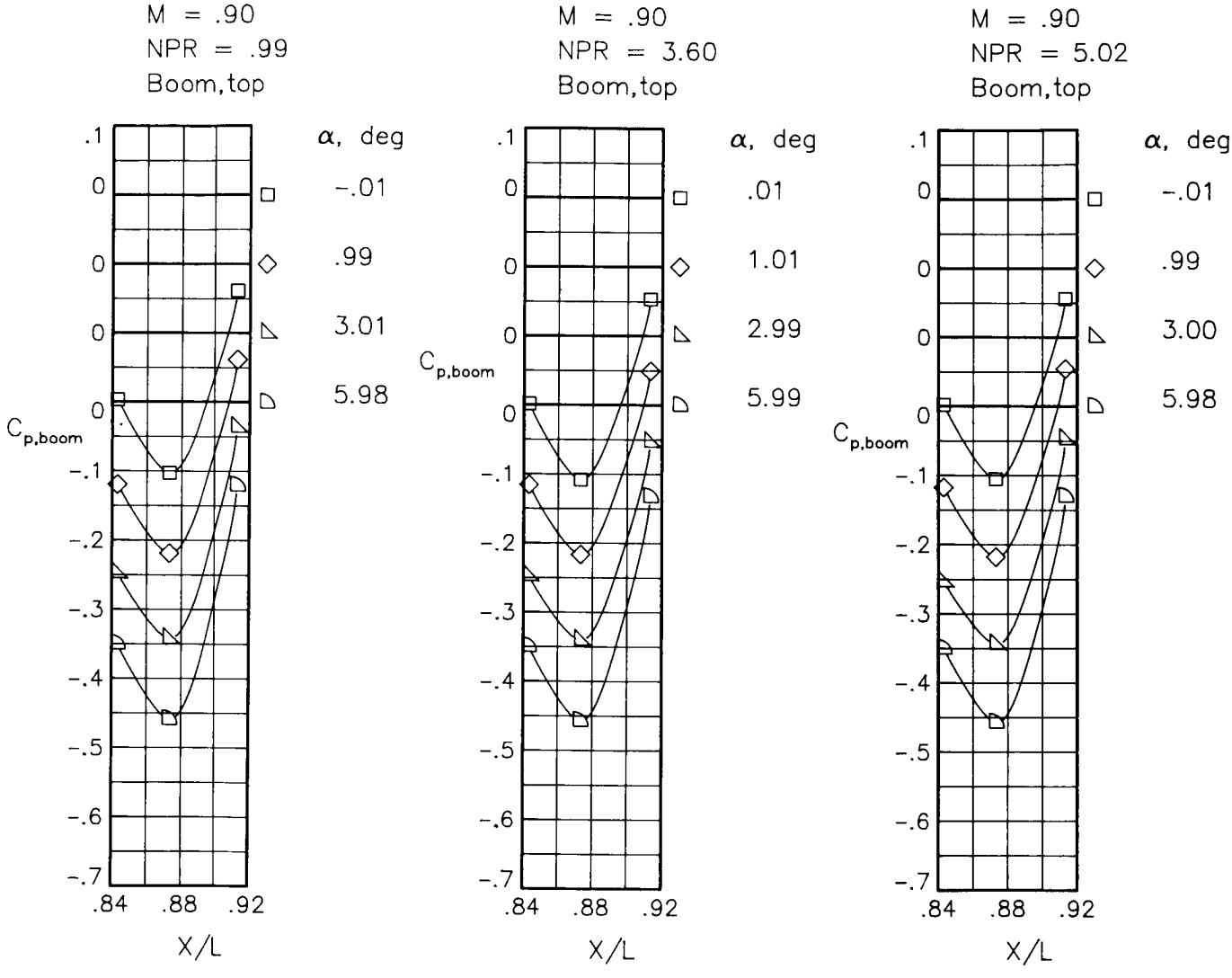

(c) M = 0.90.

Figure 61.- Concluded.

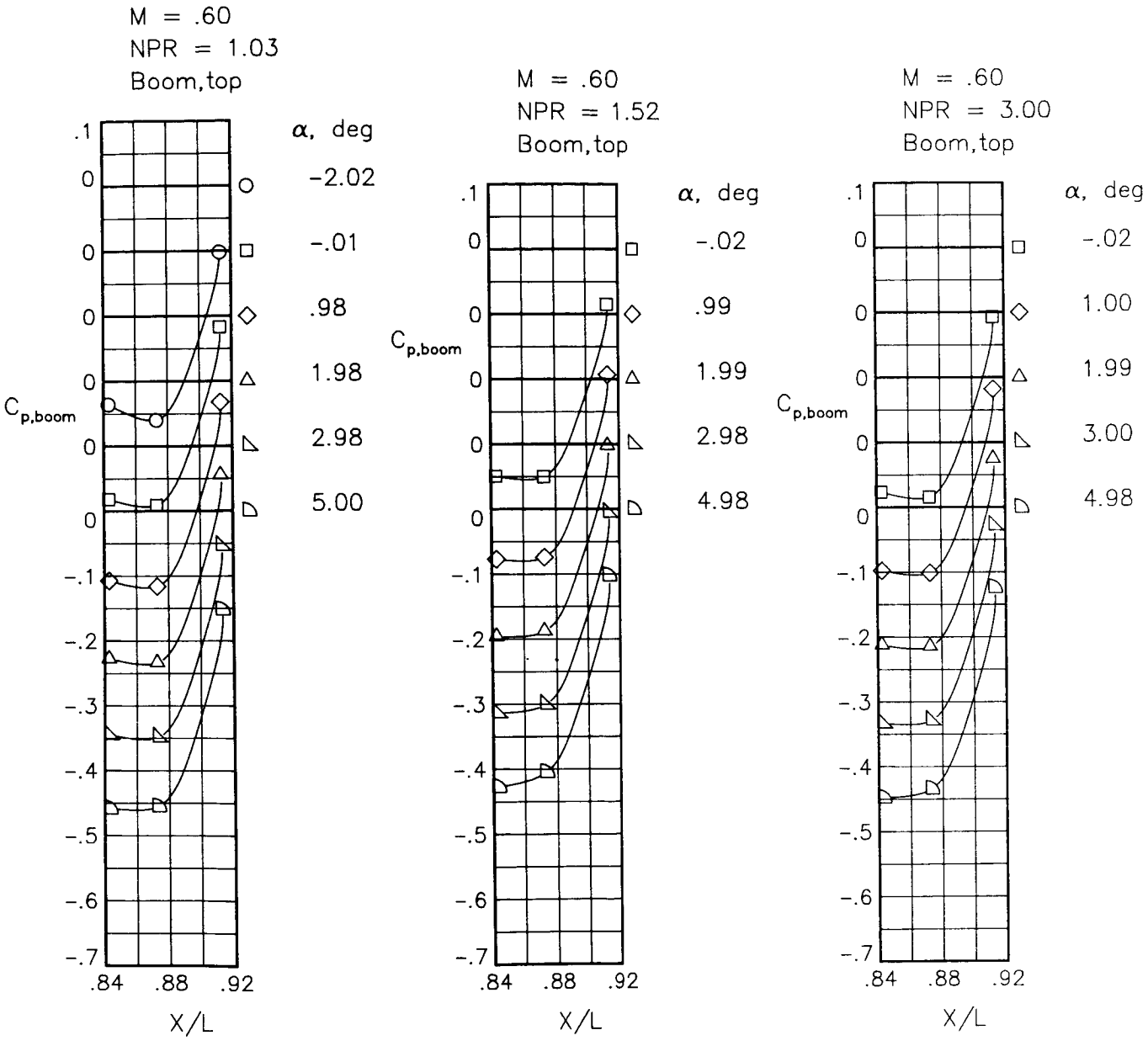

(a) M = 0.60.

Figure 62.- Static-pressure-coefficient distributions on top of tail boom for the model with all fuselage modifications. β_n = 18.45°.

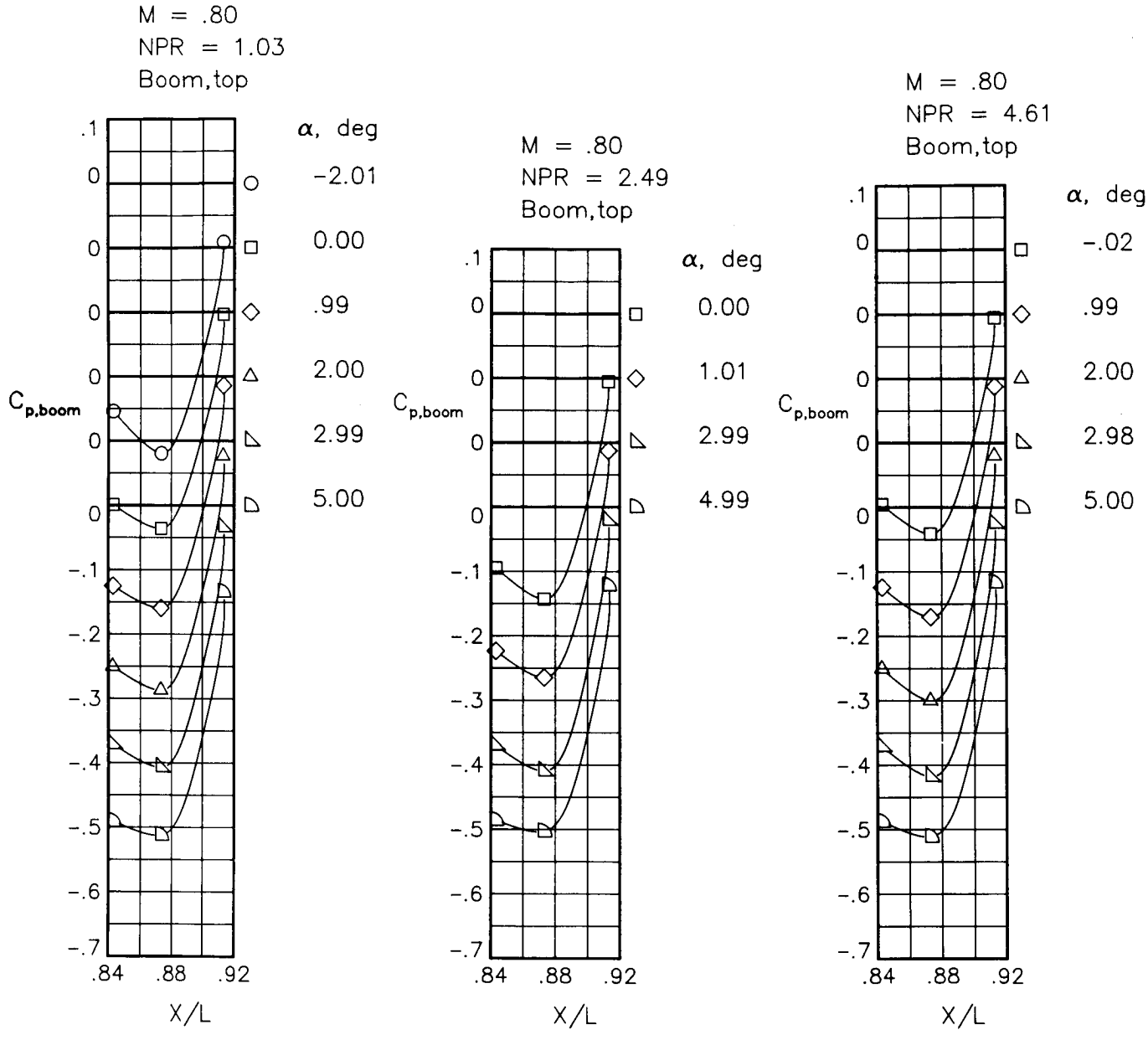

(b) M = 0.80.

Figure 62.- Continued.

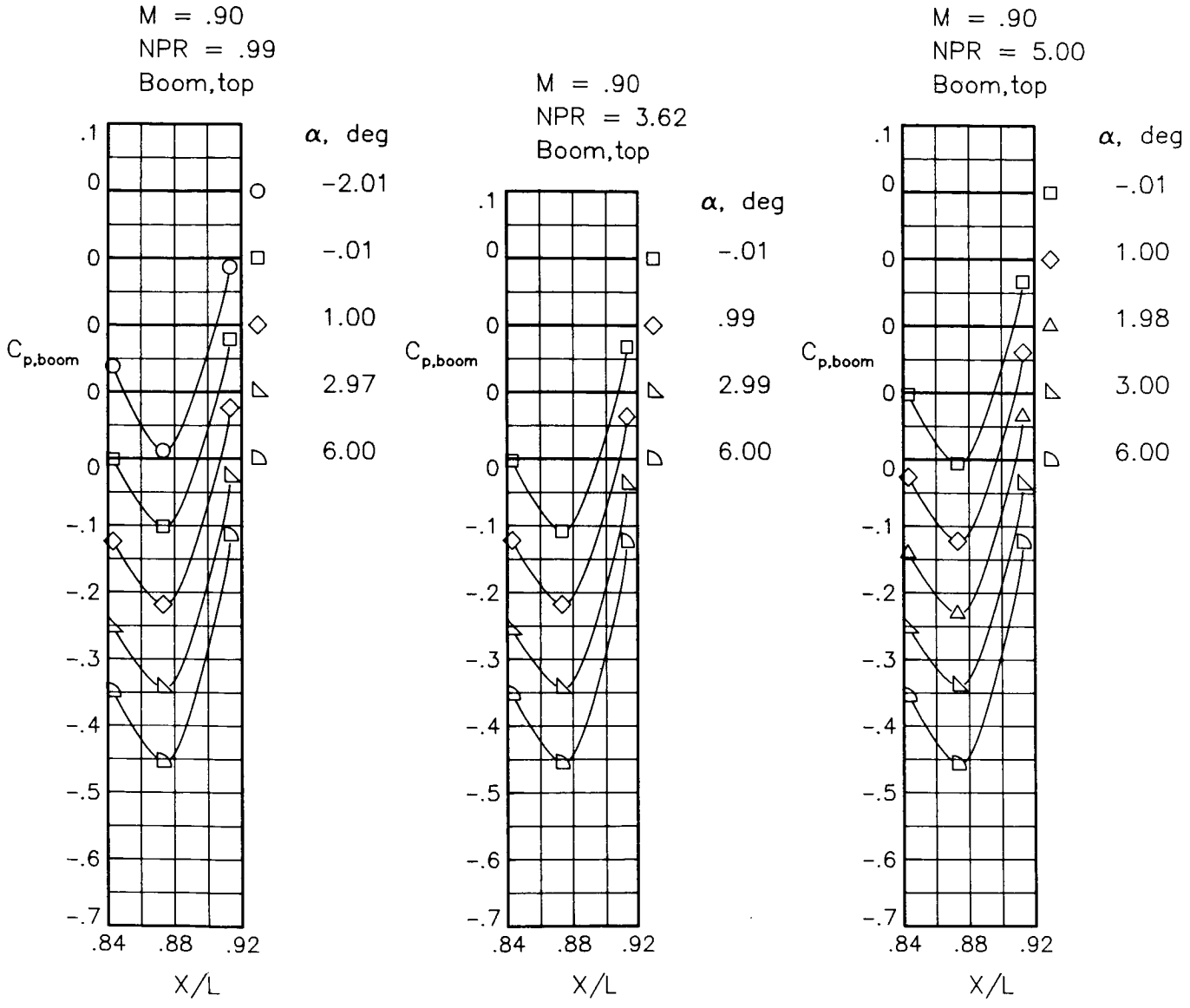

(c) M = 0.90.

Figure 62.- Concluded.

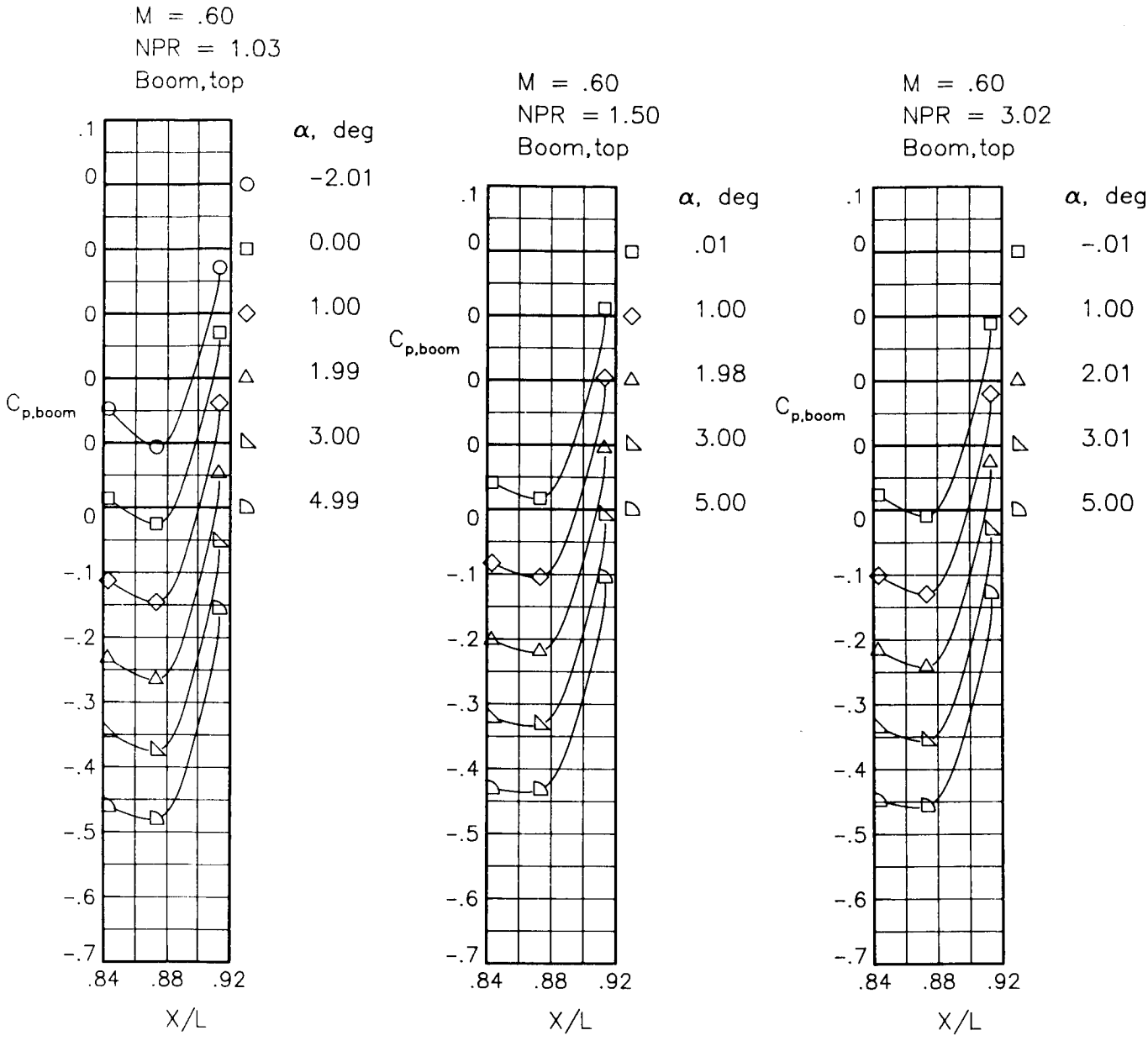

(a) M = 0.60.

Figure 63.- Static-pressure-coefficient distributions on top of tail boom for the model with all fuselage modifications. β_n = 18.45°. Repeat data.

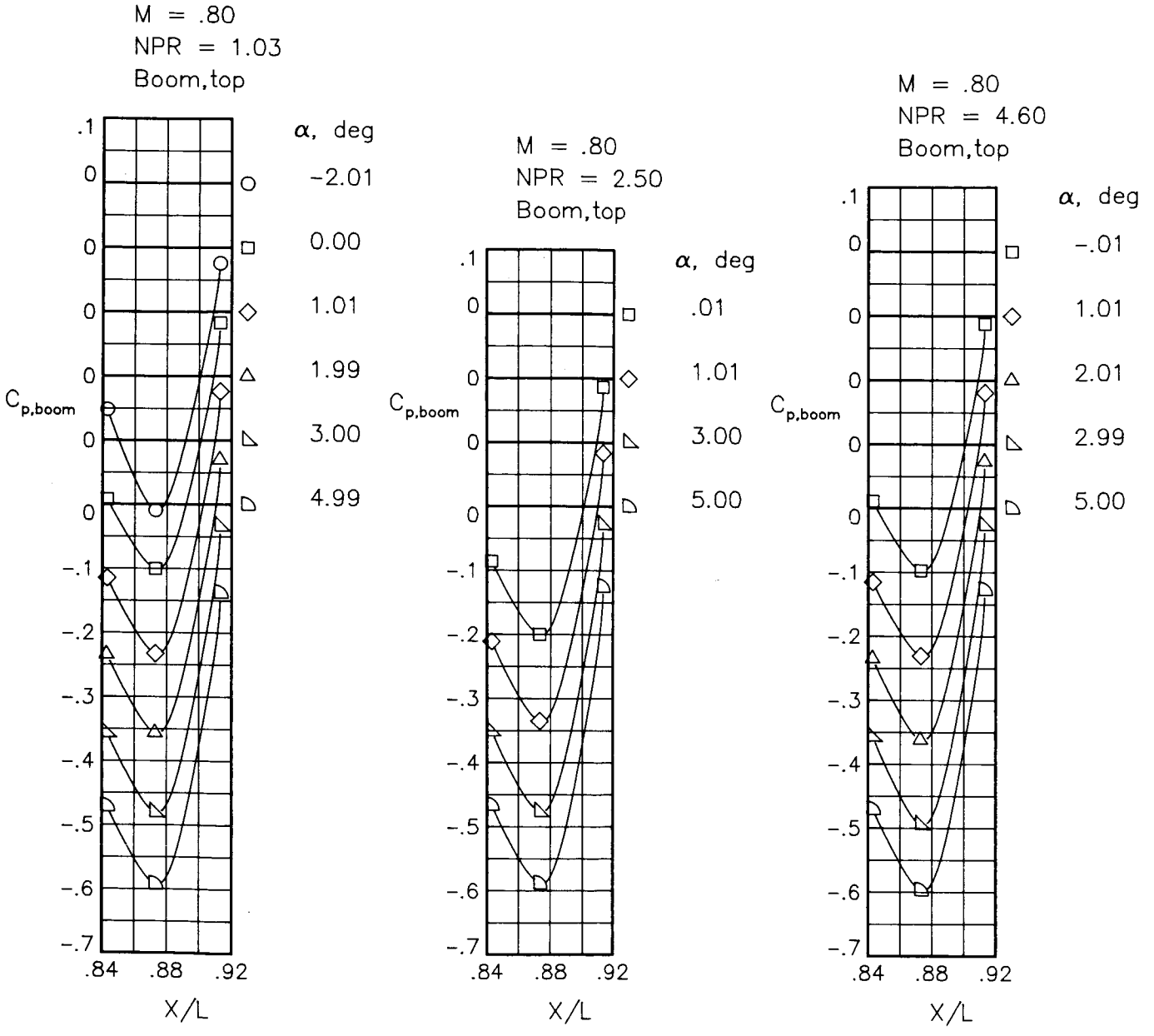

(b) M = 0.80.

Figure 63.- Continued.

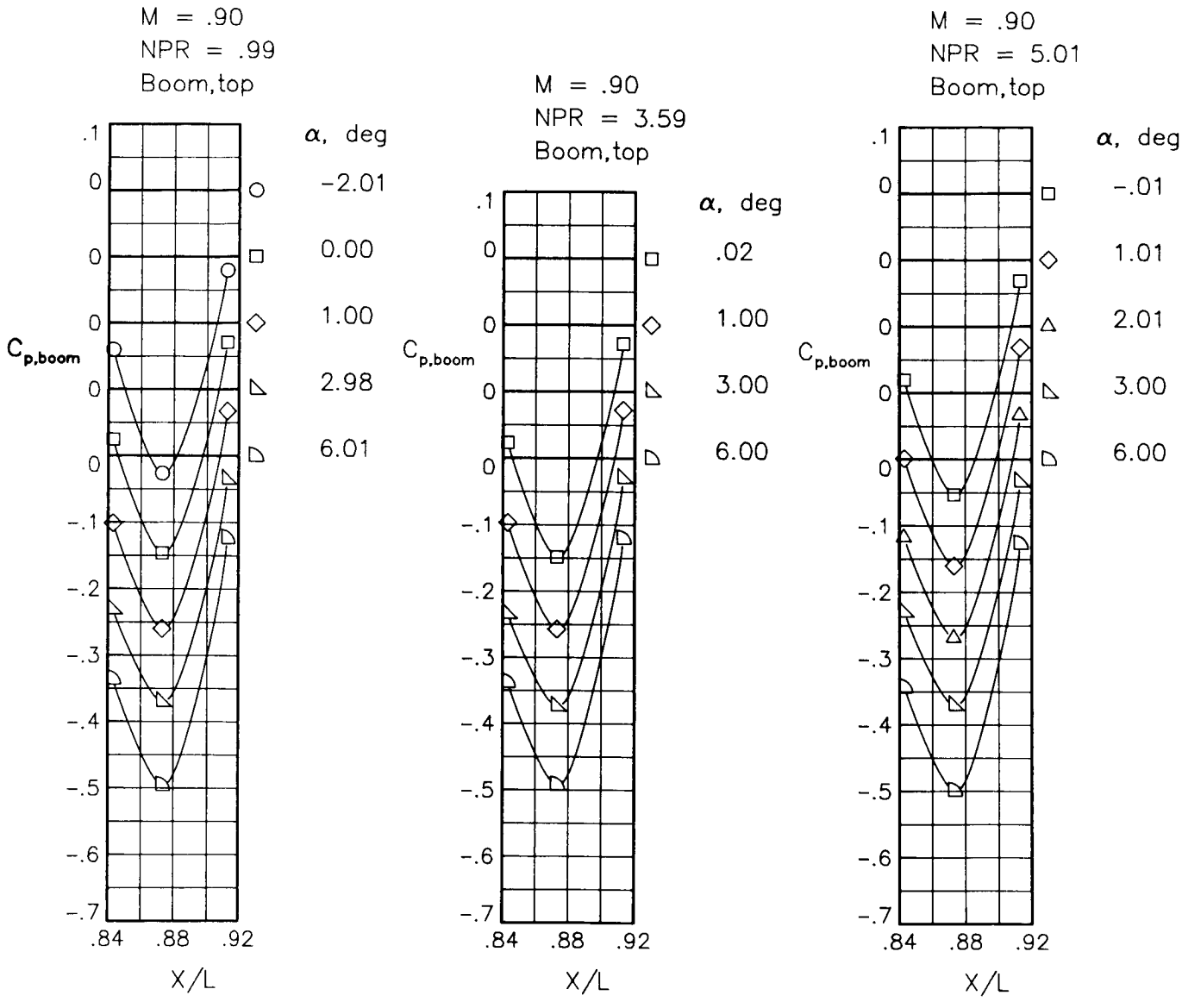

(c) M = 0.90.

Figure 63.- Concluded.

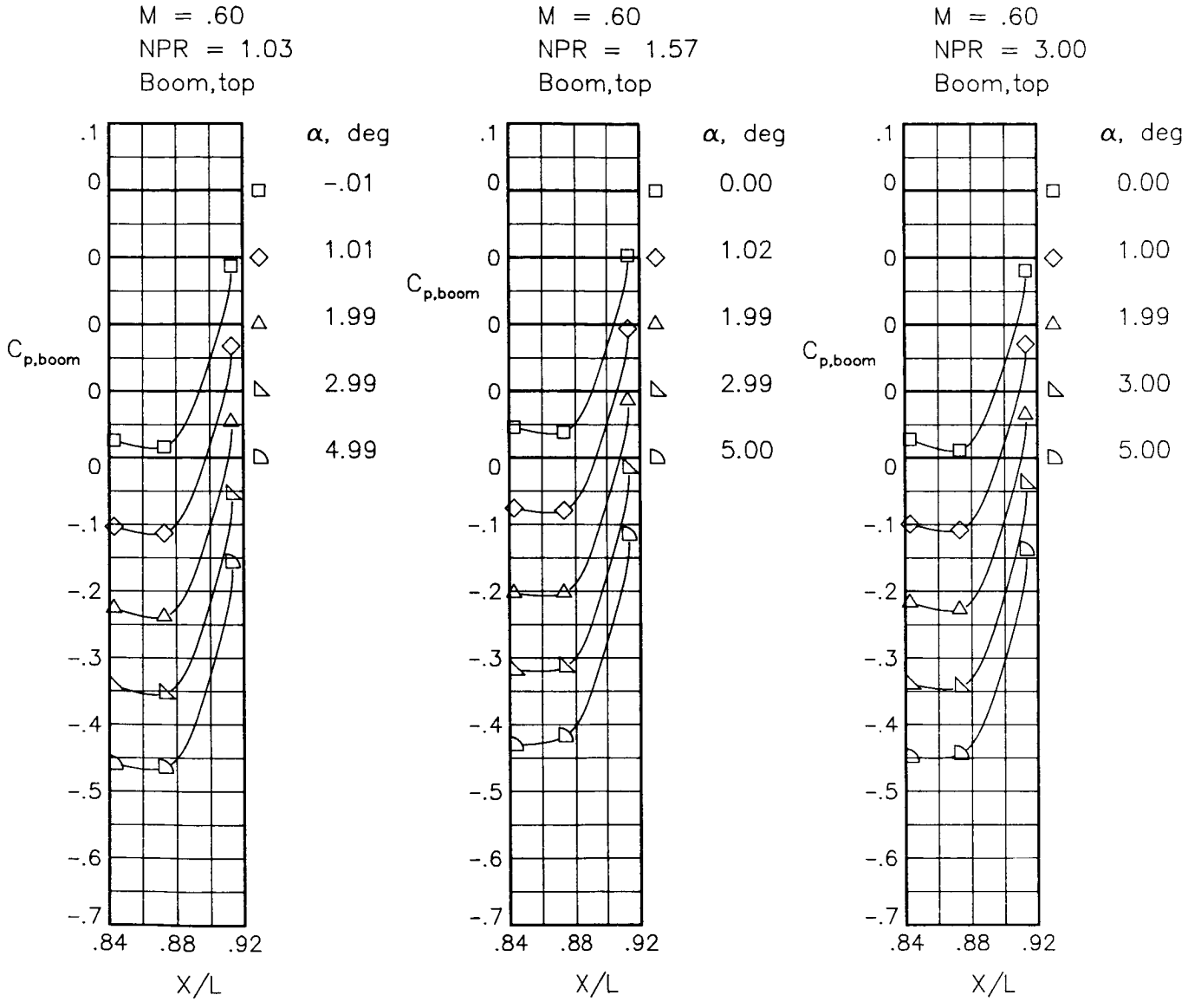

(a) M = 0.60.

Figure 64.- Static-pressure-coefficient distributions on top of tail boom for the model with all fuselage modifications. β_n = 18.45°; δ_r = -5°.

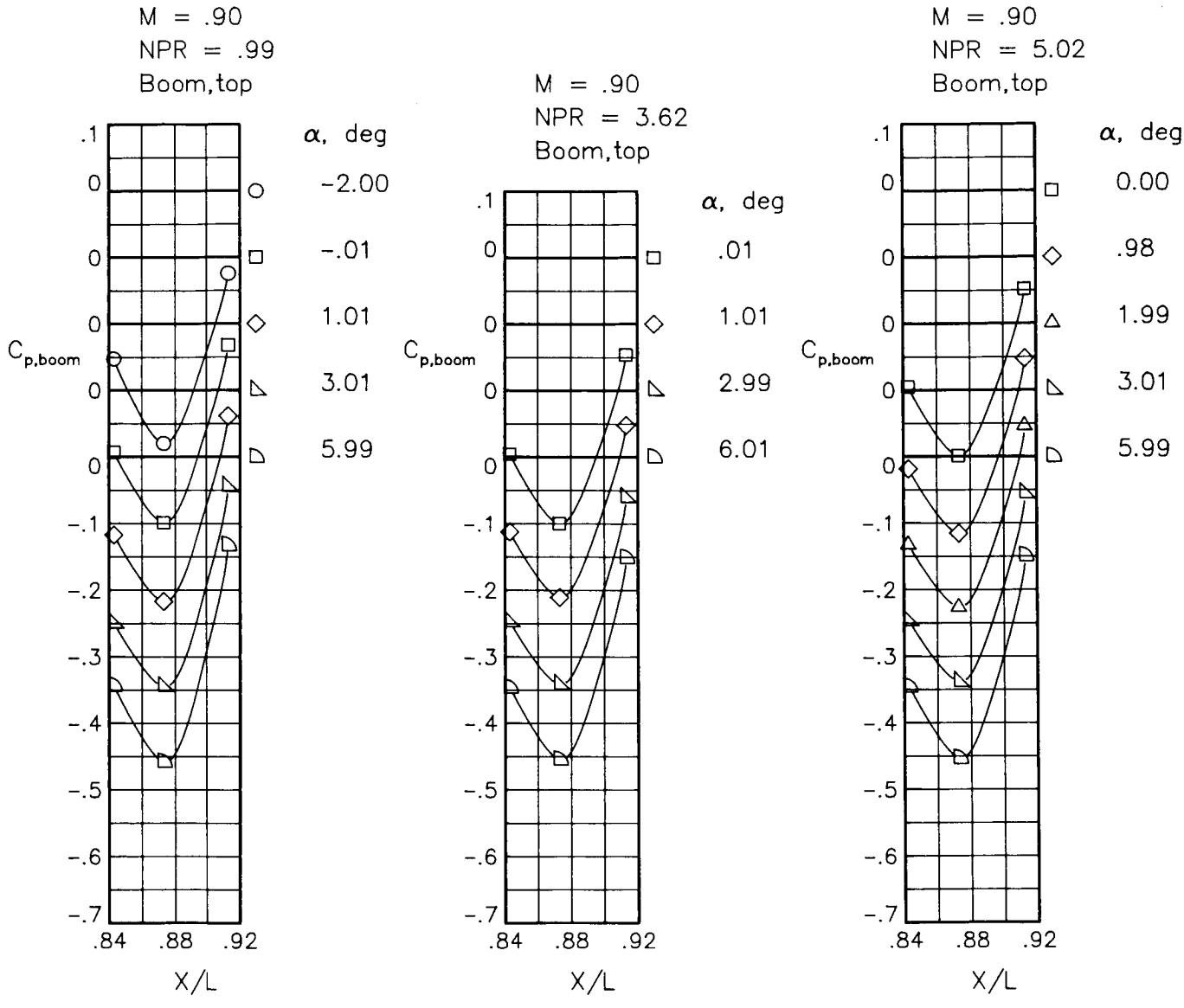

(b) M = 0.90.

Figure 64.- Concluded.

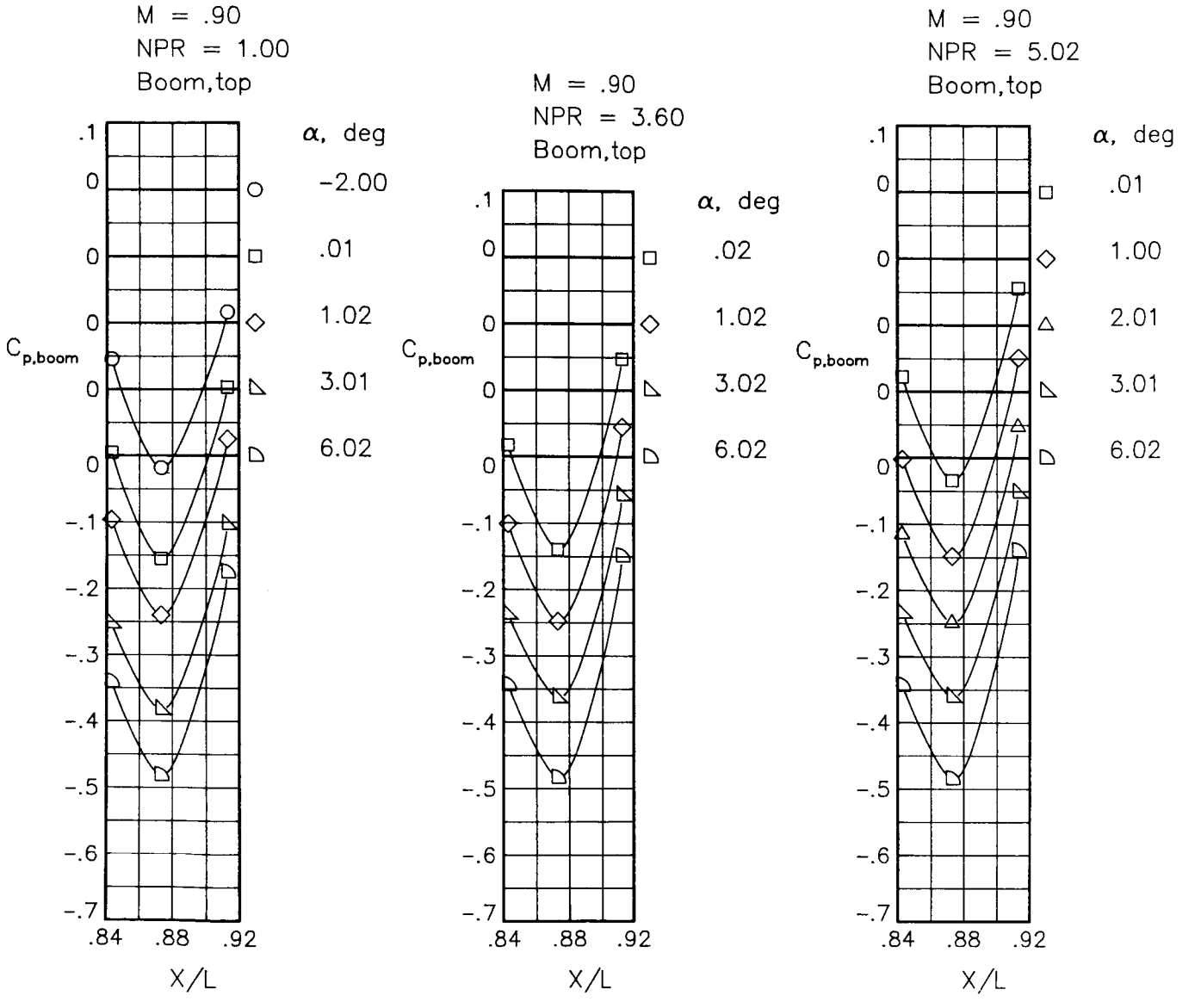

(a) M = 0.90.

Figure 65.- Static-pressure-coefficient distributions on top of tail boom for the model with all fuselage modifications. β_n = 15.05°.

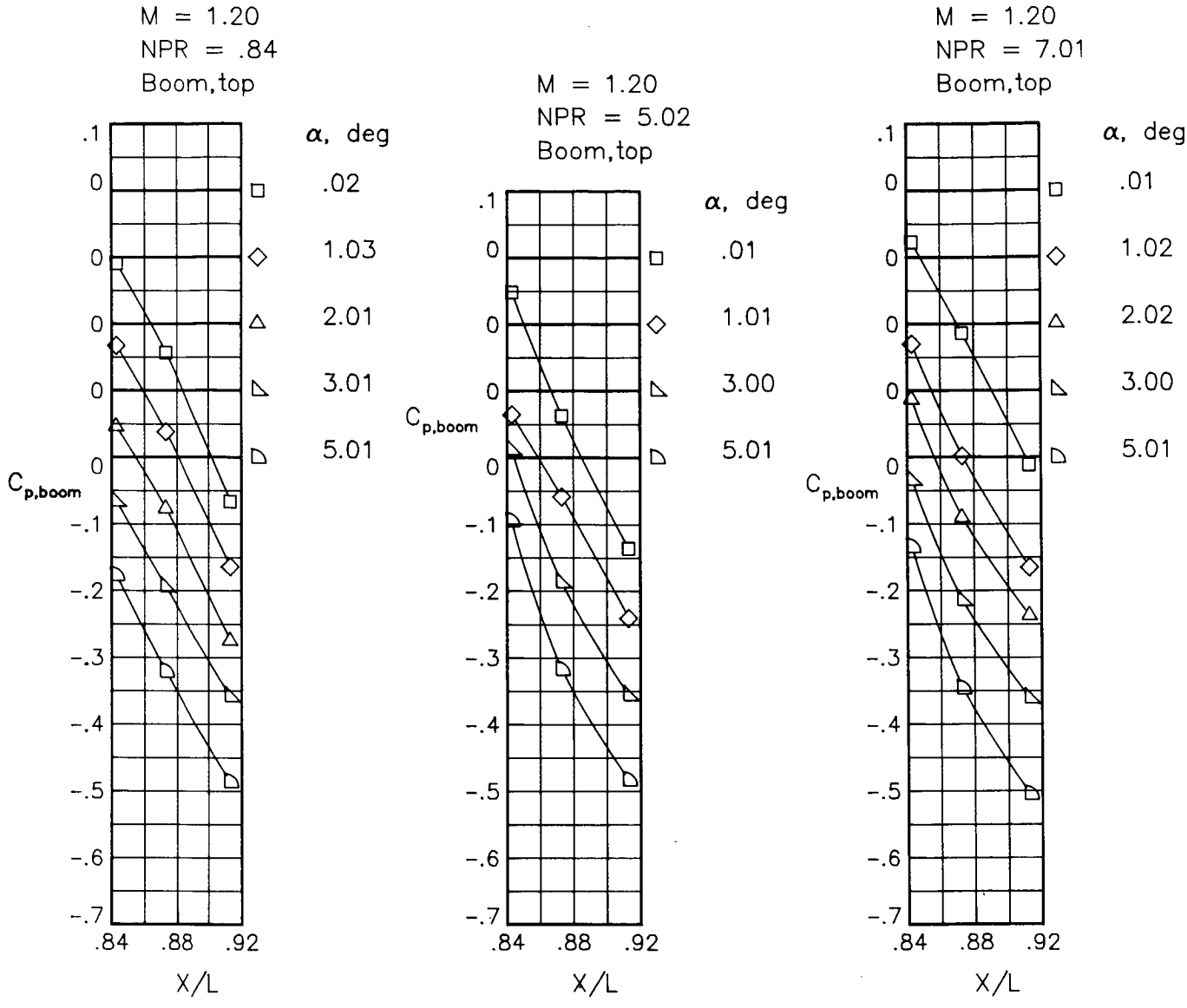

(b) M = 1.20.

Figure 65.- Concluded.

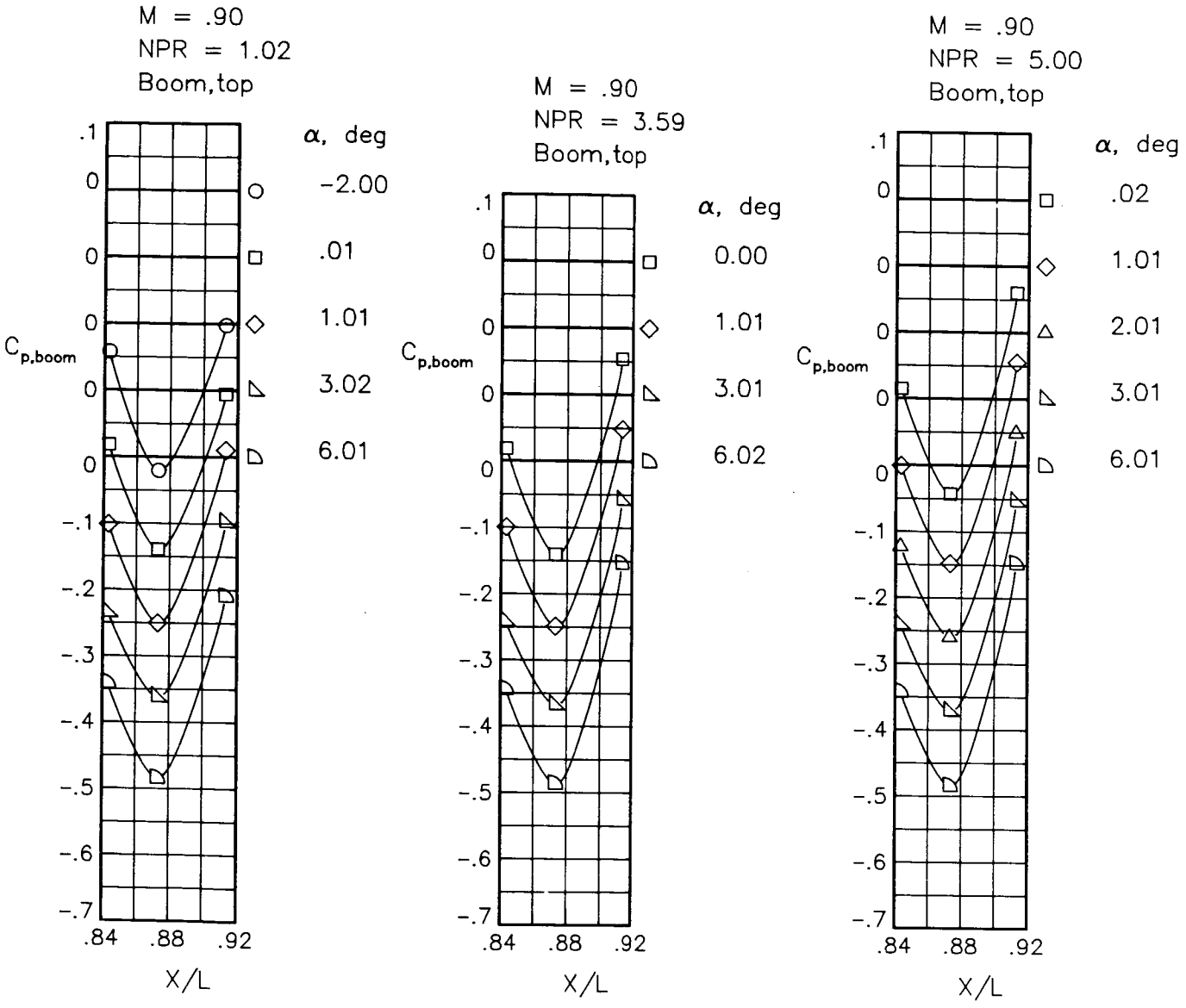

(a) M = 0.90.

Figure 66.- Static-pressure-coefficient distributions on top of tail boom for the model with all fuselage modifications. β_n = 9.63°.

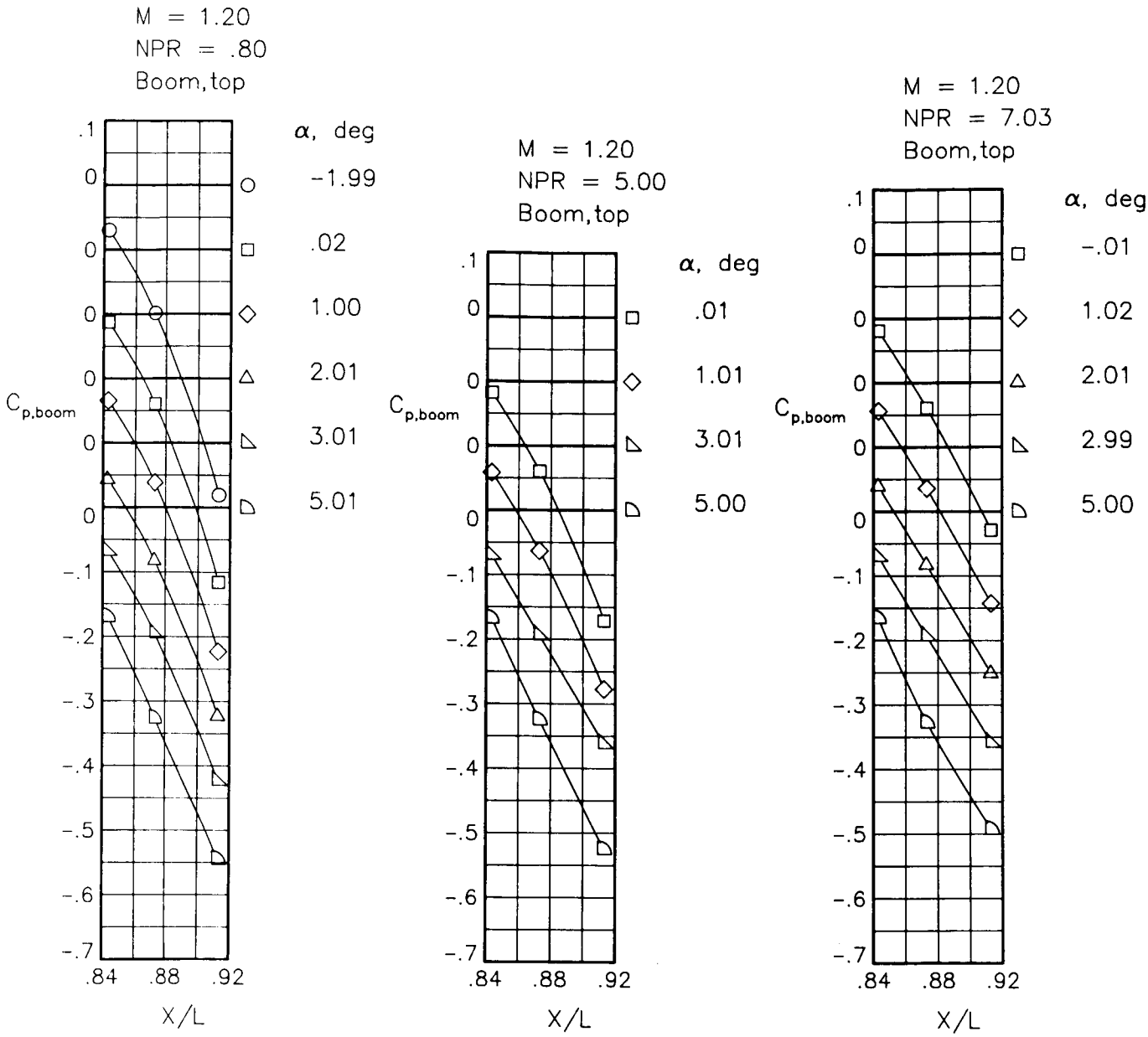

(b) M = 1.20.

Figure 66.- Concluded.

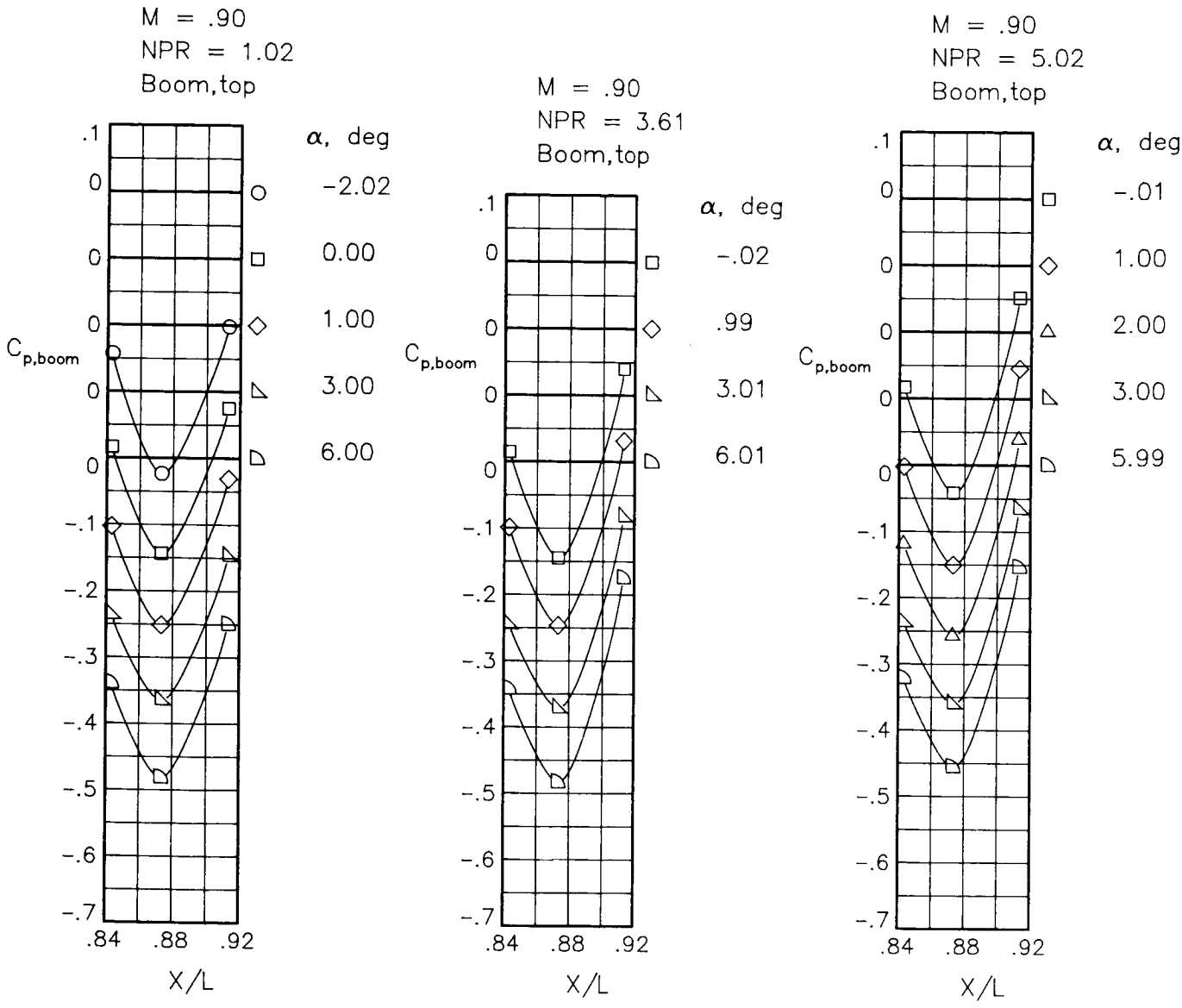

(a) M = 0.90.

Figure 67.- Static-pressure-coefficient distributions on top of tail boom for the model with all fuselage modifications. β_n = 7.72°.

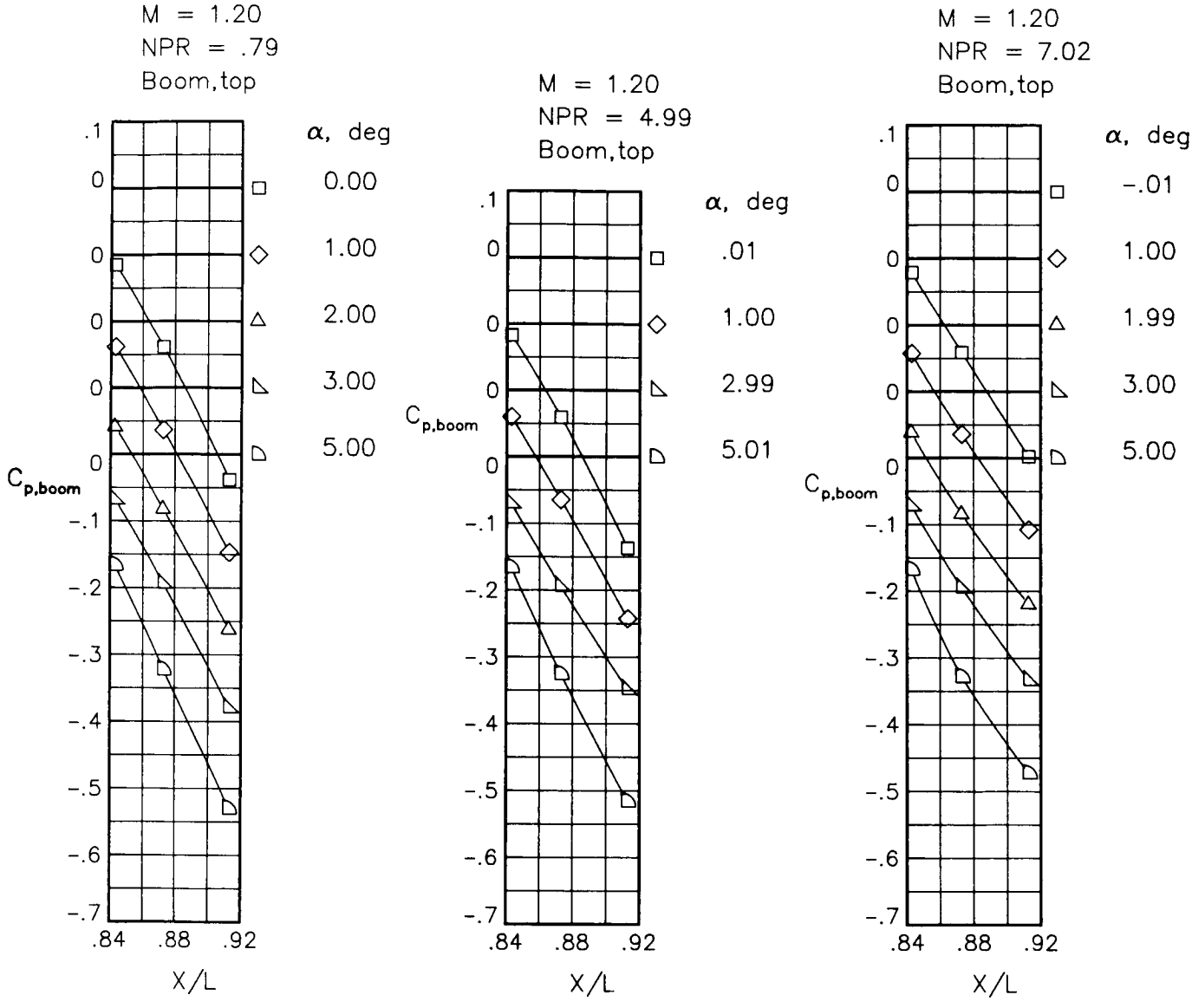

(b) M = 1.20.

Figure 67.- Concluded.

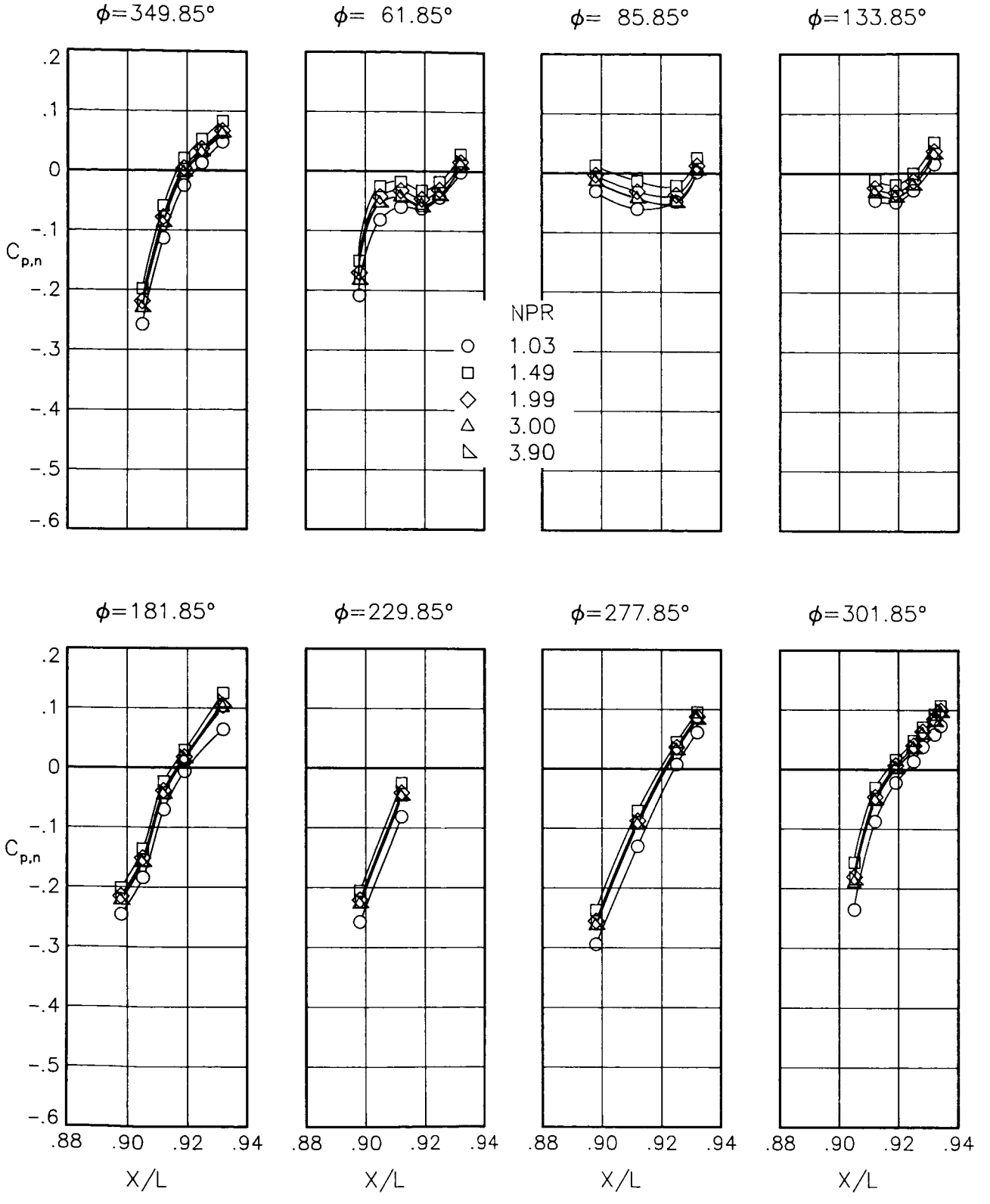

(a) M = 0.60; α = 0.00°.

Figure 68.- Static-pressure-coefficient distributions on nozzle for the unmodified model. β_n = 18.45°.

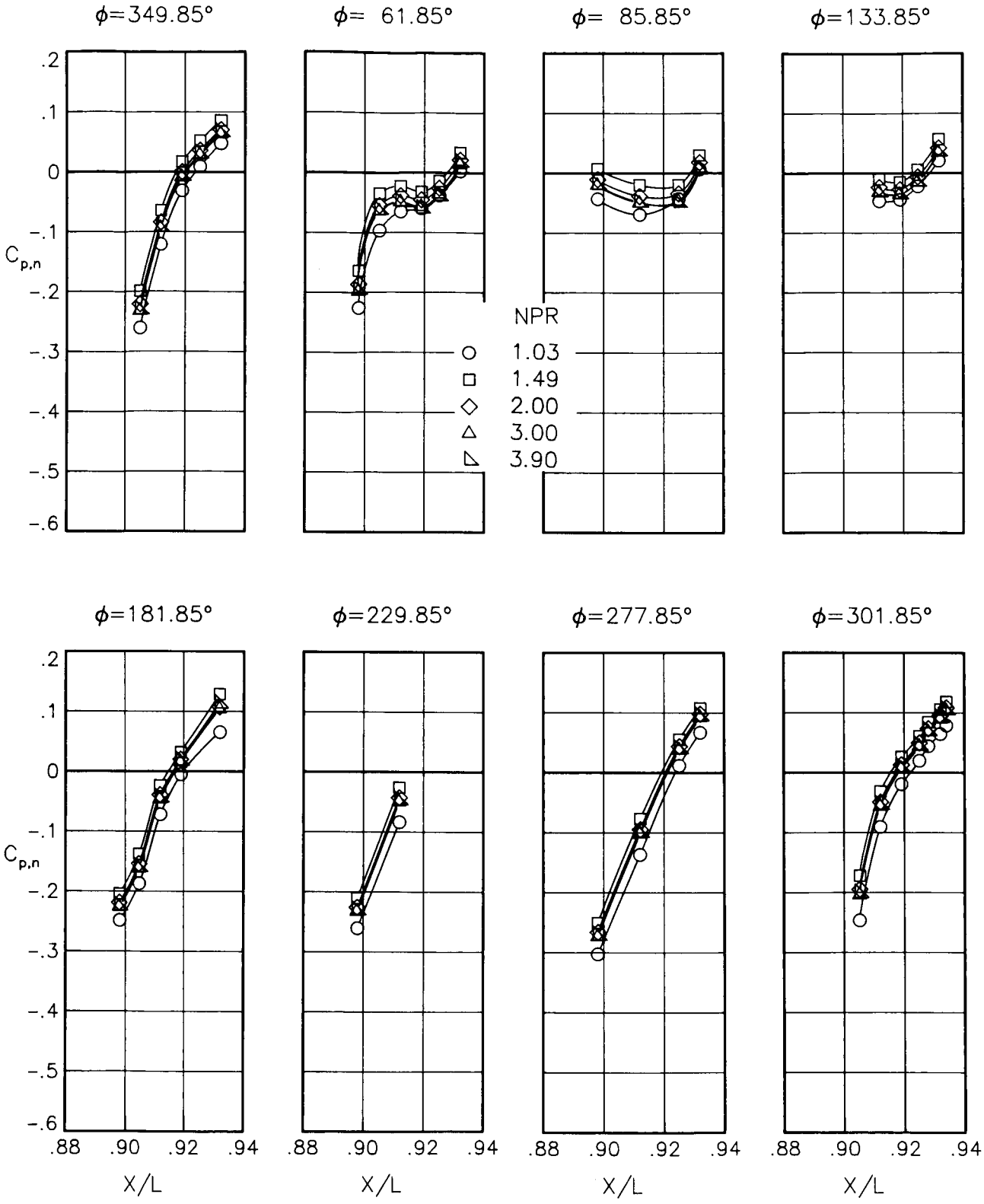

(b) M = 0.60; α = 1.00°.

Figure 68.- Continued.

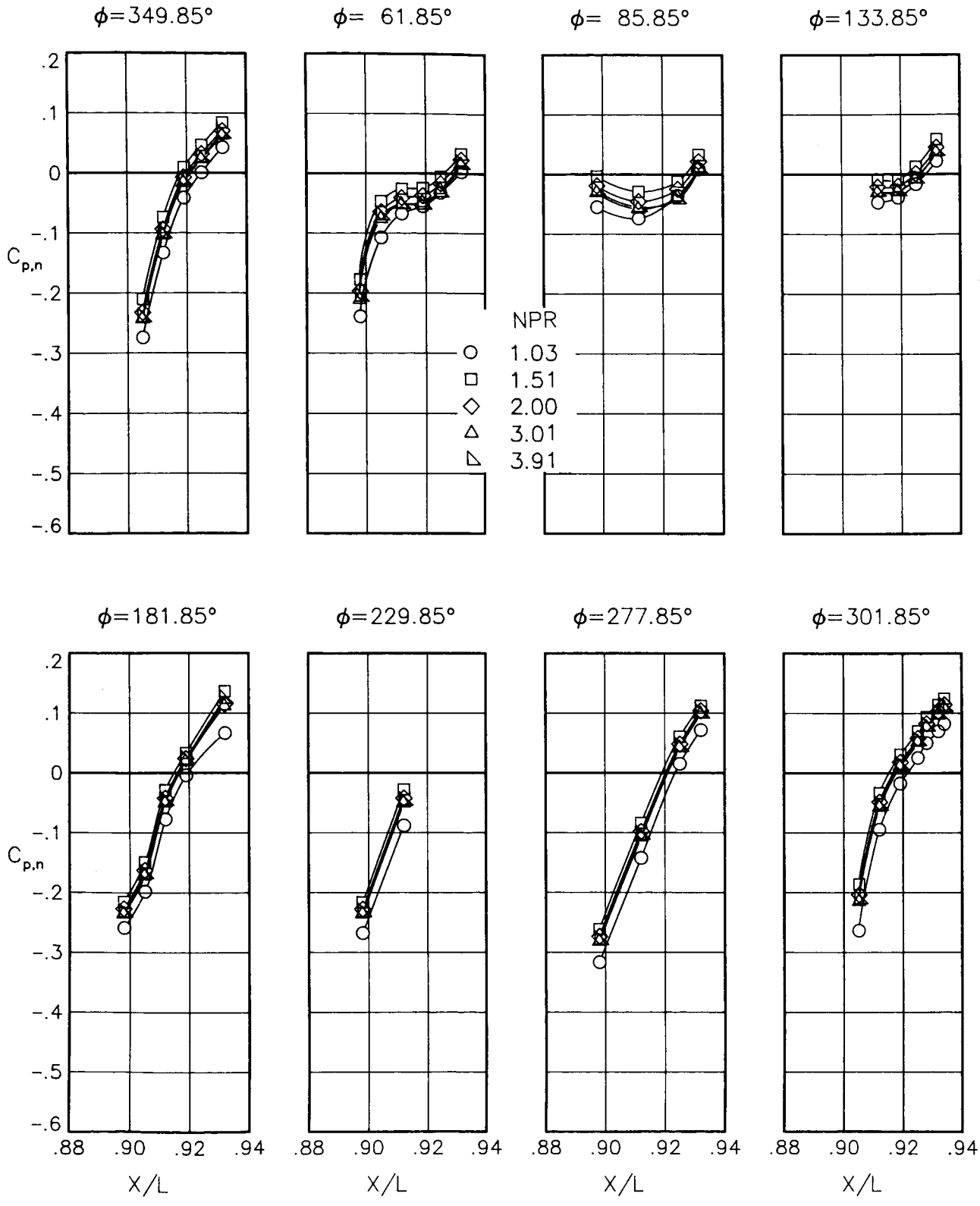

(c) M = 0.60; α = 3.00°.

Figure 68.- Continued.

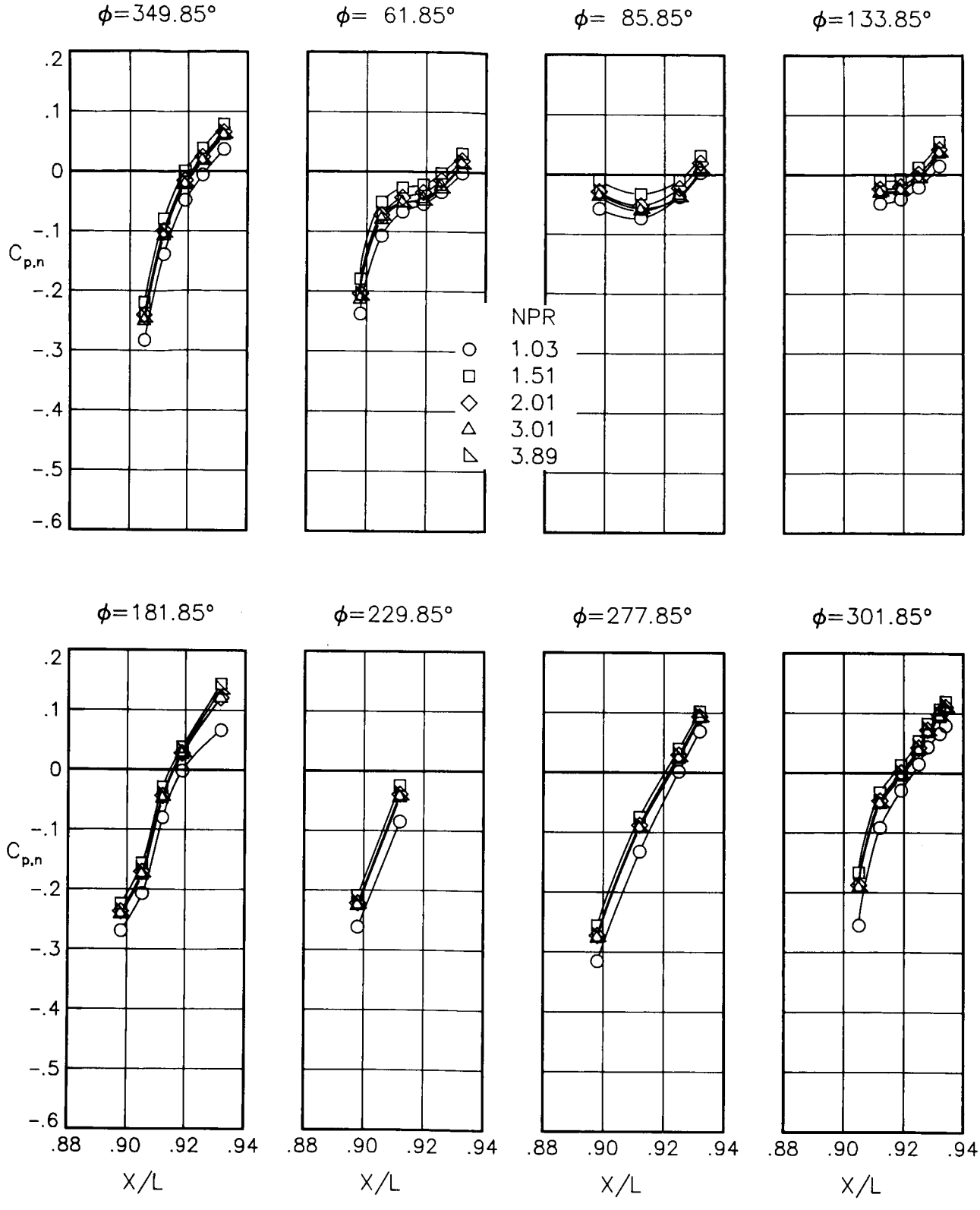

(d) M = 0.60; α = 5.00°.

Figure 68.- Continued.

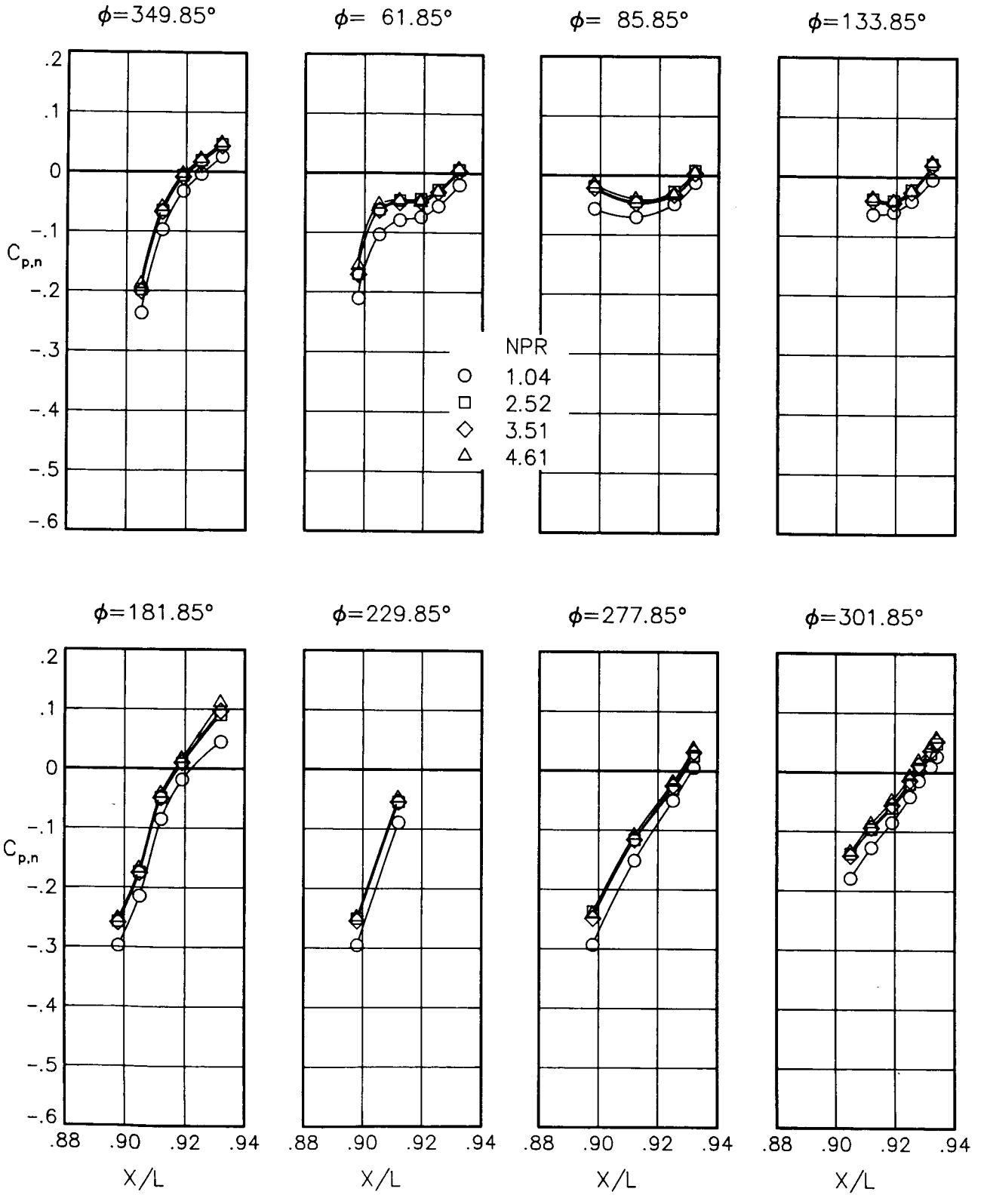

(e) M = 0.80; α = 0.00°.

Figure 68.- Continued.

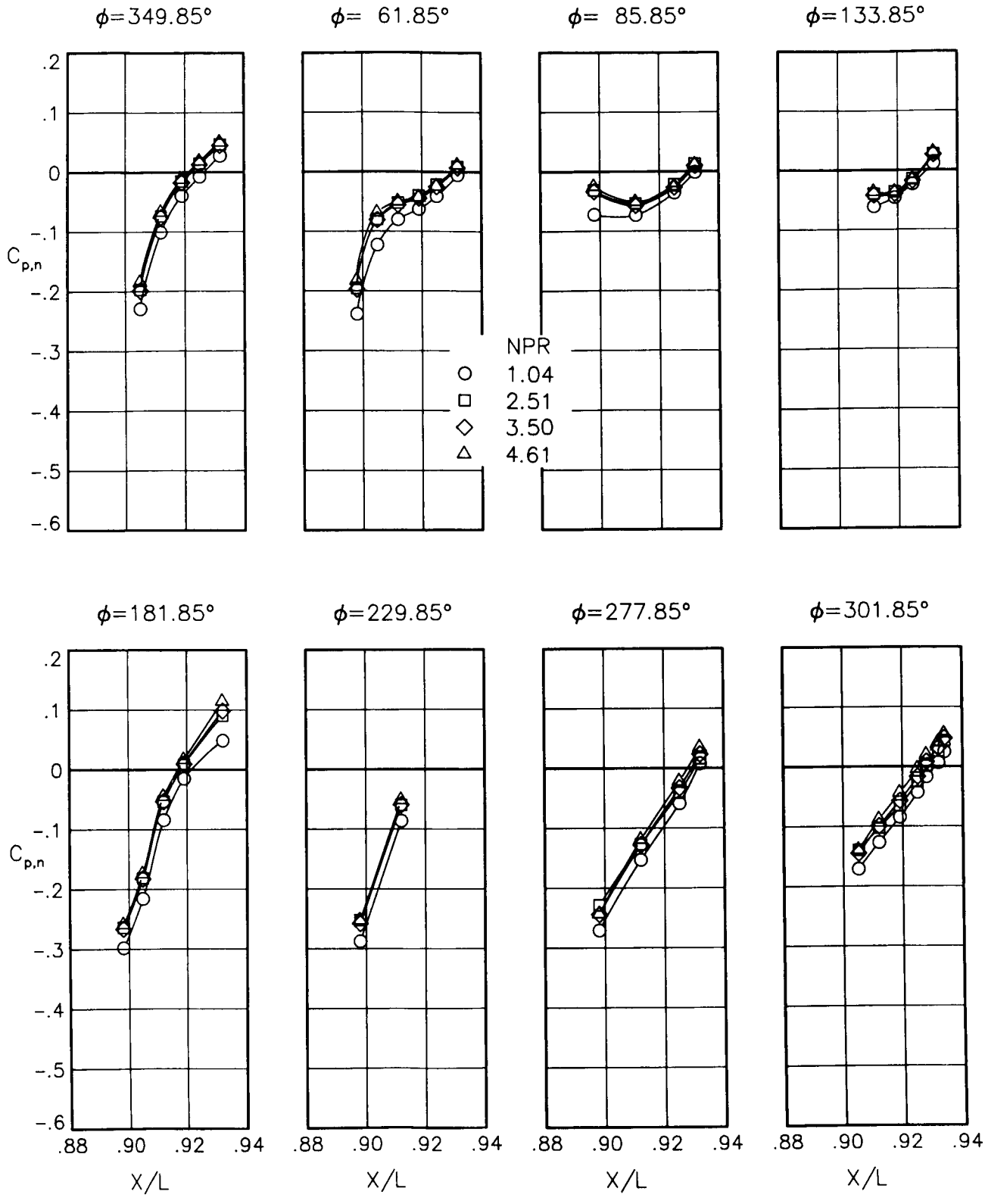

(f) M = 0.80; α = 1.00°.

Figure 68.- Continued.

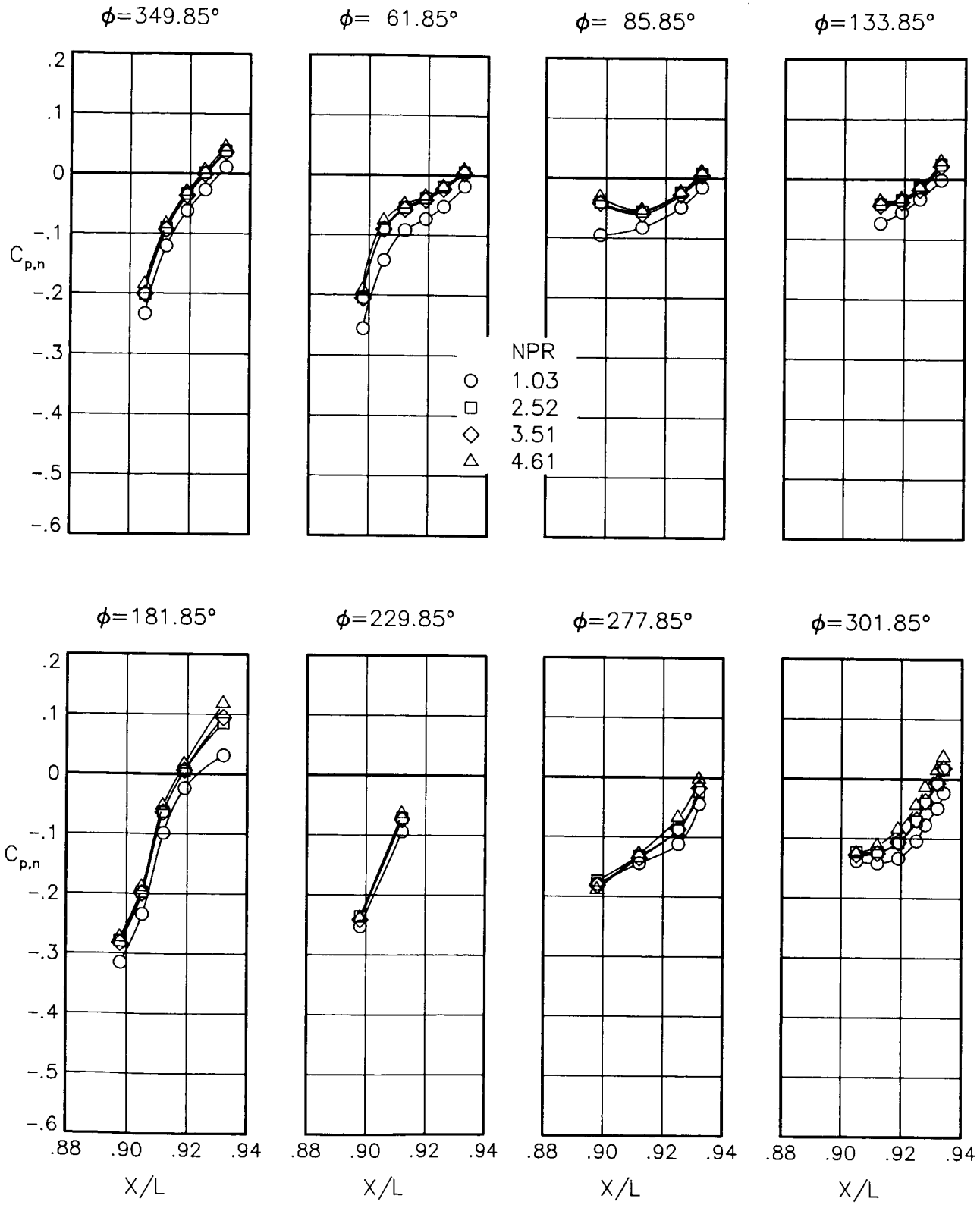

(g) M = 0.80; α = 3.00°.

Figure 68.- Continued.

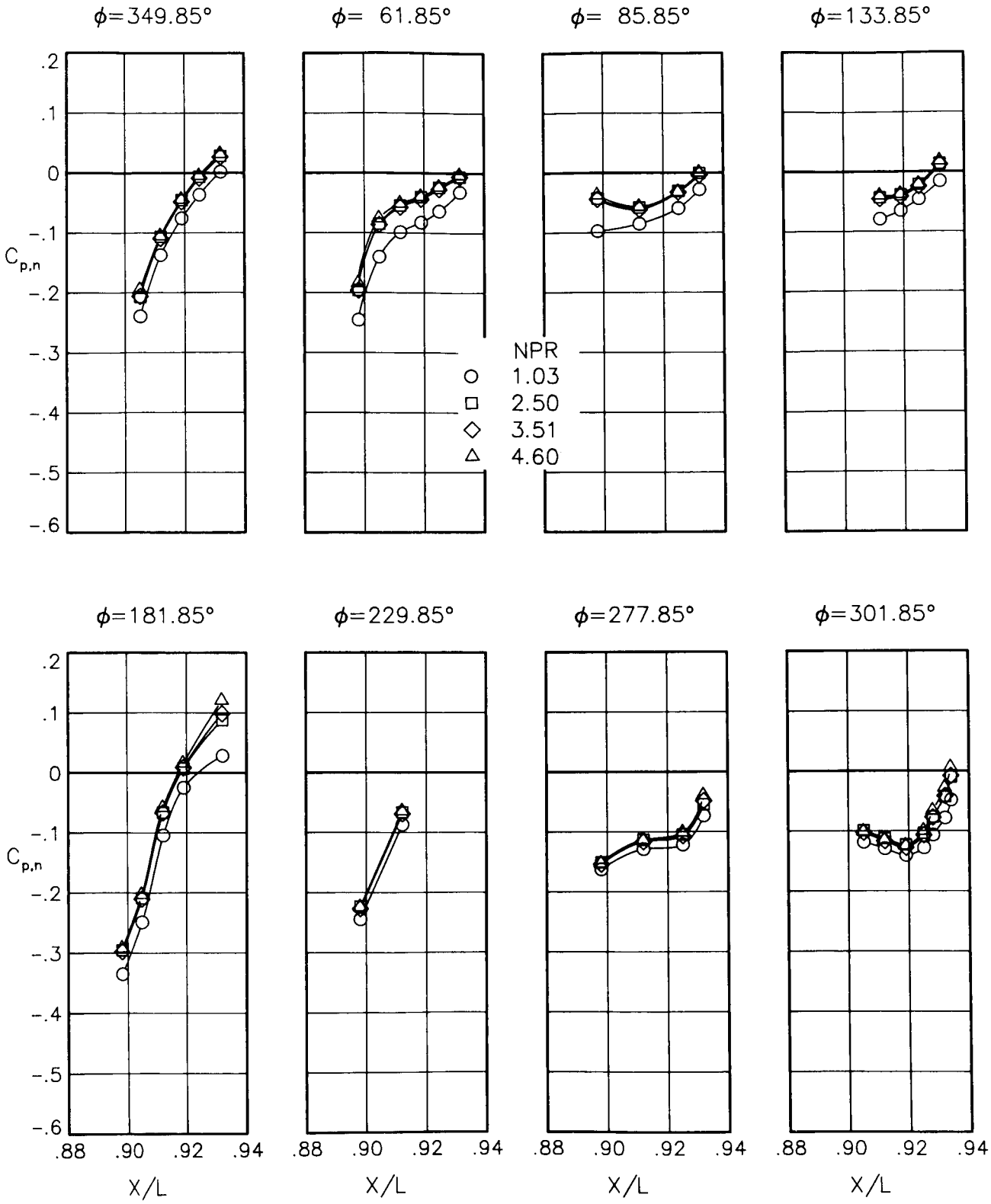

(h) M = 0.80; α = 5.00°.

Figure 68.- Continued.

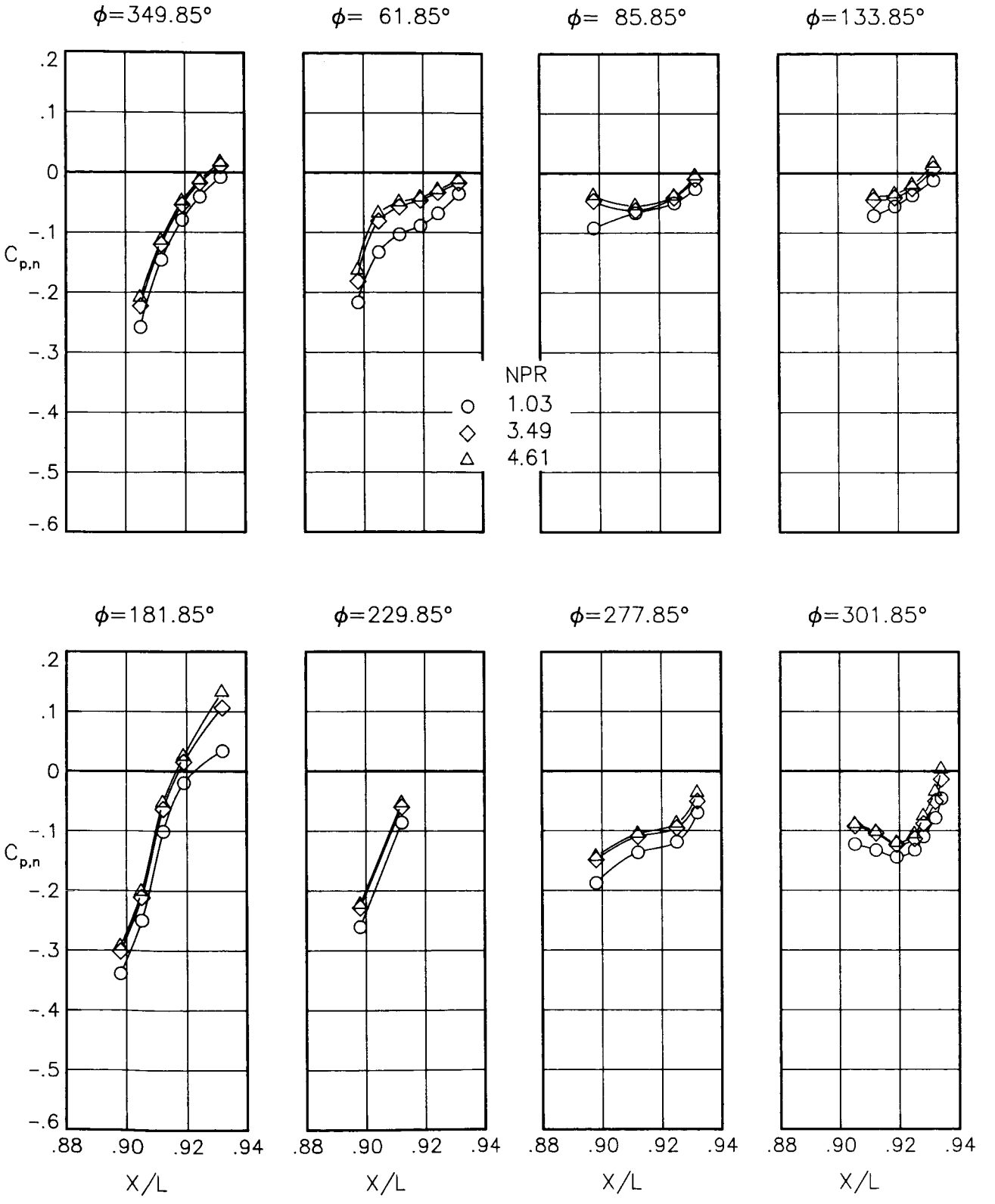

(i) M = 0.80; α = 7.00°.

Figure 68.- Continued.

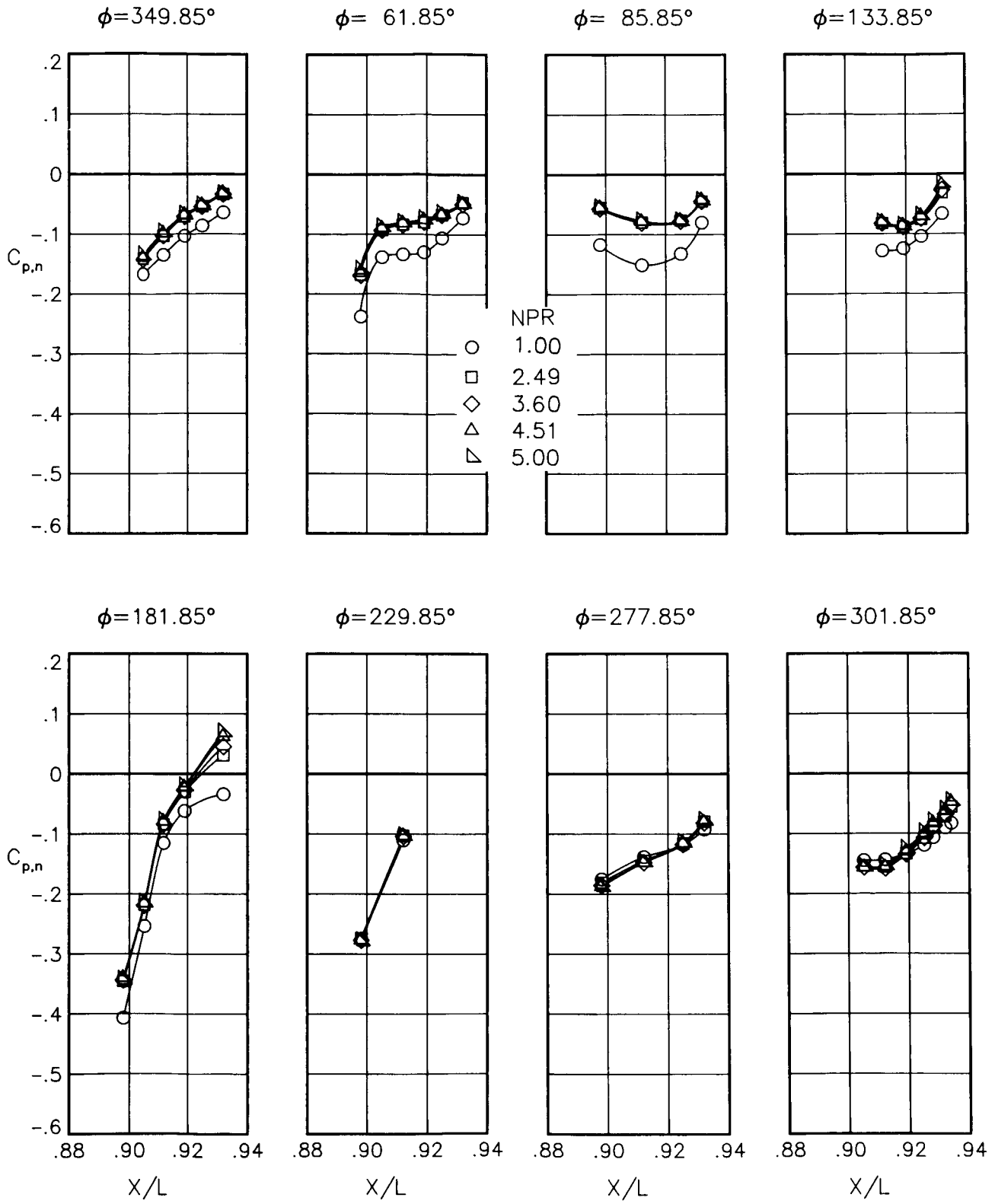

(j) M = 0.90; α = 0.00°.

Figure 68.- Continued.

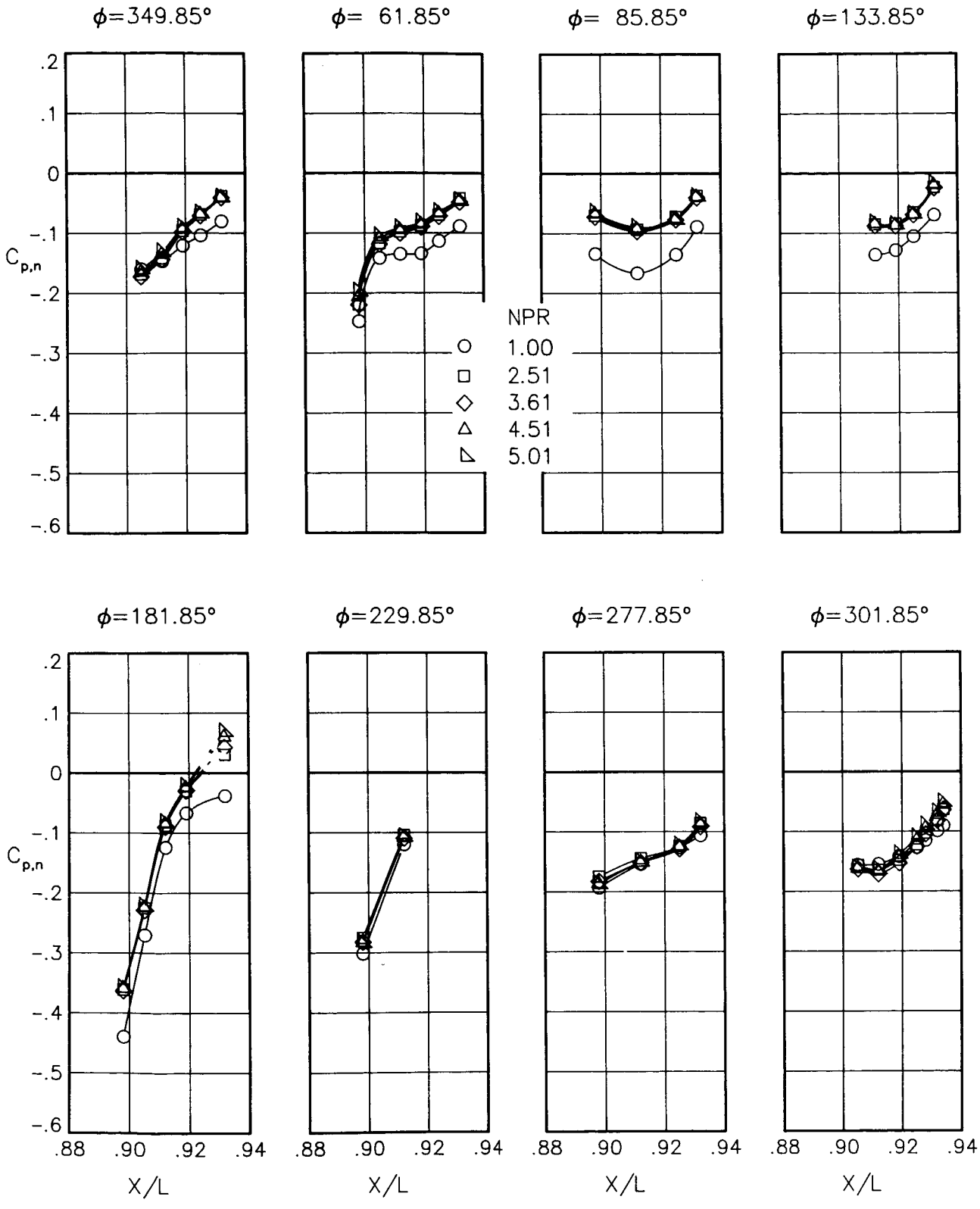

(k) M = 0.90; α = 1.00°.

Figure 68.- Continued.

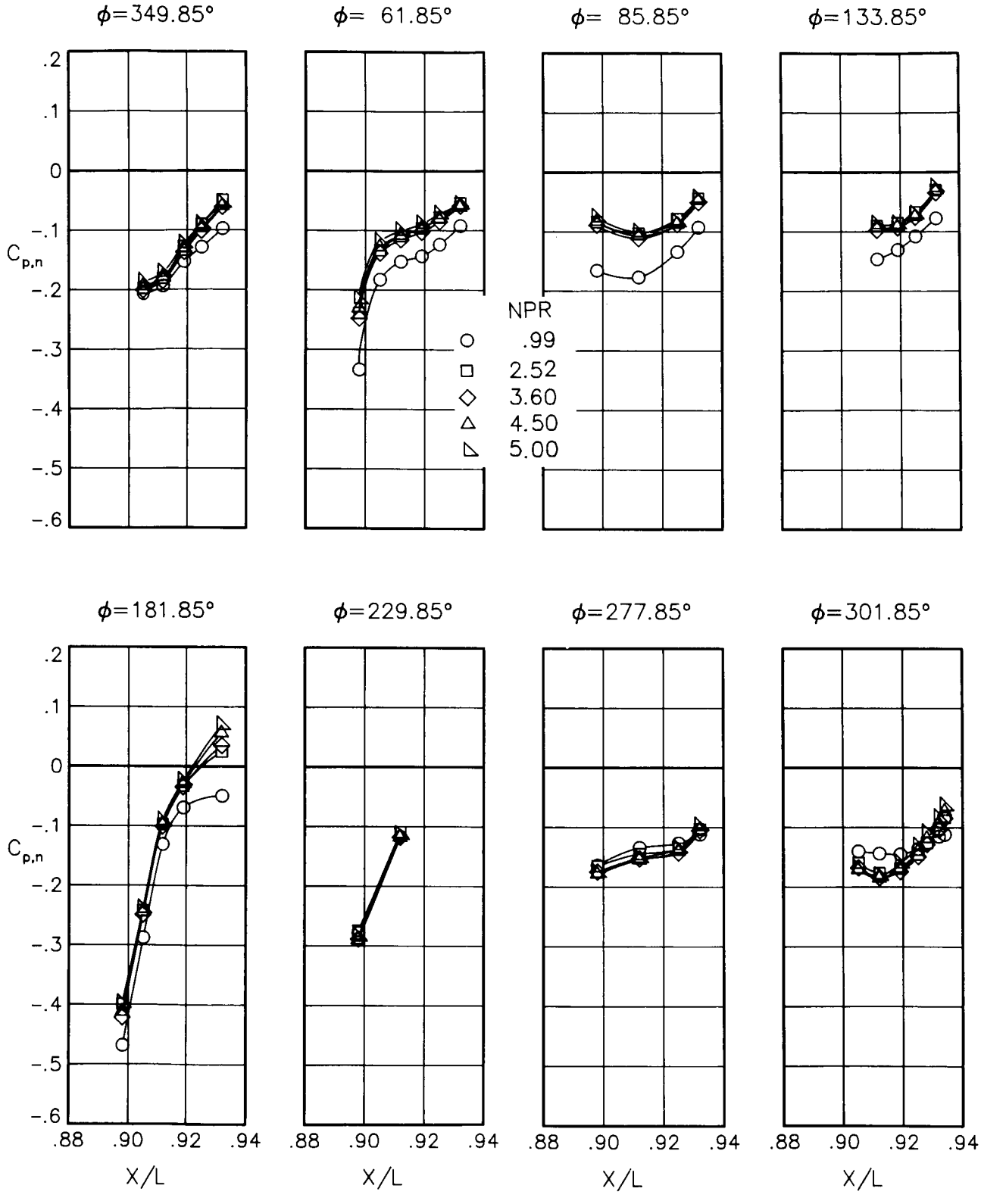

(1) M = 0.90; α = 3.00°.

Figure 68.- Continued.

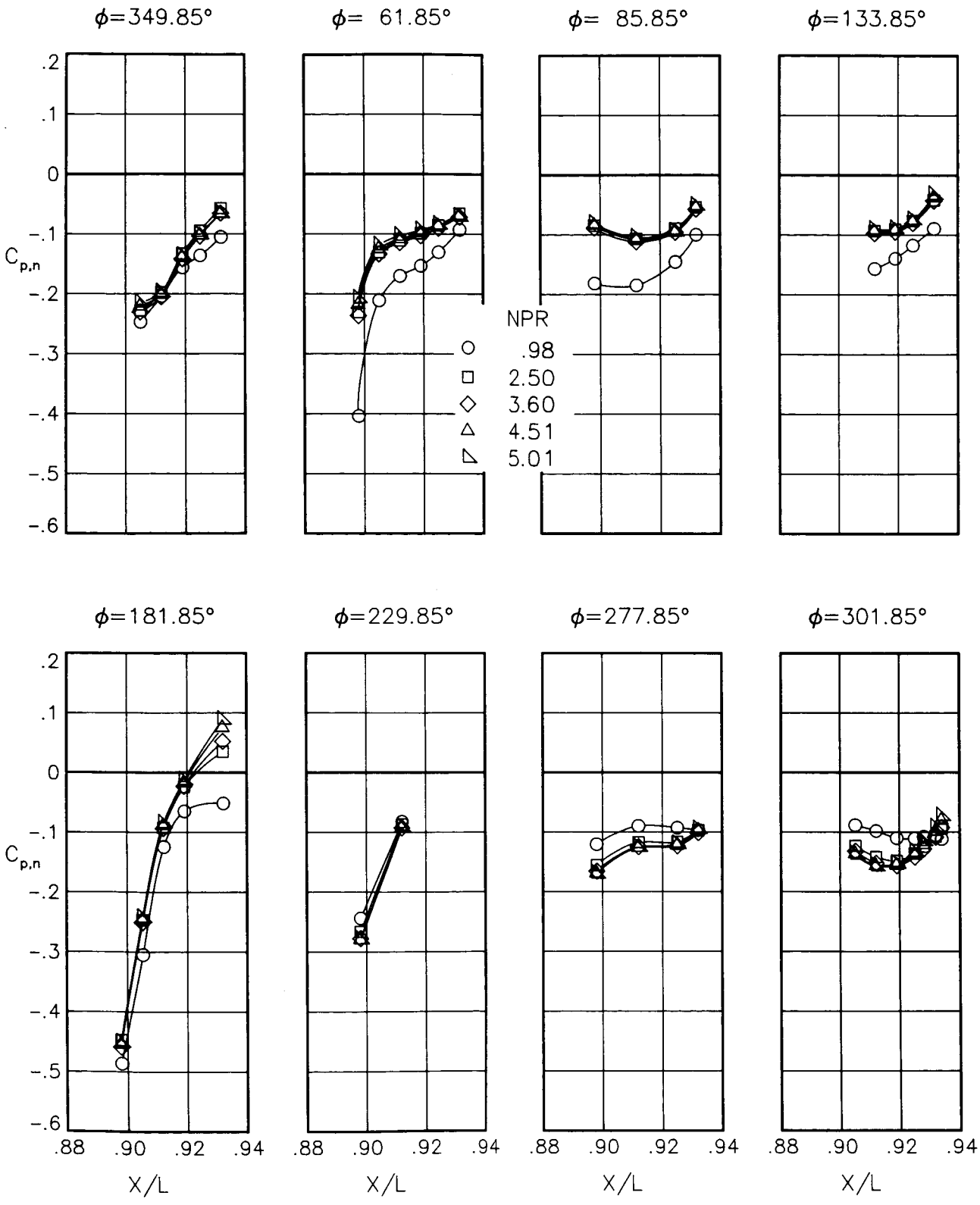

(m) M = 0.90; α = 6.00°.

Figure 68.- Concluded.

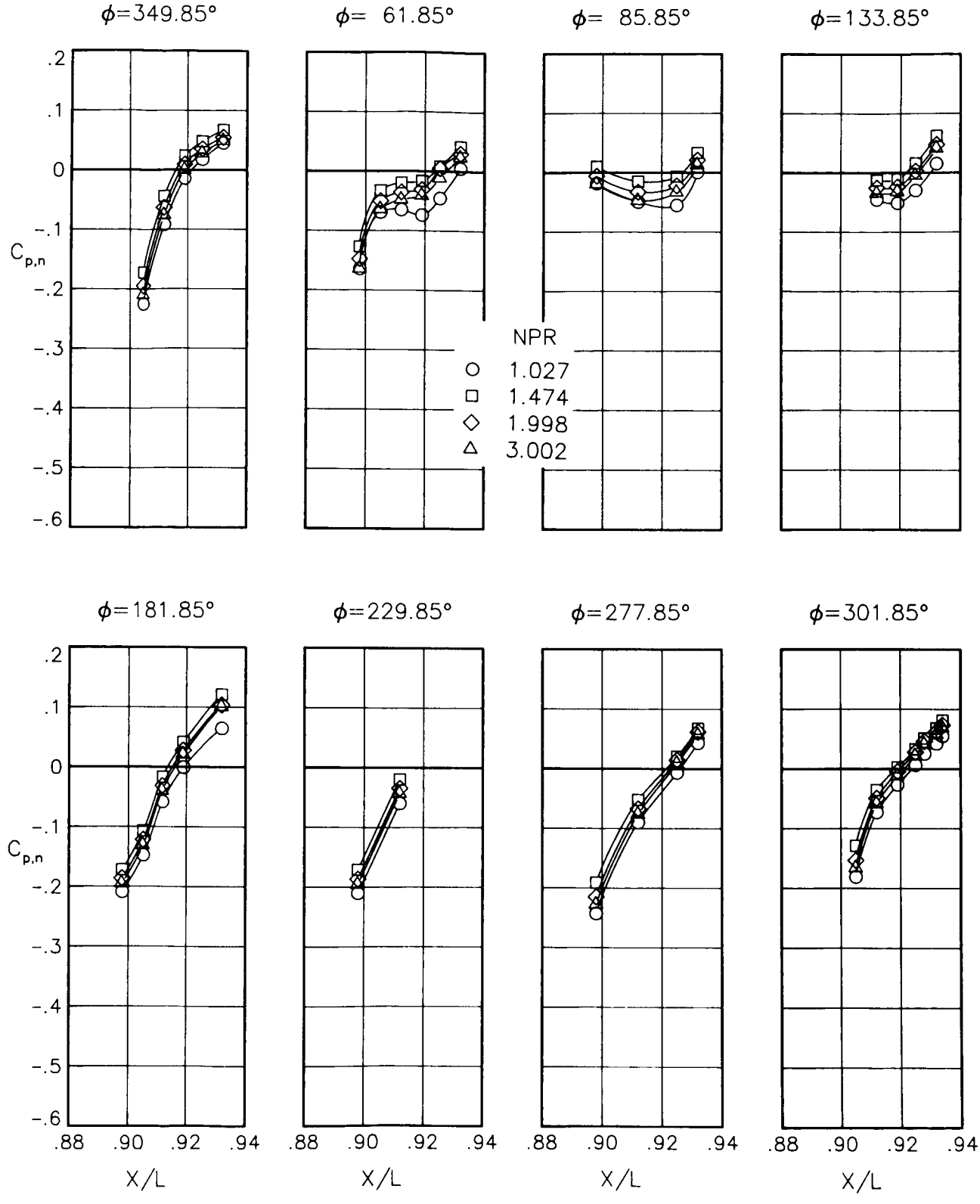

(a) M = 0.60; α = 0.00°.

Figure 69.- Static-pressure-coefficient distributions on nozzle for the model with all fuselage modifications except nose boom. β_n = 18.45°.

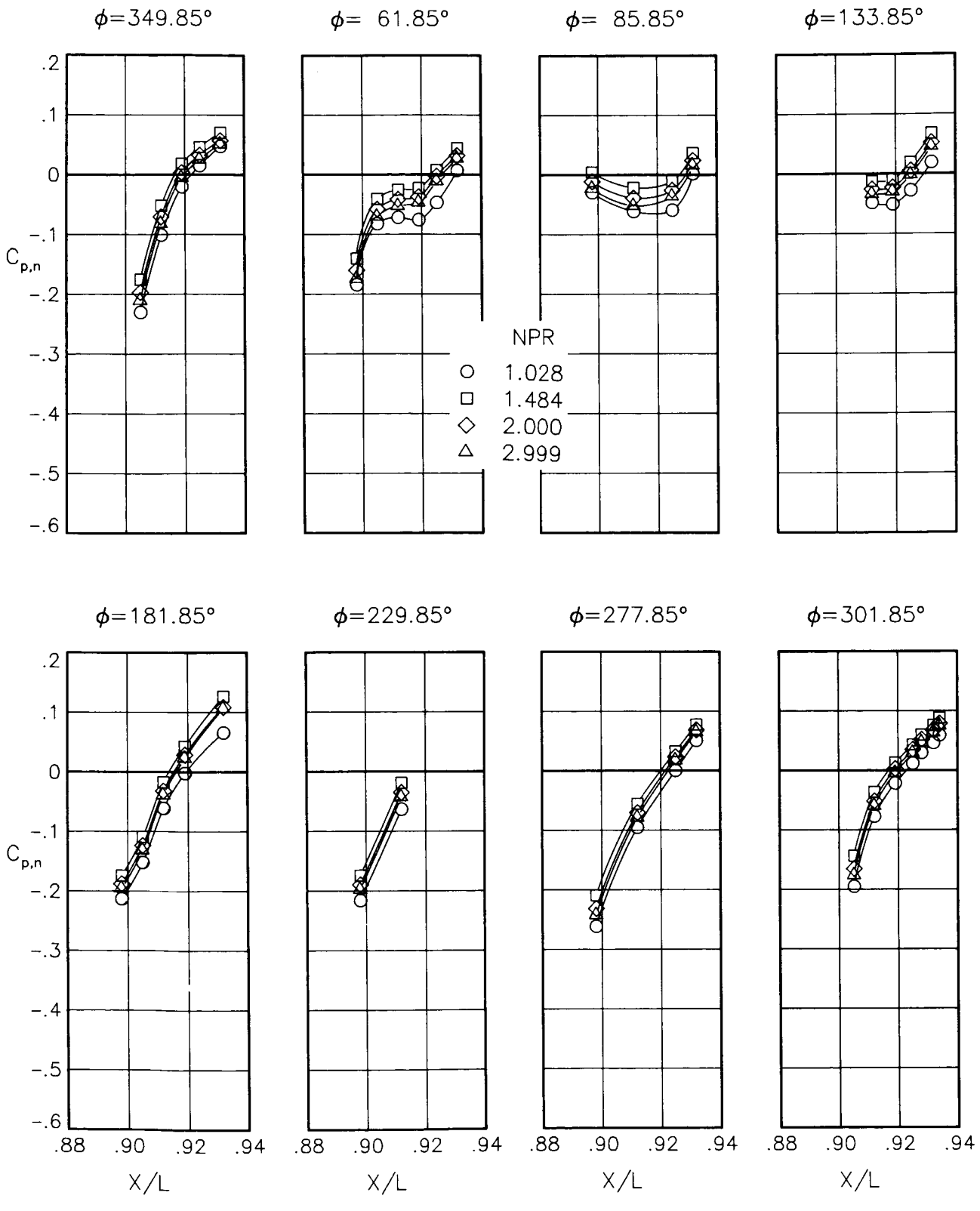

(b) M = 0.60; α = 1.00°.

Figure 69.- Continued.

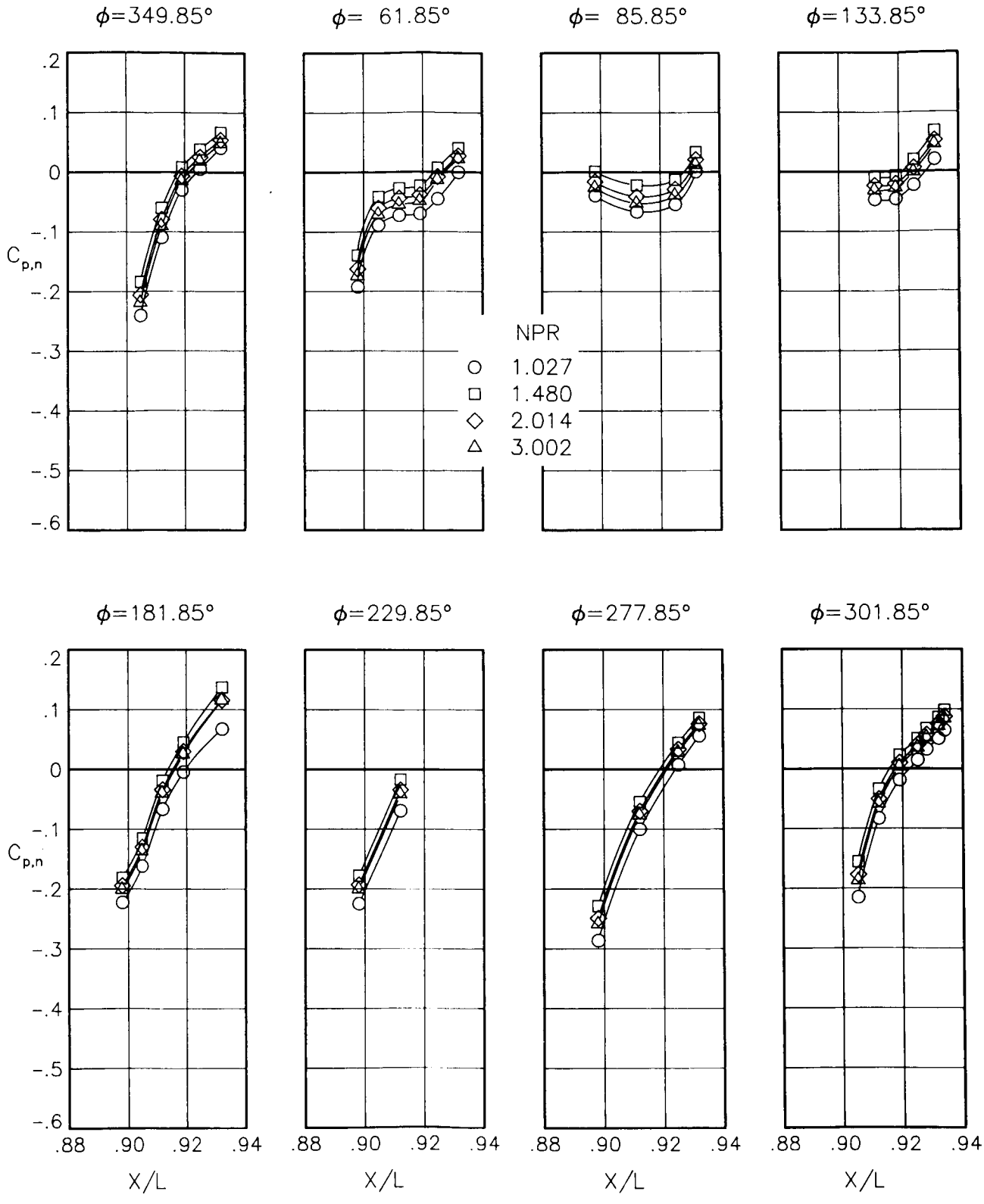

(c) M = 0.60; α = 3.00°.

Figure 69.- Continued.

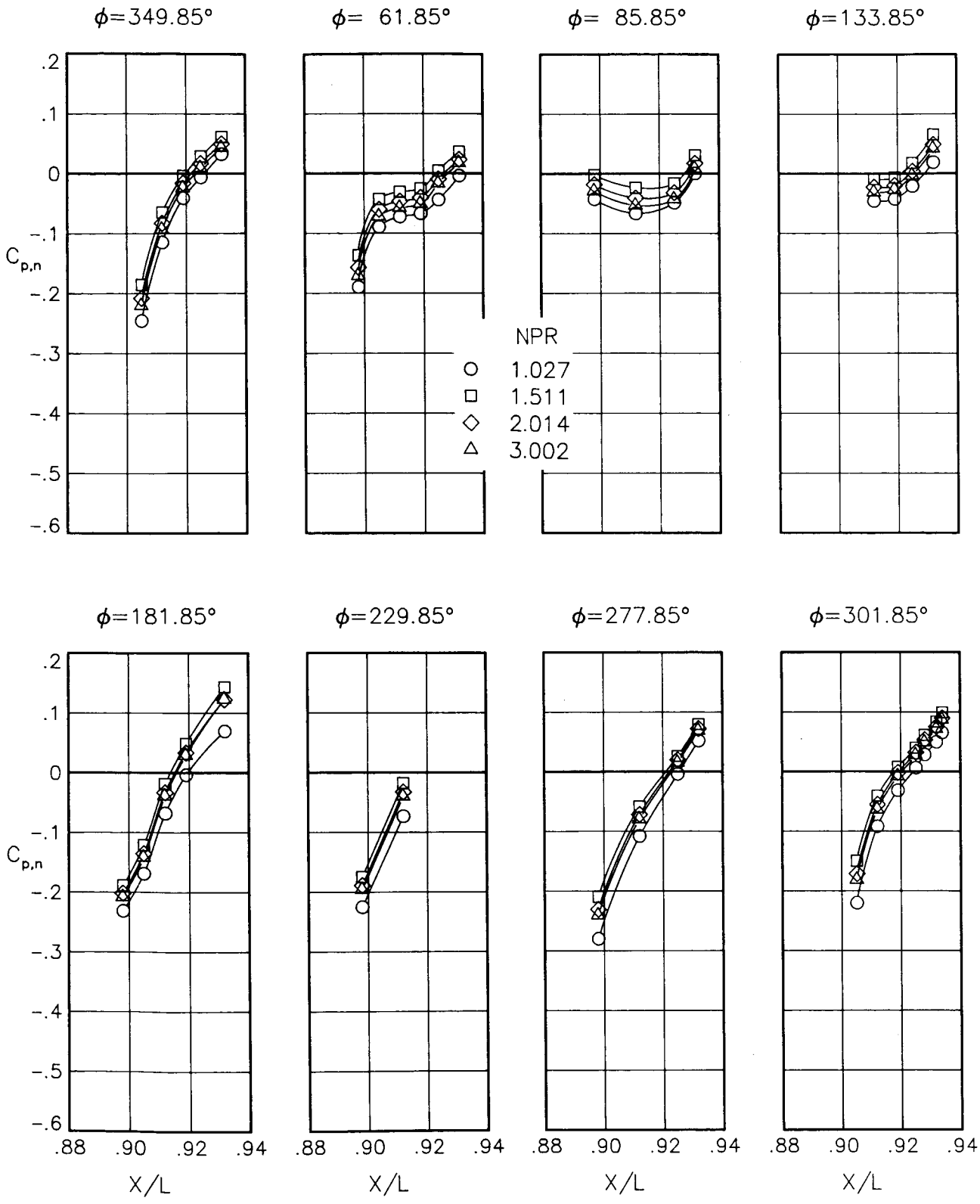

(d) M = 0.60; α = 5.00°.

Figure 69.- Continued.

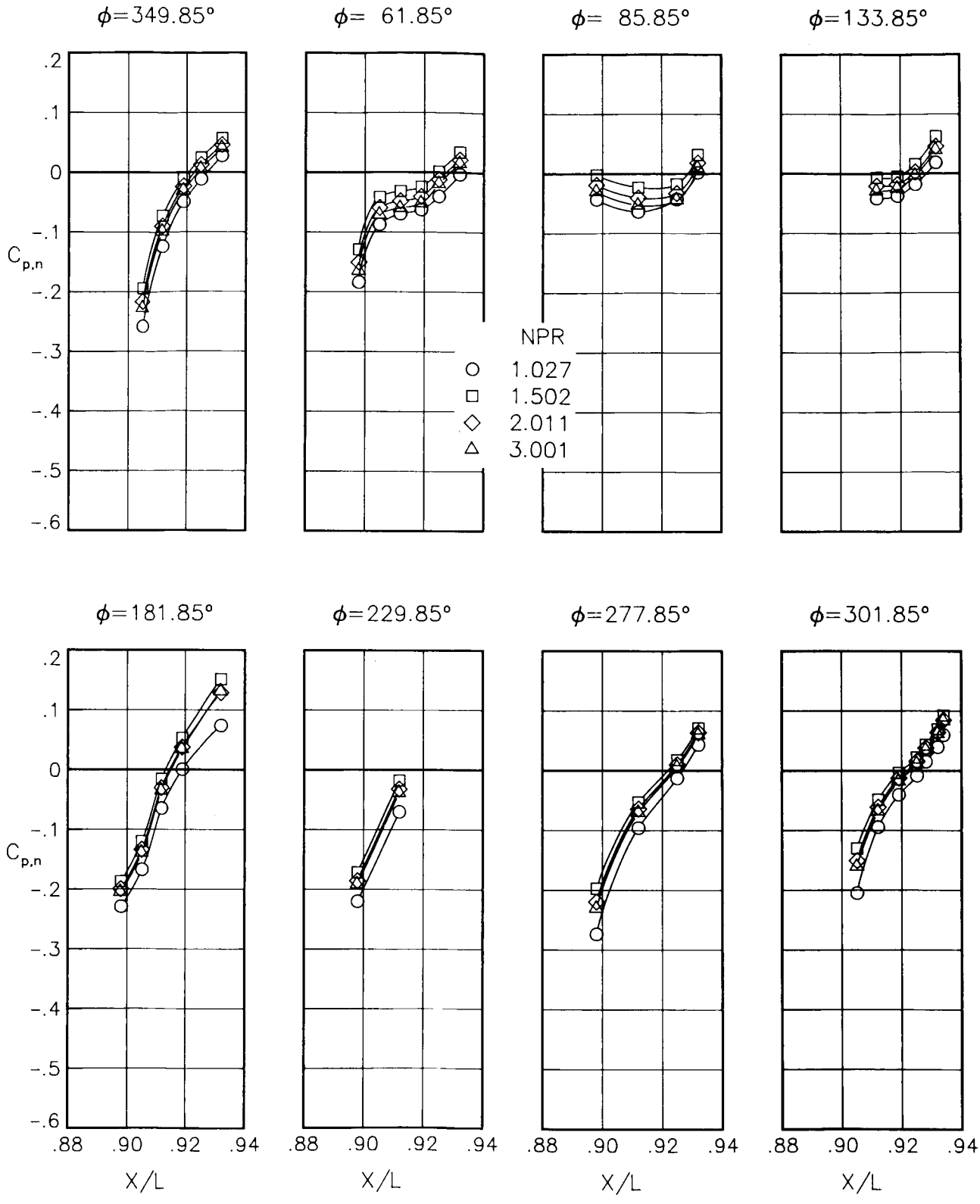

(e) M = 0.60; α = 7.00°.

Figure 69.- Continued.

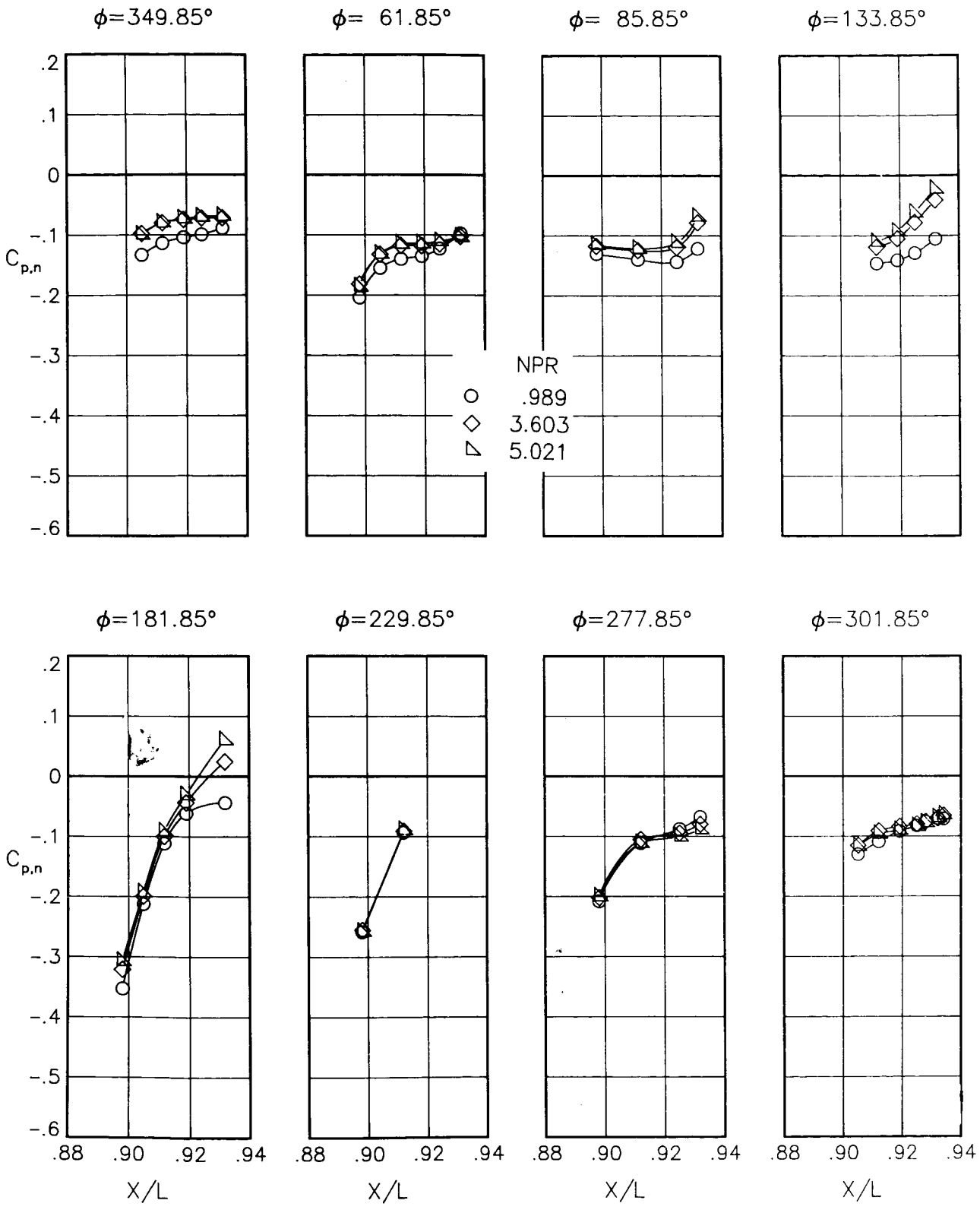

(f) M = 0.90; α = 0.00°.

Figure 69.- Continued.

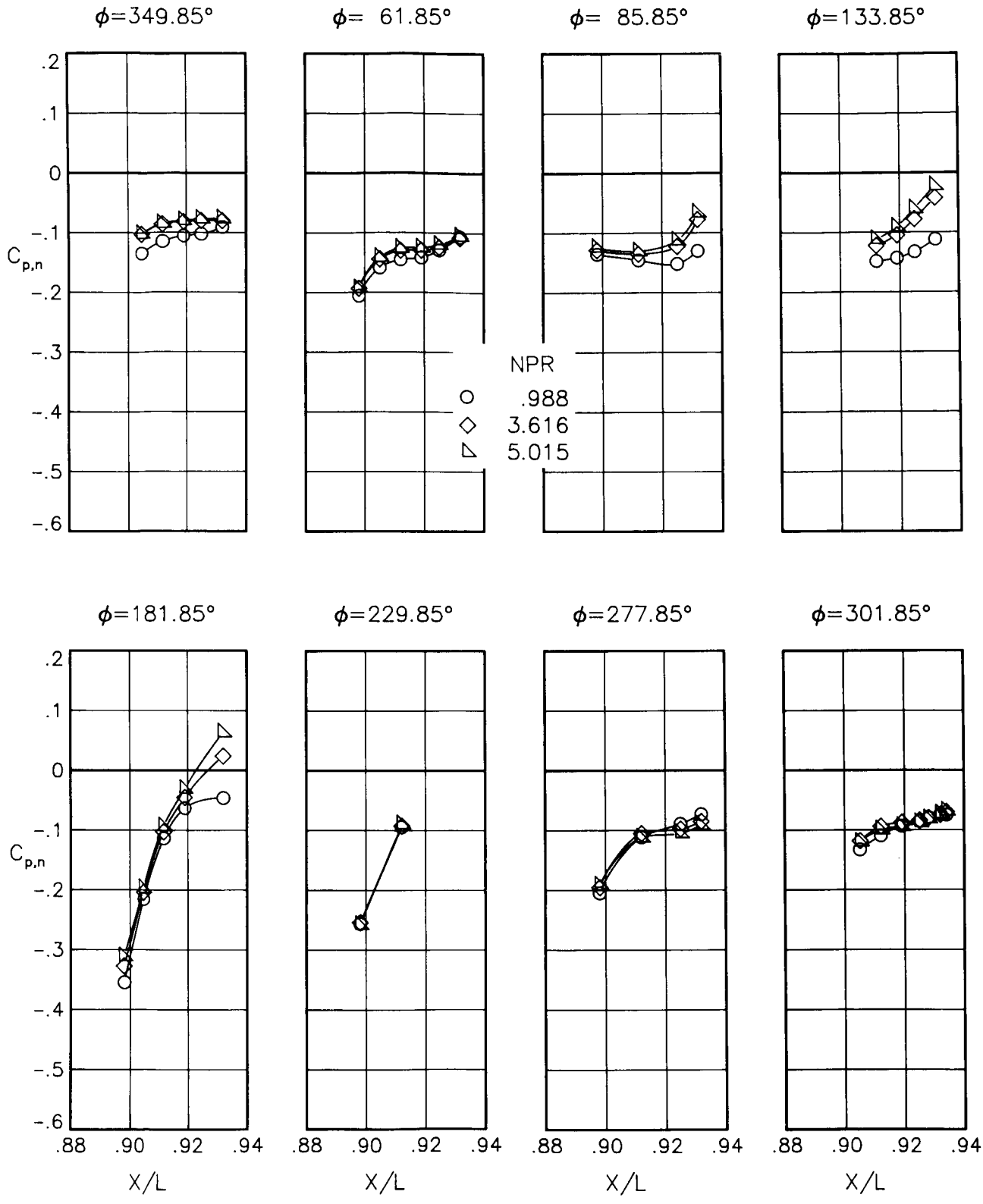

(g) M = 0.90; α = 1.00°.

Figure 69.- Continued.

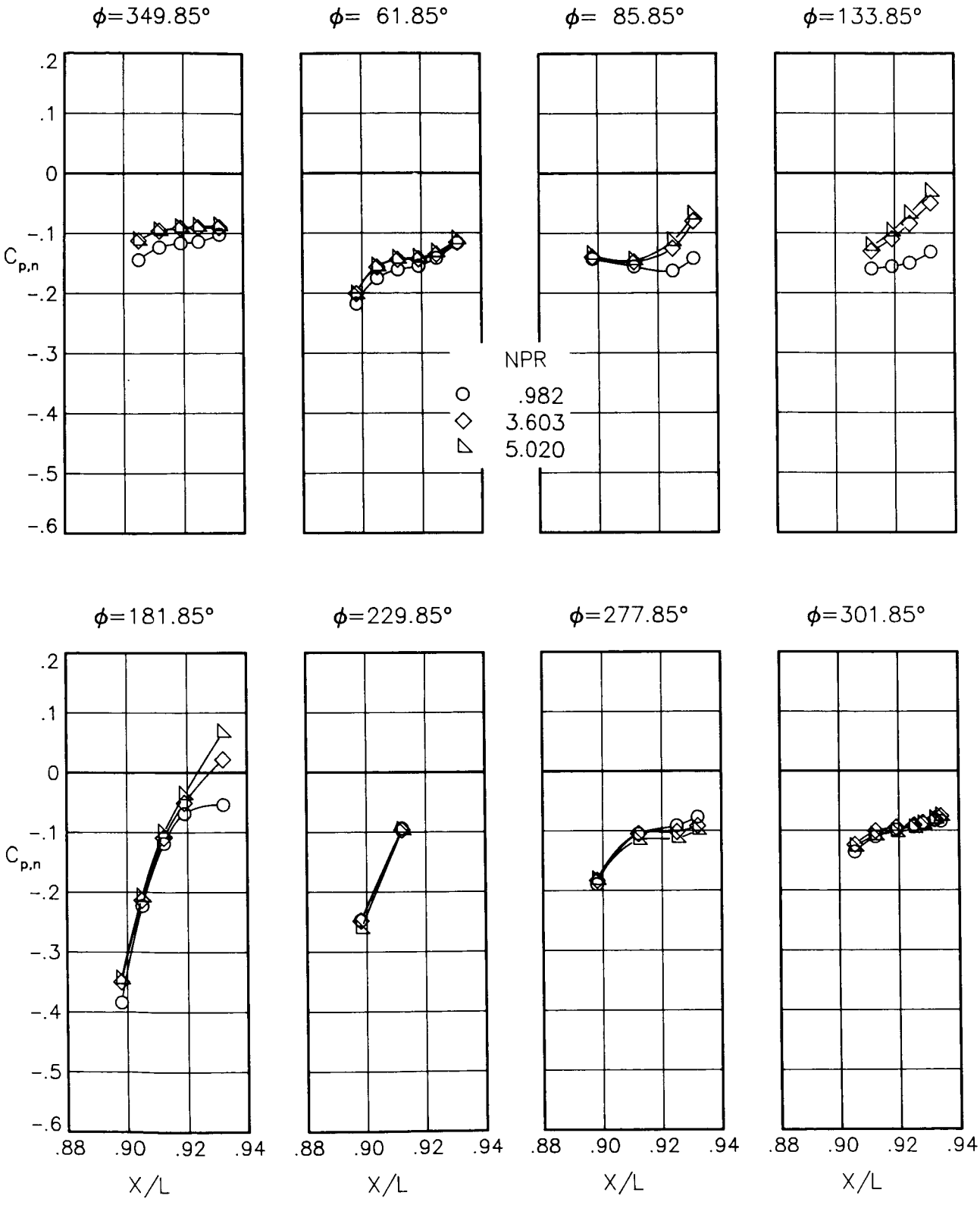

(h) M = 0.90; α = 3.00°.

Figure 69.- Continued.

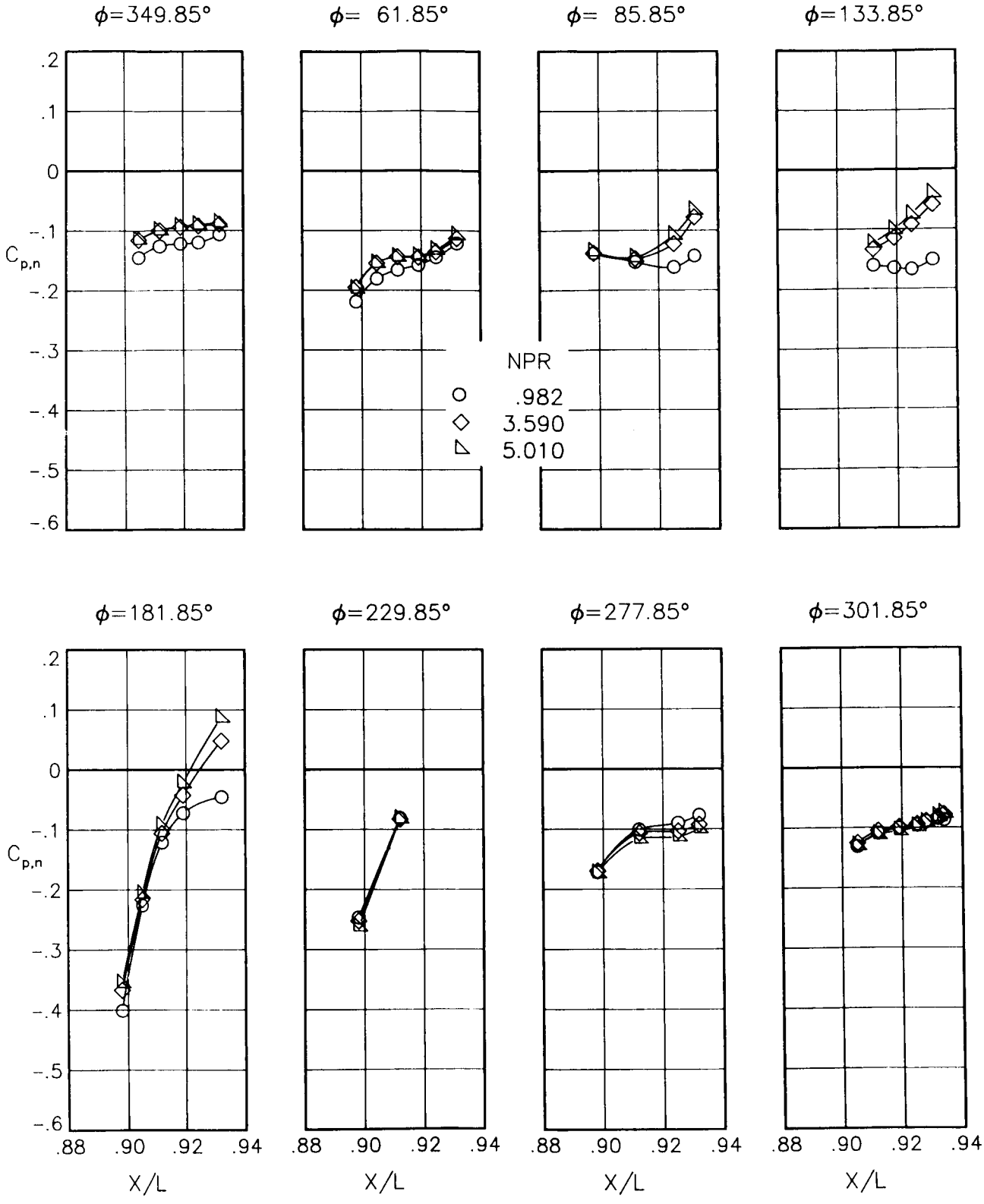

(i) M = 0.90; α = 7.00°.

Figure 69.- Concluded.

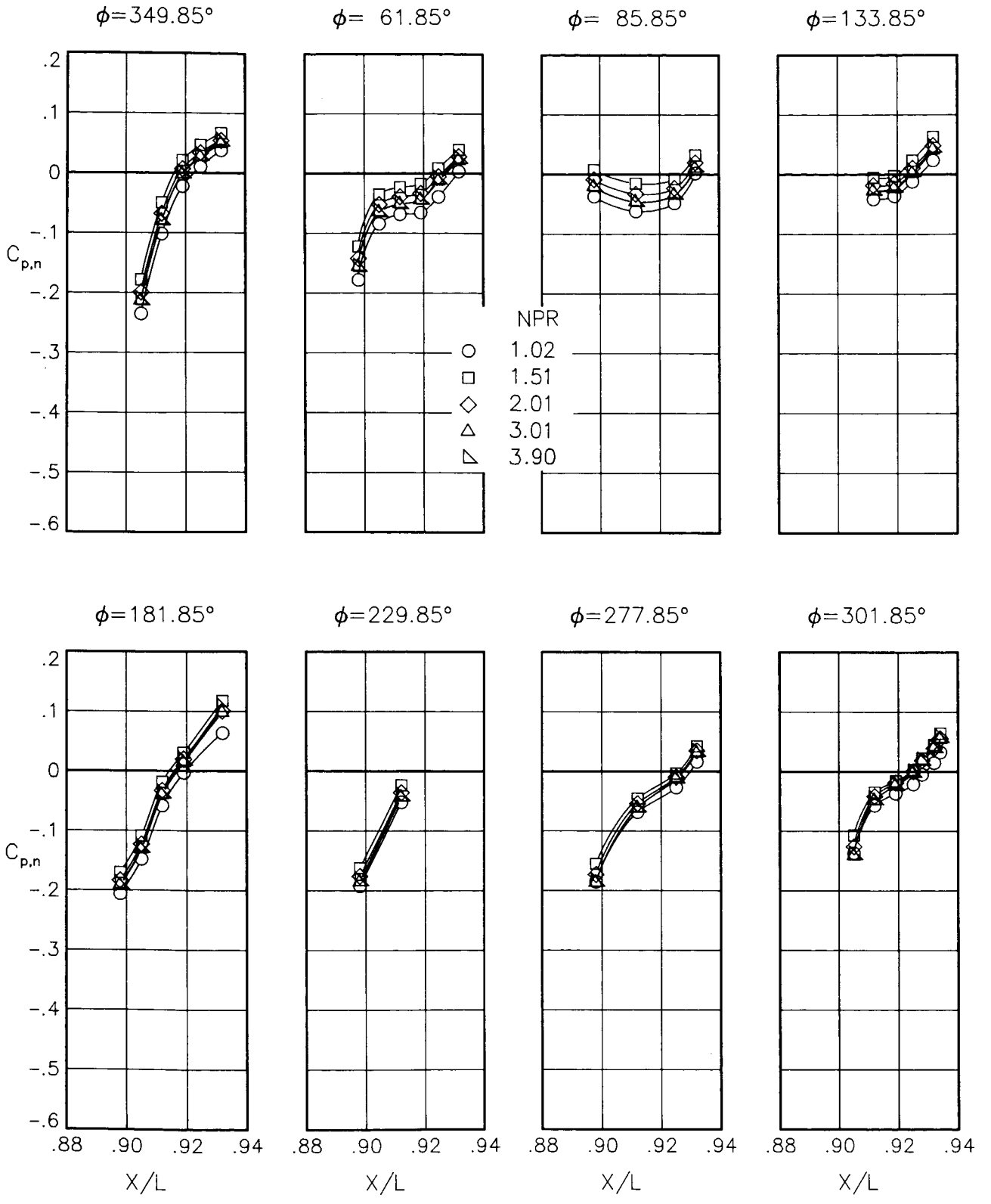

(a) M = 0.60; α = 0.00°.

Figure 70.- Static-pressure-coefficient distributions on nozzle for the model with nose booms, actuator fairings, A/B vents, and nozzle steps (no rakes). β_n = 18.45°.

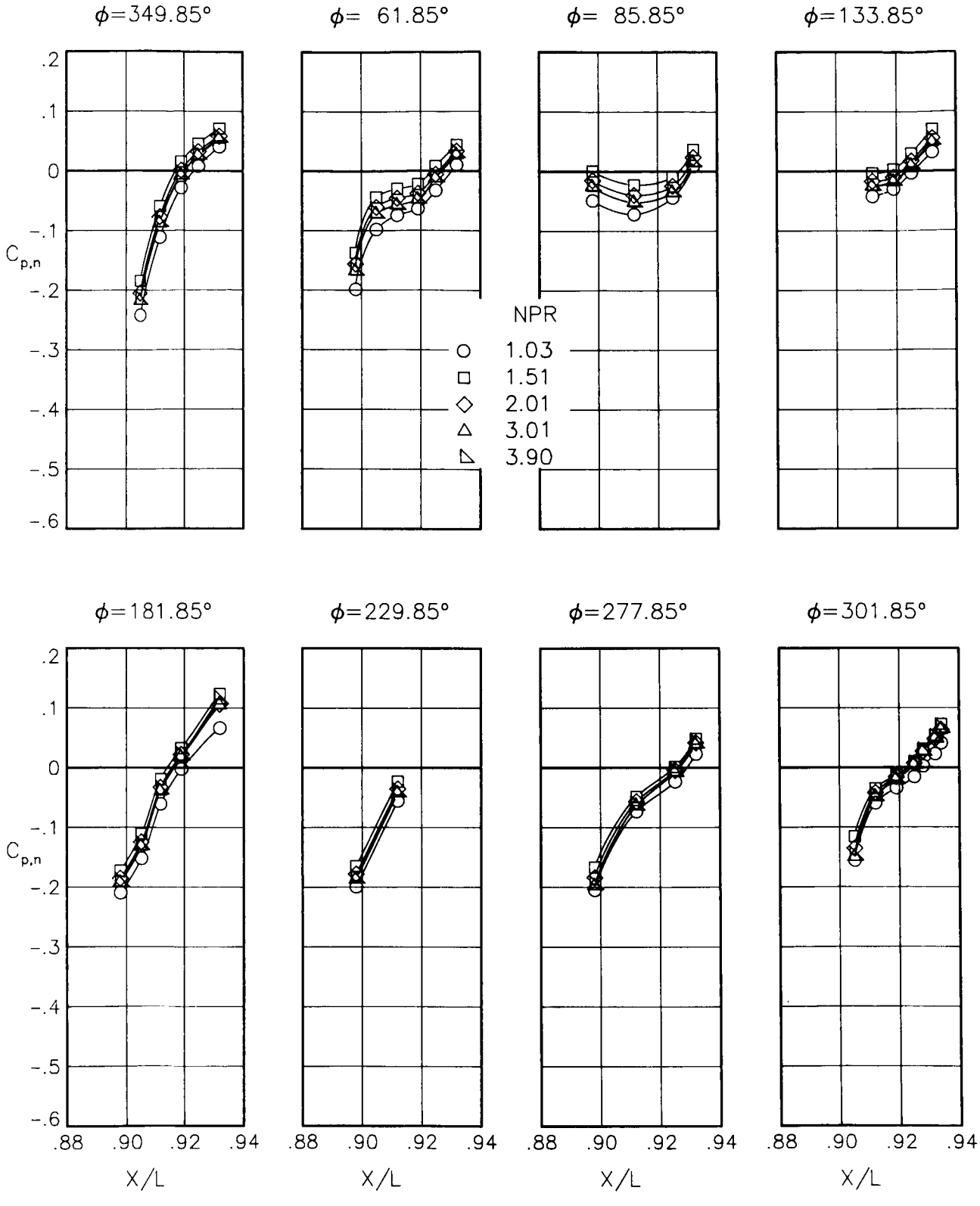

(b) M = 0.60; α = 1.00°.

Figure 70.- Continued.

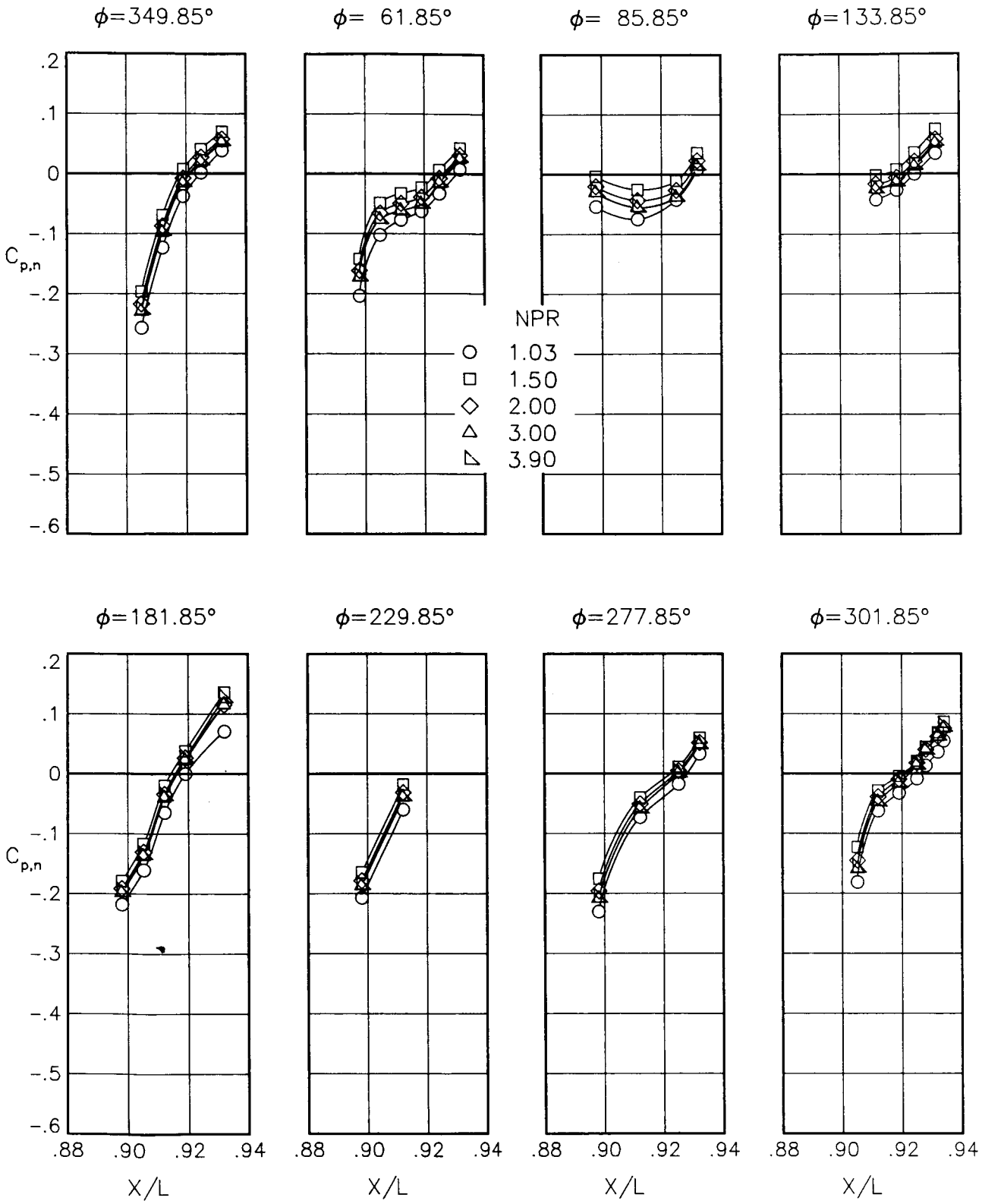

(c) M = 0.60; α = 3.00°.

Figure 70.- Continued.

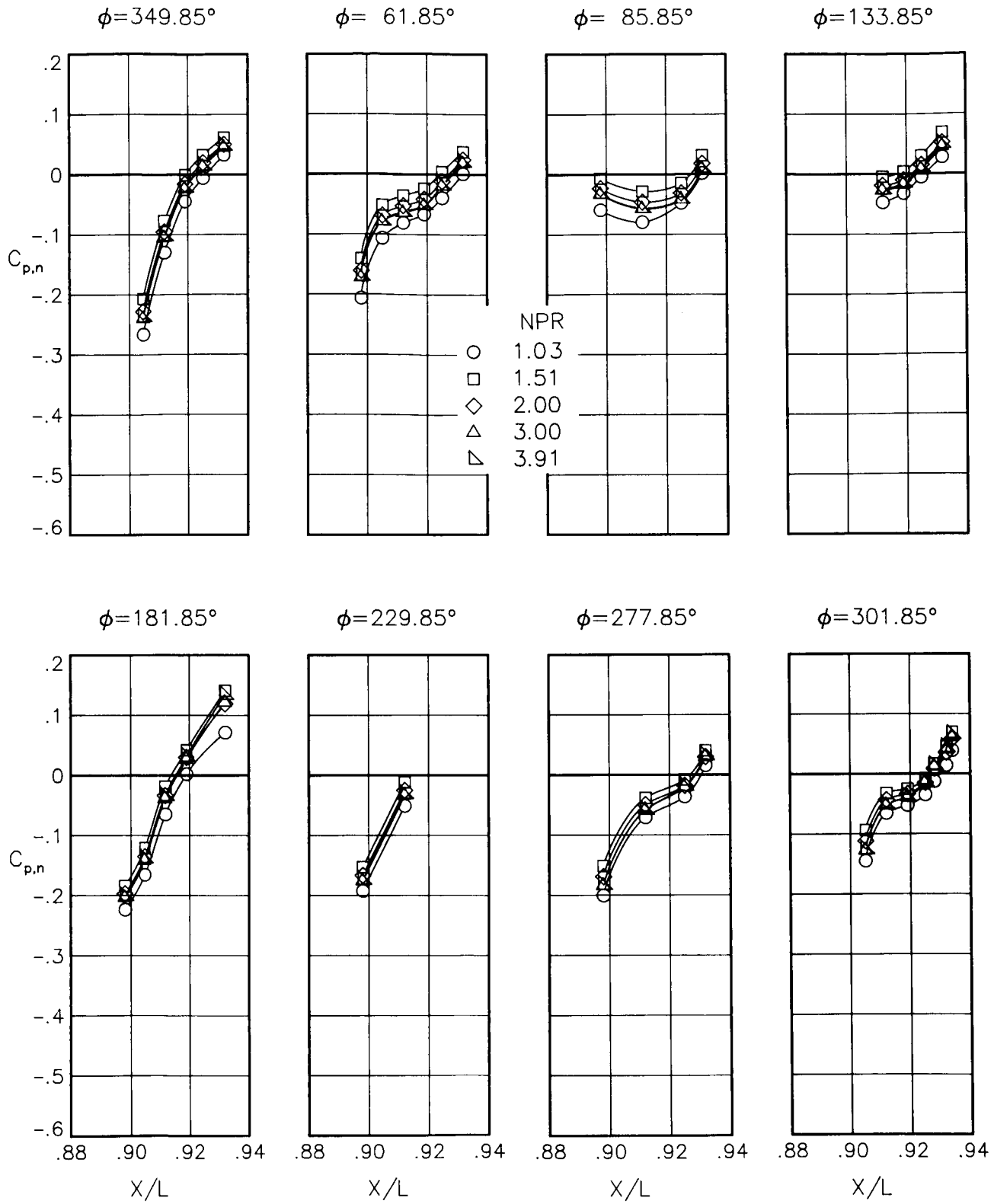

(d) M = 0.60; α = 5.00°.

Figure 70.- Continued.

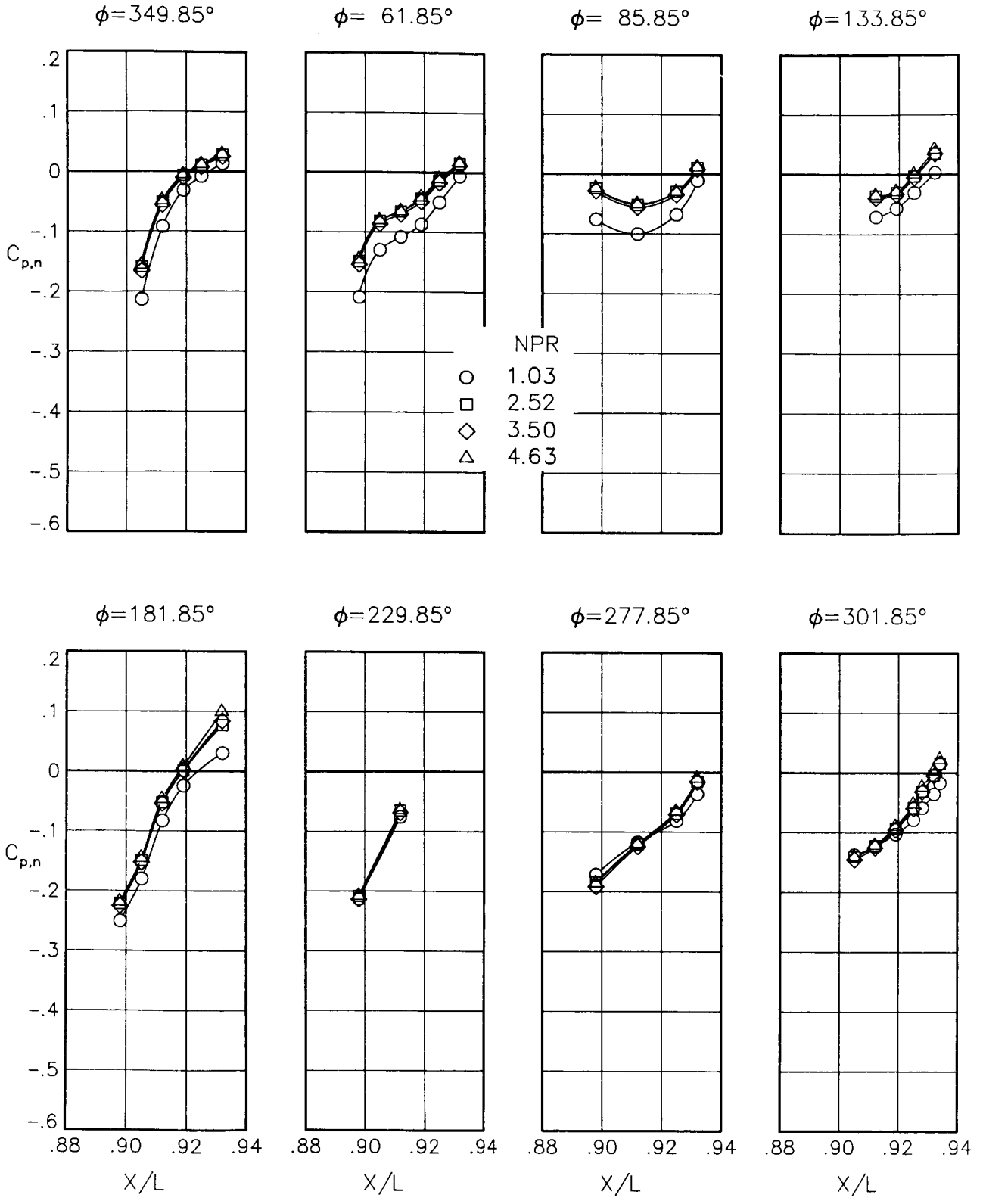

(e) M = 0.80; α = 0.00°.

Figure 70.- Continued.

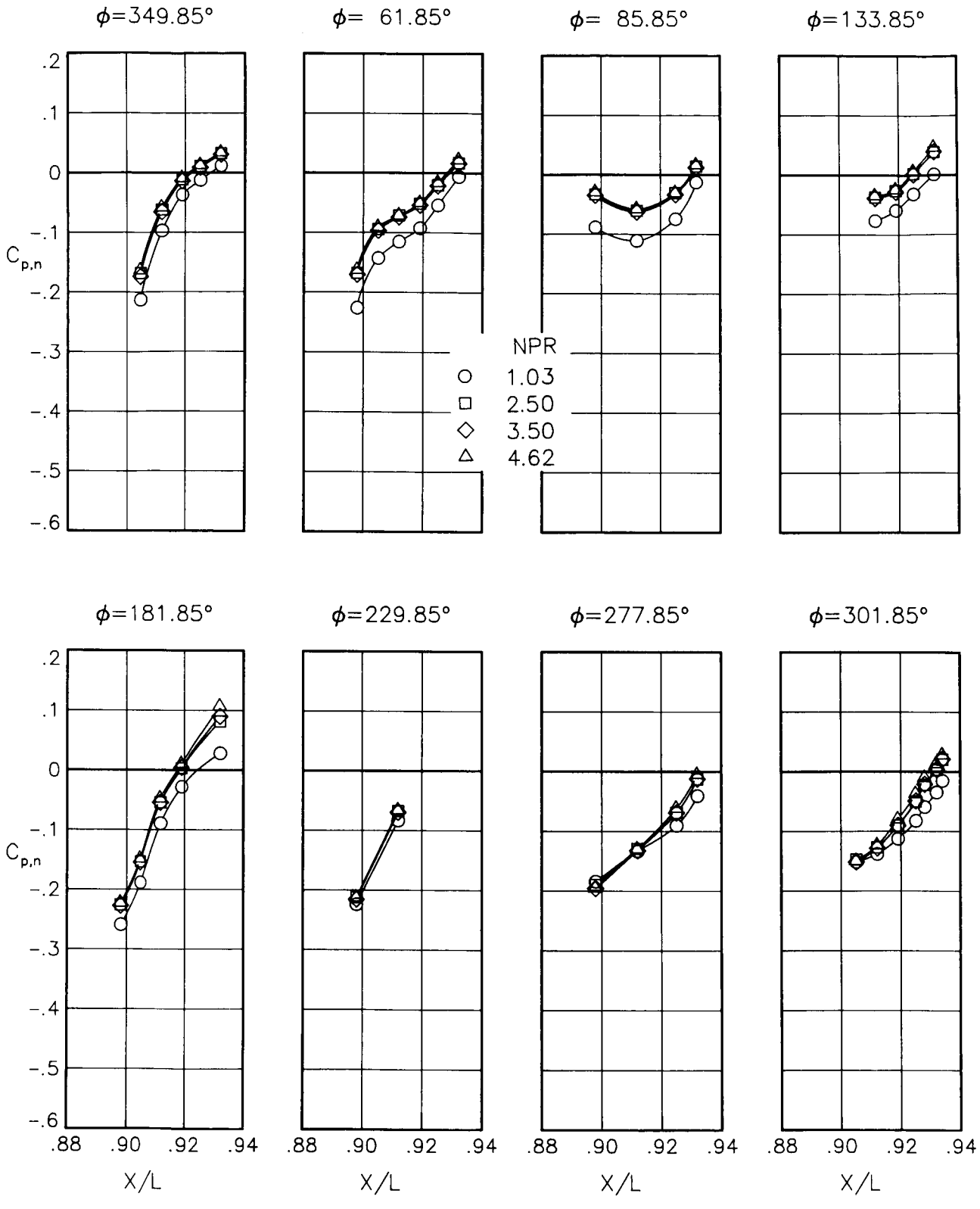

(f) M = 0.80; α = 1.00°.

Figure 70.- Continued.

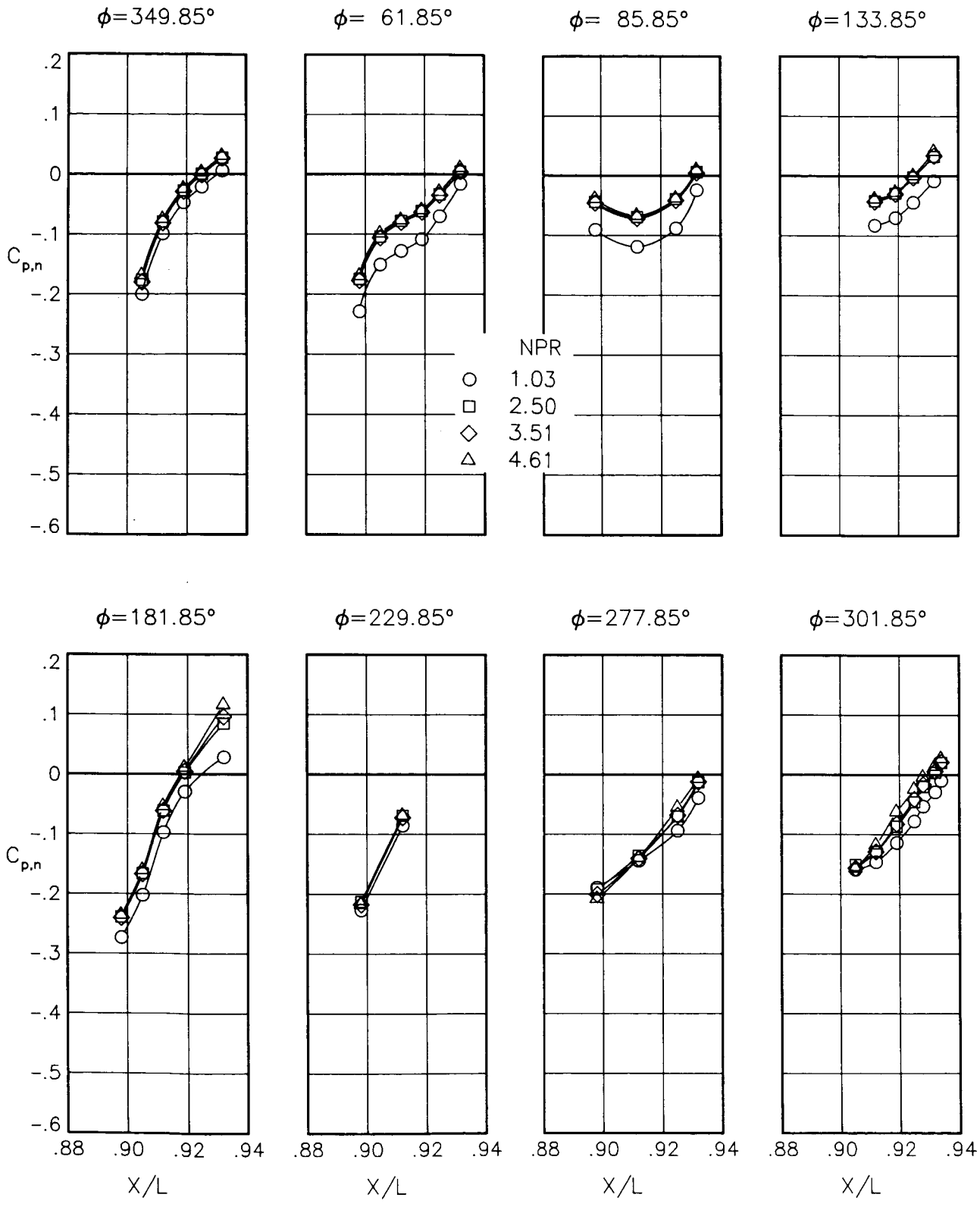

(g) M = 0.80; α = 3.00°.

Figure 70.- Continued.

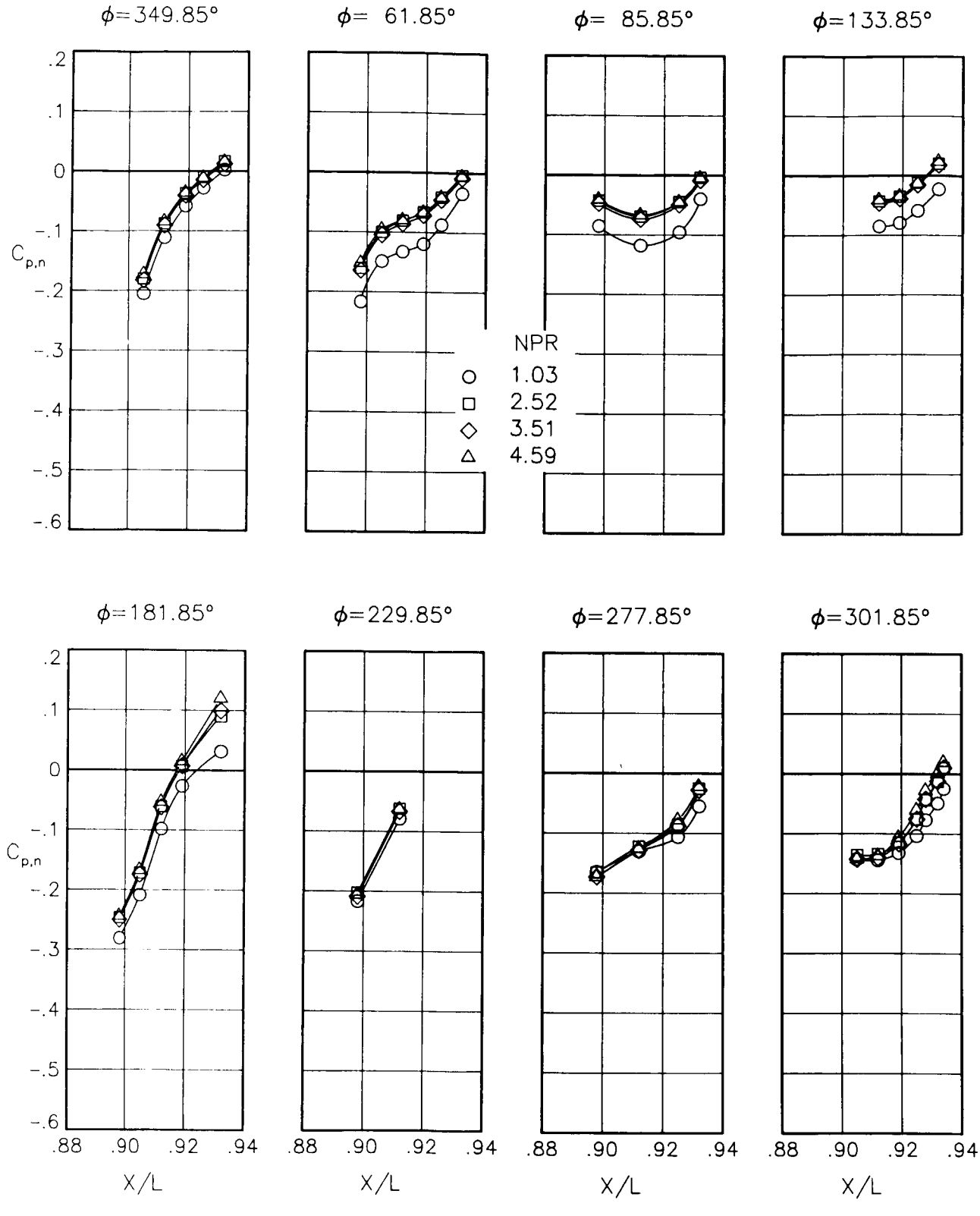

(h) M = 0.80; α = 5.00°.

Figure 70.- Continued.

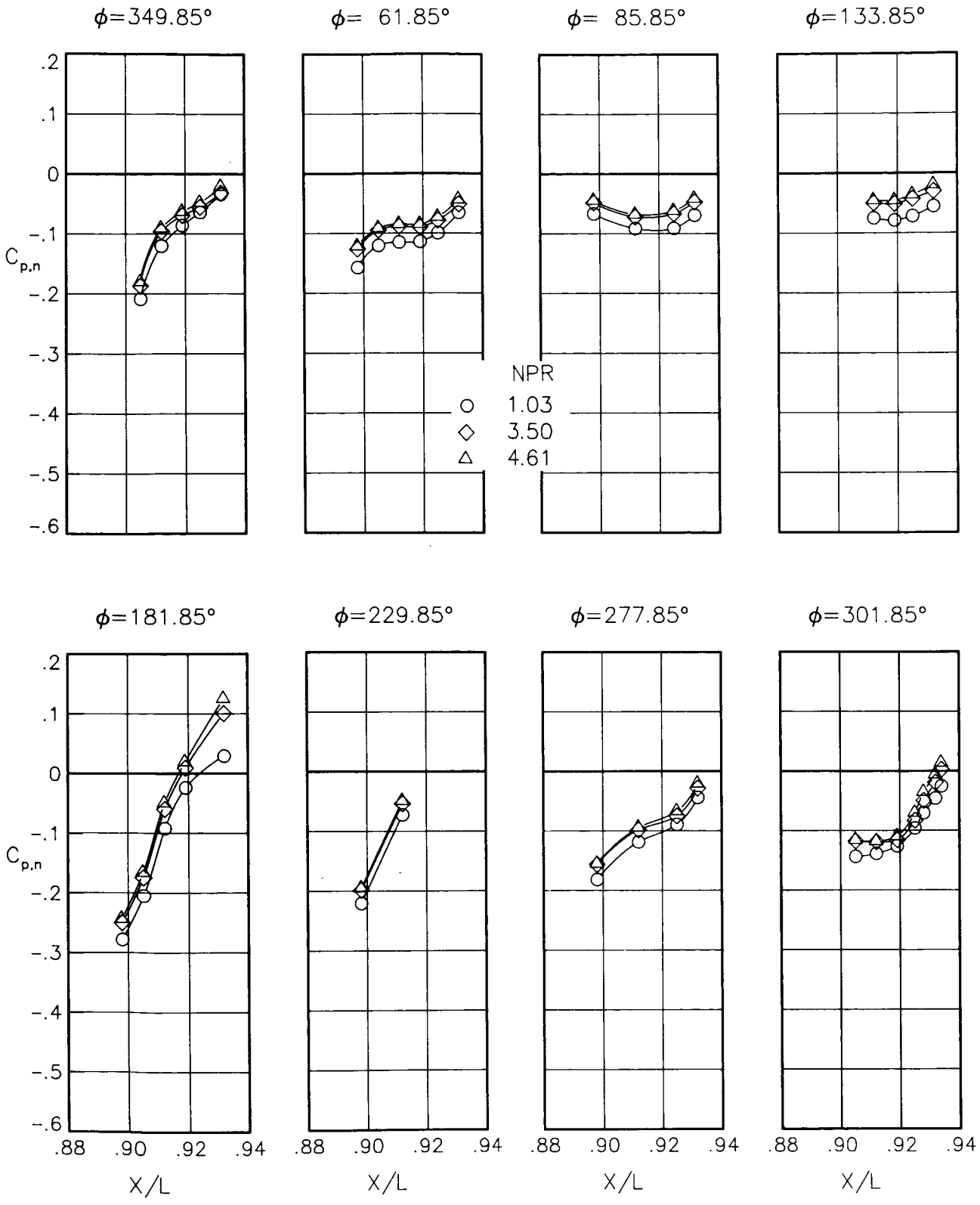

(i) M = 0.80; α = 7.00°.

Figure 70.- Continued.

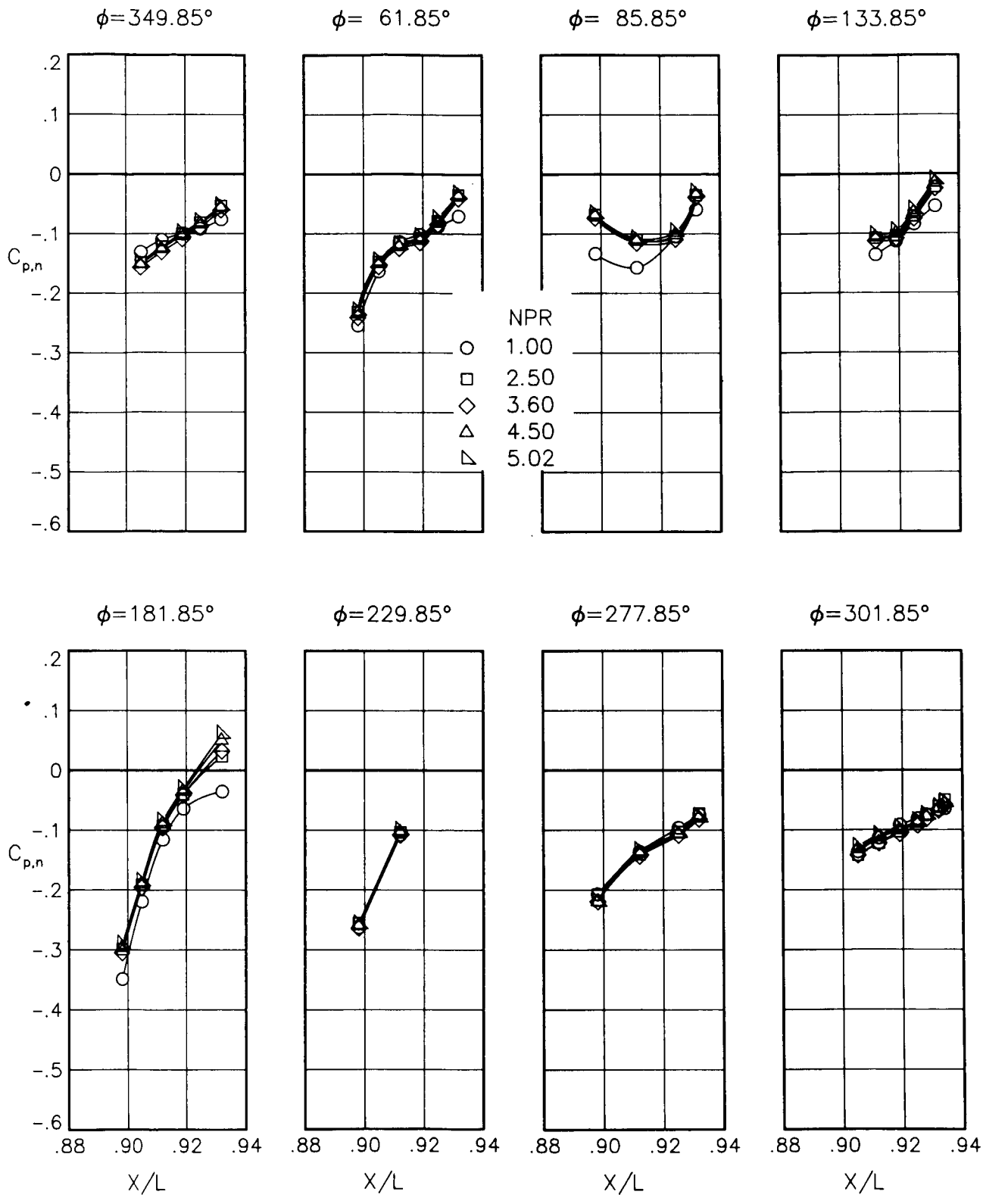

(j) M = 0.90; α = 0.00°.

Figure 70.- Continued.

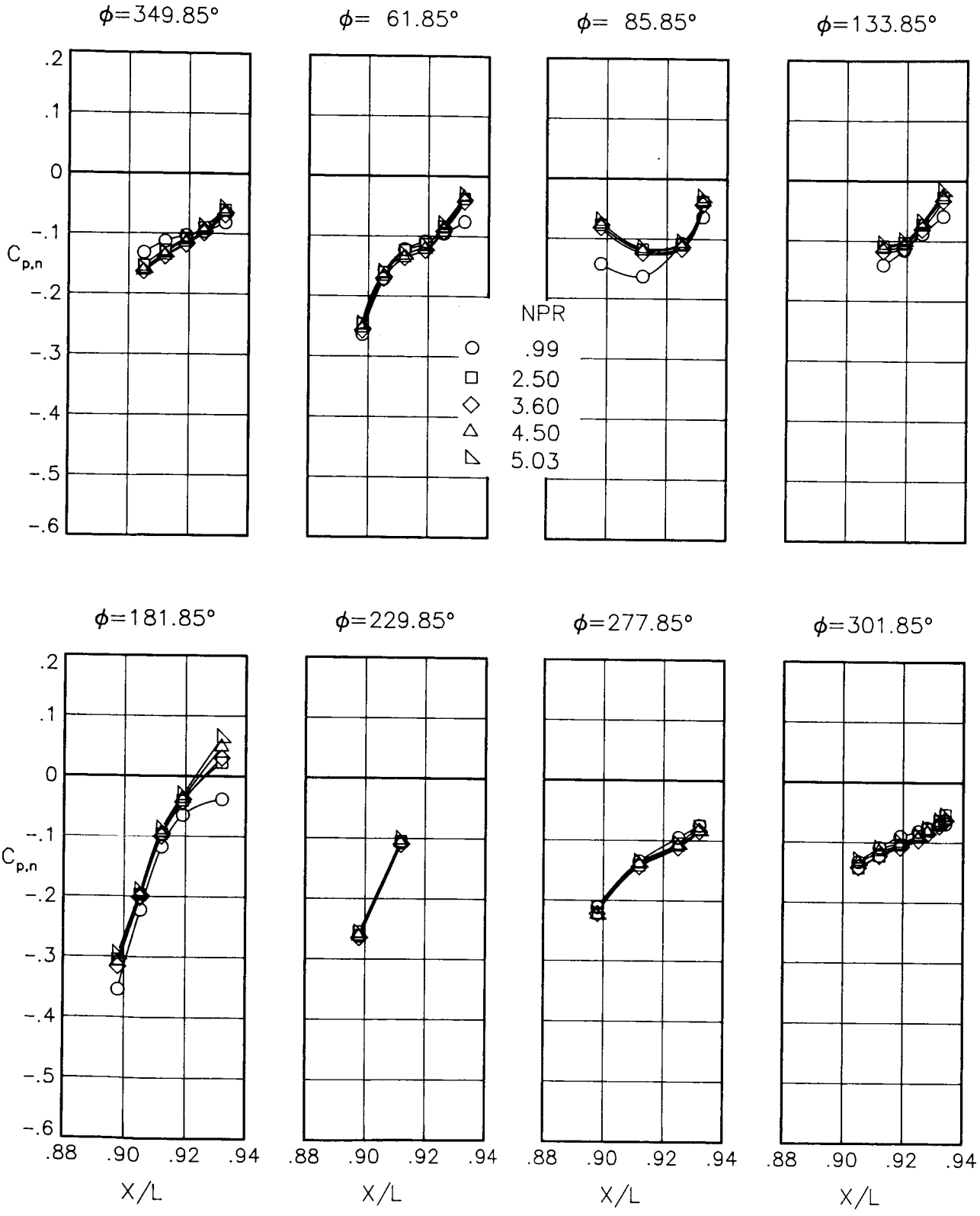

(k) M = 0.90; α = 1.00°.

Figure 70.- Continued.

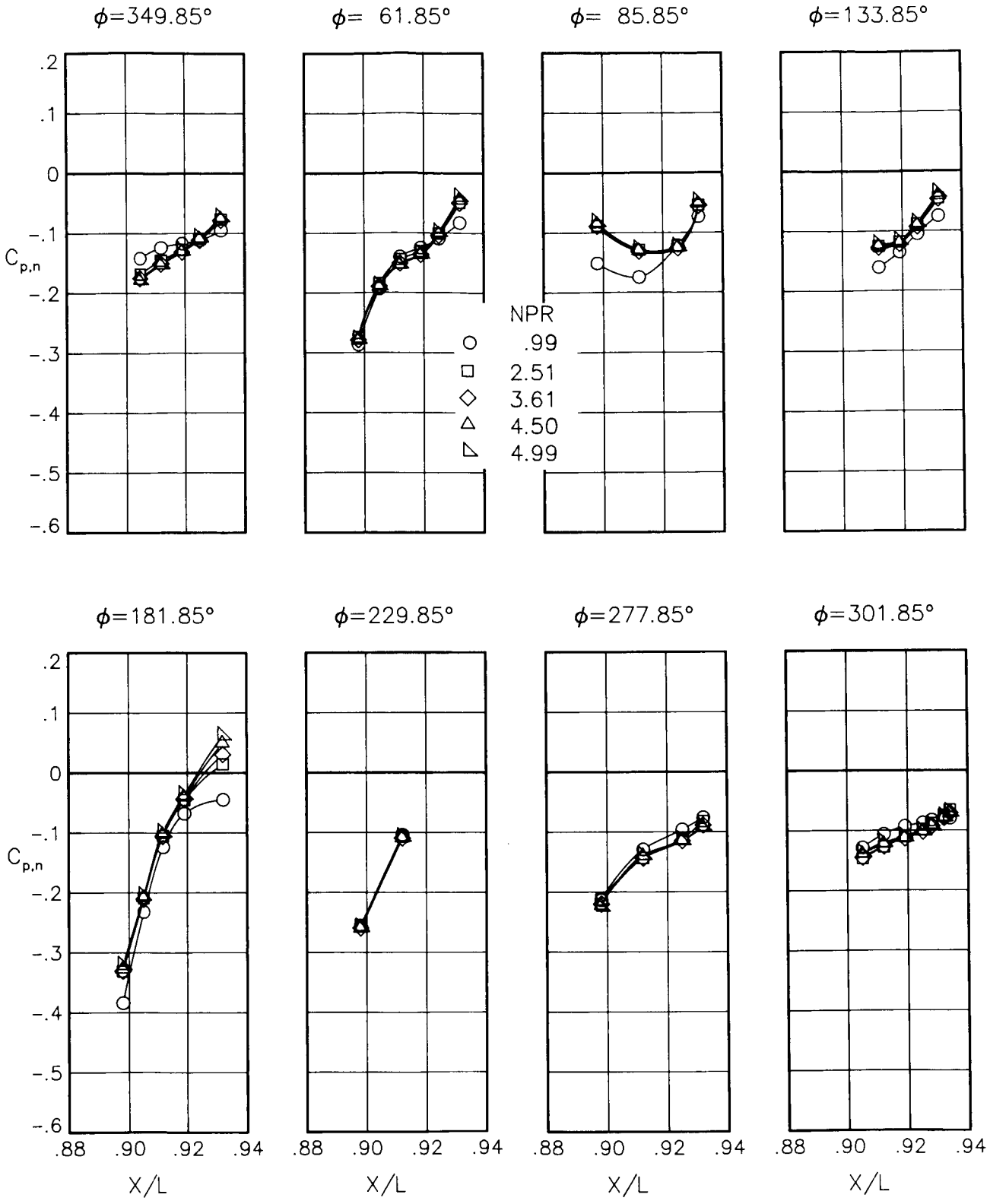

(1) M = 0.90; α = 3.00°.

Figure 70.- Continued.

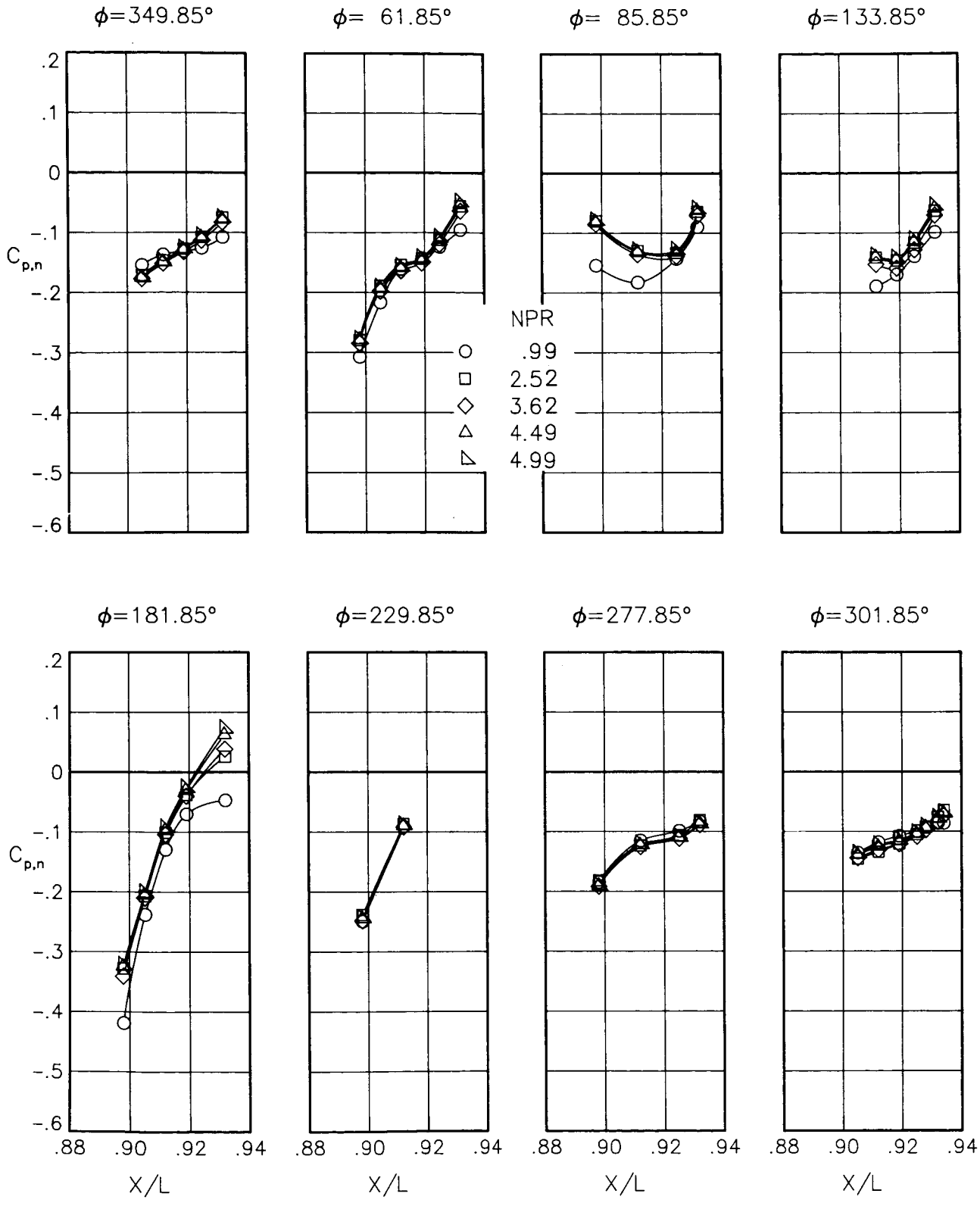

(m) M = 0.90; α = 6.00°.

Figure 70.- Concluded.

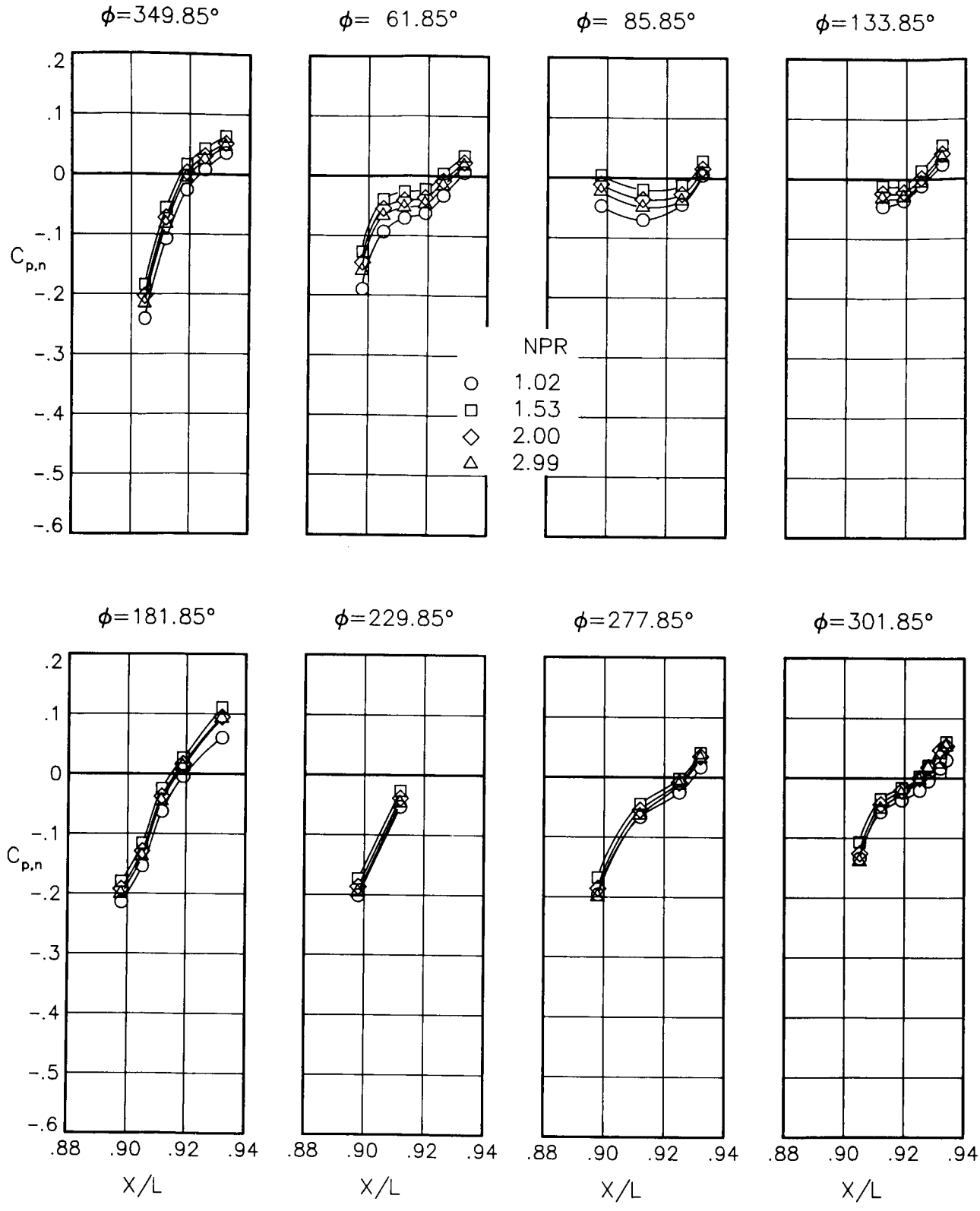

(a) M = 0.60; α = 0.00°.

Figure 71.- Static-pressure-coefficient distributions on nozzle for the model with nose boom, actuator fairings, A/B vents, and nozzle steps (no rakes). β_n = 18.45°; δ_h = -2°.

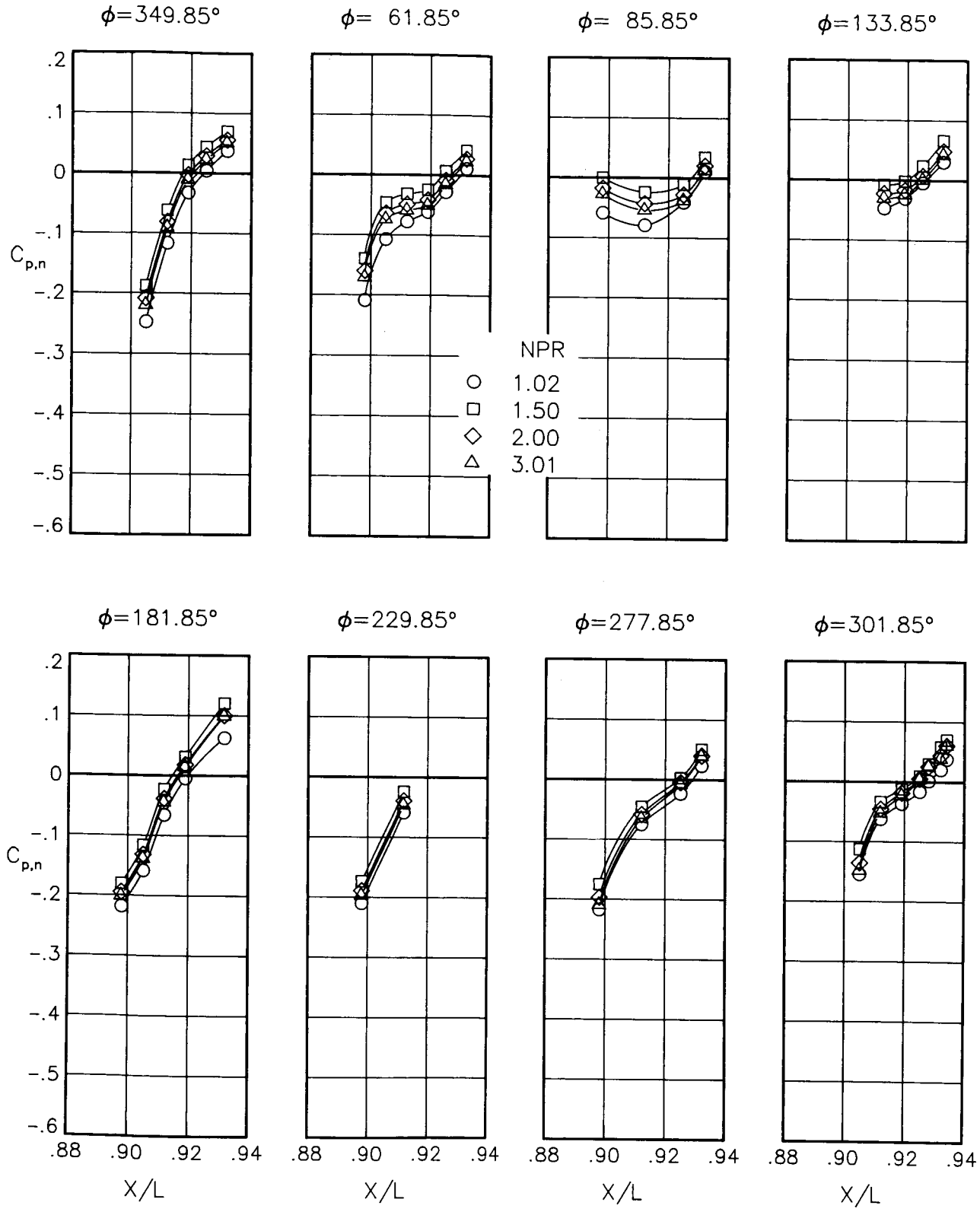

(b) M = 0.60; α = 1.00°.

Figure 71.- Continued.

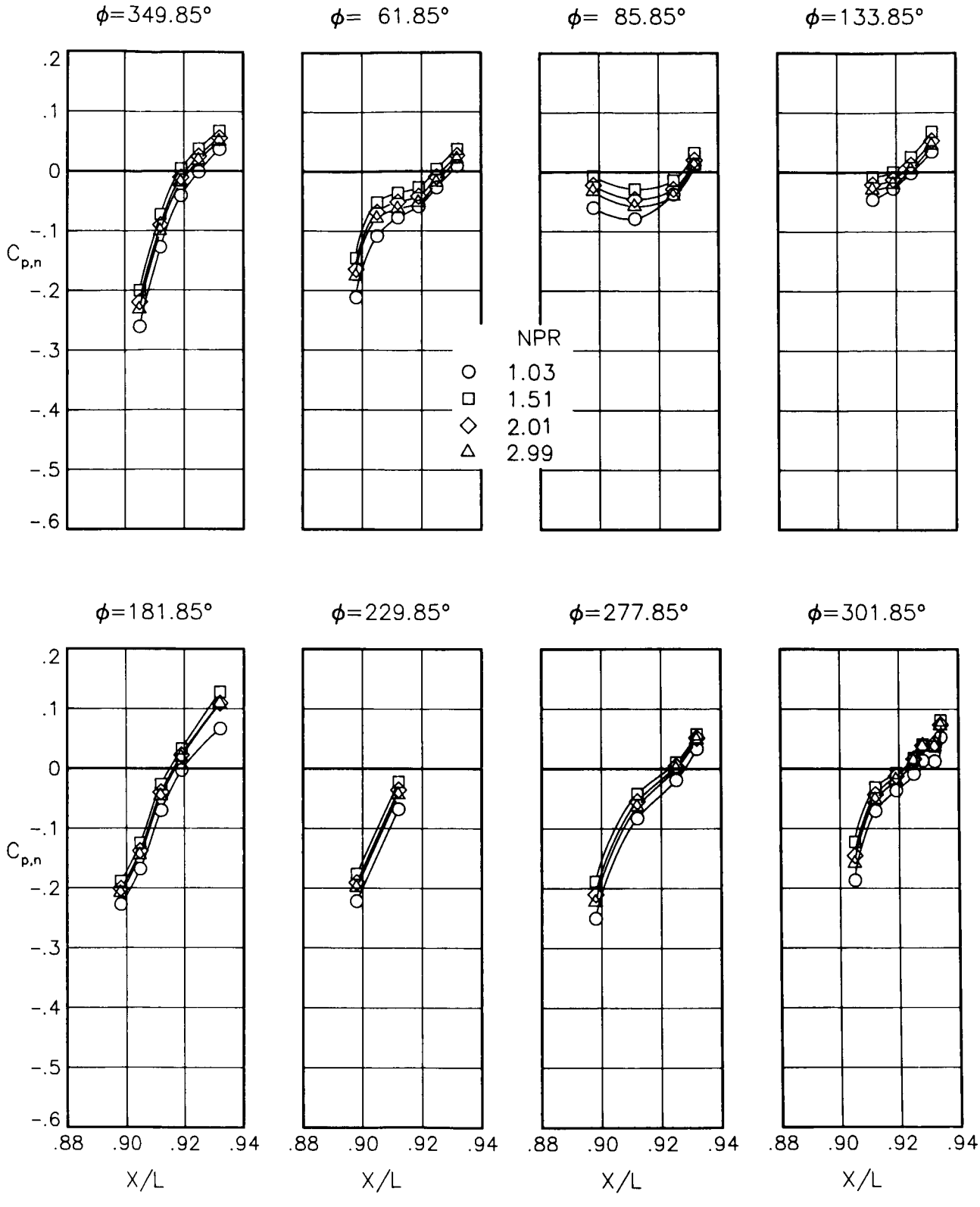

(c) M = 0.60; α = 3.00°.

Figure 71.- Continued.

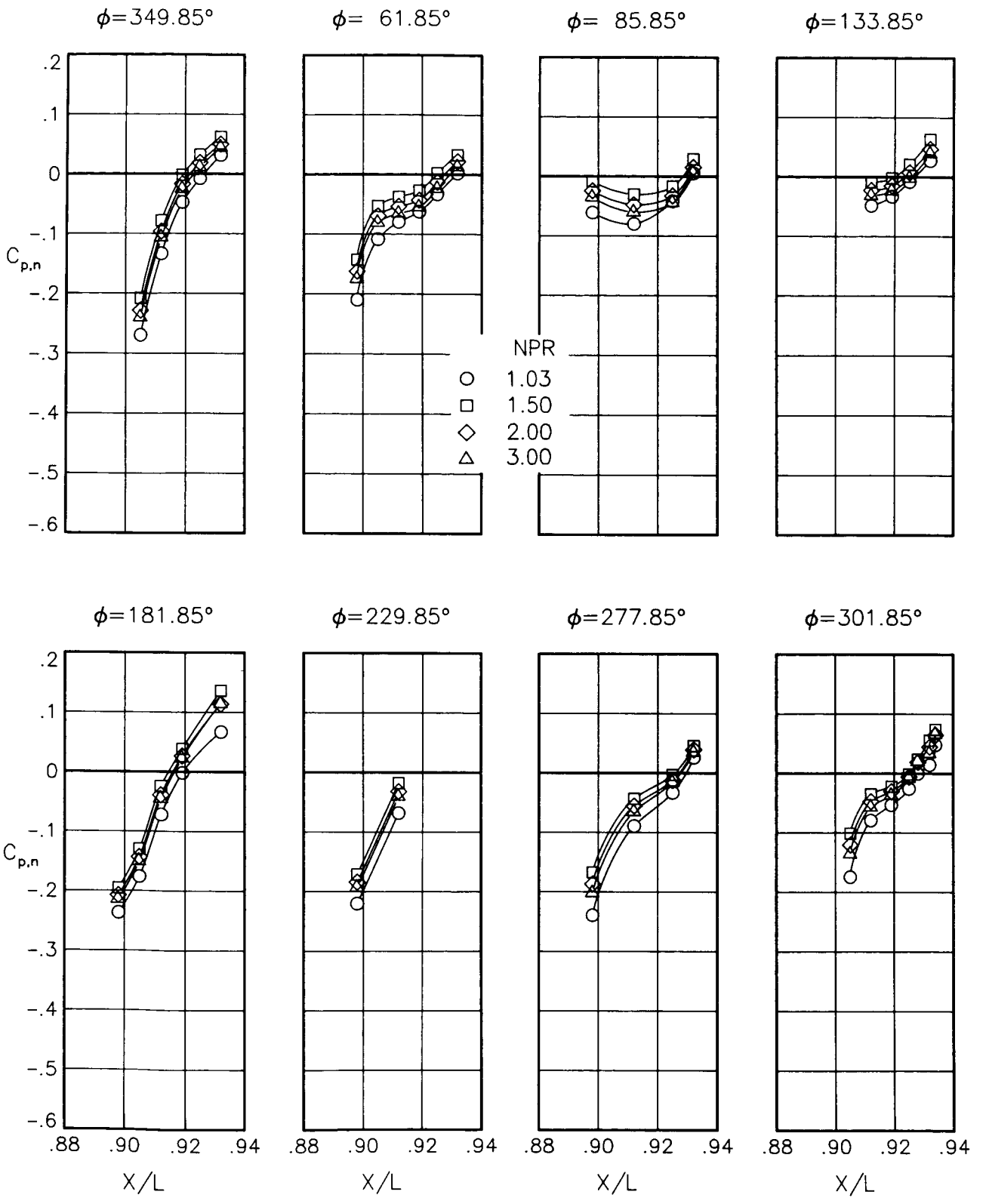

(d) M = 0.60; α = 5.00°.

Figure 71.- Continued.

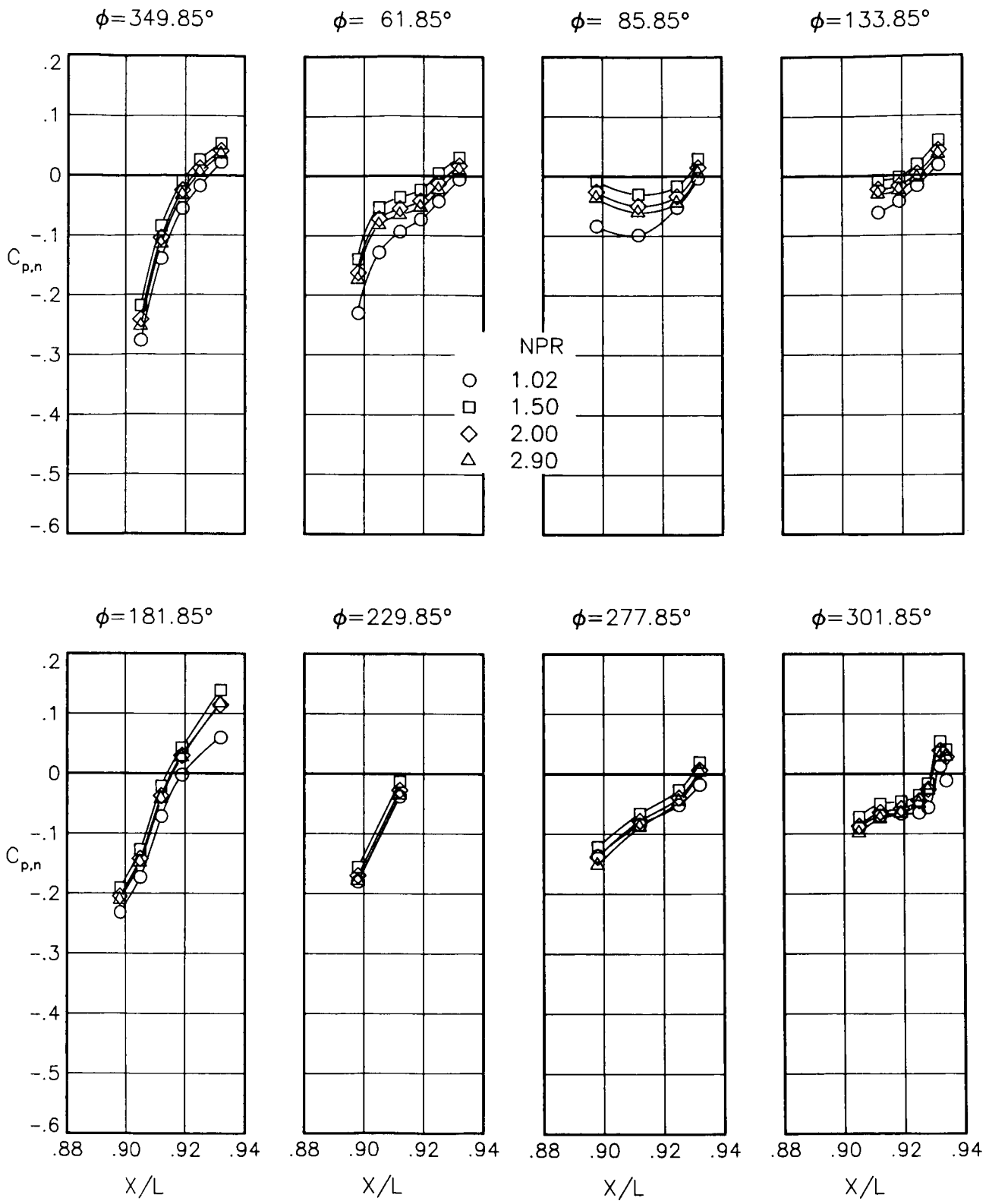

(e) M = 0.60; α = 7.00°.

Figure 71.- Continued.

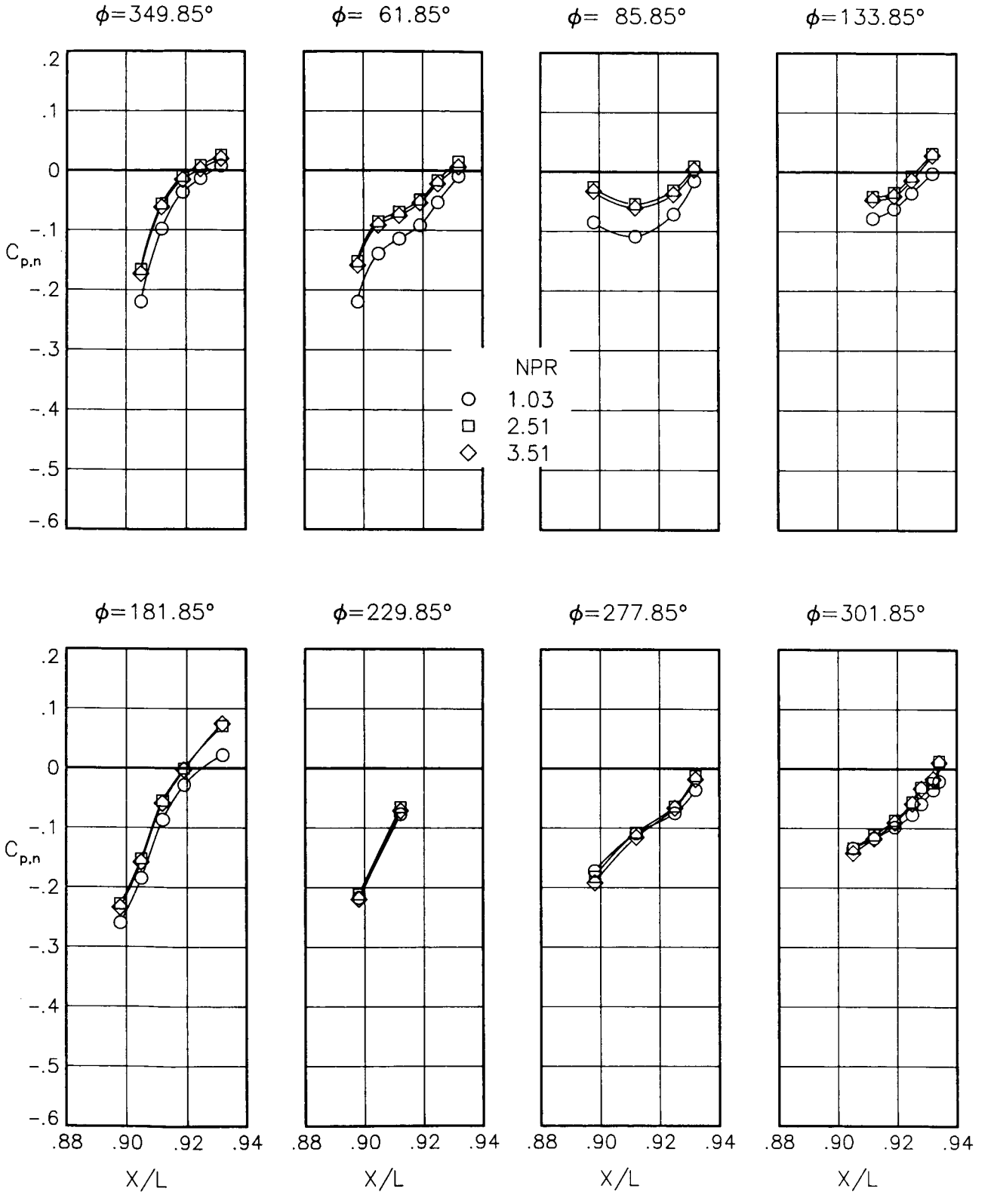

(f) M = 0.80; α = 0.00°.

Figure 71.- Continued.

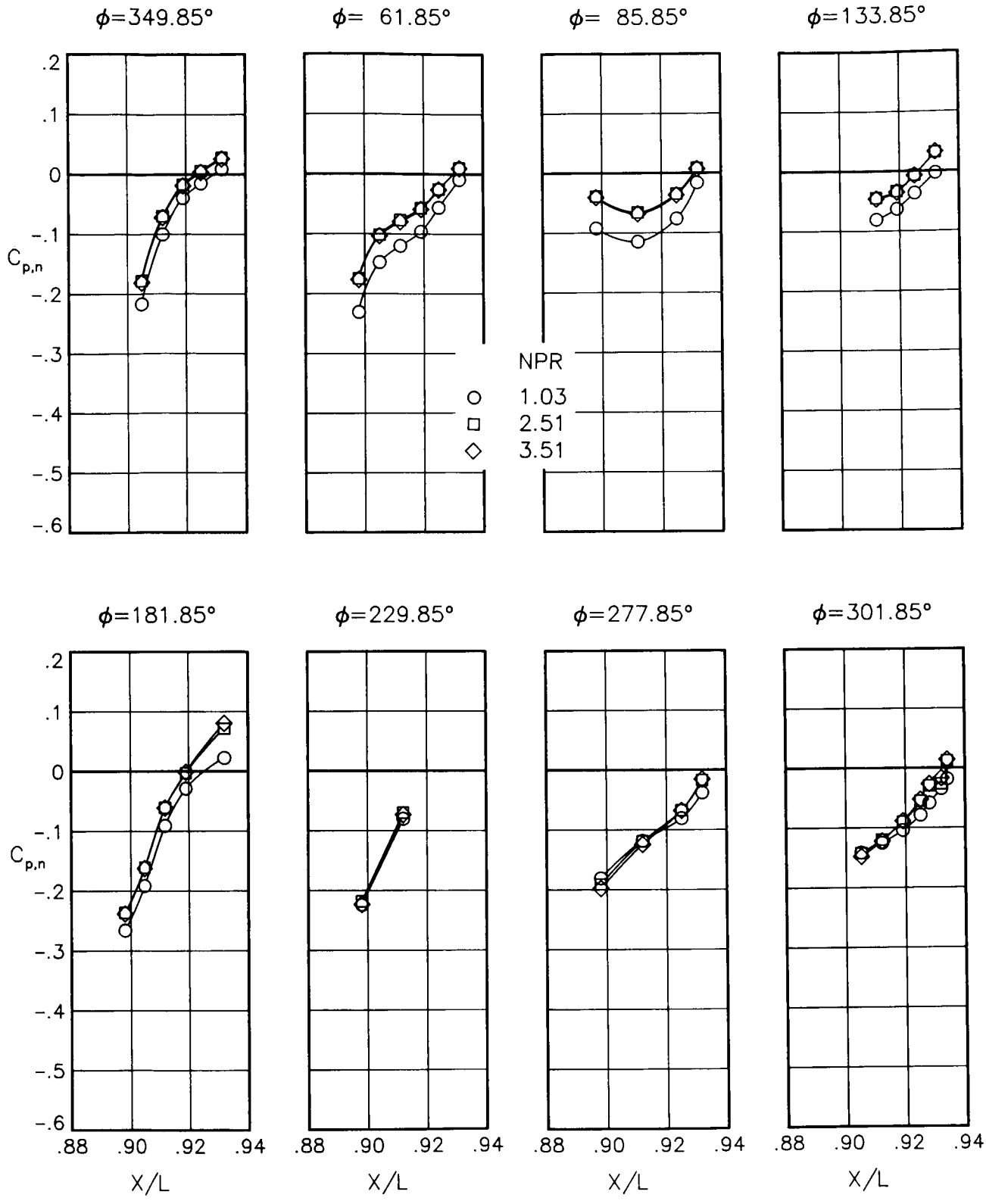

(g) M = 0.80; α = 1.00°.

Figure 71.- Continued.

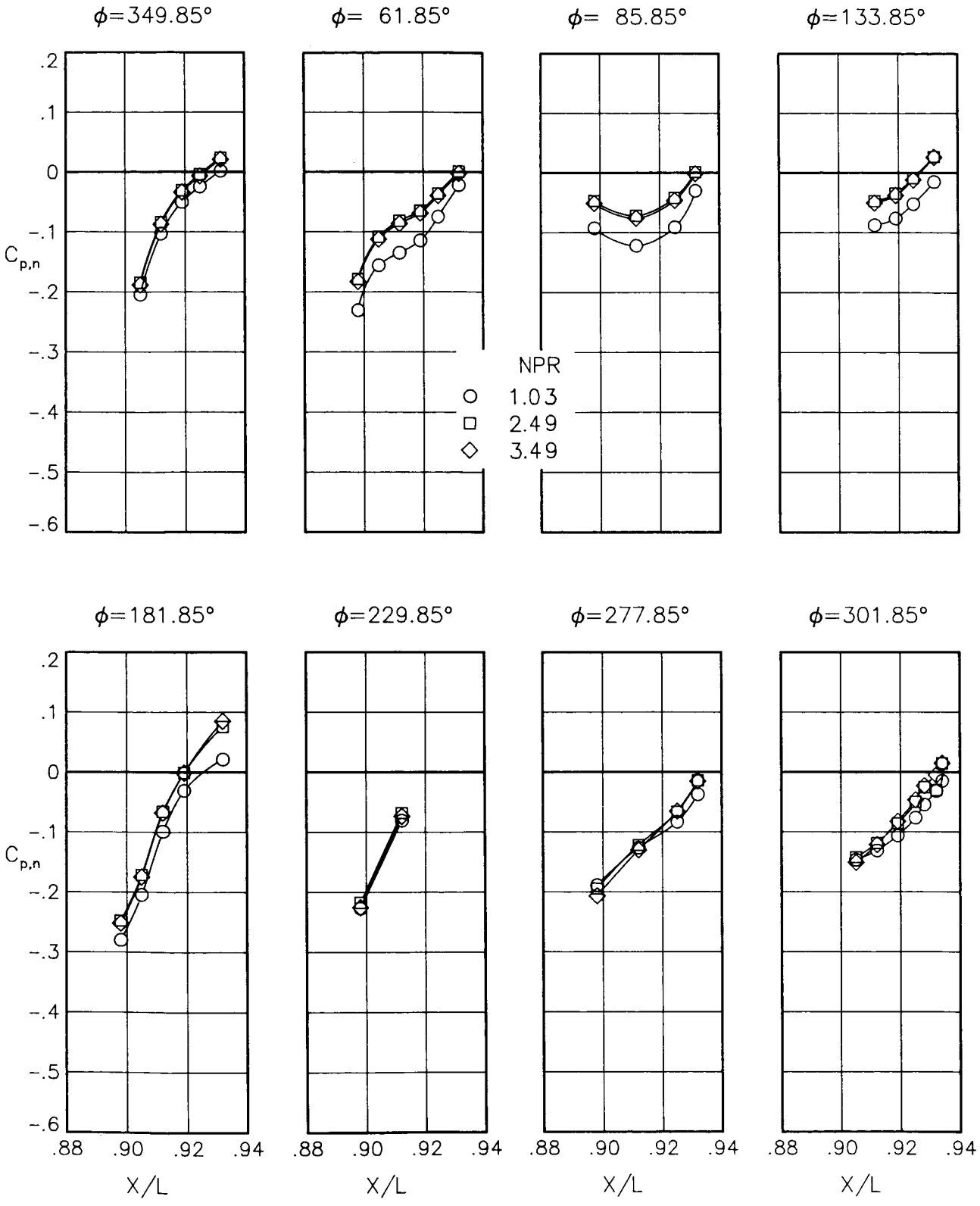

(h) M = 0.80; α = 3.00°.

Figure 71.- Continued.

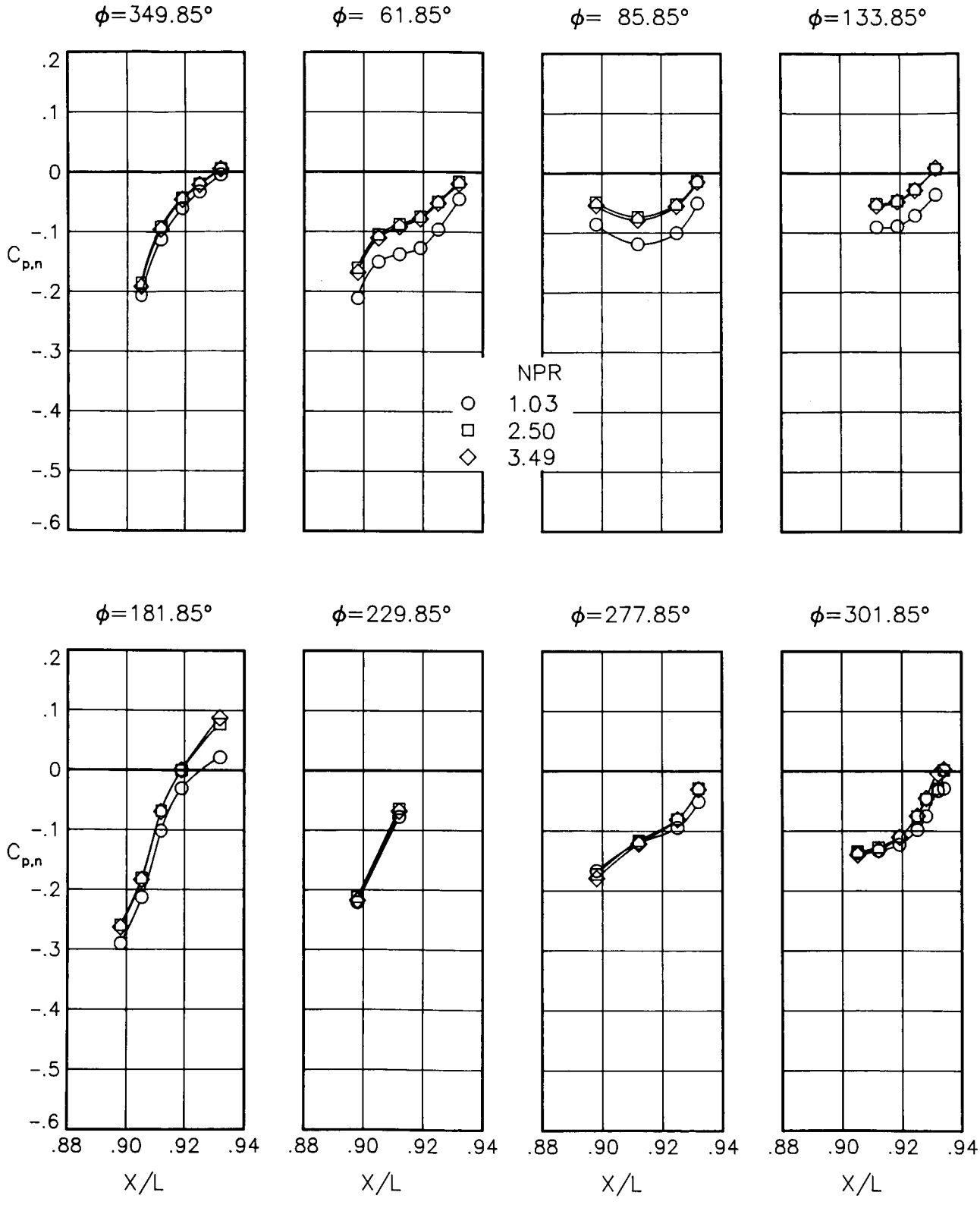

(i) M = 0.80; α = 5.00°.

Figure 71.- Continued.

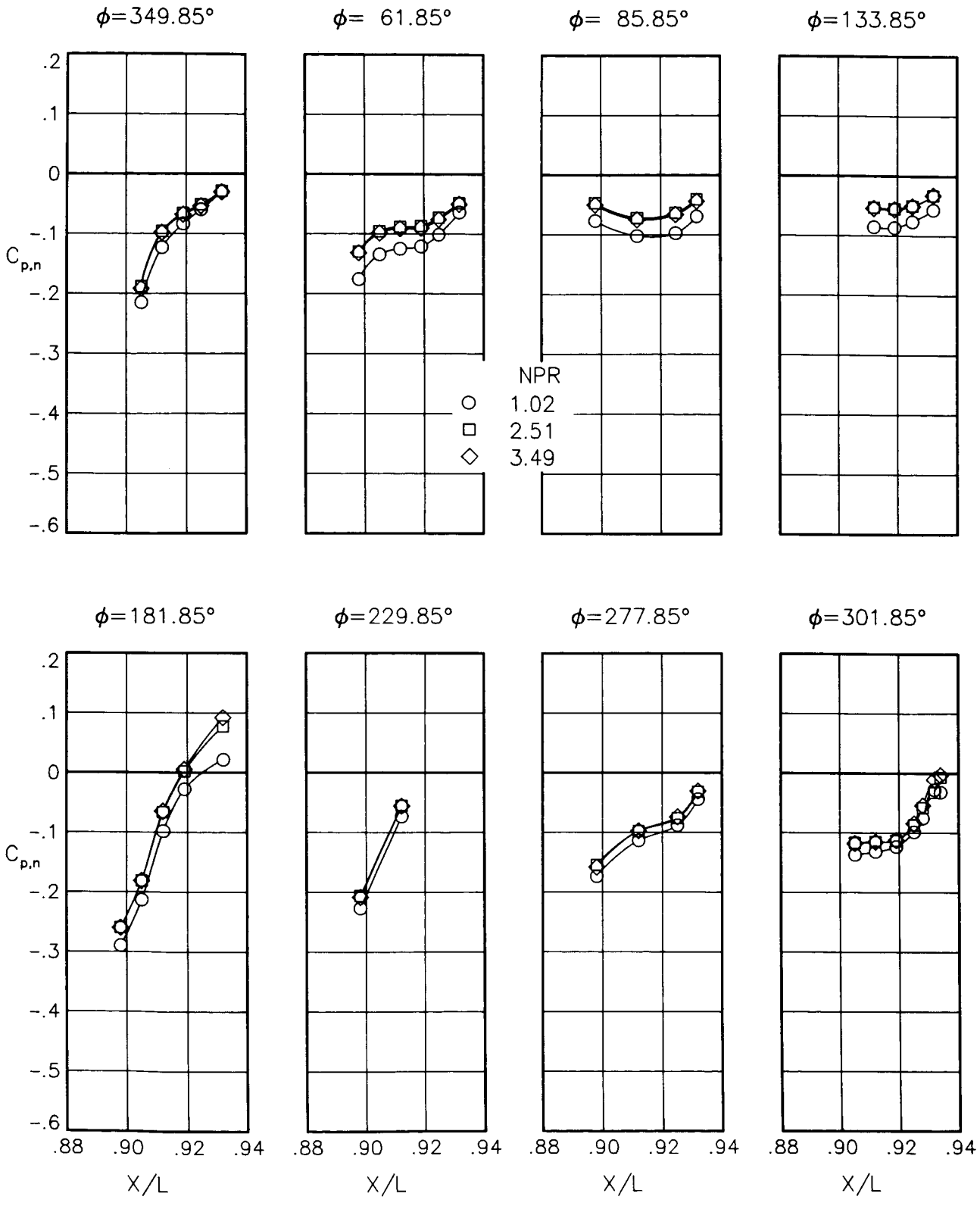

(j) M = 0.80; α = 7.00°.

Figure 71.- Continued.

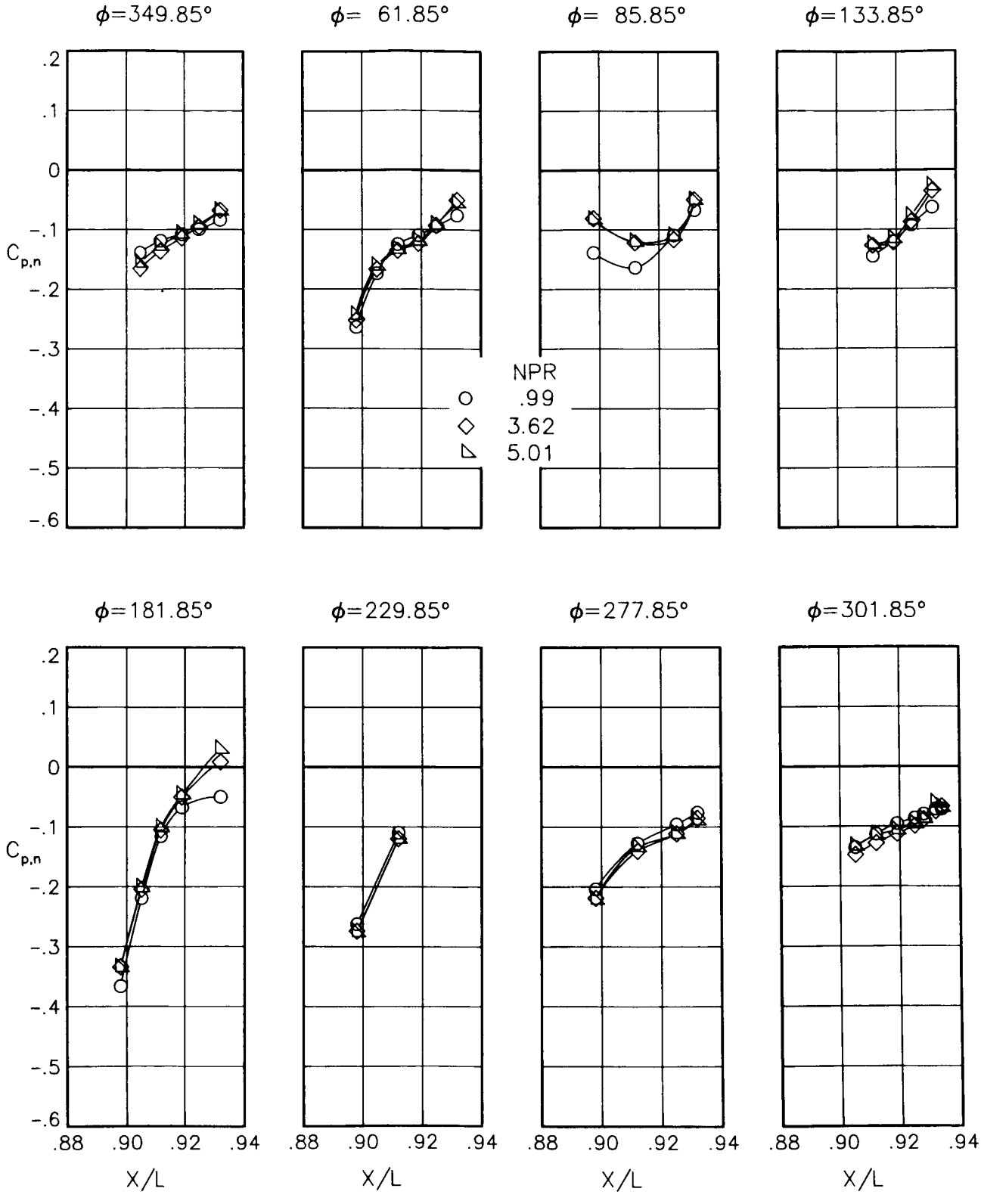

(k) M = 0.90; α = 0.00°.

Figure 71.- Continued.

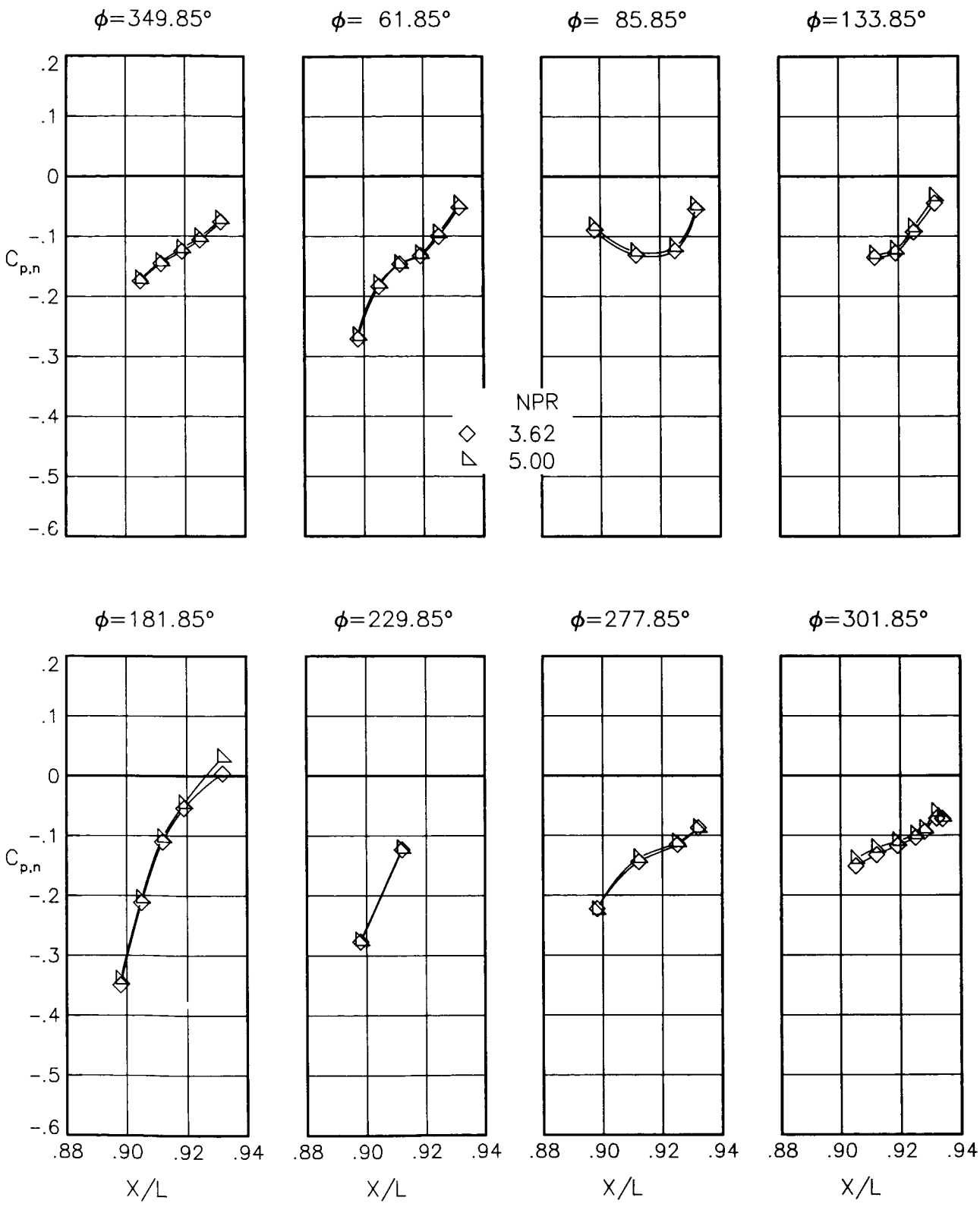

(1) M = 0.90; α = 1.00°.

Figure 71.- Continued.

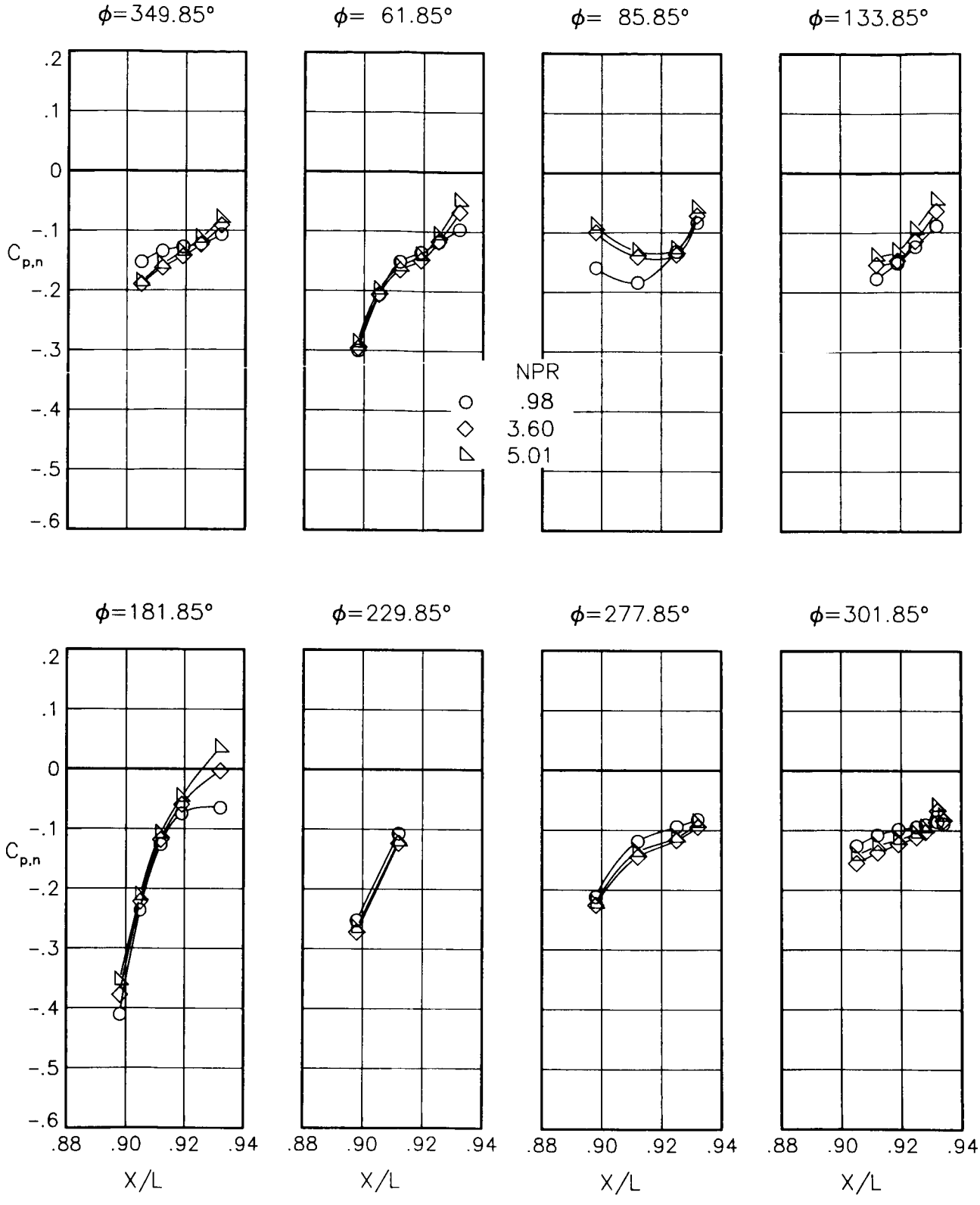

(m) M = 0.90; α = 3.00°.

Figure 71.- Continued.

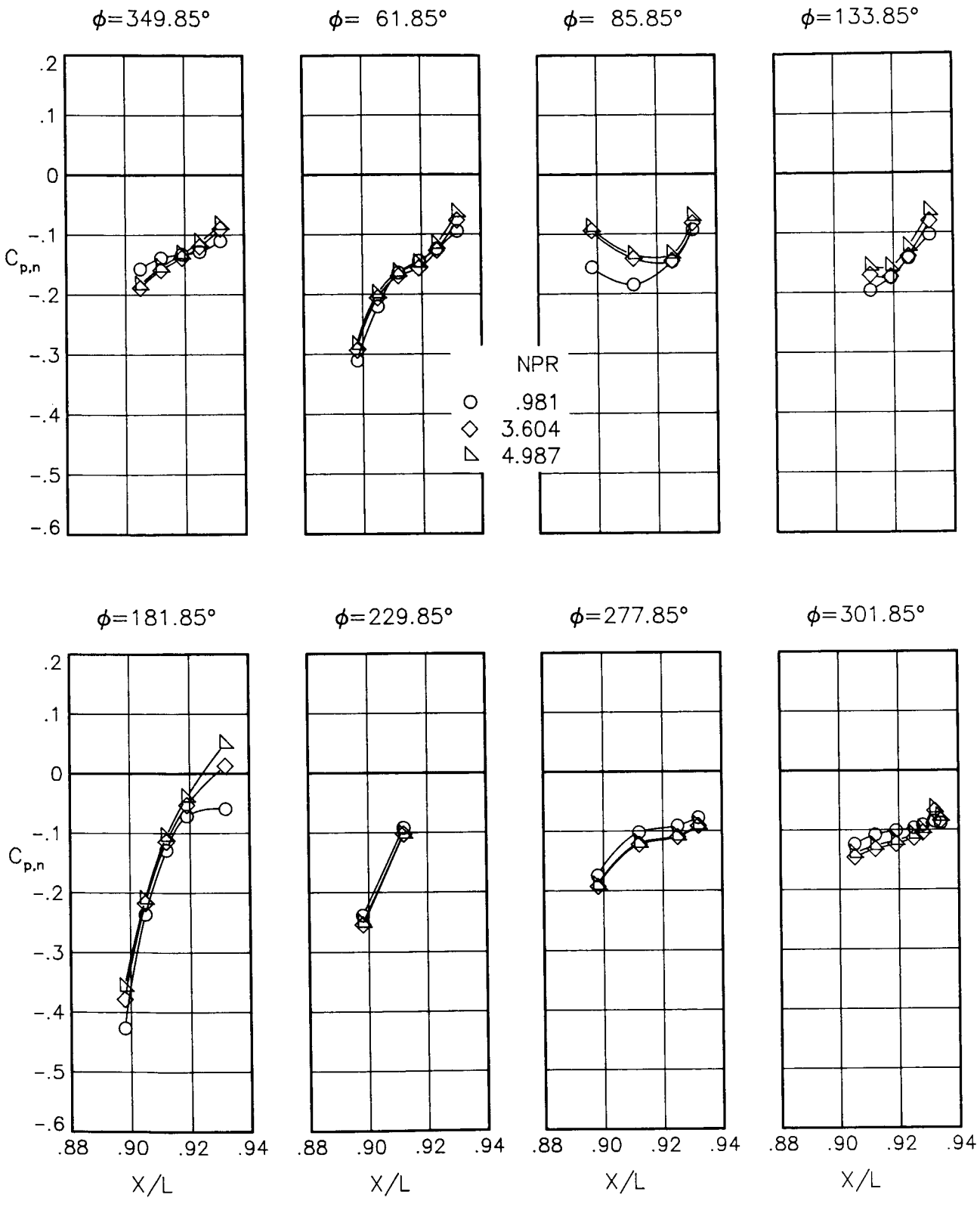

(n) M = 0.90; α = 6.00°.

Figure 71.- Concluded.

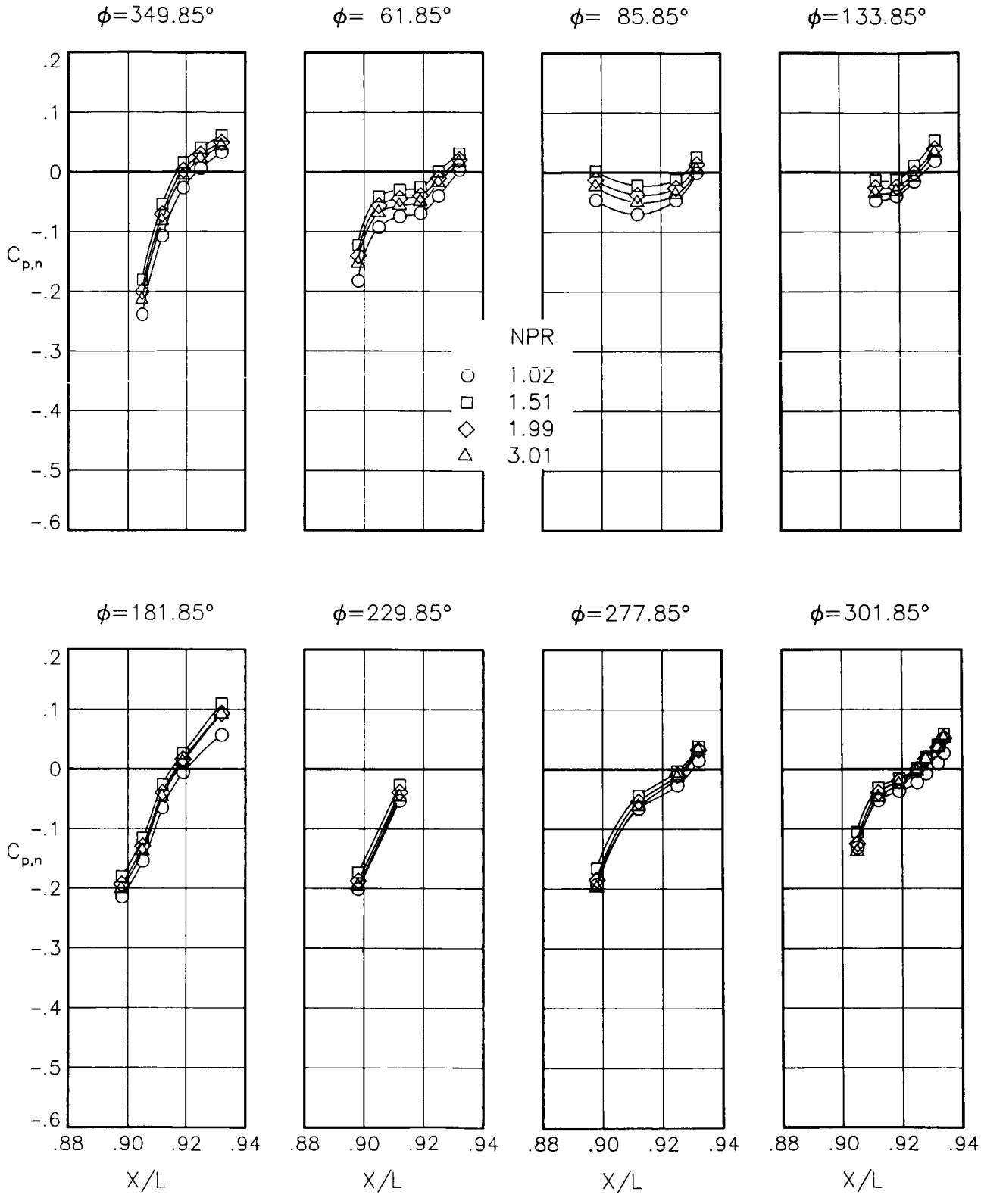

(a) M = 0.60; α = 0.00°.

Figure 72.- Static-pressure-coefficient distributions on nozzle for the model with nose boom, actuator fairings, A/B vents, nozzle steps, and right rake. β_h = 18.45°; δ_h = -2°.

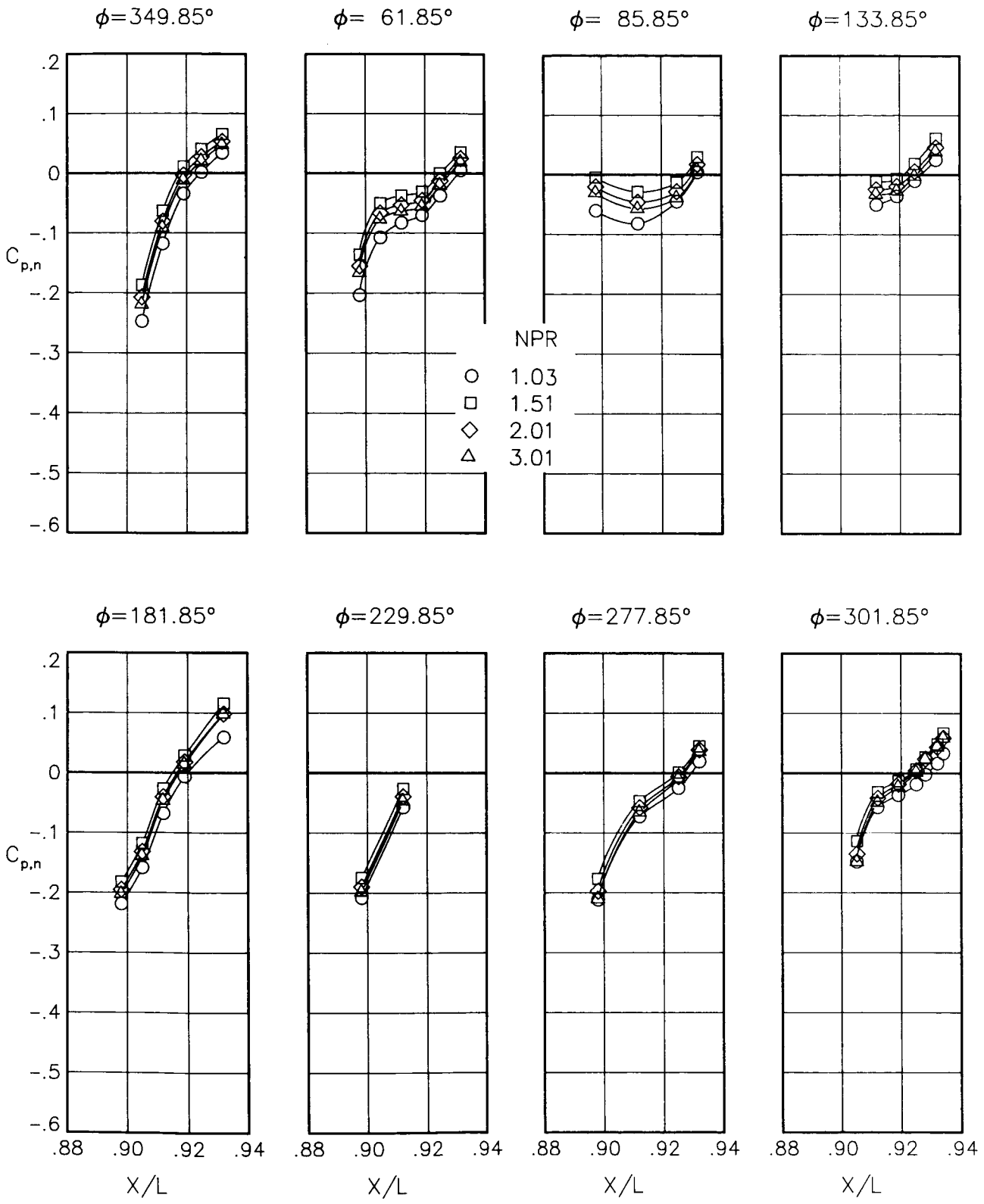

(b) M = 0.60; α = 1.00°.

Figure 72.- Continued.

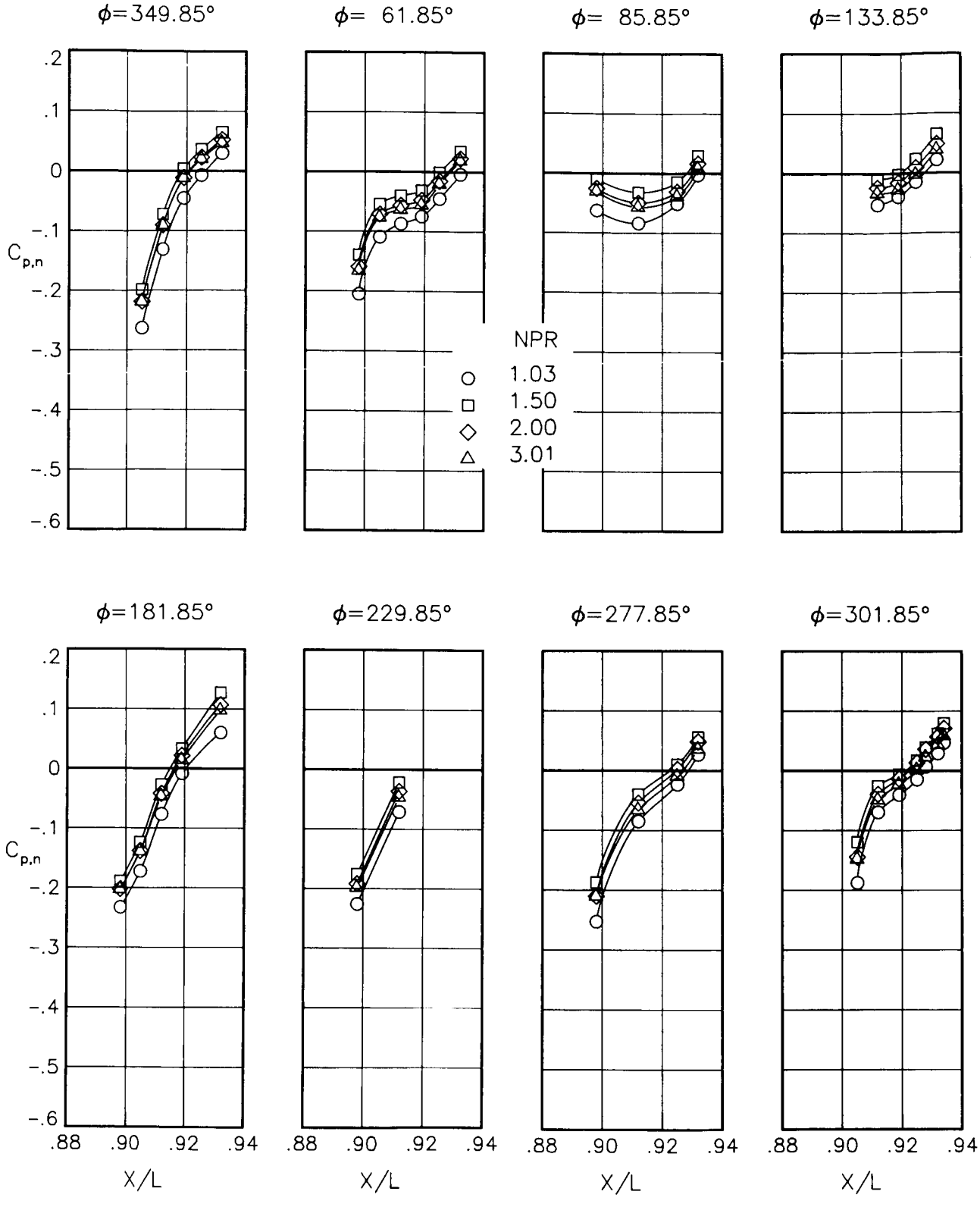

(c) M = 0.60; α = 3.00°.

Figure 72.- Continued.

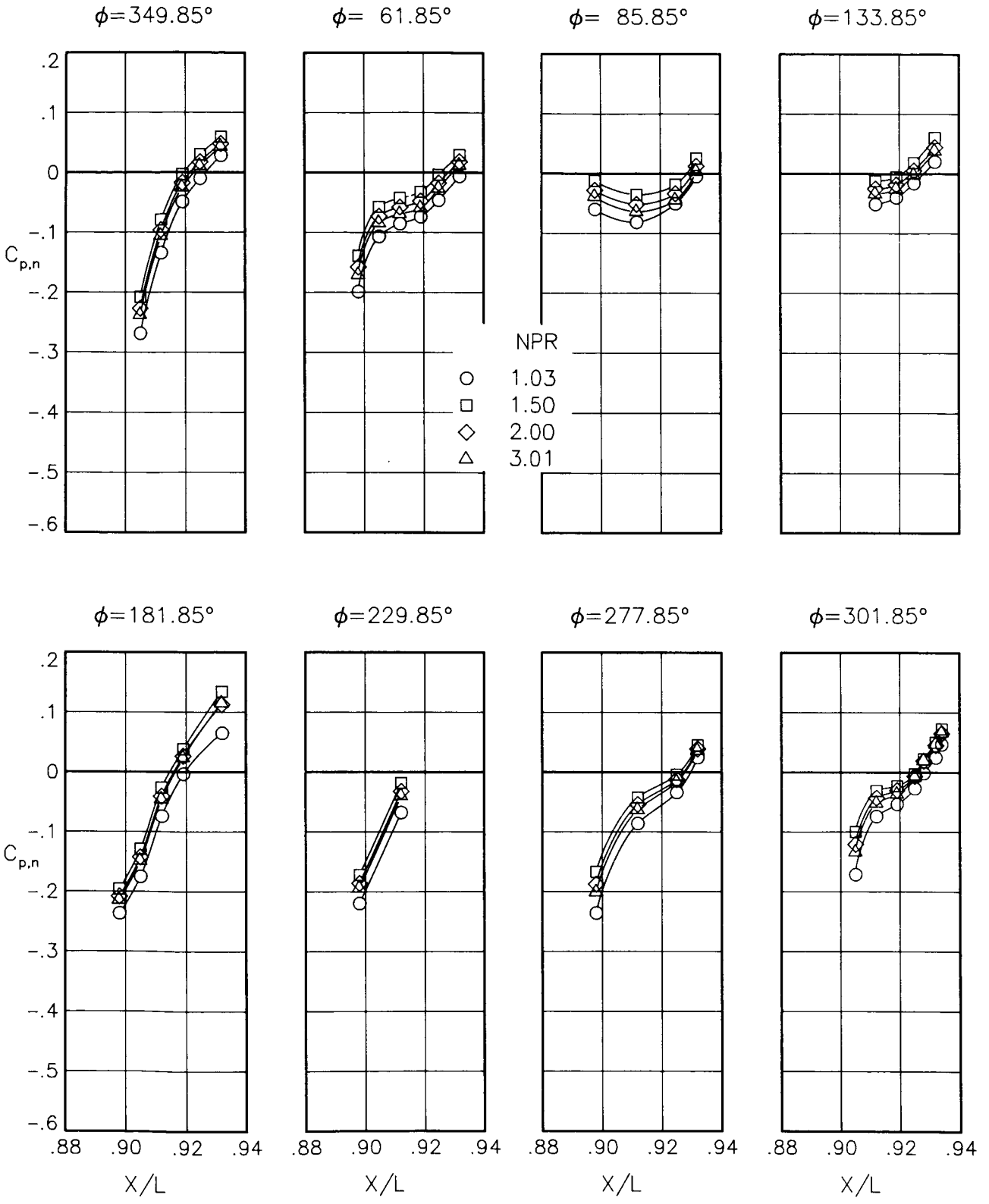

(d) M = 0.60; α = 5.00°.

Figure 72.- Continued.

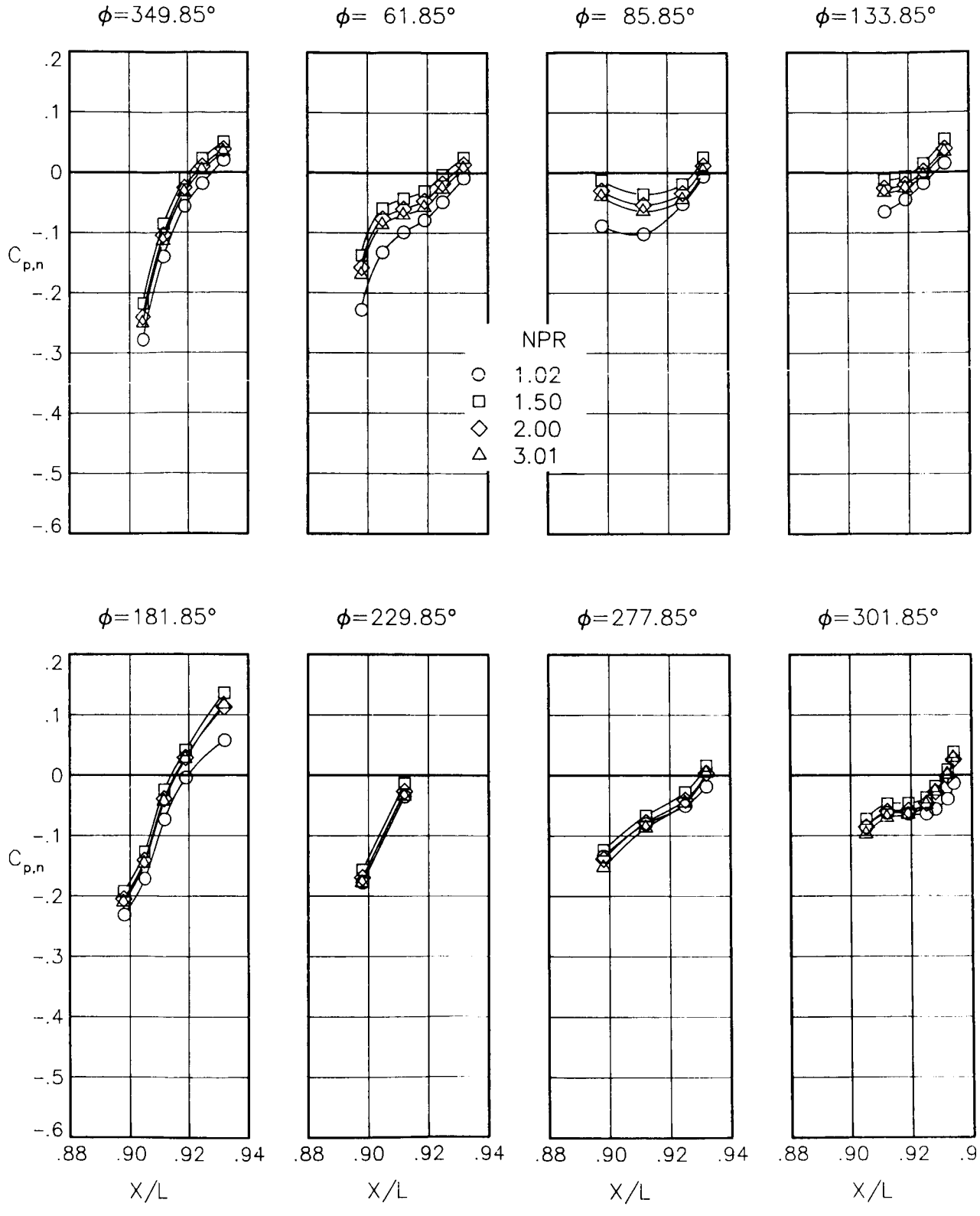

(e) M = 0.60; α = 7.00°.

Figure 72.- Continued.

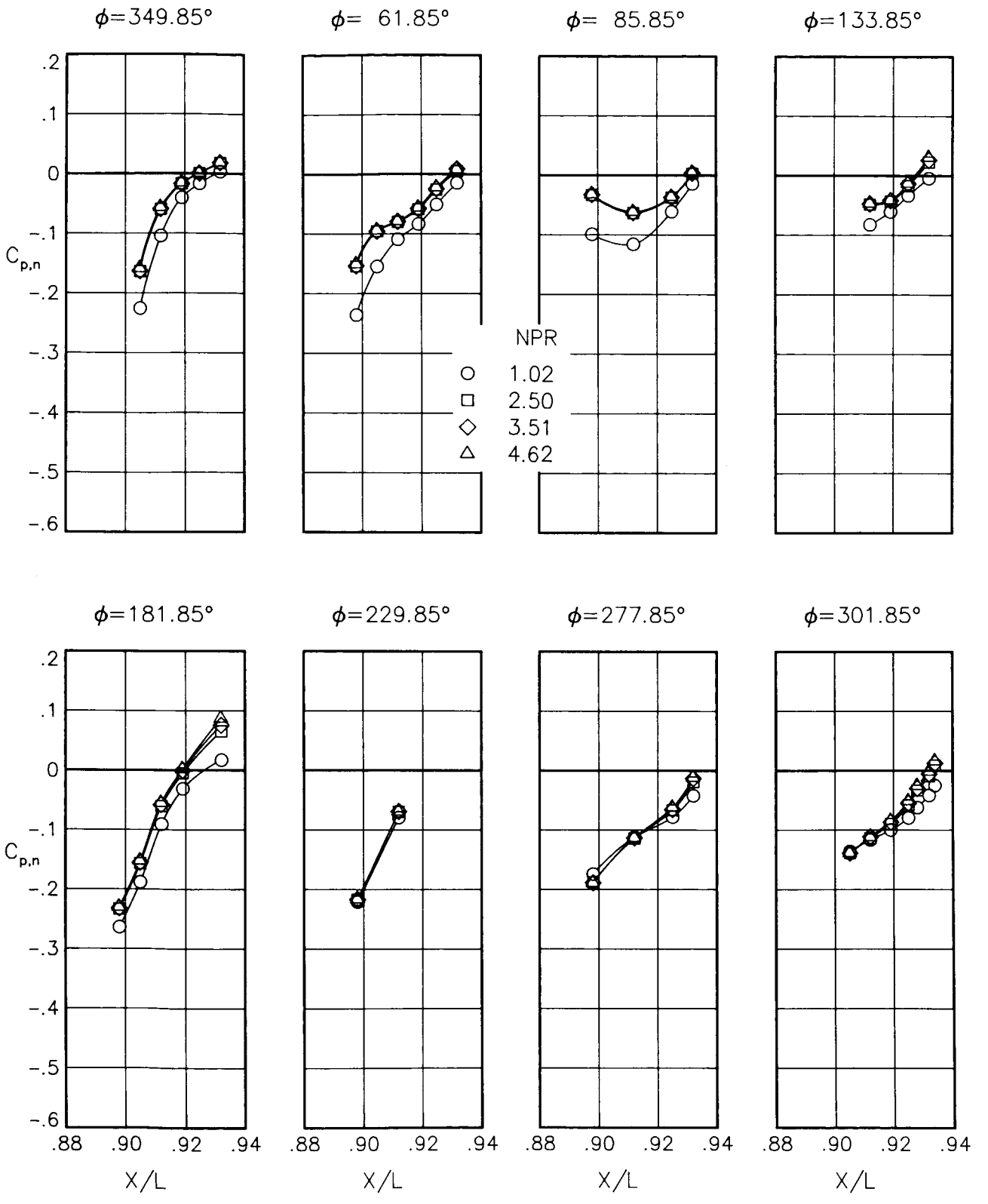

(f) M = 0.80; α = 0.00°.

Figure 72.- Continued.

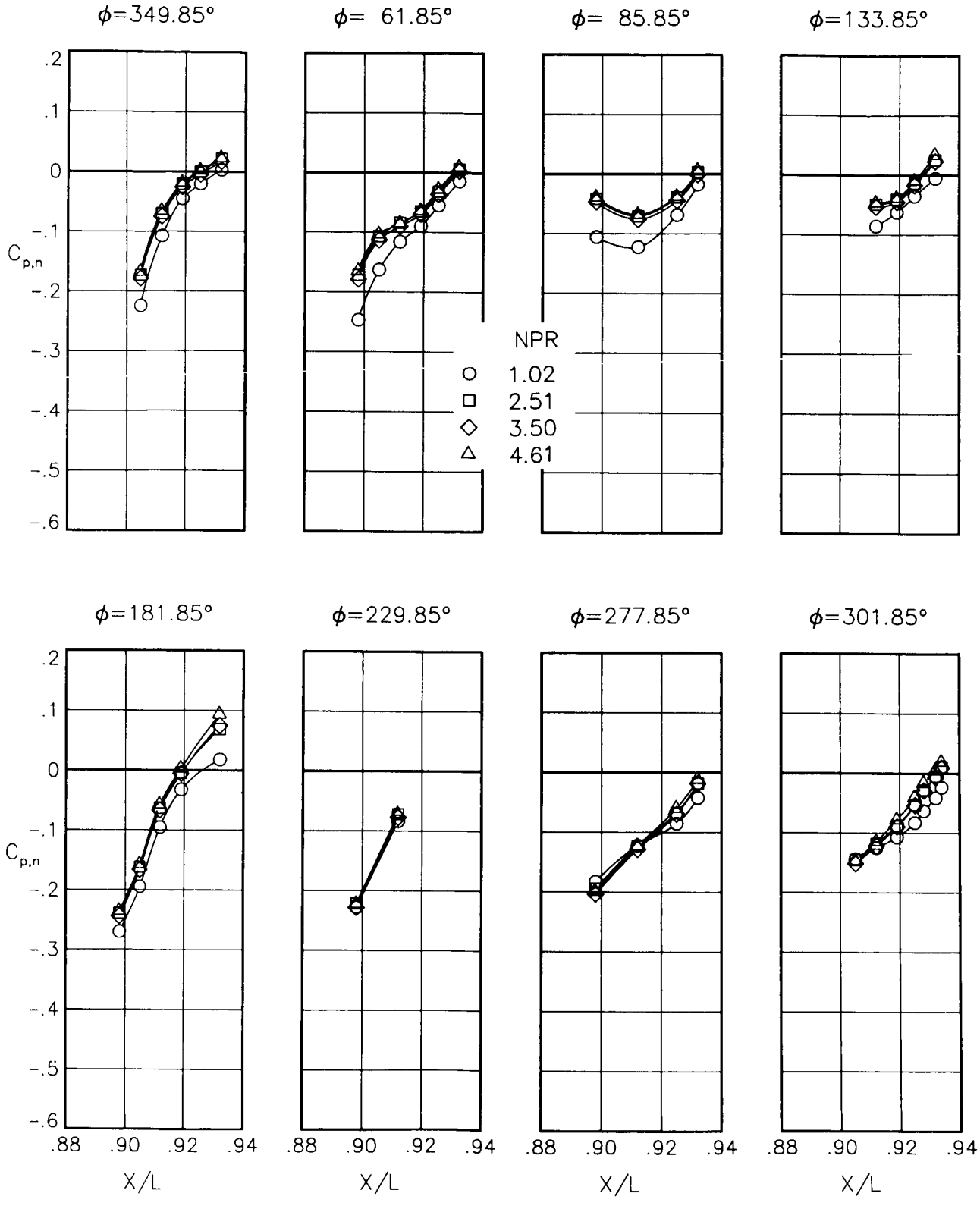

(g) M = 0.80; α = 1.00°.

Figure 72.- Continued.

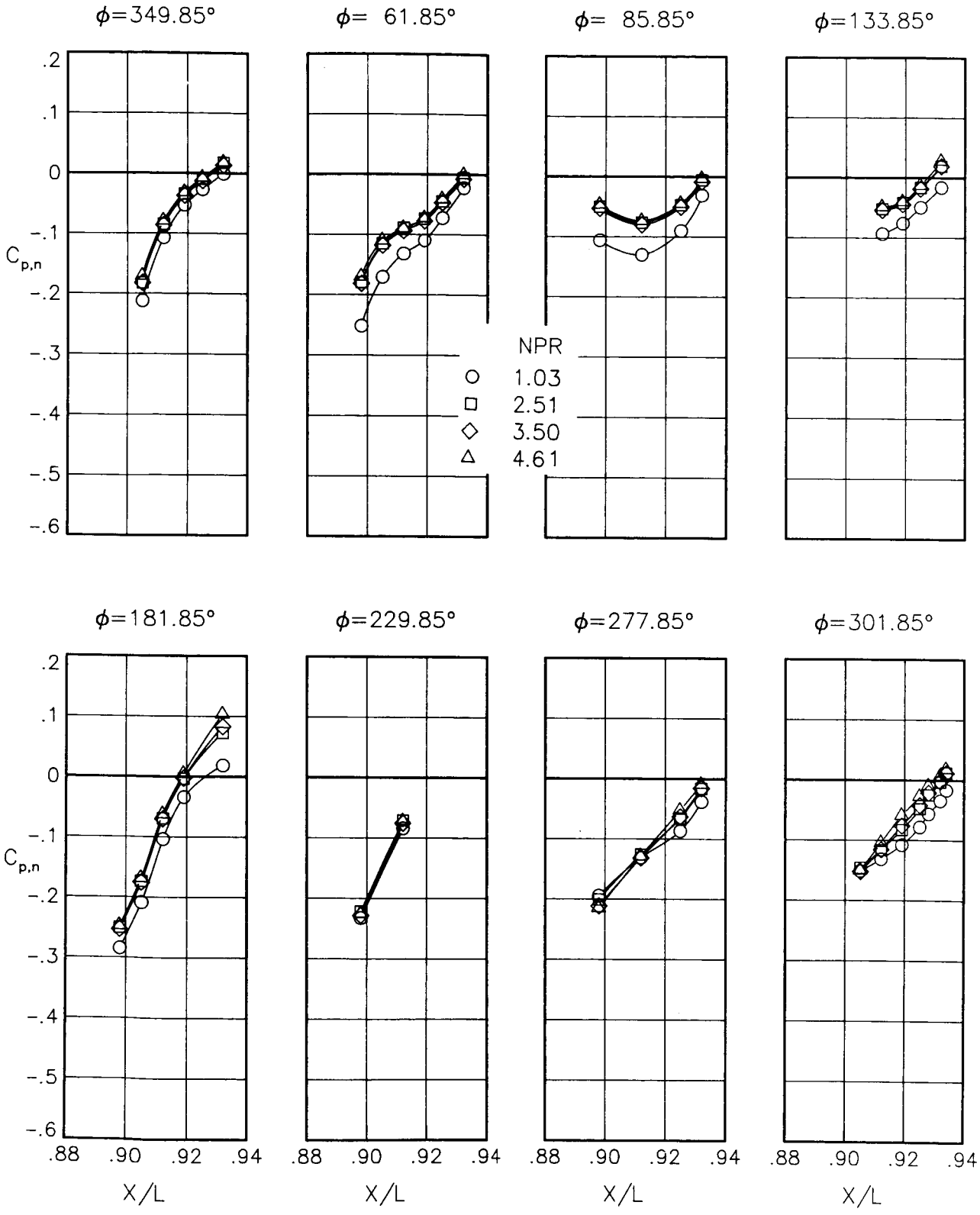

(h) M = 0.80; α = 3.00°.

Figure 72.- Continued.

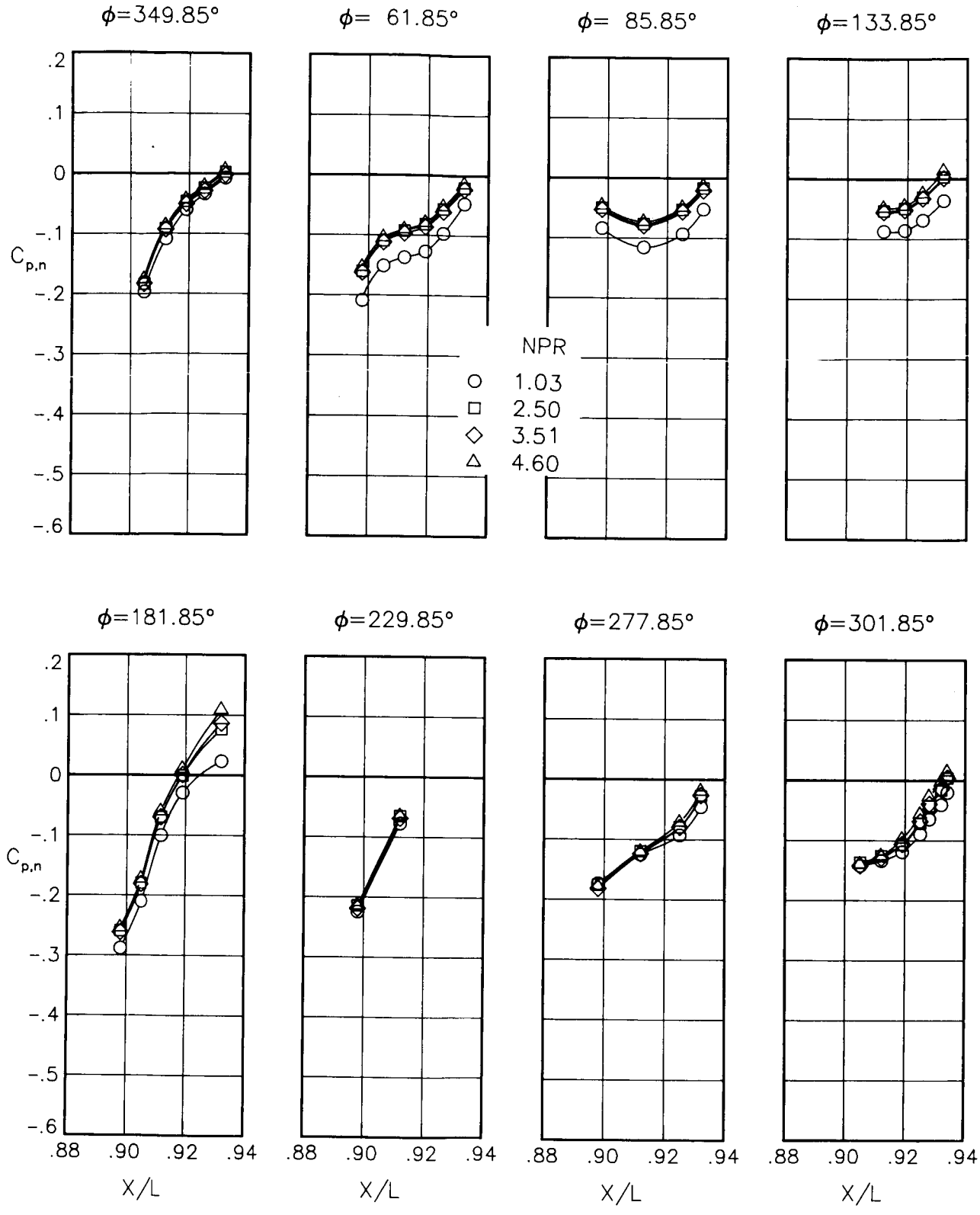

(i) M = 0.80; α = 5.00°.

Figure 72.- Continued.

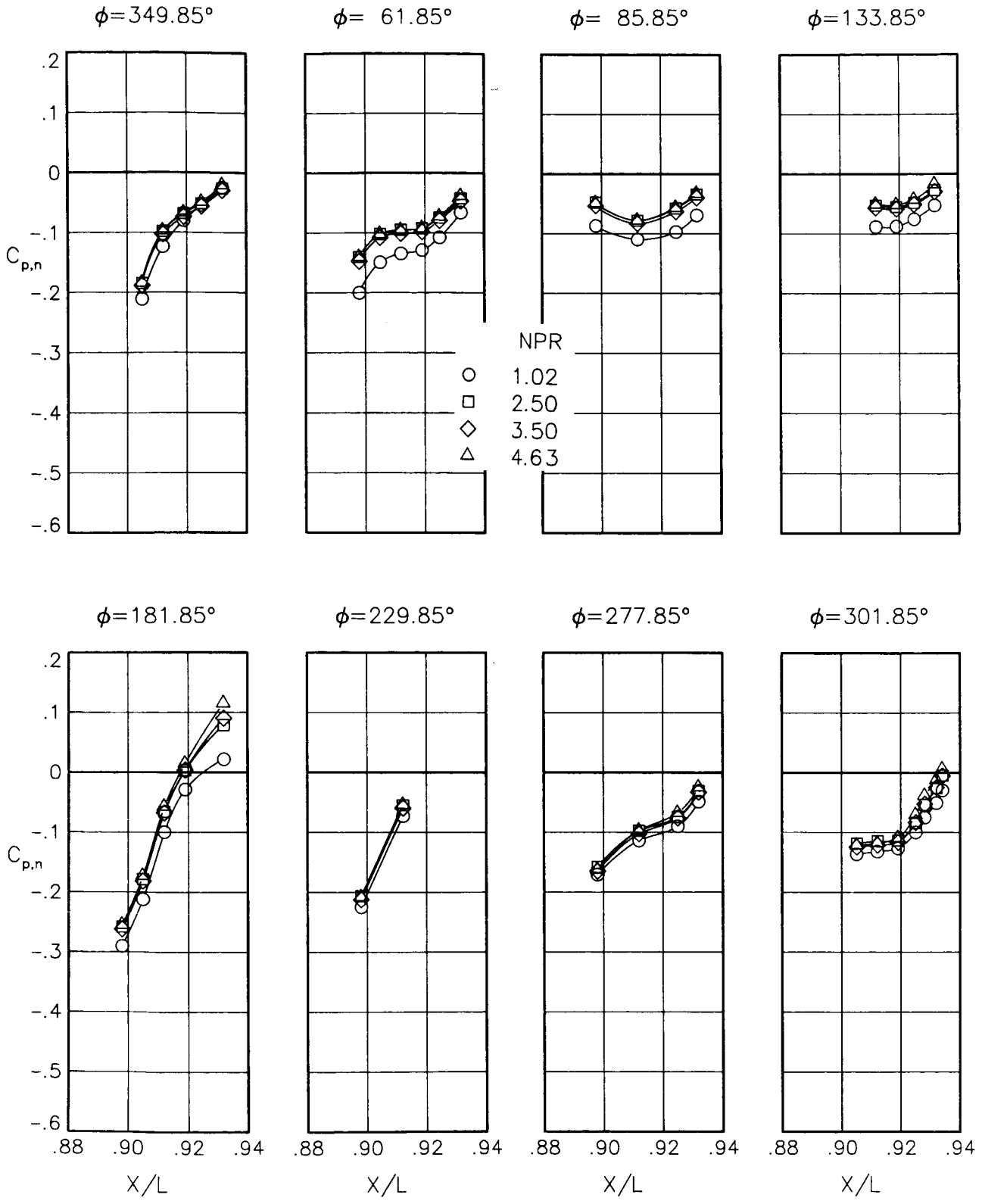

(j) M = 0.80; α = 7.00°.

Figure 72.- Continued.

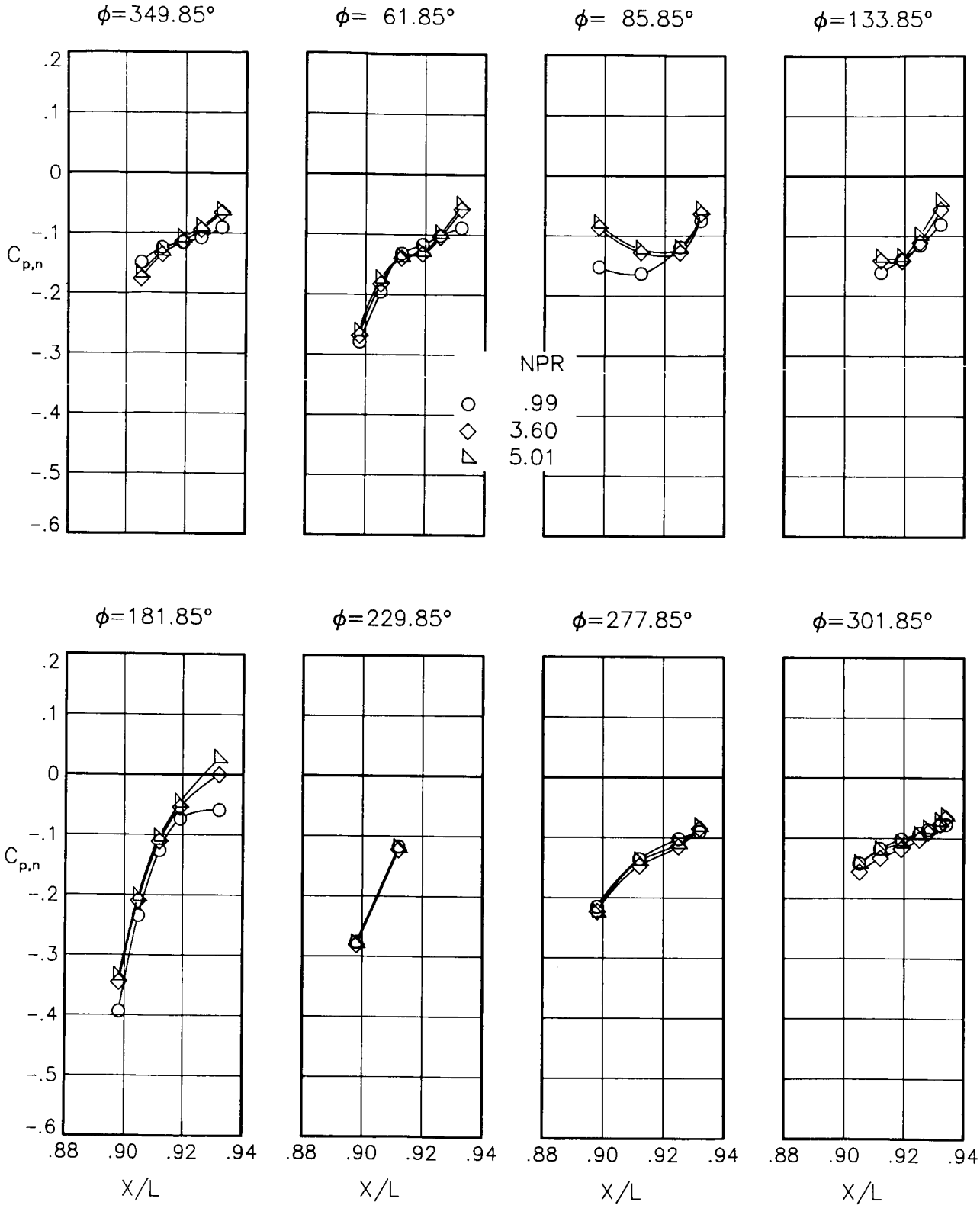

(k) M = 0.90; α = 0.00°.

Figure 72.- Continued.

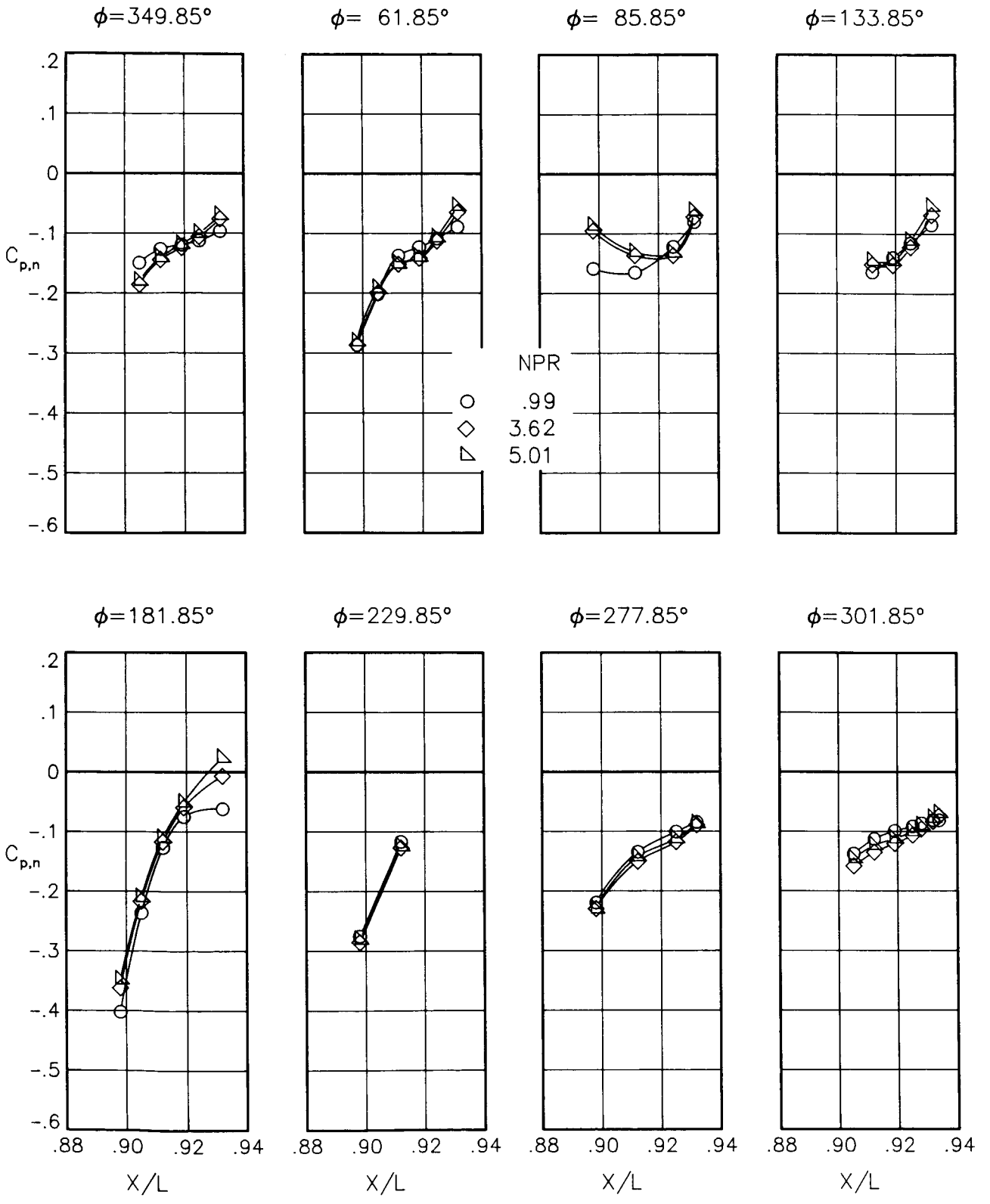

(1) M = 0.90; α = 1.00°.

Figure 72.- Continued.

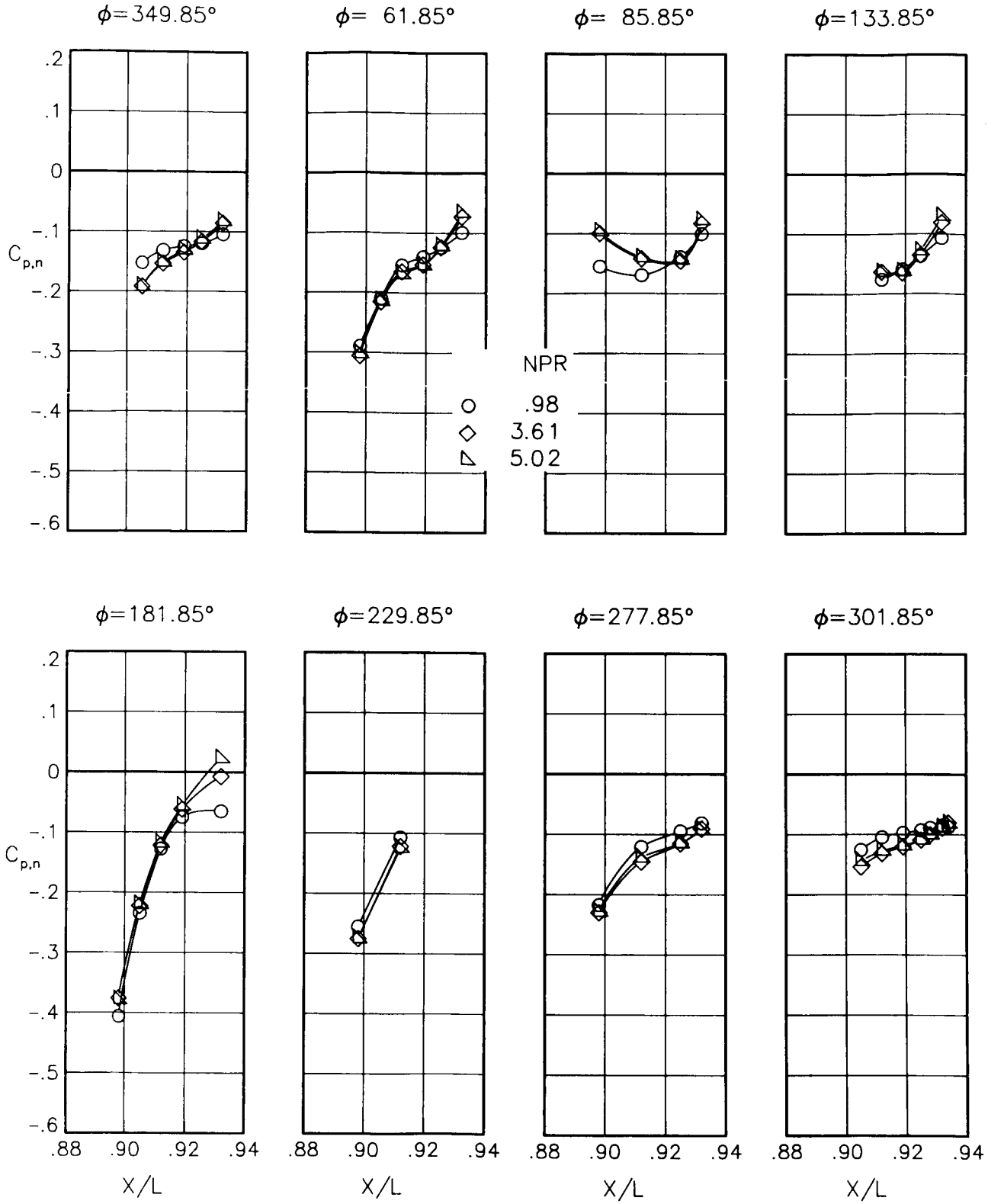

(m) M = 0.90; α = 3.00°.

Figure 72.- Continued.

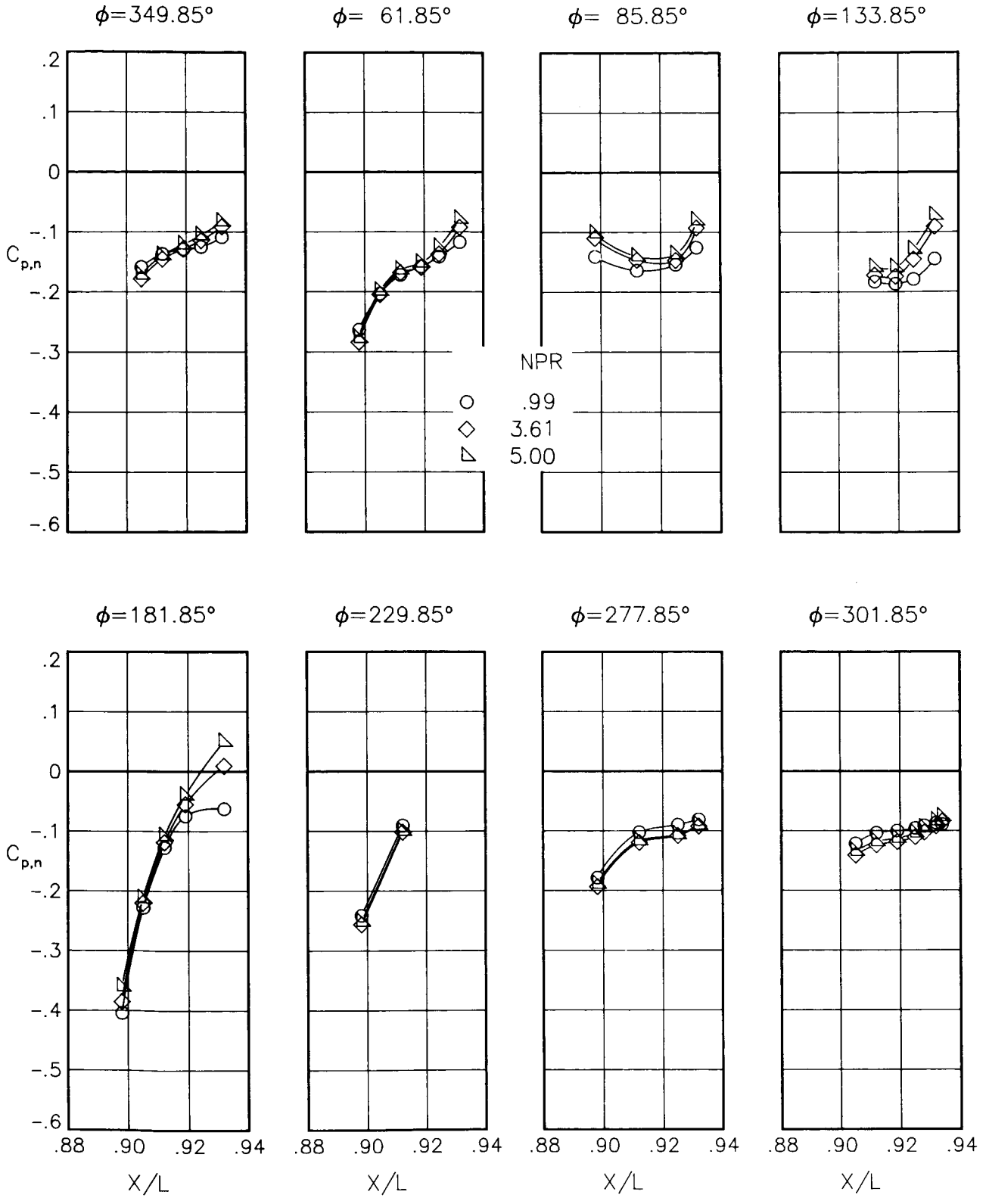

(n) M = 0.90; α = 6.00°.

Figure 72.- Concluded.

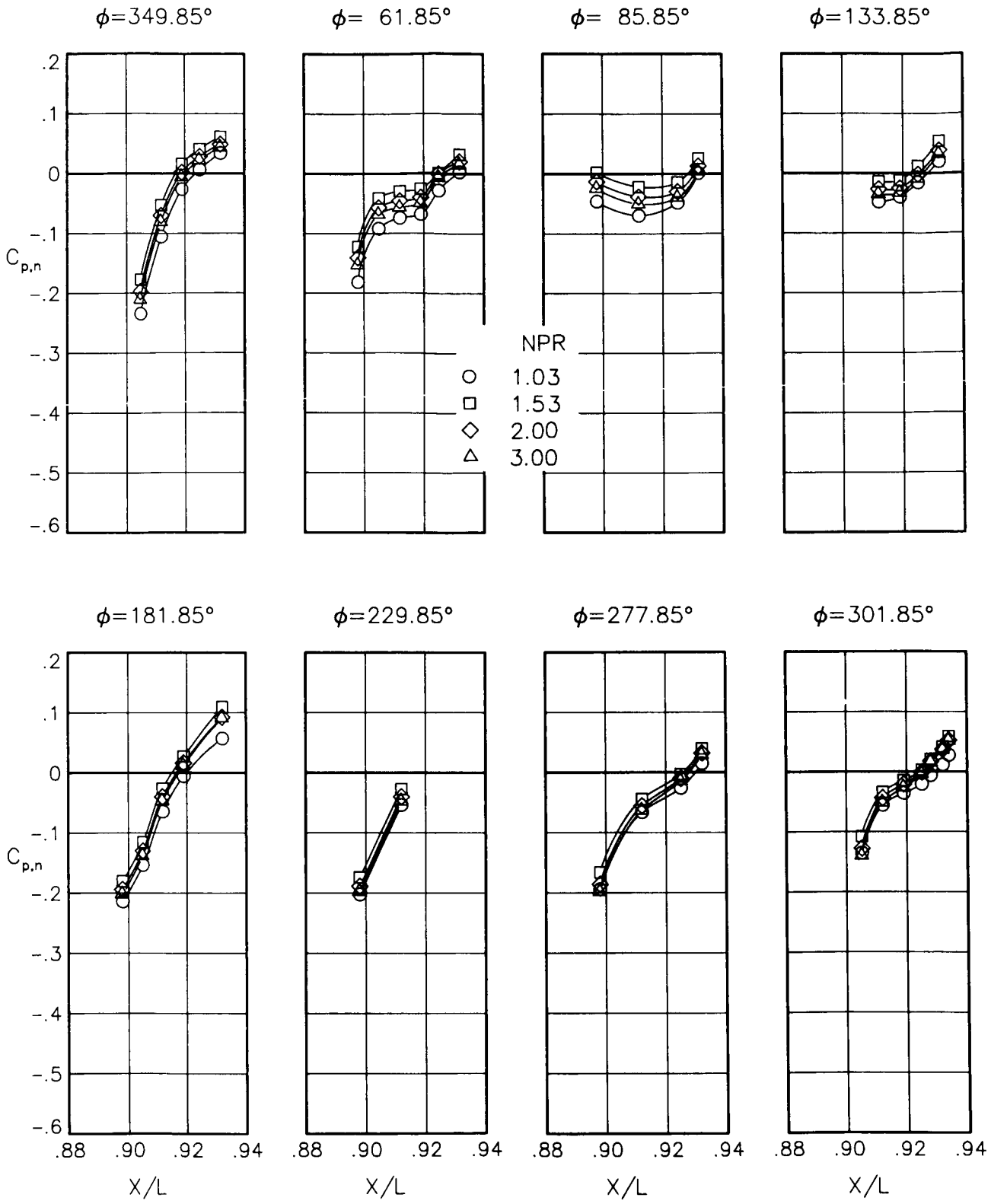

(a) M = 0.60; α = 0.00°.

Figure 73.- Static-pressure-coefficient distributions on nozzle for the model with all fuselage modifications. β_n = 18.45°; δ_h = -2°.

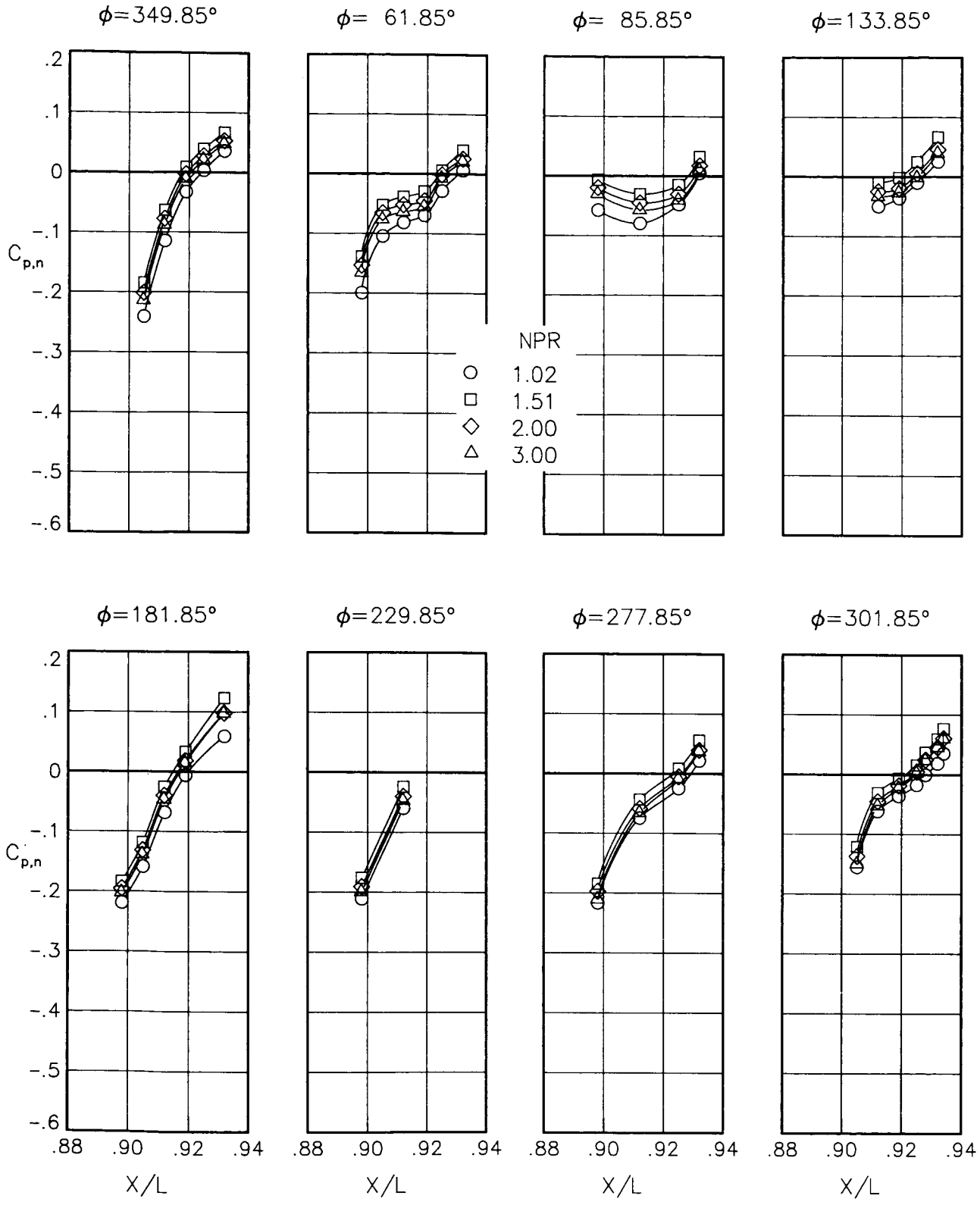

(b) M = 0.60; α = 1.00°.

Figure 73.- Continued.

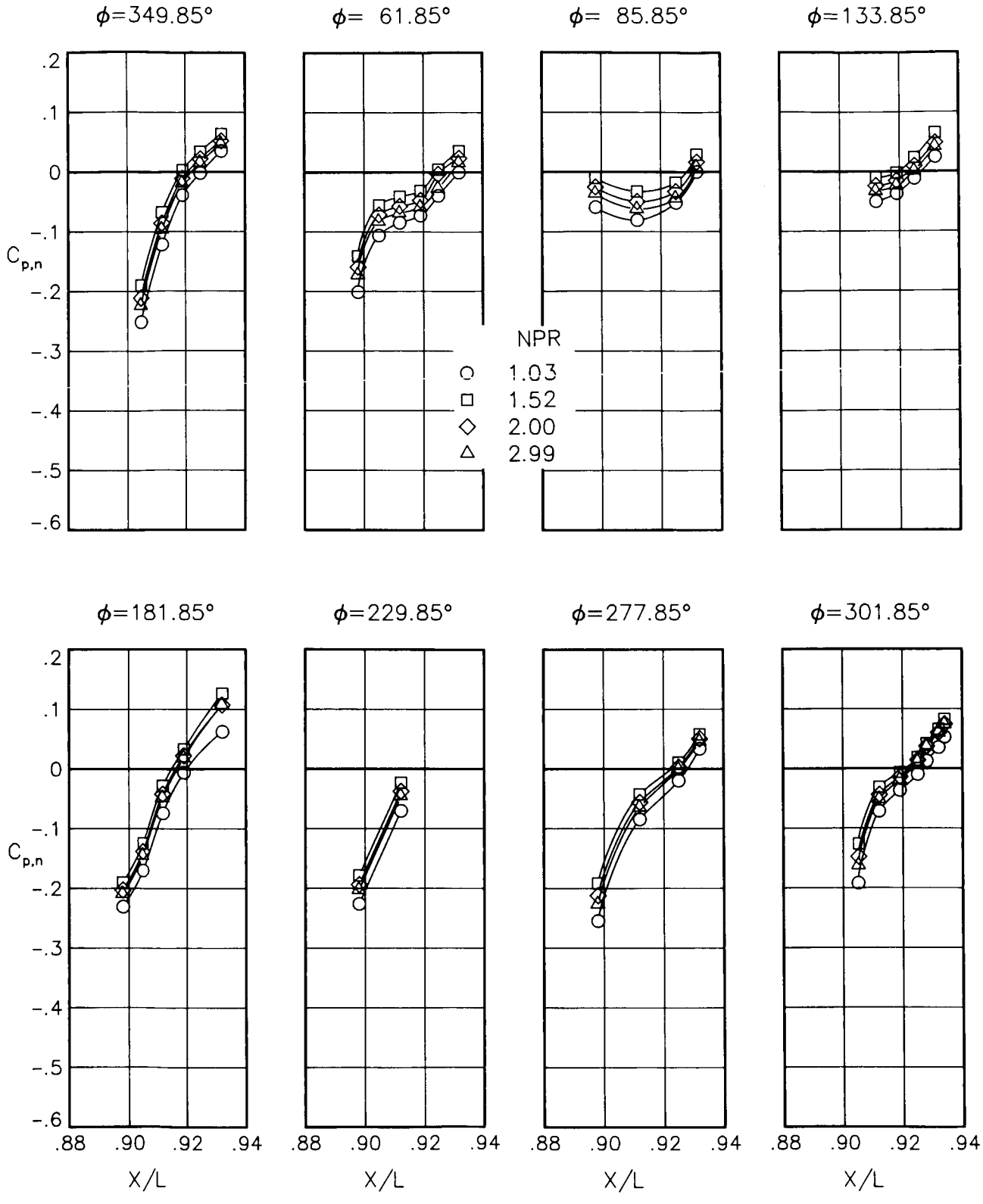

(c) M = 0.60; α = 3.00°.

Figure 73.- Continued.

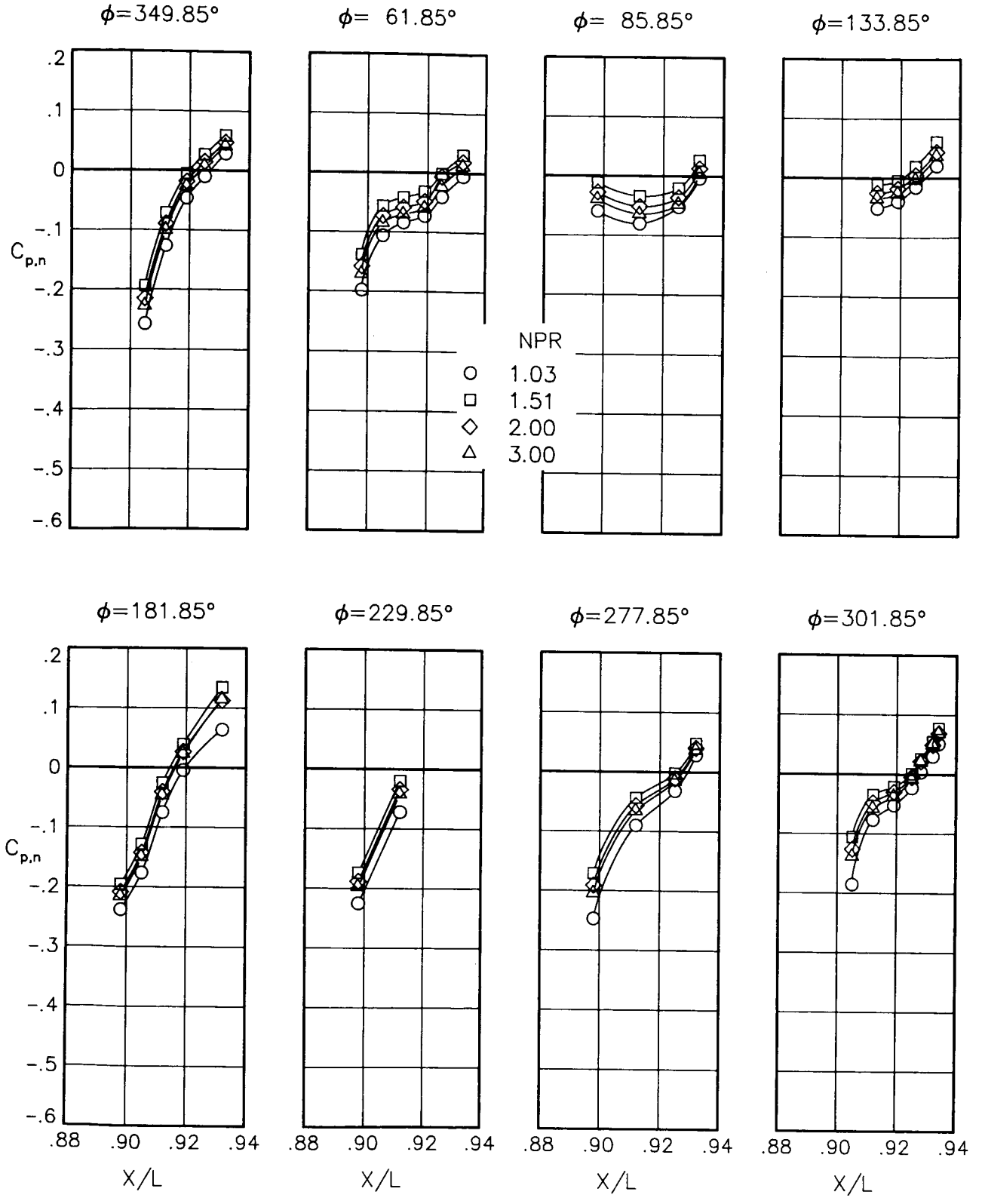

(d) M = 0.60; α = 5.00°.

Figure 73.- Continued.

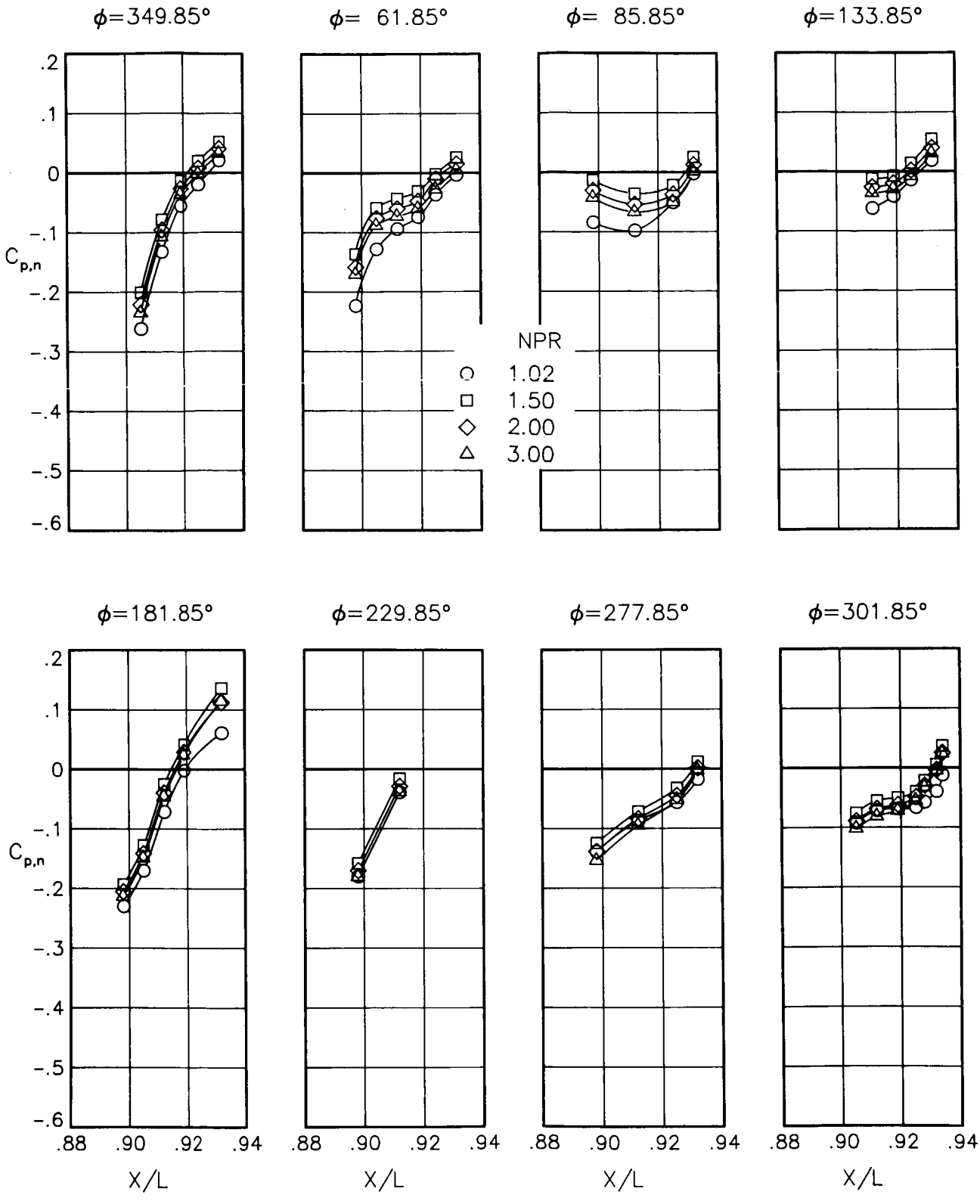

(e) M = 0.60; α = 7.00°.

Figure 73.- Continued.

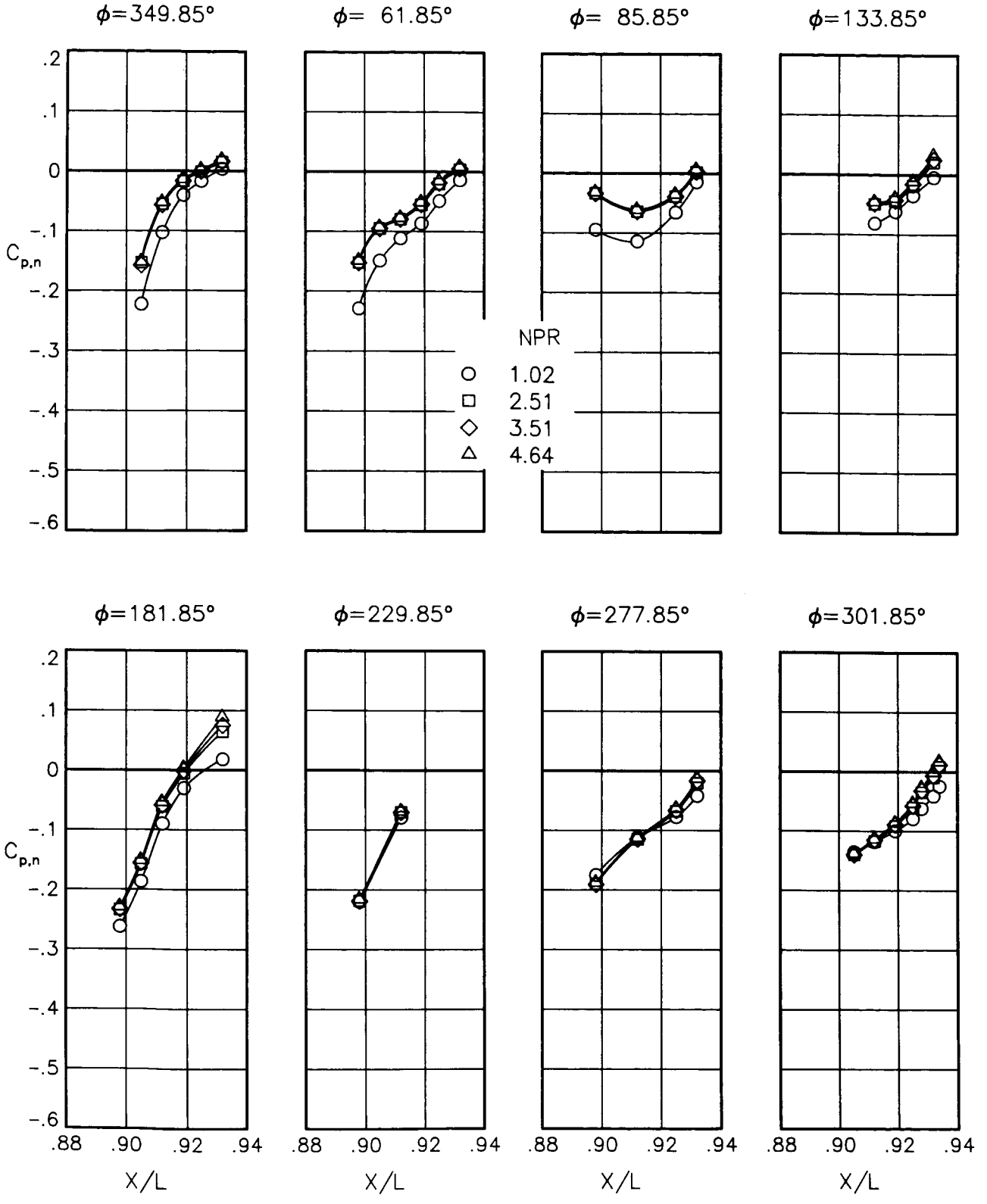

(f) M = 0.80; α = 0.00°.

Figure 73.- Continued.

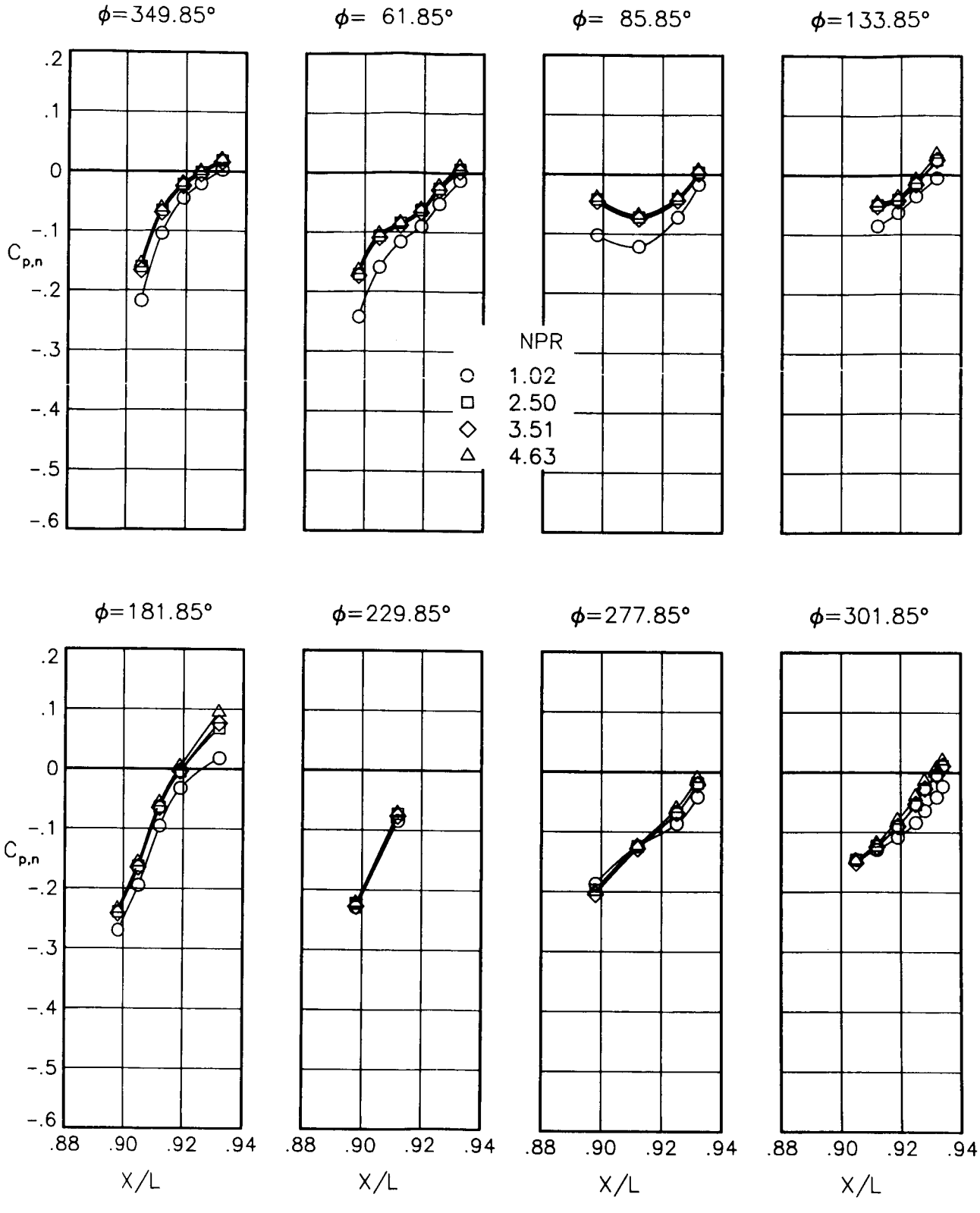

(g) M = 0.80; α = 1.00°.

Figure 73.- Continued.

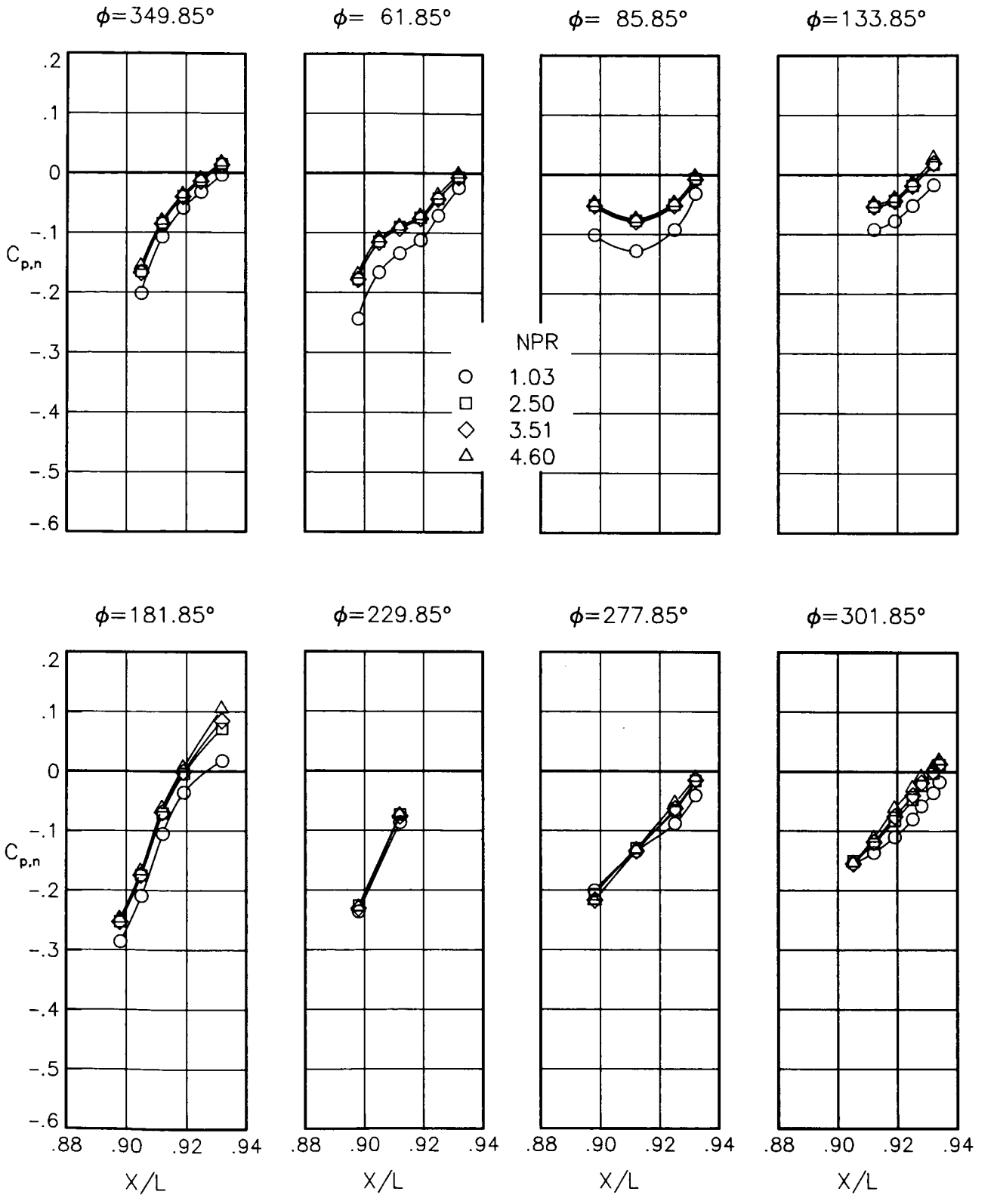

(h) M = 0.80; α = 3.00°.

Figure 73.- Continued.

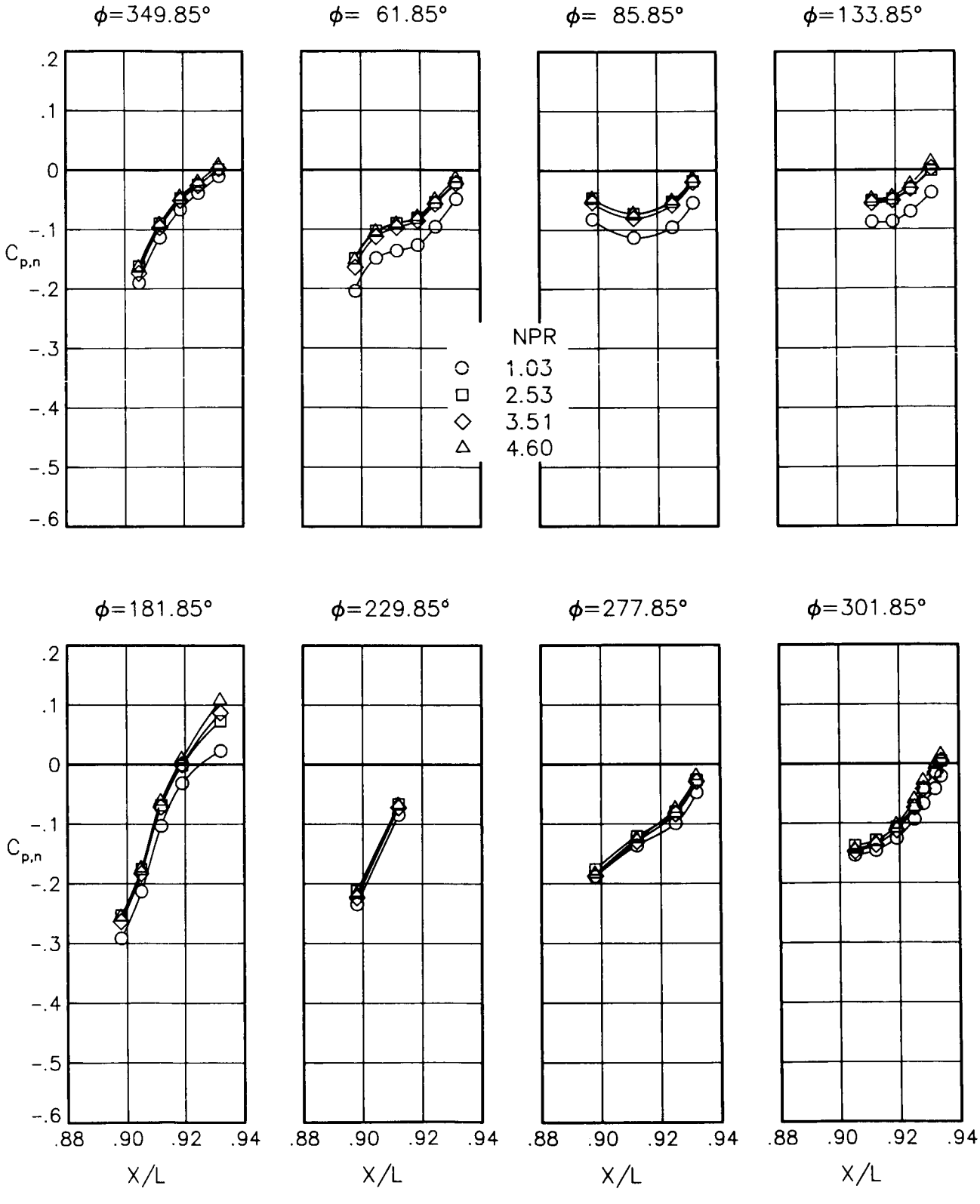

(i) M = 0.80; α = 5.00°.

Figure 73.- Continued.

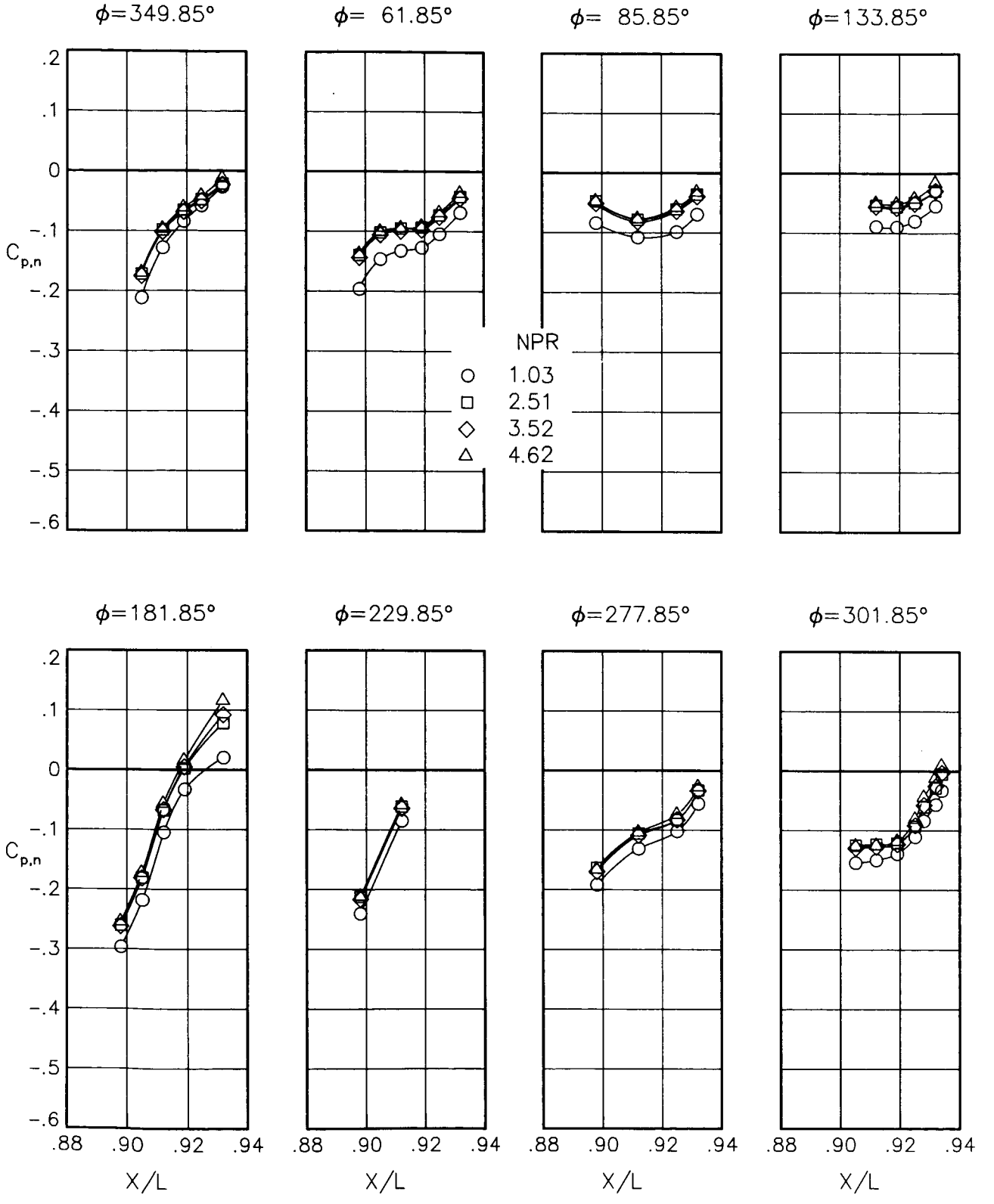

(j) M = 0.80; α = 7.00°.

Figure 73.- Continued.

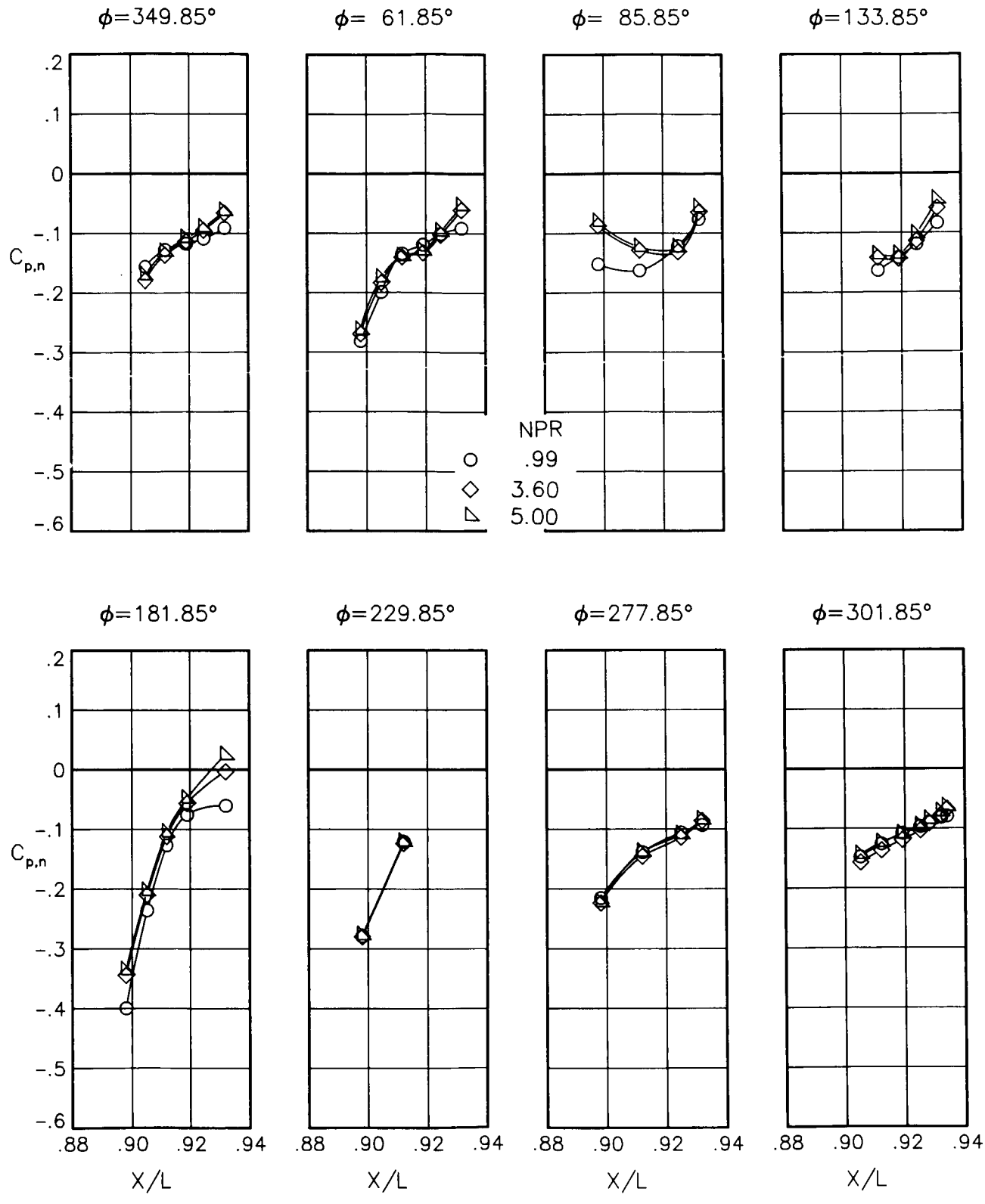

(k) M = 0.90; α = 0.00°.

Figure 73.- Continued.

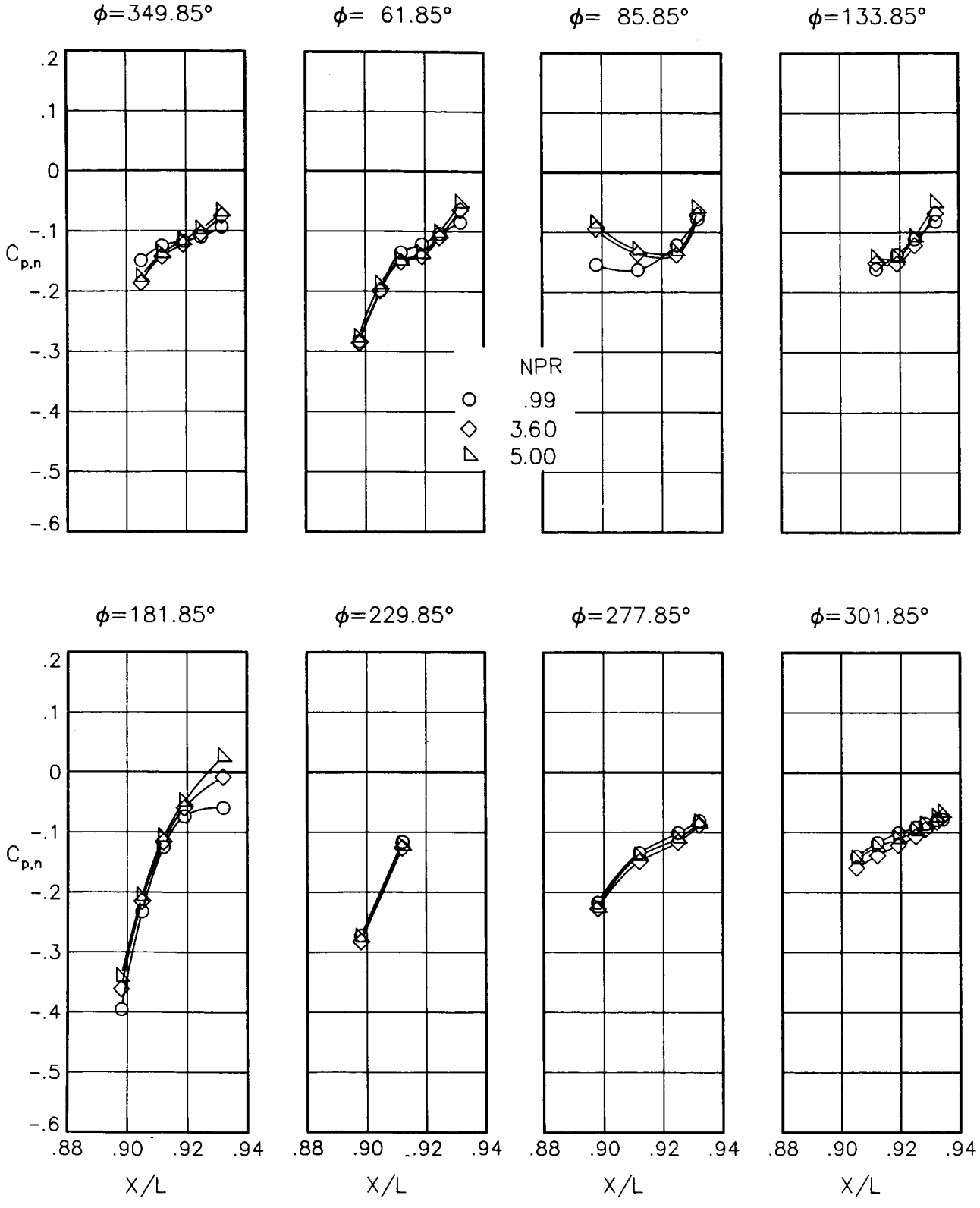

(l) M = 0.90; α = 1.00°.

Figure 73.- Continued.

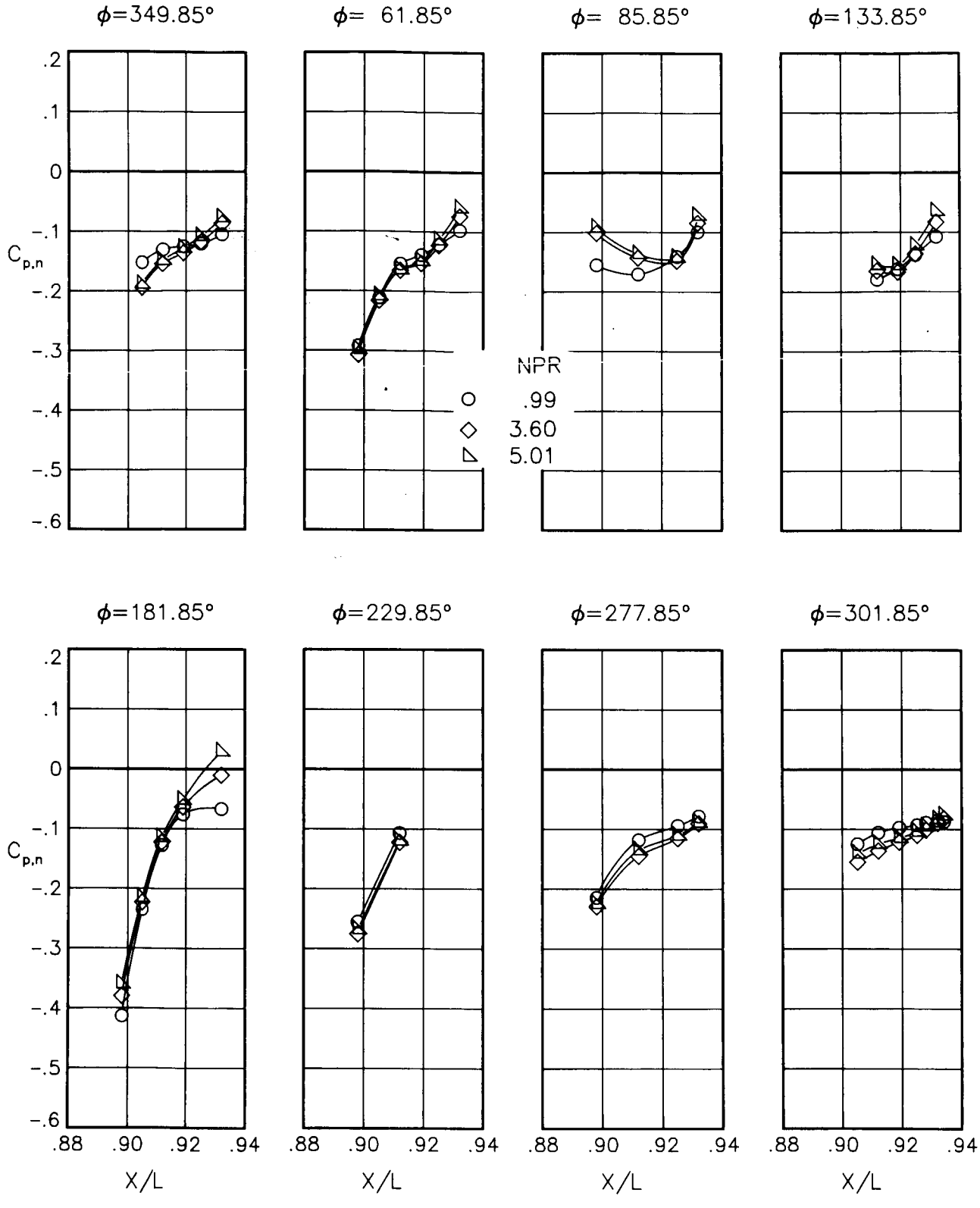

(m) M = 0.90; α = 3.00°.

Figure 73.- Continued.

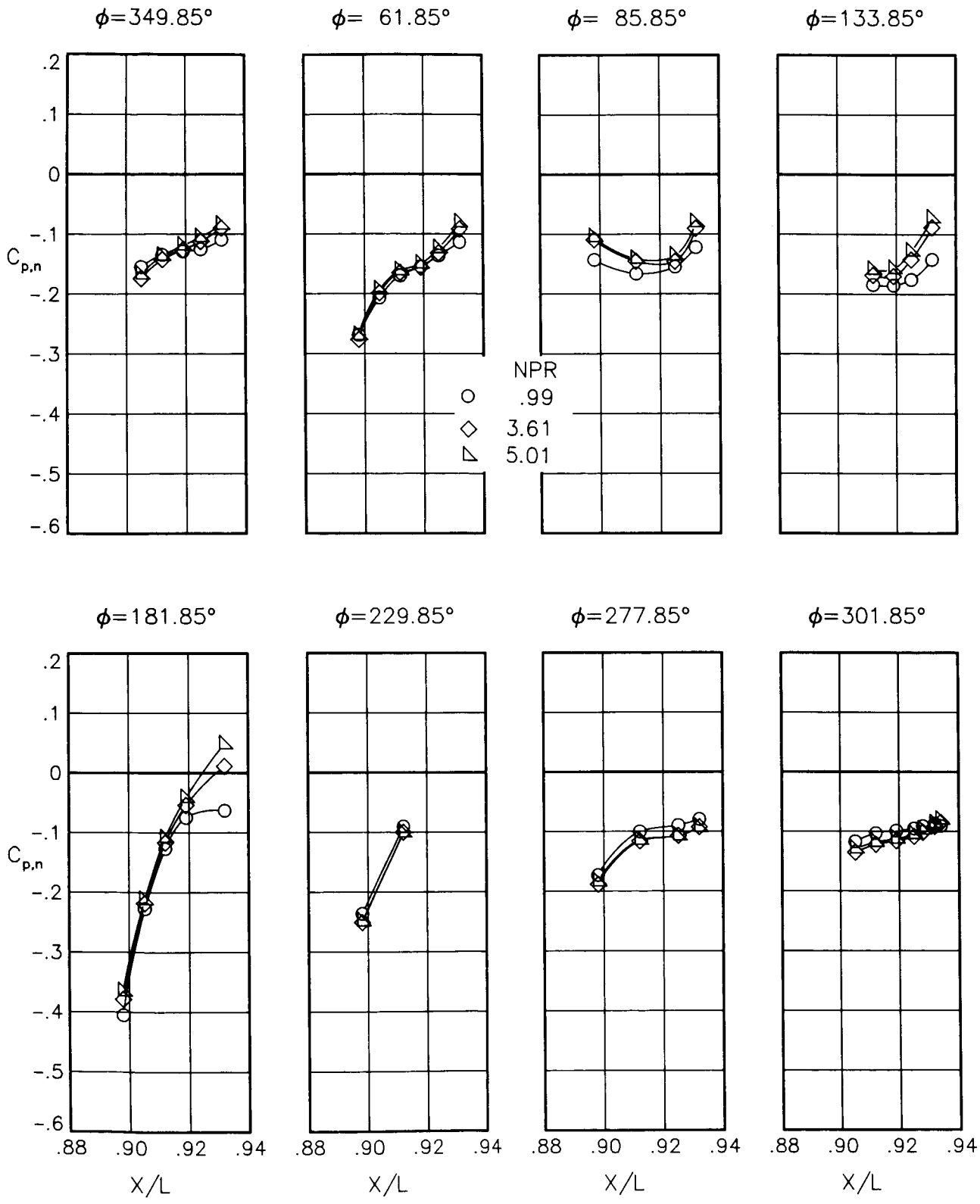

(n) M = 0.90; α = 6.00°.

Figure 73.- Concluded.

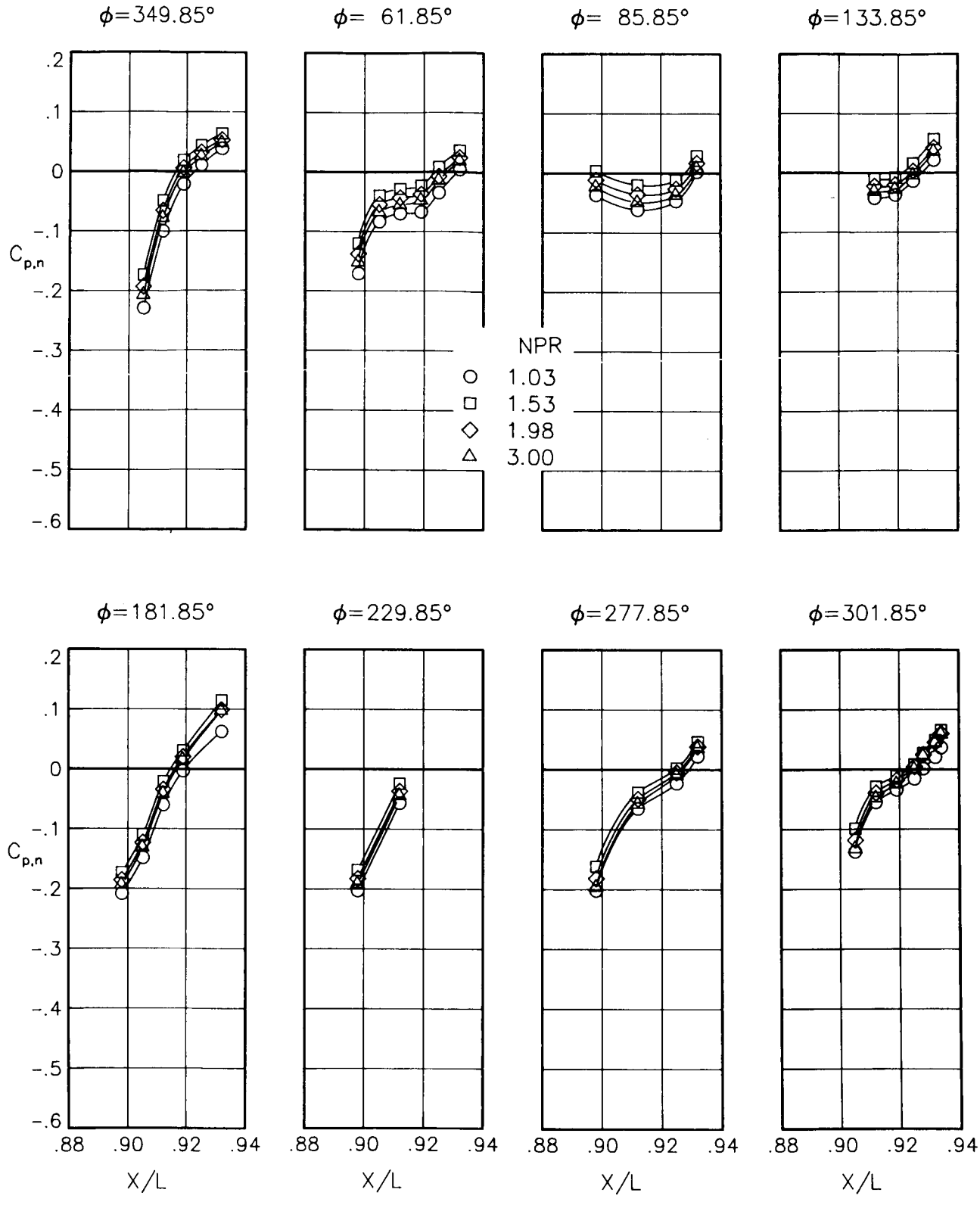

(a) M = 0.60; α = 0.00°.

Figure 74.- Static-pressure-coefficient distributions on nozzle for the model with all fuselage modifications. β_n = 18.45°.

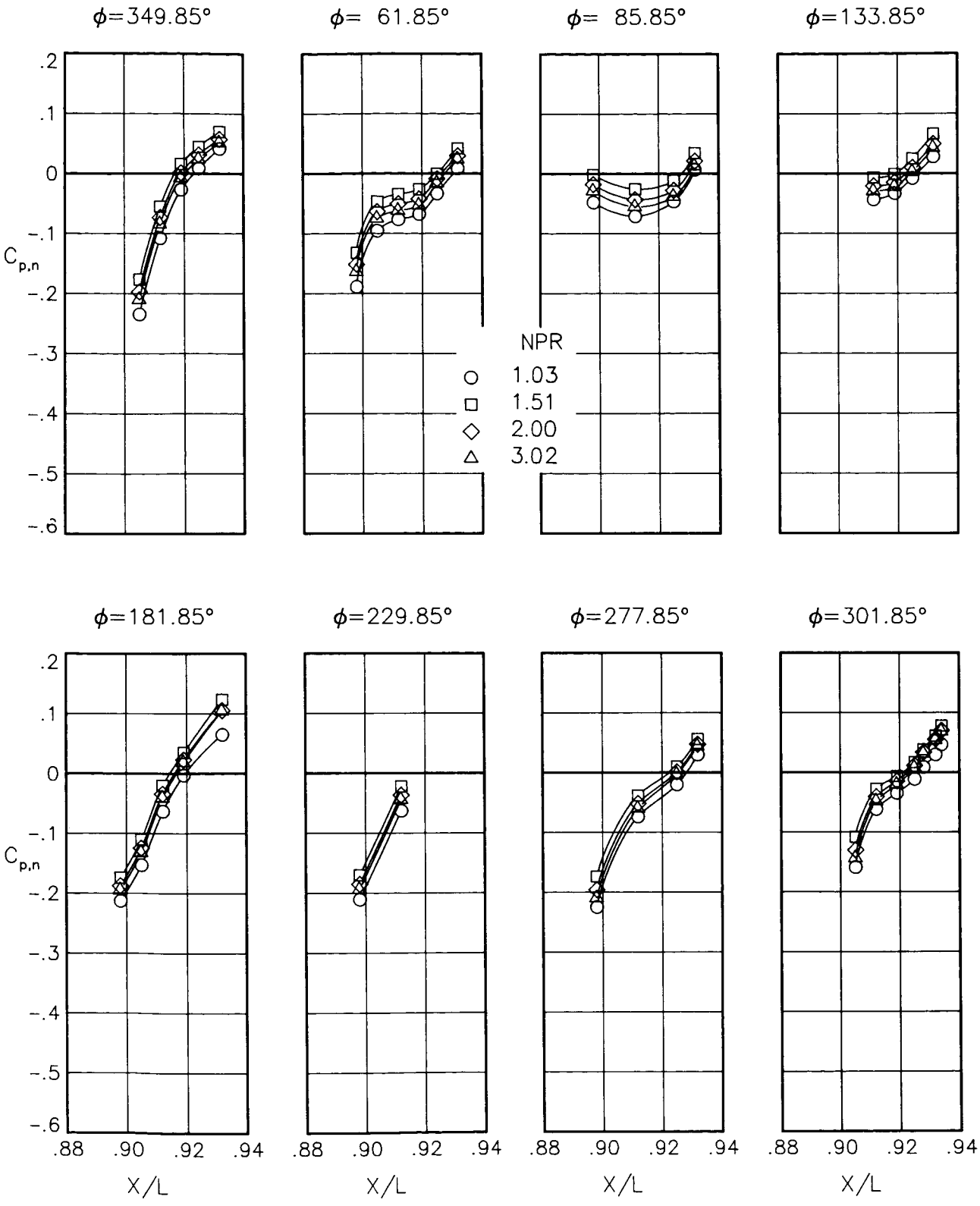

(b) M = 0.60; α = 1.00°.

Figure 74.- Continued.

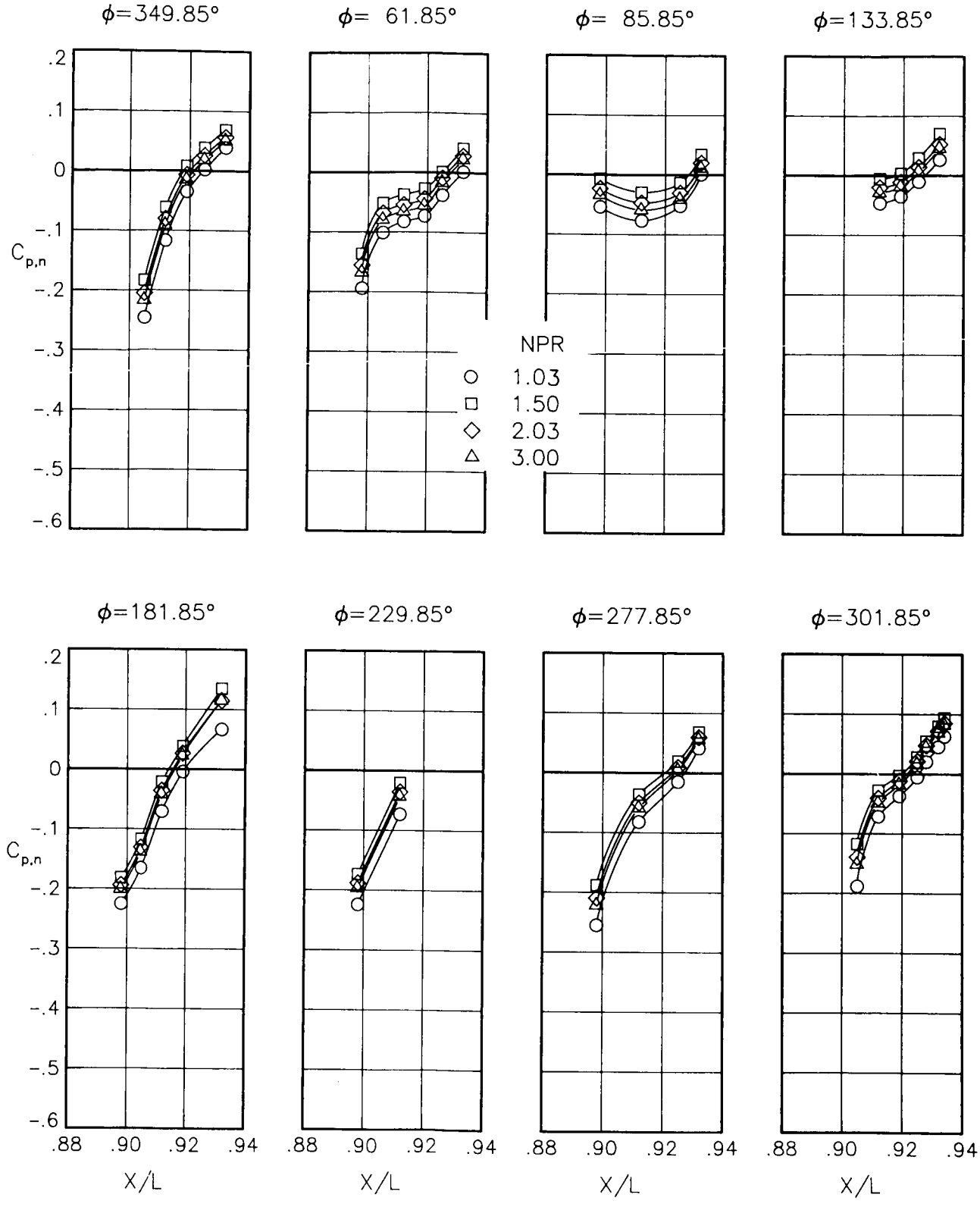

(c) M = 0.60; α = 3.00°.

Figure 74.- Continued.

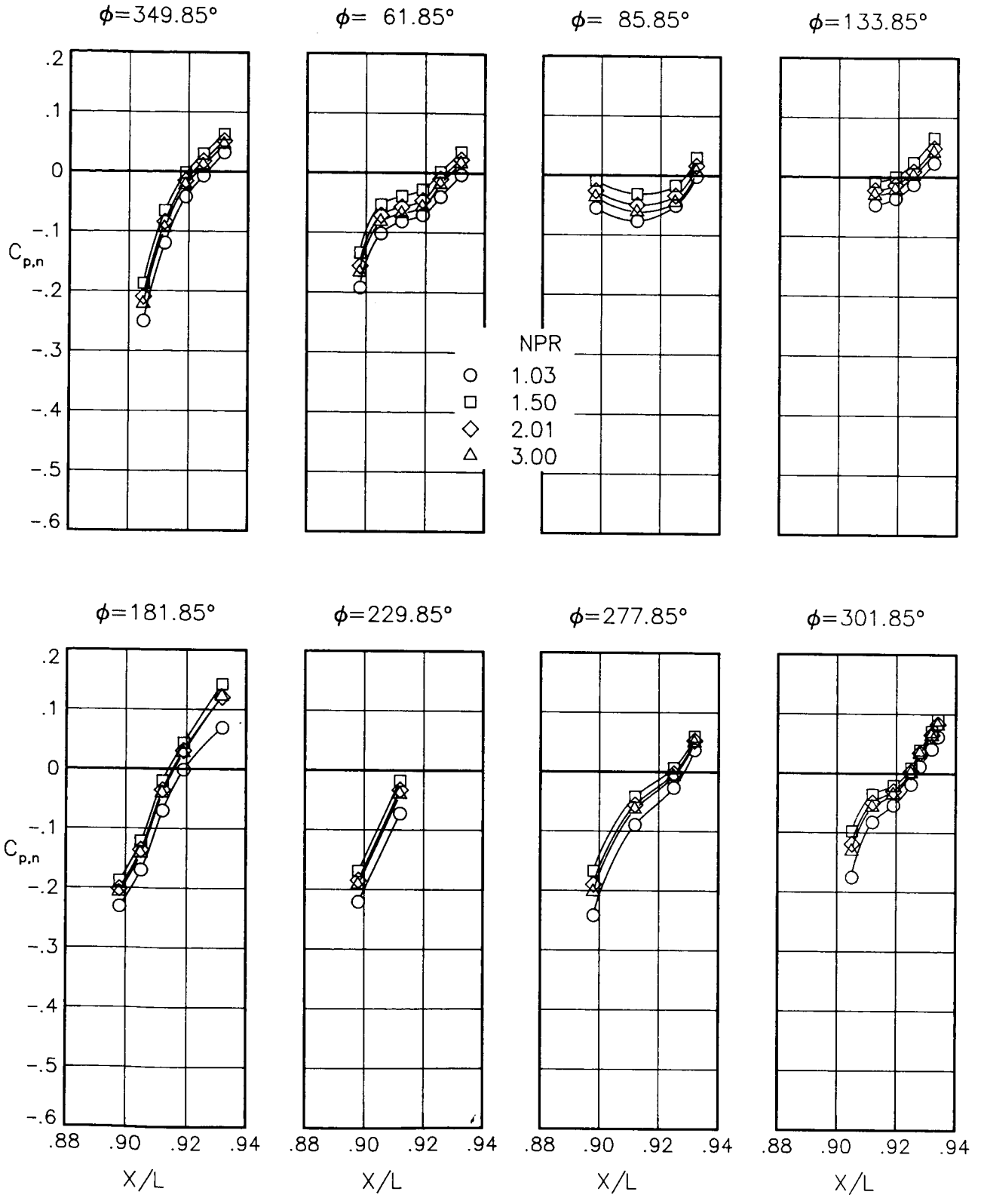

(d) M = 0.60; α = 5.00°.

Figure 74.- Continued.

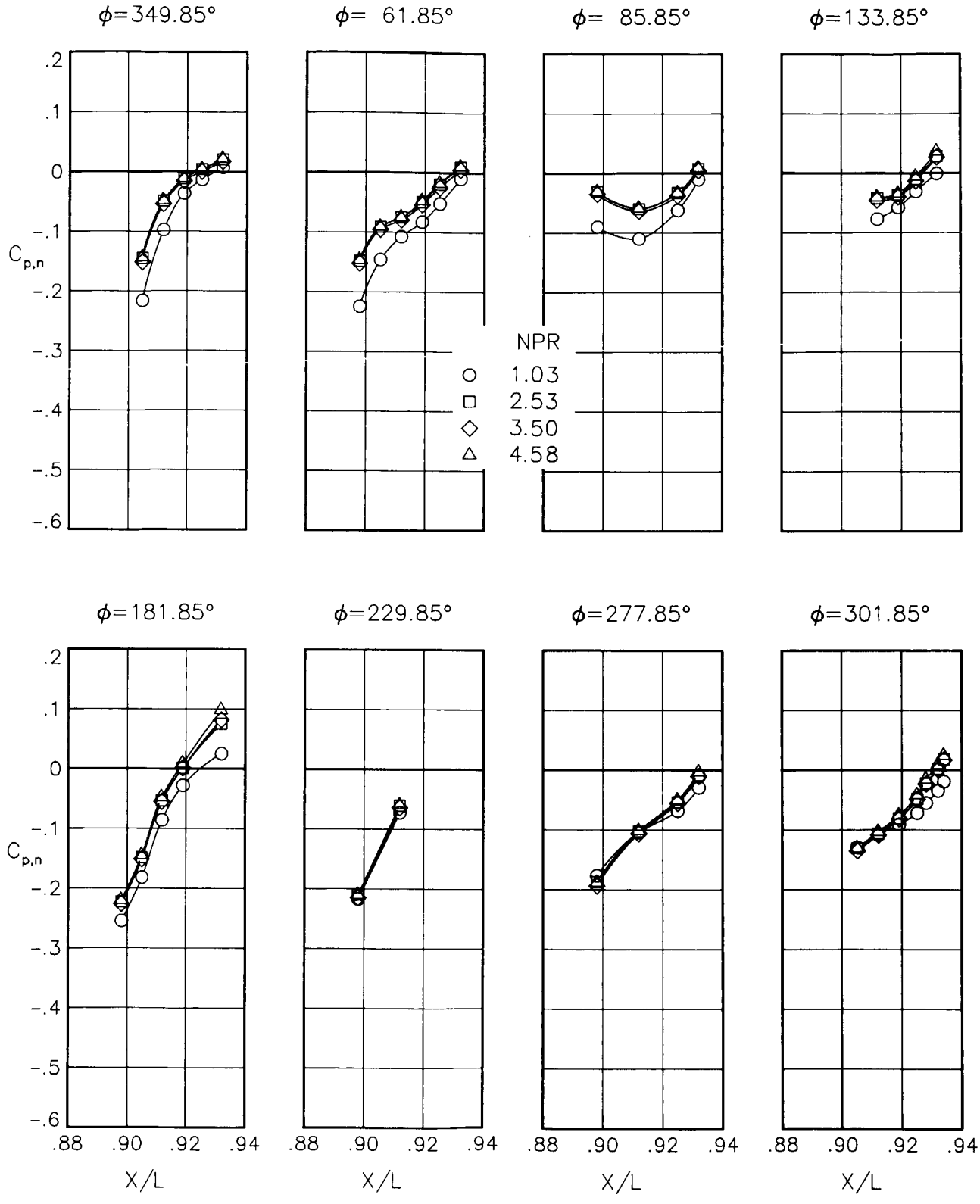

(e) M = 0.80; α = 0.00°.

Figure 74.- Continued.

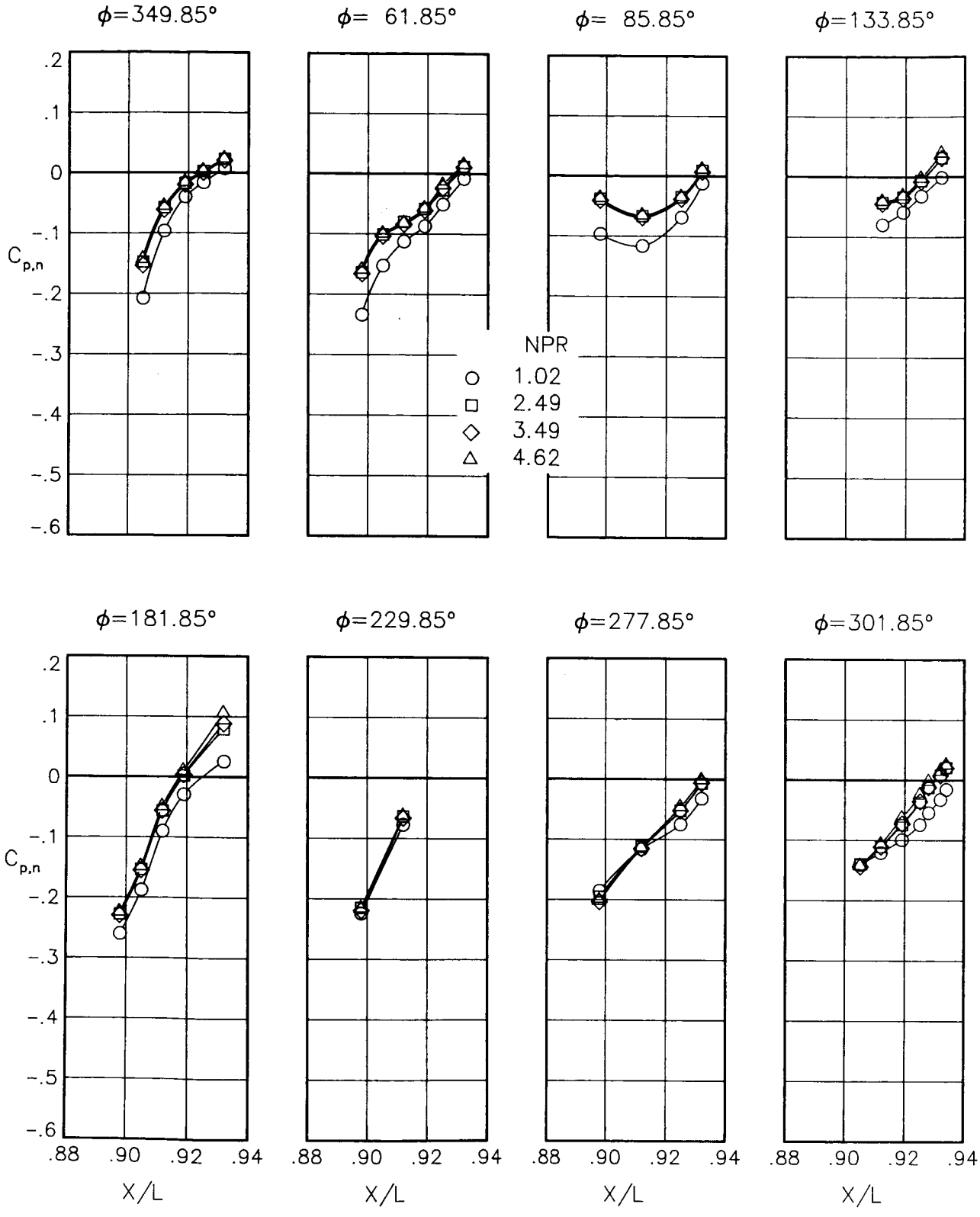

(f) M = 0.80; α = 1.00°.

Figure 74.- Continued.

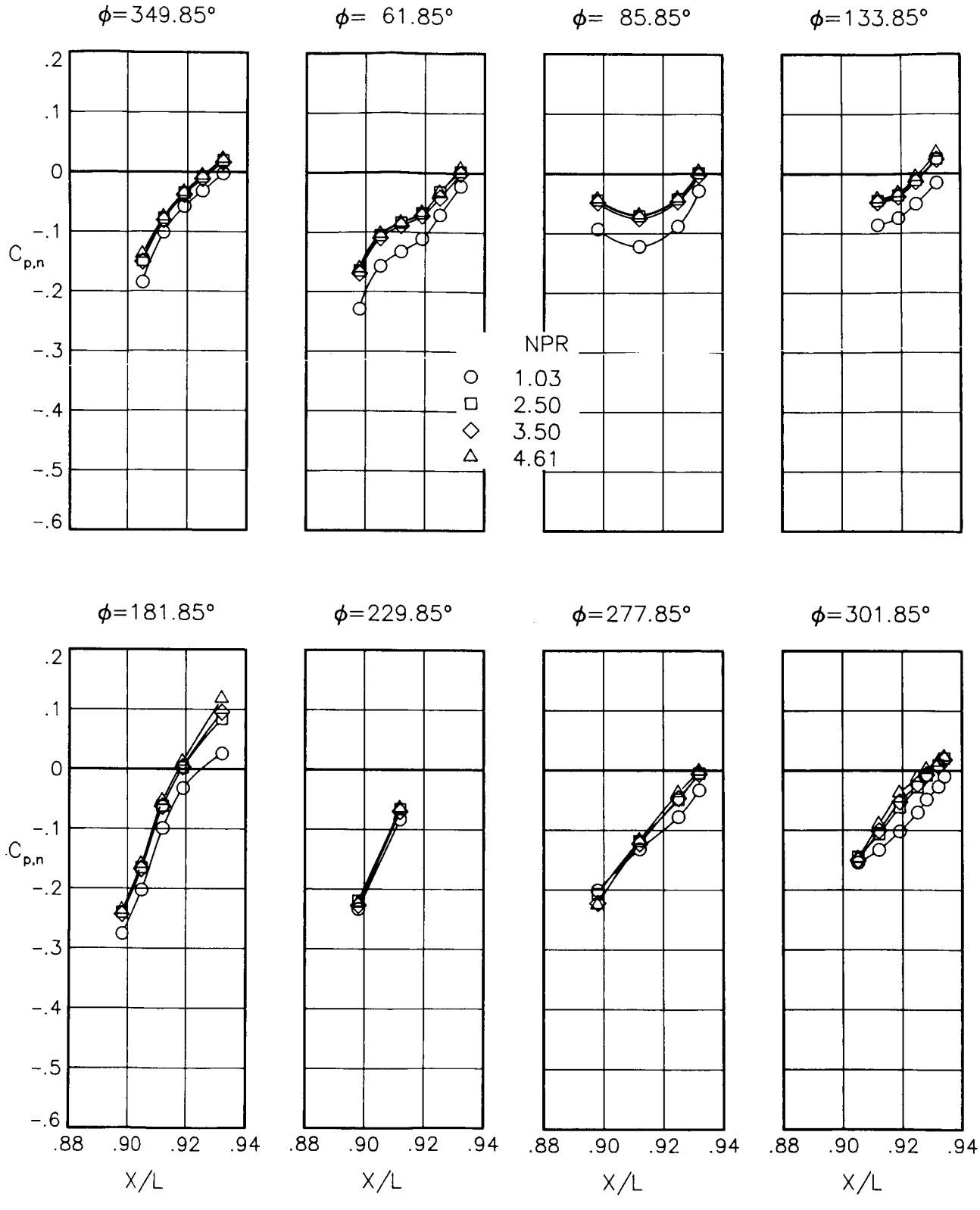

(g) M = 0.80; α = 3.00°.

Figure 74.- Continued.

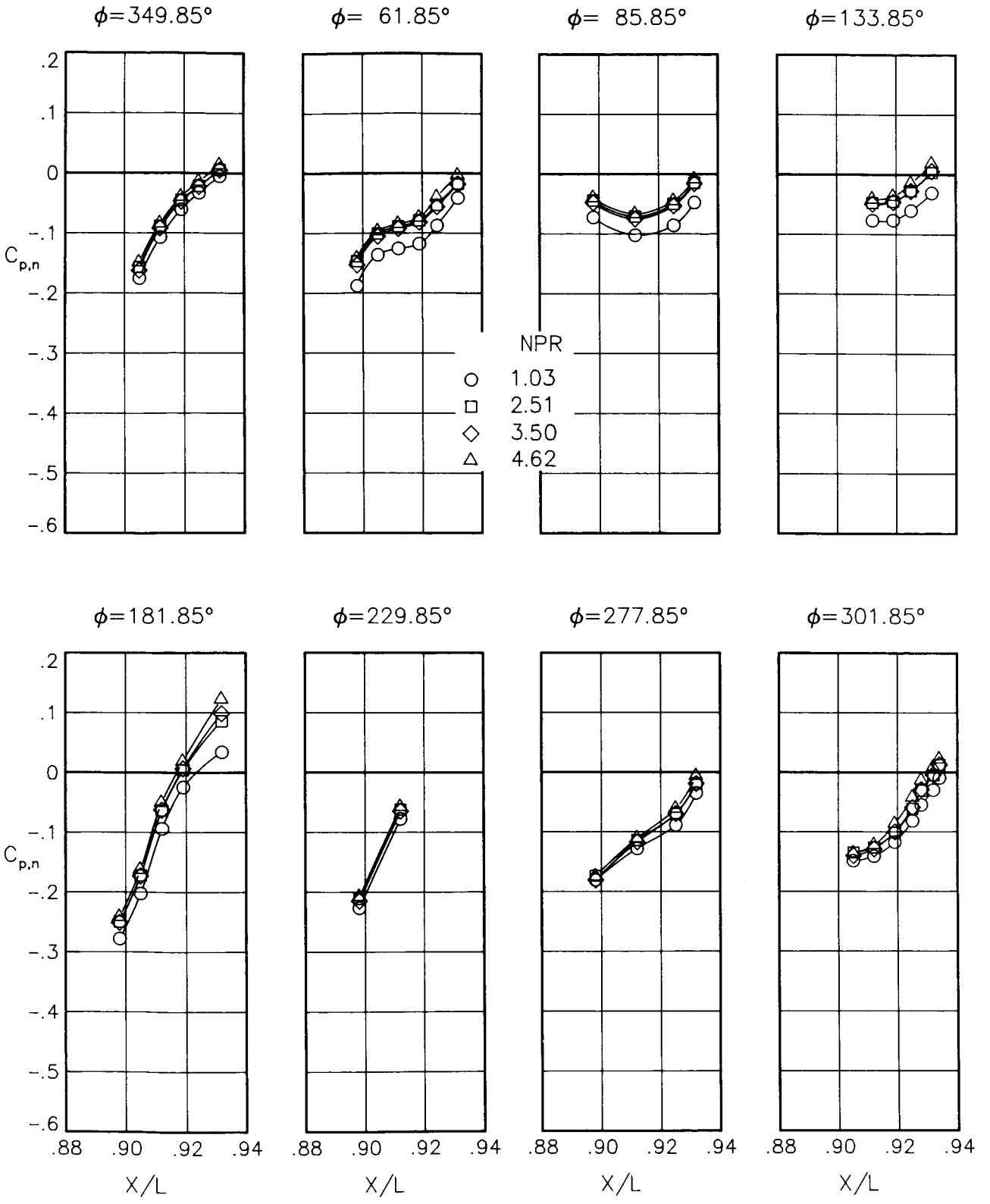

(h) M = 0.80; α = 5.00°.

Figure 74.- Continued.

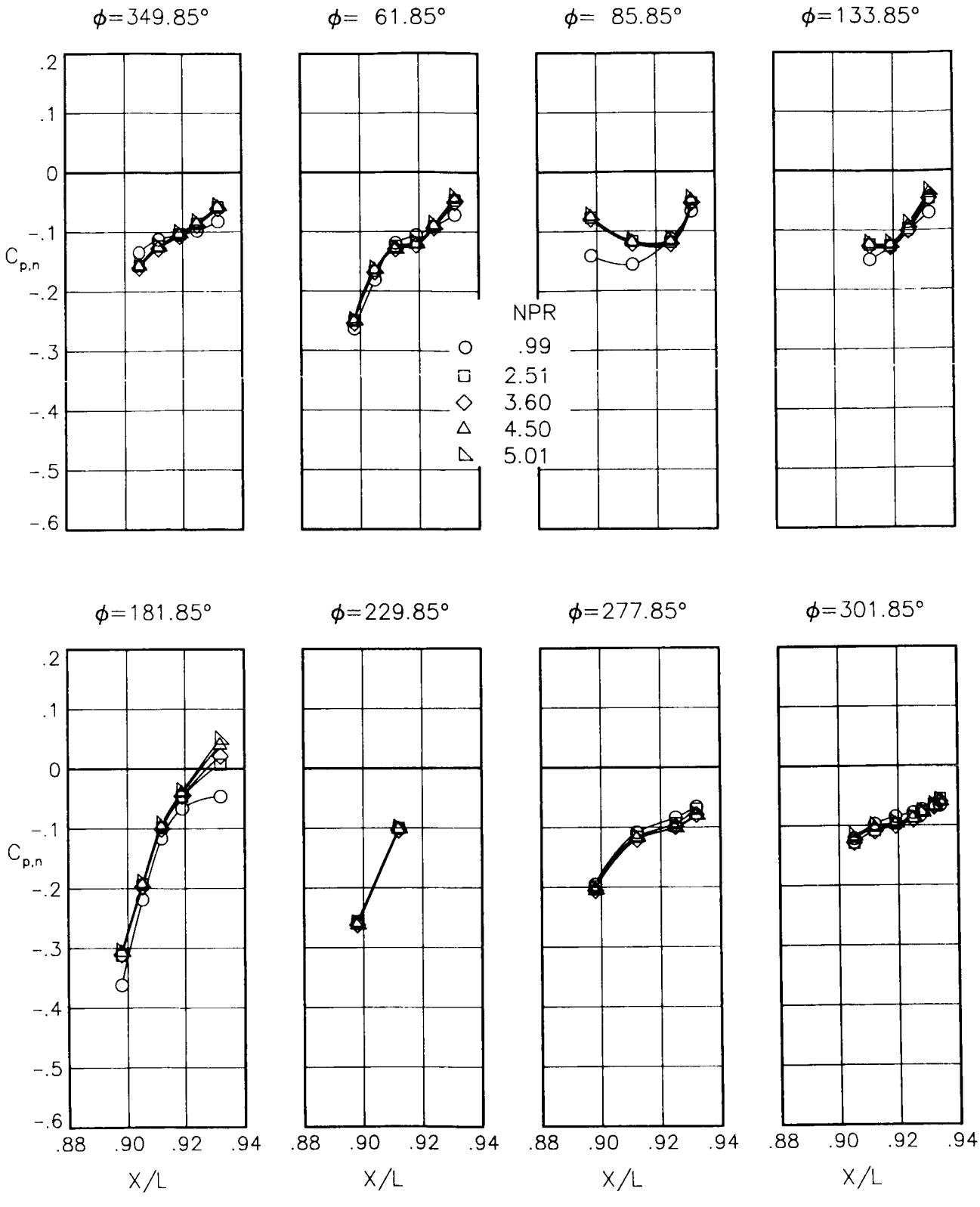

(i) M = 0.90; α = 0.00°.

Figure 74.- Continued.

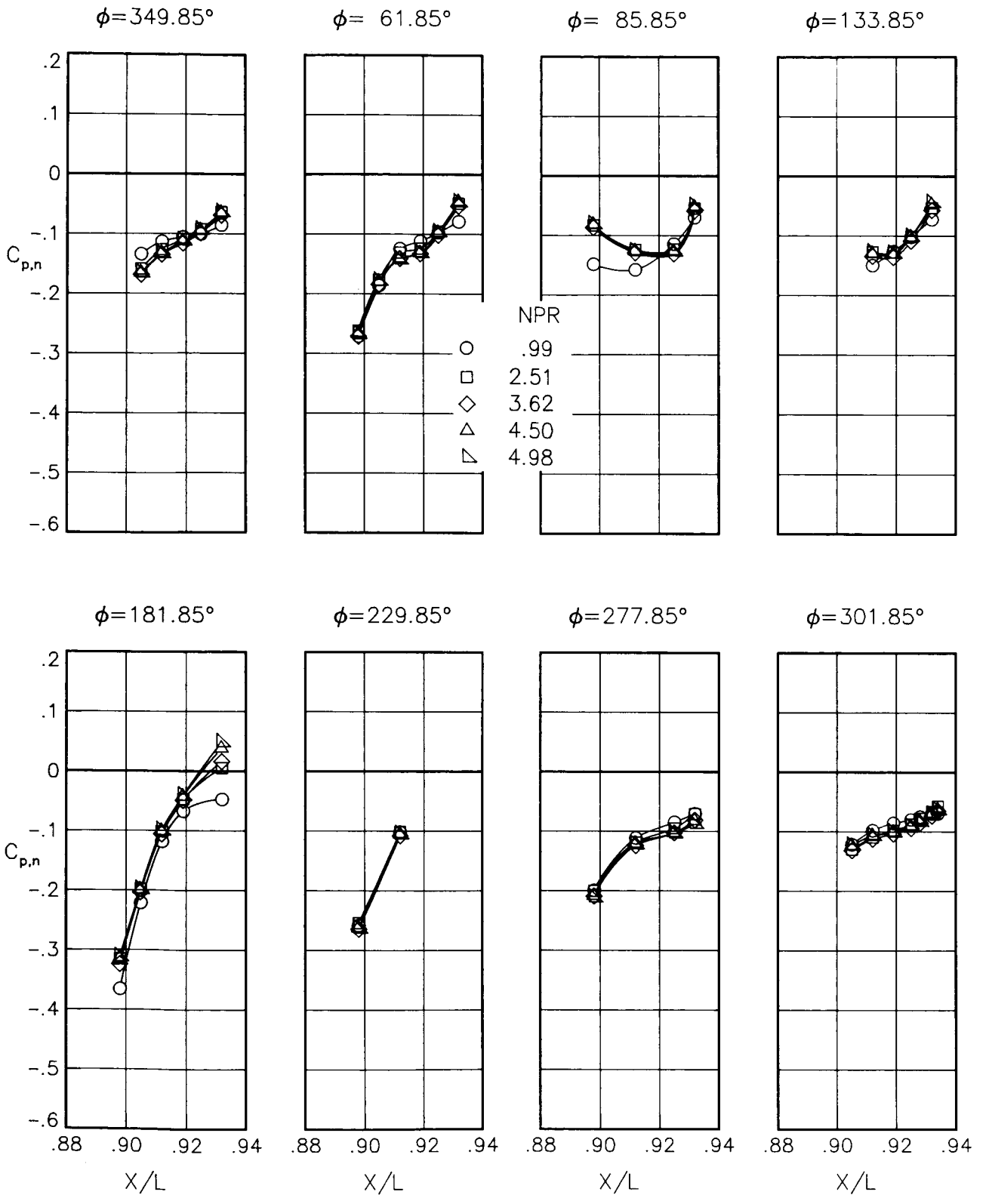

(j) M = 0.90; α = 1.00°.

Figure 74.- Continued.

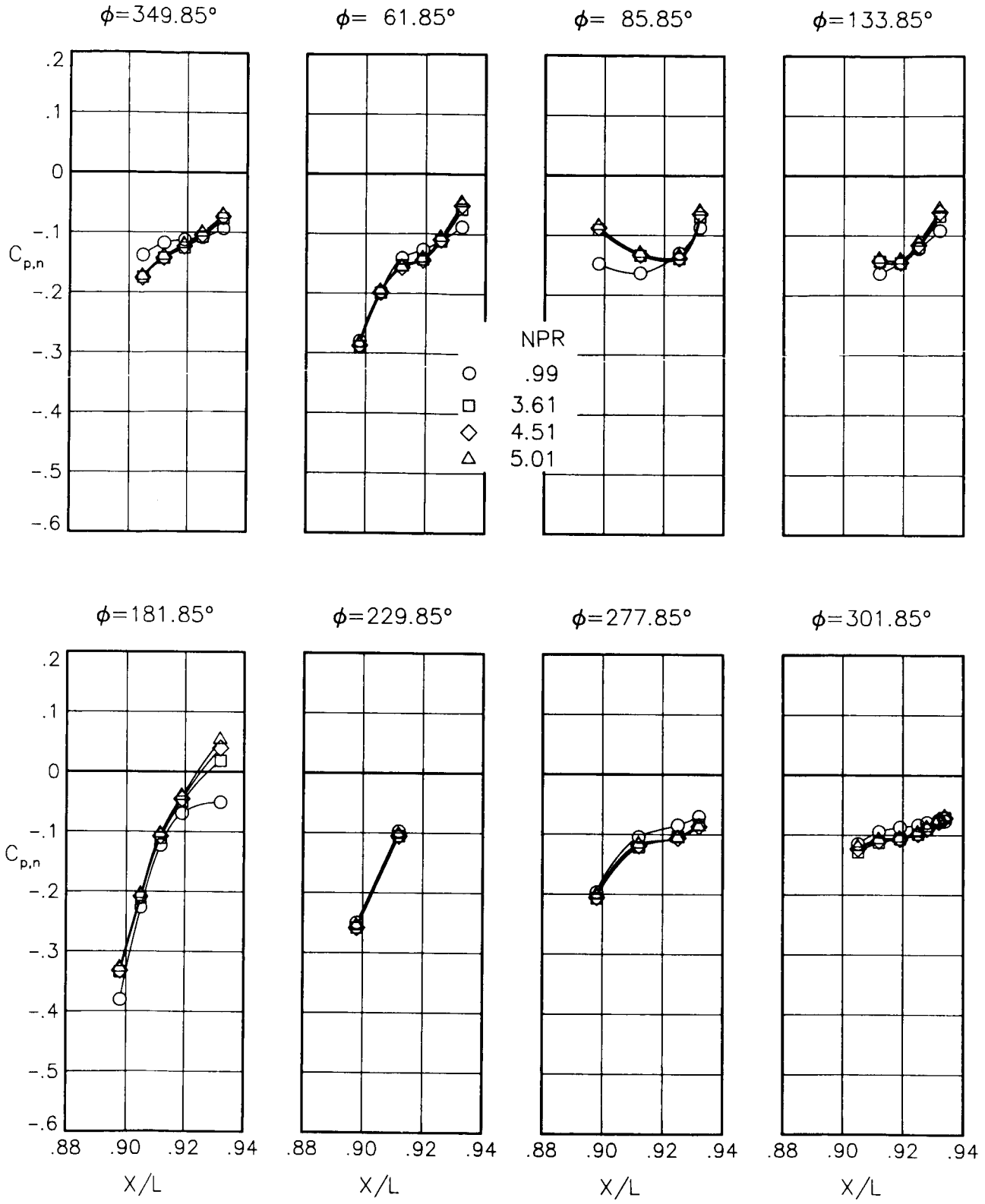

(k) M = 0.90; α = 3.00°.

Figure 74.- Continued.

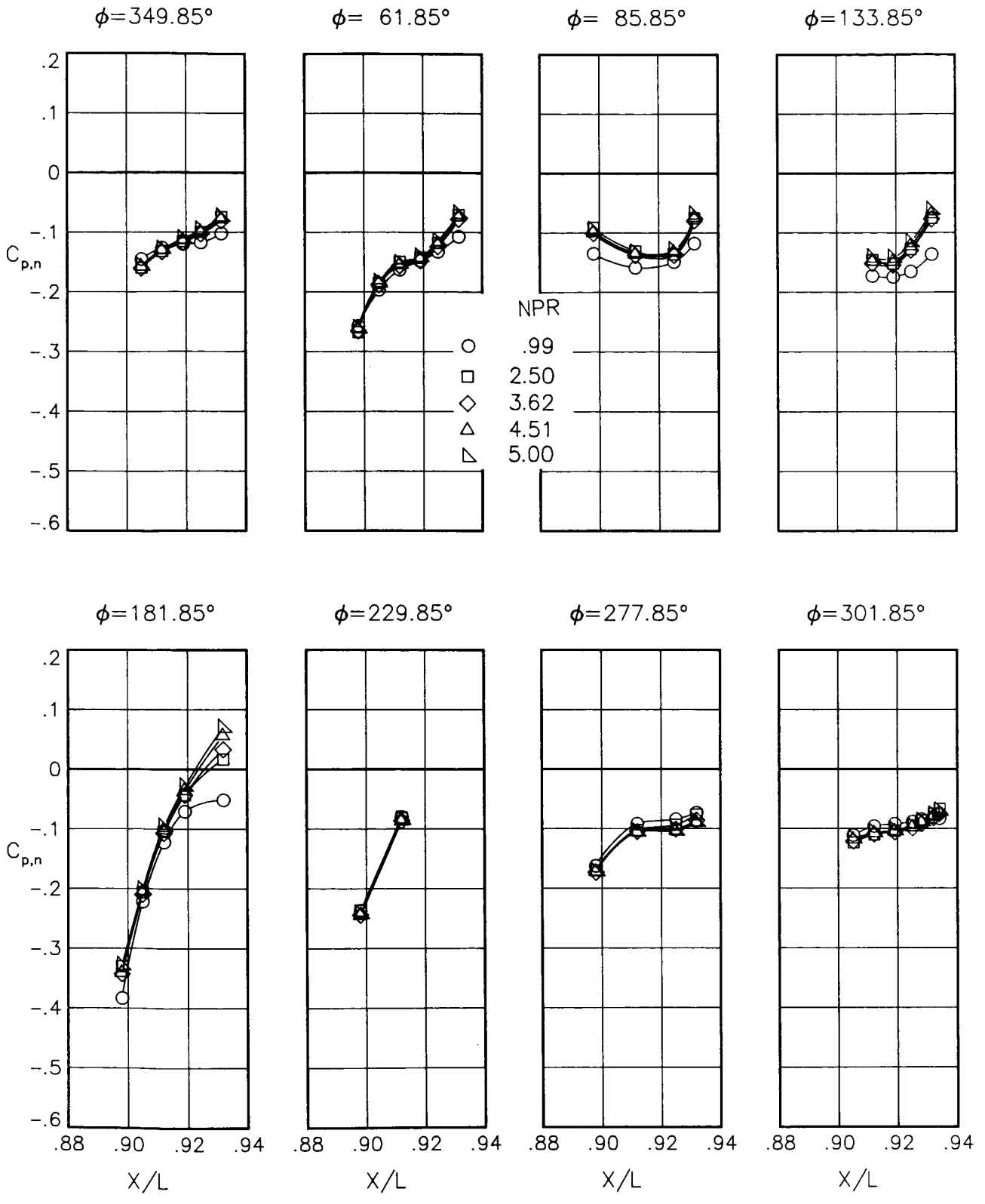

(1) M = 0.90; α = 6.00°.

Figure 74.- Concluded.

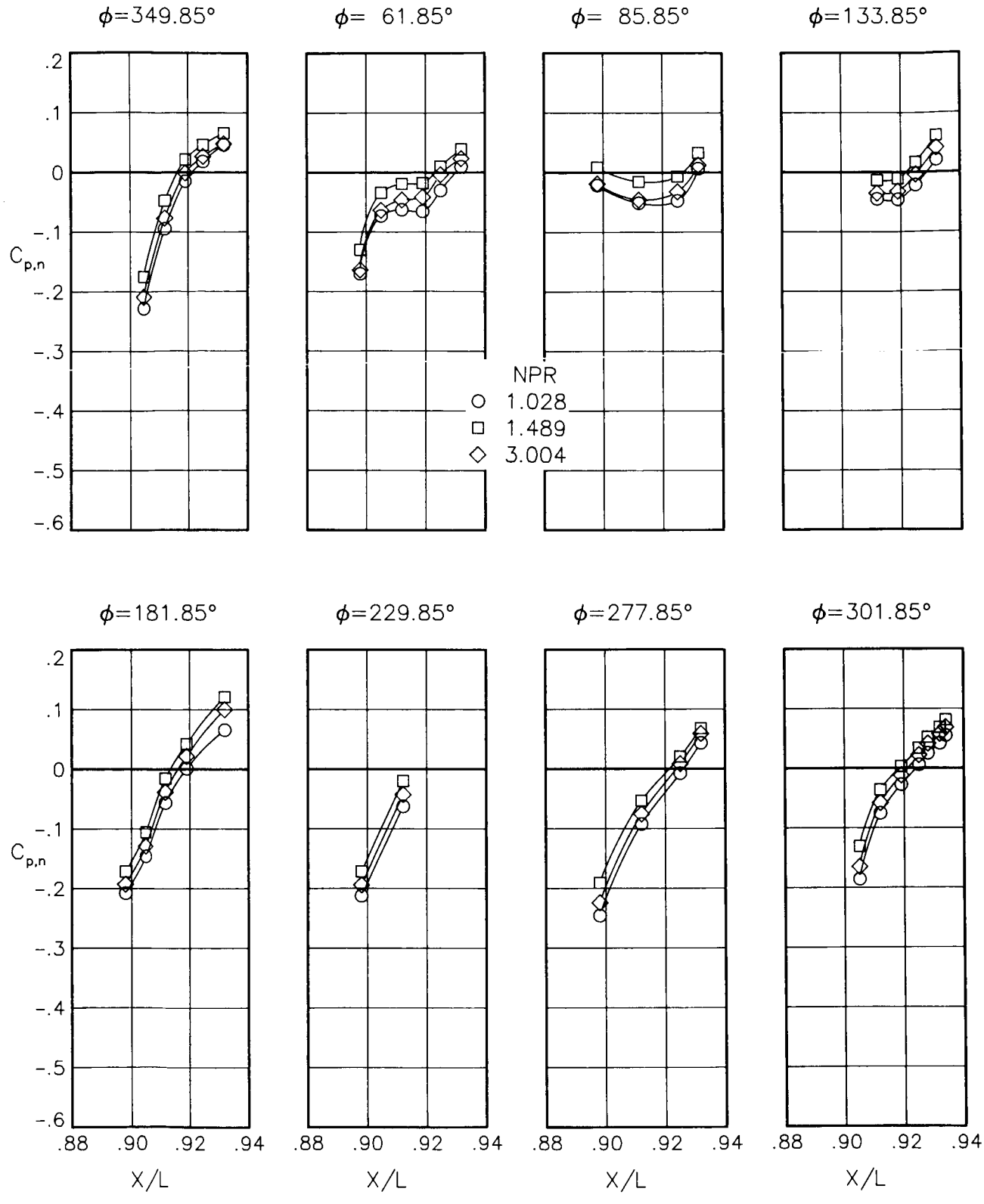

(a) M = 0.60; α = 0.00°.

Figure 75.- Static-pressure-coefficient distributions on nozzle for the model with all fuselage modifications. β_n = 18.45°. Repeat data.

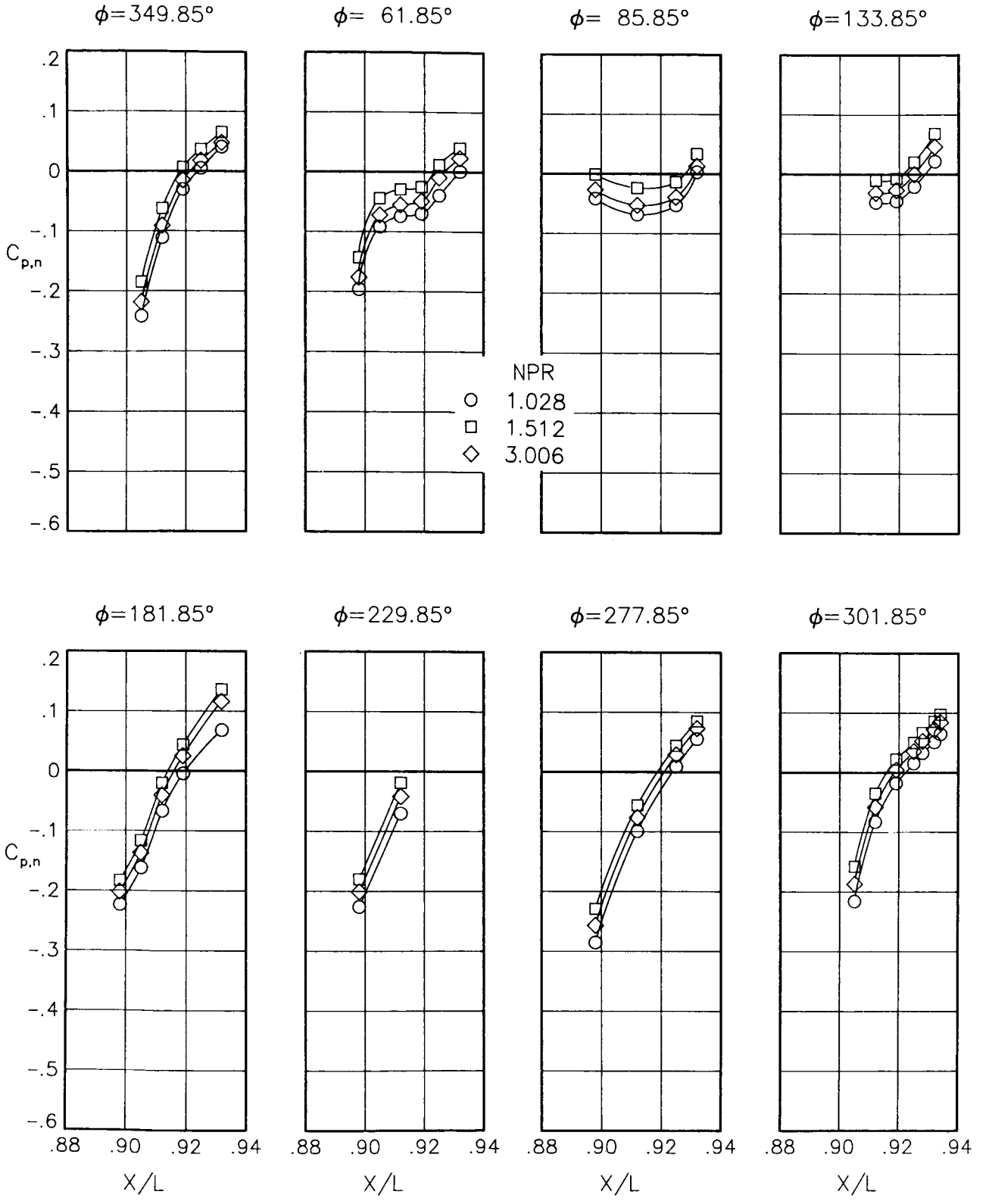

(b) M = 0.60; α = 3.00°.

Figure 75.- Continued.

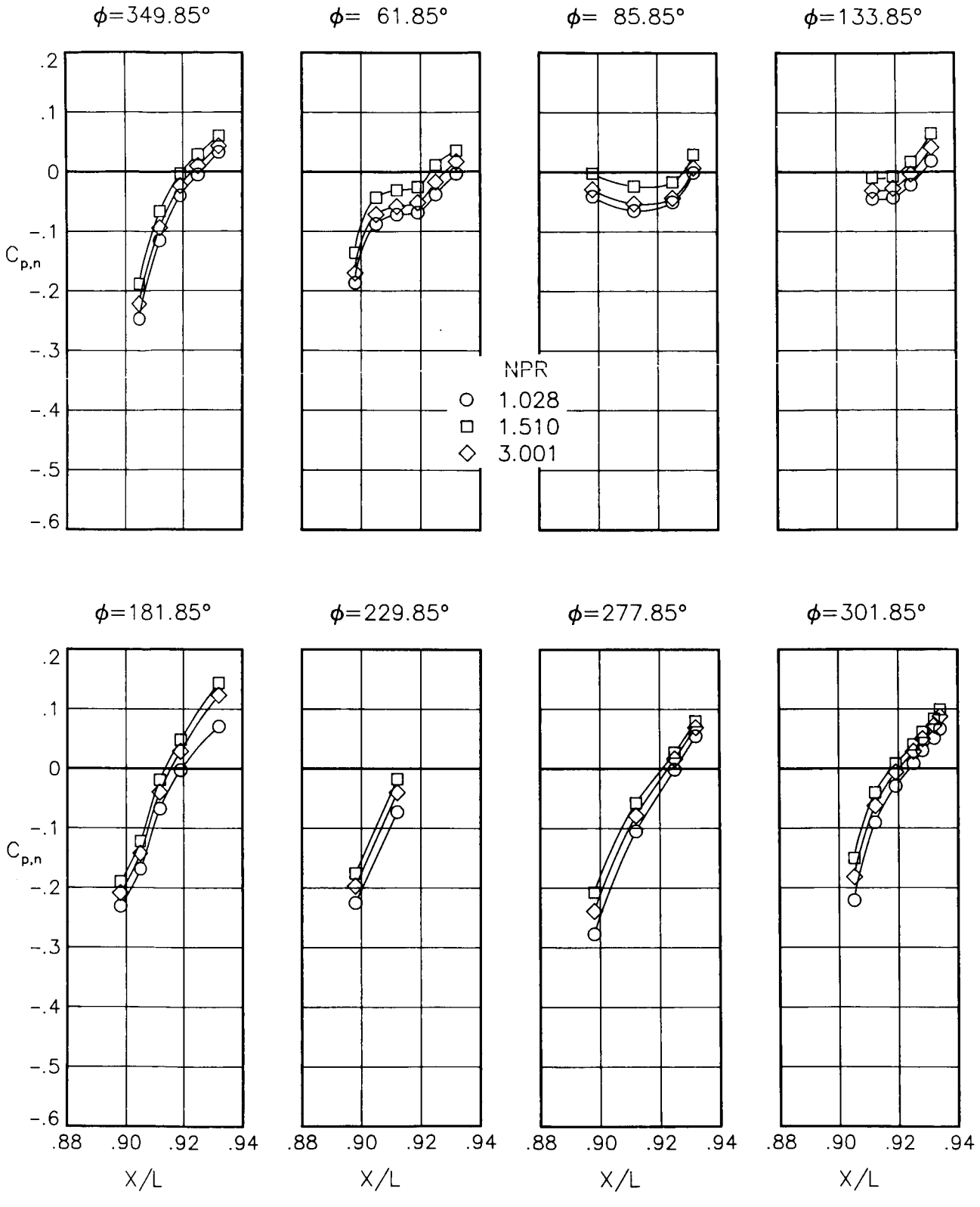

(c) M = 0.60; α = 5.00°.

Figure 75.- Continued.

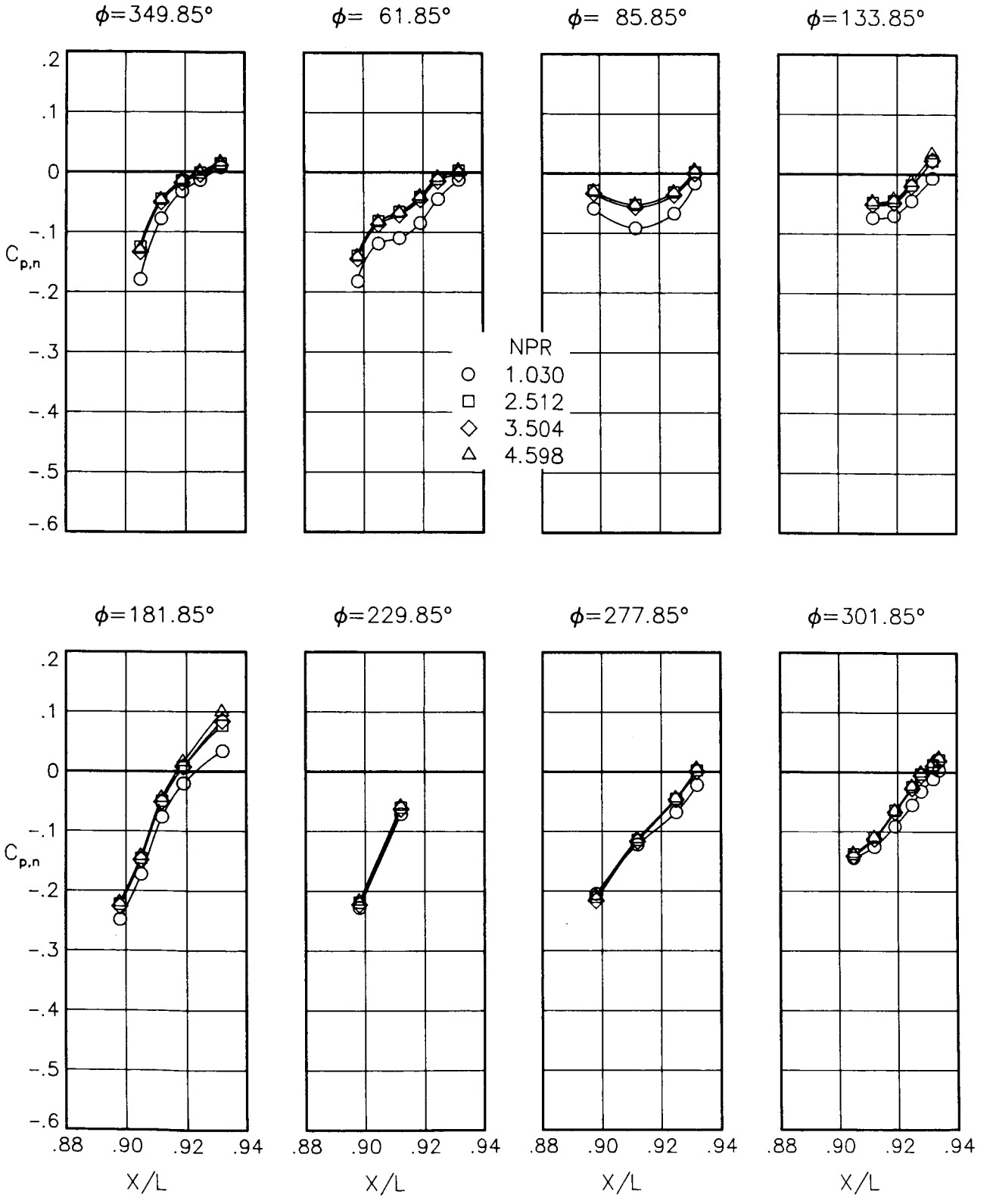

(d) M = 0.80; α = 0.00°.

Figure 75.- Continued.

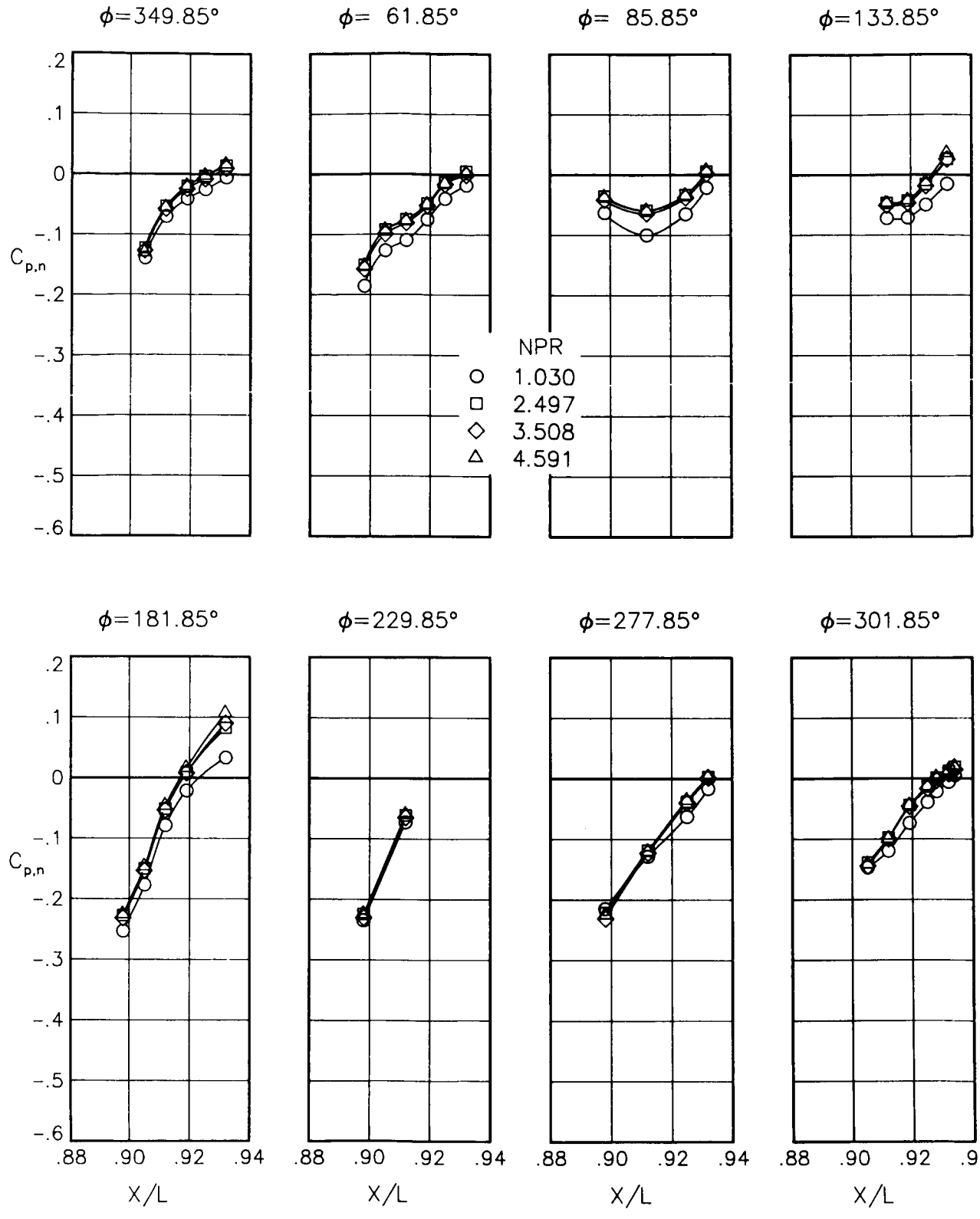

(e) M = 0.80; α = 1.00°.

Figure 75.- Continued.

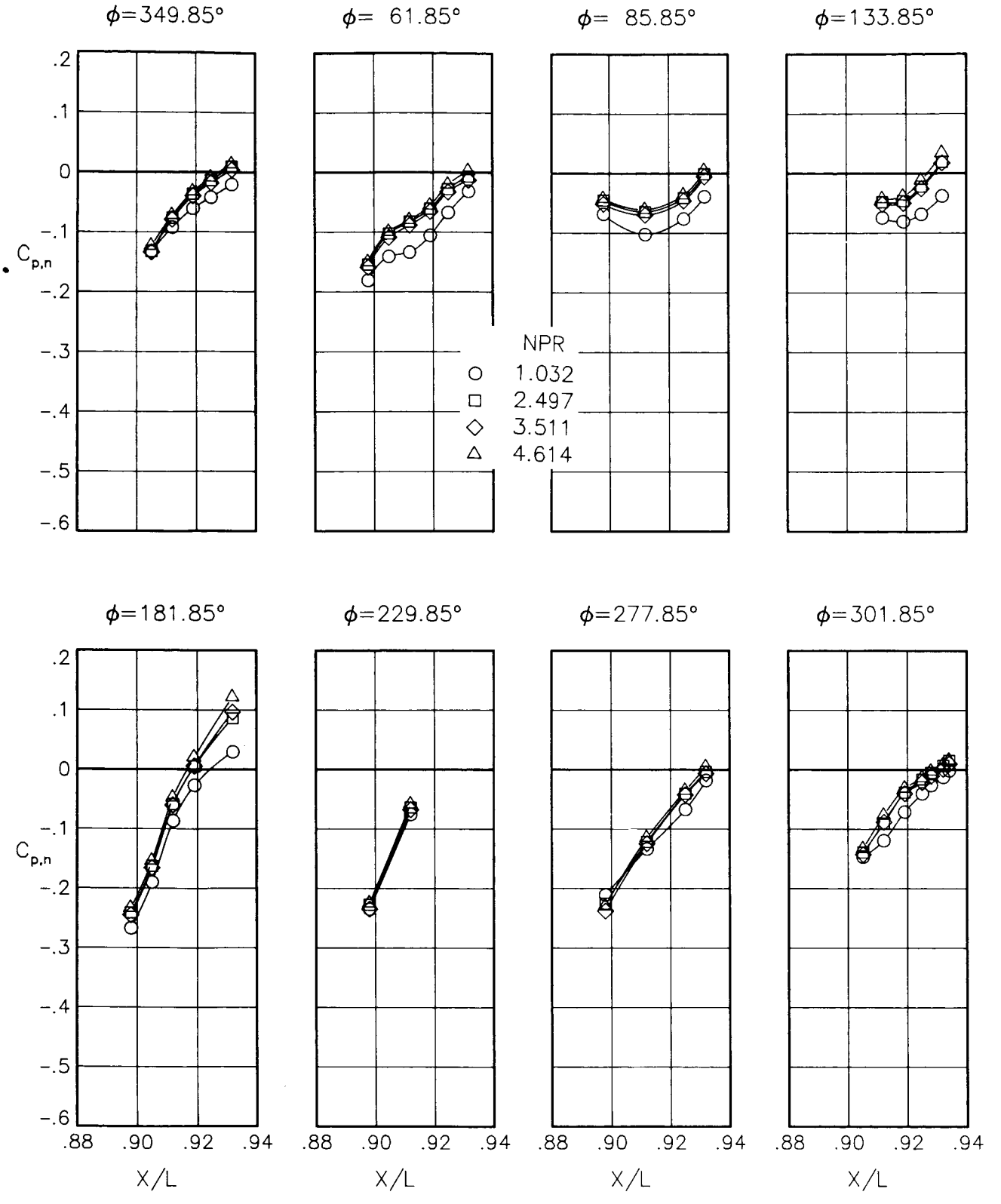

(f) M = 0.80; α = 3.00°.

Figure 75.- Continued.

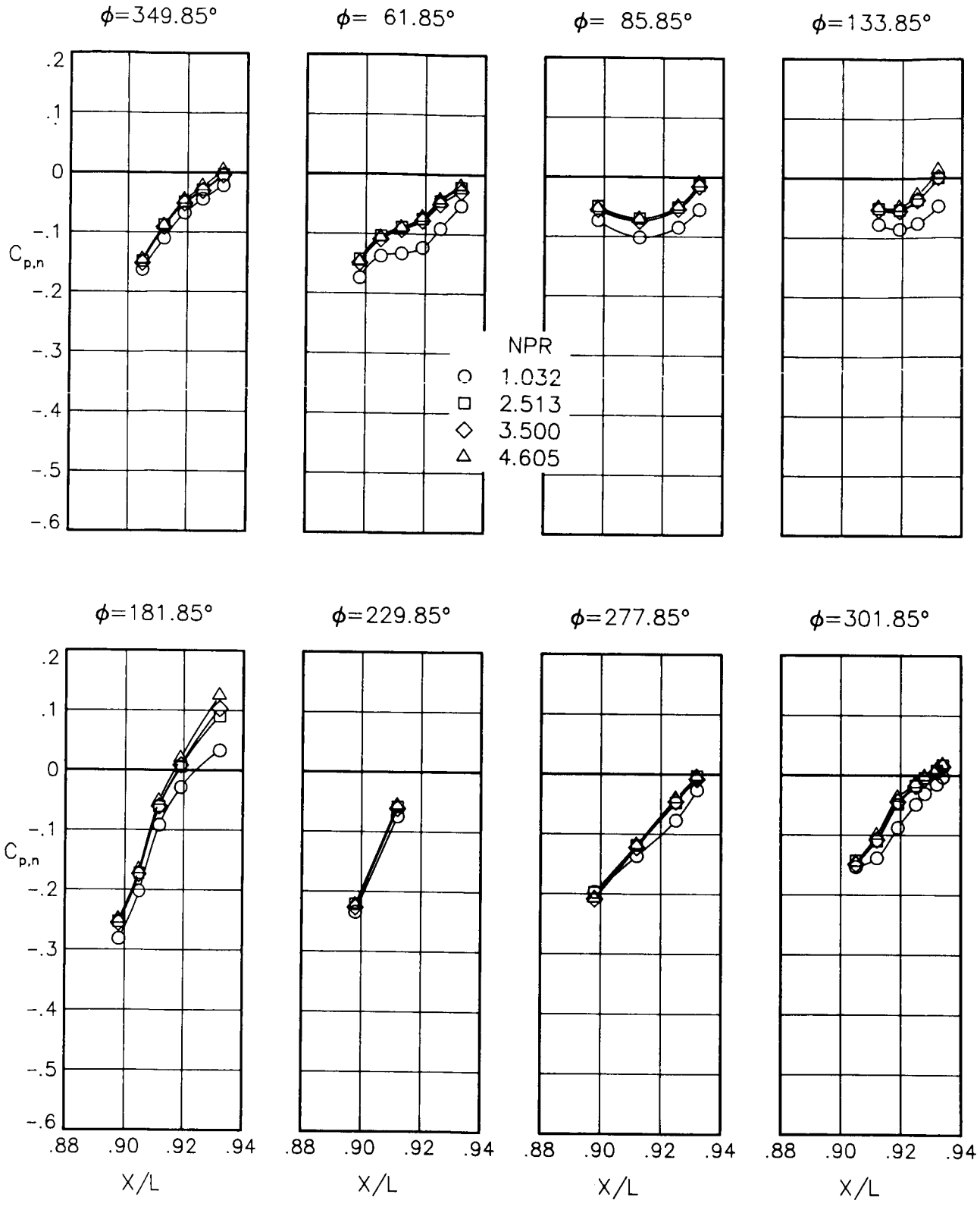

(g) M = 0.80; α = 5.00°.

Figure 75.- Continued.

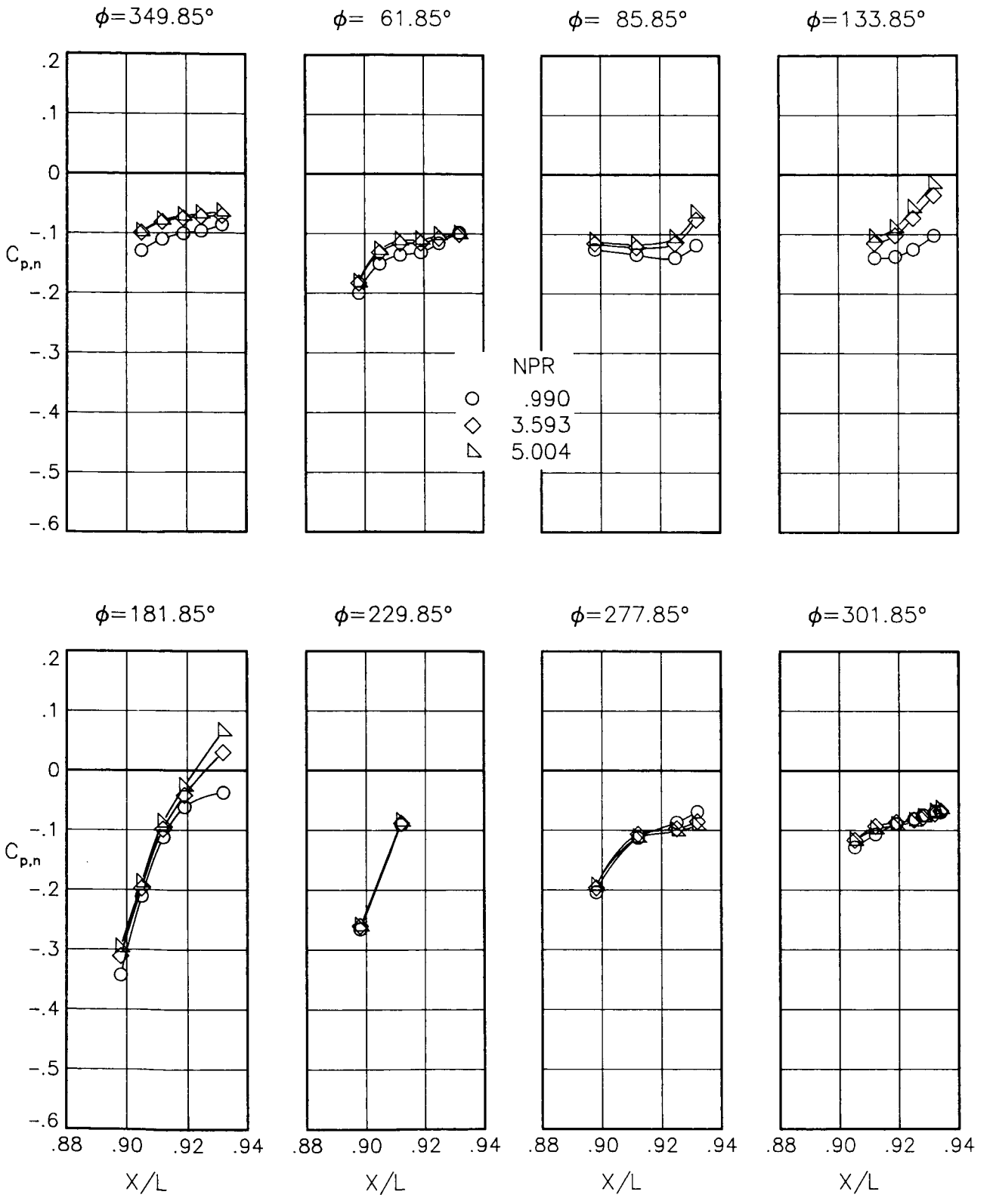

(h) M = 0.90; α = 0.00°.

Figure 75.- Continued.

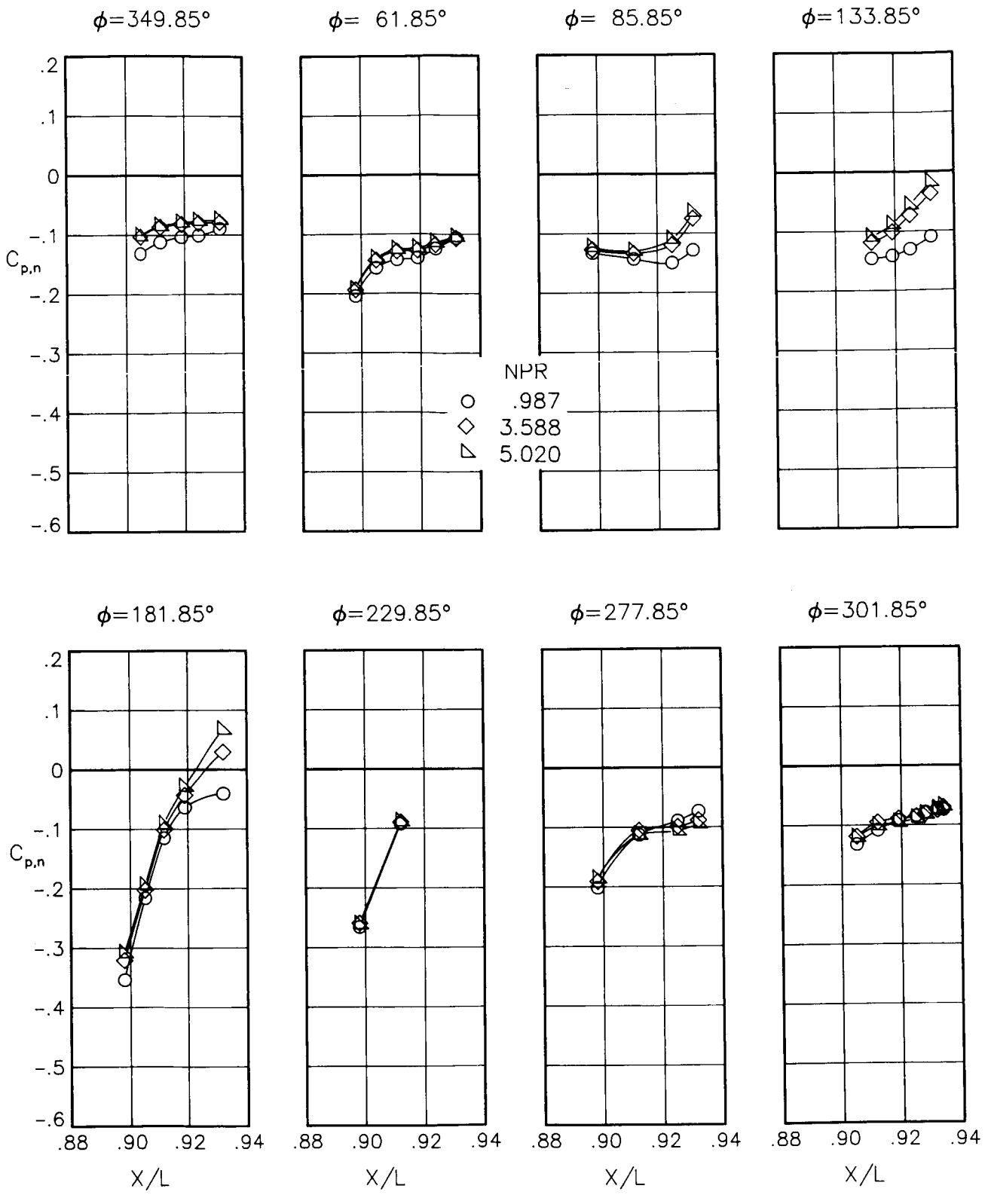

(i) M = 0.90; α = 1.00°.

Figure 75.- Continued.

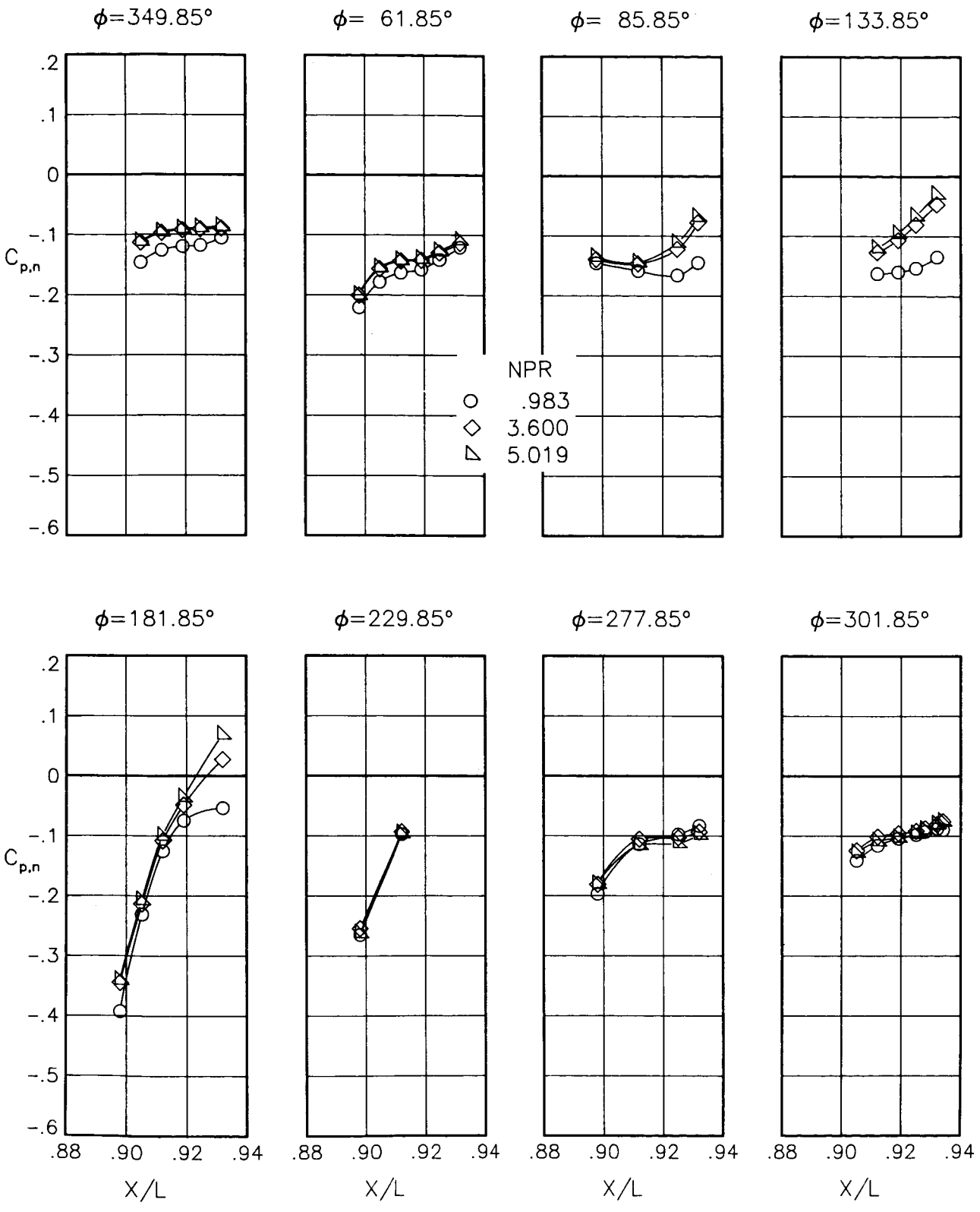

(j) M = 0.90; α = 3.00°.

Figure 75.- Continued.

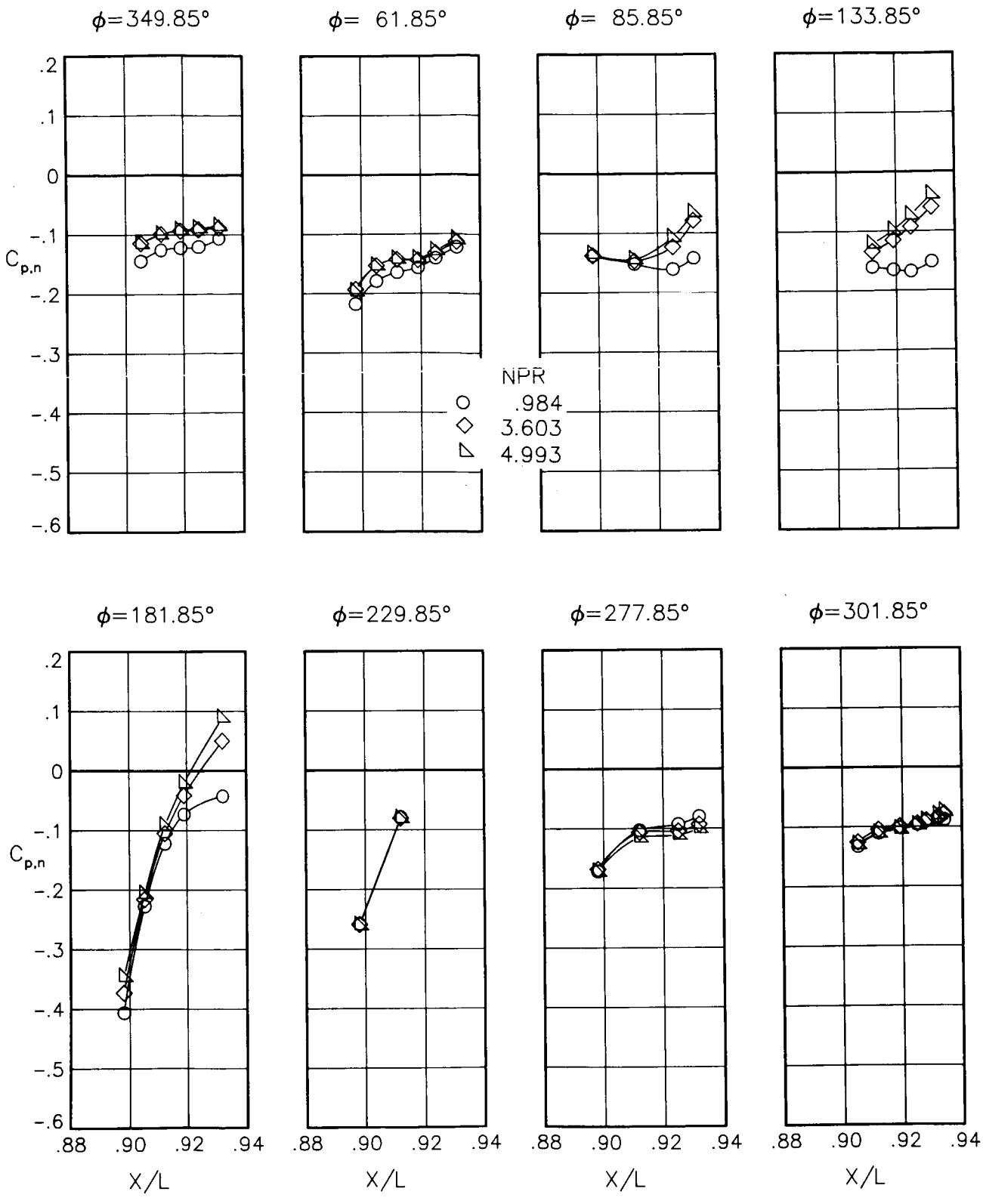

(k) M = 0.90; α = 6.00°.

Figure 75.- Concluded.

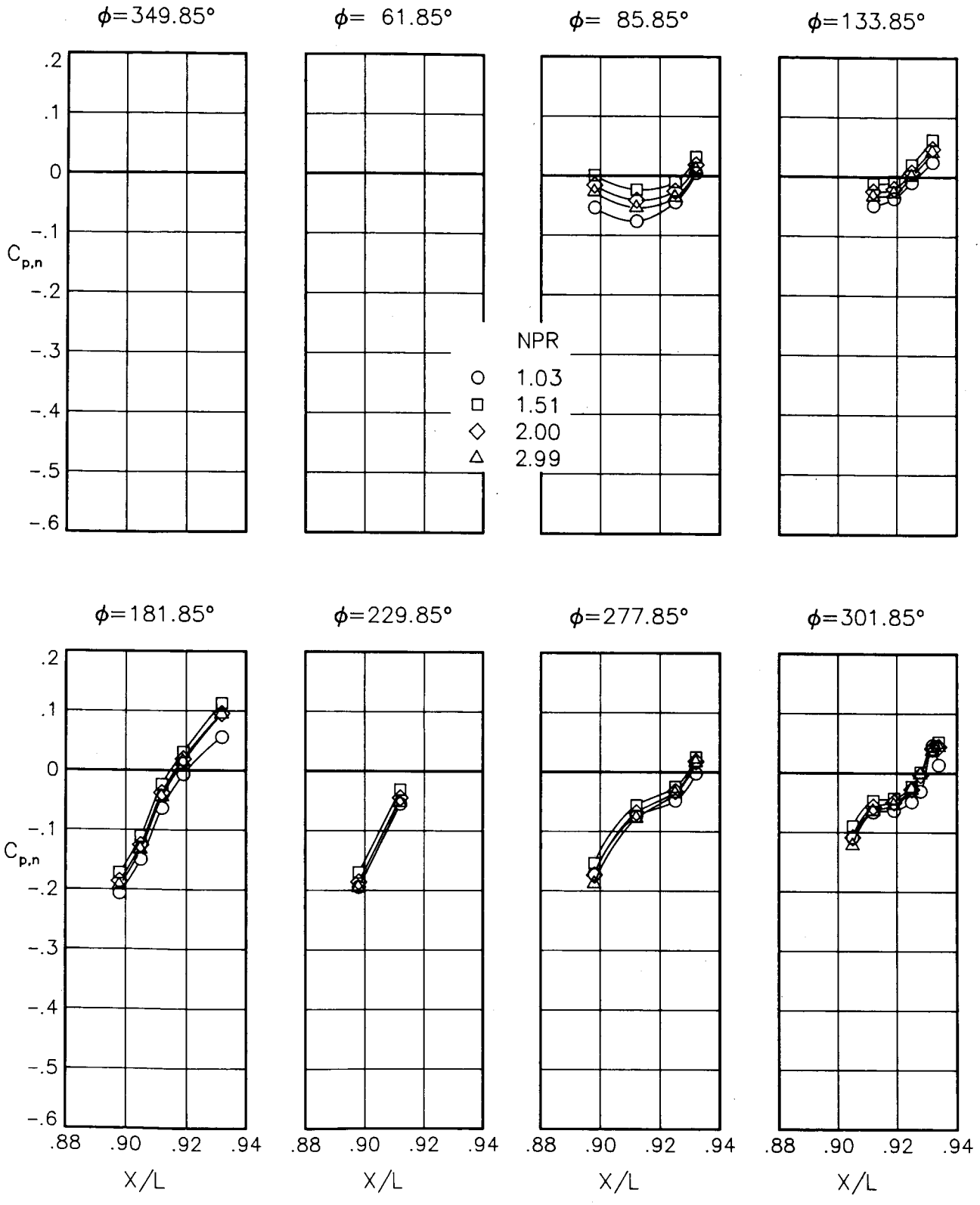

(a) M = 0.60; α = 0.00°.

Figure 76.- Static-pressure-coefficient distributions on nozzle for the model with all fuselage modifications. β_n = 18.45°; δ_r = -5°.

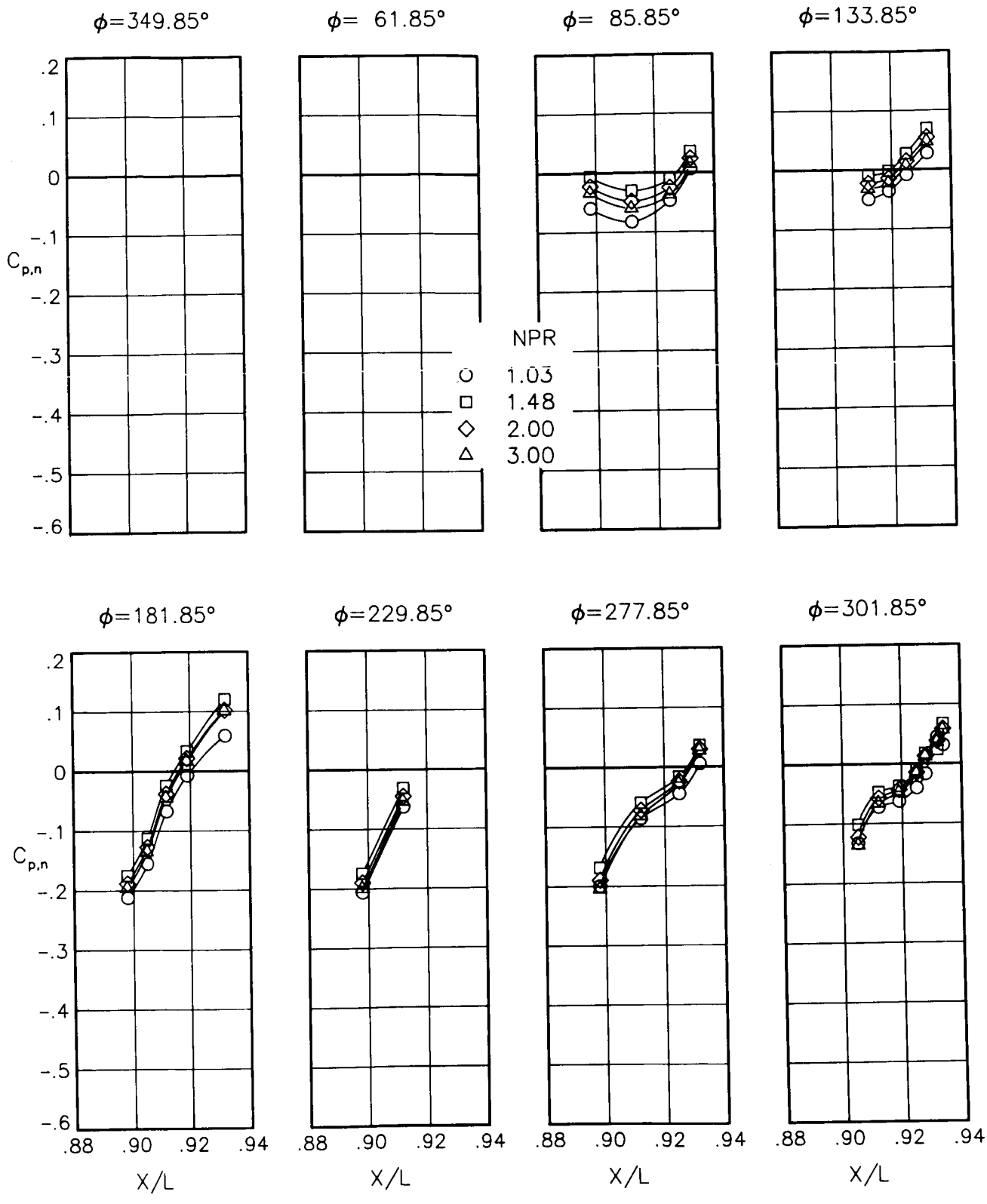

(b) M = 0.60; α = 1.00°.

Figure 76.- Continued.

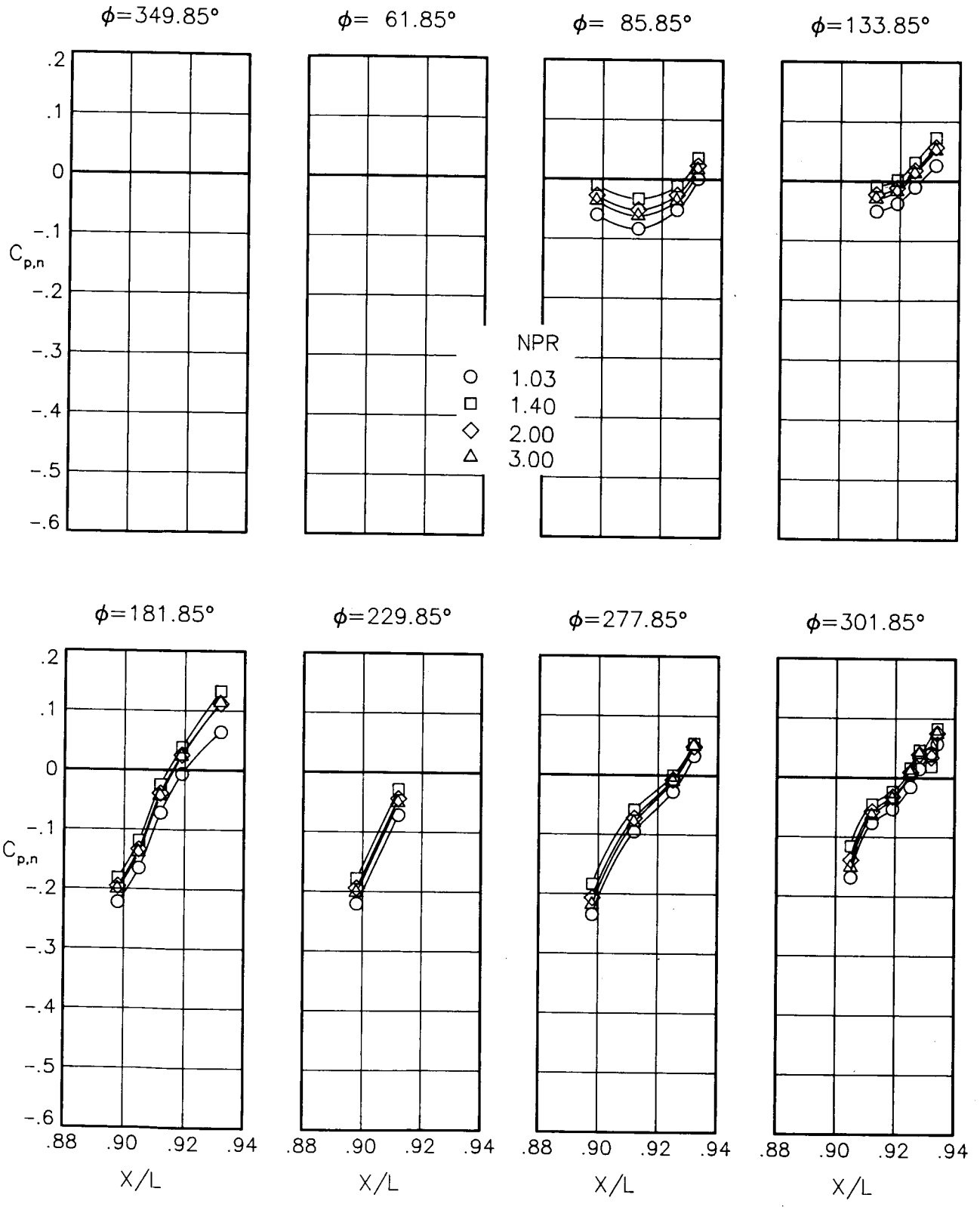

(c) M = 0.60; α = 3.00°.

Figure 76.- Continued.

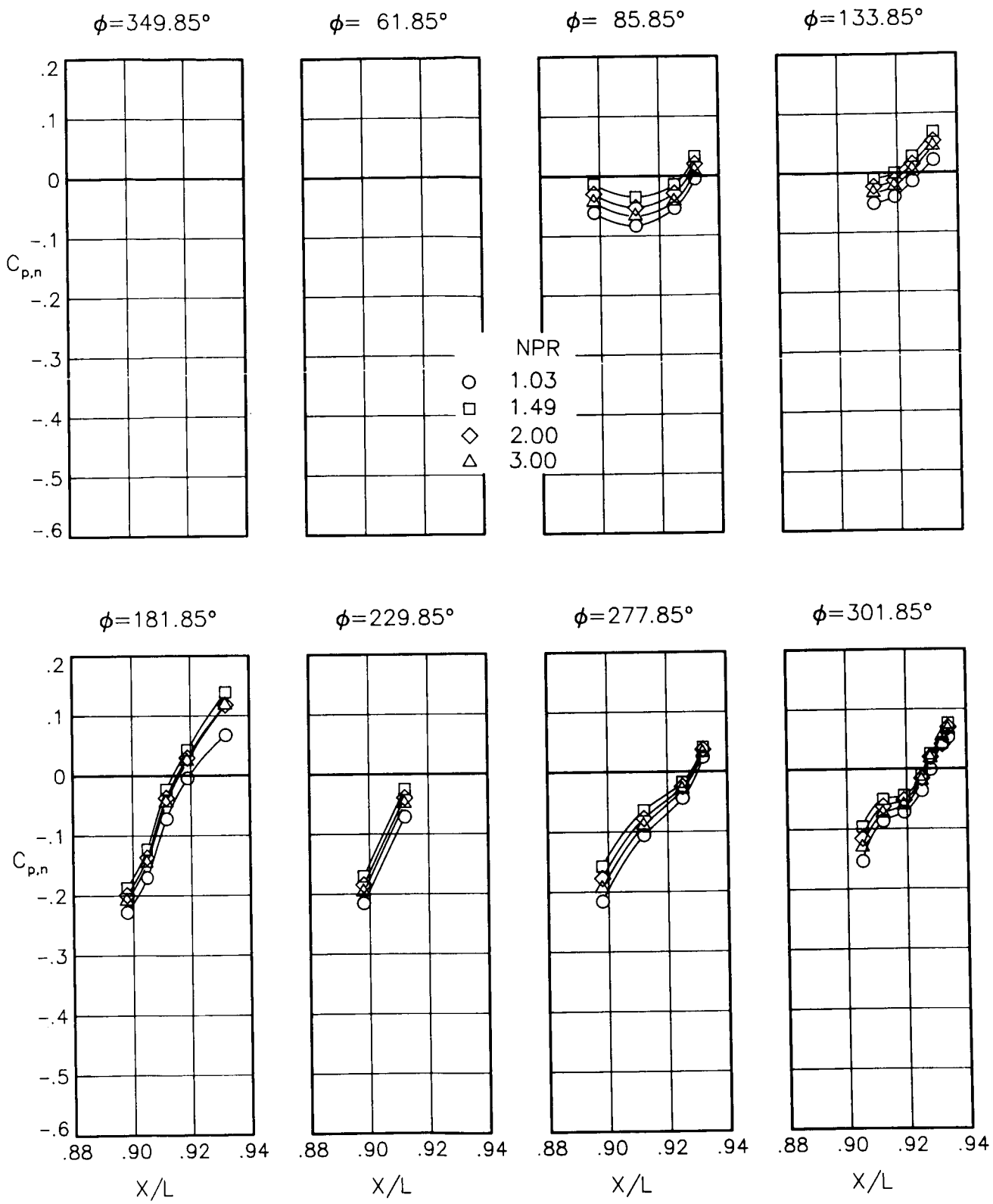

(d) M = 0.60; α = 5.00°.

Figure 76.- Continued.

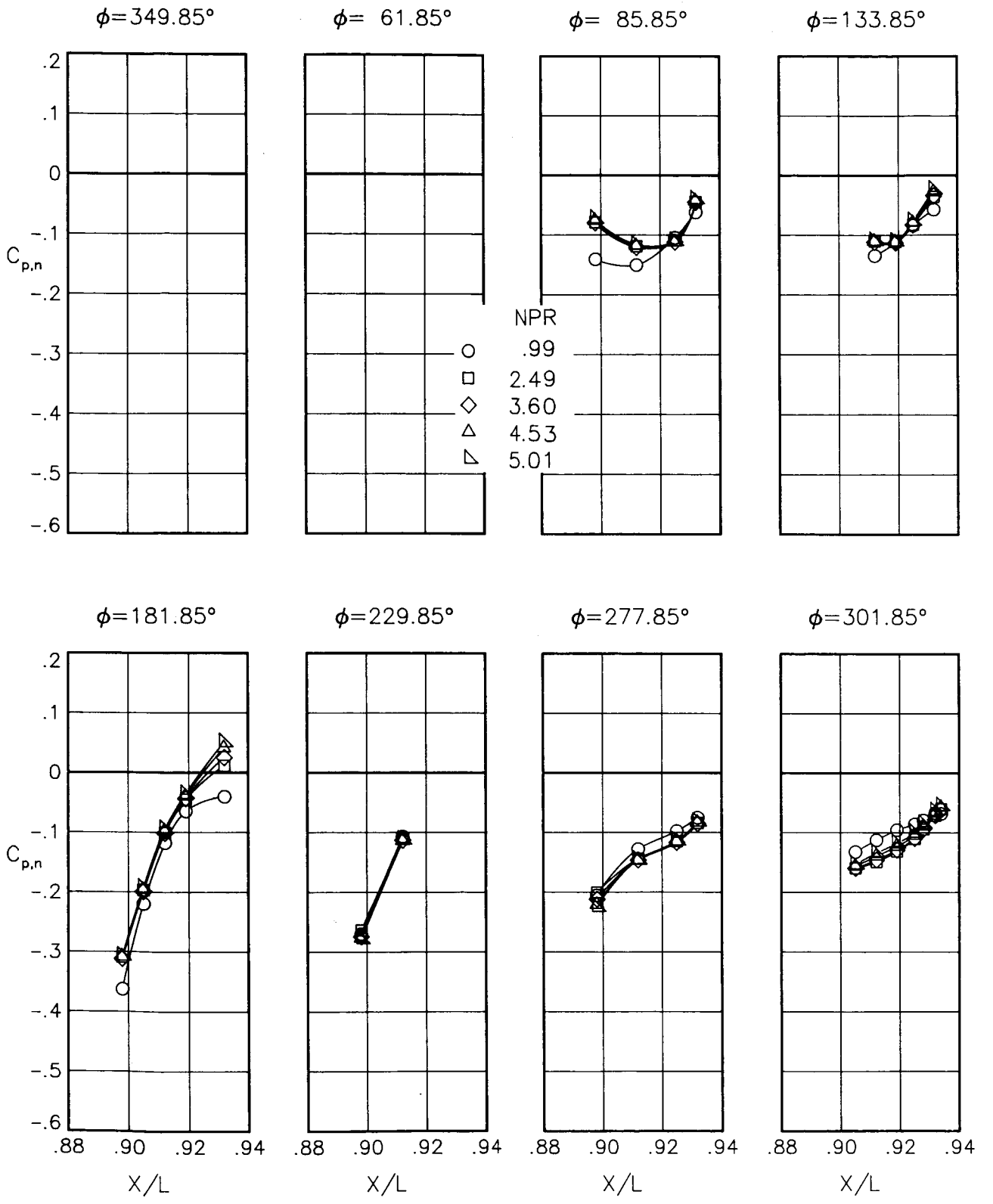

(e) M = 0.90; α = 0.00°.

Figure 76.- Continued.

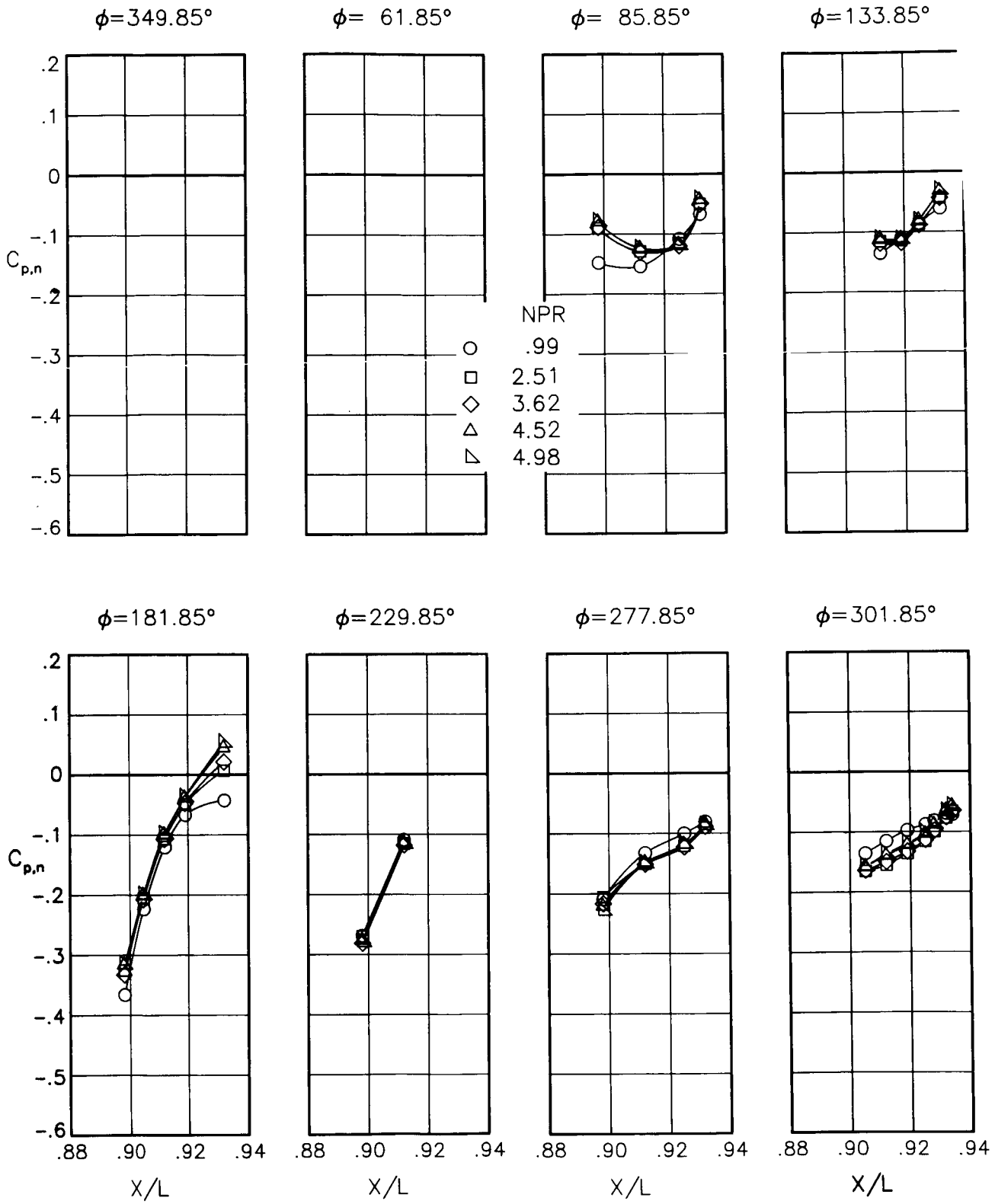

(f) M = 0.90; α = 1.00°.

Figure 76.- Continued.

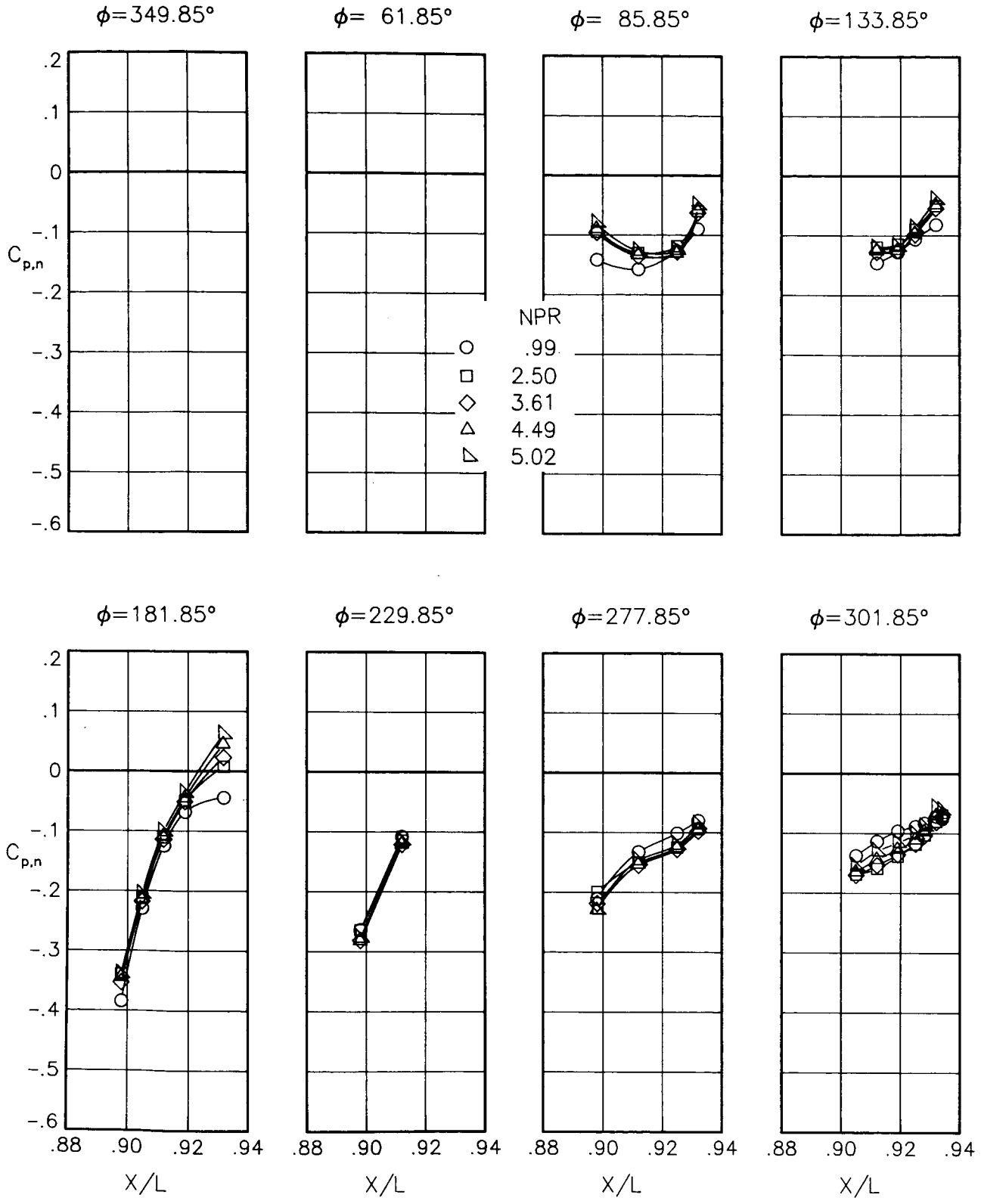

(g) M = 0.90; α = 3.00°.

Figure 76.- Continued.

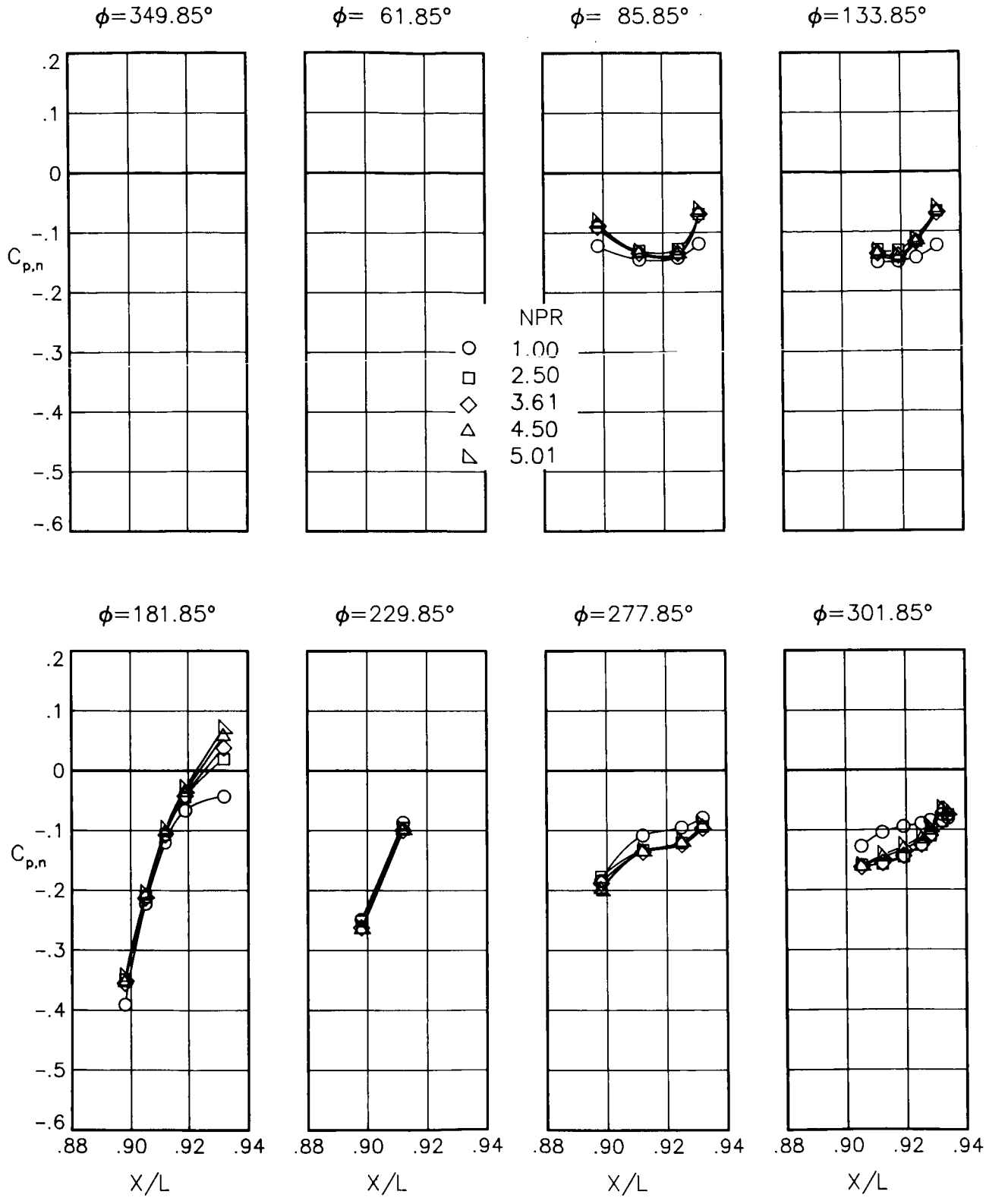

(h) M = 0.90; α = 6.00°.

Figure 76.- Concluded.

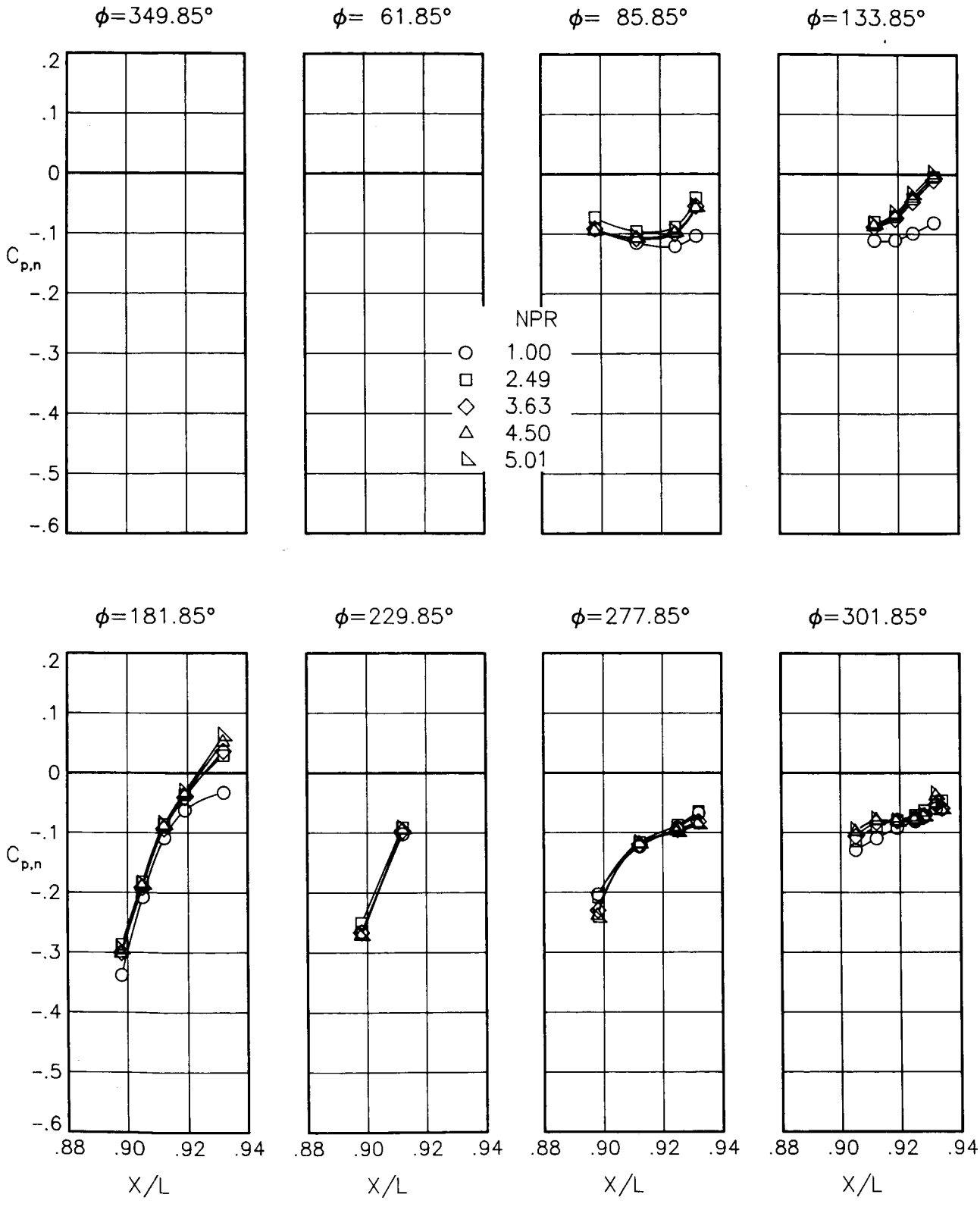

(a) M = 0.90; α = 0.00°.

Figure 77.- Static-pressure-coefficient distributions on nozzle for the model with all fuselage modifications. β_L = 18.45°; β_R = 15.05°.

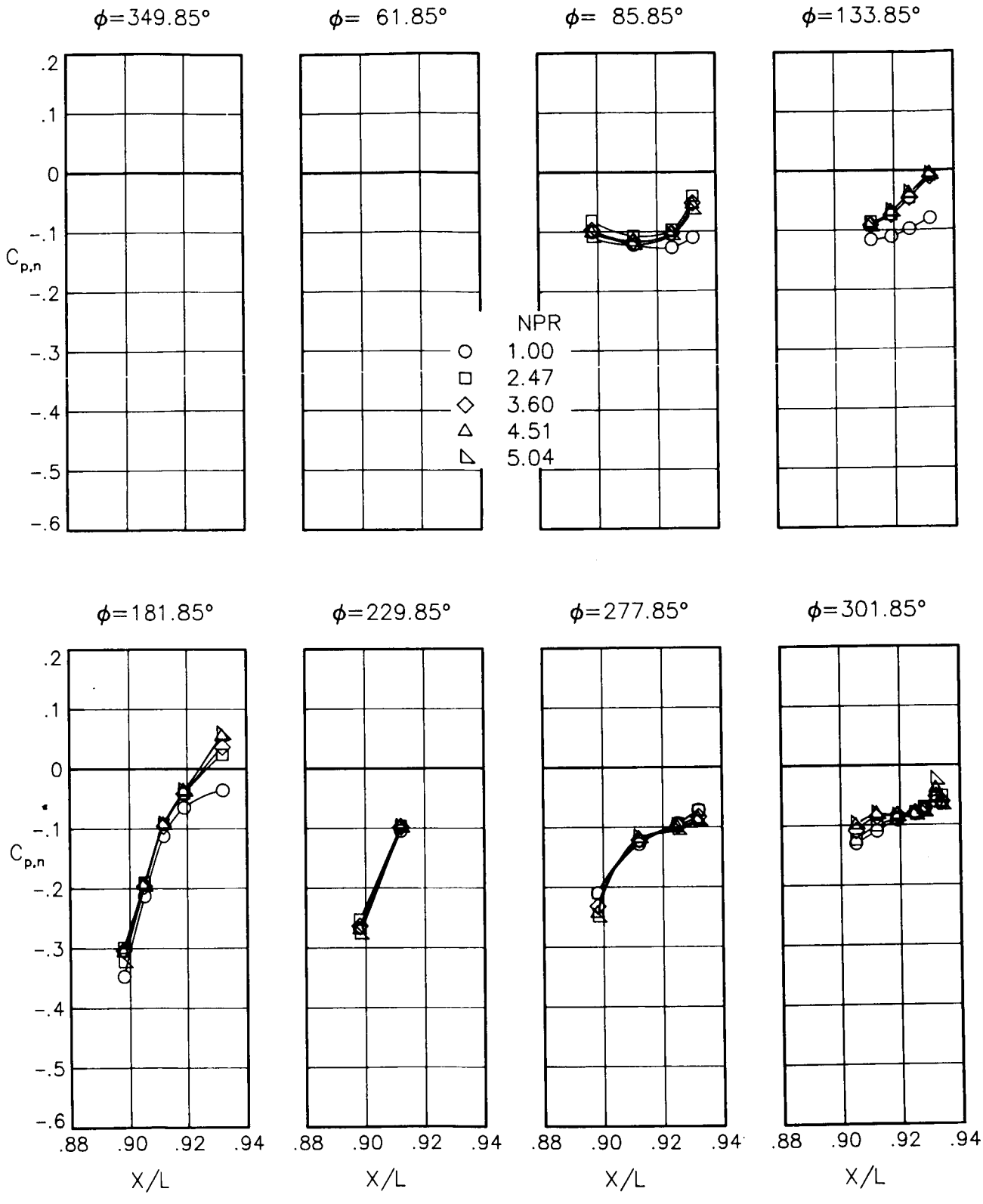

(b) M = 0.90; α = 1.00°.

Figure 77.- Continued.

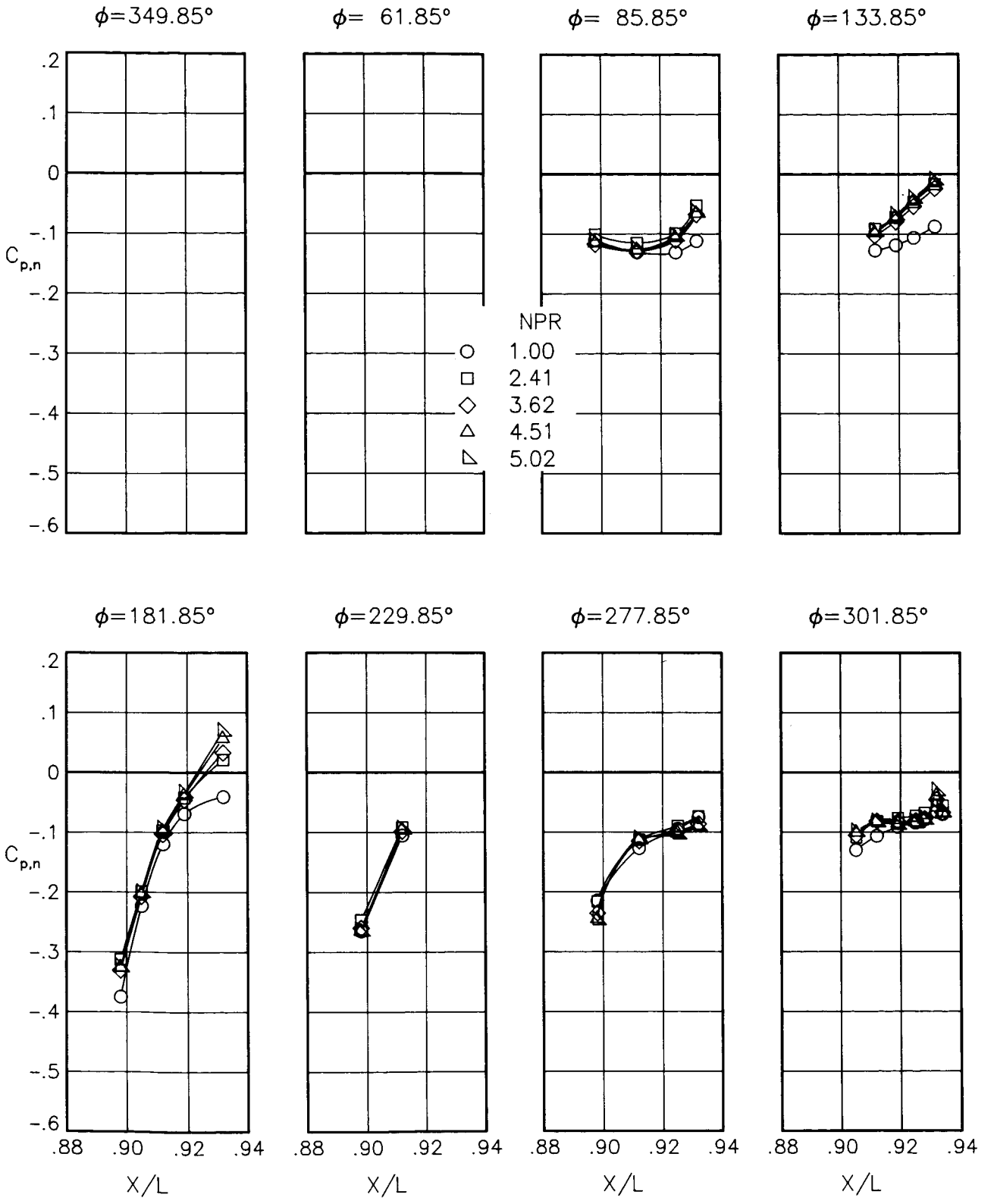

(c) M = 0.90; α = 3.00°.

Figure 77.- Continued.

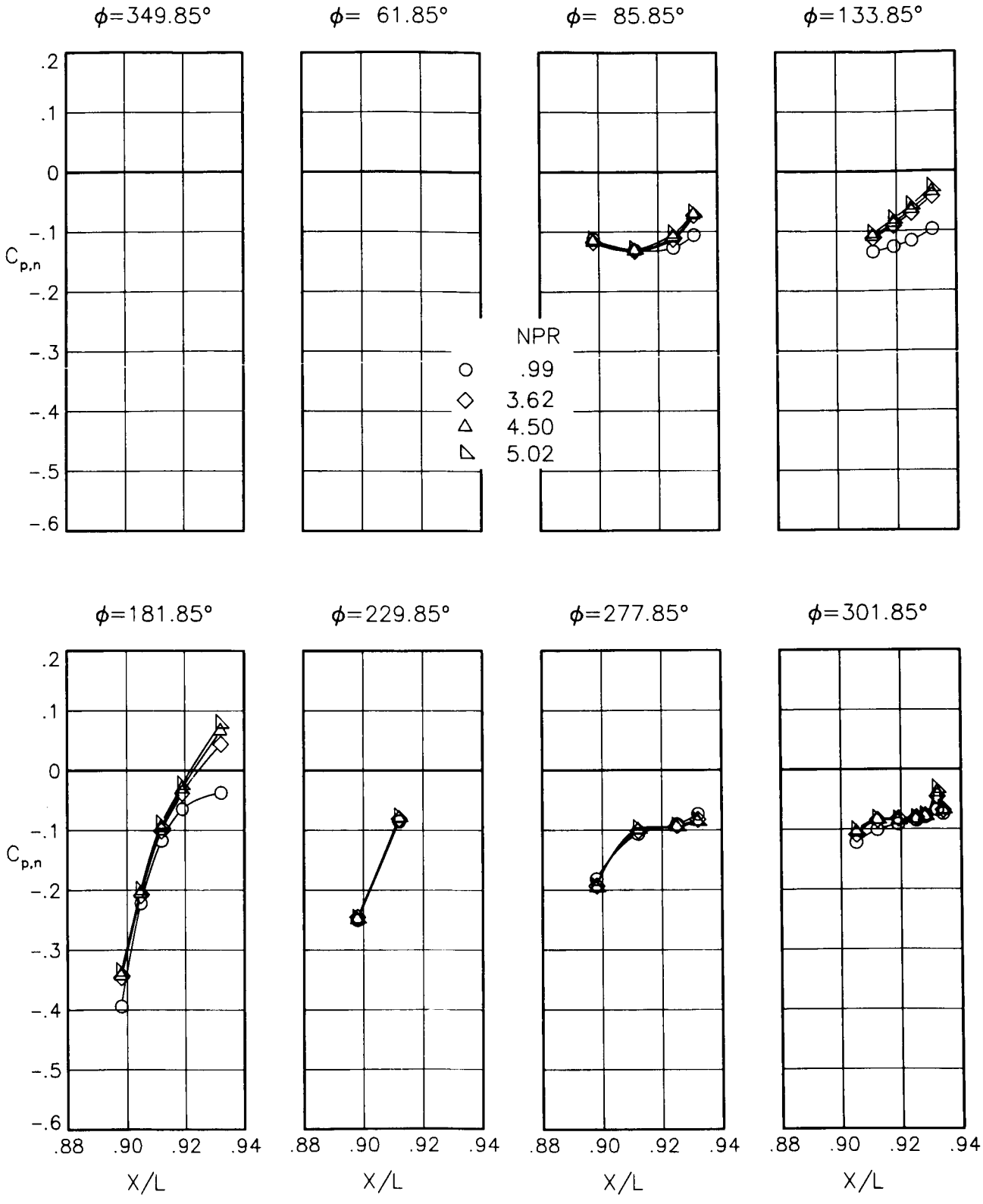

(d) M = 0.90; α = 6.00°.

Figure 77.- Concluded.

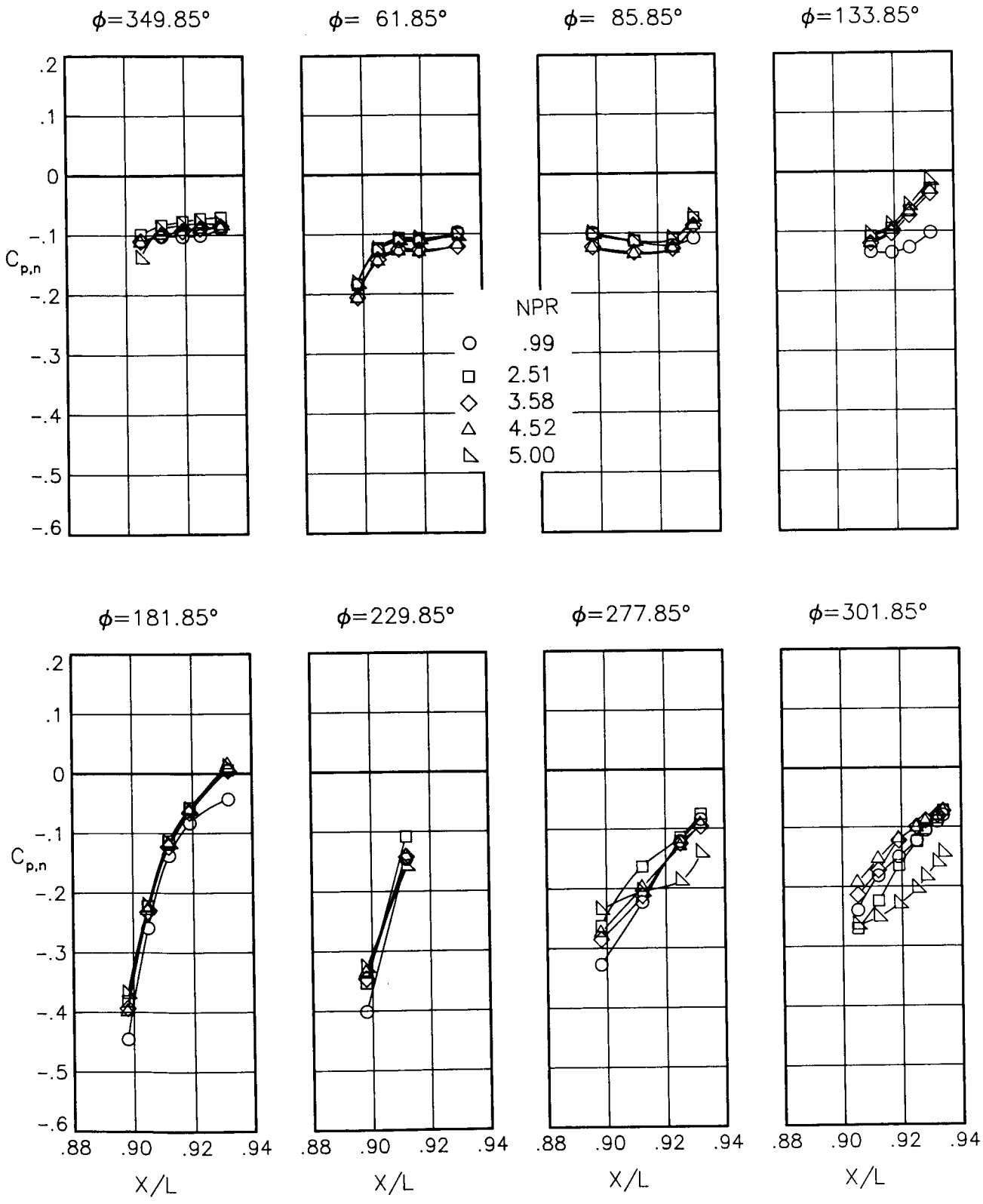

(a) M = 0.90; α = 0.00°.

Figure 78.- Static-pressure-coefficient distributions on nozzle for the model with all fuselage modifications. β_L = 18.45°; β_R = 15.05°; δ_h = -3°.

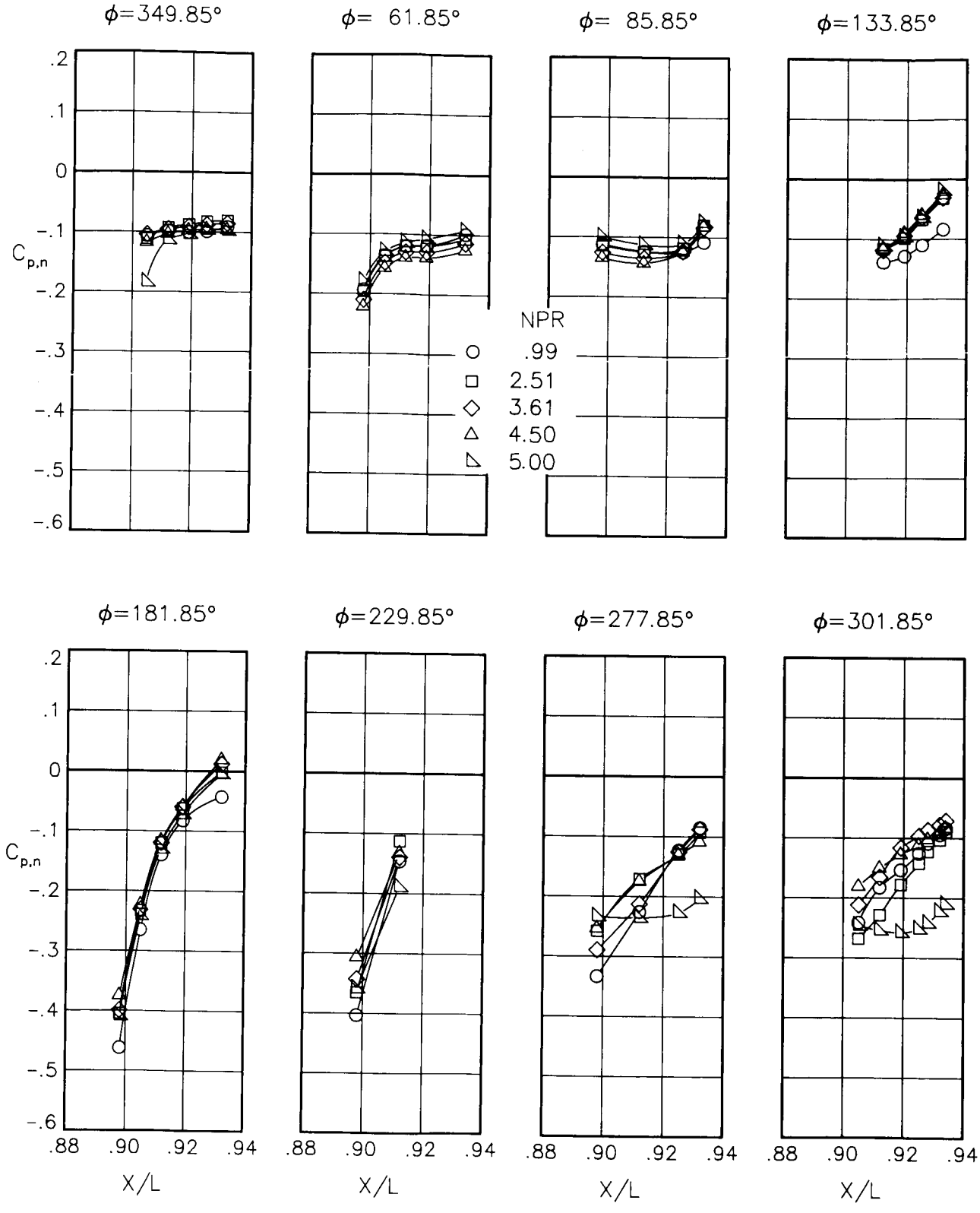

(b) M = 0.90; α = 1.00°.

Figure 78.- Continued.

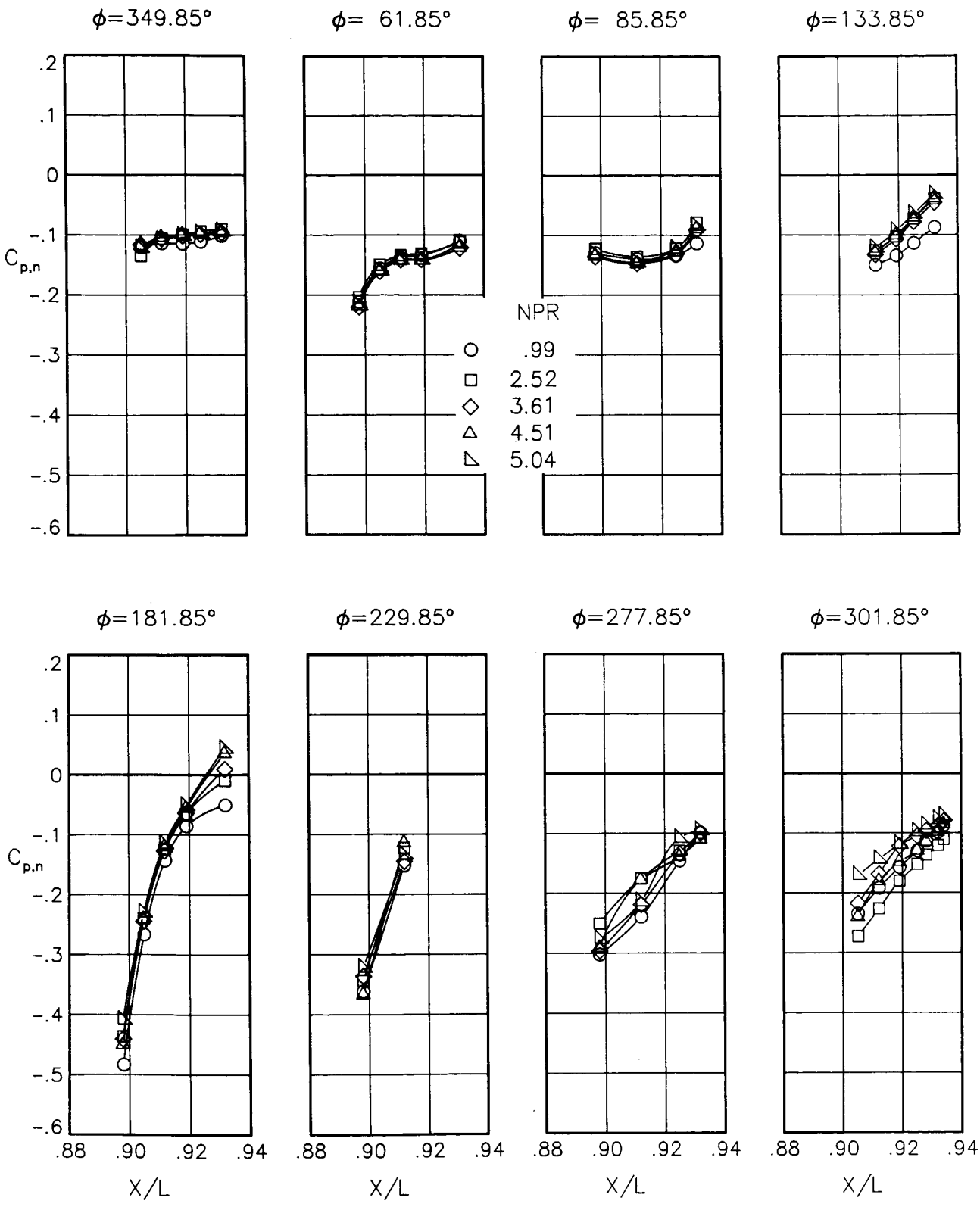

(c) M = 0.90; α = 3.00°.

Figure 78.- Continued.

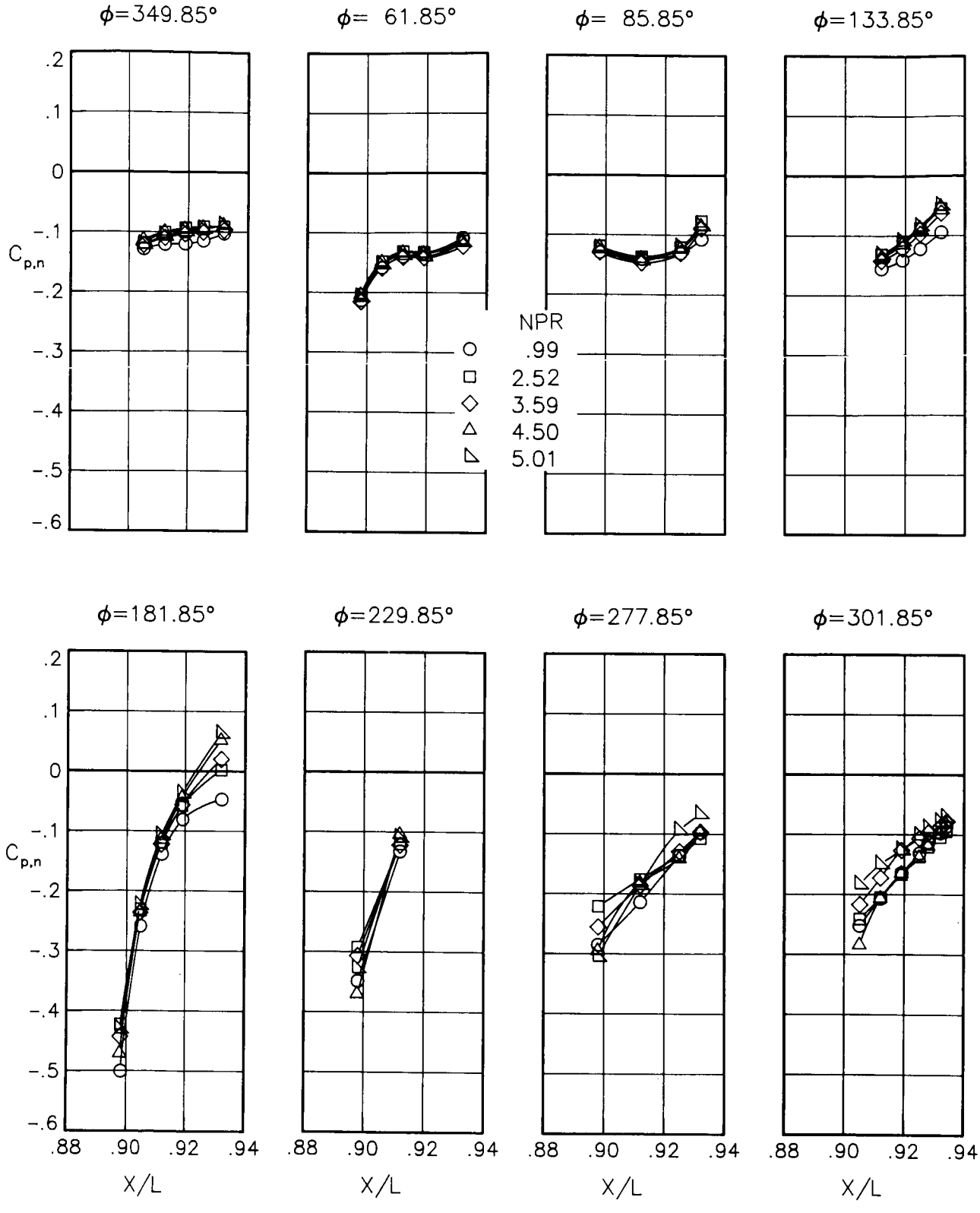

(d) M = 0.90; α = 6.00°.

Figure 78.- Concluded.

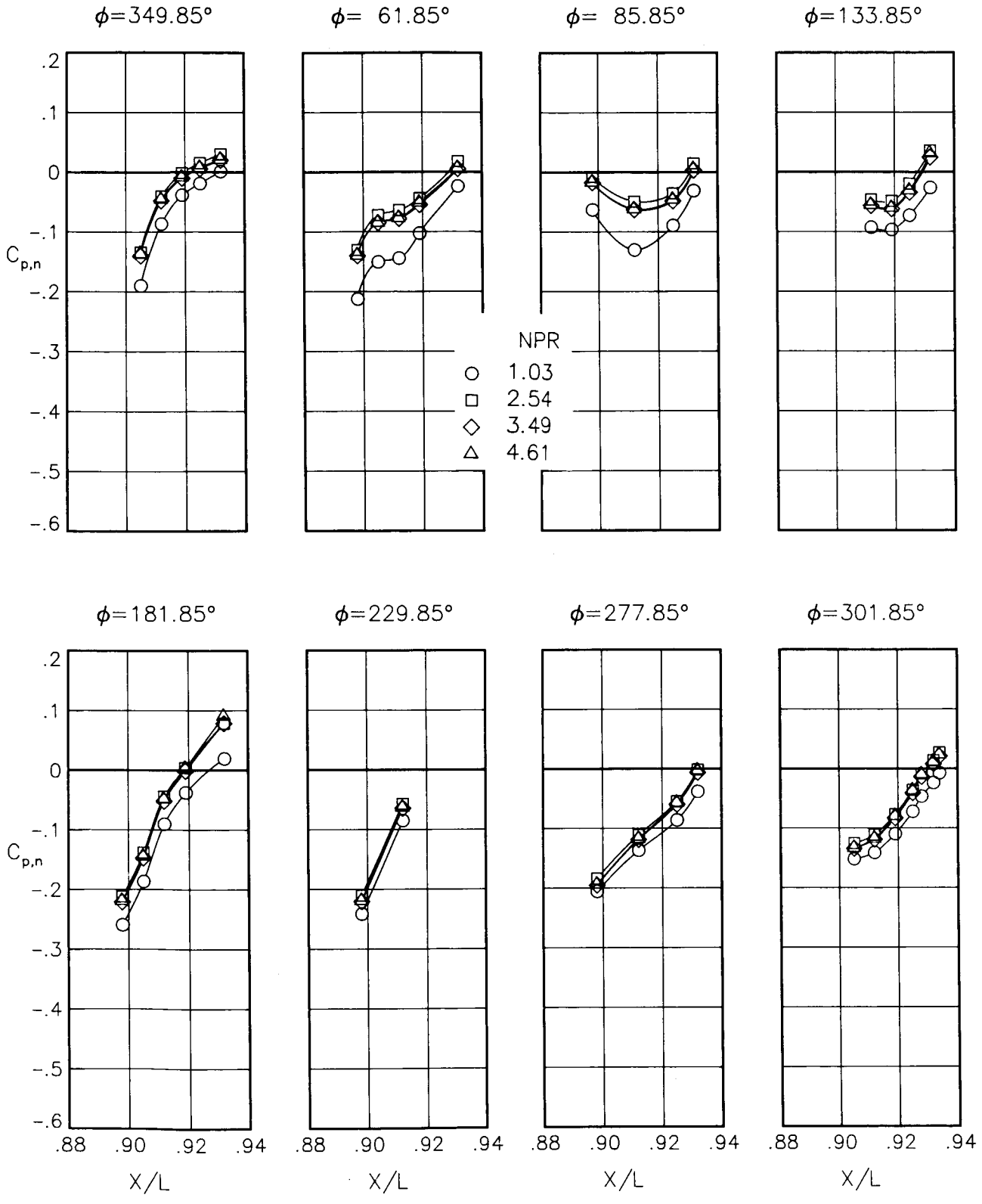

(a) M = 0.80; α = 0.00°.

Figure 79.- Static-pressure-coefficient distributions on nozzle for the model with all fuselage modifications. β_L = 18.45°; β_R = 9.63°; δ_h = -2°.

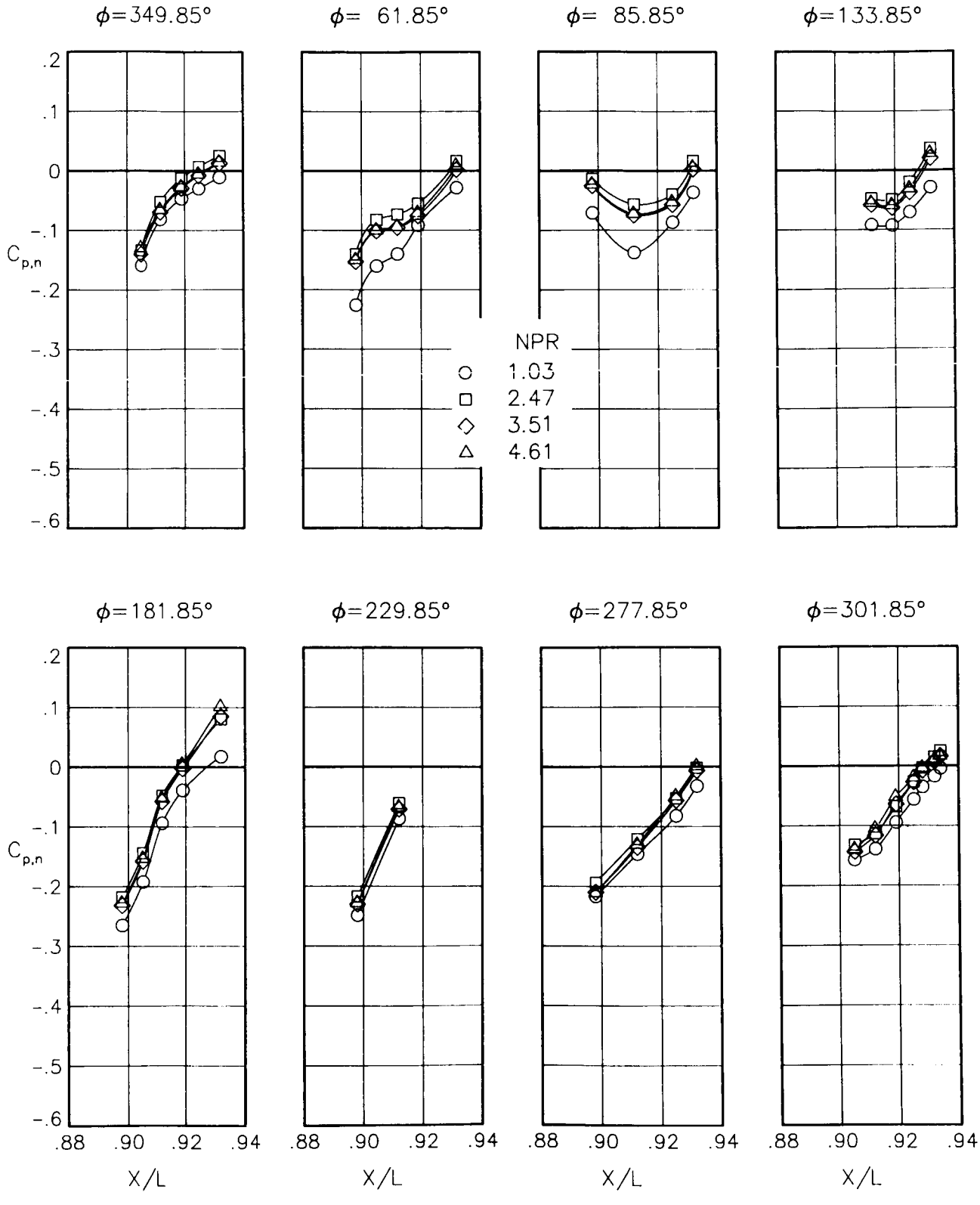

(b) M = 0.80; α = 1.00°.

Figure 79.- Continued.

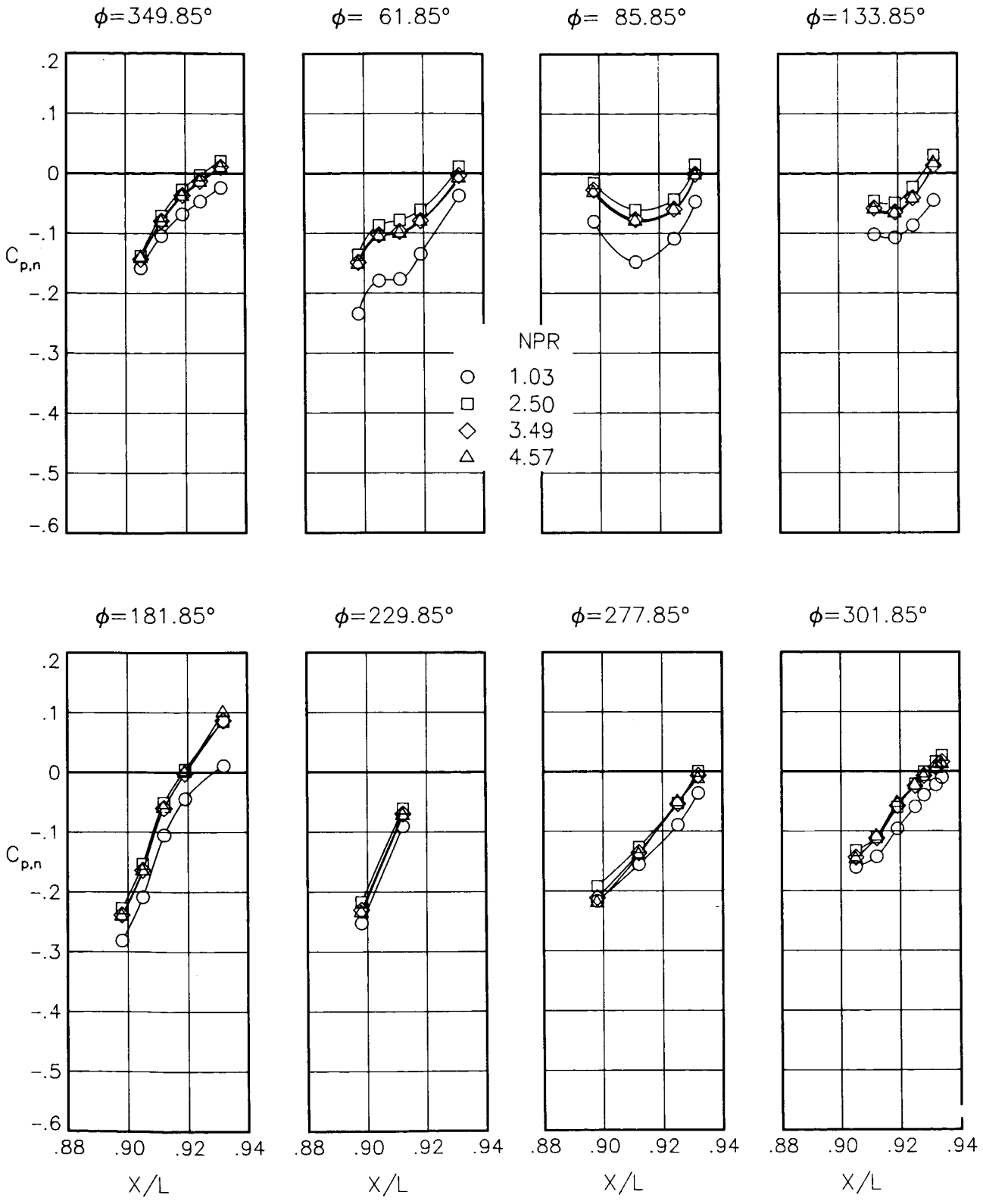

(c) M = 0.80; α = 3.00°.

Figure 79.- Continued.

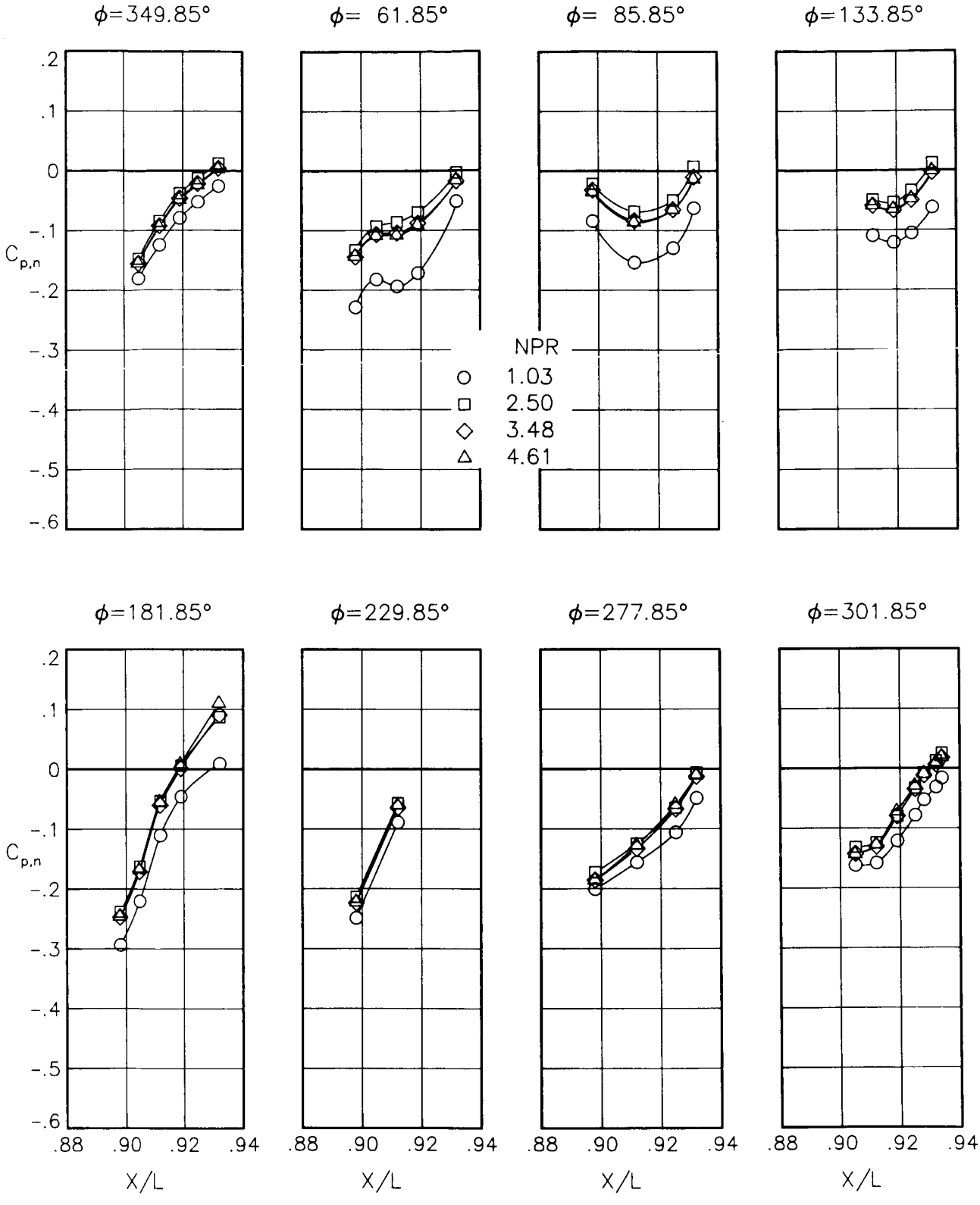

(d) M = 0.80; α = 5.00°.

Figure 79.- Continued.

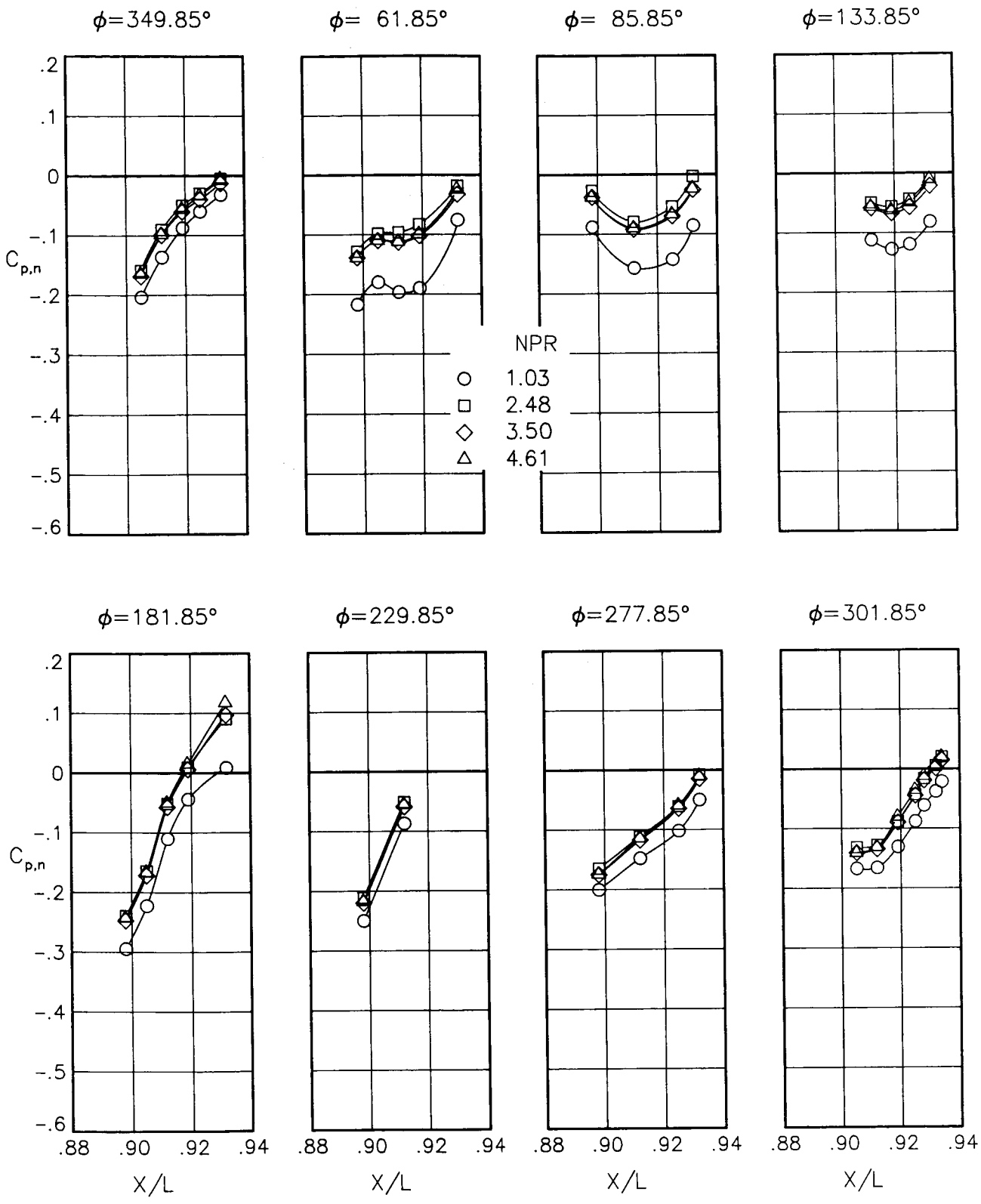

(e) M = 0.80; α = 7.00°.

Figure 79.- Continued.

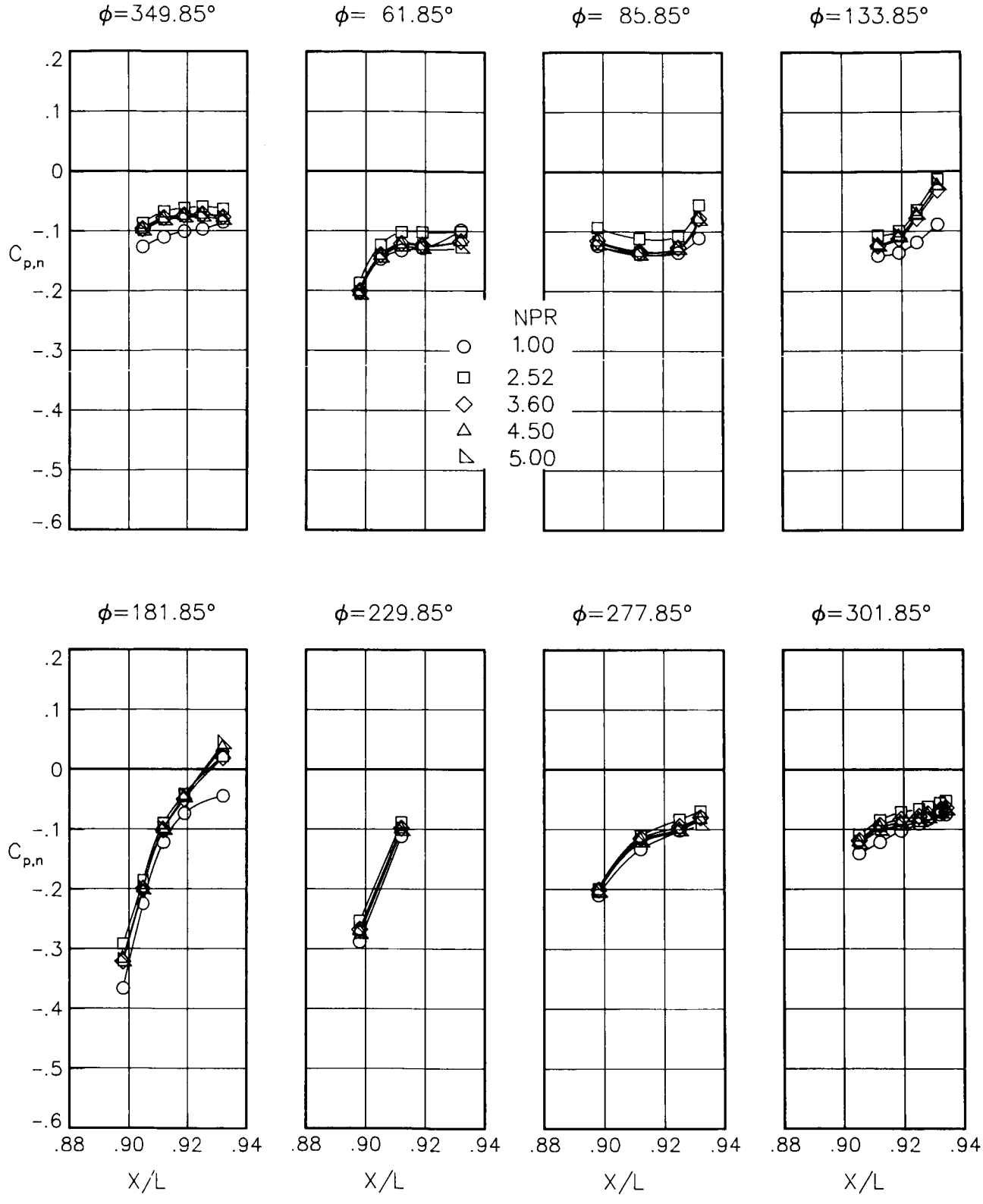

(f) M = 0.90; α = 0.00°.

Figure 79.- Continued.

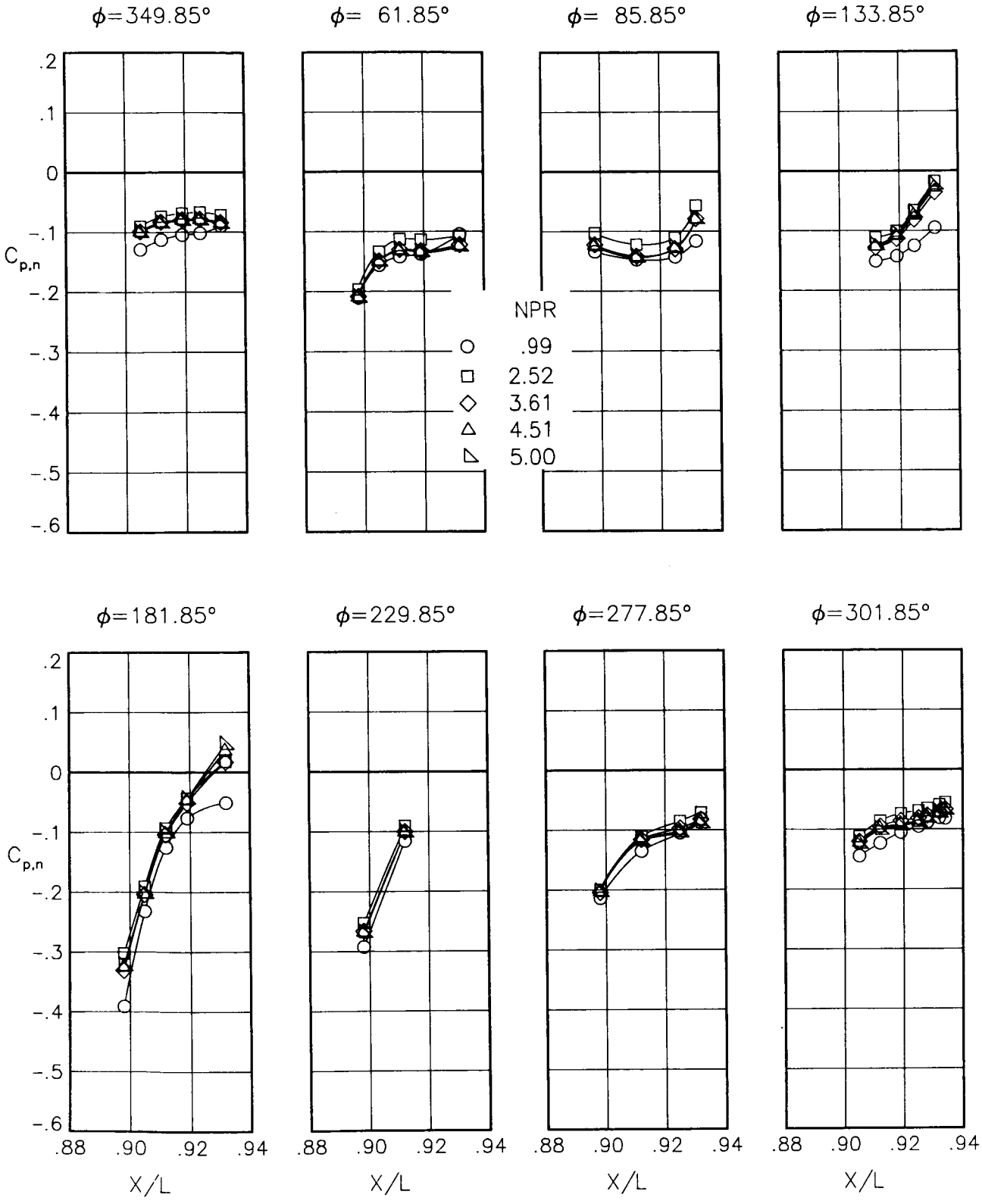

(g) M = 0.90; α = 1.00°.

Figure 79.- Continued.

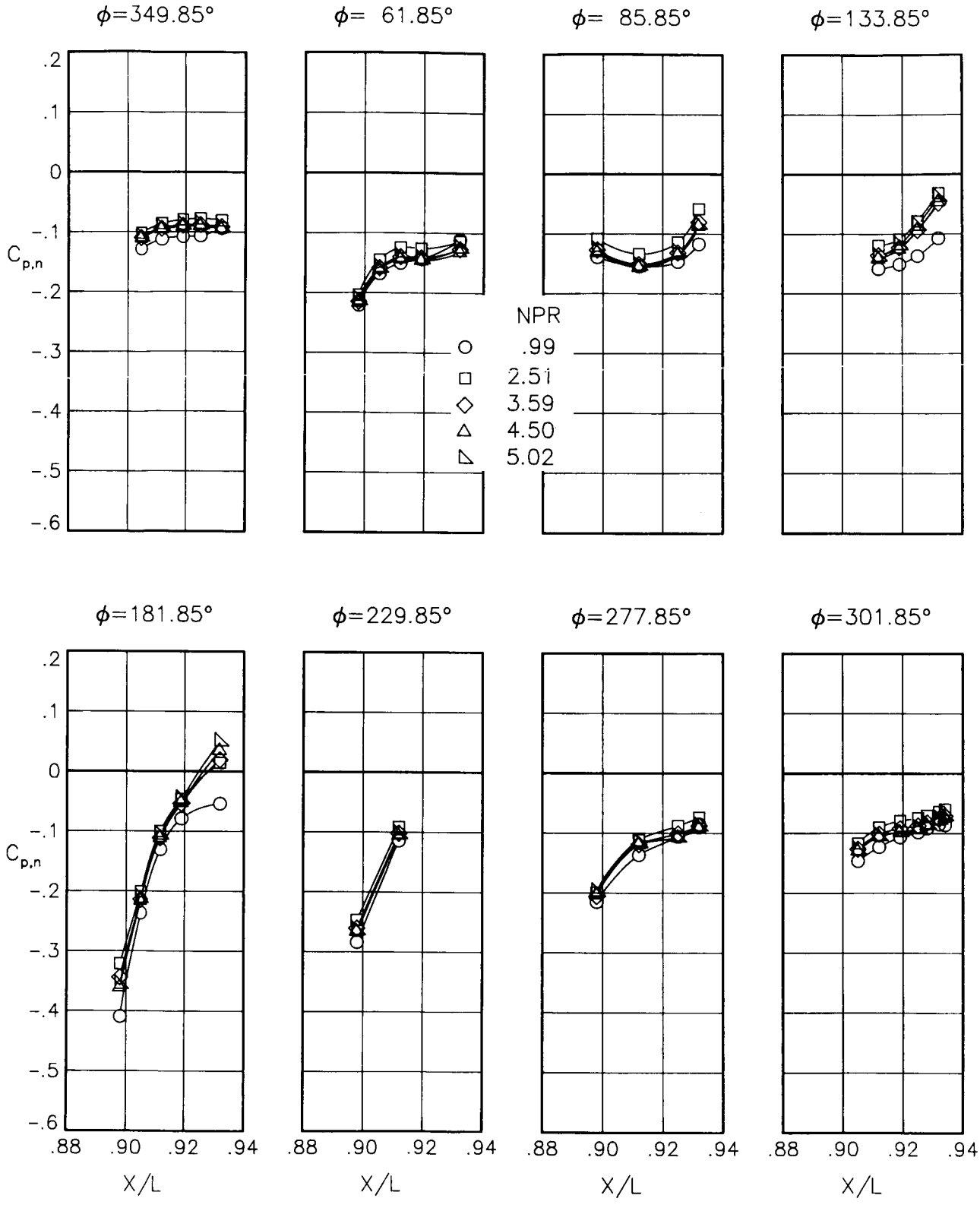

(h) M = 0.90; α = 3.00°.

Figure 79.- Continued.

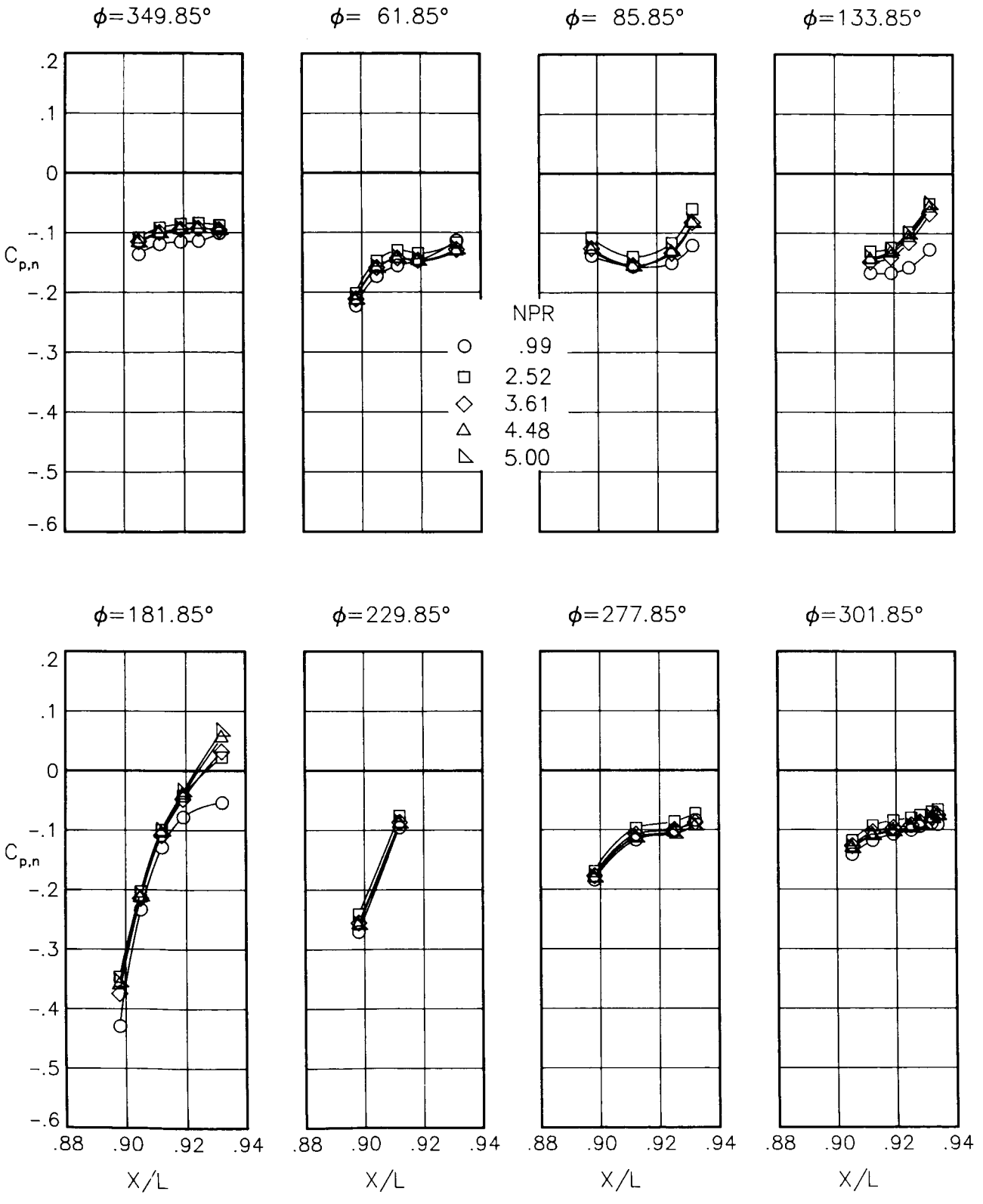

(i) M = 0.90; α = 6.00°.

Figure 79.- Concluded.

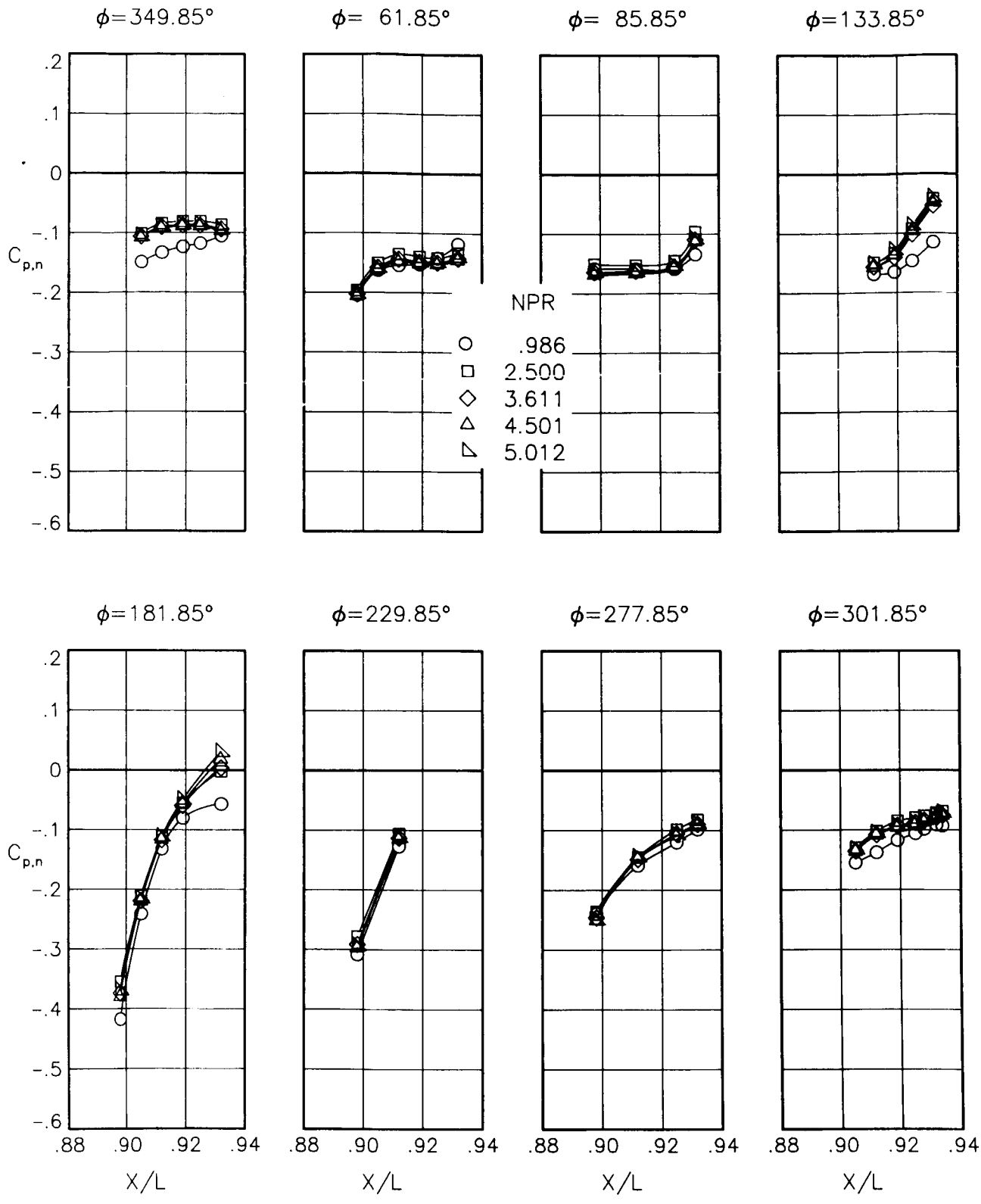

(a) M = 0.90; α = 0.00°.

Figure 80.- Static-pressure-coefficient distributions on nozzle for the model with all fuselage modifications. β_L = 18.45°; β_R = 7.72°; δ_h = -4°.

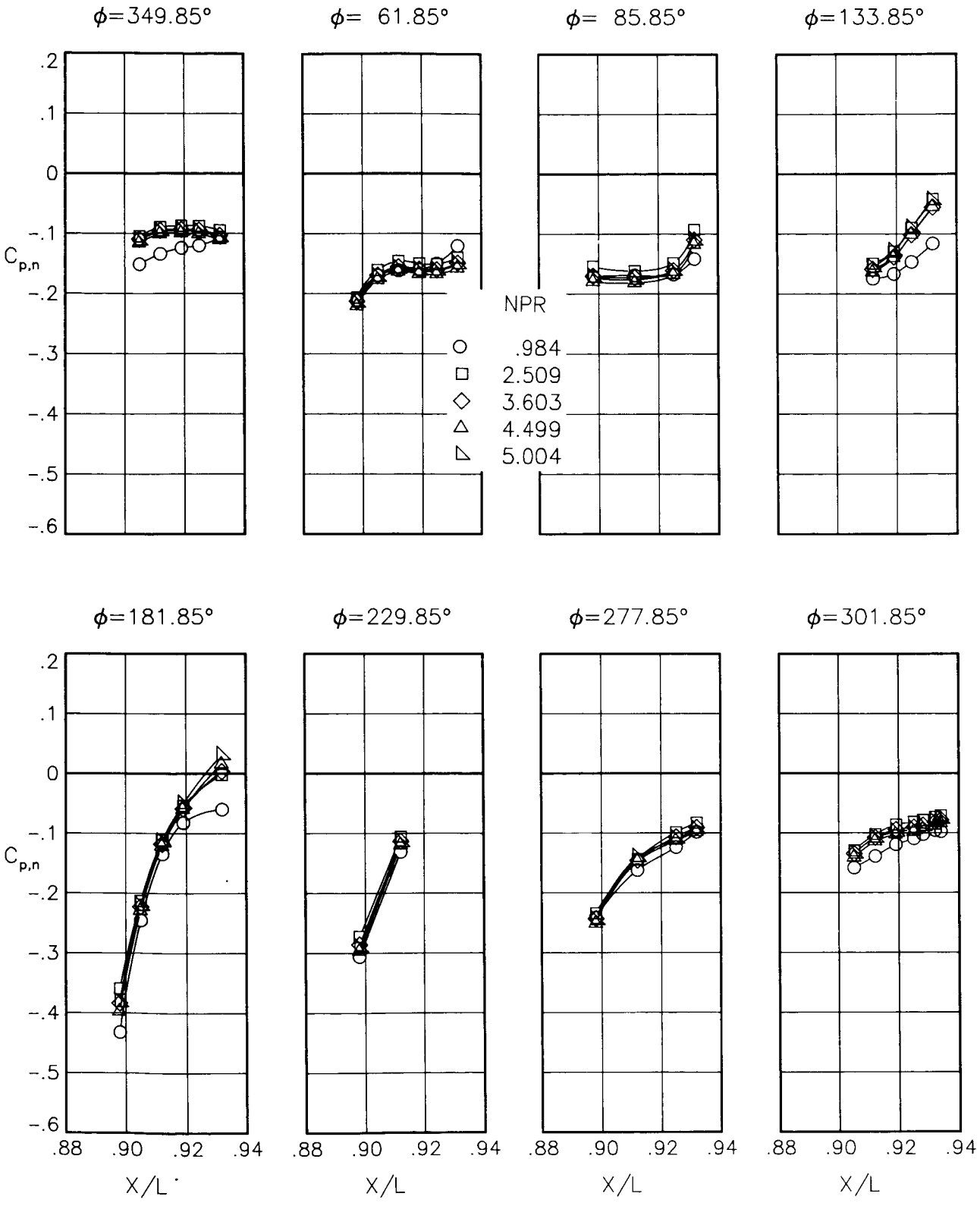

(b) M = 0.90; α = 1.00°.

Figure 80.- Continued.

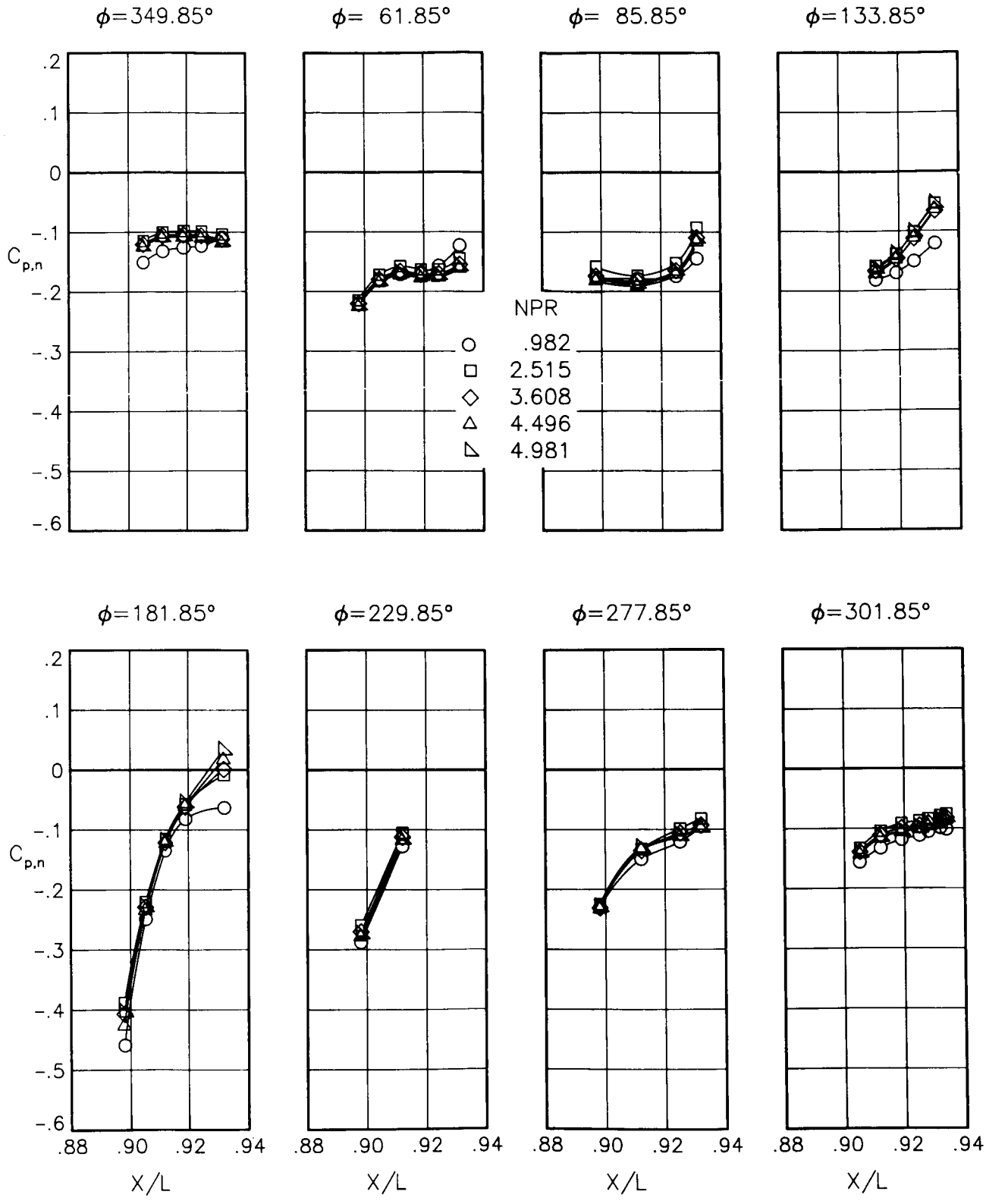

(c) M = 0.90; α = 3.00°.

Figure 80.- Continued.

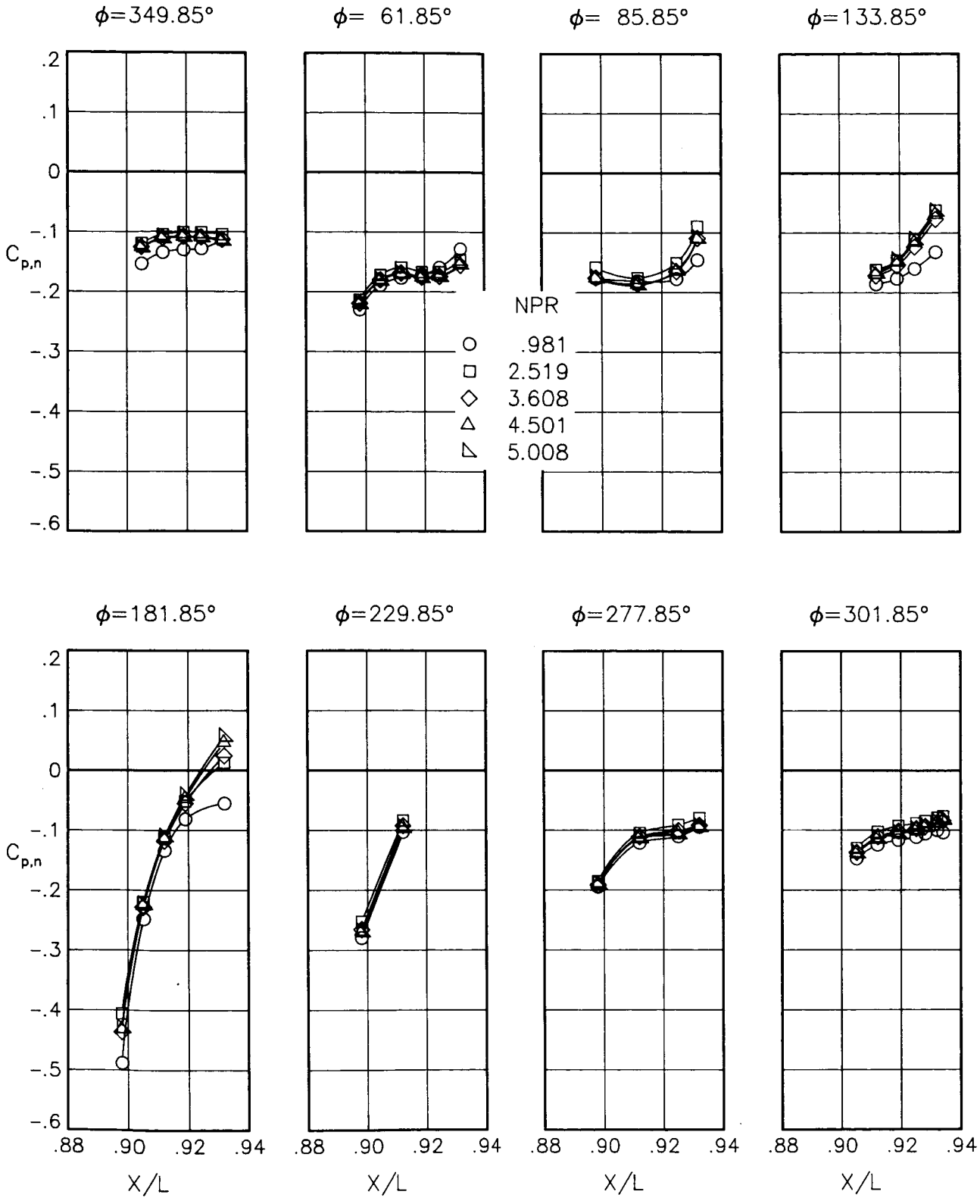

(d) M = 0.90; α = 6.00°.

Figure 80.- Concluded.

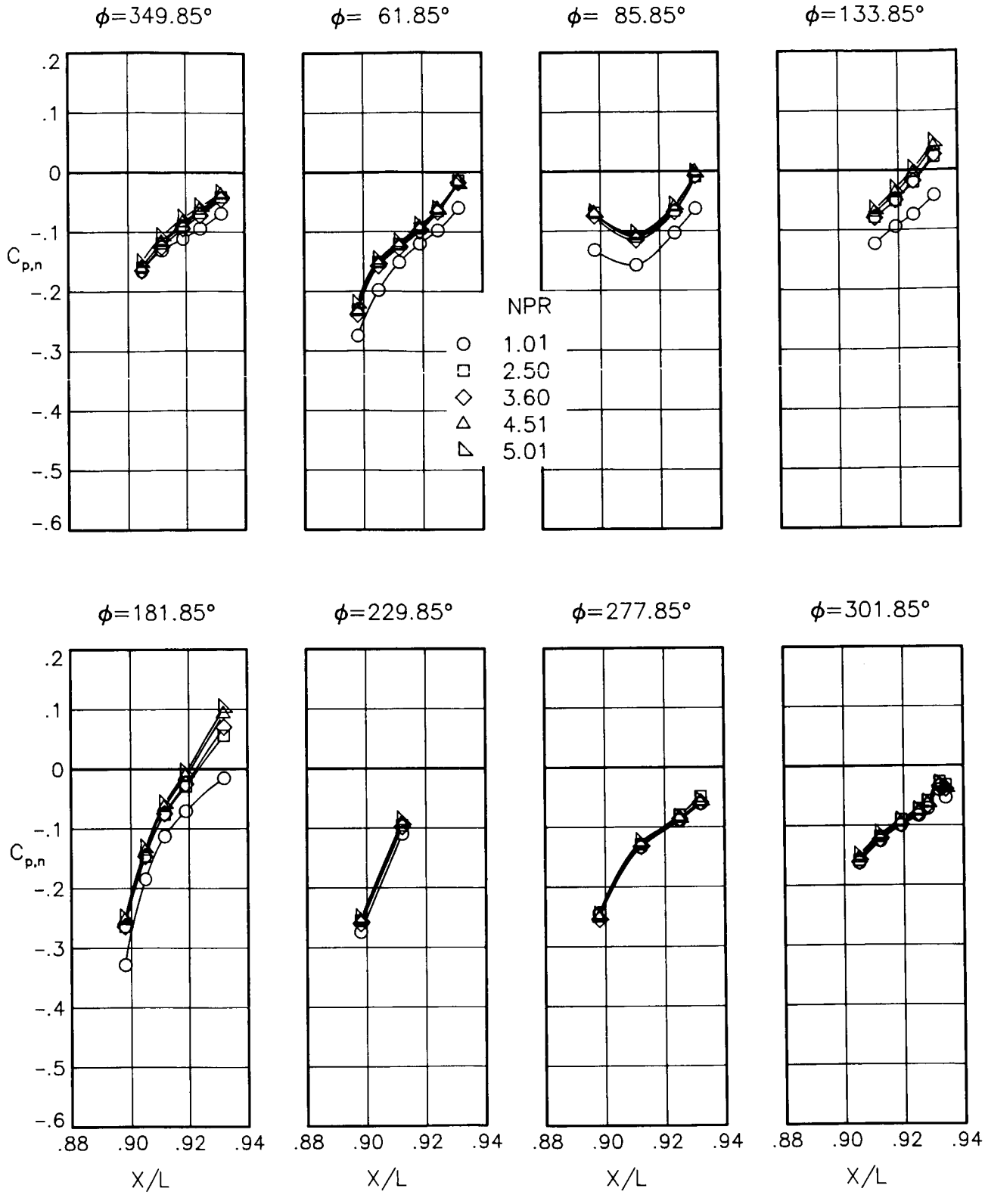

(a) M = 0.90; α = 0.00°.

Figure 81.- Static-pressure-coefficient distributions on nozzle for the model with all fuselage modifications. β_n = 15.05°.

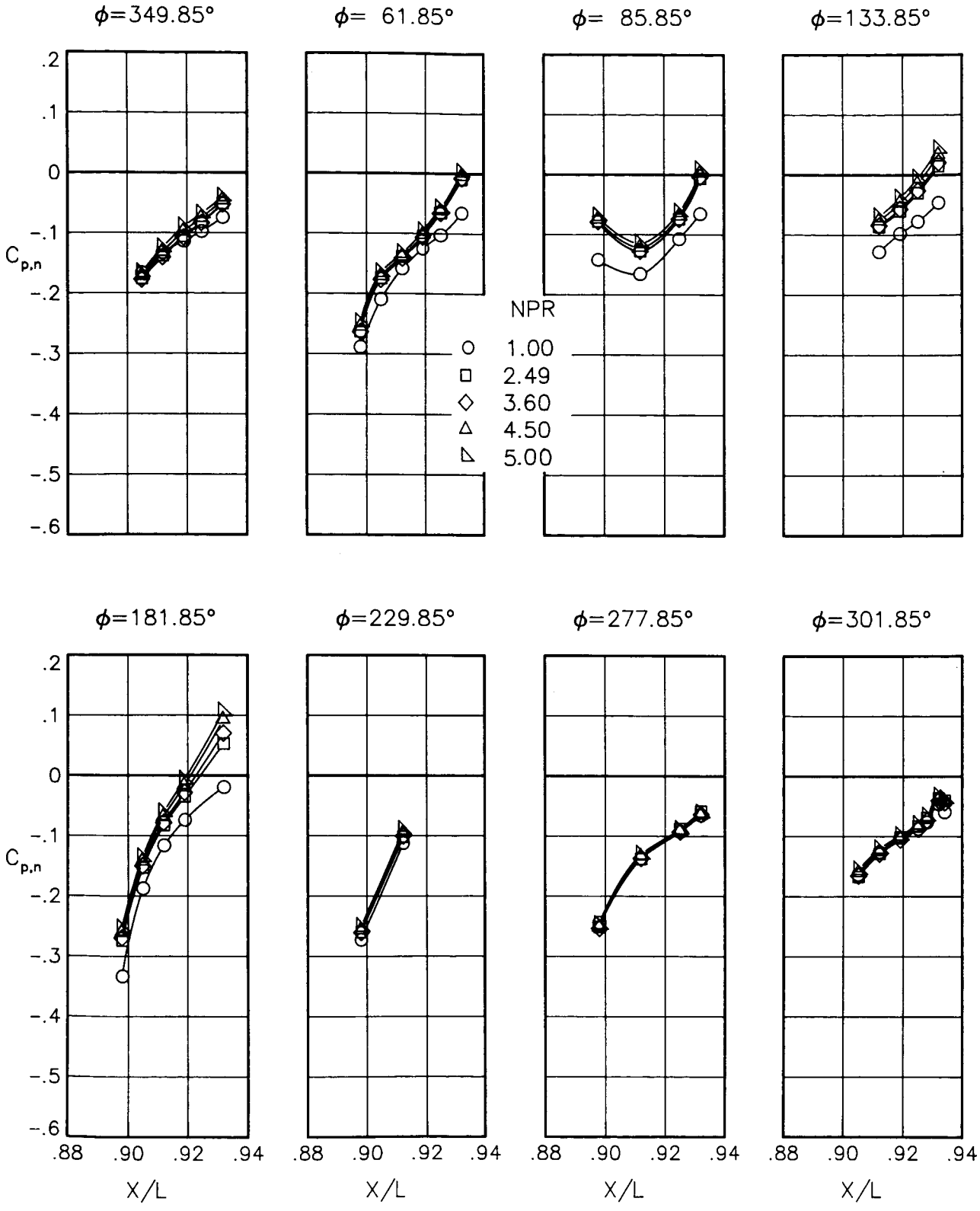

(b) M = 0.90; α = 1.00°.

Figure 81.- Continued.

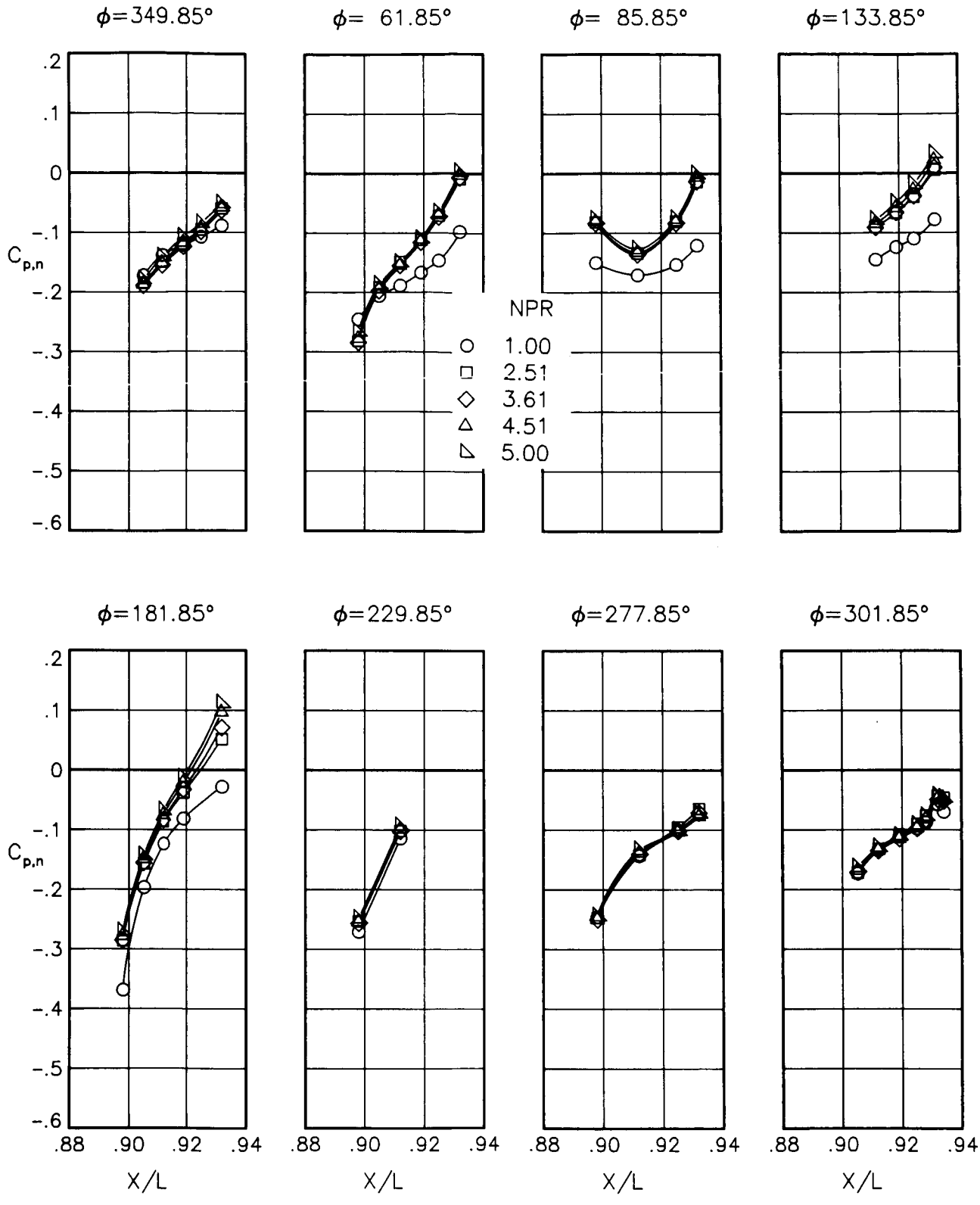

(c) M = 0.90; α = 3.00°.

Figure 81.- Continued.

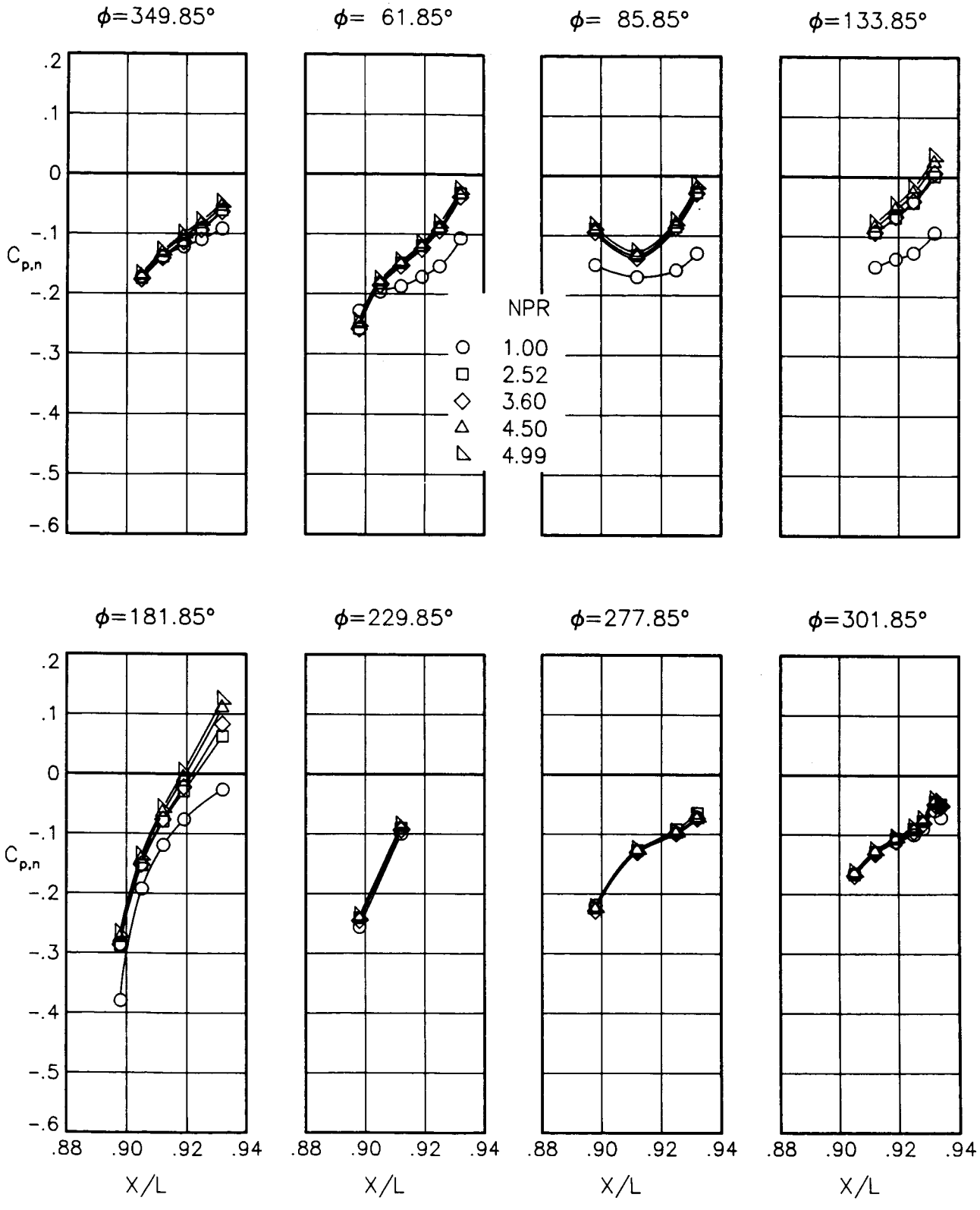

(d) M = 0.90; α = 6.00°.

Figure 81.- Continued.

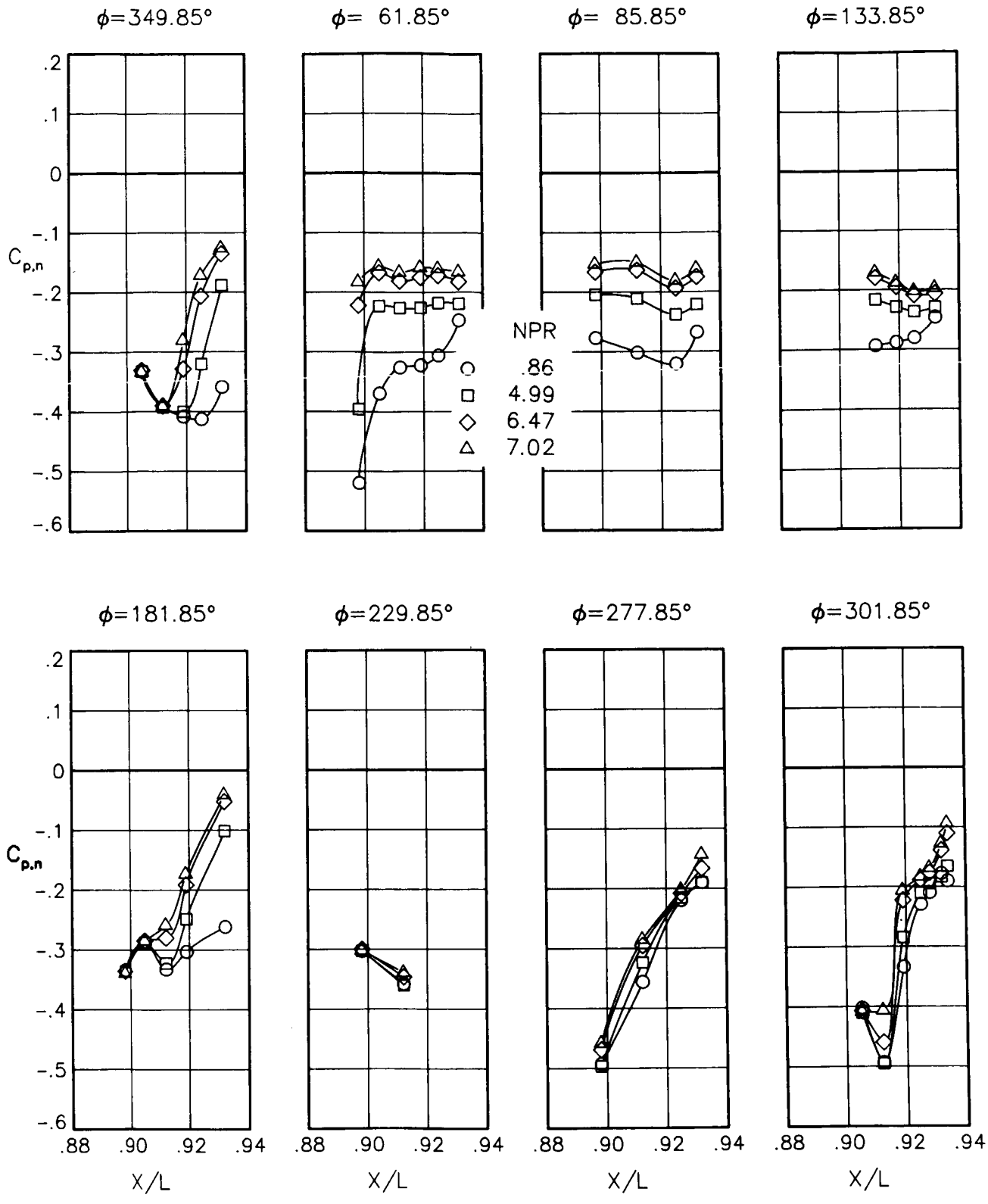

(e) M = 1.20; α = 0.00°.

Figure 81.- Continued.

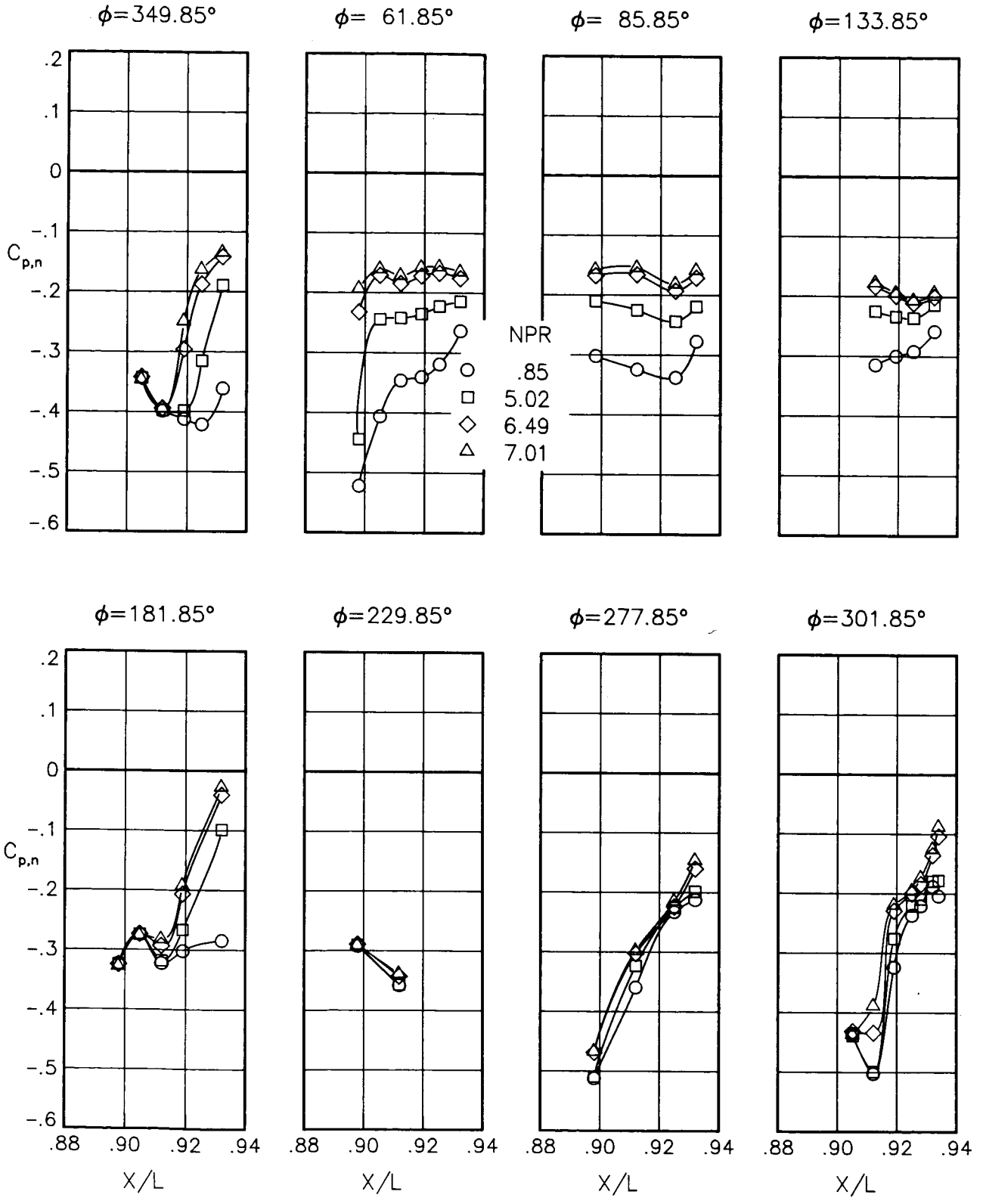

(f) M = 1.20; α = 1.00°.

Figure 81.- Continued.

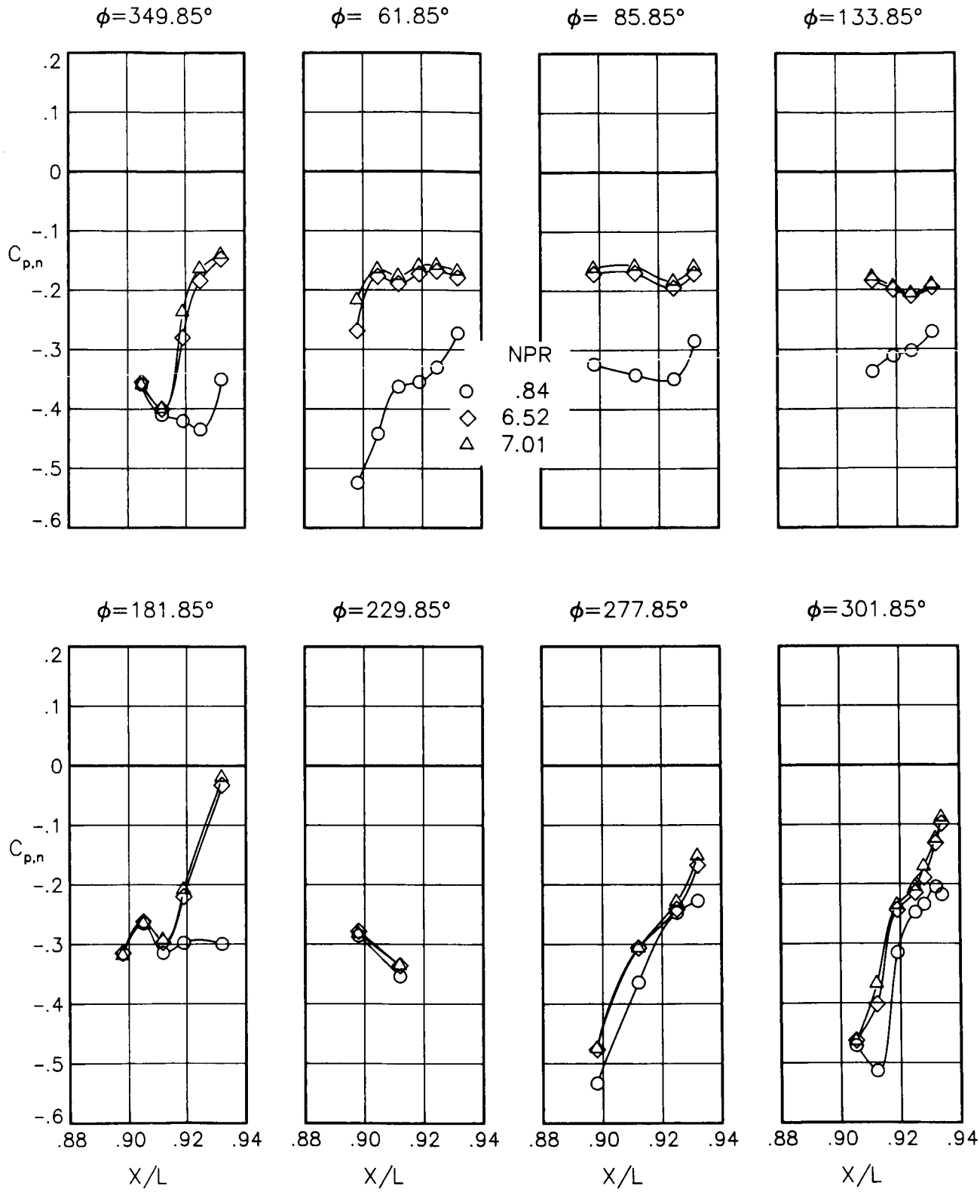

(g) M = 1.20; α = 2.00°.

Figure 81.- Continued.

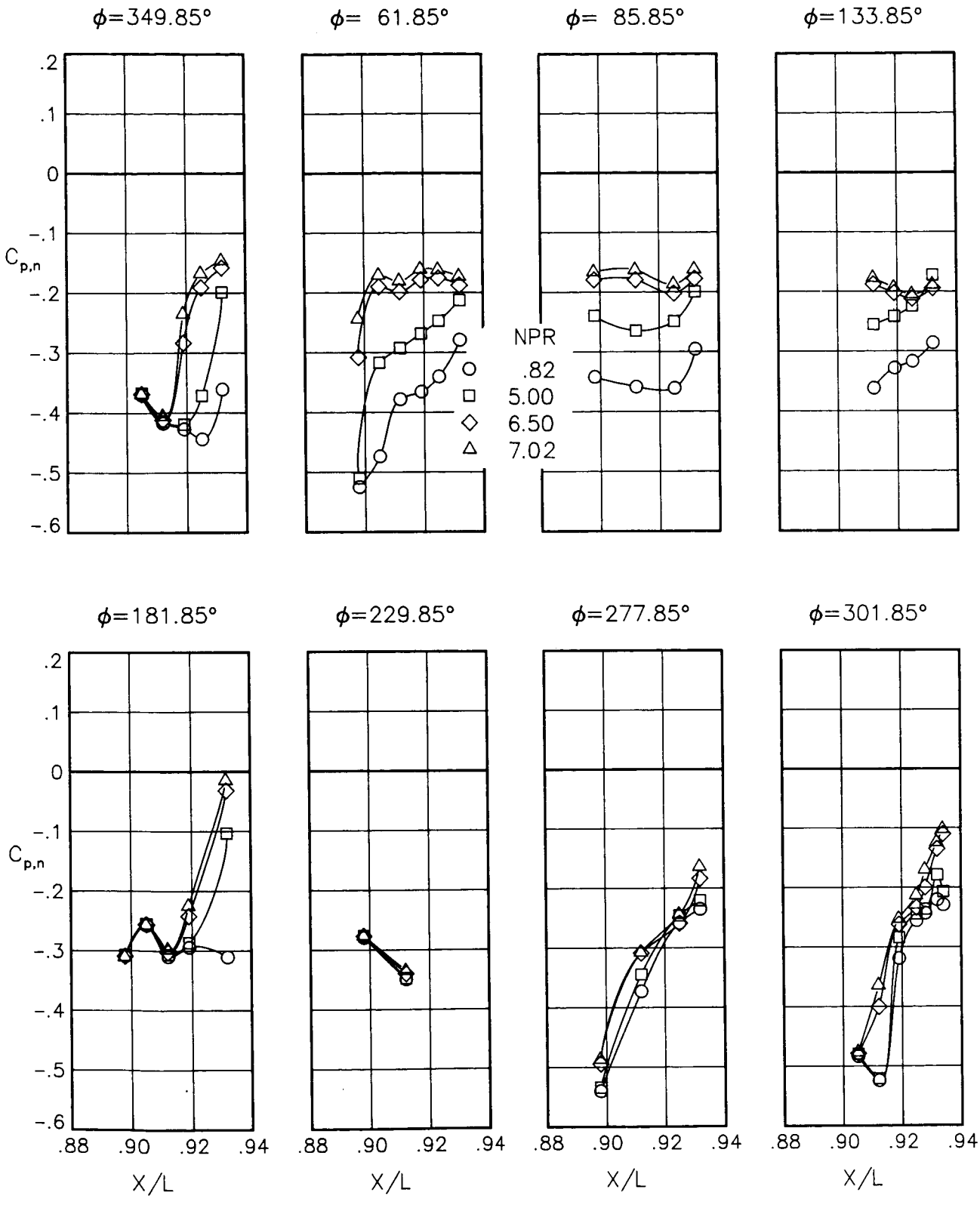

(h) M = 1.20; α = 3.00°.

Figure 81.- Continued.

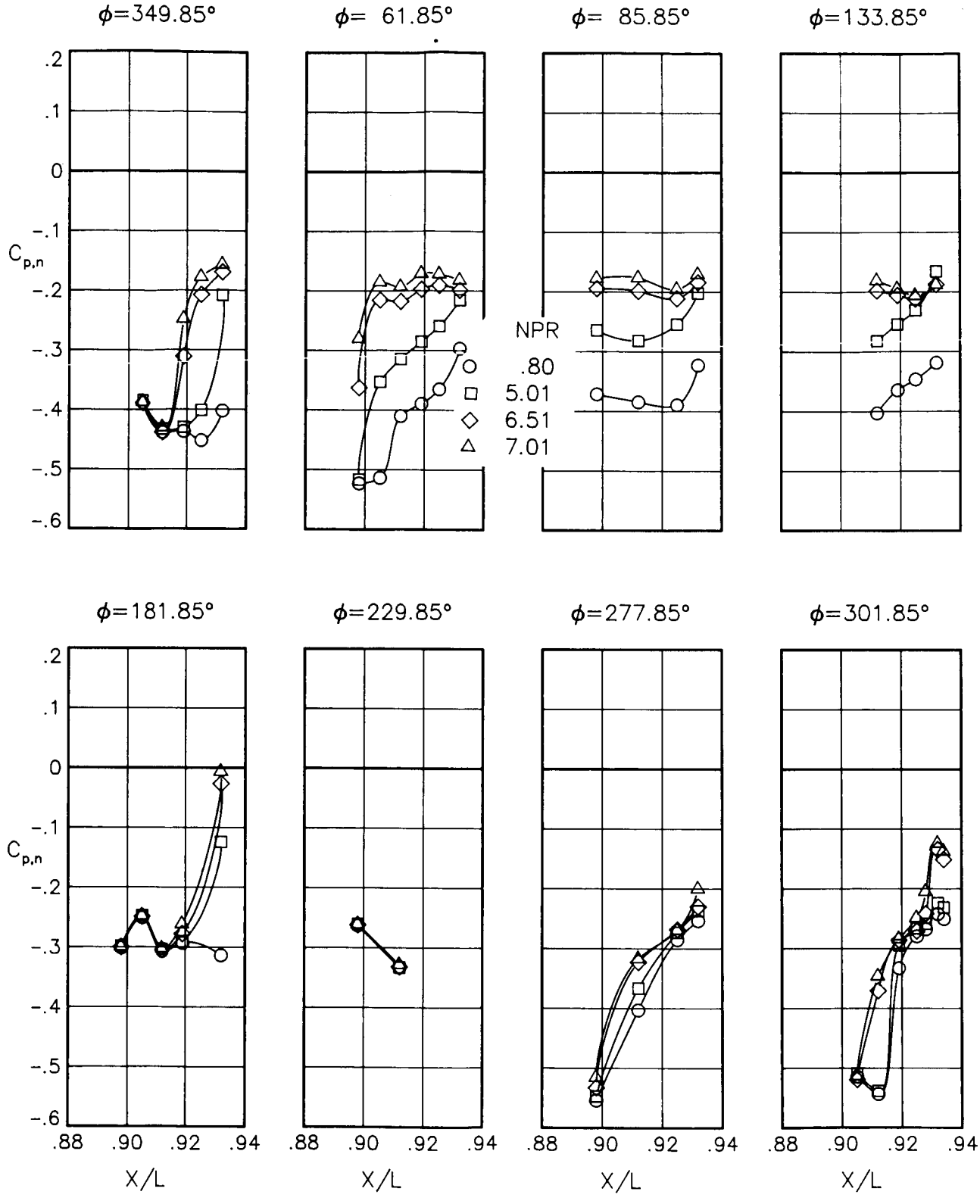

(i) M = 1.20; α = 5.00°.

Figure 81.- Concluded.

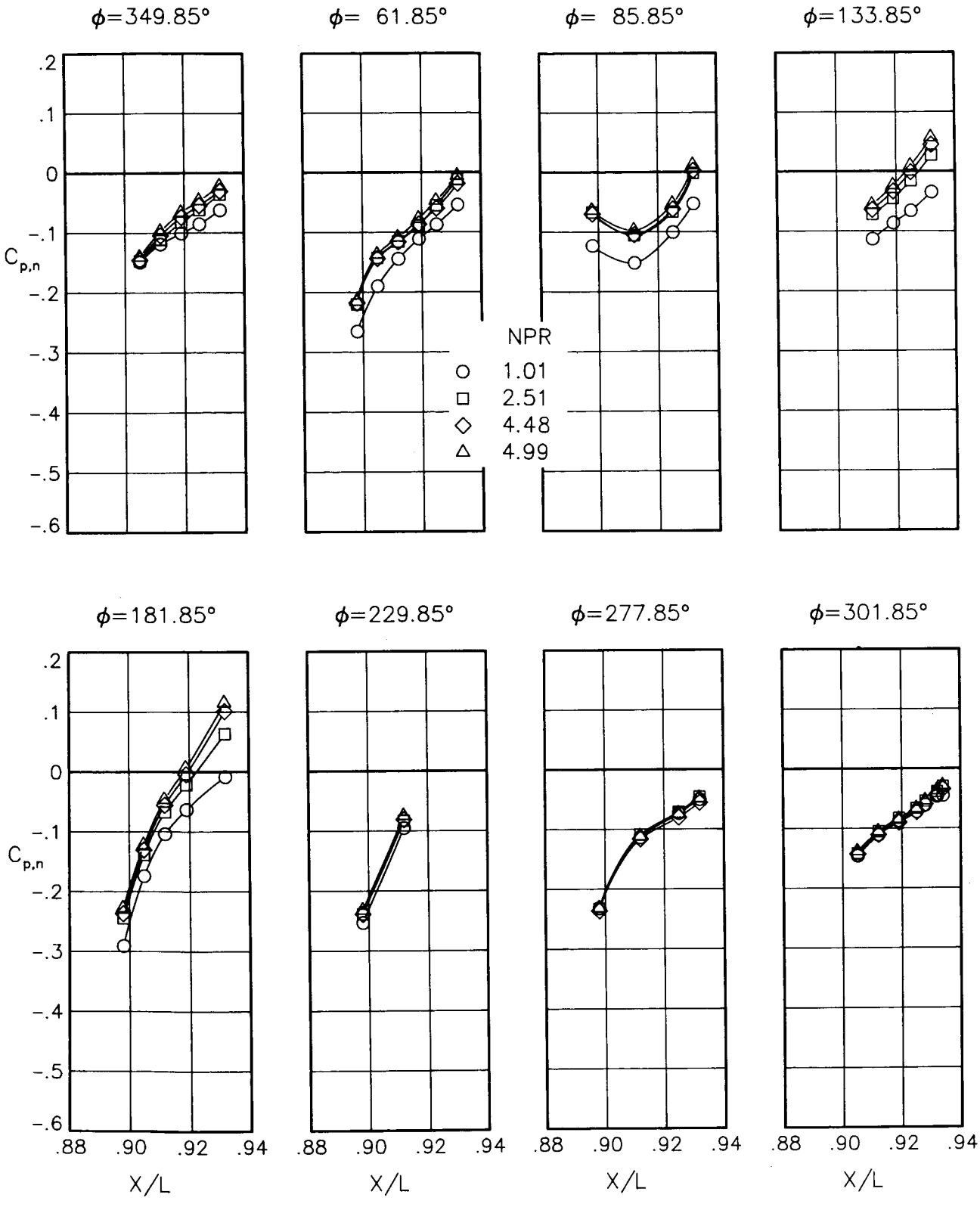

(a) M = 0.90; α = 0.00°.

Figure 82.- Static-pressure-coefficient distributions on nozzle for the model with all fuselage modifications. β_n = 15.05°; δ_h = 2°.

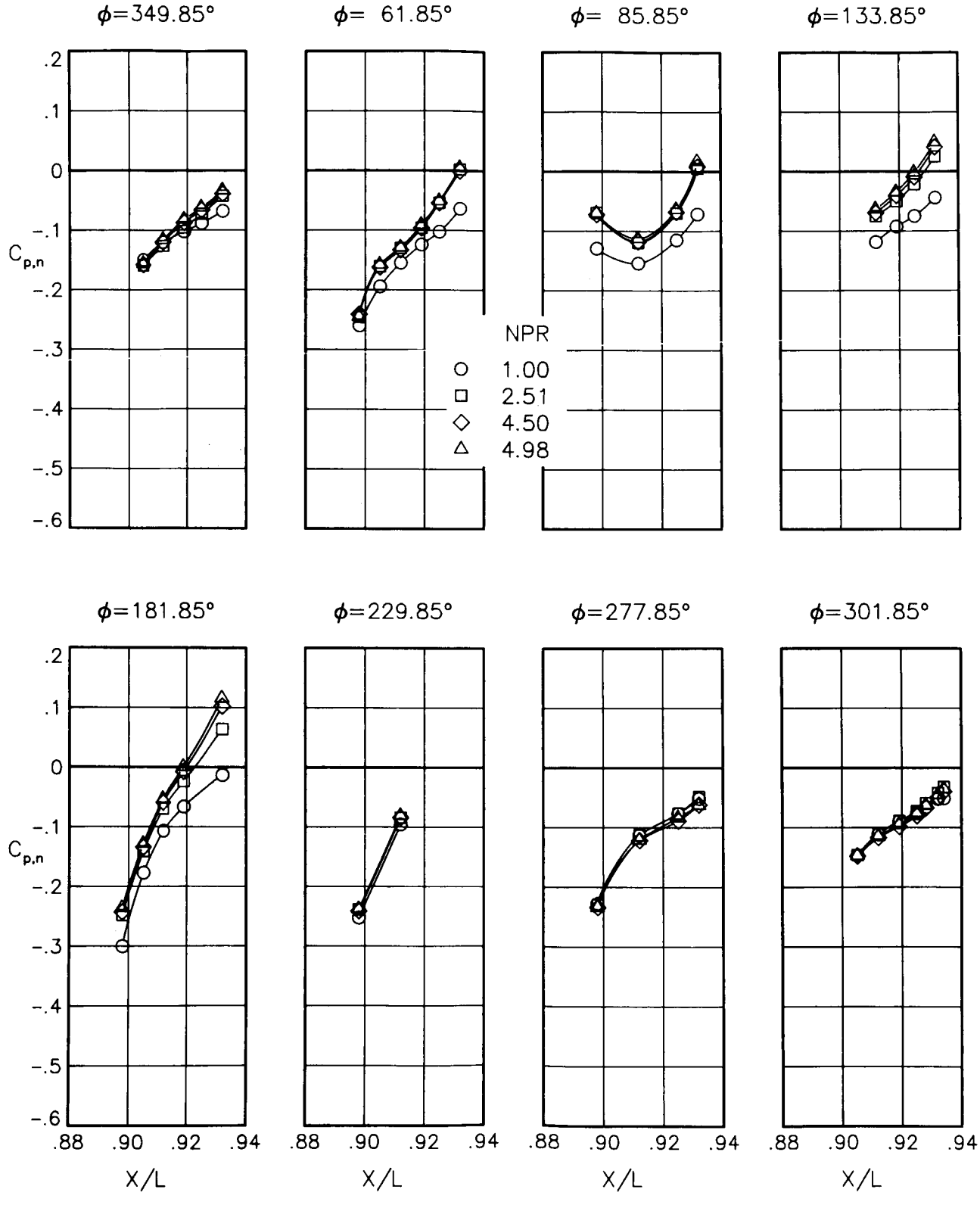

(b) M = 0.90; α = 1.00°.

Figure 82.- Continued.

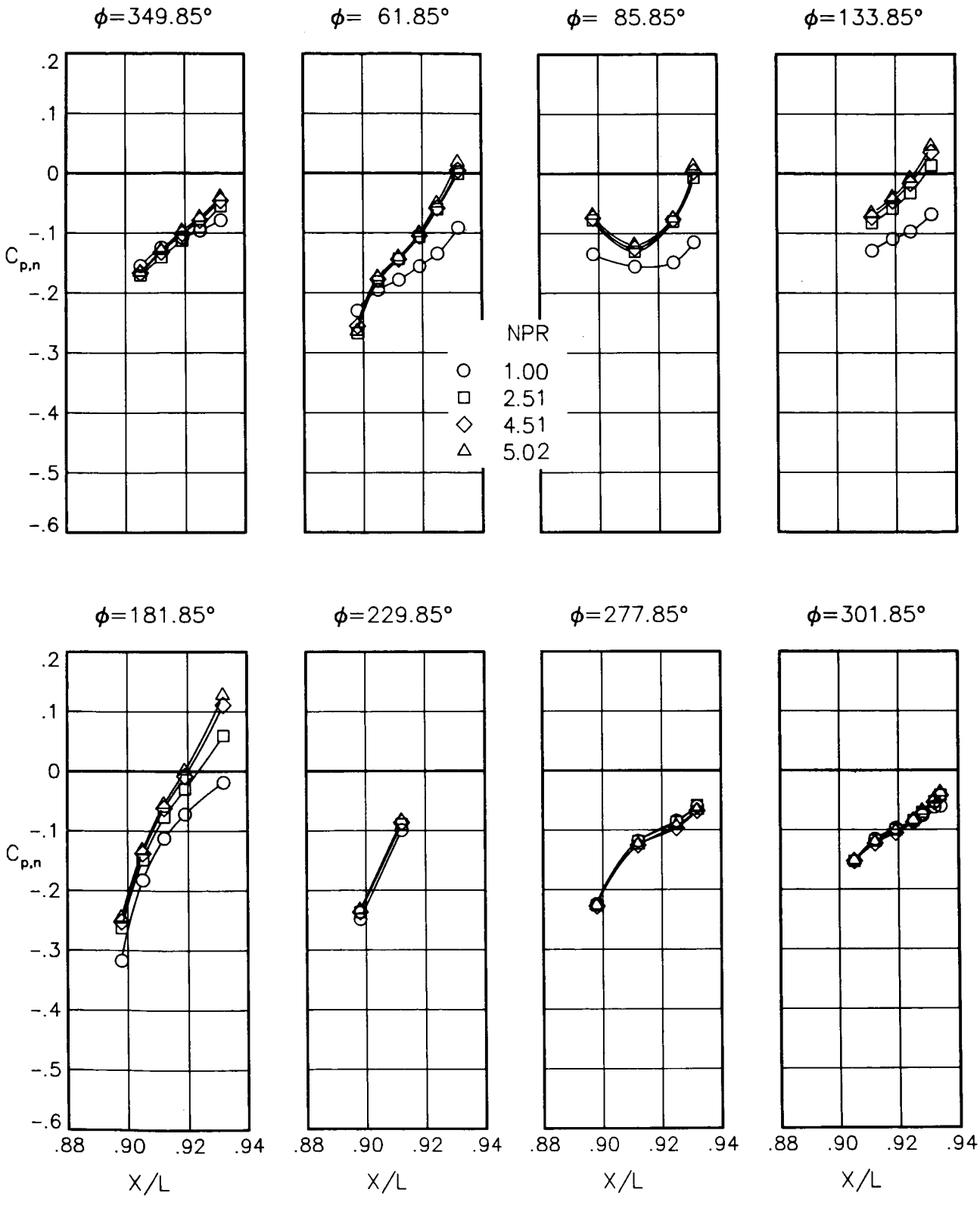

(c) M = 0.90; α = 3.00°.

Figure 82.- Continued.

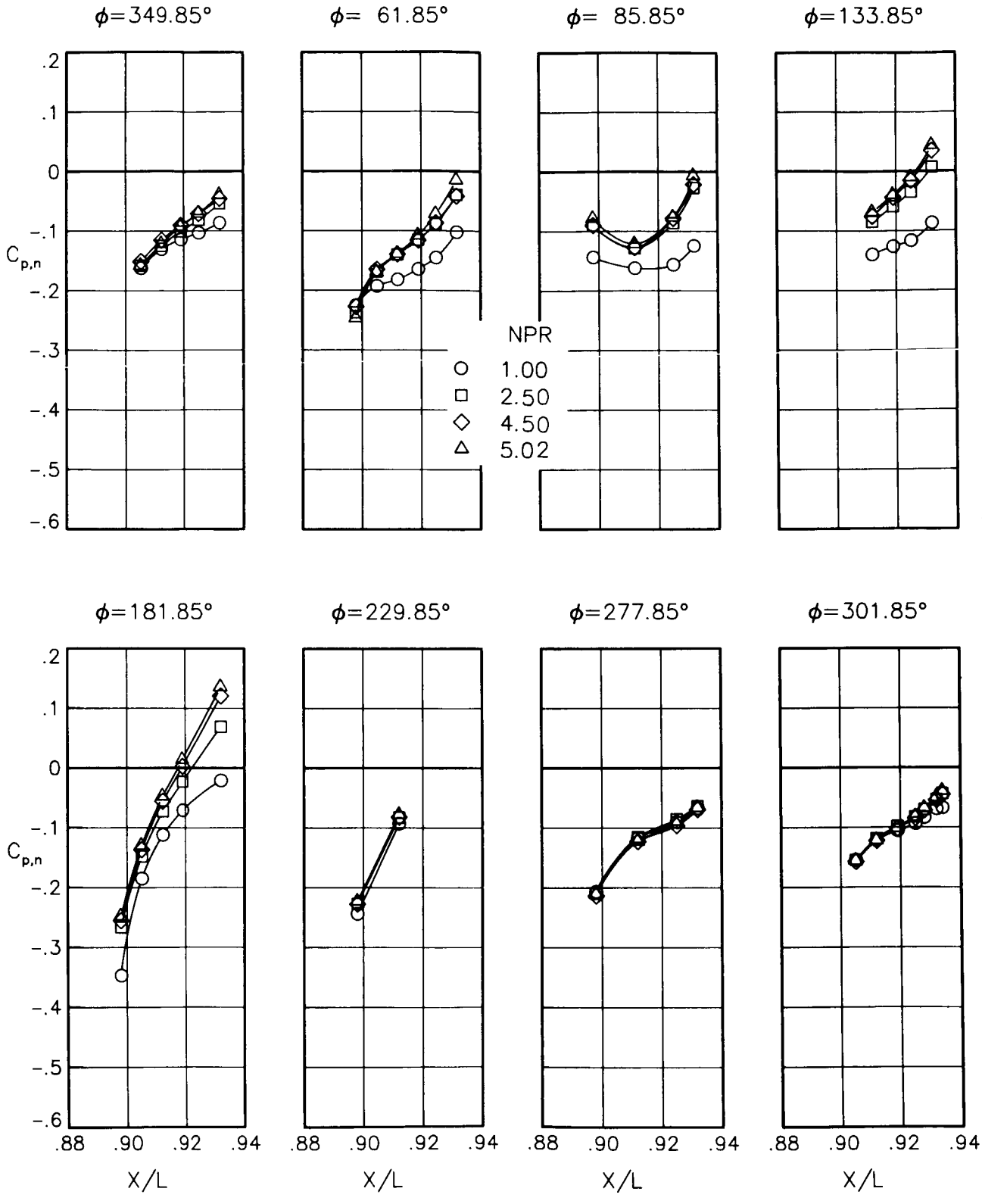

(d) M = 0.90; α = 6.00°.

Figure 82.- Continued.

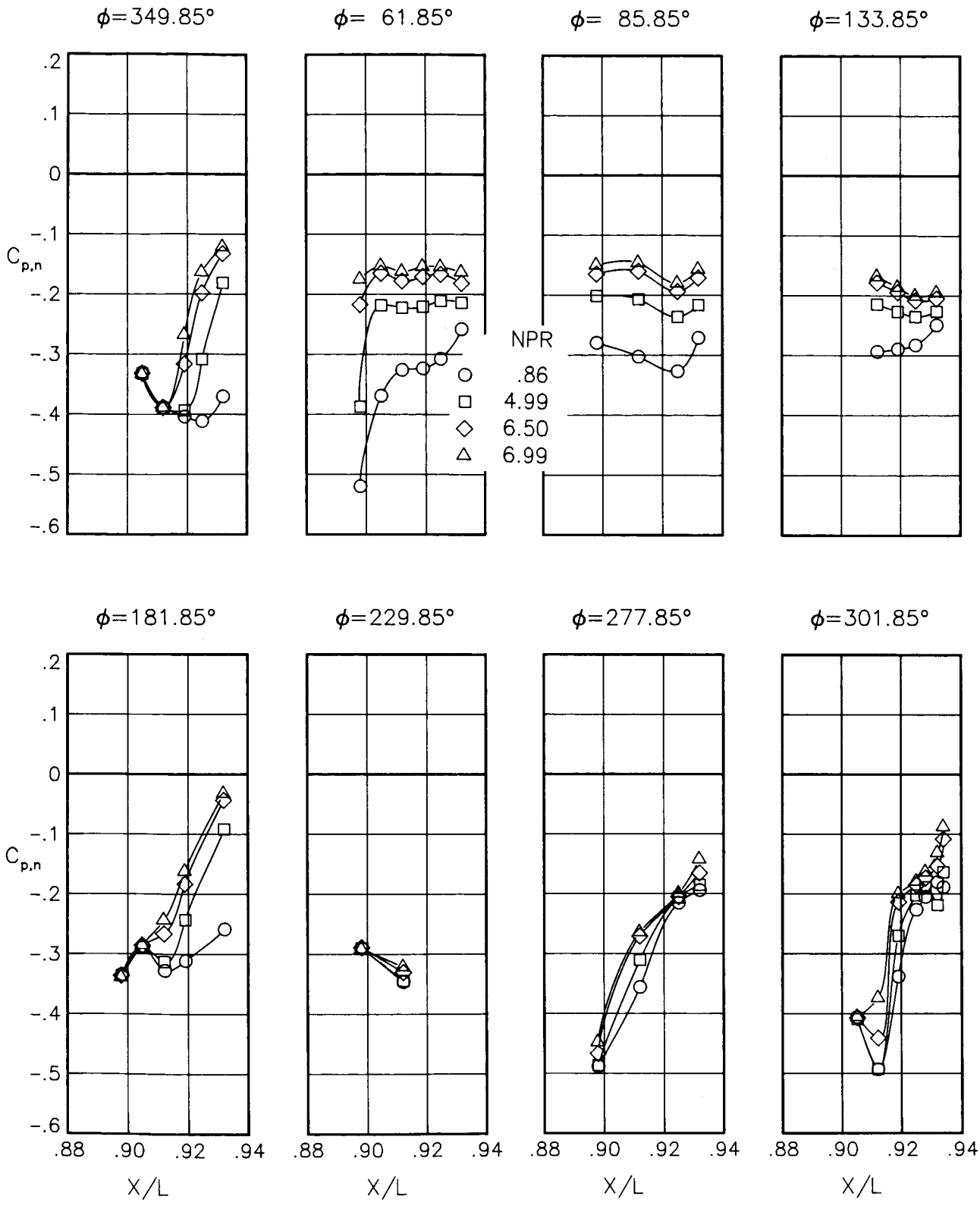

(e) M = 1.20; α = 0.00°.

Figure 82.- Continued.

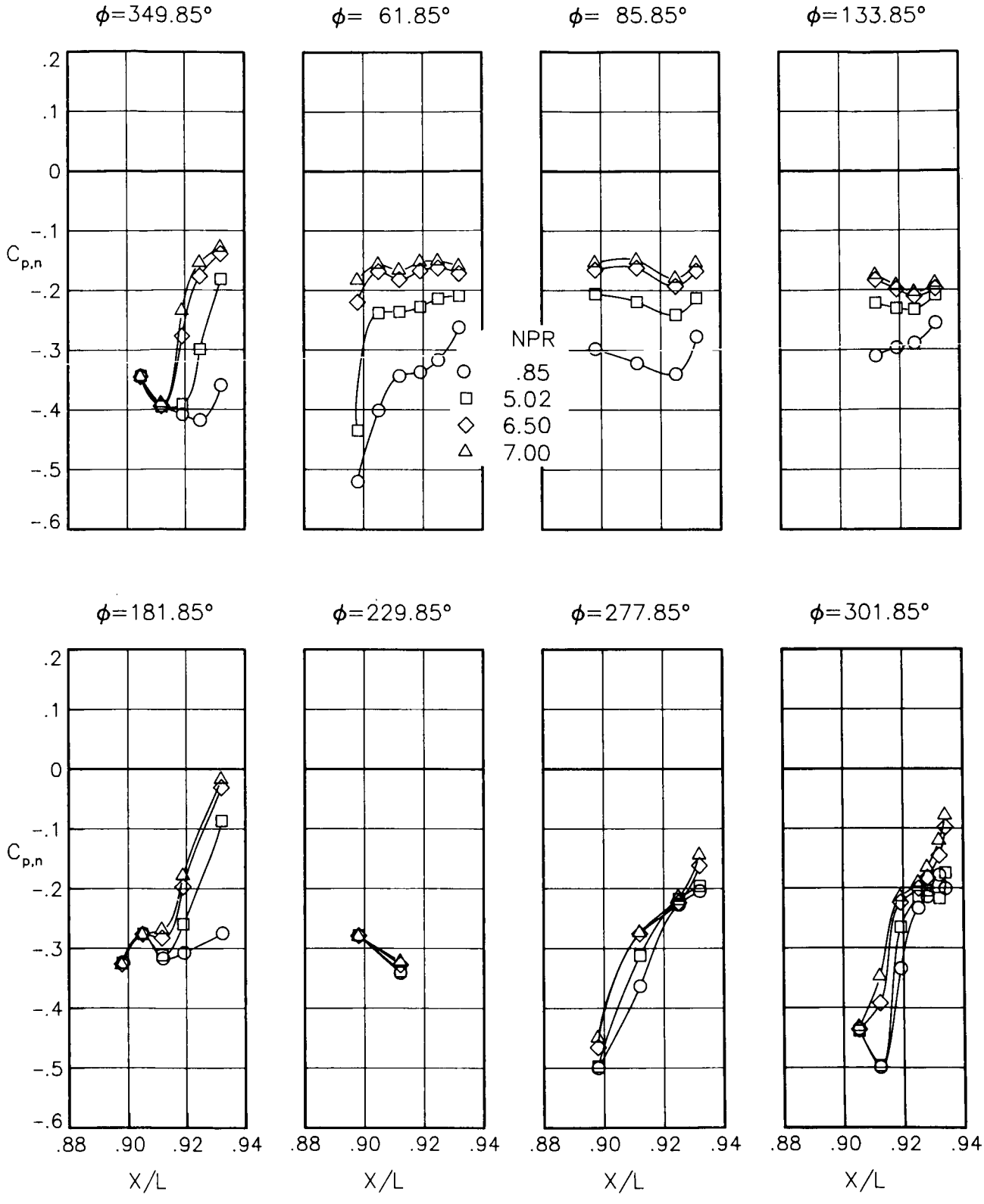

(f) M = 1.20; α = 1.00°.

Figure 82.- Continued.

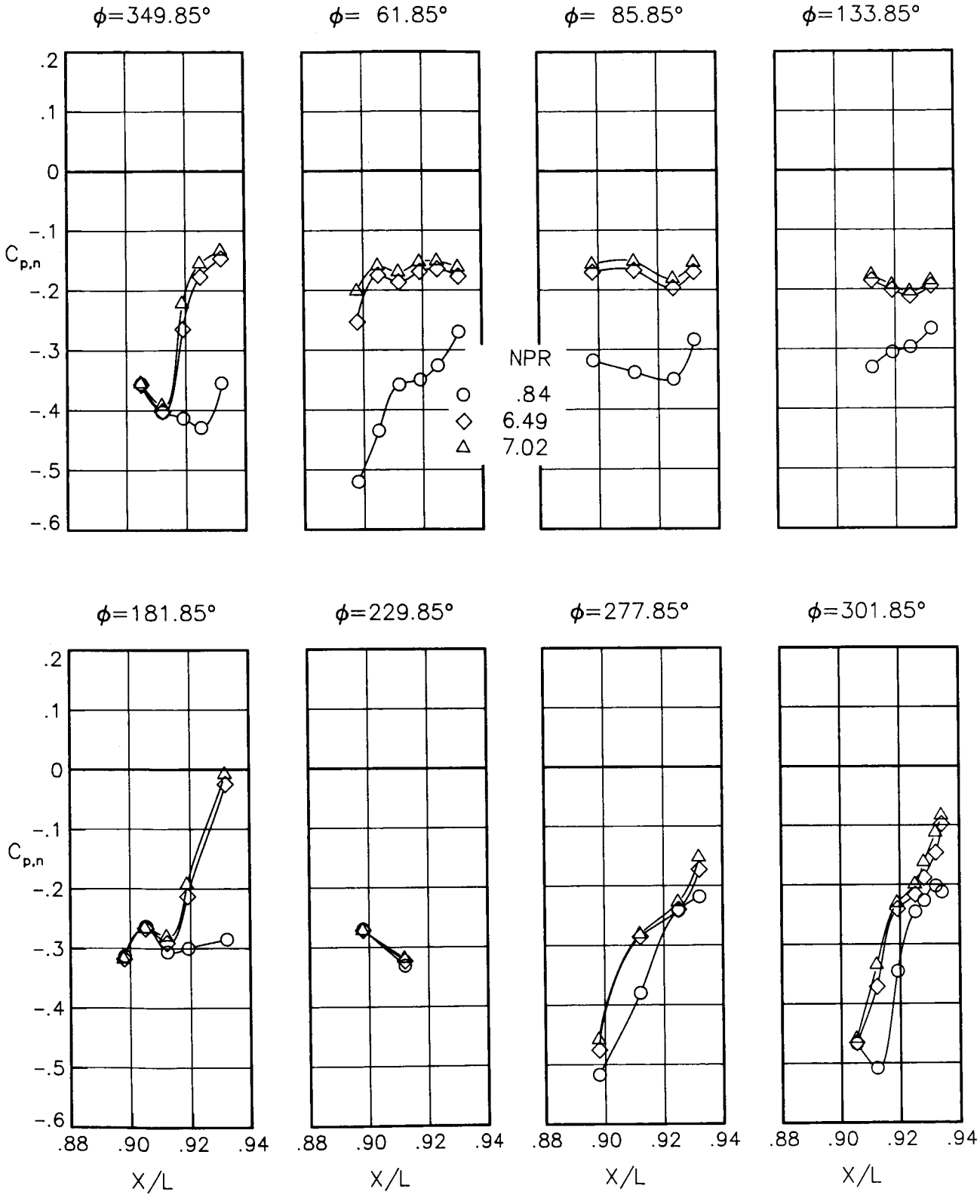

(g) M = 1.20; α = 2.00°.

Figure 82.- Continued.

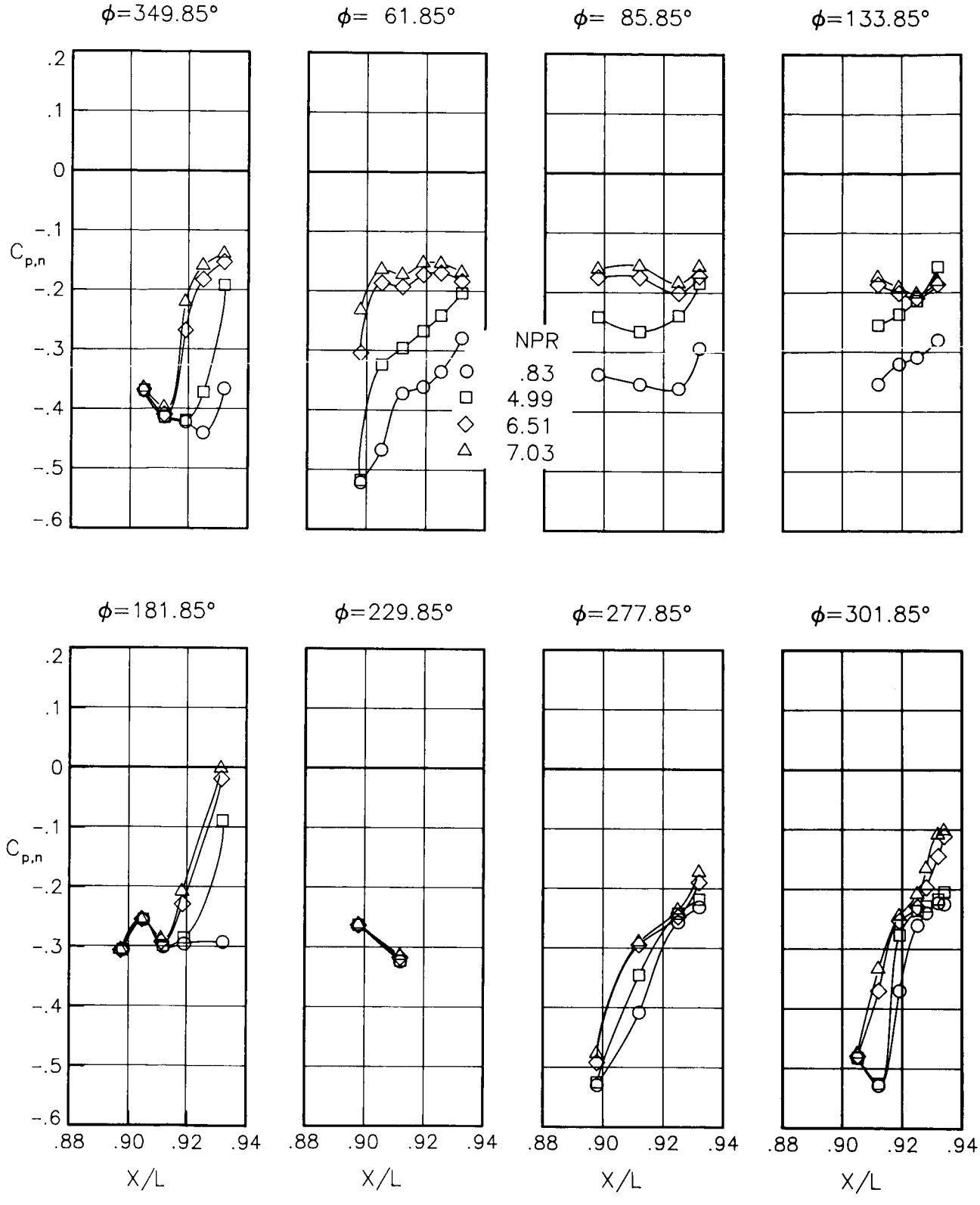

(h) M = 1.20; α = 3.00°.

Figure 82.- Concluded.

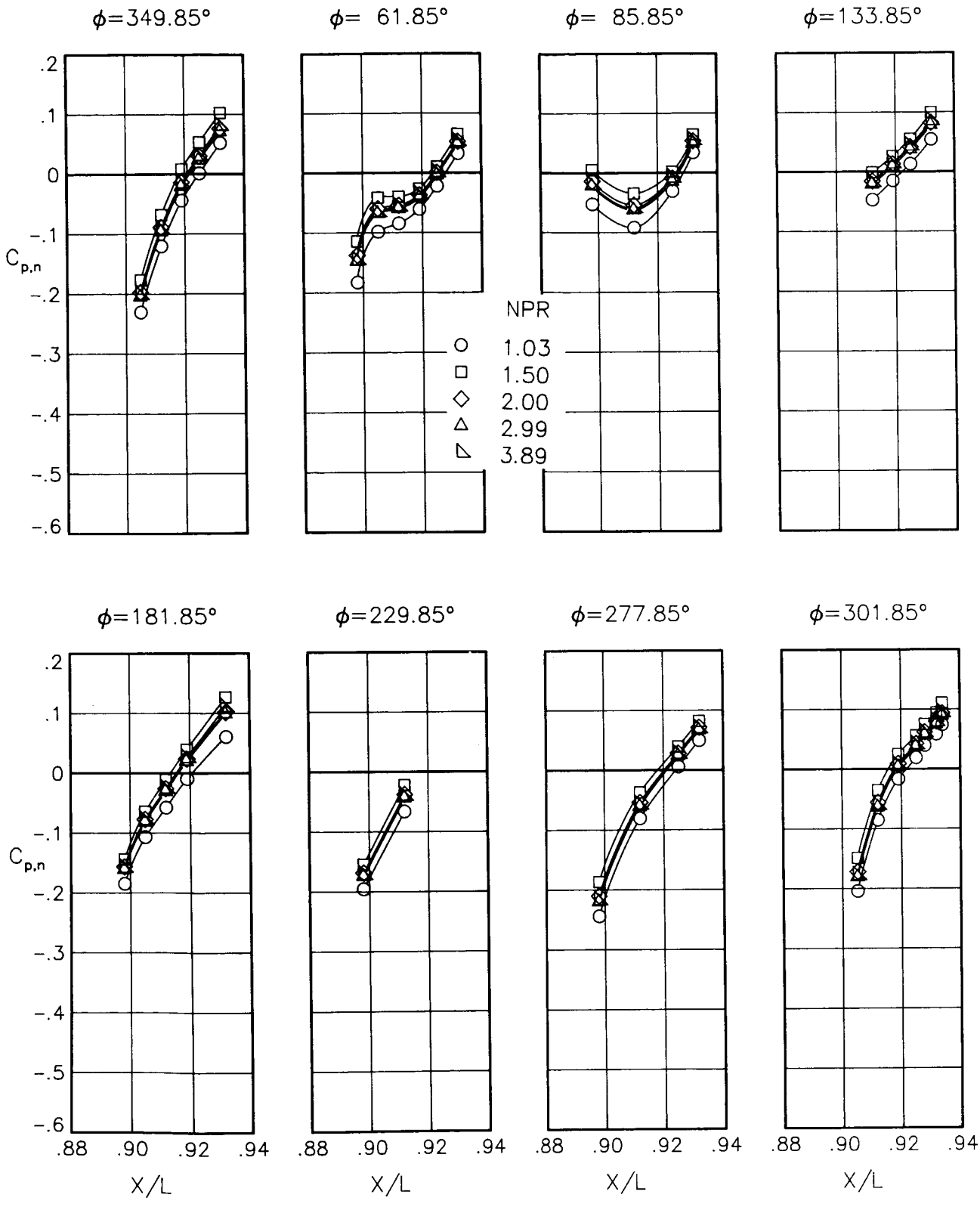

(a) M = 0.60; α = 0.00°.

Figure 83.- Static-pressure-coefficient distributions on nozzle for the model with all fuselage modifications. β_L = 15.05°; β_R = 18.45°.

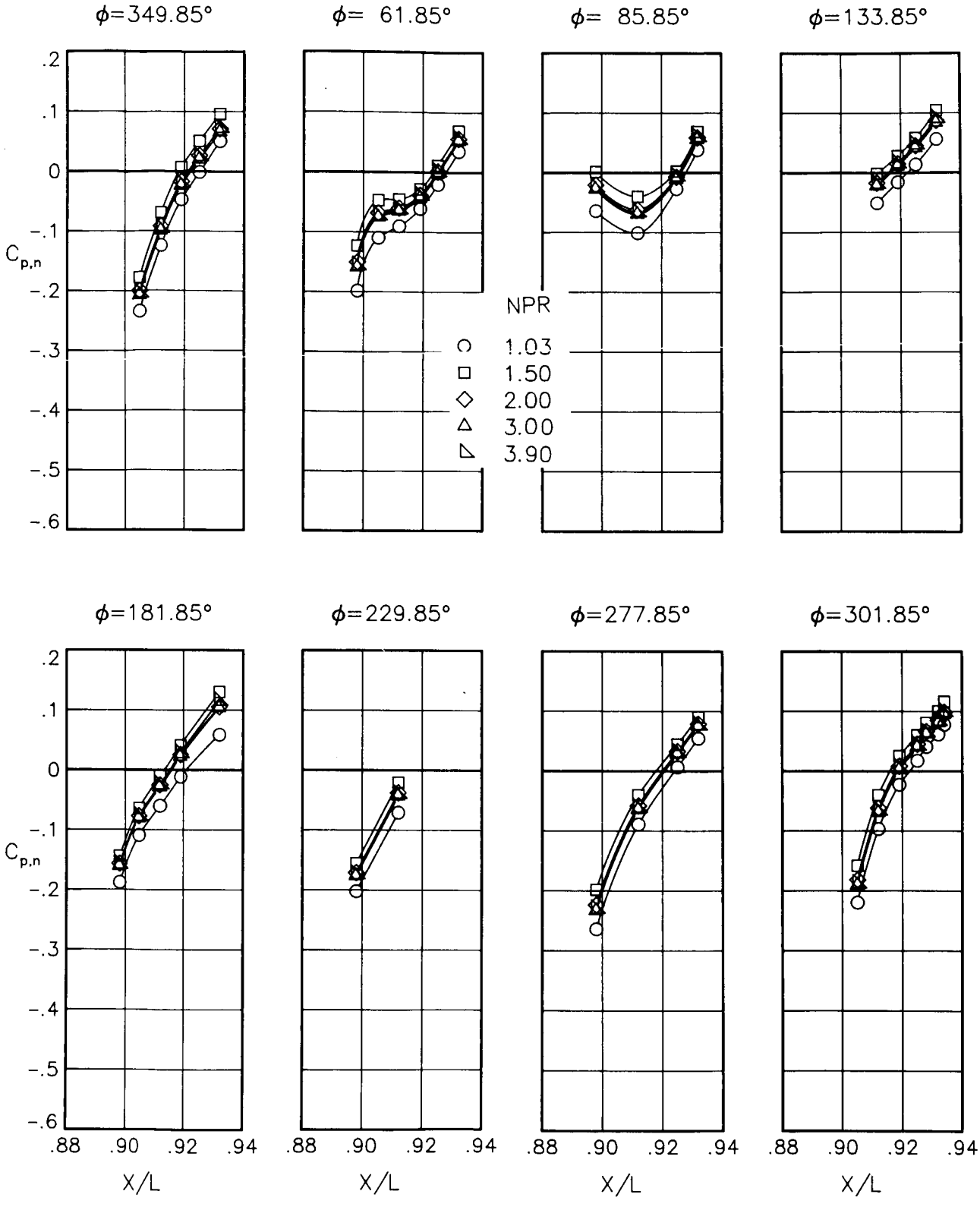

(b) M = 0.60; α = 1.00°.

Figure 83.- Continued.

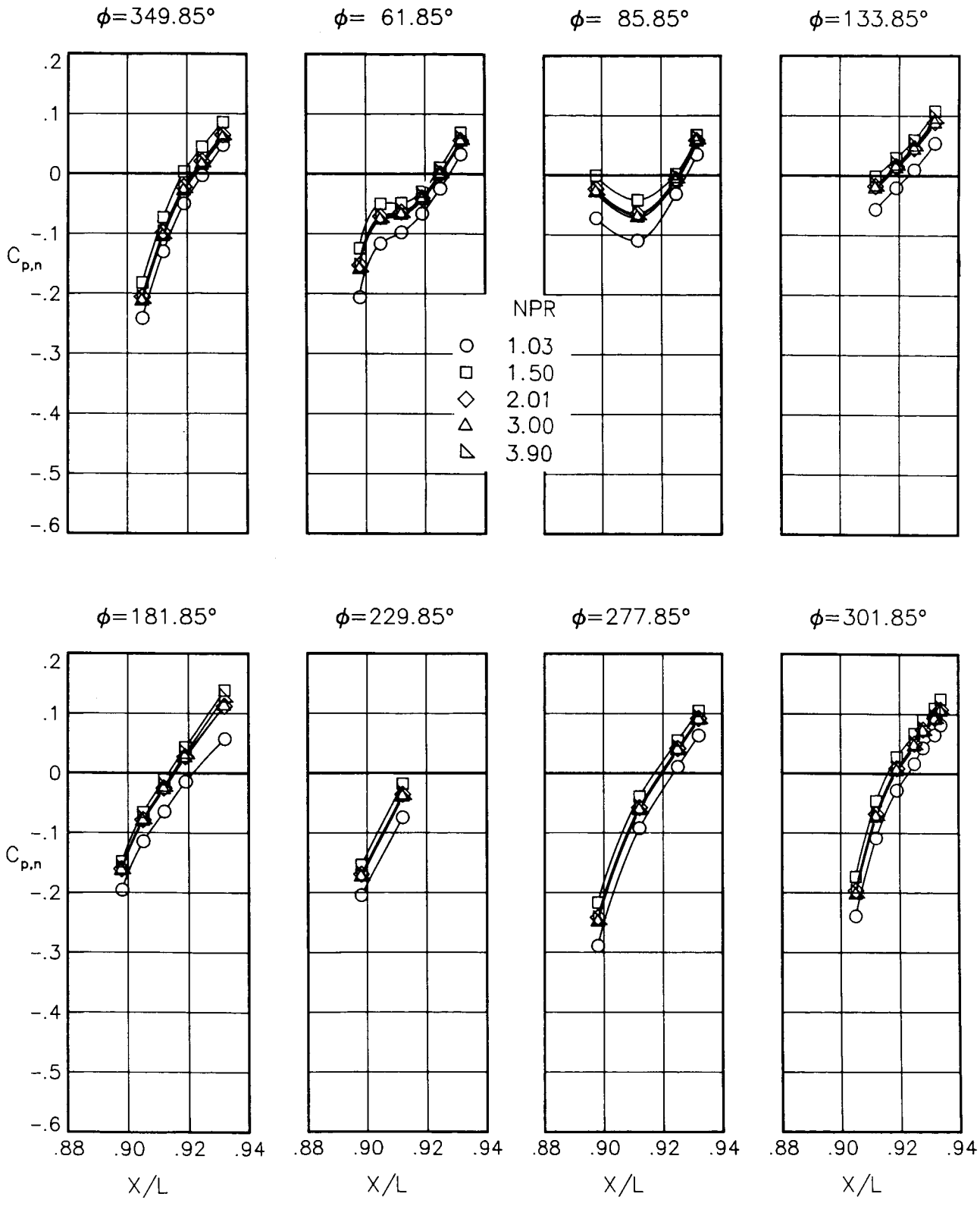

(c) M = 0.60; α = 3.00°.

Figure 83.- Continued.

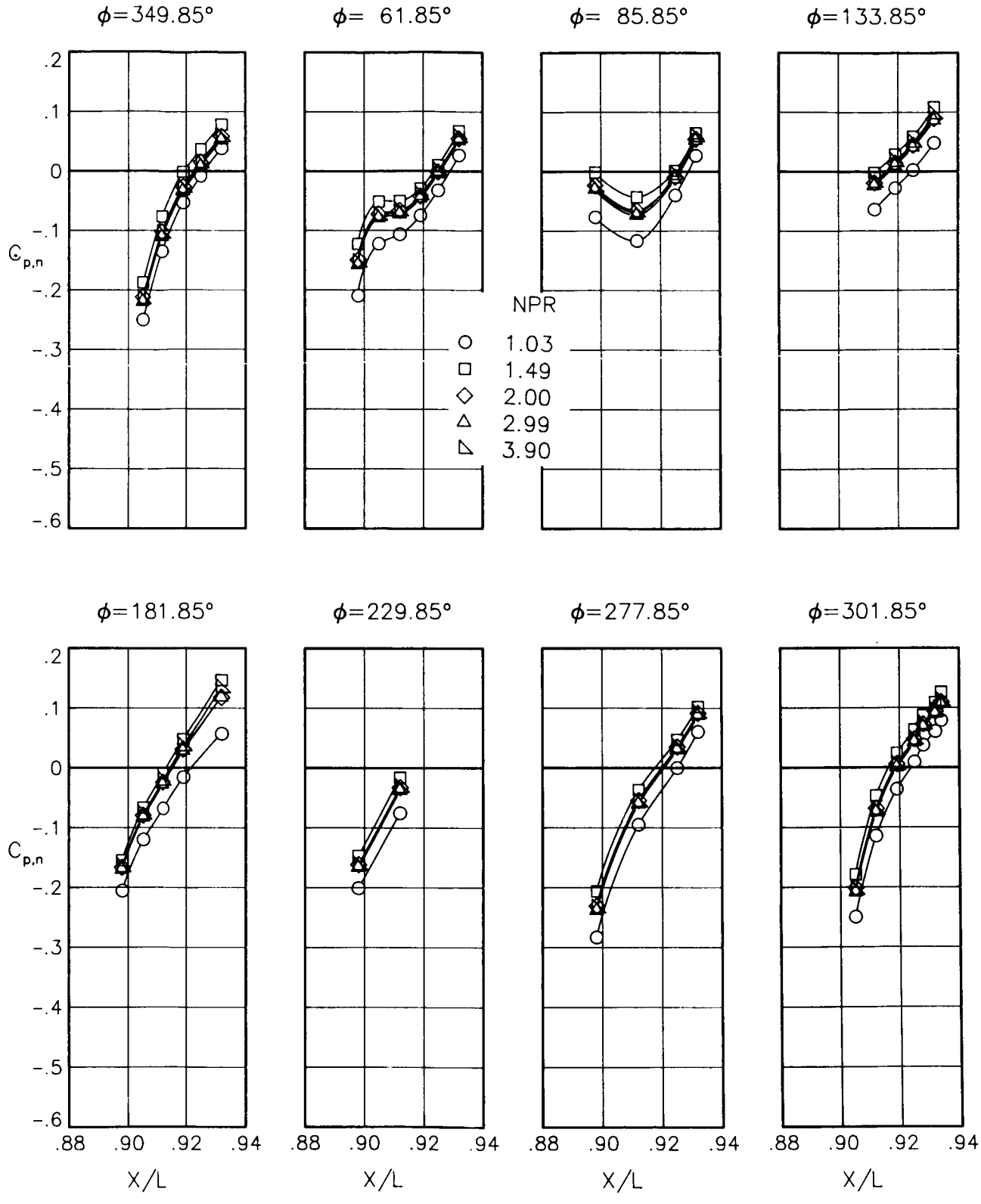

(d) M = 0.60; α = 5.00°.

Figure 83.- Continued.

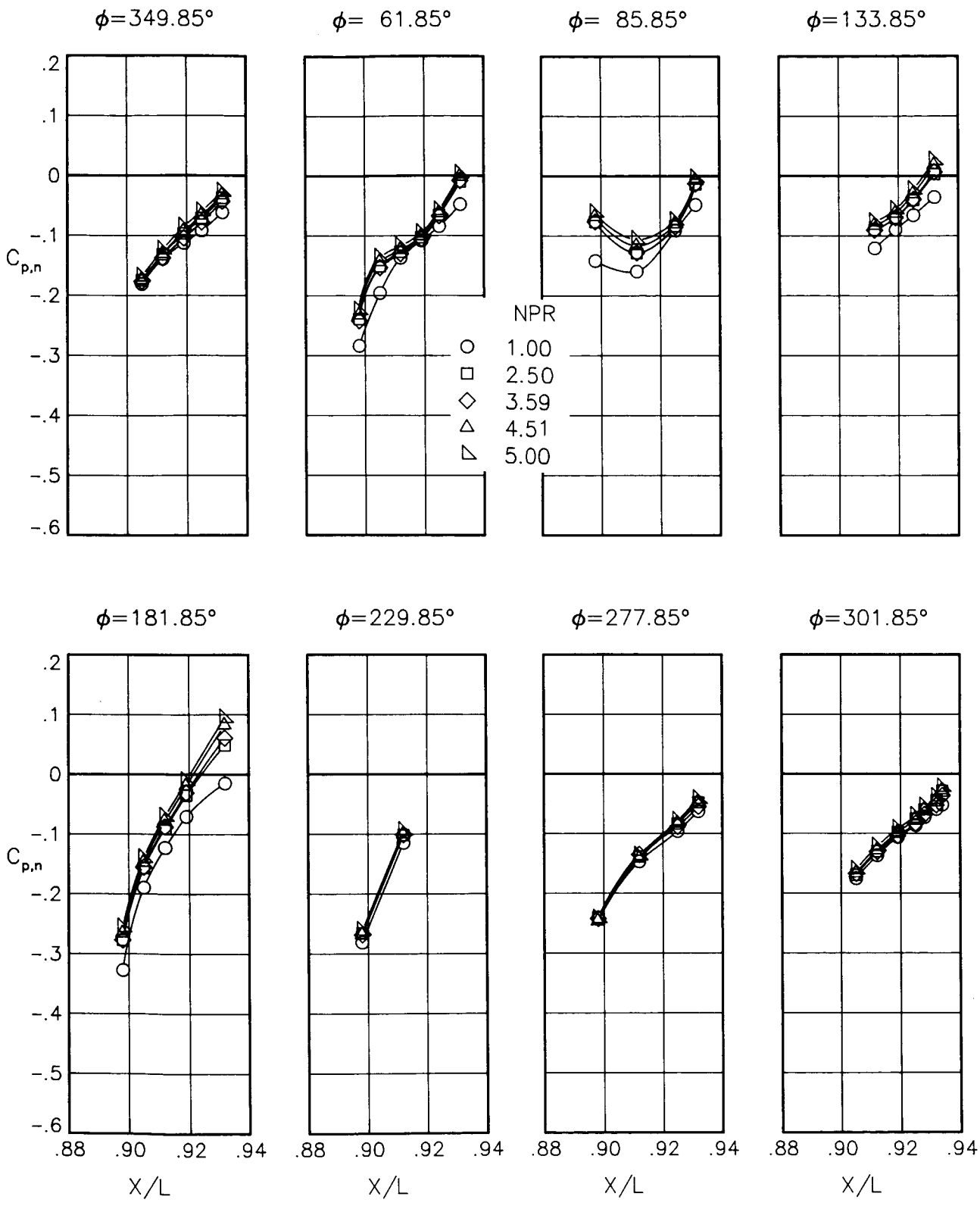

(e) M = 0.90; α = 0.00°.

Figure 83.- Continued.

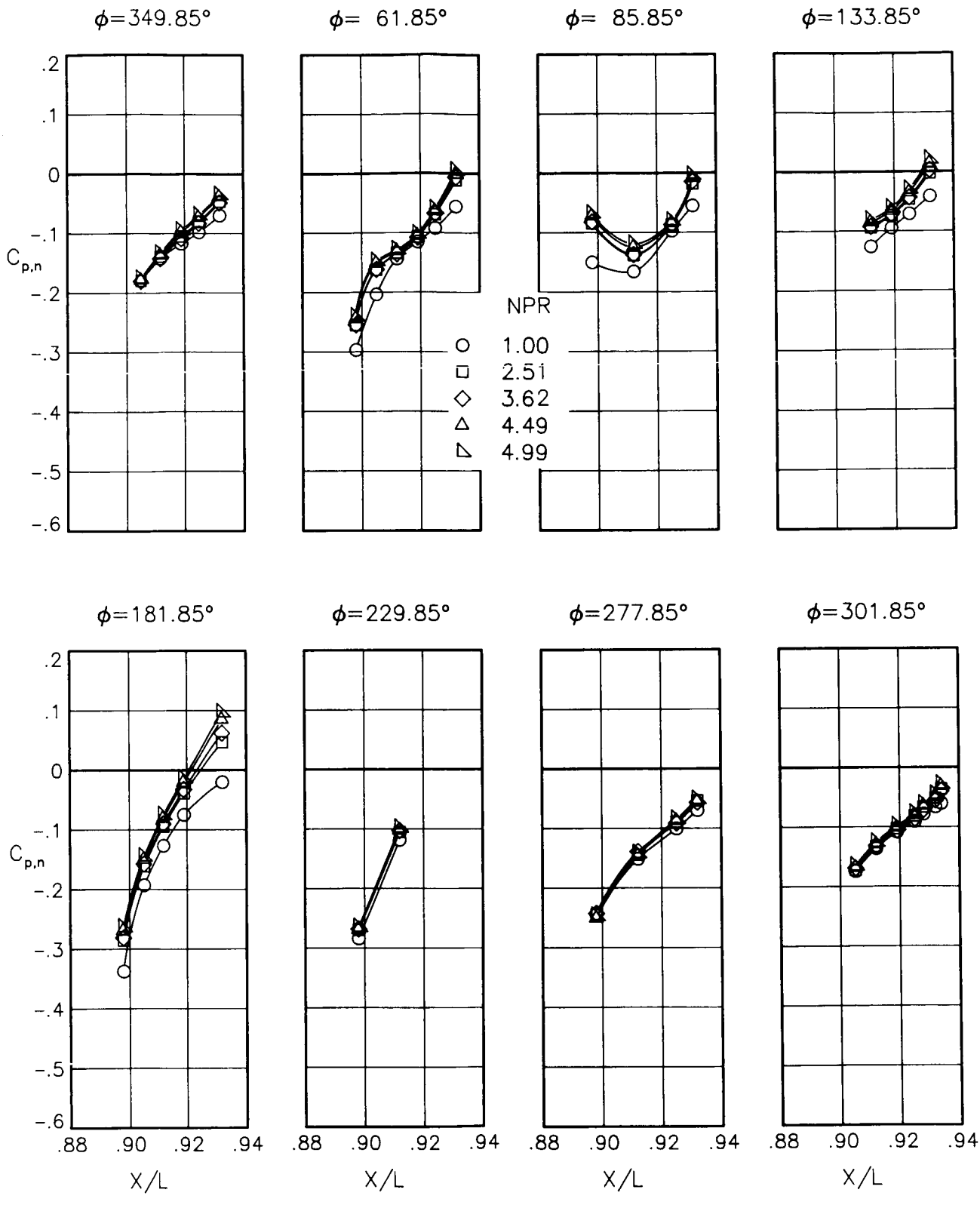

(f) M = 0.90; α = 1.00°.

Figure 83.- Continued.

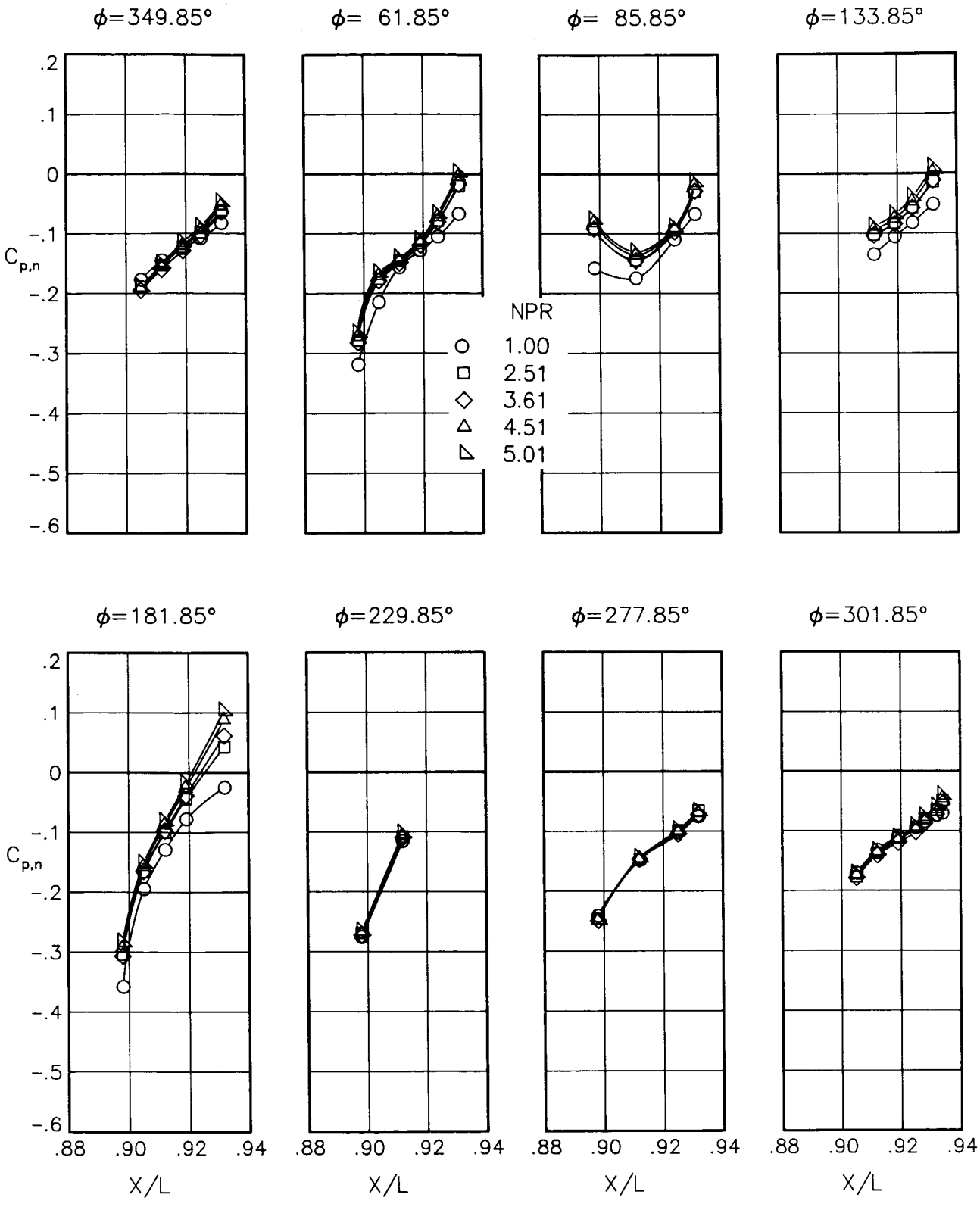

(g) M = 0.90; α = 3.00°.

Figure 83.- Continued.

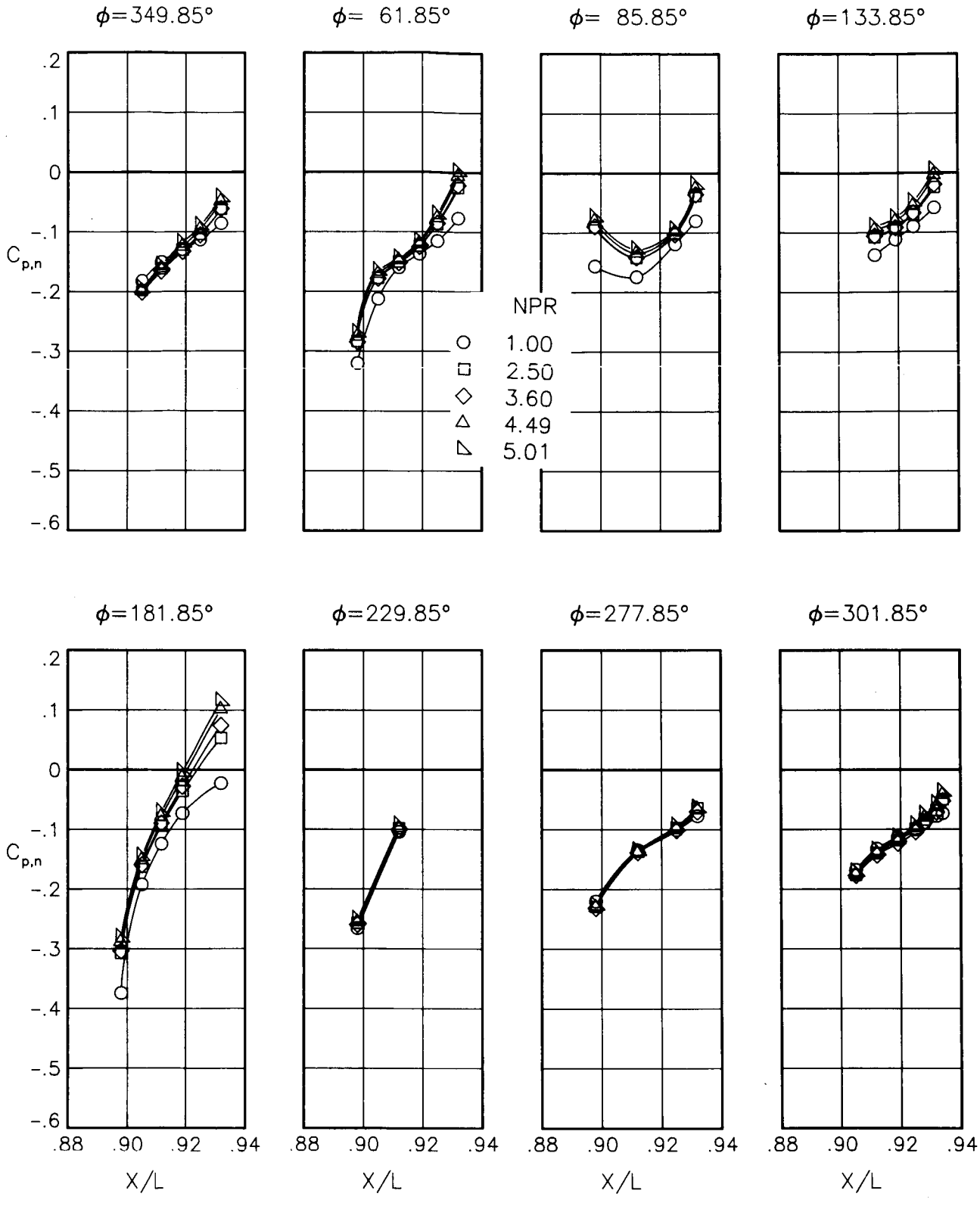

(h) M = 0.90; α = 6.00°.

Figure 83.- Concluded.

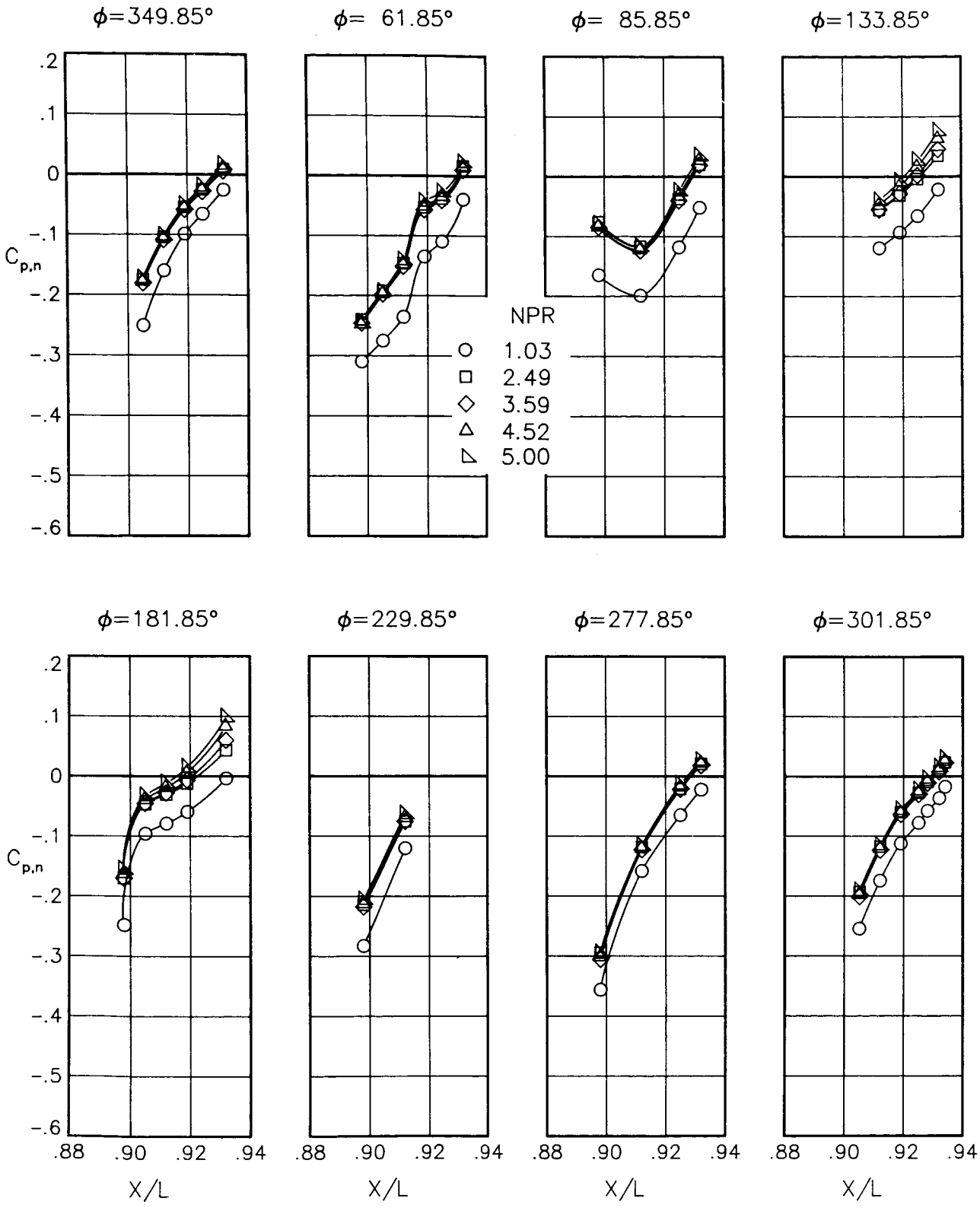

(a) M = 0.90; α = 0.00°.

Figure 84.- Static-pressure-coefficient distributions on nozzle for the model with all fuselage modifications. β_n = 9.63°.

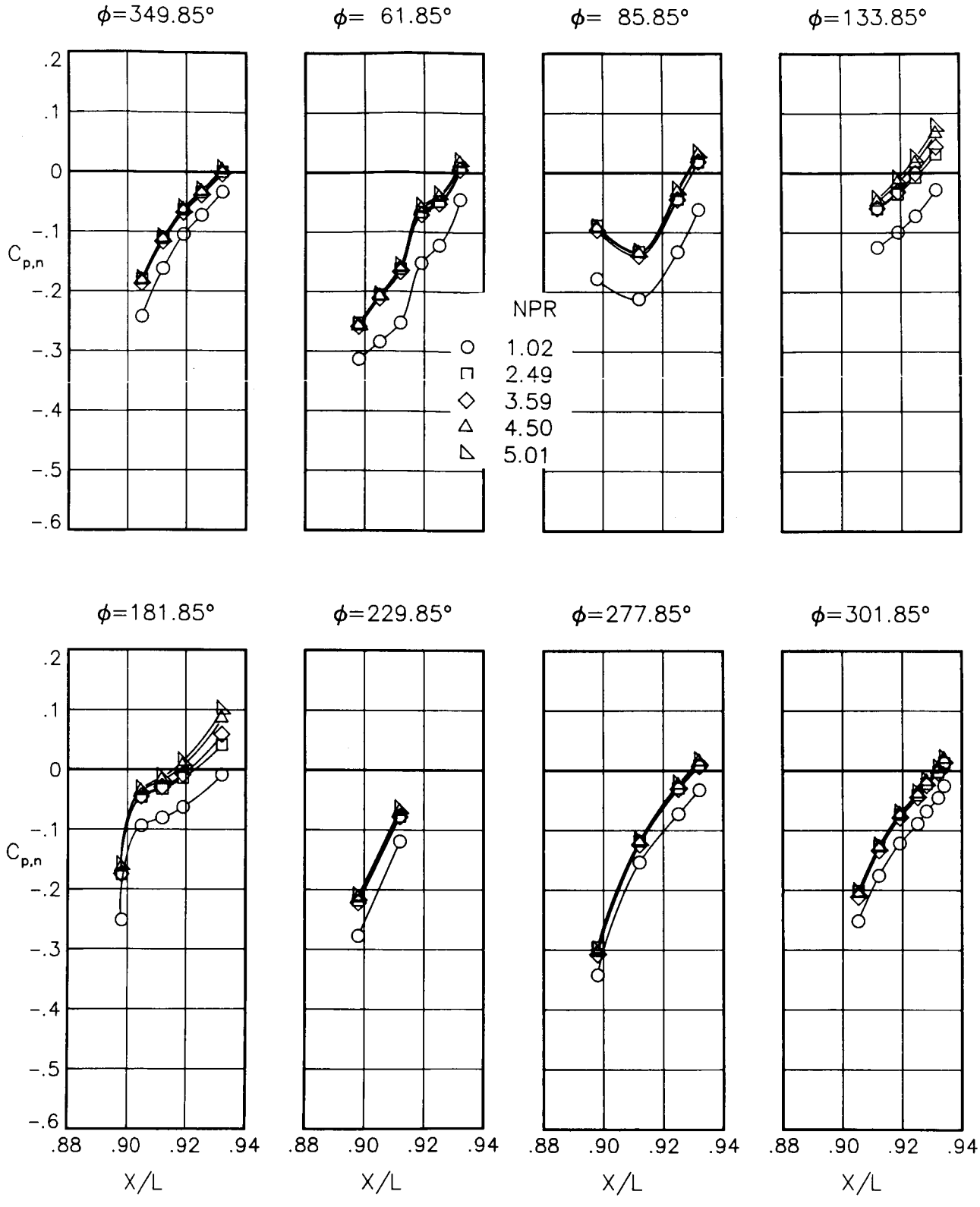

(b) M = 0.90; α = 1.00°.

Figure 84.- Continued.

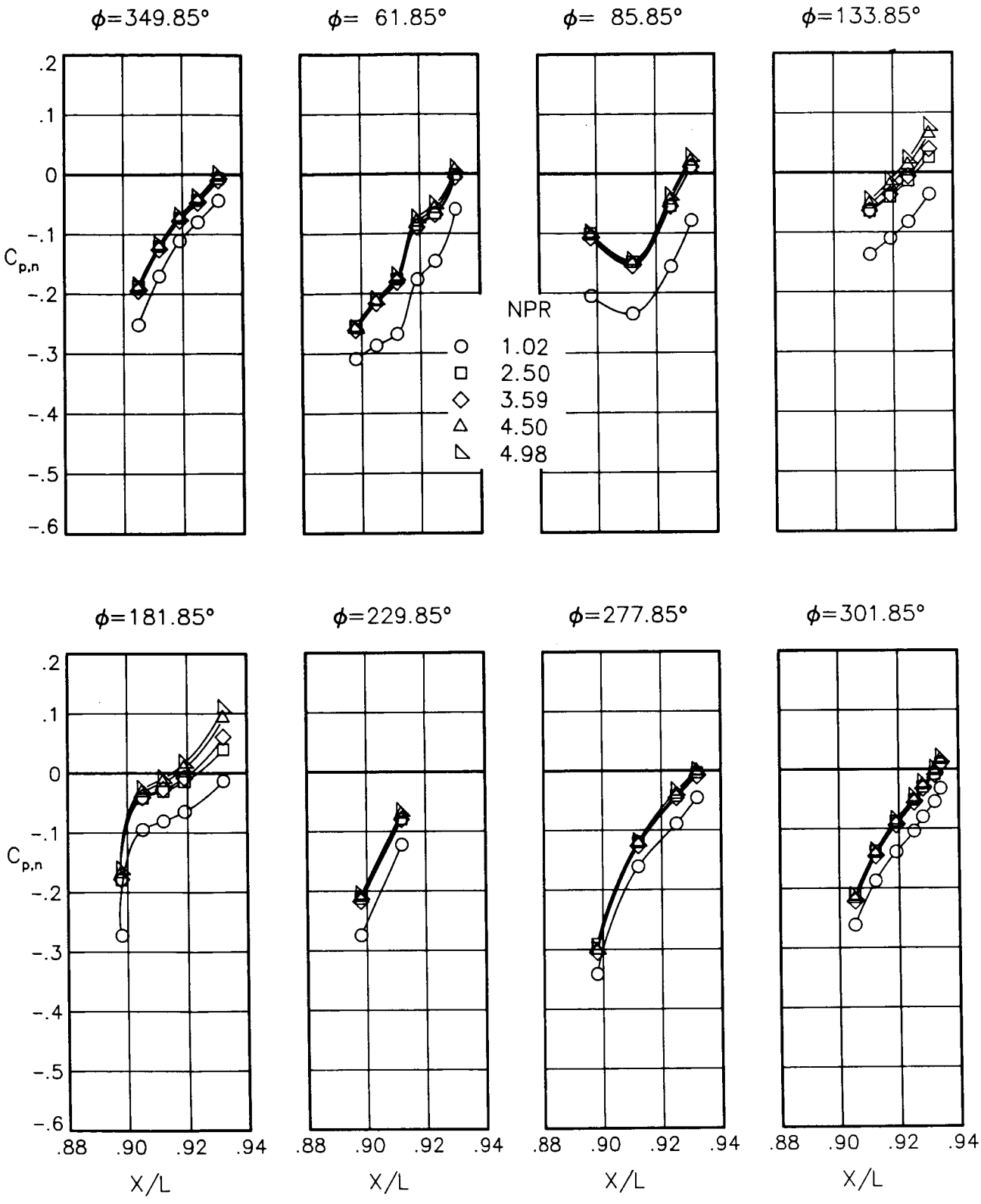

(c) M = 0.90; α = 3.00°.

Figure 84.- Continued.

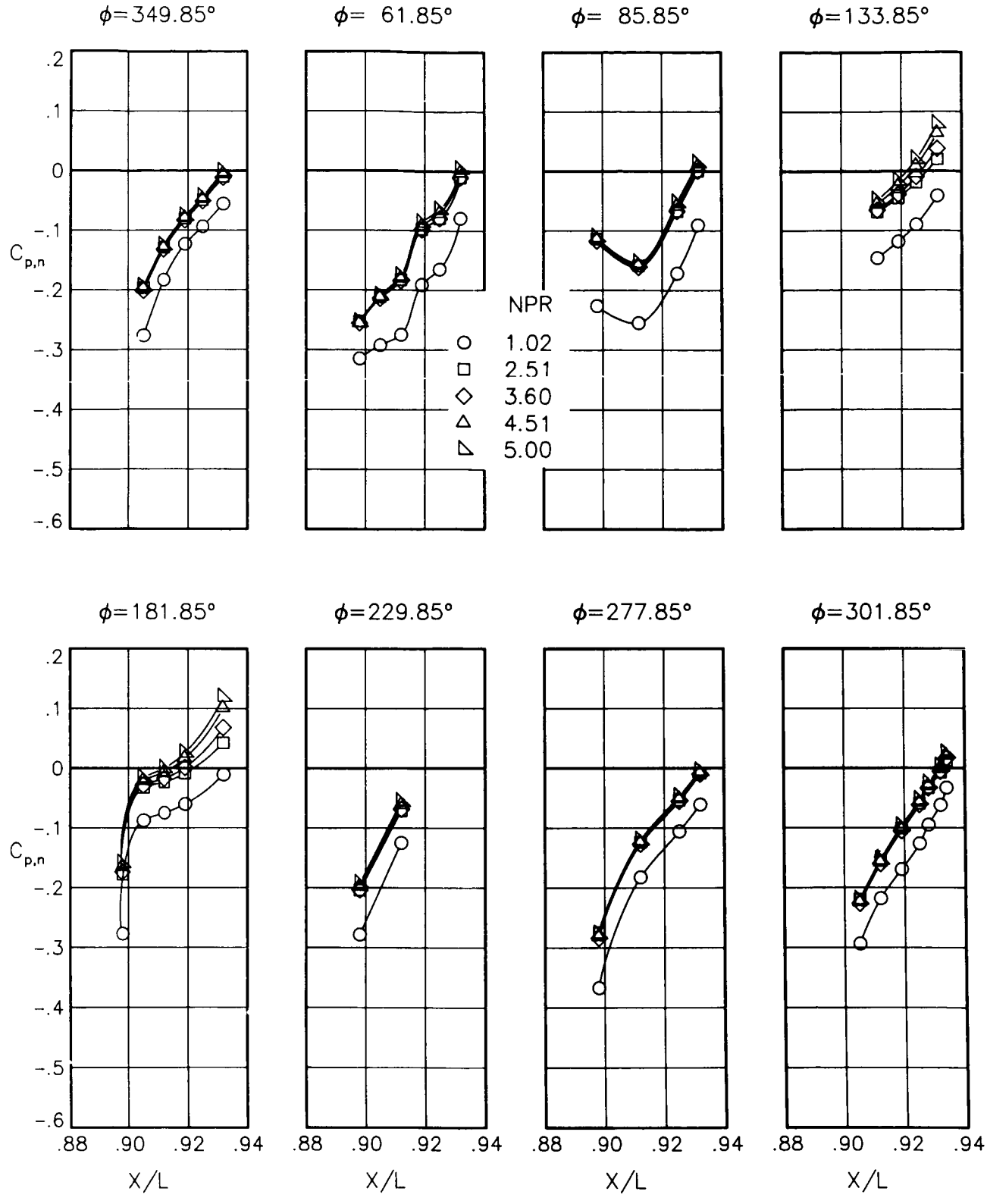

(d) M = 0.90; α = 6.00°.

Figure 84.- Continued.

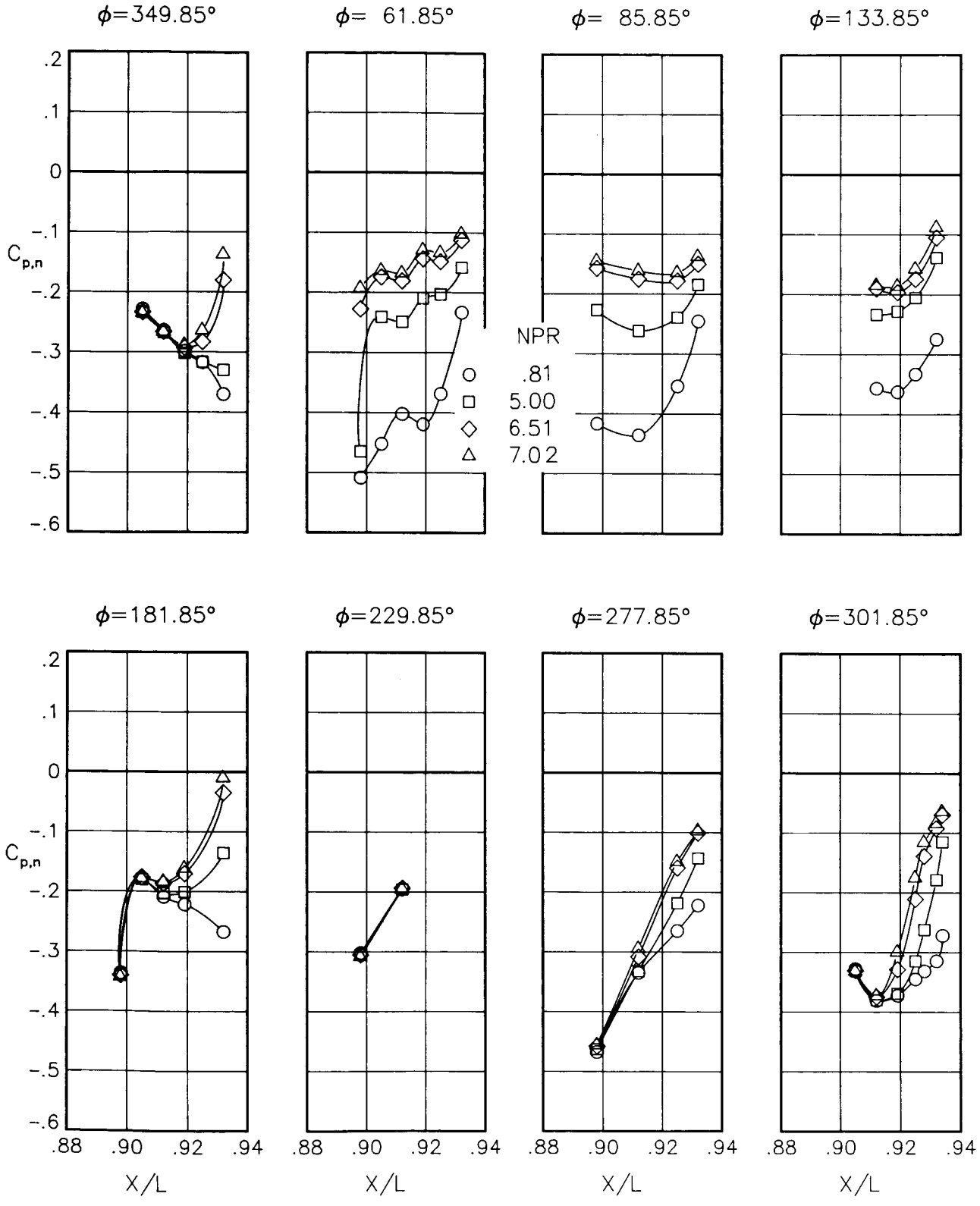

(e) M = 1.20; α = 0.00°.

Figure 84.- Continued.

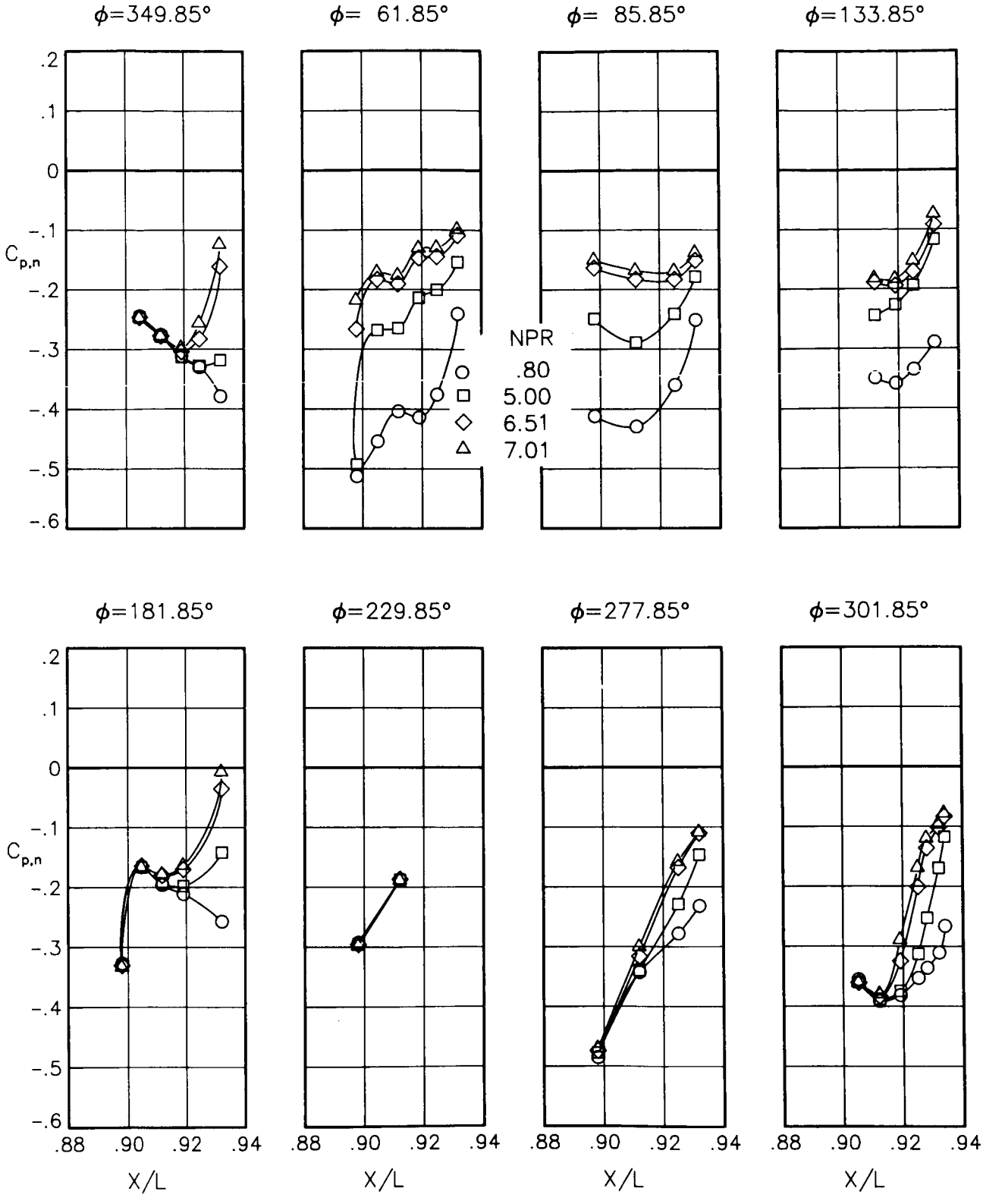

(f) M = 1.20; α = 1.00°.

Figure 84.- Continued.

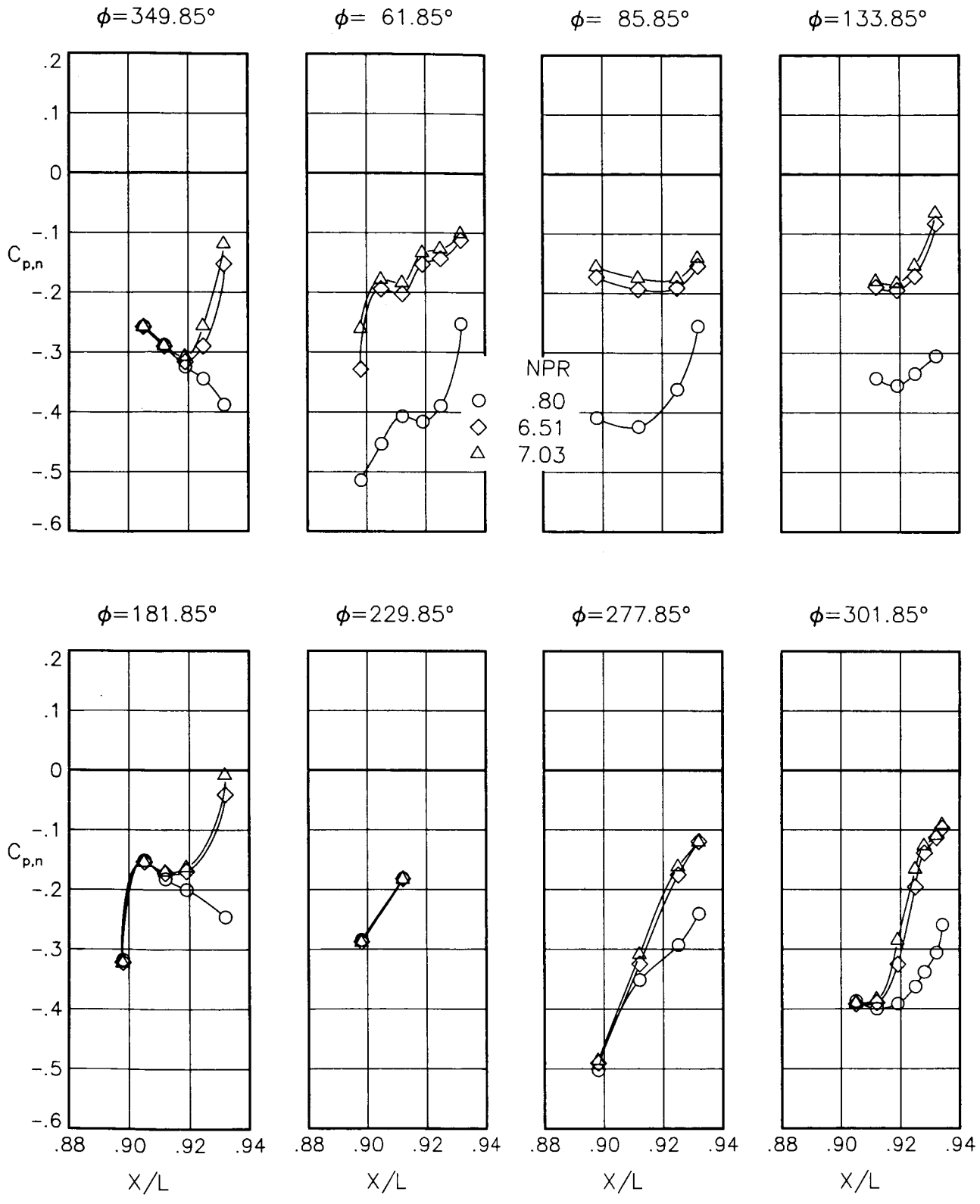

(g) M = 1.20; α = 2.00°.

Figure 84.- Continued.

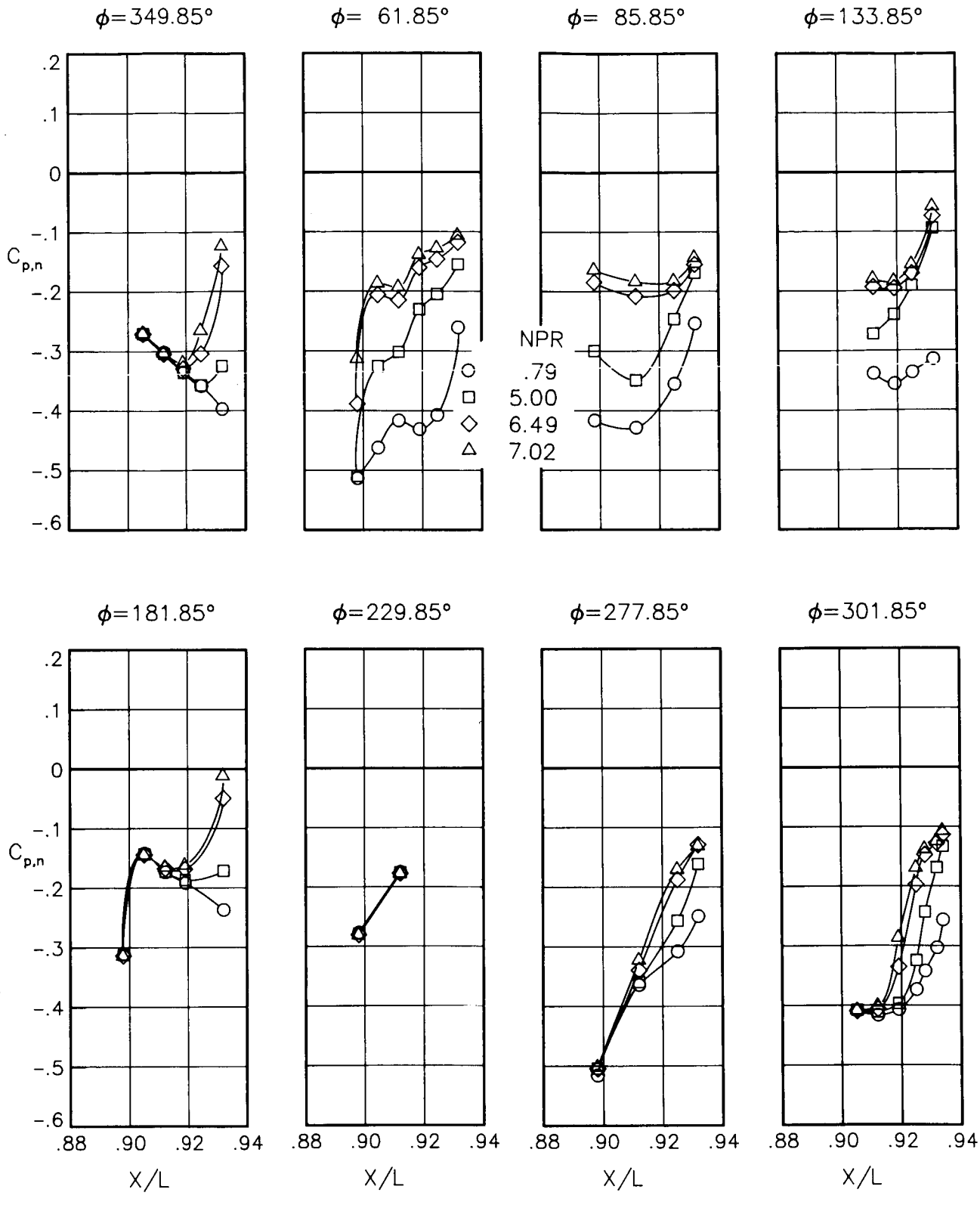

(h) M = 1.20; α = 3.00°.

Figure 84.- Continued.

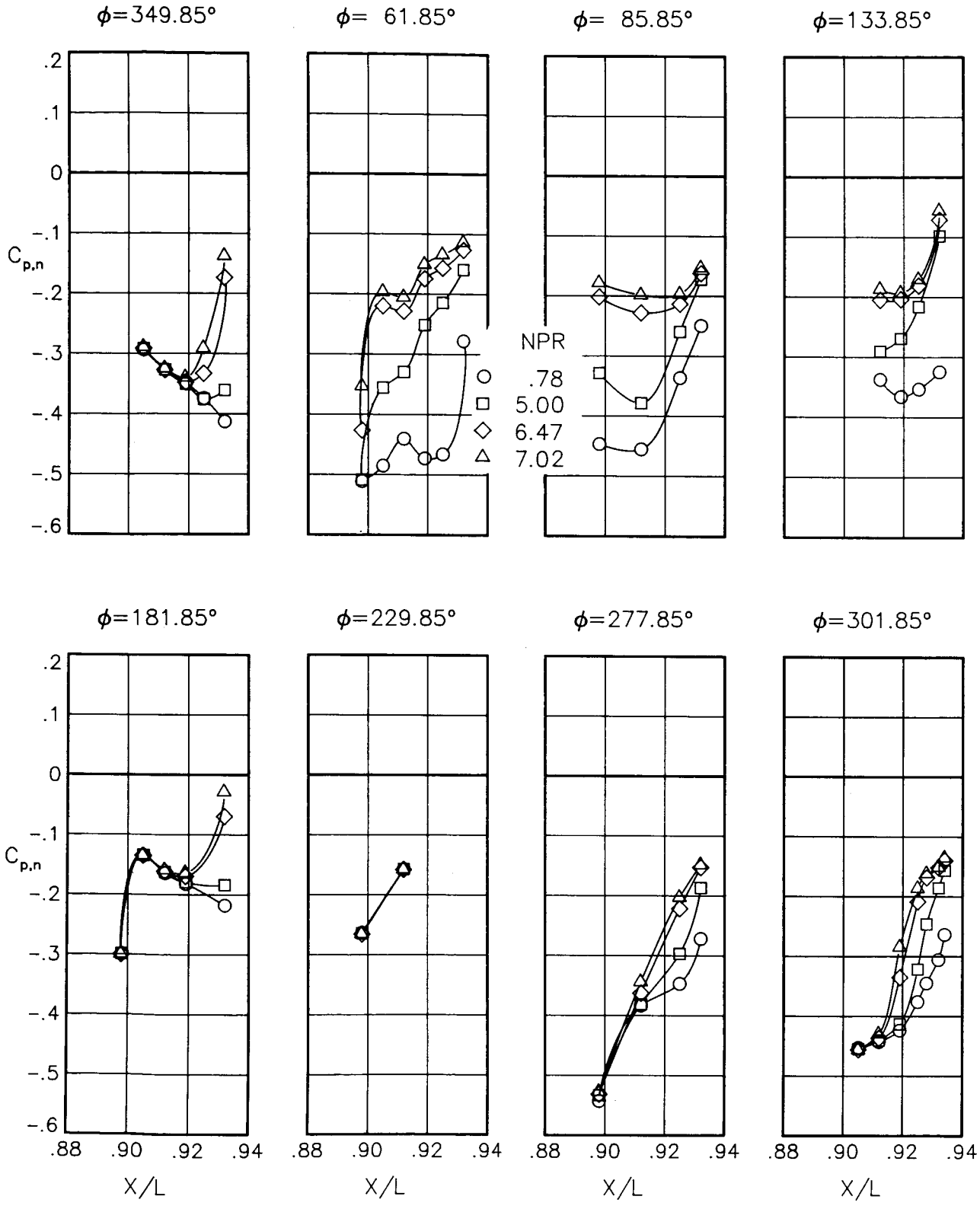

(i) M = 1.20; α = 5.00°.

Figure 84.- Concluded.

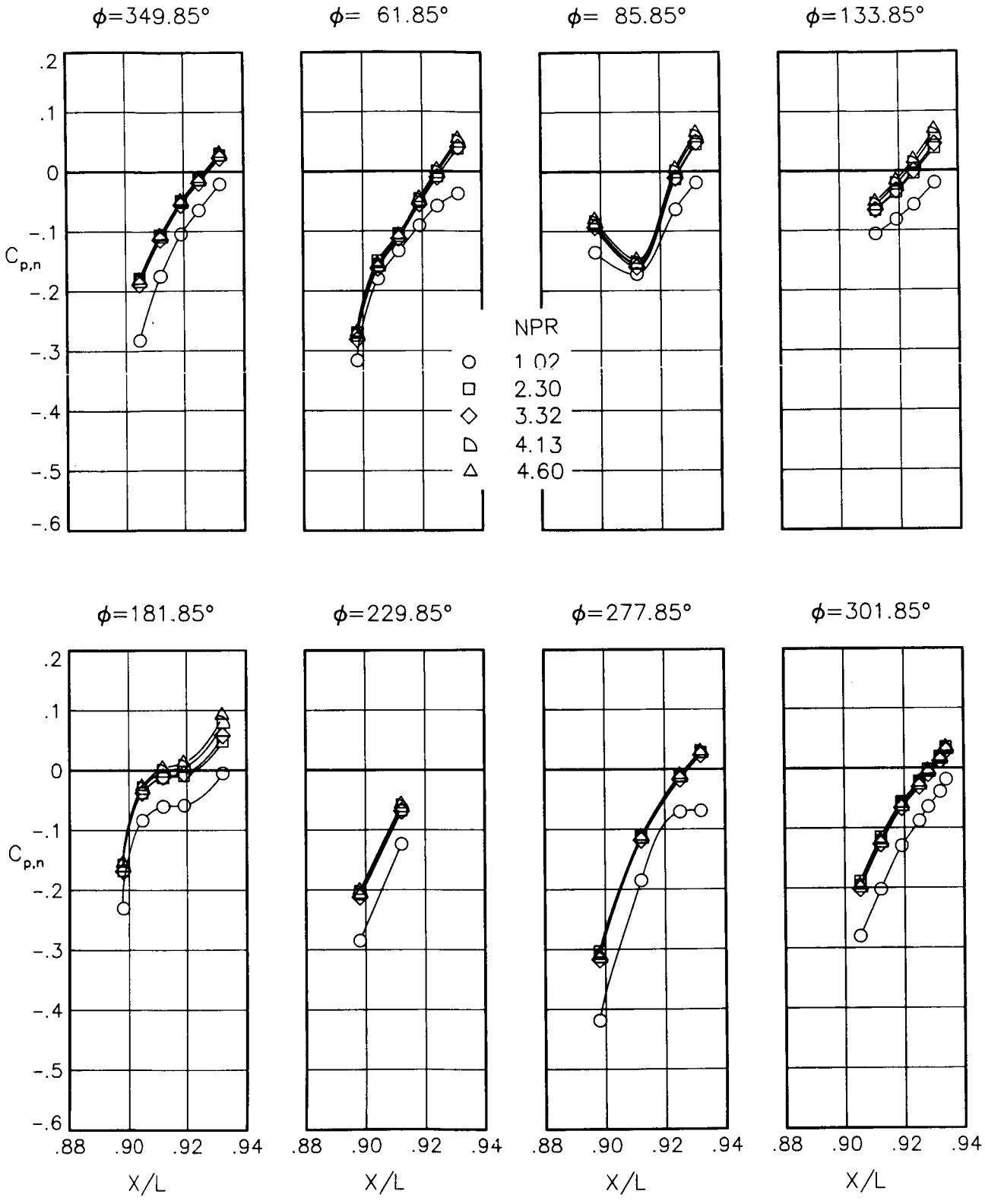

(a) M = 0.90; α = 0.00°.

Figure 85.- Static-pressure-coefficient distributions on nozzle for the model with all fuselage modifications. β_L = 9.63°; β_R = 15.05°; δ_h = 2.5°.

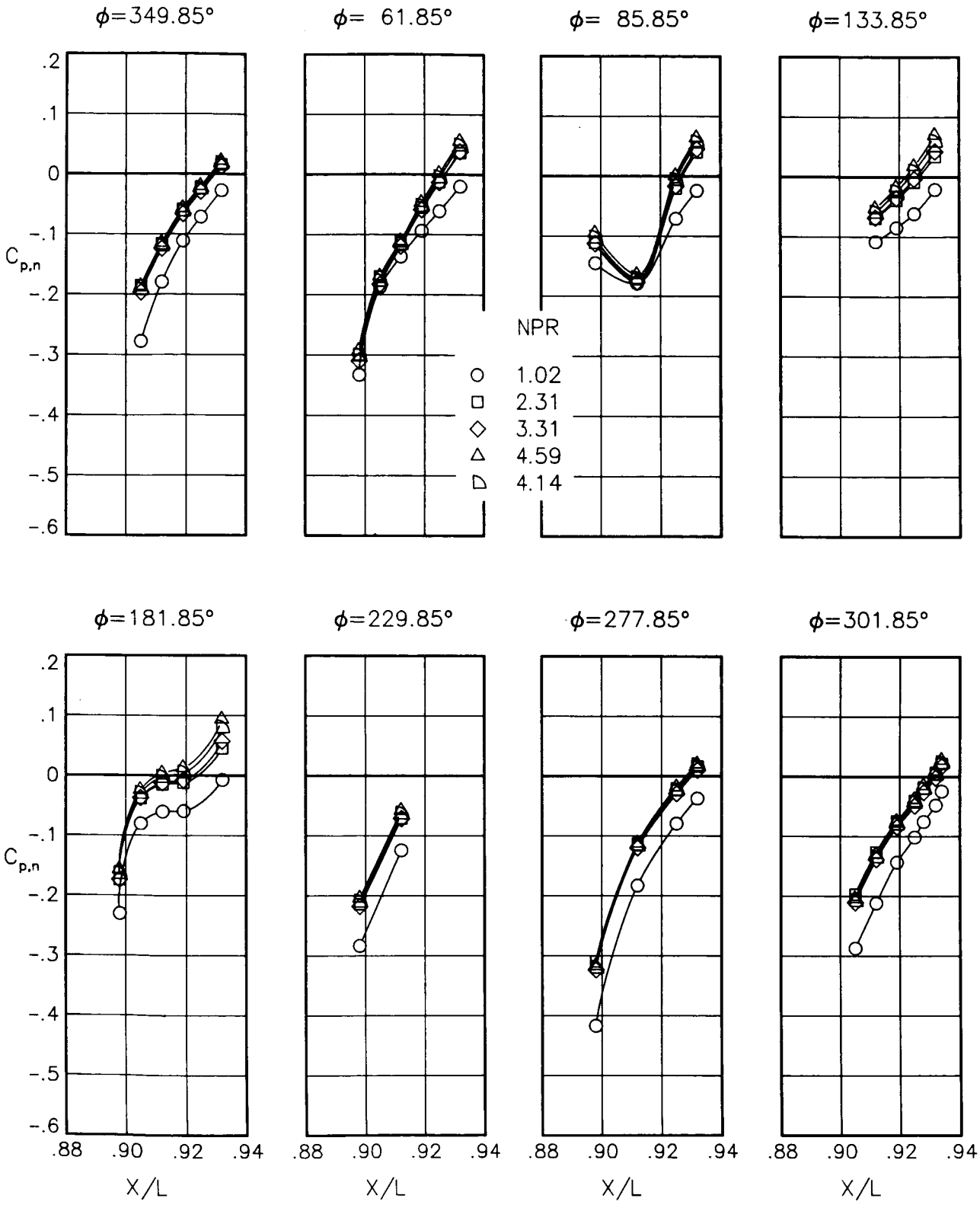

(b) M = 0.90; α = 1.00°.

Figure 85.- Continued.

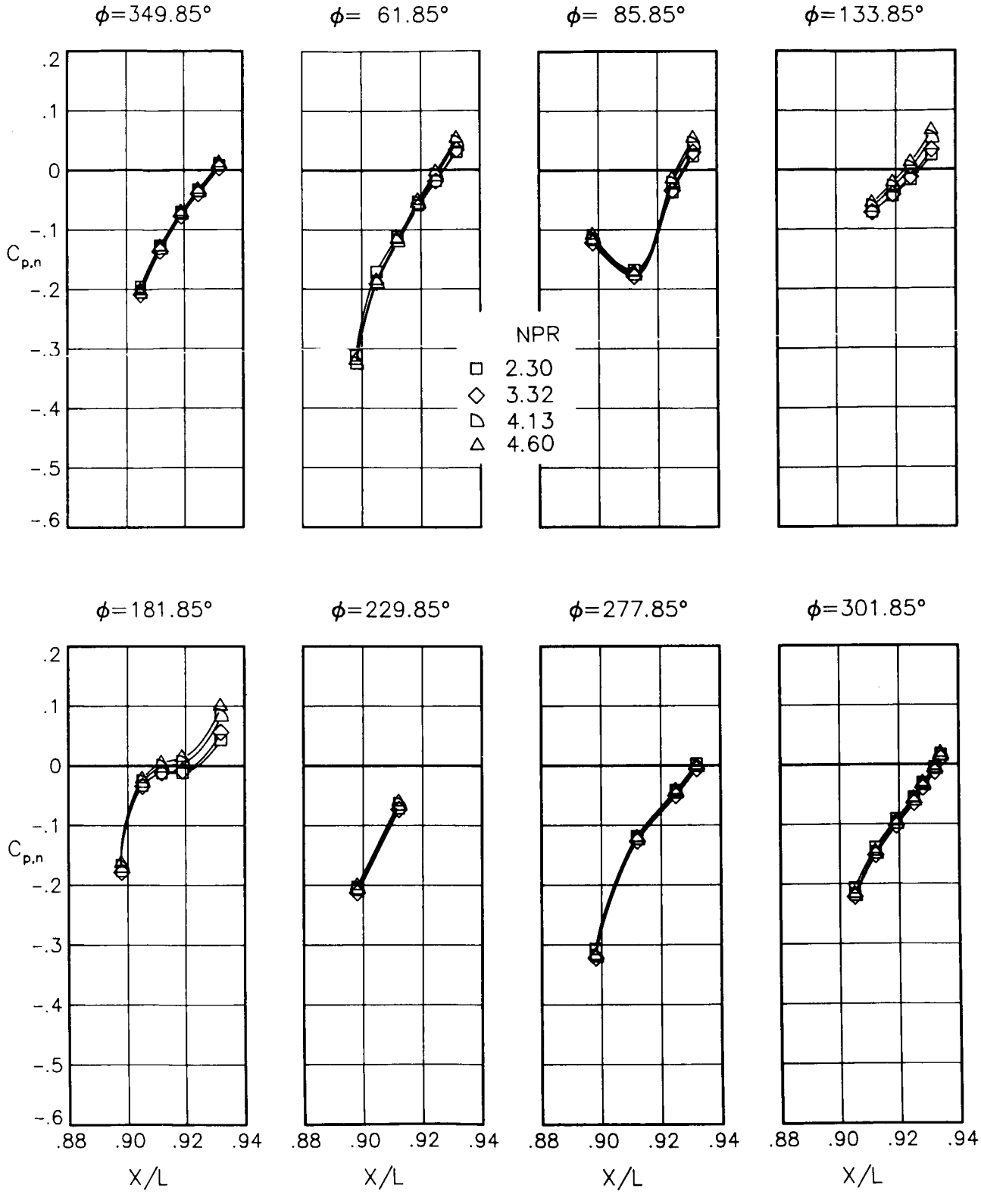

(c) M = 0.90; α = 3.00°.

Figure 85.- Continued.

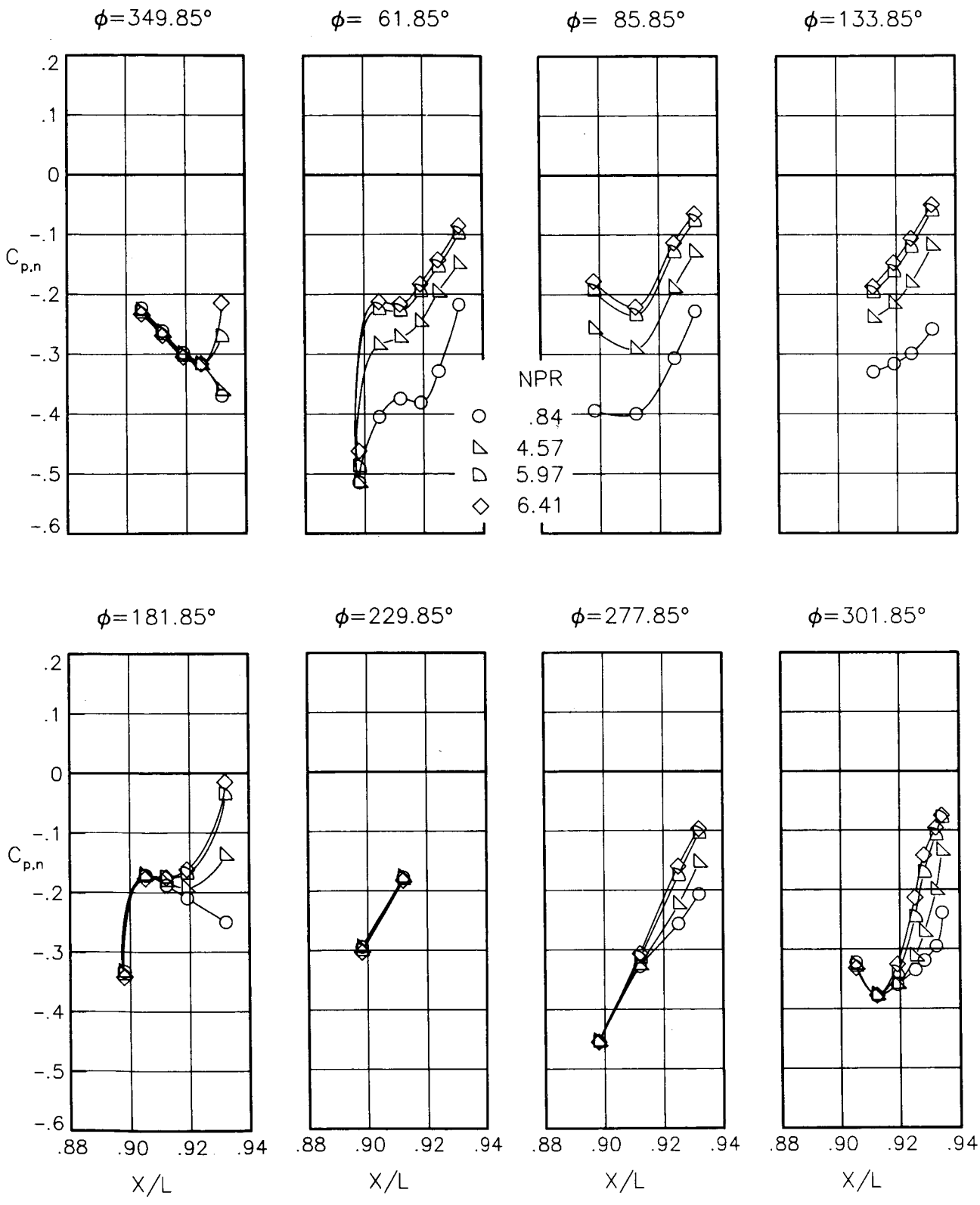

(d) M = 1.20; α = 0.00°.

Figure 85.- Continued.

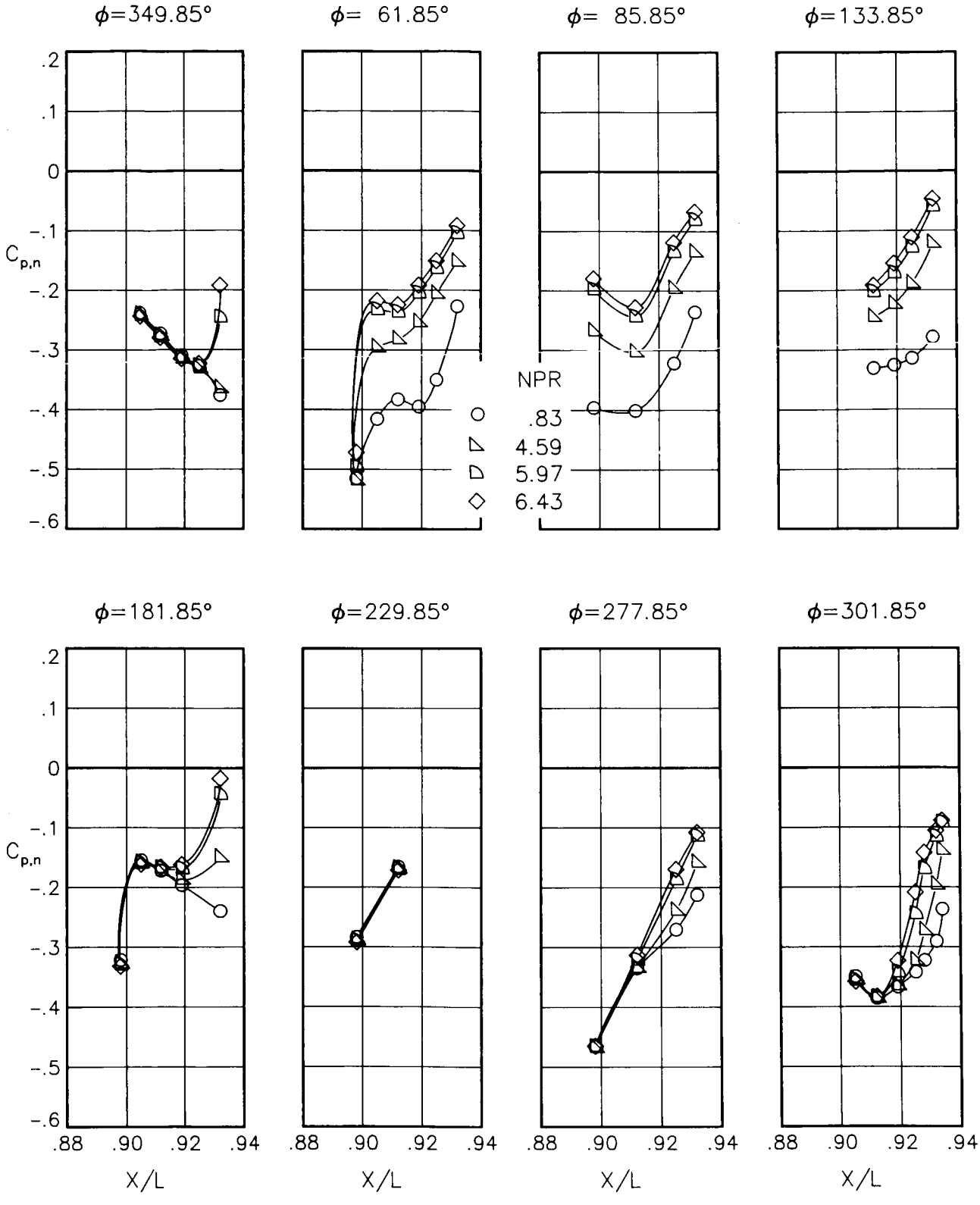

(e) M = 1.20; α = 1.00°.

Figure 85.- Continued.

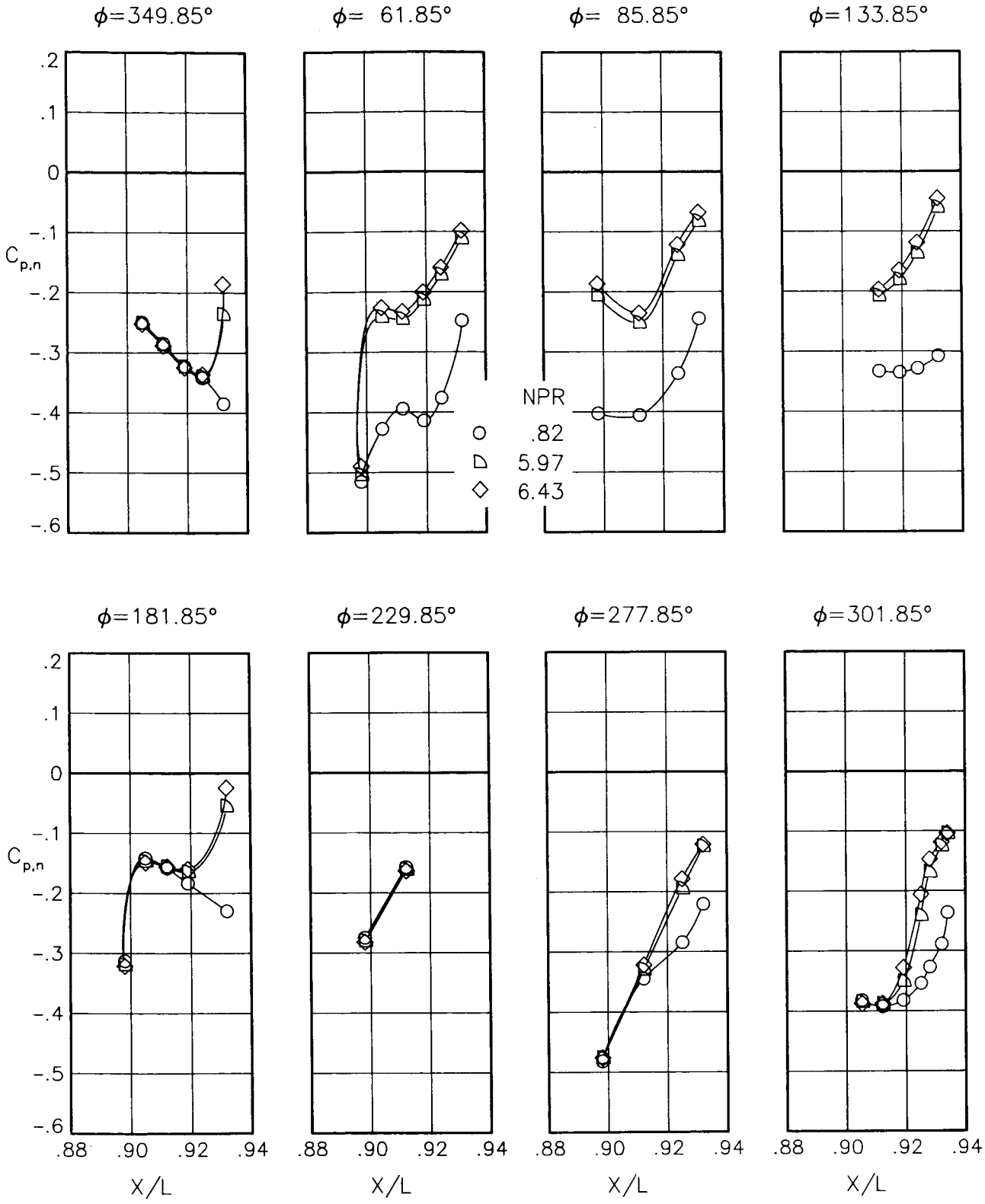

(f) M = 1.20; α = 2.00°.

Figure 85.- Continued.

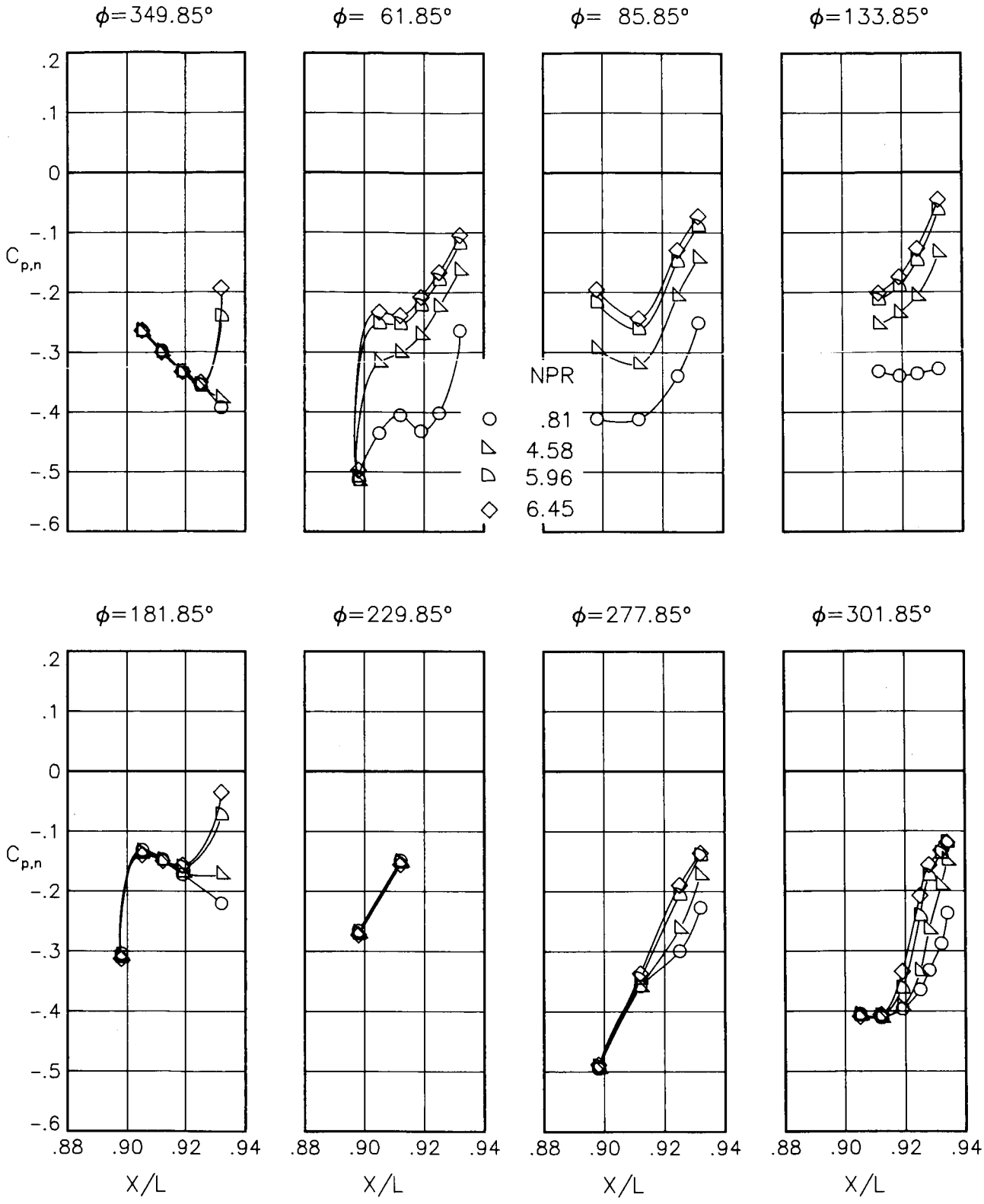

(g) M = 1.20; α = 3.00°.

Figure 85.- Concluded.

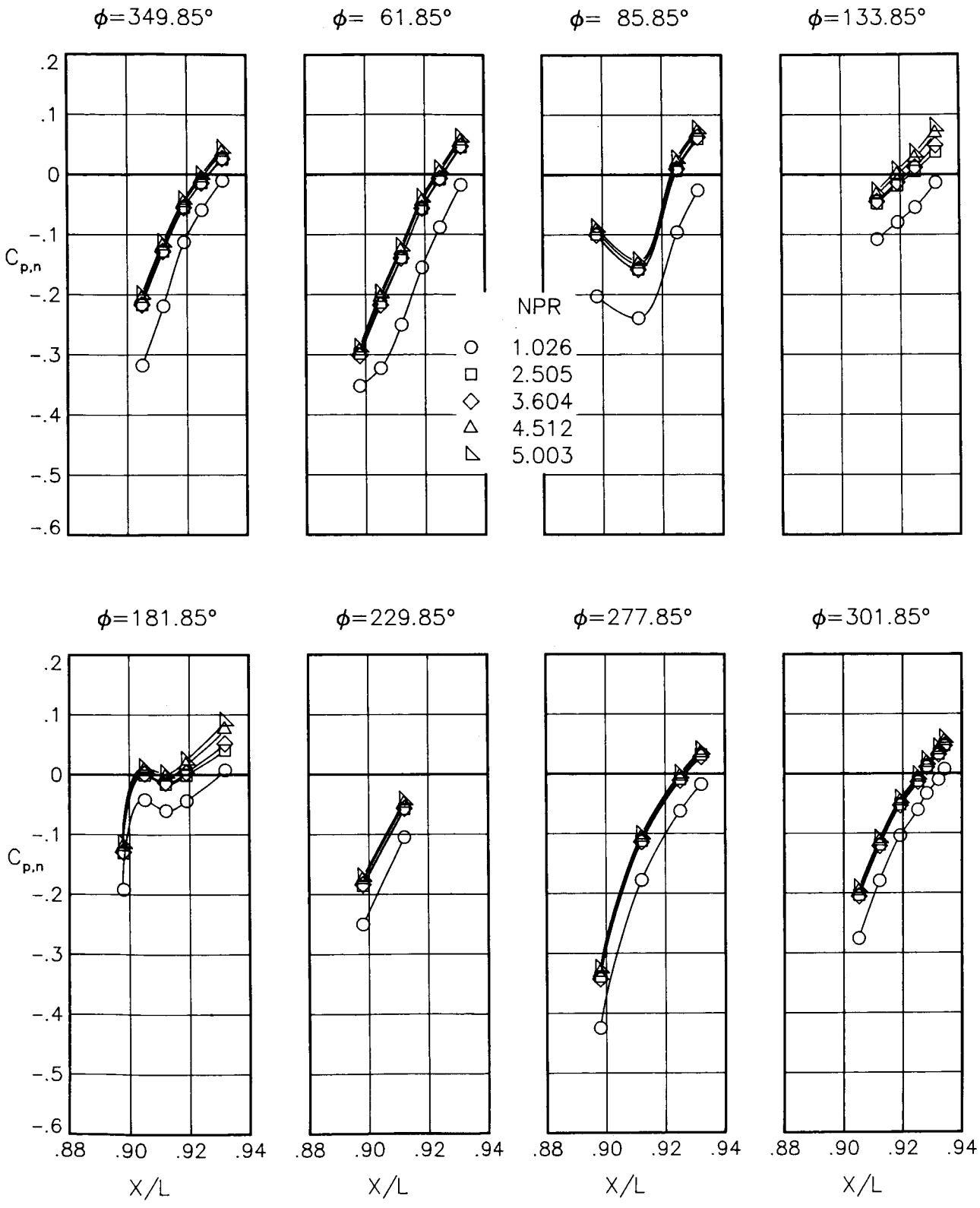

(a) M = 0.90; α = 0.00°.

Figure 86.- Static-pressure-coefficient distributions on nozzle for the model with all fuselage modifications. β_n = 7.72°.

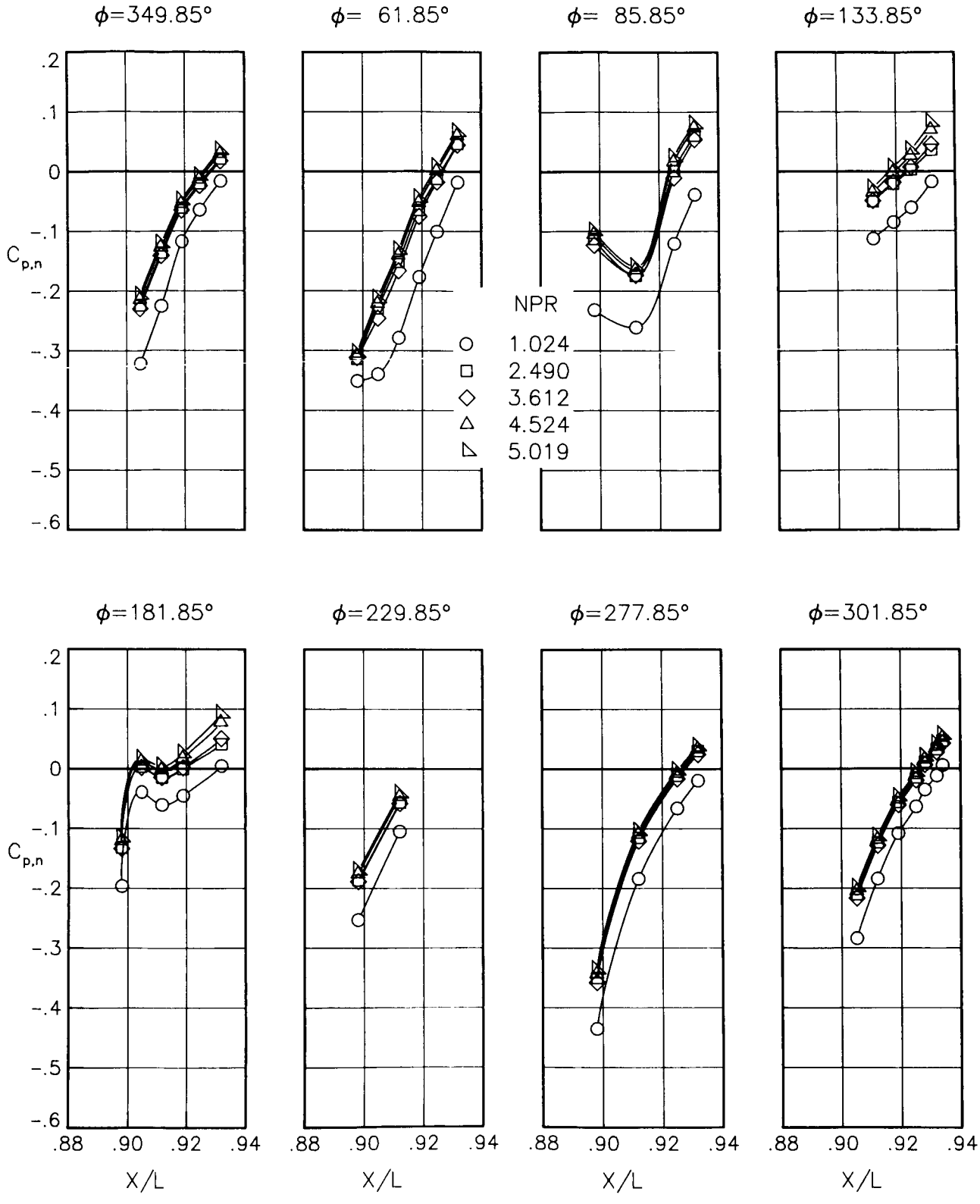

(b) M = 0.90; α = 1.00°.

Figure 86.- Continued.

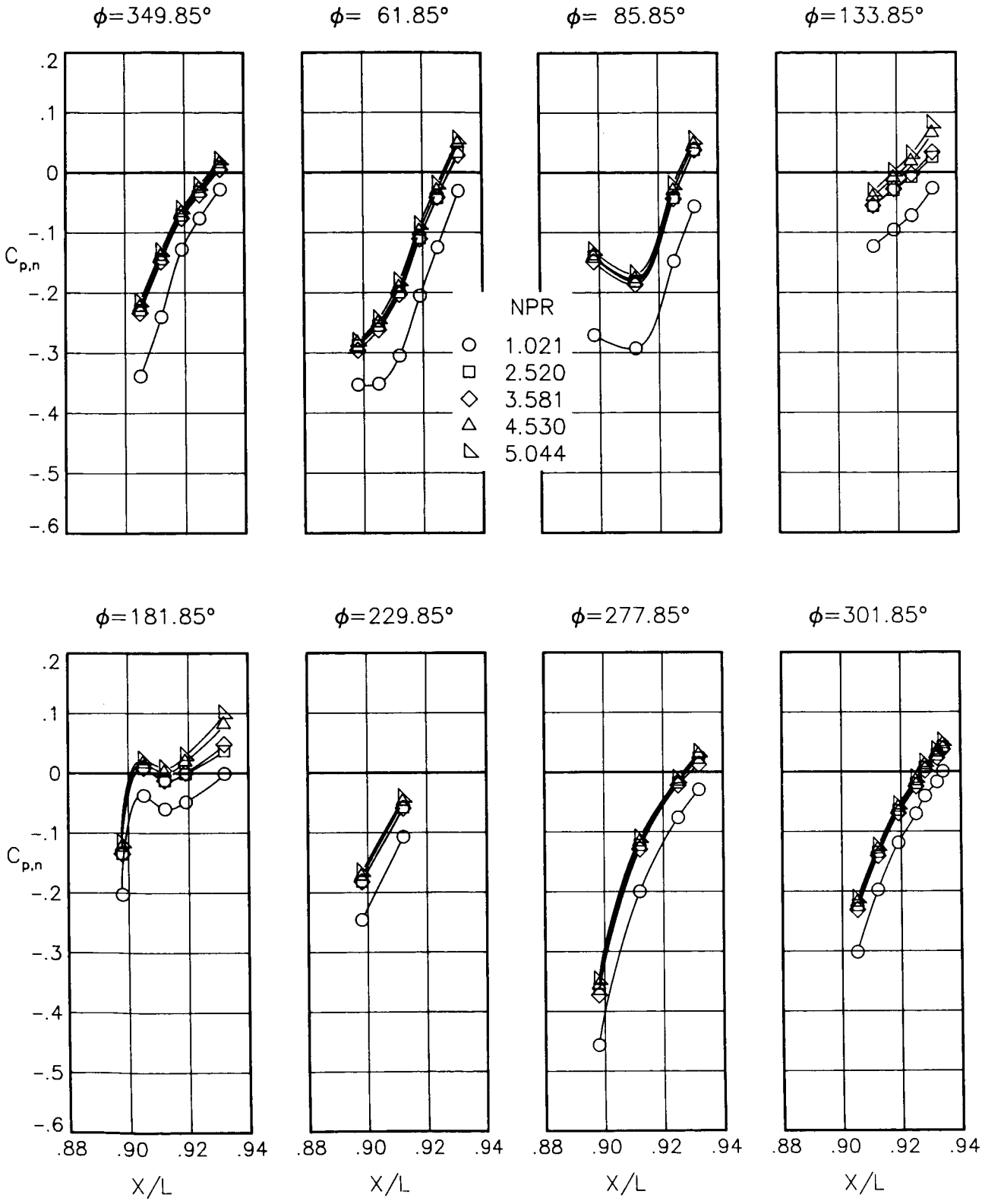

(c) M = 0.90; α = 3.00°.

Figure 86.- Continued.

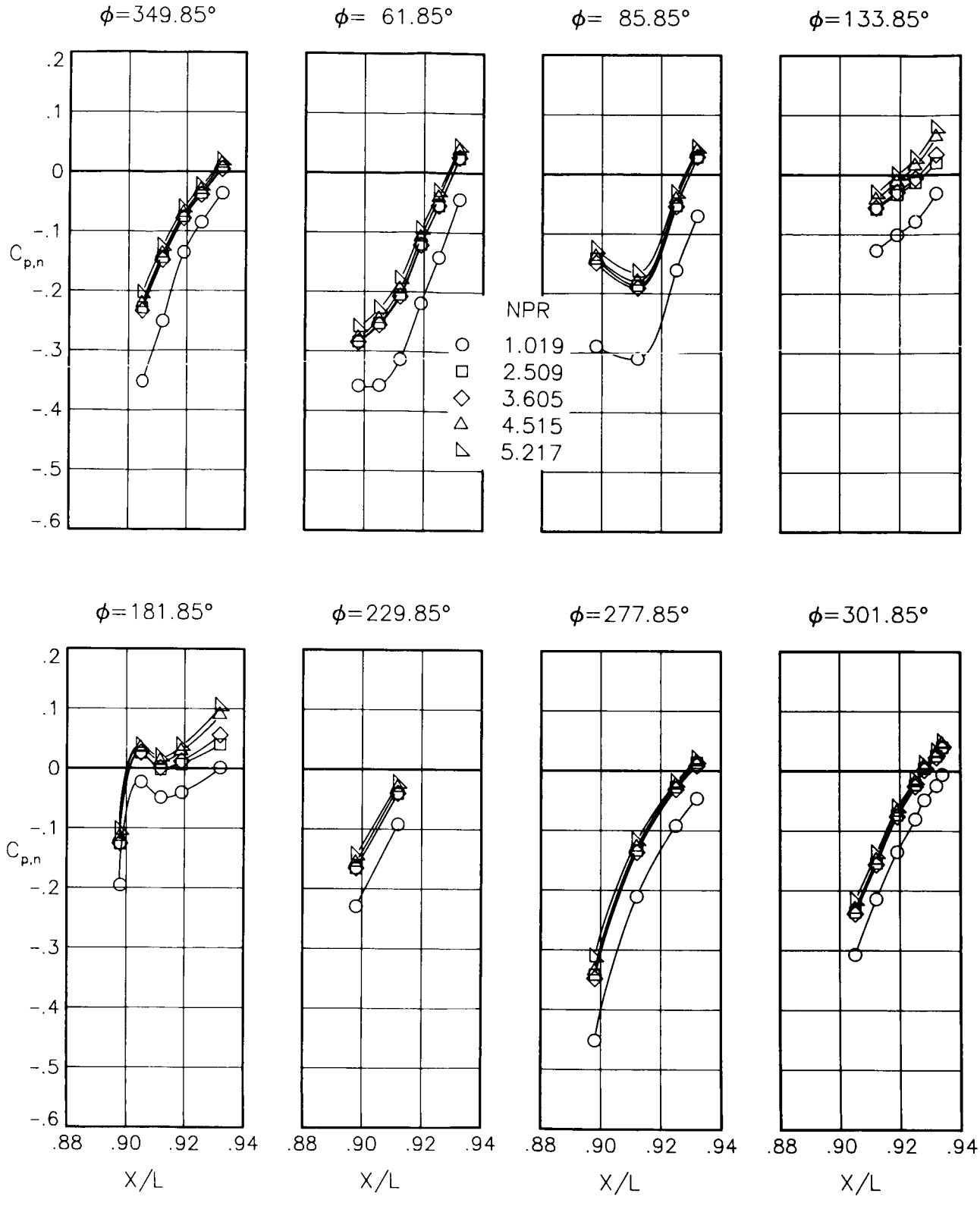

(d) M = 0.90; α = 6.00°.

Figure 86.- Continued.

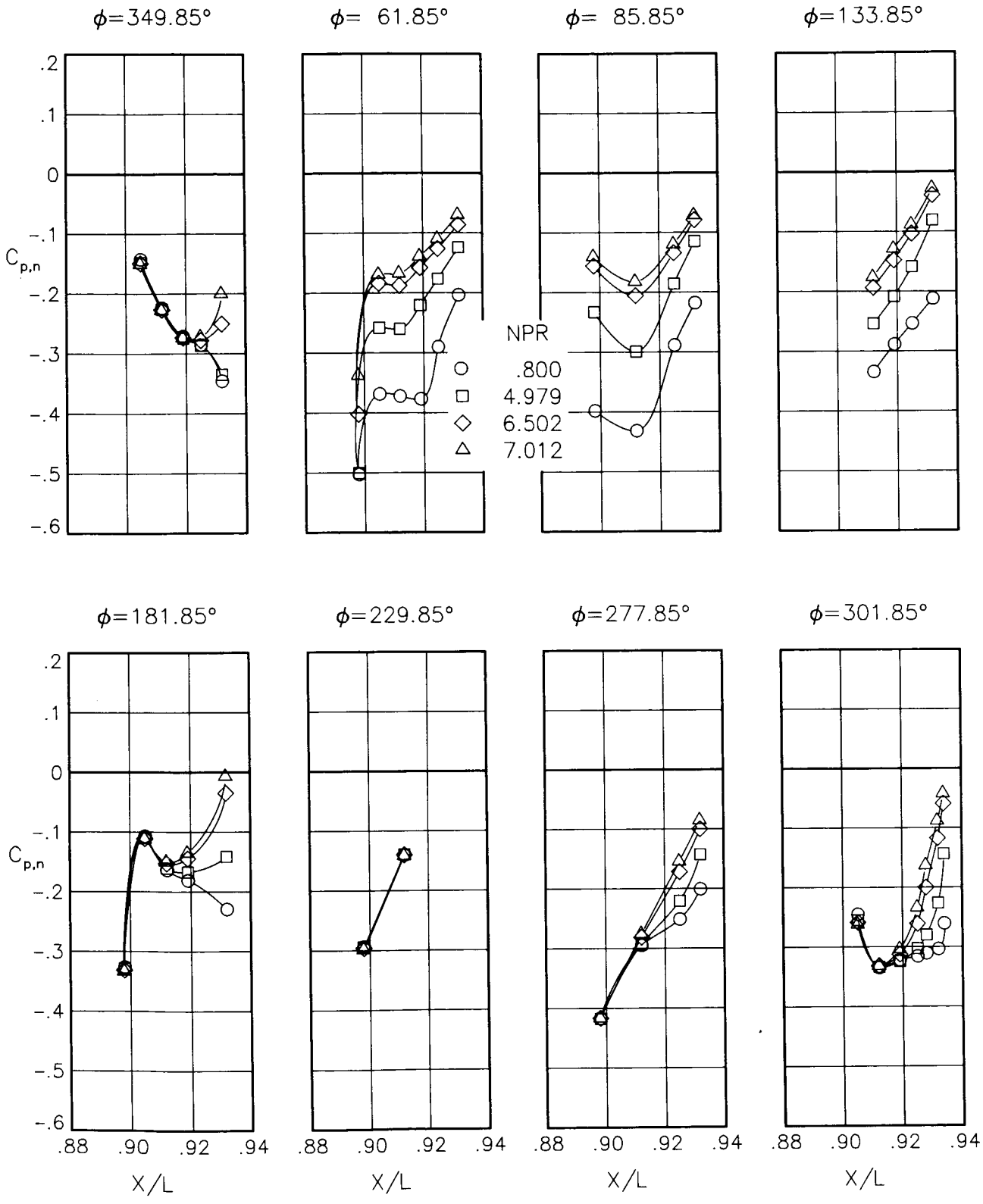

(e) M = 1.20; α = 0.00°.

Figure 86.- Continued.

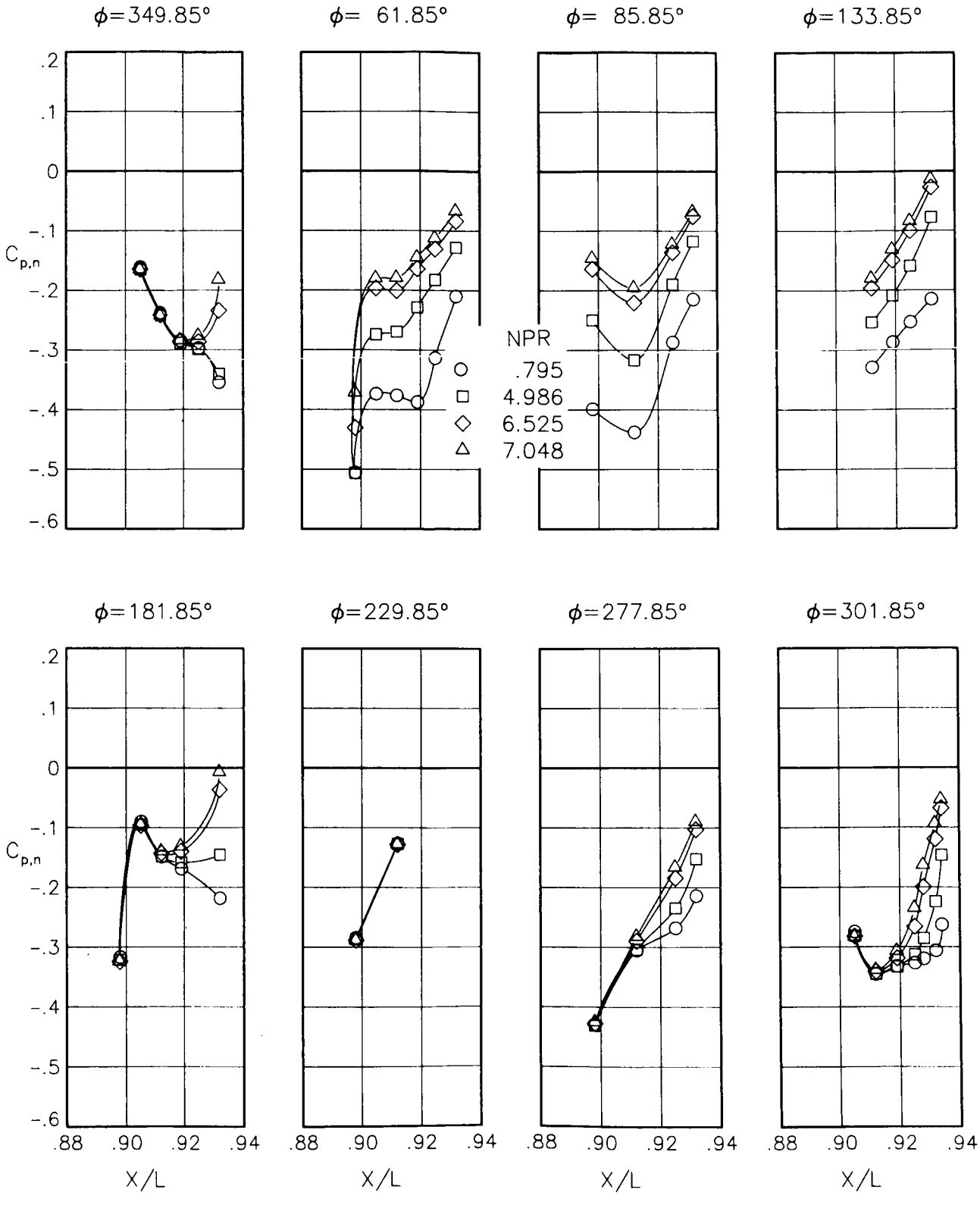

(f) M = 1.20; α = 1.00°.

Figure 86.- Continued.

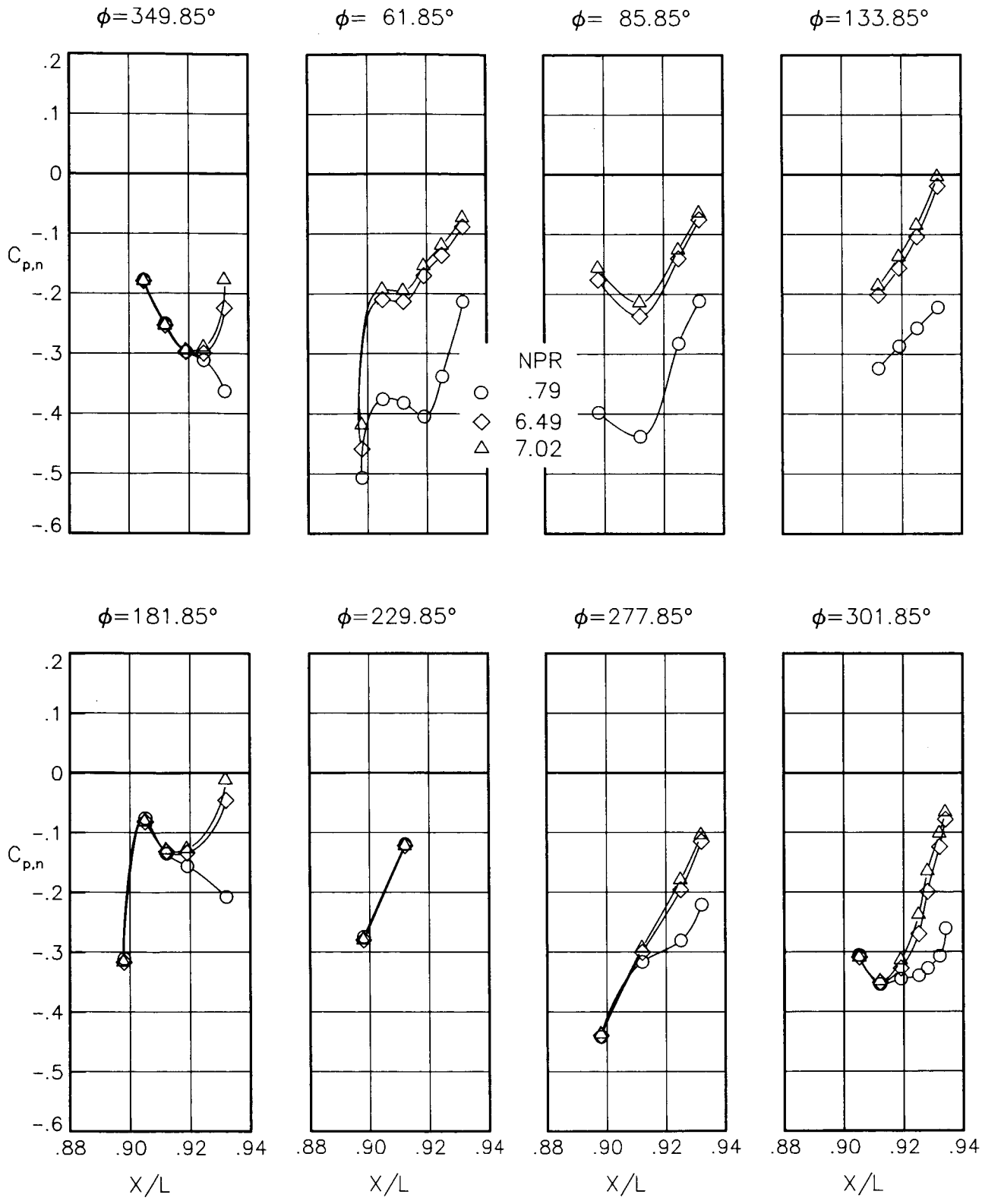

(g) M = 1.20; α = 2.00°.

Figure 86.- Continued.

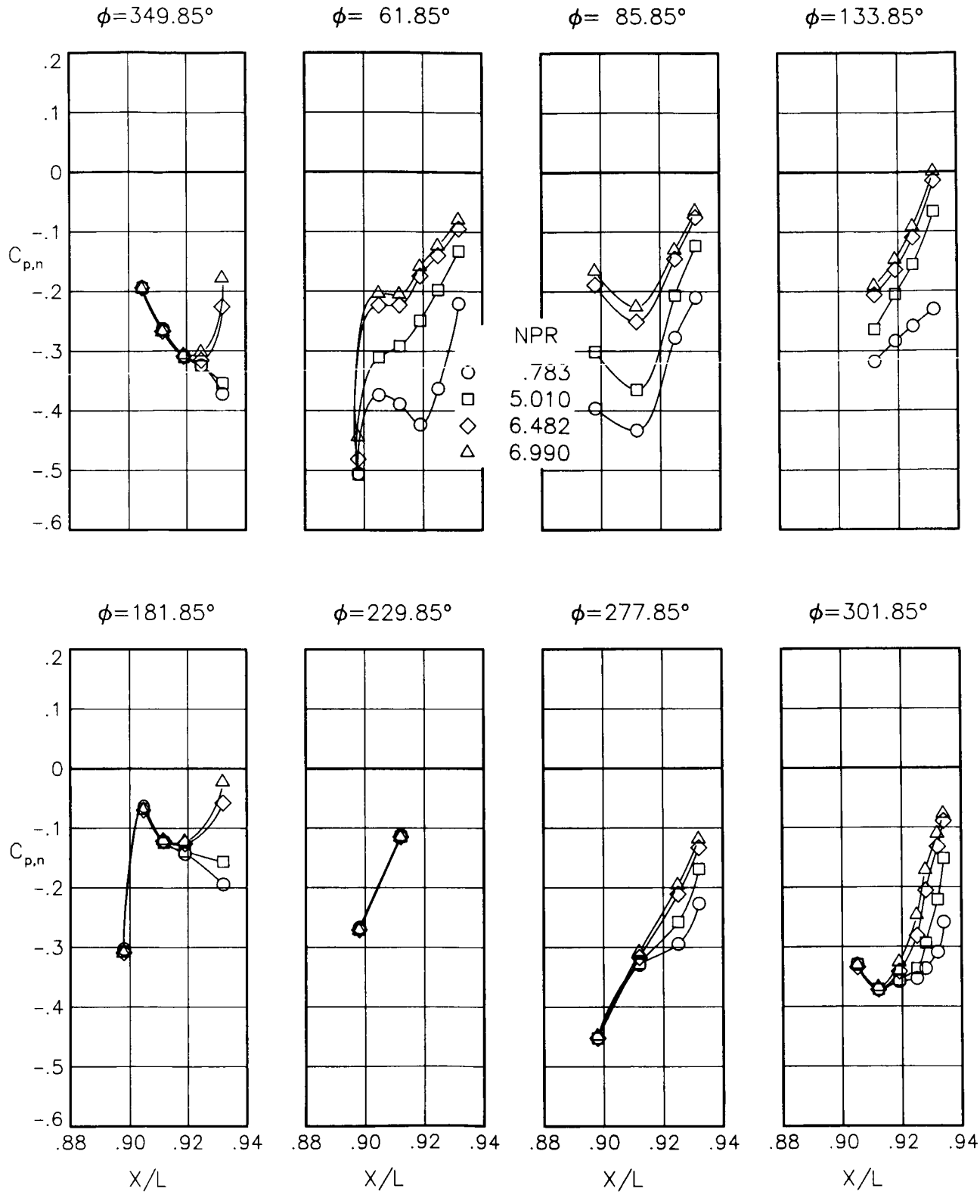

(h) M = 1.20; α = 3.00°.

Figure 86.- Continued.

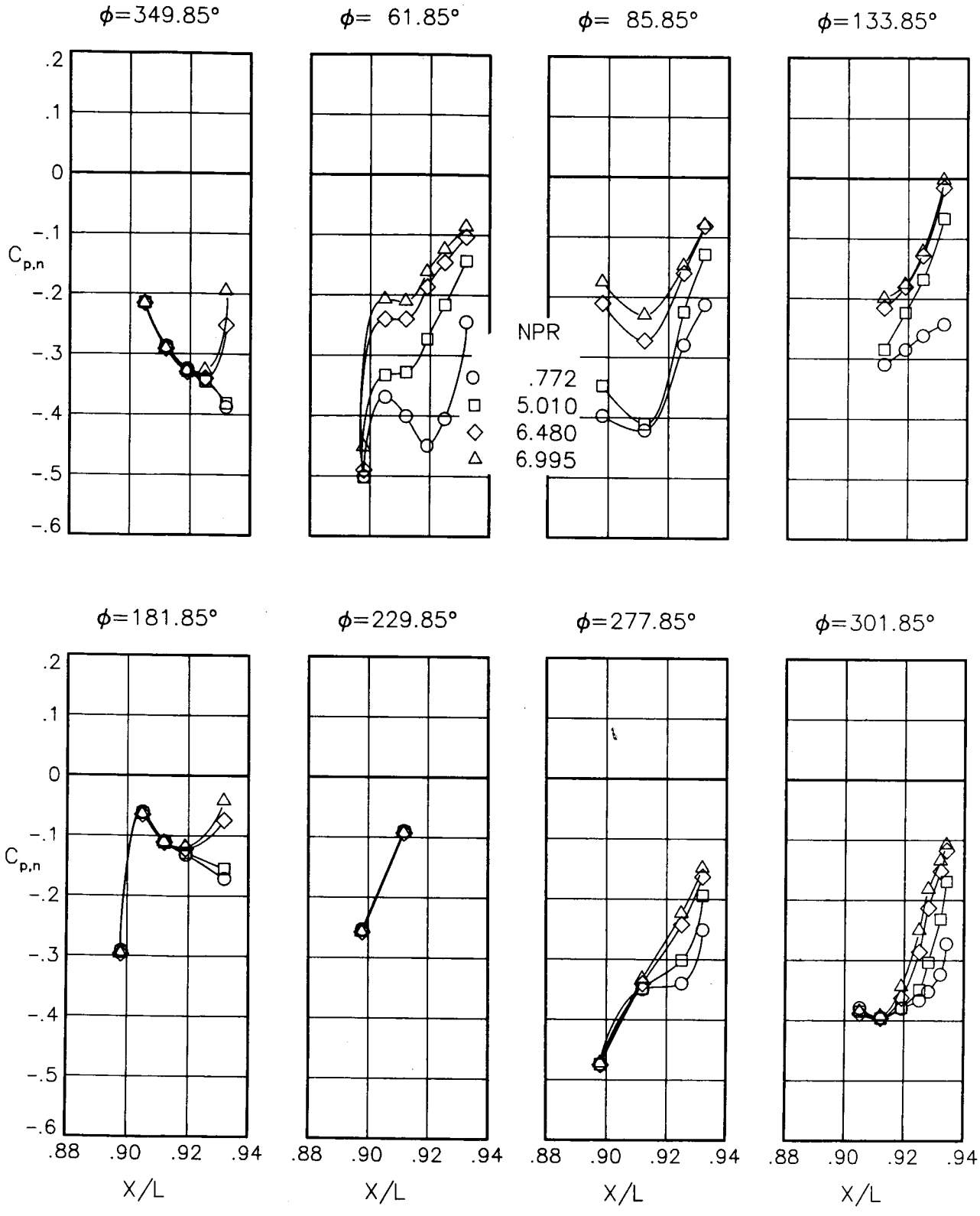

(i) M = 1.20; α = 5.00°.

Figure 86.- Concluded.

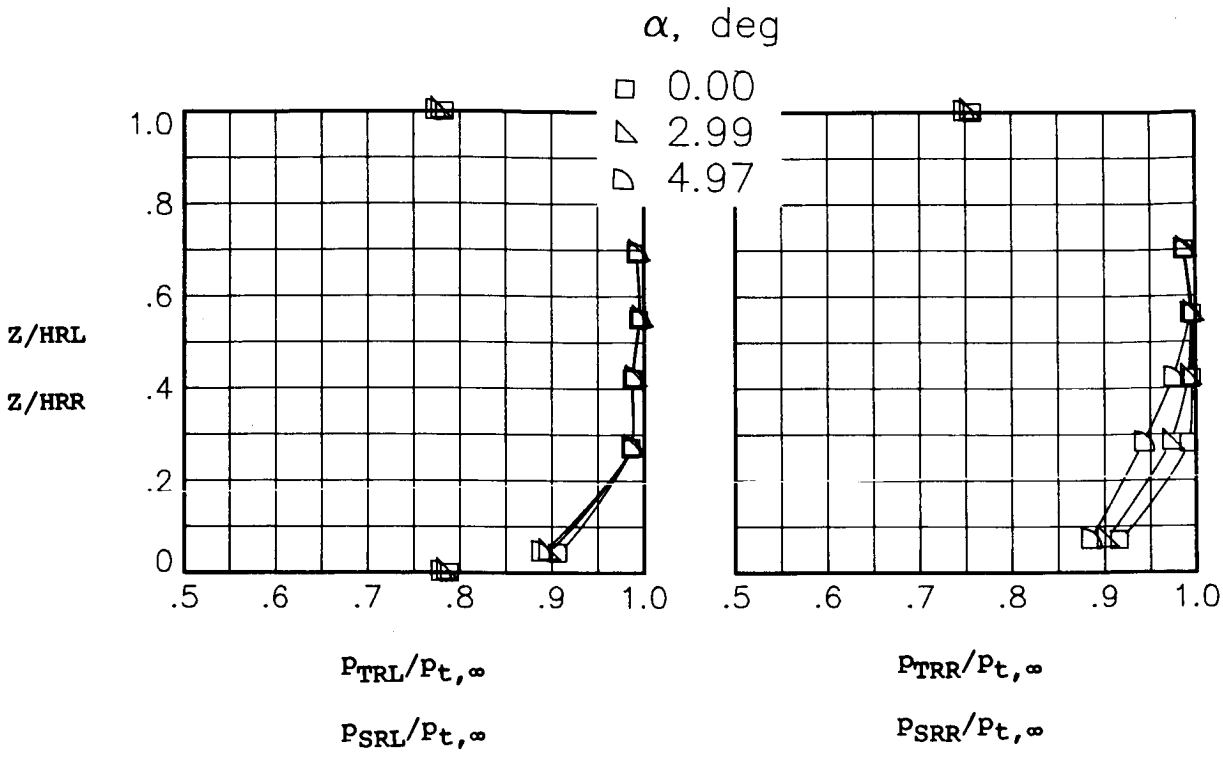

(a) M = 0.60; NPR = 1.03.

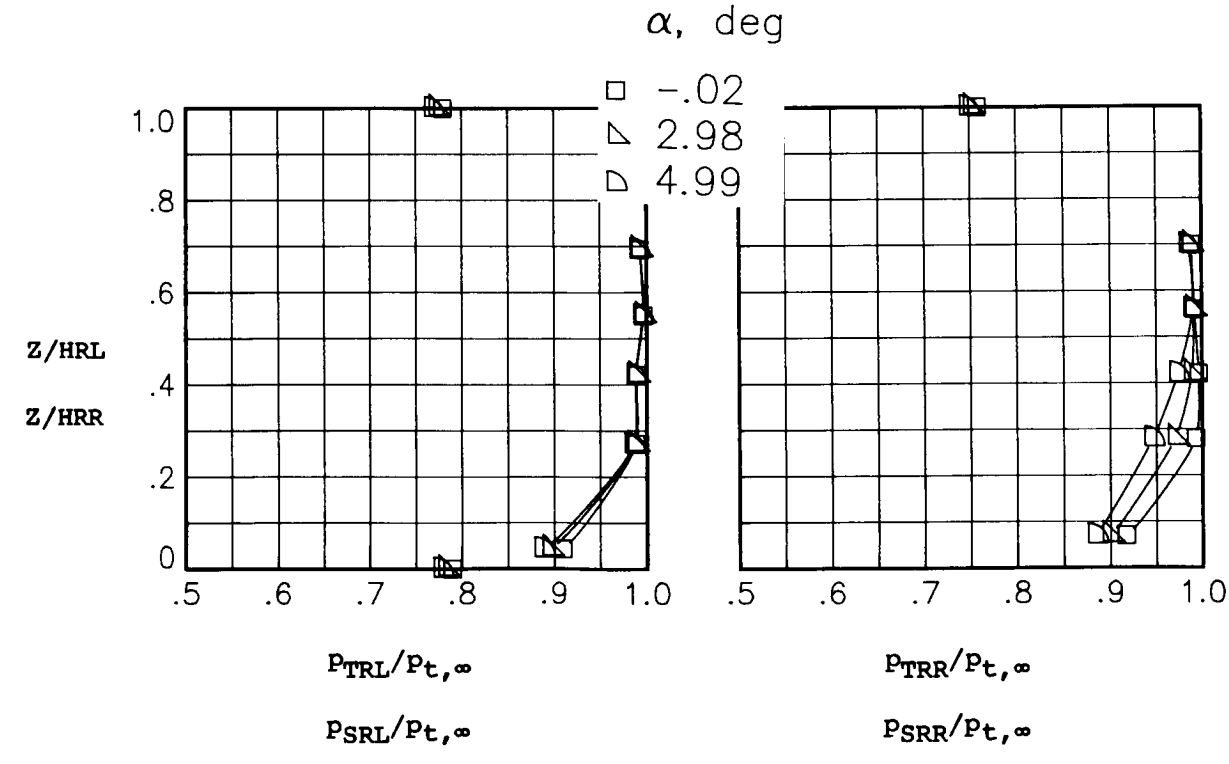

(b) M = 0.60; NPR = 3.00.

Figure 87.- Boundary-layer static- and total-pressure profiles for the model with all fuselage modifications except nose boom. β_n = 18.45°.

Z/HRL Left — Forward
Z/HRR Rt — Aft

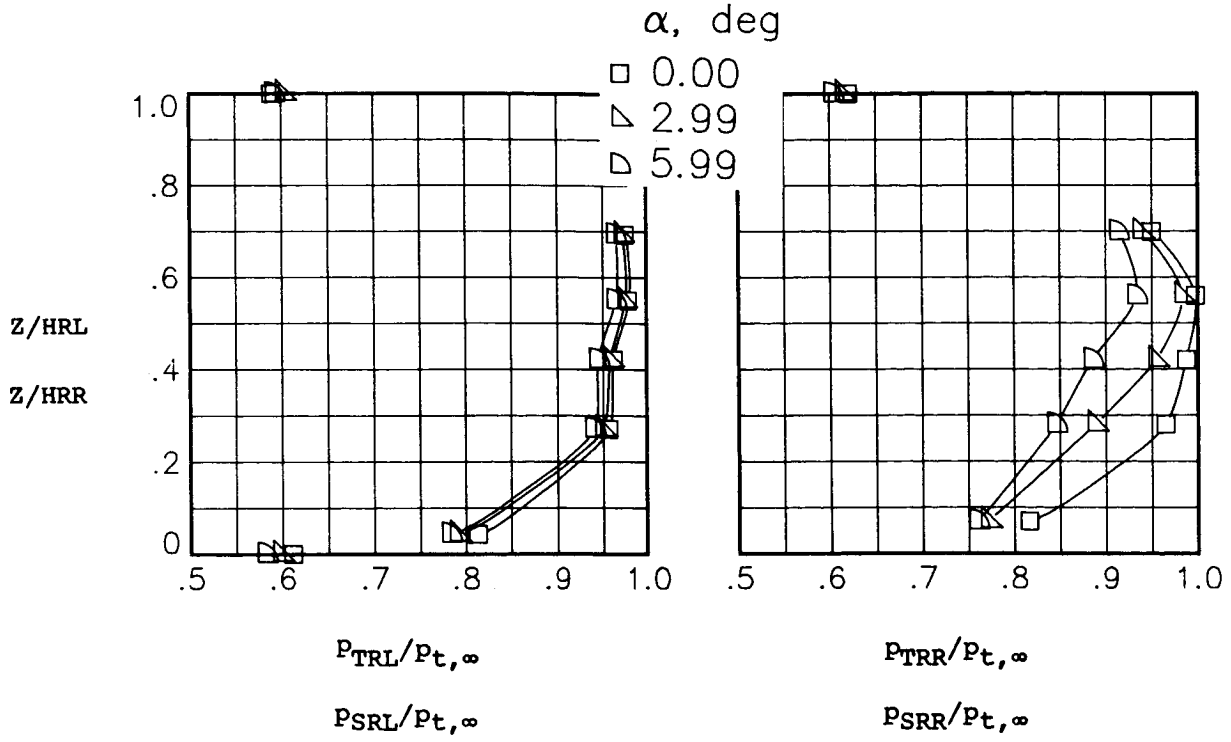

(c) M = 0.90; NPR = 0.99.

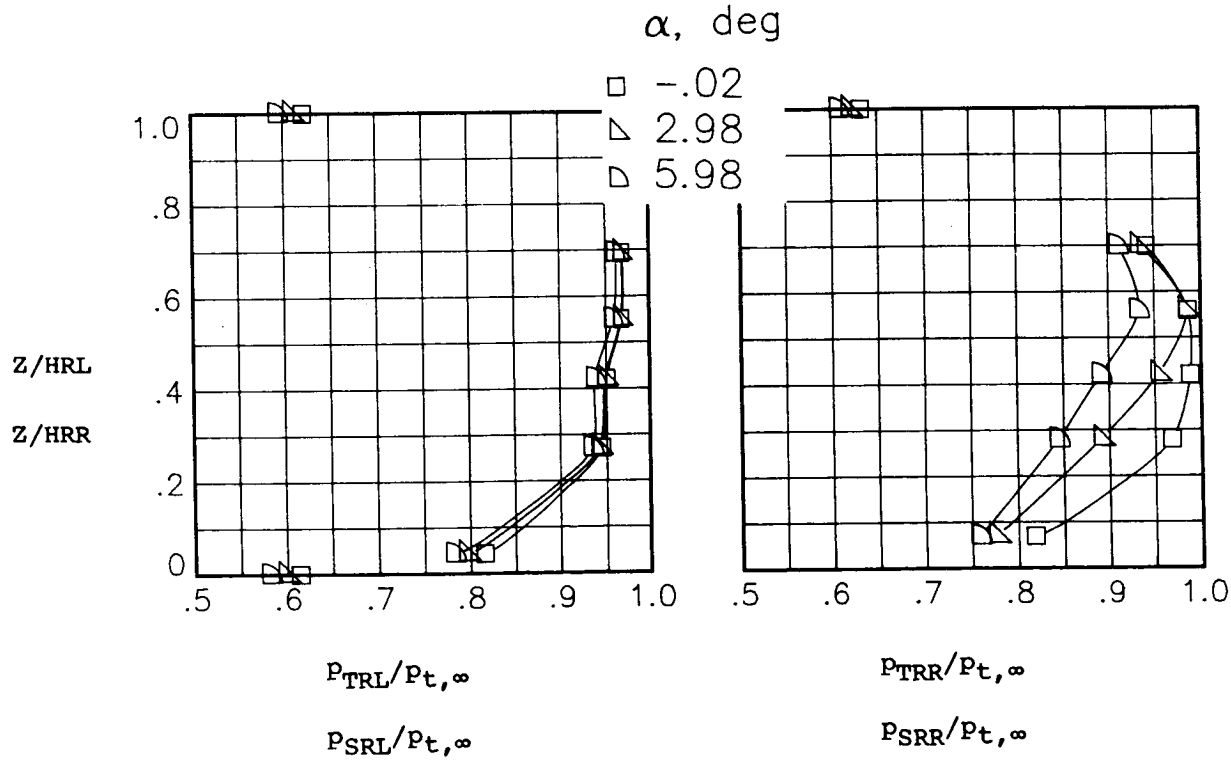

(d) M = 0.90; NPR = 5.02.

Figure 87.- Concluded.

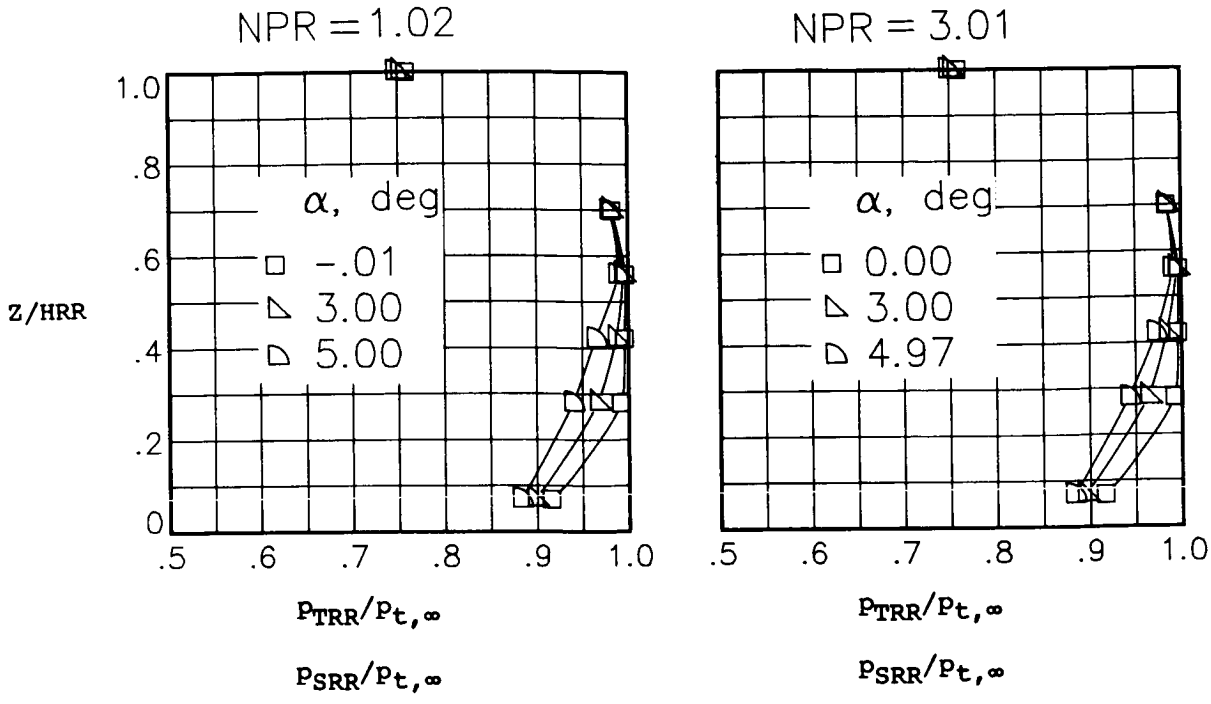

(a) M = 0.60.

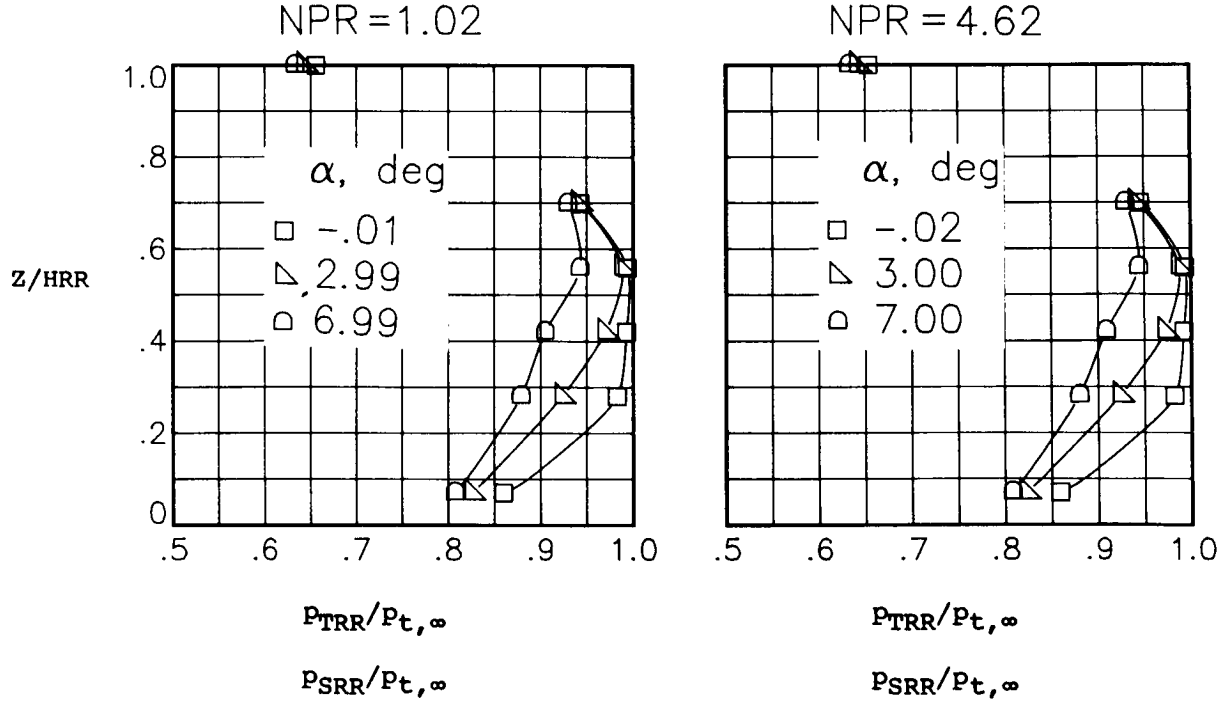

(b) M = 0.80.

Figure 88.- Boundary-layer static- and total-pressure profiles for the model with nose boom, actuator fairings, A/B vents, nozzle steps, and right rake. β_n = 18.45°; δ_n = -2°.

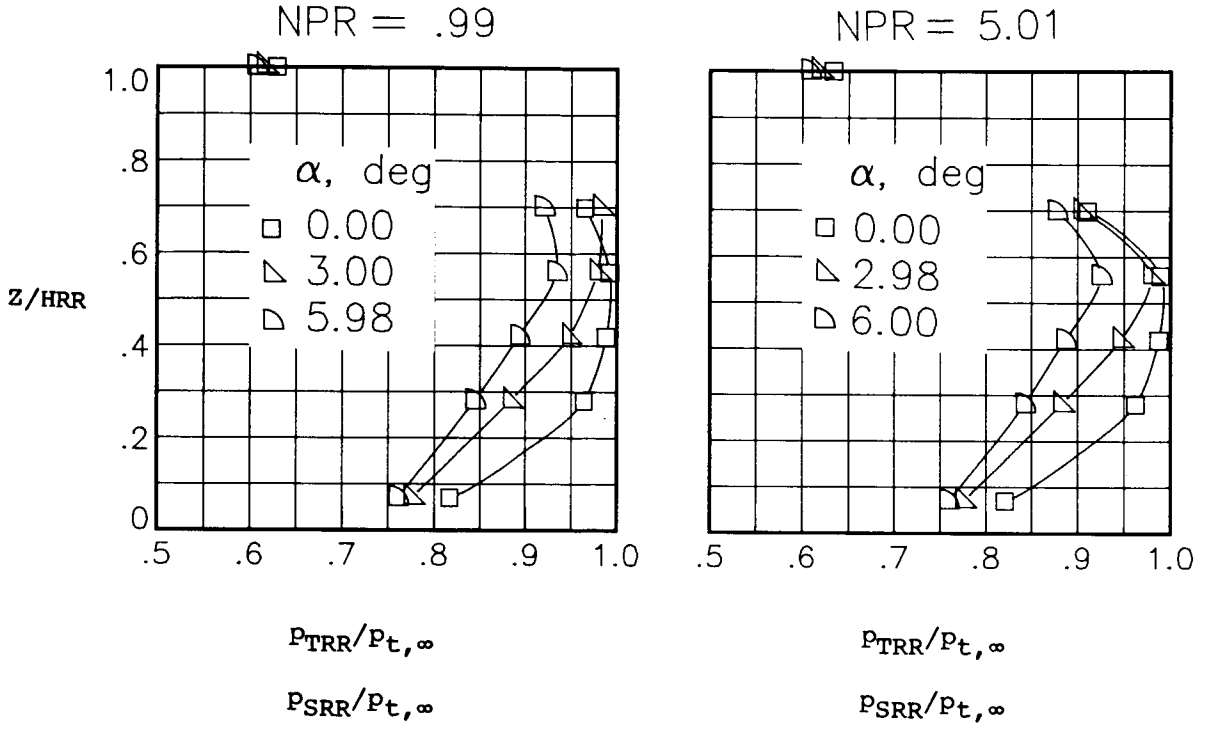

(c) M = 0.90.

Figure 88.- Concluded.

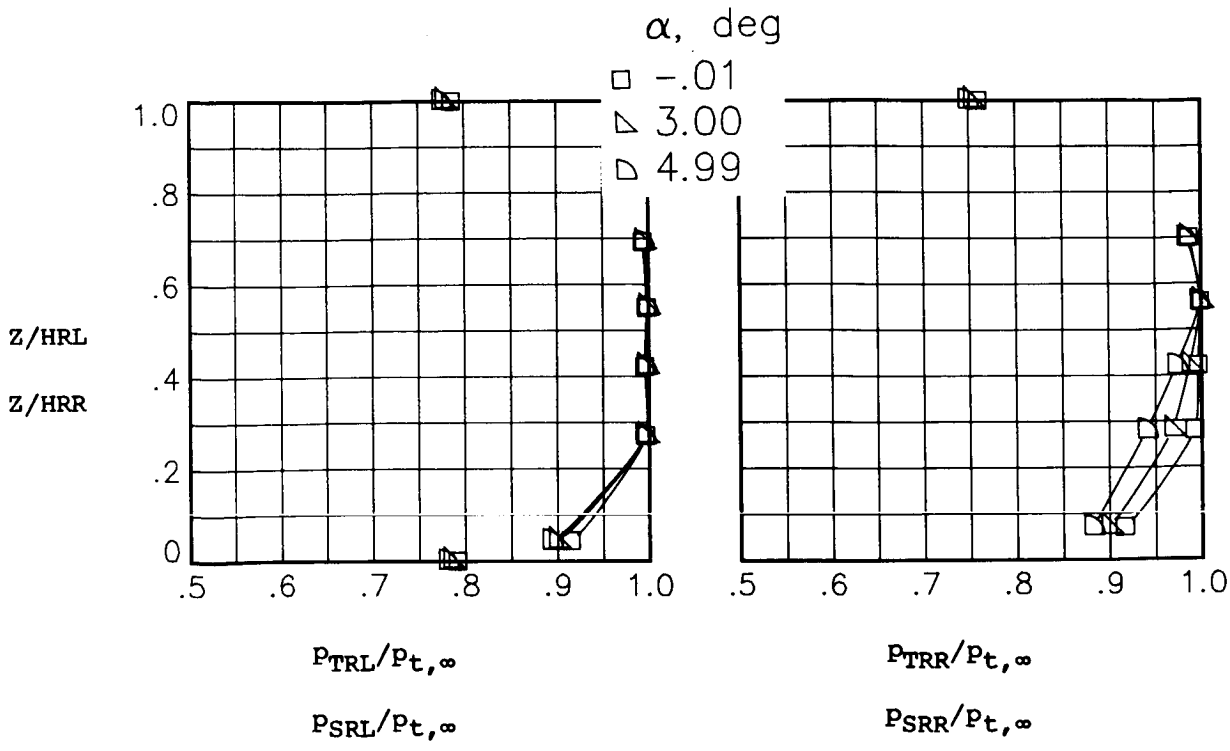

(a) M = 0.60; NPR = 1.02.

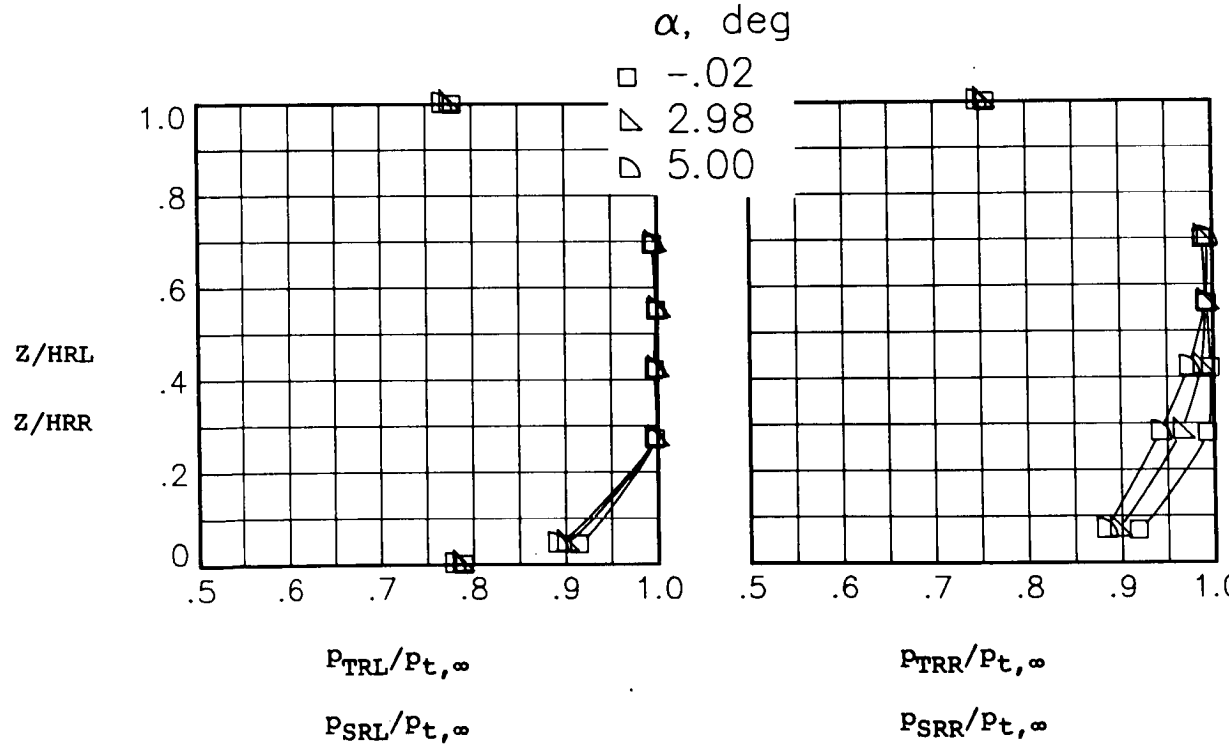

(b) M = 0.60; NPR = 3.00.

Figure 89.- Boundary-layer static- and total-pressure profiles for the model with all fuselage modifications. β_n = 18.45°; δ_h = -2°.

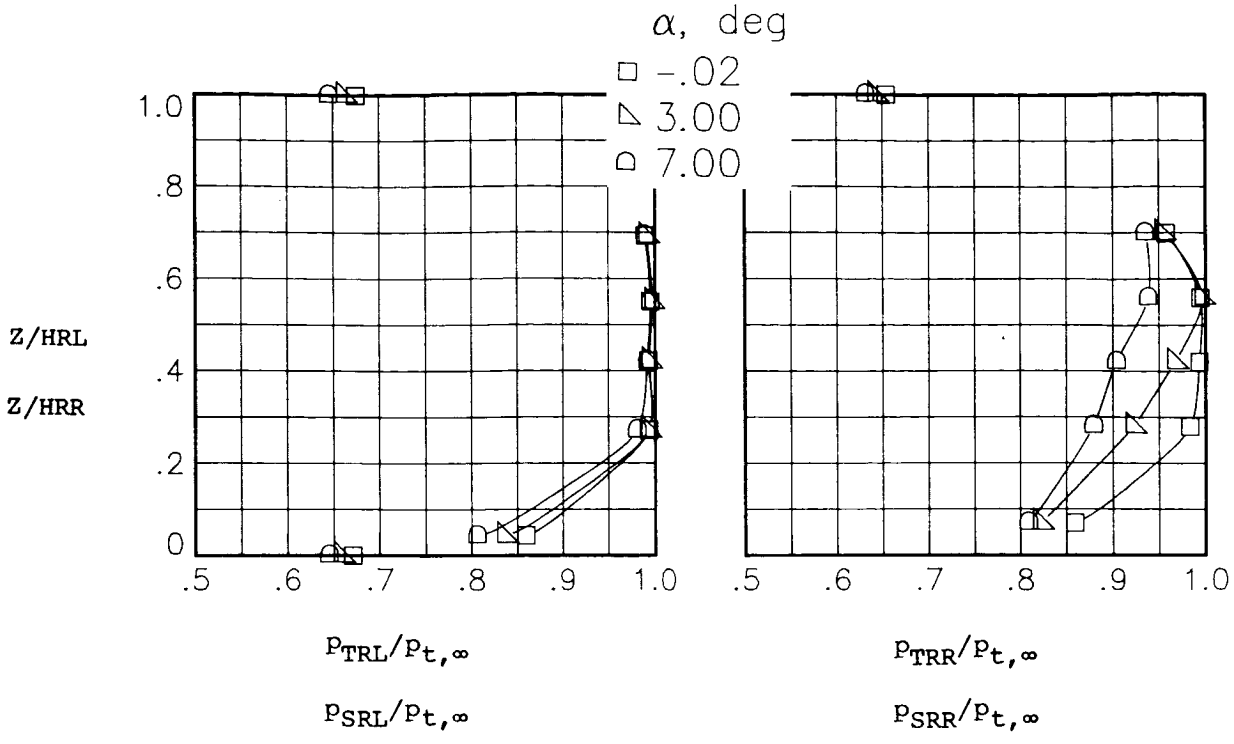

(c) M = 0.80; NPR = 1.02.

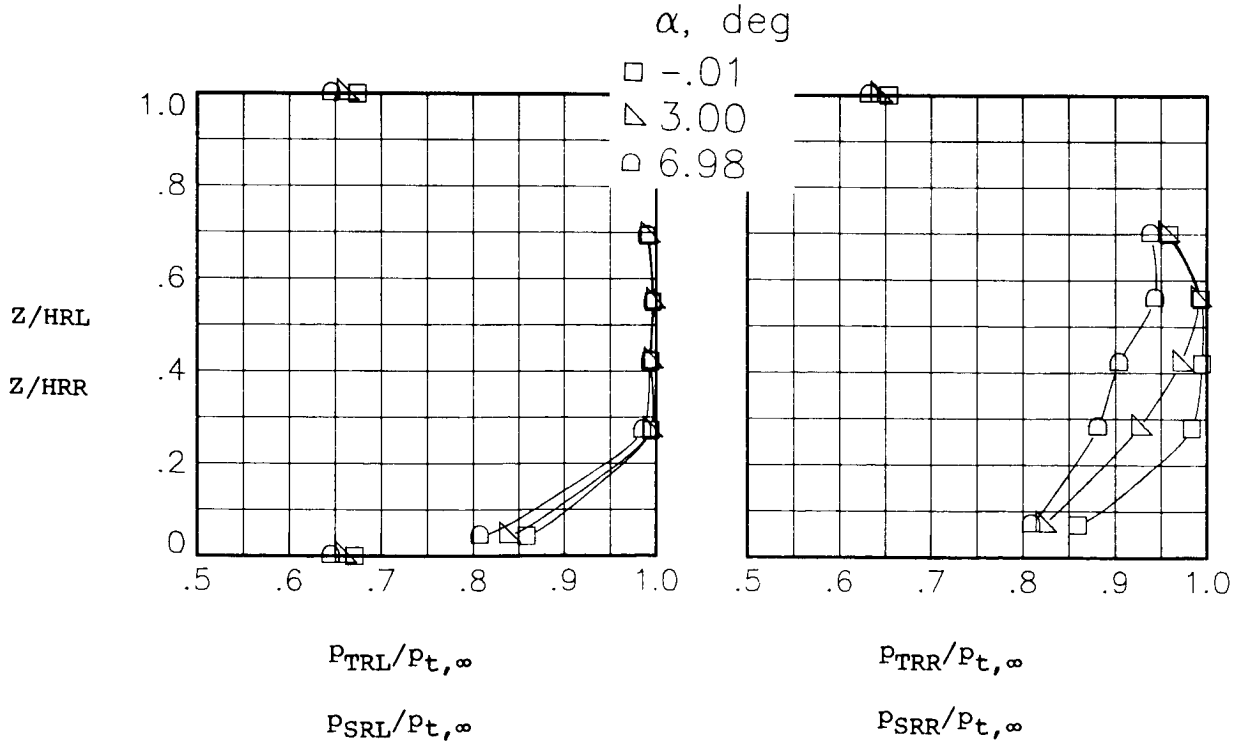

(d) M = 0.80; NPR = 4.64.

Figure 89.- Continued.

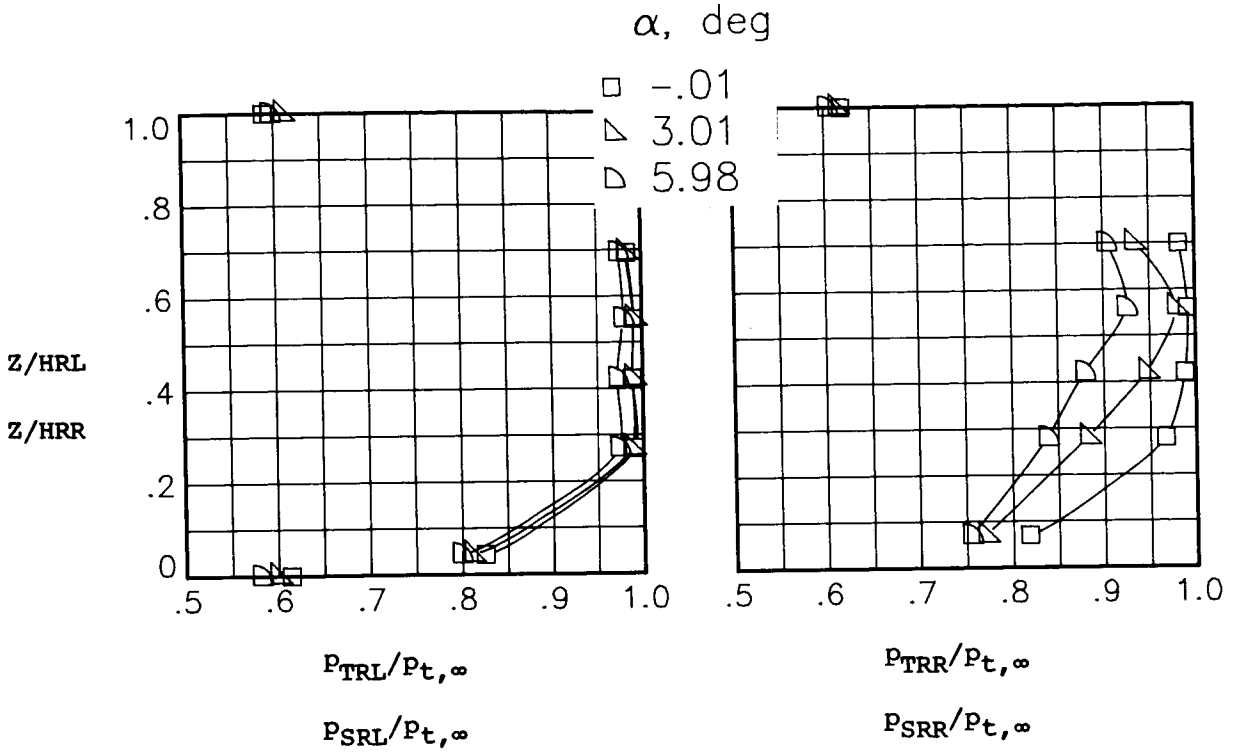

(e) M = 0.90; NPR = 0.99.

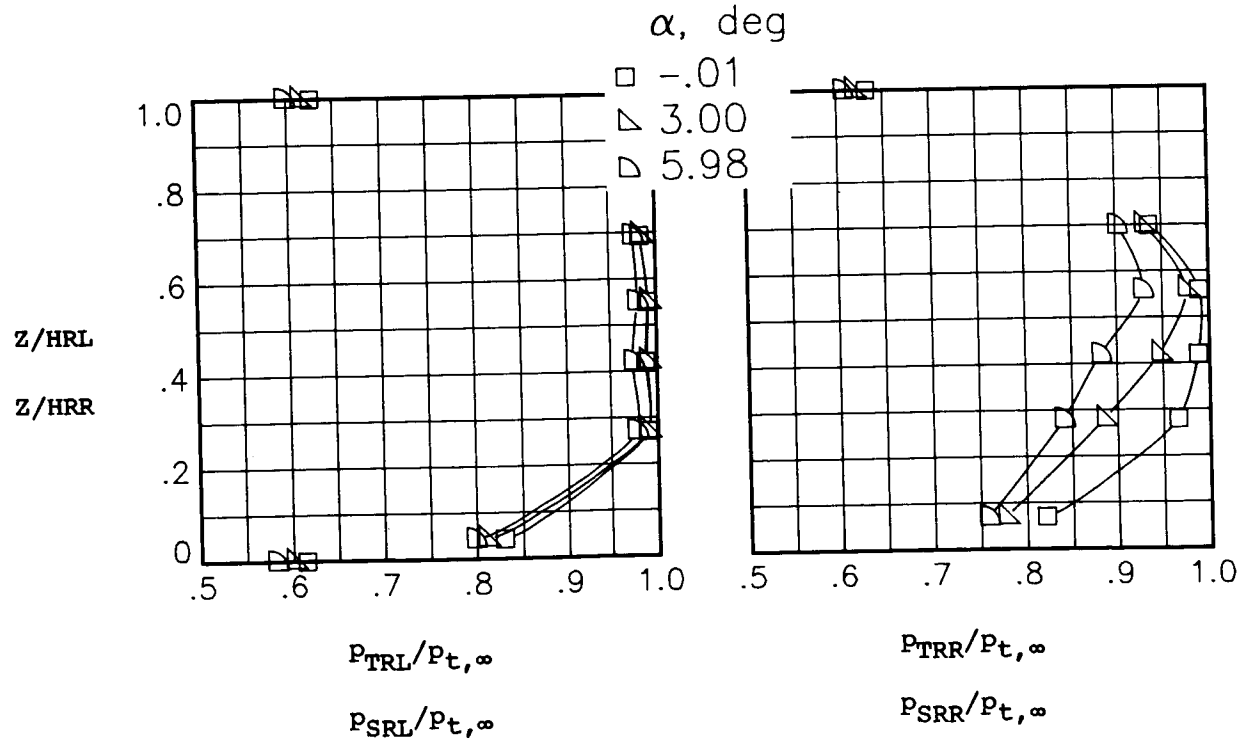

(f) M = 0.90; NPR = 5.00.

Figure 89.- Concluded.

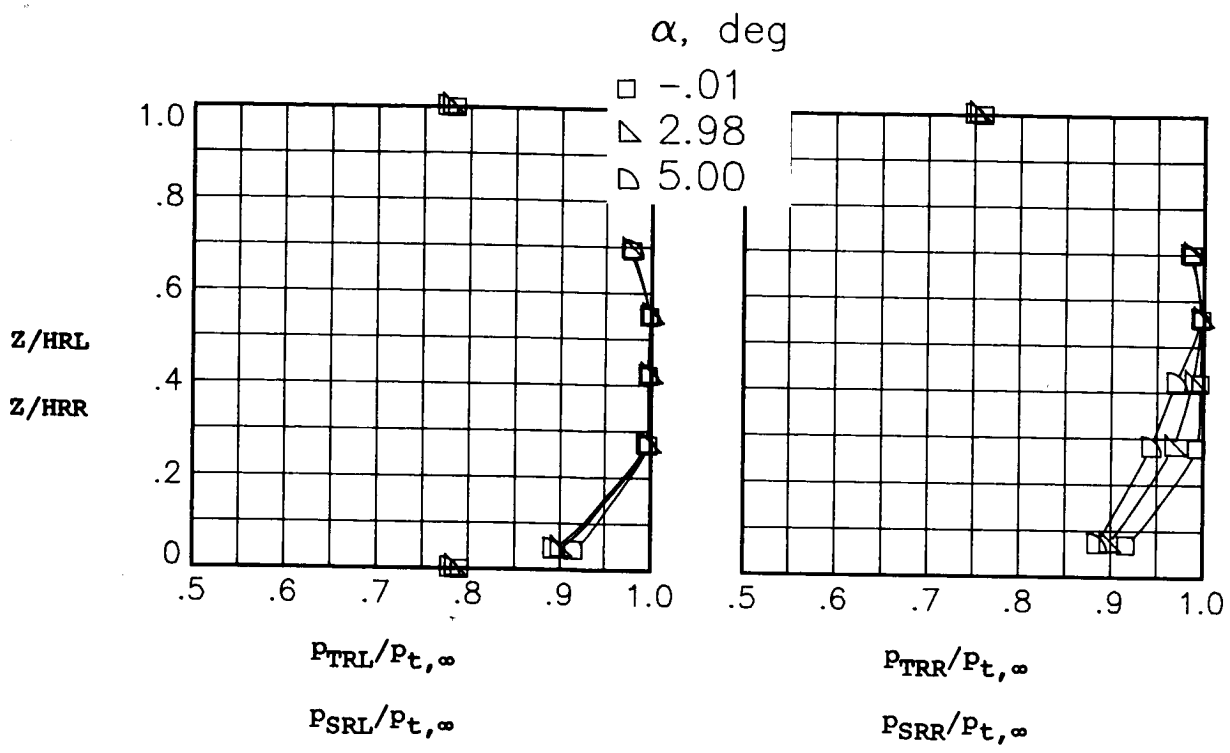

(a) M = 0.60; NPR = 1.03.

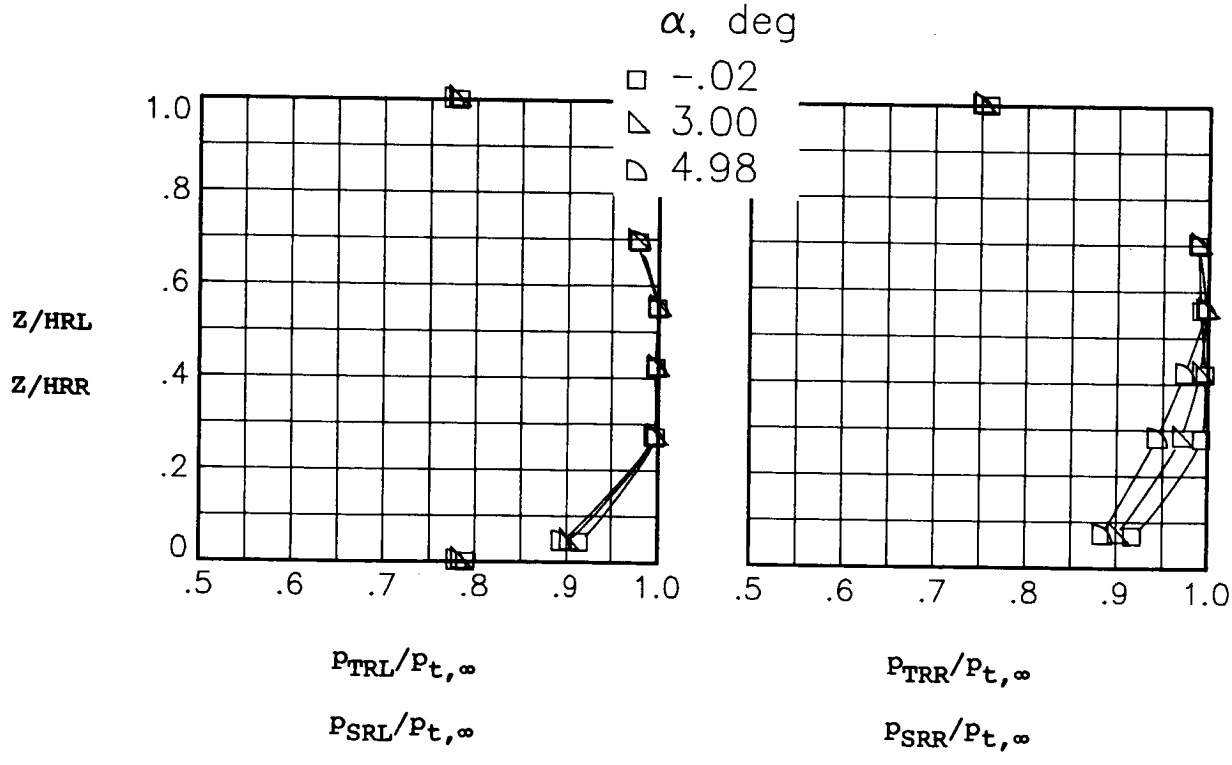

(b) M = 0.60; NPR = 3.00.

Figure 90.- Boundary-layer static- and total-pressure profiles for the model with all fuselage modifications. β_n = 18.45°.

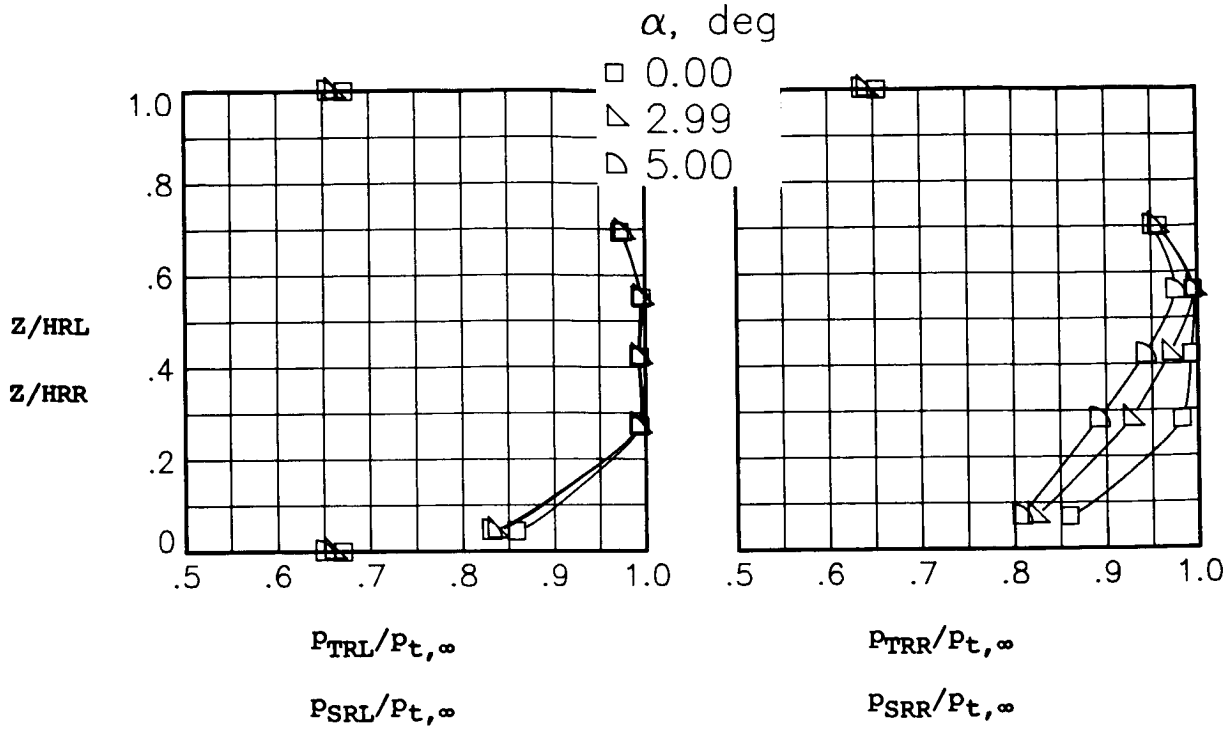

(c) M = 0.80; NPR = 1.02.

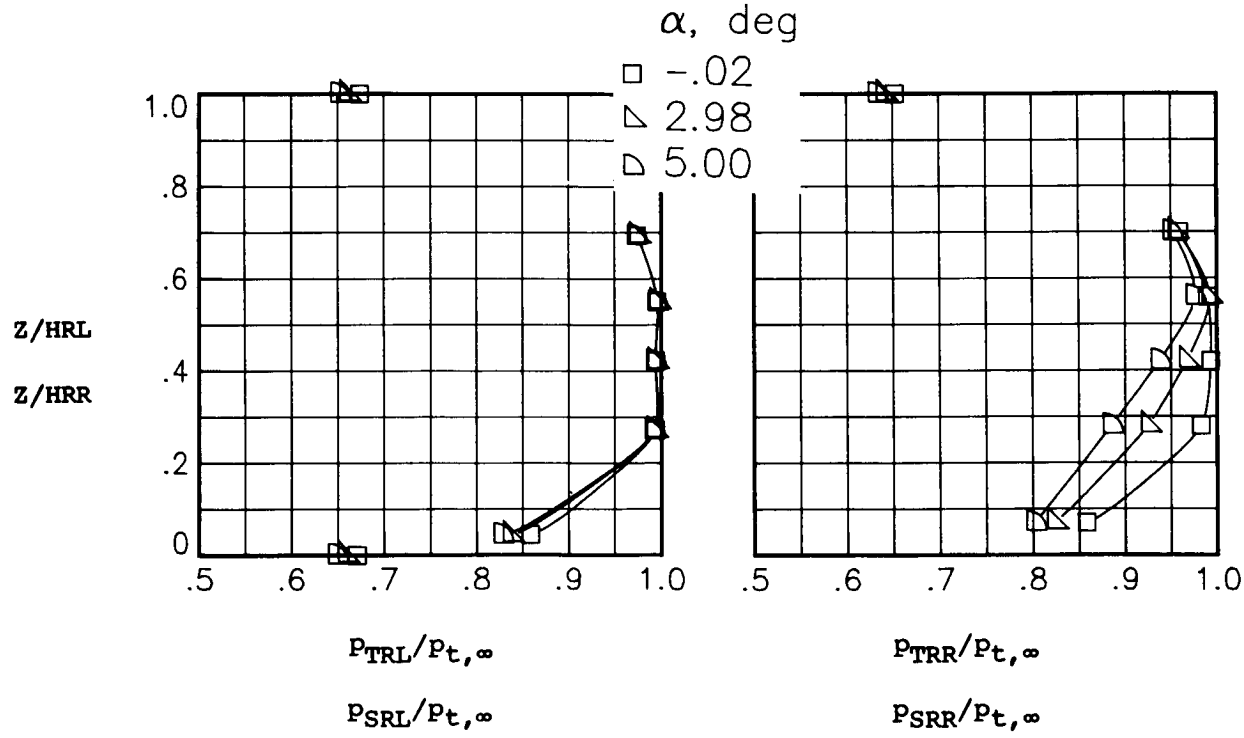

(d) M = 0.80; NPR = 4.58.

Figure 90.- Continued.

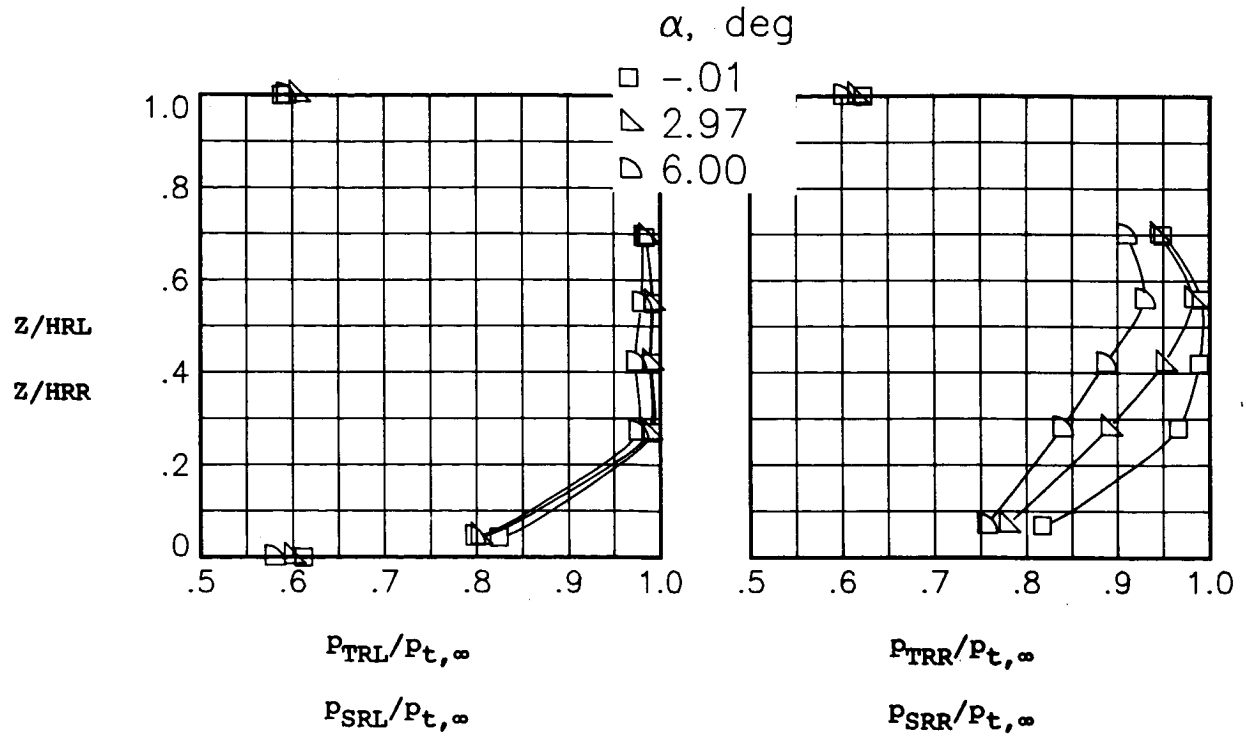

(e) M = 0.90; NPR = 0.99.

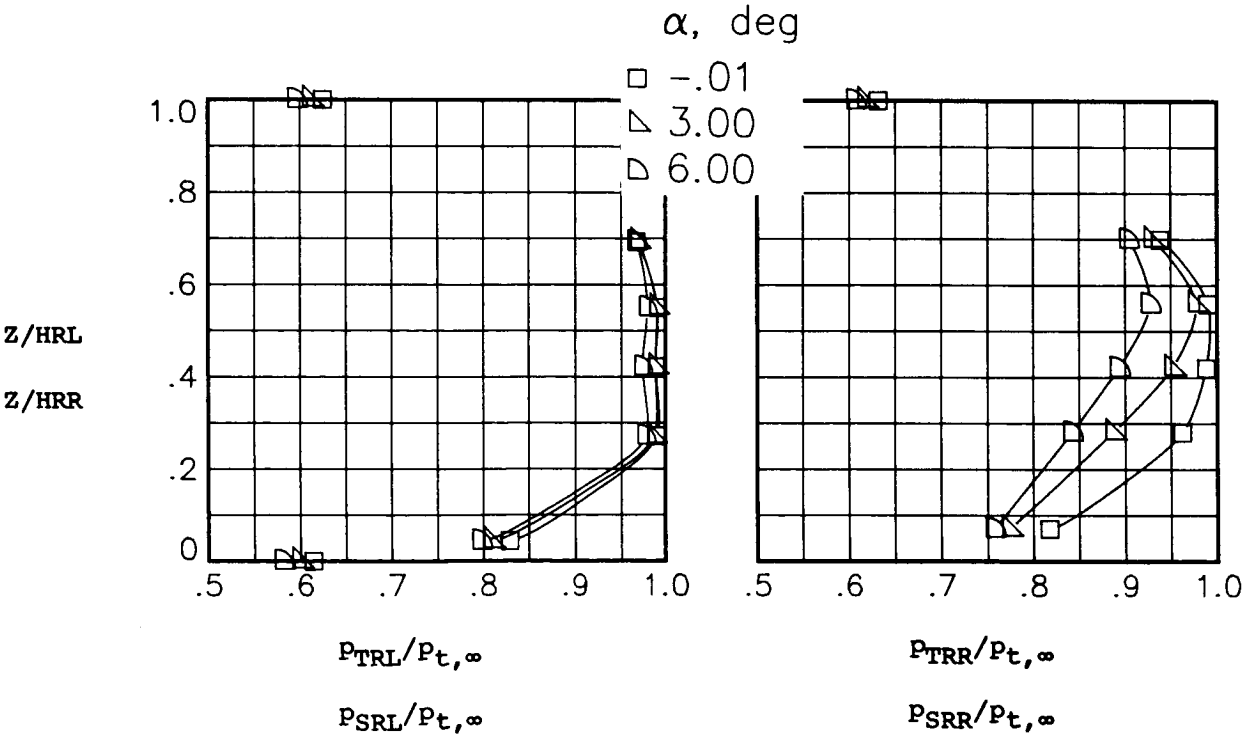

(f) M = 0.90; NPR = 5.01.

Figure 90.- Concluded.

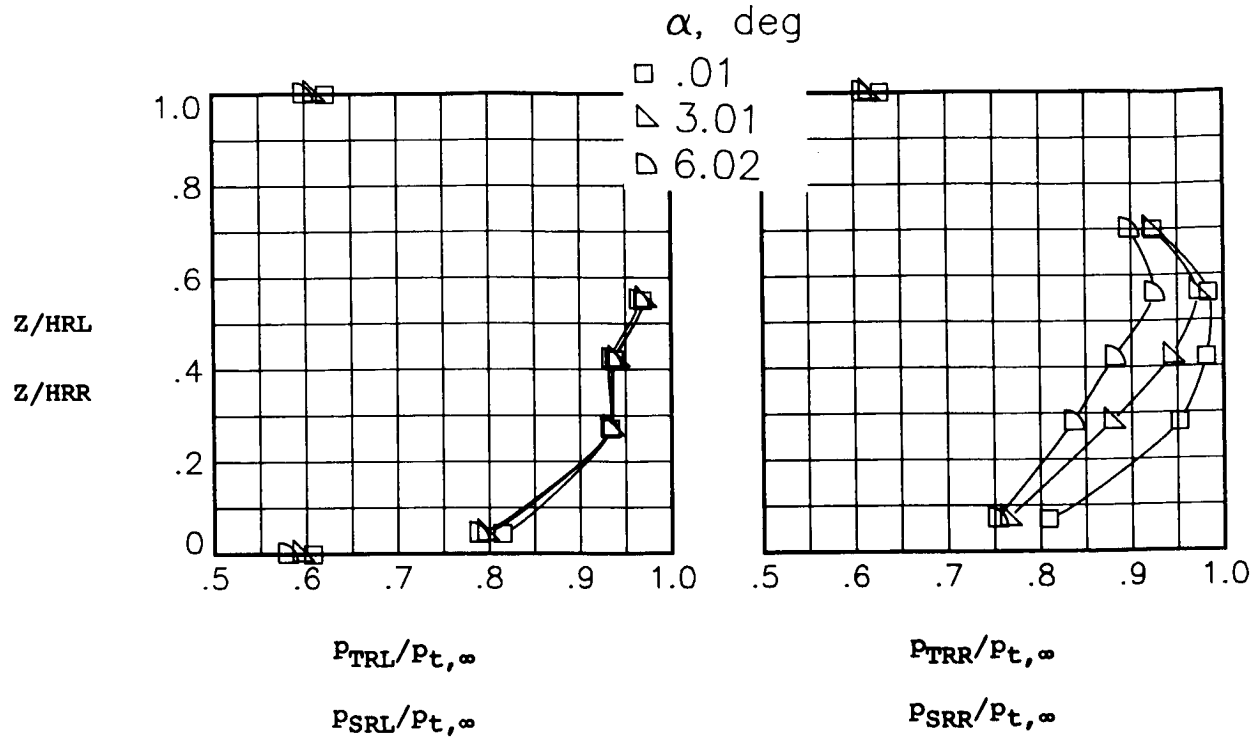

(a) M = 0.90; NPR = 1.01.

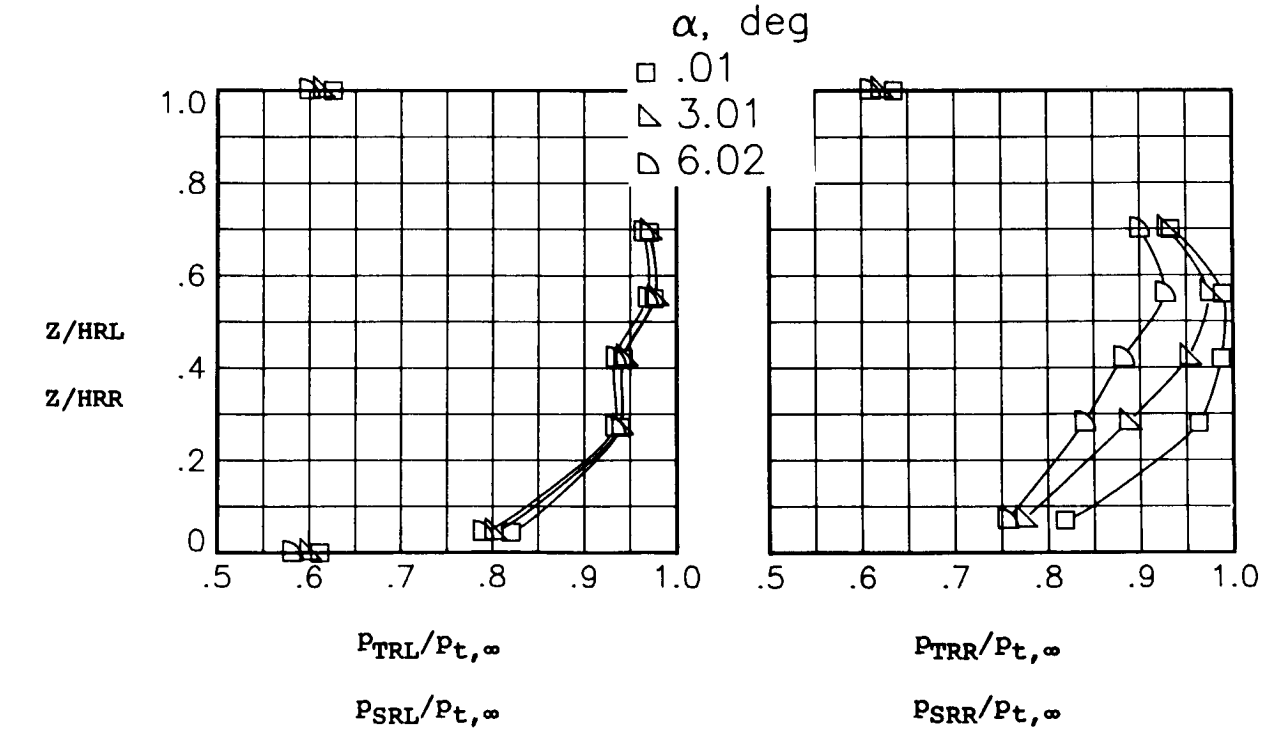

(b) M = 0.90; NPR = 5.01.

Figure 91.- Boundary-layer static- and total-pressure profiles for the model with all fuselage modifications. β_n = 15.05°.

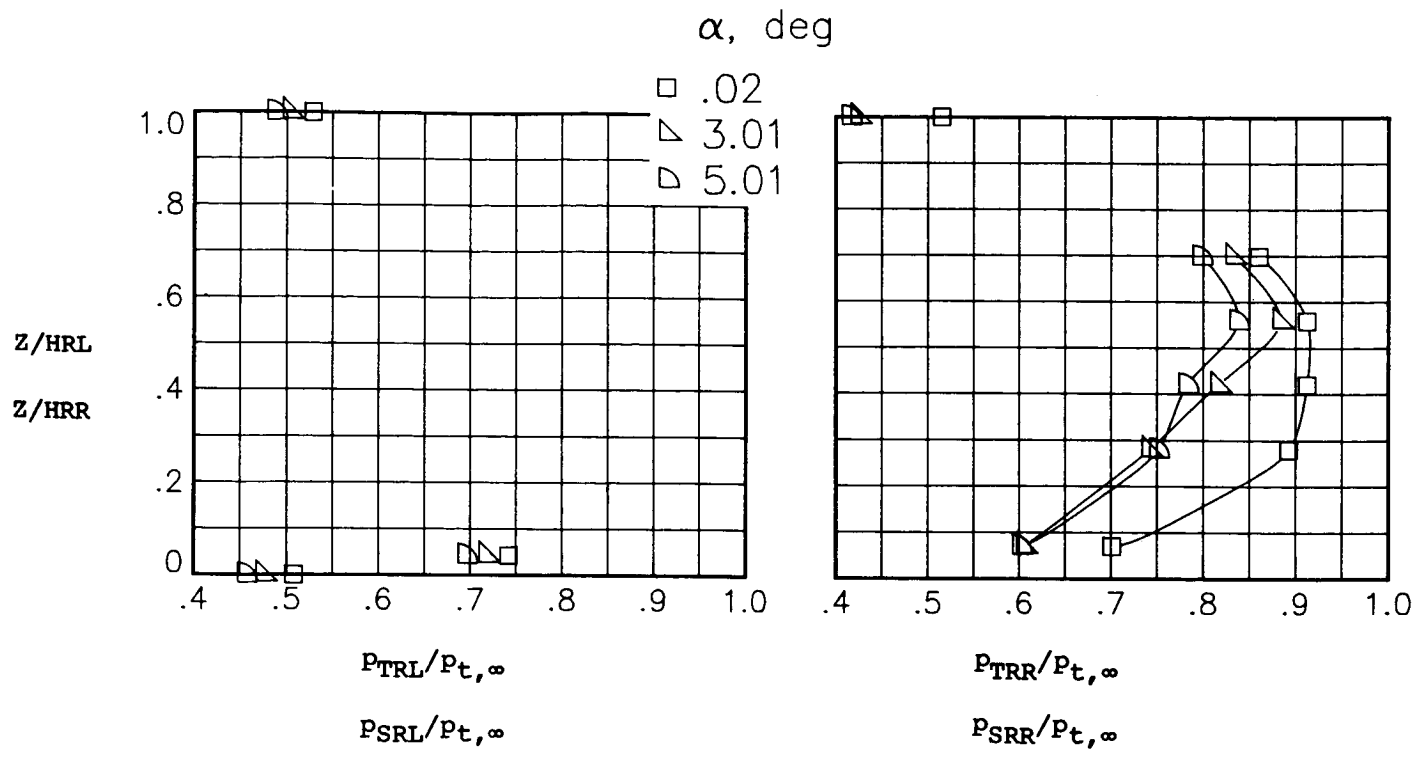

(c) M = 1.20; NPR = 0.86.

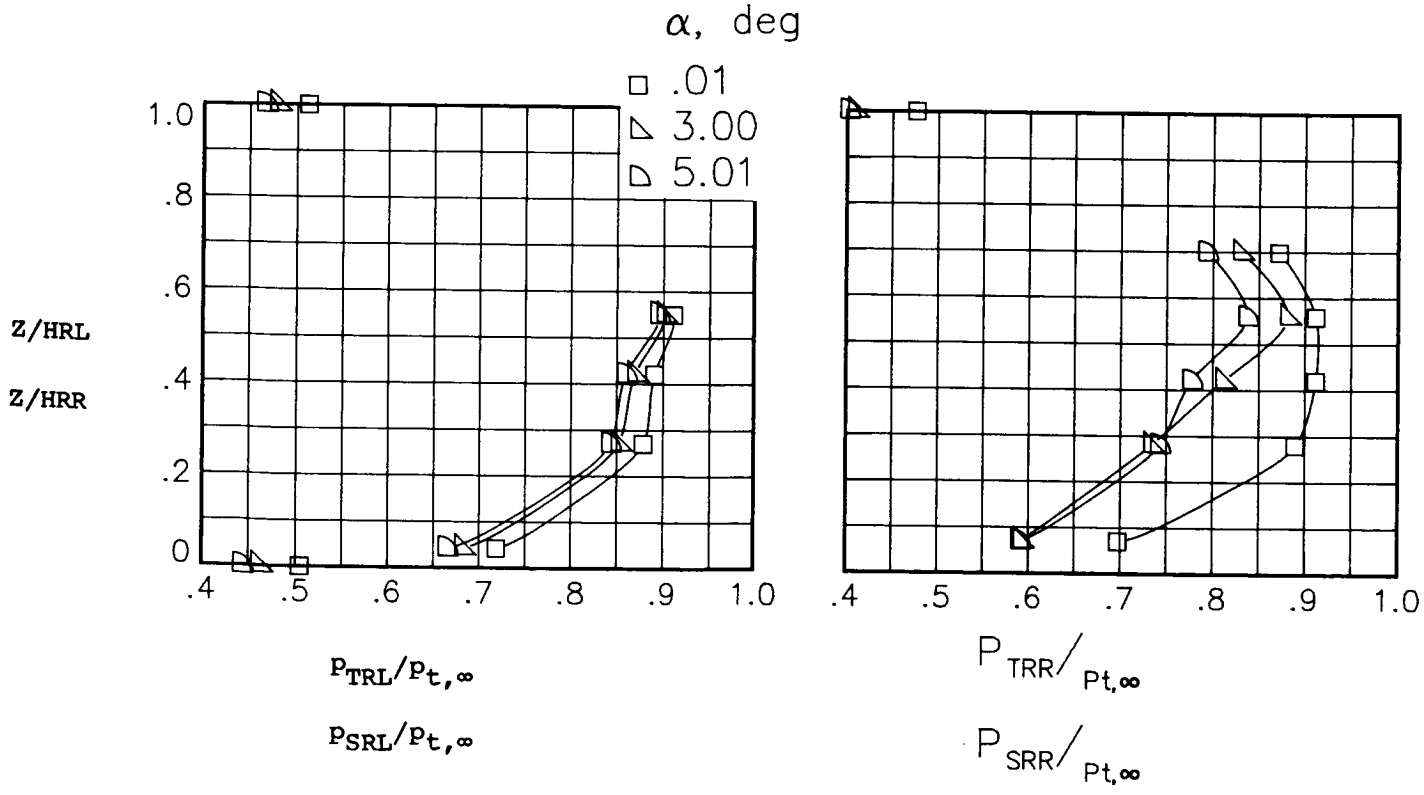

(d) M = 1.20; NPR = 7.02.

Figure 91.- Concluded.

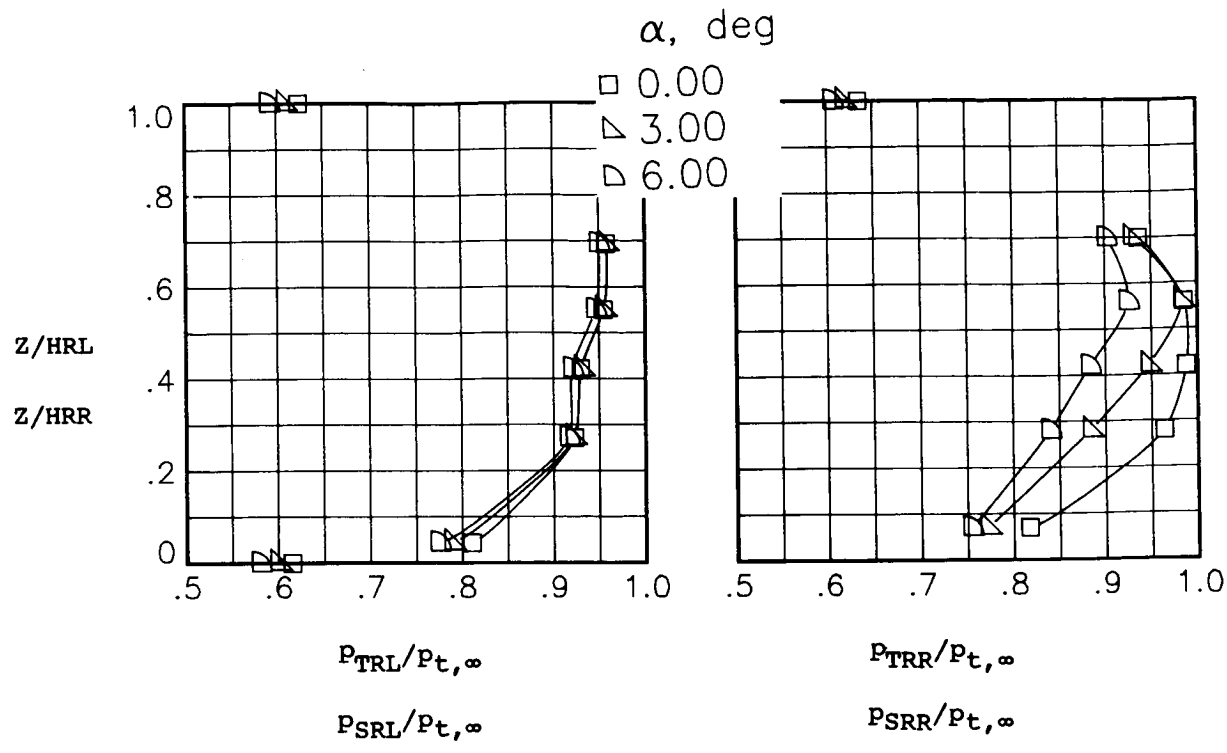

(a) M = 0.90; NPR = 1.03.

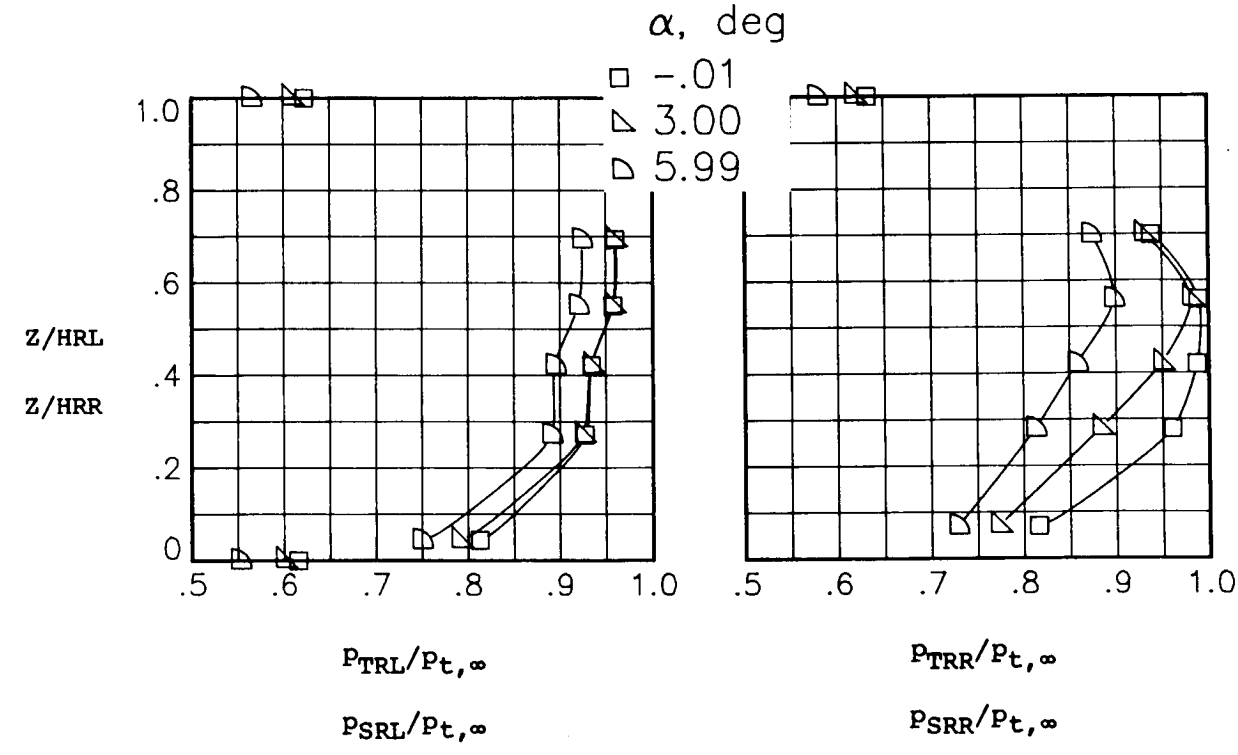

(b) M = 0.90; NPR = 5.00.

Figure 92.- Boundary-layer static- and total-pressure profiles for the model with all fuselage modifications. β_n = 7.72°.

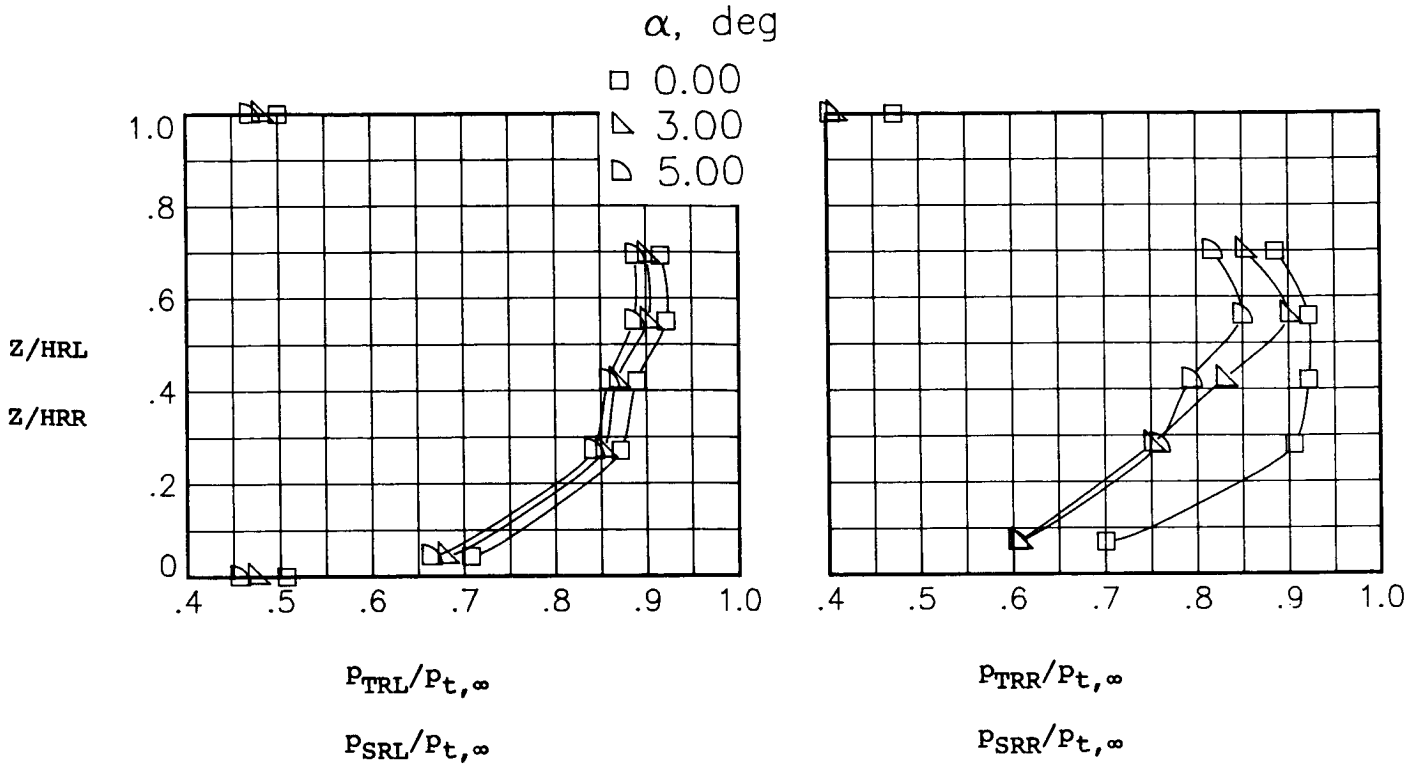

(c) M = 1.20; NPR = 0.80.

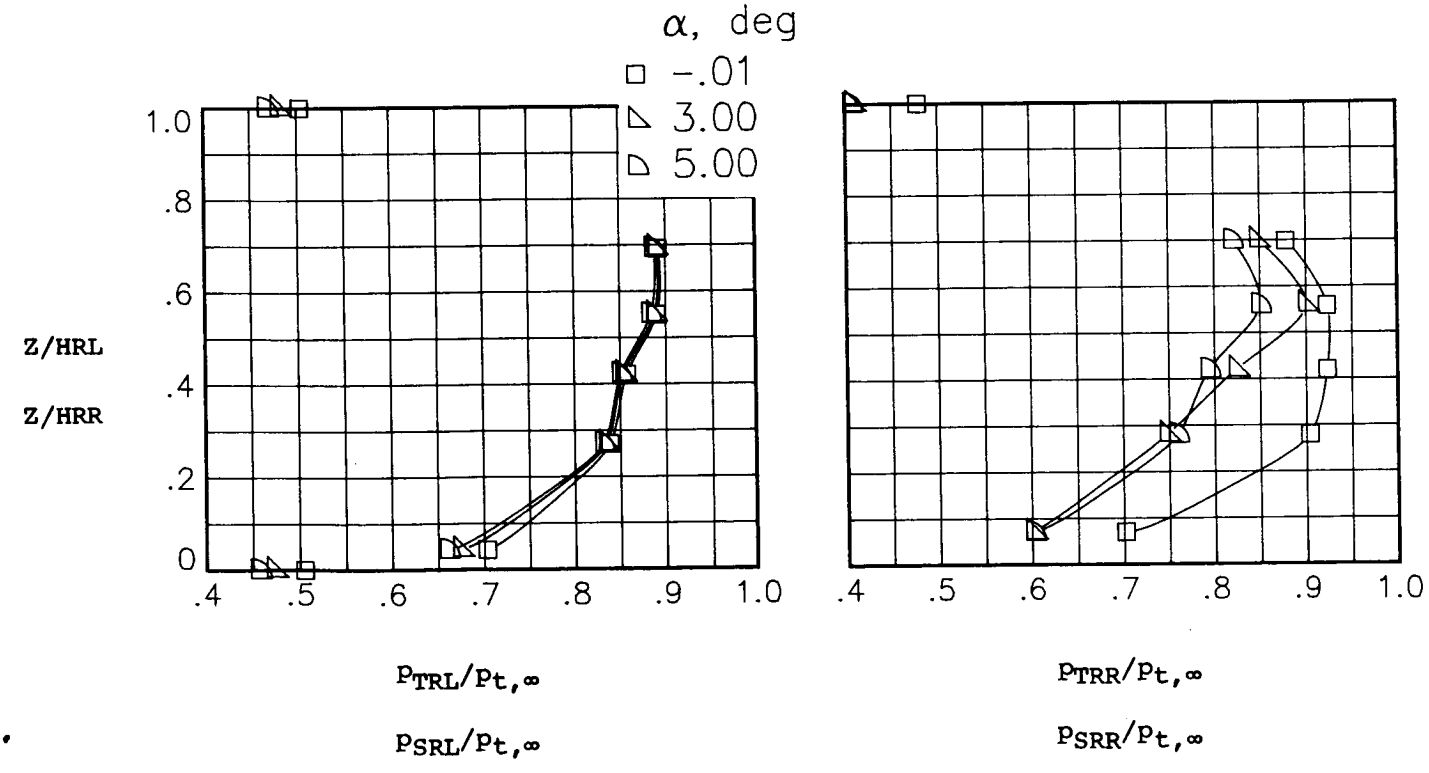

(d) M = 1.20; NPR = 7.01.

Figure 92.- Concluded.

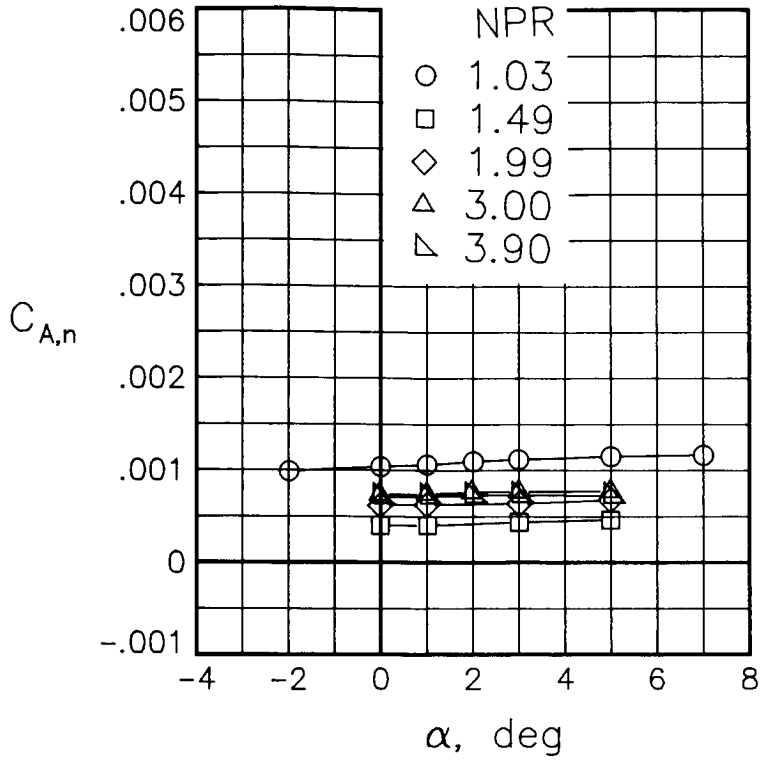

(a) M = 0.60.

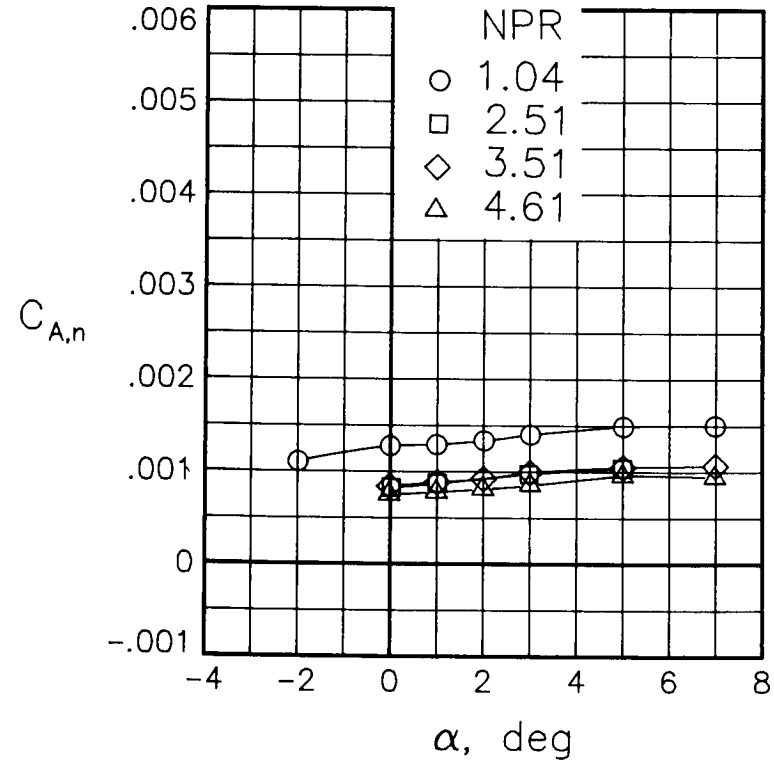

(b) M = 0.80.

Figure 93.- Integrated axial-force coefficient for the left-hand nozzle of the unmodified model. β_n = 18.45°.

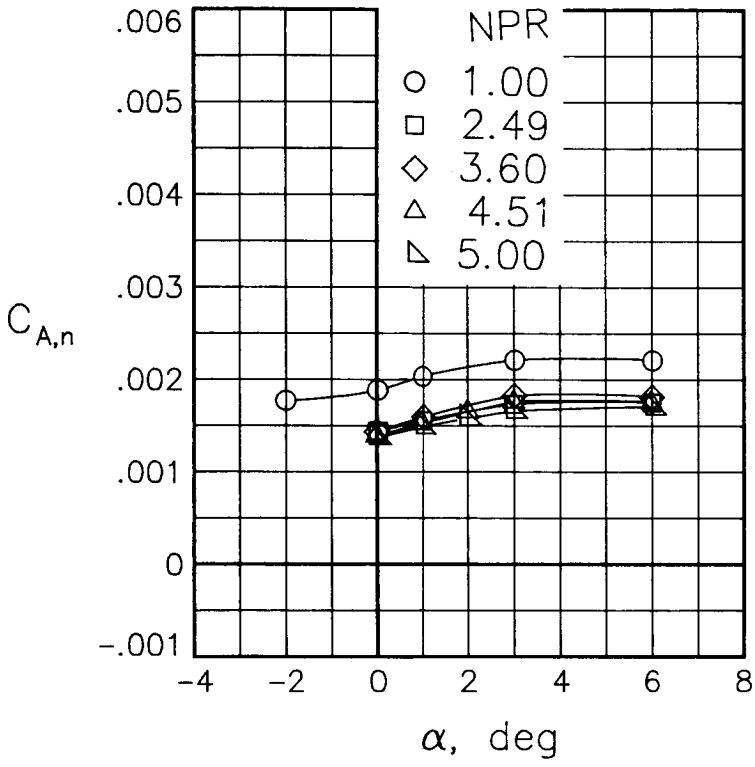

(c) M = 0.90.

Figure 93.- Concluded.

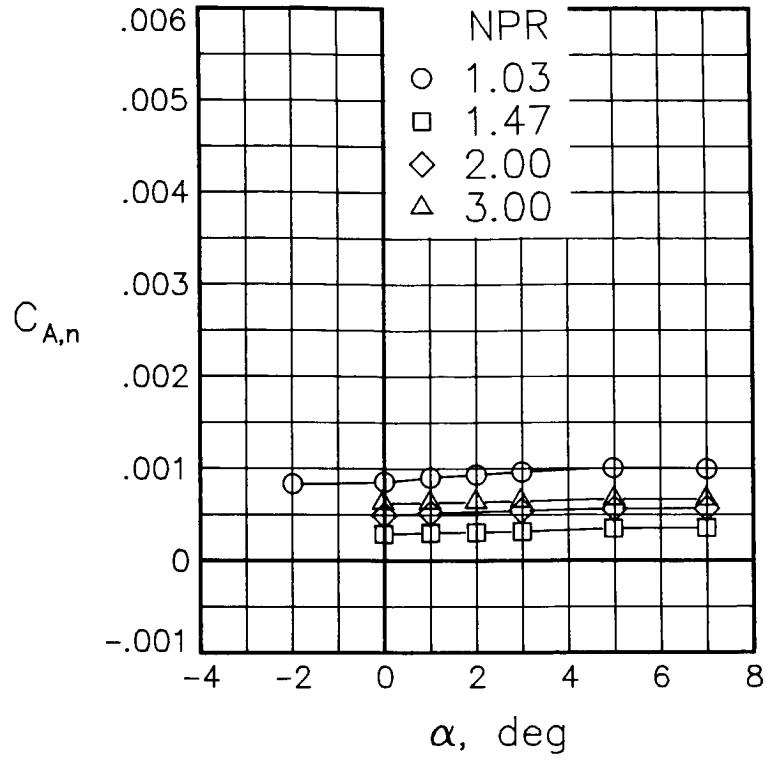

(a) M = 0.60.

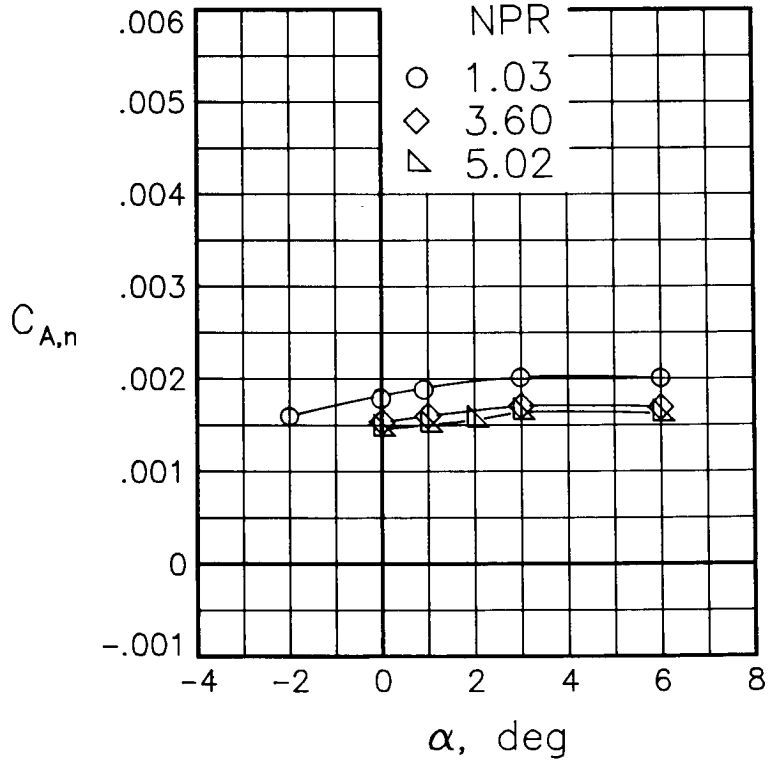

(b) M = 0.90.

Figure 94.- Integrated axial-force coefficient for the left-hand nozzle of the model with all fuselage modifications except nose boom. β_n = 18.45°.

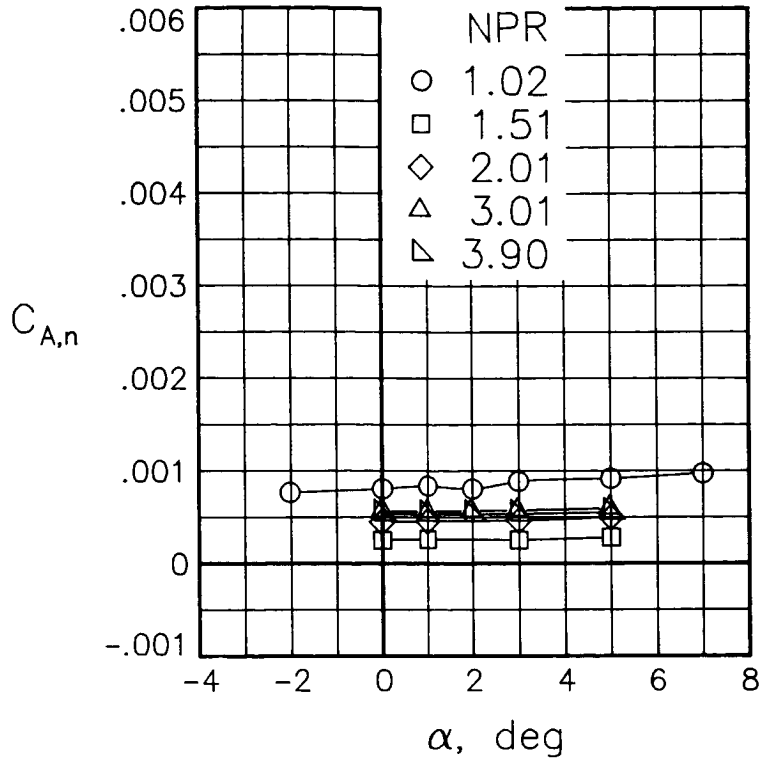

(a) M = 0.60.

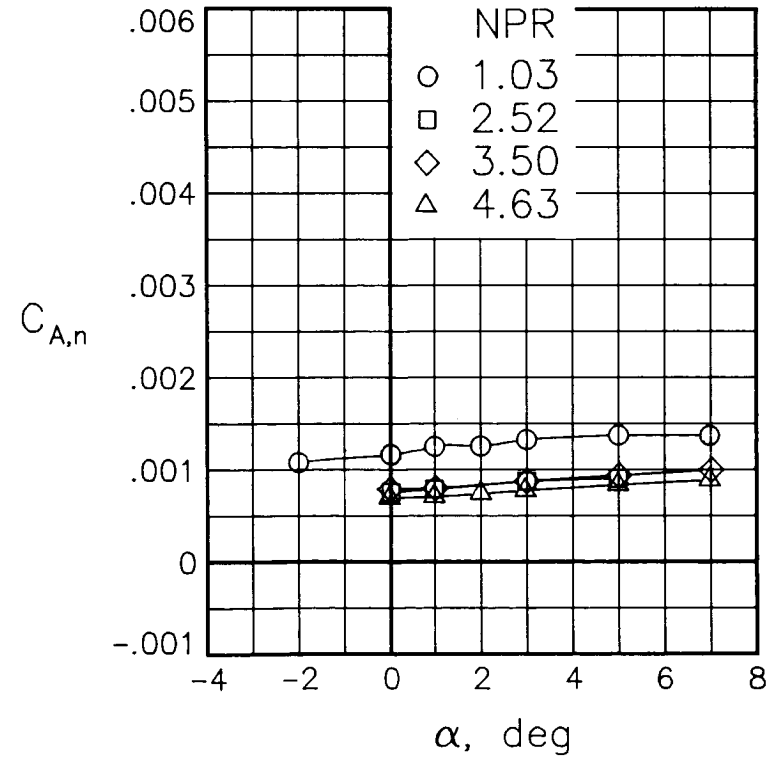

(b) M = 0.80.

Figure 95.- Integrated axial-force coefficient for the left-hand nozzle of the model with nose boom, actuator fairings, A/B vents, and nozzle steps (no rakes). β_n = 18.45°.

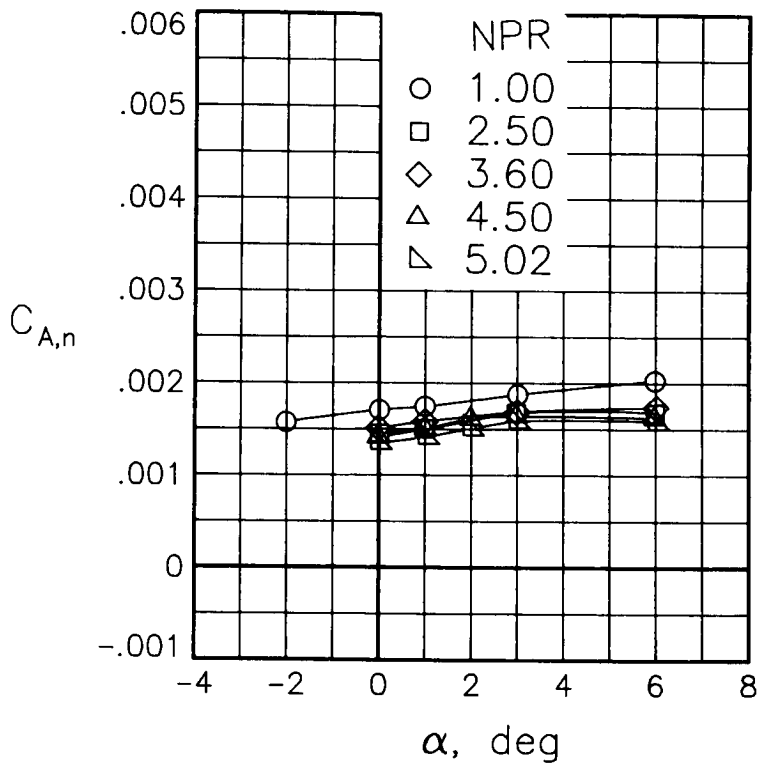

(c) M = 0.90.

Figure 95.- Concluded.

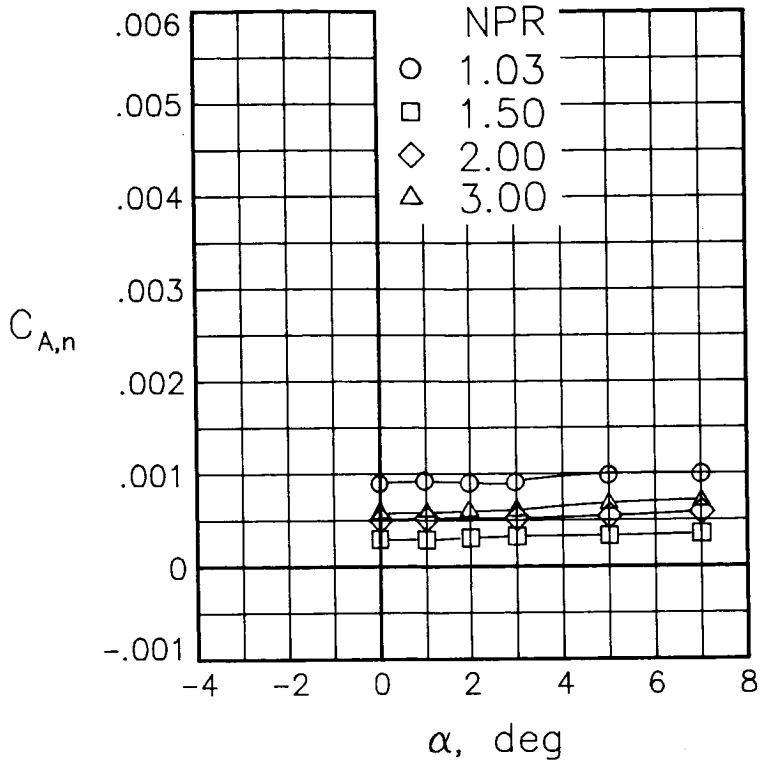

(a) M = 0.60.

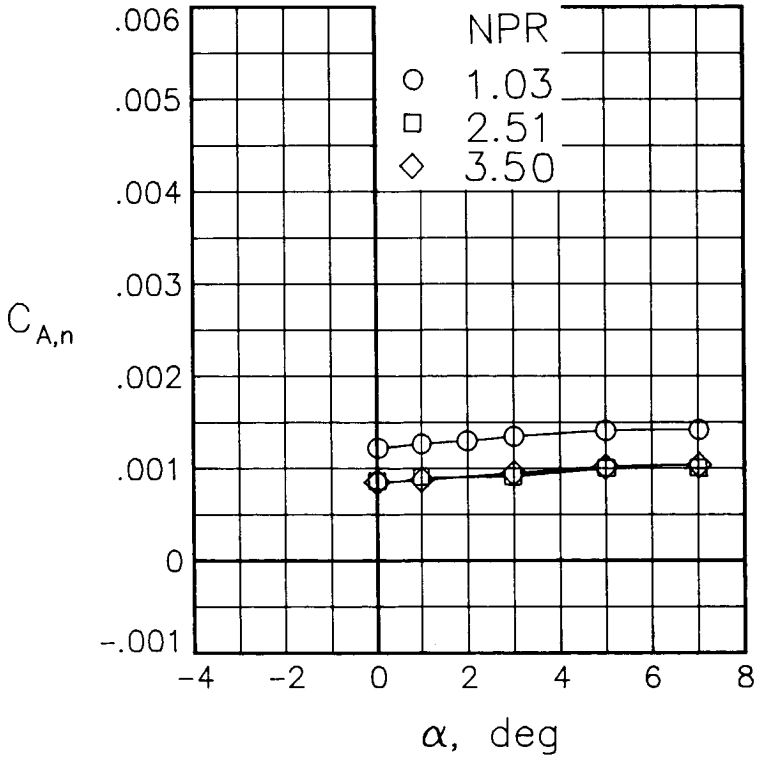

(b) M = 0.80.

Figure 96.- Integrated axial-force coefficient for the left-hand nozzle of the model with nose boom, actuator fairings, A/B vents, and nozzle steps (no rakes). β_n = 18.45°; δ_h = -2°.

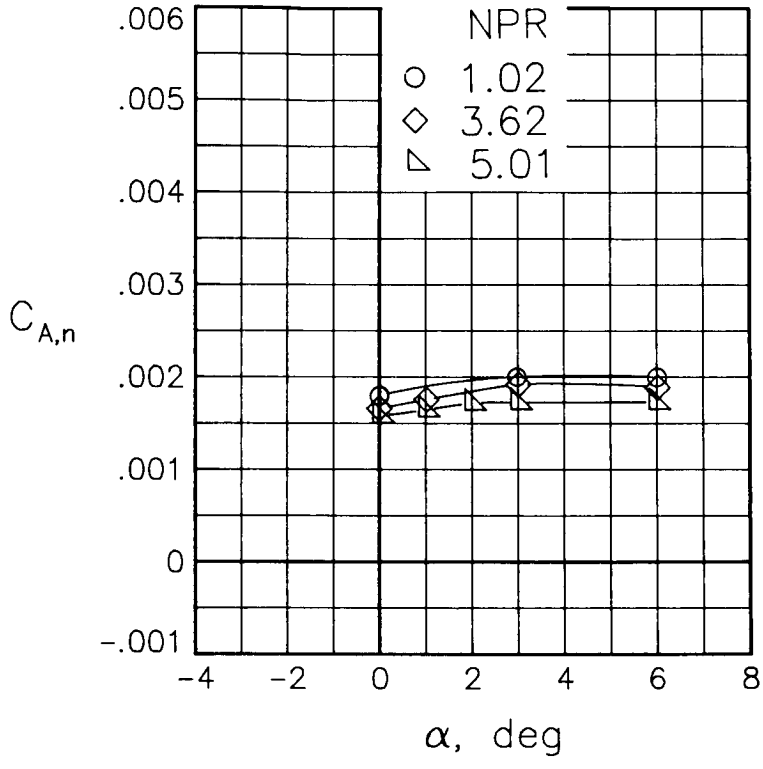

(c) M = 0.90.

Figure 96.- Concluded.

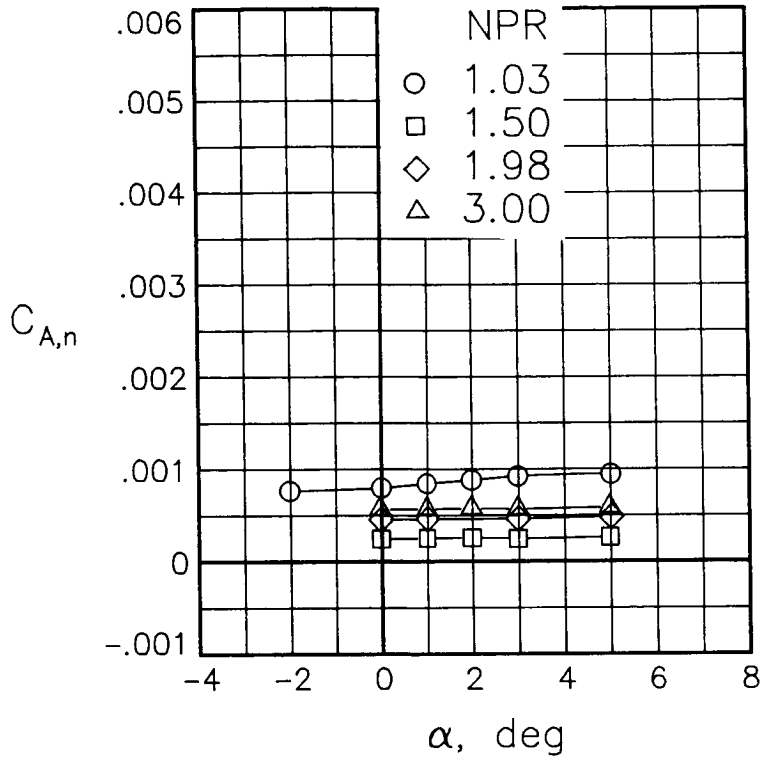

(a) M = 0.60.

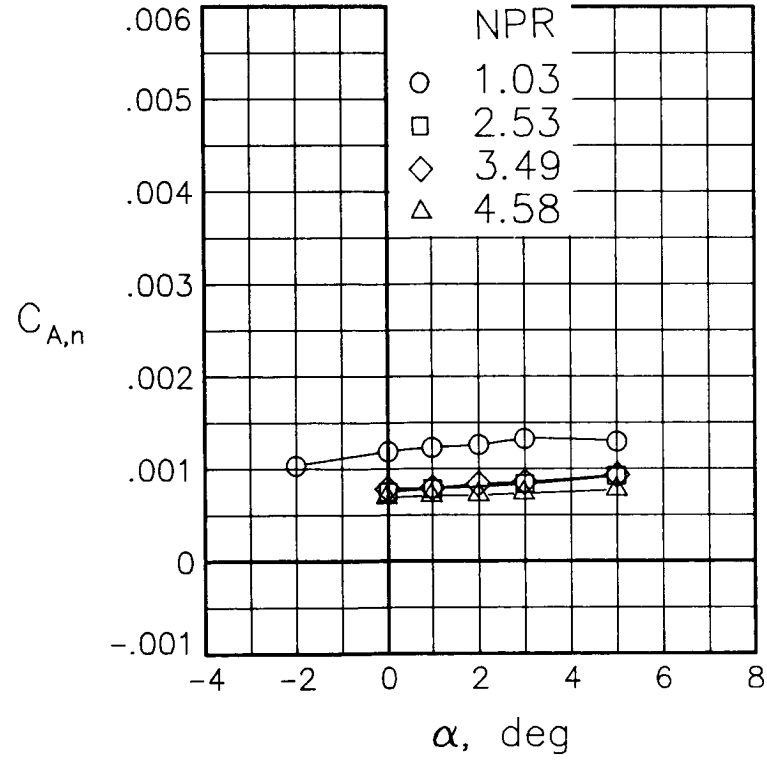

(b) M = 0.80.

Figure 97.- Integrated axial-force coefficient for the left-hand nozzle of the model with all fuselage modifications. β_n = 18.45°.

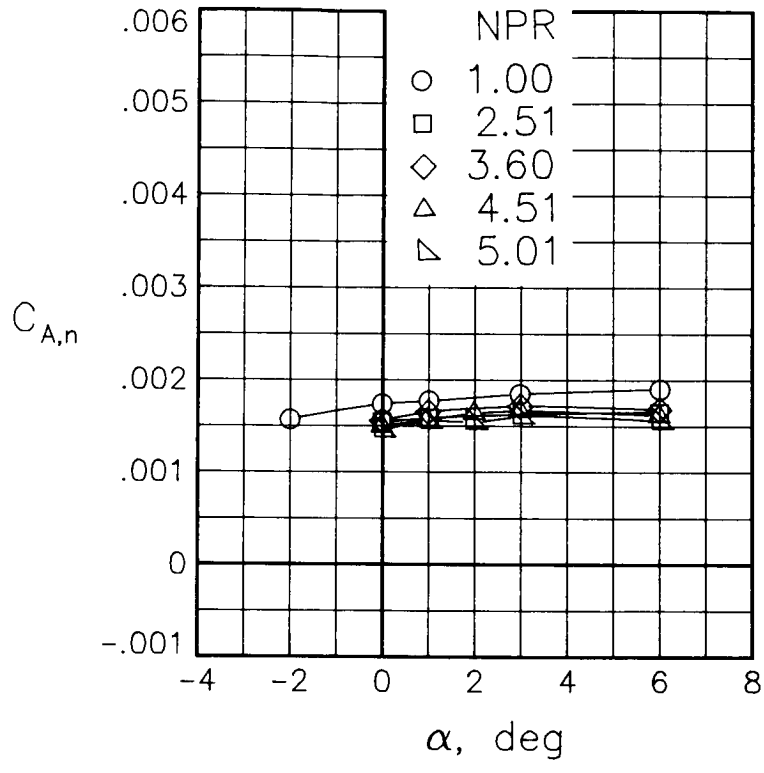

(c) M = 0.90.

Figure 97.- Concluded.

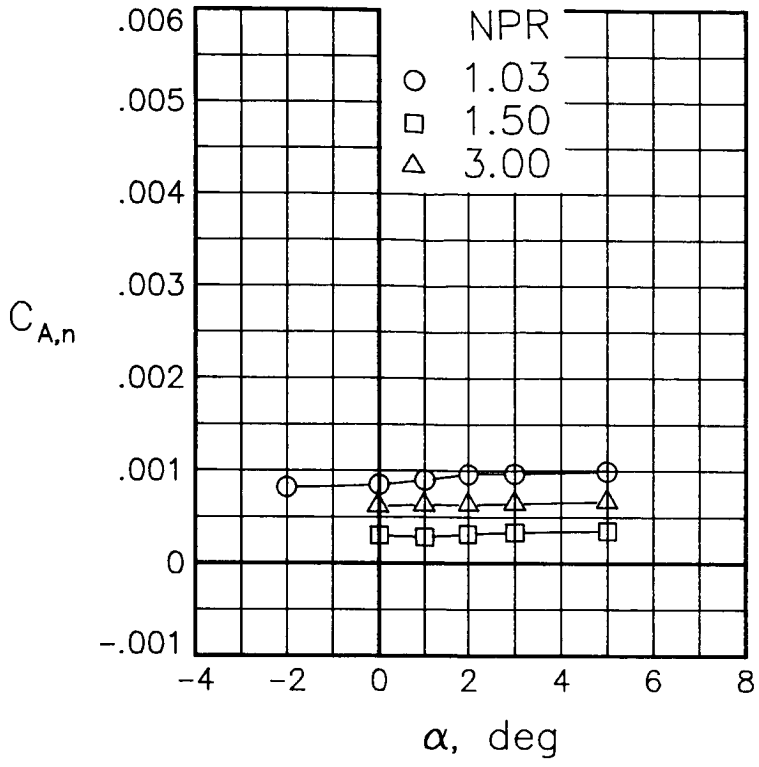

(a) M = 0.60.

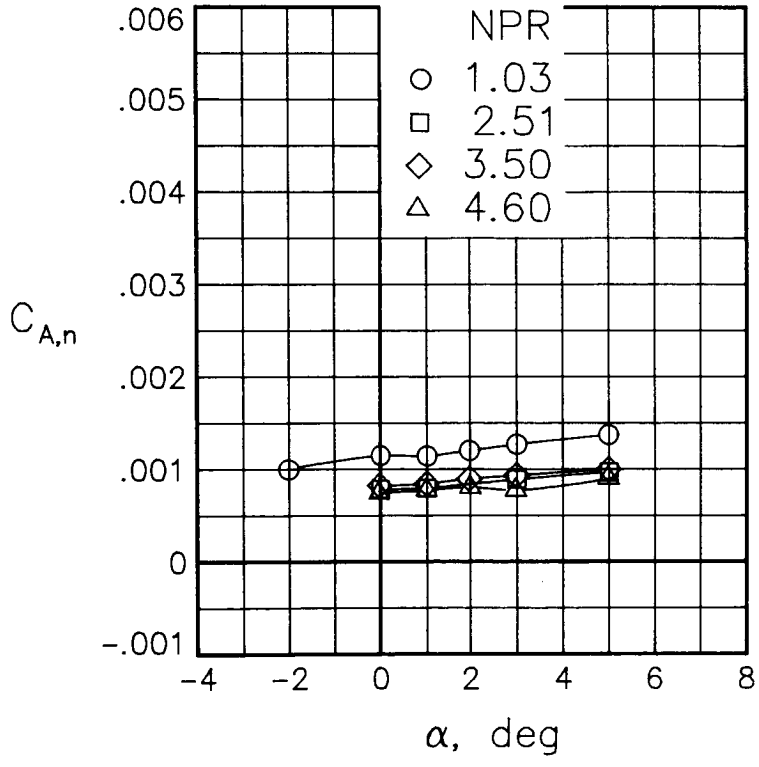

(b) M = 0.80.

Figure 98.- Integrated axial-force coefficient for the left-hand nozzle of the model with fuselage modifications. β_n = 18.45°. Repeat data.

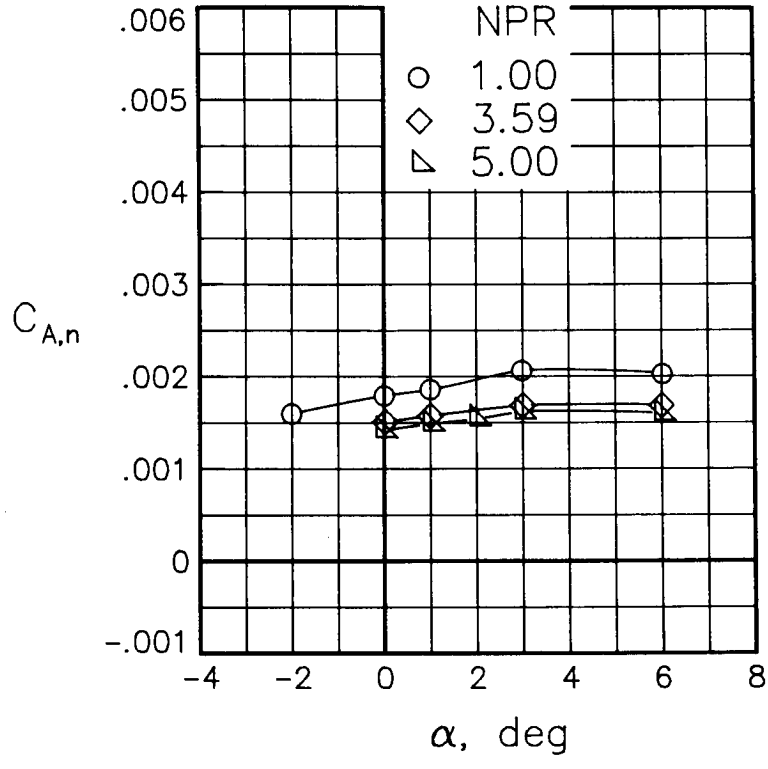

(c) M = 0.90.

Figure 98.- Concluded.

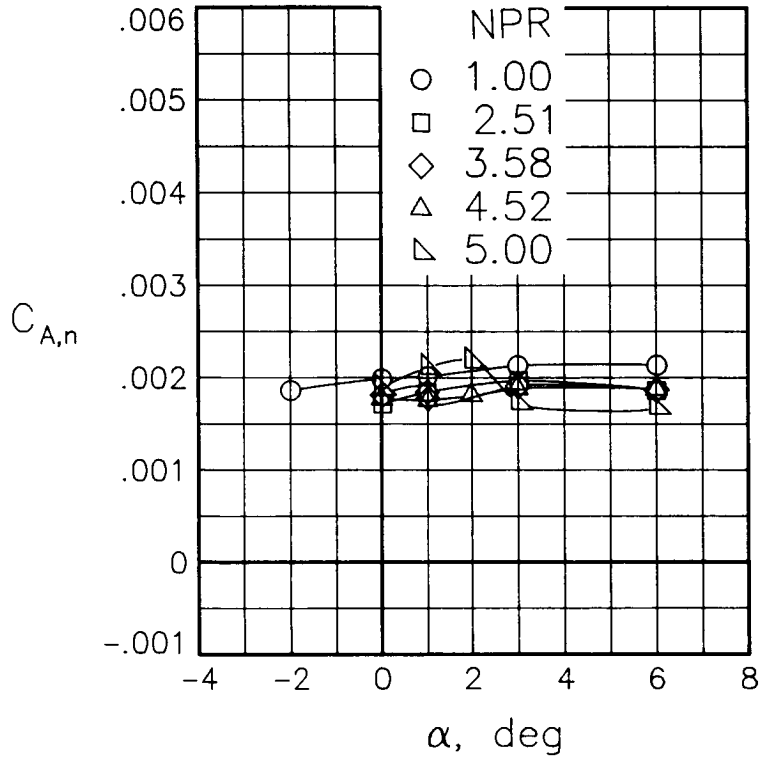

Figure 99.- Integrated axial-force coefficient at M = 0.90 for the left-hand nozzle of the model with all fuselage modifications. β_L = 18.45°; β_R = 15.05°; δ_h = -5°.

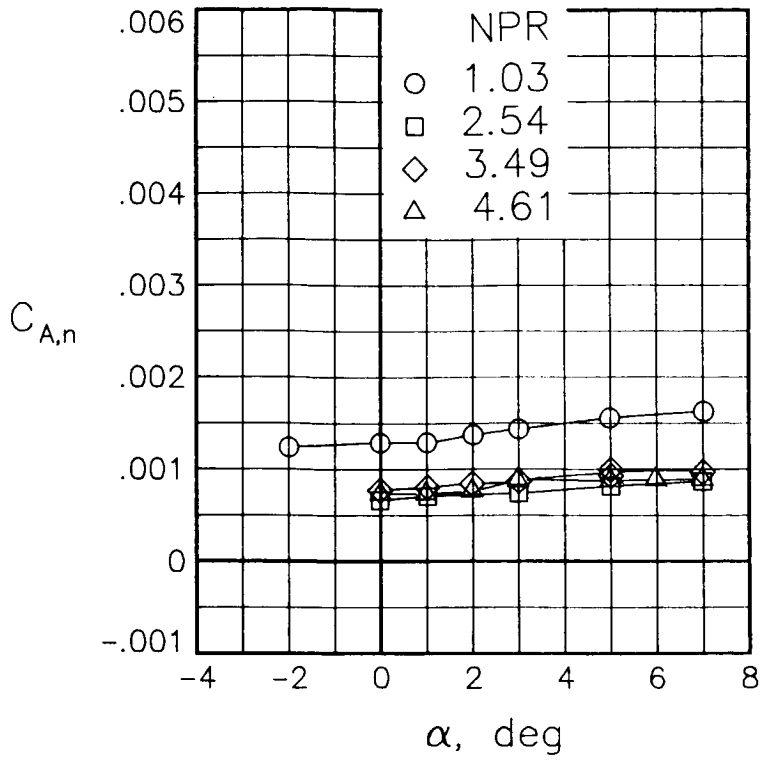

(a) M = 0.80.

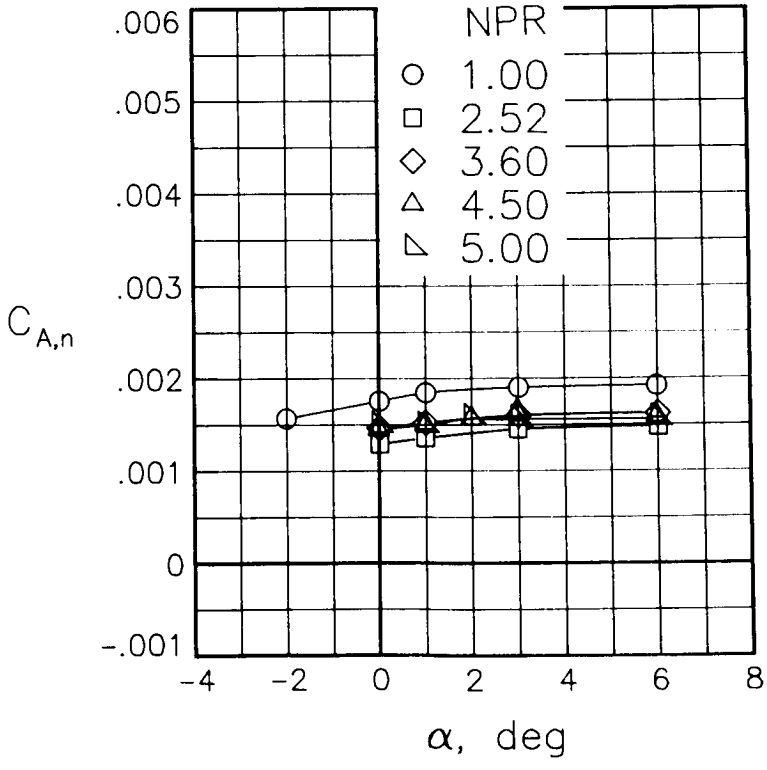

(b) M = 0.90.

Figure 100.- Integrated axial-force coefficient for the left-hand nozzle of the model with all fuselage modifications. β_L = 18.45°; β_R = 9.63°; δ_h = -2°.

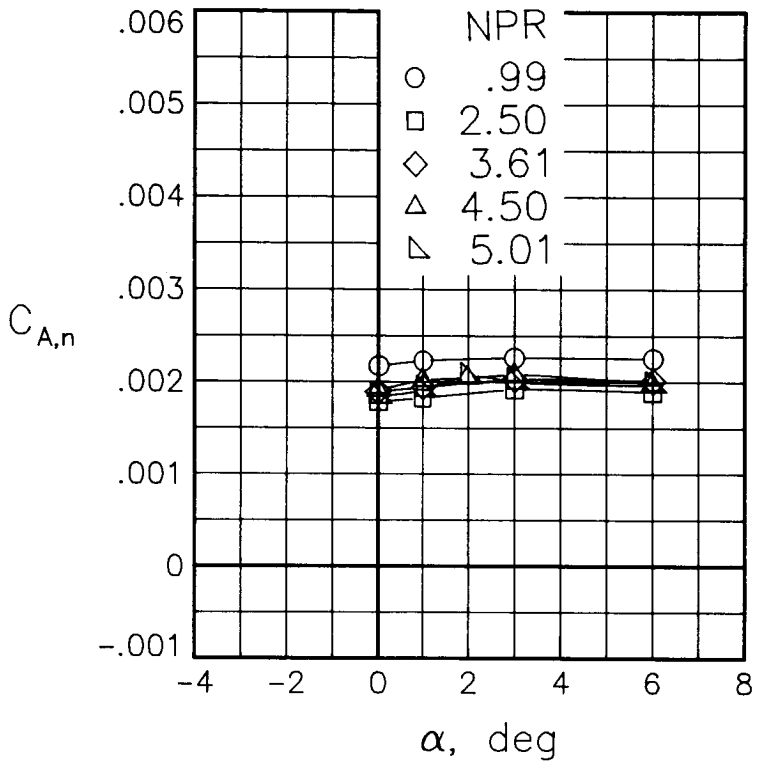

Figure 101.- Integrated axial-force coefficient at M = 0.90 for the left-hand nozzle of the model with all fuselage modifications. β_L = 18.45°; β_R = 7.72°; δ_h = -4°.

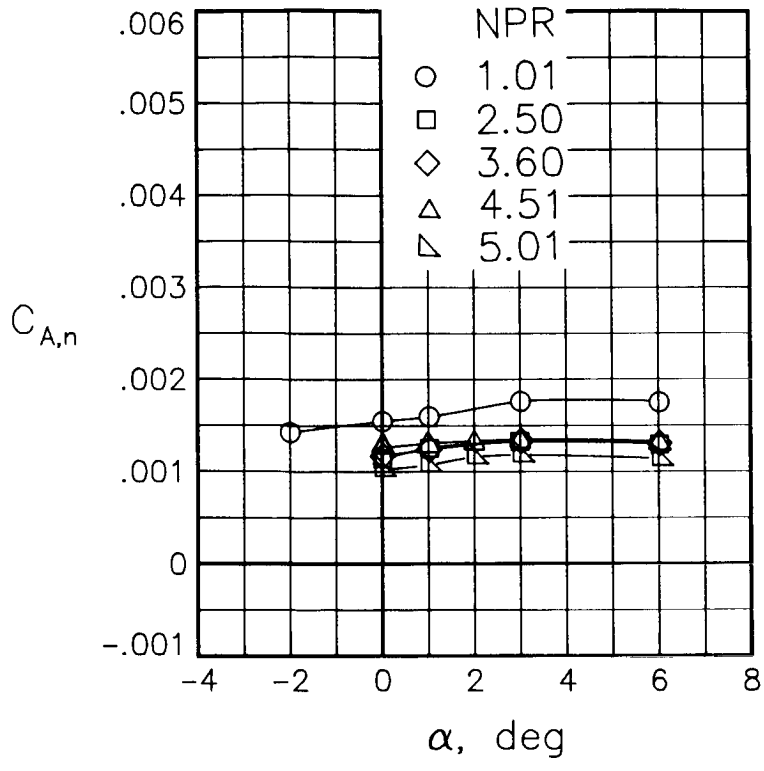

(a) M = 0.90.

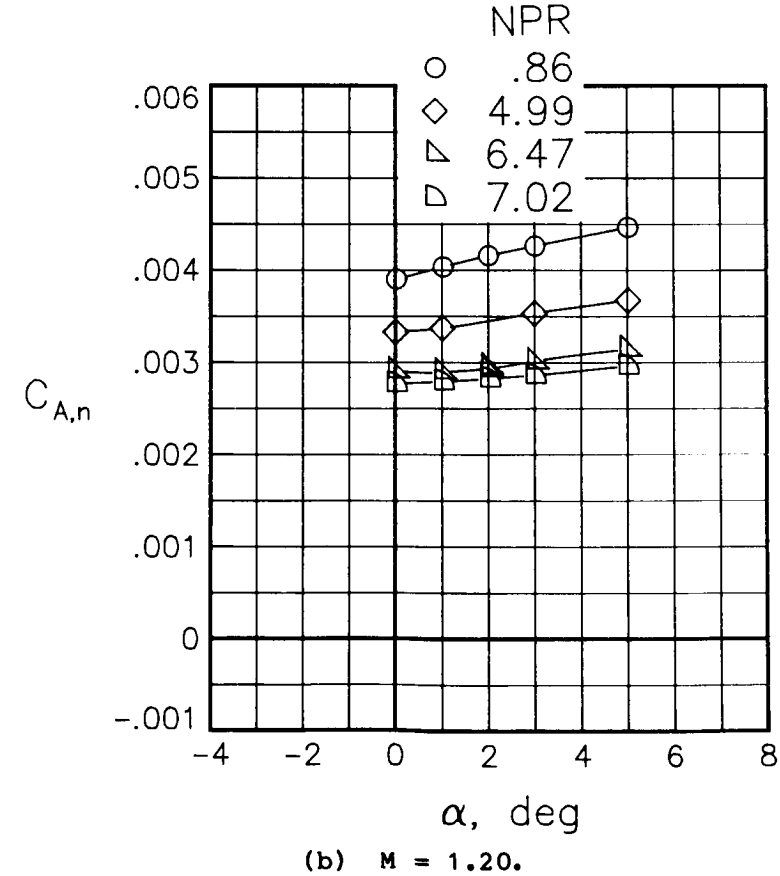

(b) M = 1.20.

Figure 102.- Integrated axial-force coefficient for the left-hand nozzle of the model with all fuselage modifications. β_n = 15.05°.

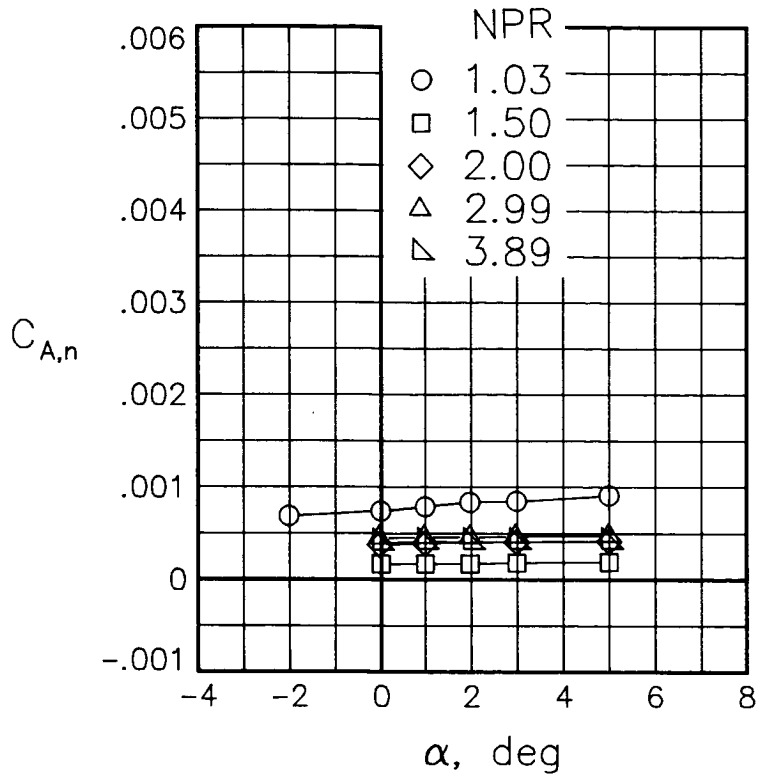

(a) M = 0.60.

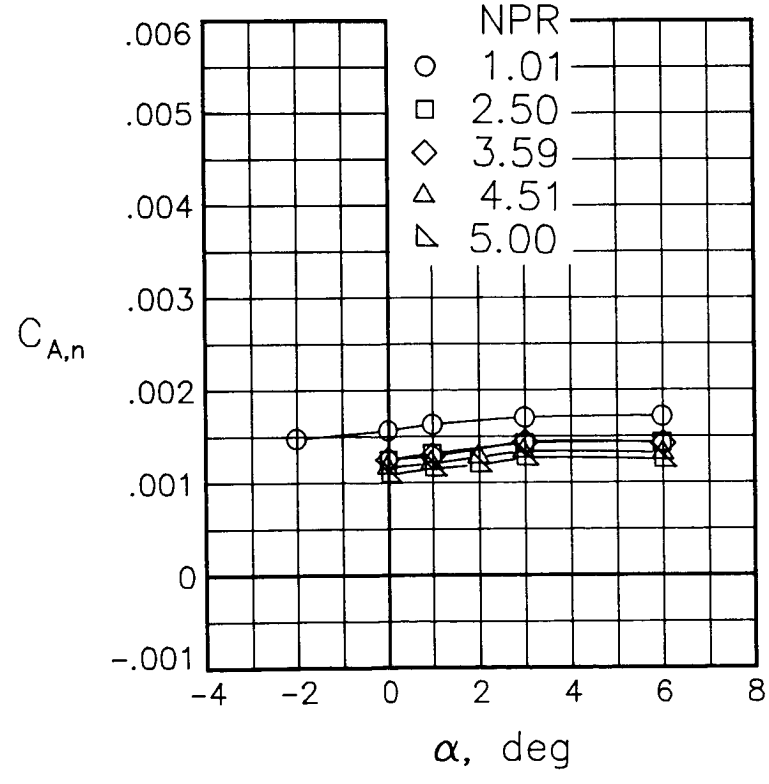

(b) M = 0.90.

Figure 103.- Integrated axial-force coefficient for the left-hand nozzle of the model with all fuselage modifications. β_L = 15.05°; β_R = 18.45°.

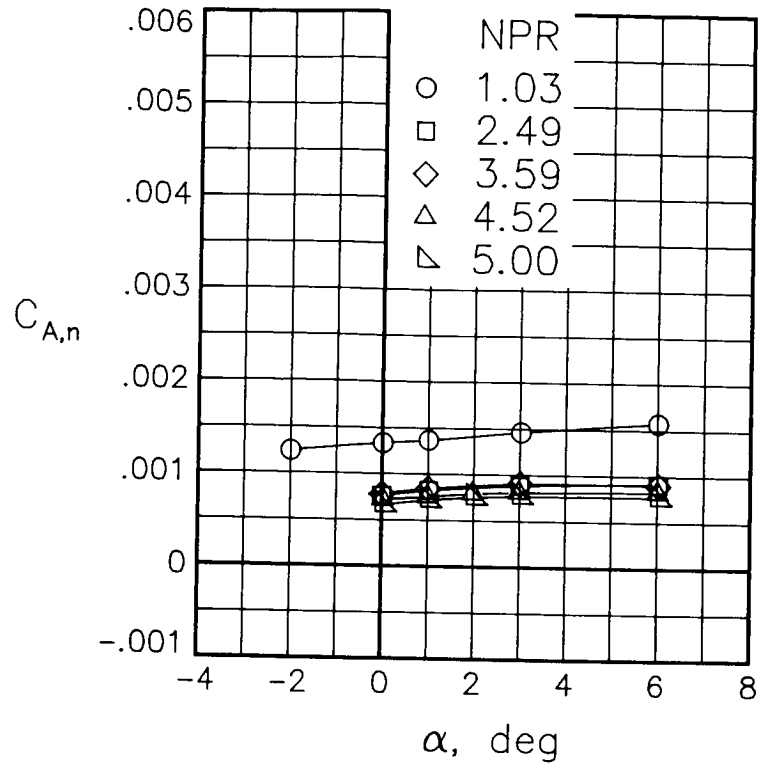

(a) M = 0.90.

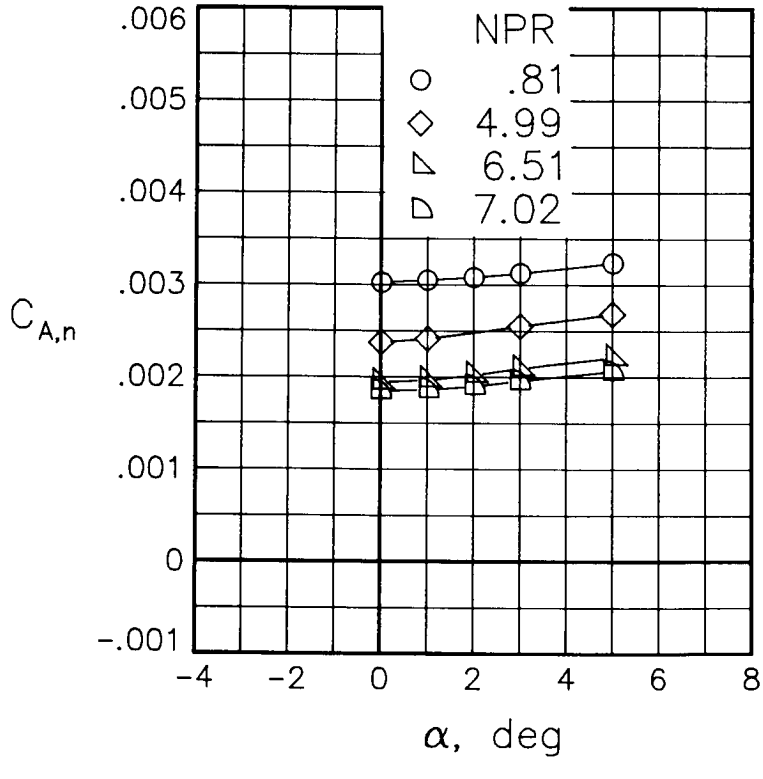

(b) M = 1.20.

Figure 104.- Integrated axial-force coefficient for the left-hand nozzle of the model with all fuselage modifications. β_n = 9.63°.

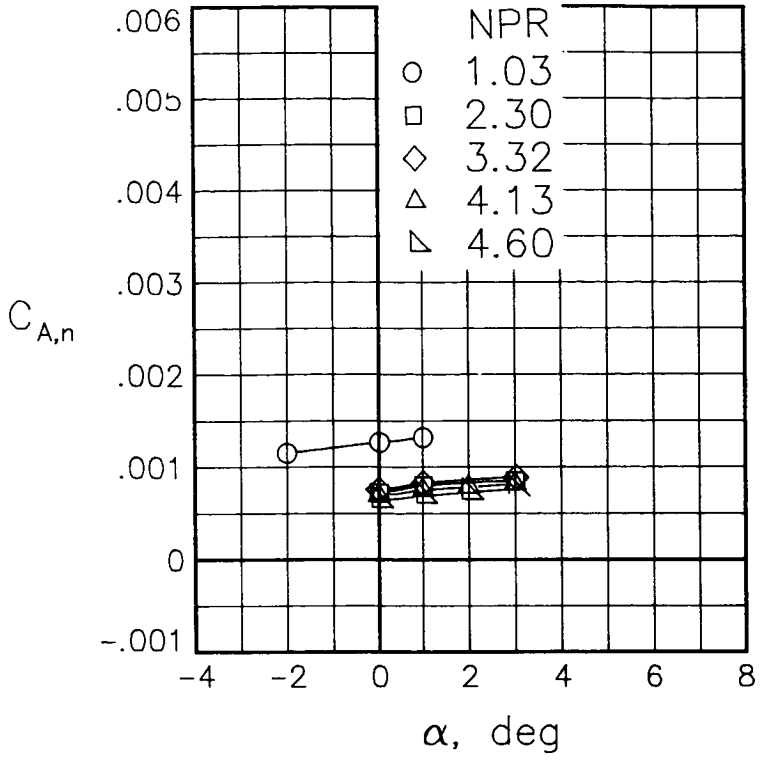

(a) M = 0.90.

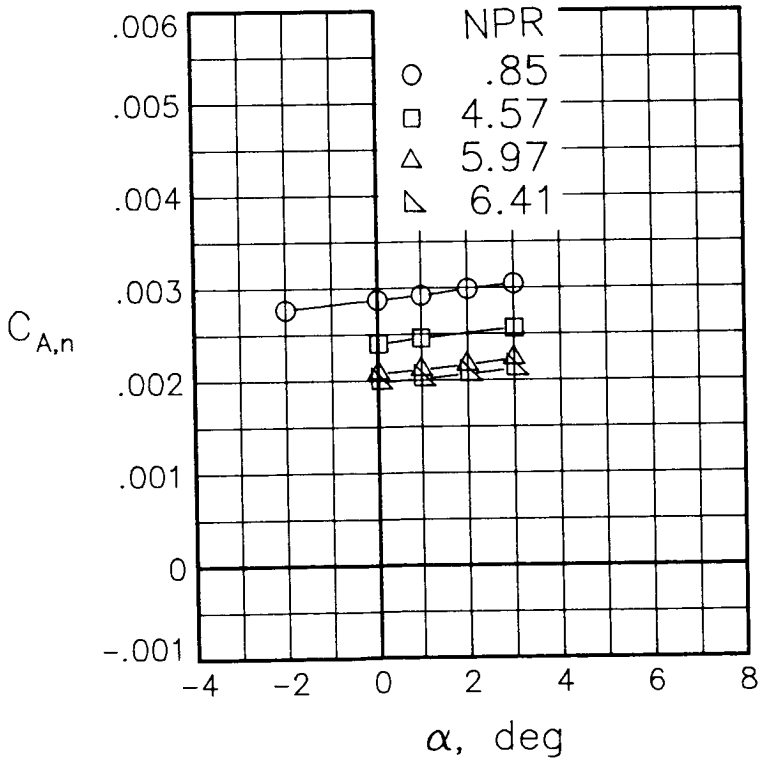

(b) M = 1.20.

Figure 105.- Integrated axial-force coefficient for the left-hand nozzle of the model with all fuselage modifications. β_L = 9.63°; β_R = 15.05°; δ_h = 2.5°.

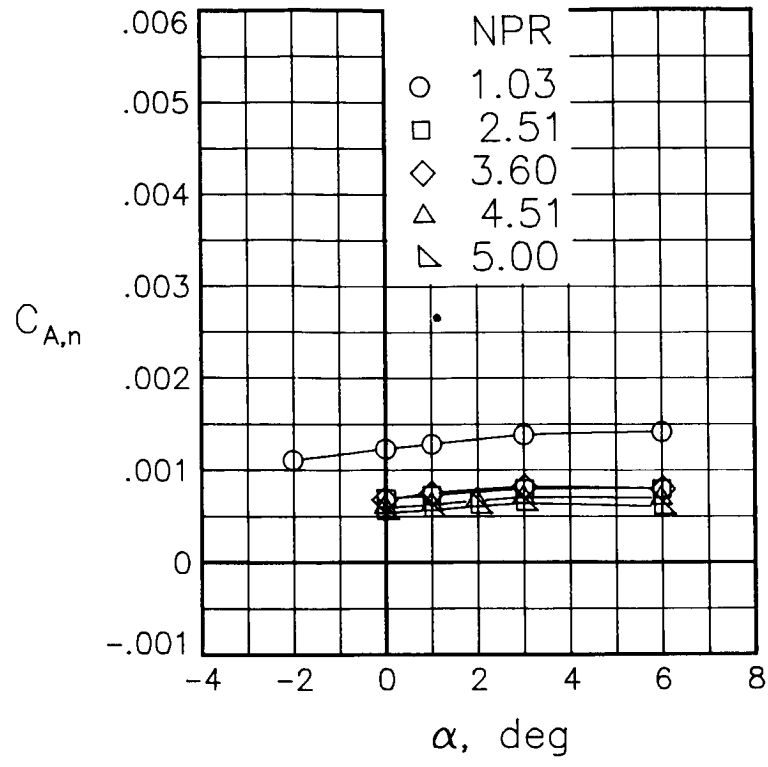

(a) M = 0.90.

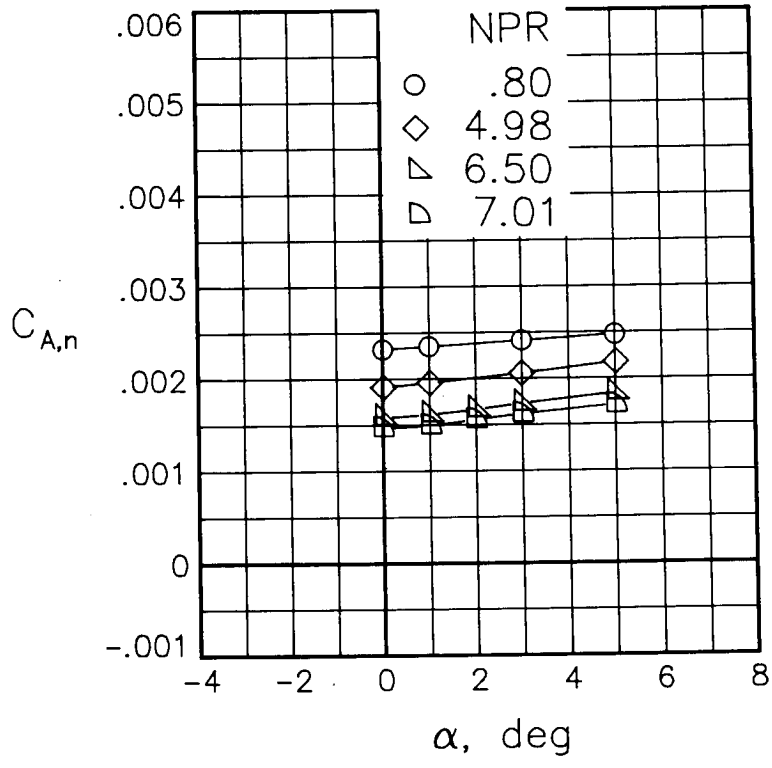

Figure 106.- Integrated axial-force coefficient for the left-hand nozzle of the model with all fuselage modifications. β_n = 7.72°.

☆U.S. GOVERNMENT PRINTING OFFICE:1984 -739 -010/ 17 REGION NO. 4

1. Report No.	2. Government Accession No.	3. Recipient's Catalog No.
NASA TP-2333		

4. Title and Subtitle	5. Report Date
FUSELAGE AND NOZZLE PRESSURE DISTRIBUTIONS OF A 1/12-SCALE F-15 PROPULSION MODEL AT TRANSONIC SPEEDS - EFFECT OF FUSELAGE MODIFICATIONS AND NOZZLE VARIABLES	August 1984
	6. Performing Organization Code: 505-43-90-07

7. Author(s)	8. Performing Organization Report No.
Odis C. Pendergraft, Jr., and George T. Carson, Jr.	L-15755
	10. Work Unit No.

9. Performing Organization Name and Address	11. Contract or Grant No.
NASA Langley Research Center Hampton, VA 23665	
	13. Type of Report and Period Covered: Technical Paper

12. Sponsoring Agency Name and Address	14. Sponsoring Agency Code
National Aeronautics and Space Administration Washington, DC 20546	

15. Supplementary Notes

16. Abstract

Static-pressure-coefficient distributions on the forebody, afterbody, and nozzles of a 1/12-scale F-15 propulsion model have been determined in the Langley 16-Foot Transonic Tunnel for Mach numbers from 0.60 to 1.20, angles of attack from -2° to 7°, and ratio of jet total pressure to free-stream static pressure from 1 (jet off) up to about 7, depending on Mach number. The effects of nozzle geometry (both symmetric and asymmetric) and horizontal-tail deflection on the pressure distributions were investigated. Boundary-layer total-pressure profiles were also determined at two locations ahead of the nozzles on the top nacelle surface. Reynolds number varied from about 1.0×10^7 to 1.3×10^7 per meter, depending on Mach number.

17. Key Words (Suggested by Author(s))	18. Distribution Statement
Fuselage modification effects Nozzle afterbody flow field Nozzle axial force Fuselage boundary layer Nozzle geometry and power effects	Unclassified - Unlimited Subject Category 02

19. Security Classif. (of this report)	20. Security Classif. (of this page)	21. No. of Pages	22. Price
Unclassified	Unclassified	467	A20

N-305 For sale by the National Technical Information Service, Springfield, Virginia 22161 NASA-Langley, 1984

National Aeronautics and Space Administration

Washington, D.C.
20546

Official Business
Penalty for Private Use, $300

SPECIAL FOURTH CLASS MAIL
BOOK

Postage and Fees Paid
National Aeronautics and
Space Administration
NASA-451

U.S. MAIL

5 2 IU,A, 840720 S00151DS
DEPT OF THE AIR FORCE
ARNOLD ENG DEVELOPMENT [illegible]TER(AFSC)
ATTN: LIBRARY/DOCUMENTS
ARNOLD AF STA TN 37389

NASA

POSTMASTER: If Undeliverable (Section 158 Postal Manual) Do Not Return